The Development of the Lung Metastatic Niche in Murine Breast Cancer



A Thesis Submitted for the Degree of

Doctor of Philosophy

By

Salwa Sulaiman Lin

St Edmund Hall

University of Oxford

Trinity Term 2023

Supervisors:

Professor Adrian L. Harris

Professor Alison H. Banham

Professor Sarah De Val

The Development of the Lung Metastatic Niche in Murine Breast Cancer

Word count:49548

Abstract

Cancer metastasis causes 90% of cancer deaths. Patients with secondary lung metastases often show only modest responses to chemotherapy, immunotherapy, and anti-angiogenic therapy, and can develop resistance. Remodelling of the metastatic niche and the use of alternative, non-angiogenic, vascularisation pathways such as vessel co-option are thought to contribute to resistance to therapies. However, there is only limited knowledge about the molecular mechanism underlying metastatic niche formation, and the expression profile of genes driving tumour vessel co-option is poorly understood. In part, this is due to the paucity of *in vitro* and *in vivo* models that accurately recapitulate the metastatic niche in human cancers. Here, I developed a preclinical E0771 breast cancer (BC) lung metastasis mouse model with which I investigated tumour vessel development and the metastatic niche. First, MRI imaging and histological assessments were used to study vessel growth patterns, suggesting the predominant use of vessel co-option by metastases at an early stage of development, while the induction of angiogenesis was seen during the progression to subpleural metastases. Next, I combined metastatic niche labelling with single-cell RNA sequencing (scRNA-seq) to study the transcriptome of the stroma during metastatic progression. This analysis detected a shift in endothelial cell (EC) subtypes between early and late metastatic timepoints. Interestingly, co-opted capillaries were found to enhance their OXPHOS-related genes and downregulate genes linked to tight junctions, suggesting a hyperpermeability response that may facilitate tumour cell extravasation. Further analysis of this scRNA-seq data also identified cancer-associated mesenchymal cells (CAMCs) in the late metastatic niche, which acted as the primary source of the pro-angiogenic factor VEGFA. Lineage tracing analysis using Wt1-CreERT2;tdTomato reporter mice also examined whether pleural mesothelial cells exhibited pro-metastatic capacity, but suggested that they had little capacity, migrating only underneath the subpleura and few co-expressed CAMC markers. This finding was supported by the scRNA-seq data, which suggested that pleural mesothelial cells partially contribute to the growth of the subpleural metastases but were not the primary origin of the CAMC subtypes. In conclusion, analysis of this preclinical lung metastasis model has enabled me to demonstrate the temporal and spatial heterogeneity present within the metastatic niche and distal cells, and to interrogate the gene expression patterns involved in vessel co-opting and angiogenic metastases. This data could provide important information when selecting vascular drugs to target early vs late metastasis, whilst this extensive transcriptome dataset of lung stromal cells in the metastatic niche and distal regions can provide a basis for further research into the mechanisms involved.

Declaration

I declare that this thesis represents my own work and has not been previously submitted, in whole or in part, for a degree, diploma, any other qualification. Except where stated otherwise by reference or acknowledgment, the work presented is entirely my own. Work previously accepted for submission and collaborator contributions are list below:

- **Figure 1-10:** image adapted with permission from “Vascular patterns in primary and secondary pulmonary tumours in the dog,” by A. M. Jonas, C. B. Carrington, 1969, *The American journal of pathology, 56*(1), 79–95. Copyright Elsevier (1969).
- **MRI imaging and analysis of a murine model of breast cancer lung metastasis**
  Conducted by Dr Sean Smart’s team (Dr. Veerle Kersemans and Dr. Danny Allen), at the Oncology pre-clinical imaging facility at the University of Oxford, Oxford, United Kingdom.
- **Bioinformatic analysis of the scRNA-seq experiment**
  Conducted by three collaborating bioinformaticians: Dr. Thomas Carroll (Ludwig Institute for Cancer Research, Nuffield Department of Medicine, University of Oxford, United Kingdom), Badran Elshenawy (Department of Oncology, University of Oxford, Oxford, United Kingdom), and Dr. Fahad AlMesned (Bioinformatics Section, National Institute of Neurological Disorders and Stroke, National Institutes of Health, Bethesda, MD 20892, USA)
- **Raman spectral measurements of non-tumour and tumour-bearing lung tissue sections**
  In collaboration with Professor. Wei Huang, the work was conducted by Dr. Jiabao Xu, at the Department of Engineering Science at the University of Oxford, Oxford, United Kingdom
- **Generation of the metastatic niche labelling tumour cells**
  In collaboration with Professor. Ilaria Malanchi, her team (Dr. Victoria Bridgeman and Dr. Luigi Ombrato) designed and conducted the transduction of E077t tumour cells with the metastatic niche labelling lentiviral vector at the Francis Crick Institute, London, United Kingdom.

Dedication

I dedicate my dissertation work to my parents for their endless love and encouragement along my journey.

And to my country, Saudi Arabia for giving me this educational opportunity and for their unwavering support.

Acknowledgements

I extend my profound appreciation to Professor Adrian Harris, my primary supervisor, whose unwavering guidance, and thought-provoking discussions were instrumental in inspiring me to think outside the box. Additionally, I would like to express my heartfelt gratitude to Professors Sarah De Val and Alison Banham, my co-supervisors, for their unparalleled support throughout my DPhil journey. Their expertise, insightful recommendations, and meticulous feedback were pivotal in assisting me in completing my thesis.

I am especially indebted to Professor Francesco Pezzella for his invaluable feedback, and the insightful histological evaluation he provided on this work. I am also deeply thankful to Taif University, my funding body whose financial support made this research endeavour possible.

This thesis would not present a comprehensive story without the collaboration of Dr. Sean Smart, Dr. Veerle Kersemans, Dr. Danny Allen (MRI imaging and analysis), Dr. Victoria Bridgeman (from Professor Ilaria Malanchi's laboratory), Dr. Thomas Carroll, Badran Elshenawy (from Professor Francesca Buffa's laboratory), Dr. Fahad Almesned (bioinformatic analysis), Dr. Jiabao Xu (from Professor Wei Huang's laboratory, Raman spectral measurement) and Dr. Andia Redpath (from Professor Nicola Smart’s laboratory, insightful discussions about the *Wt1-CreERT2*; tdTomato reporter murine model).

I would also like to extend my gratitude to my laboratory mentors, Dr. Christos Zois, Dr. Helen Sheldon, and Professor Sarah De Val's team for their practical guidance and valuable advice. Special thanks to Dr. Neil Ashley (scRNA-seq experiment), Dr. Karla Watson, Dr. Jordan Tanner, Roo Bhasin, Douglas Passos, Magdalena Hutchins, Daniel Andrew, Natalie Cowley, and Sara Close (assistance in animal work), Dr. Christoffer Lagerholm and Dr. Rhodri Wilson (Confocal microscopy assistance), and Indrika Ratnayaka (tissue sectioning).

I wish to express my deep appreciation to St Edmund Hall, my college at the University of Oxford, for their annual grant supporting academic-related expenses.

While my DPhil journey undoubtedly involved immense dedication, the surreal experience of studying in Oxford was made more manageable by the support of my friends: Dr. Rita Alonaizan, Raood Ahmad, Sarah Batawi, Esra Sengul, Dr. Raheleh Niavarani, Vinnycius Pereira Almeida, Dr. Berna Bou Tayeh, Dr. Lucija Fleisinger, Mary Strevens, Magda Essa, and Doe Doe Tsang, who looked after me during the COVID-19 pandemic. Special thanks to Dr. Fahad Almesned, Dr. Antonella D'Amore, Dr. Ahmad Salman, Mohammed Salih,

Faisal Alshref, Abeer Alharbi, and Nahla Bakhamis for their prompt responses to my scientific and thesis writing queries at any time I would show up.

Last but foremost, my family played an indispensable role in making my DPhil studies abroad possible, particularly my parents, who provided daily encouragement and stood by me during the challenges of the COVID-19 pandemic. I am forever grateful to my mother (Fatima Kasim) for being my steadfast anchor and always being there when I needed her. Enormous thanks to my father (Sulaiman Lin) for his unwavering support and for accompanying me to many countries to showcase my research, attend workshops, and meet esteemed scientists in the field. Special thanks also go to my sisters (Dalia and Hayat), brothers (Bander and Abdulelah), brother-in-law (Ahmad bin Selim) for their unwavering support. I would like to extend my thanks to my niece (Noor) and nephews (Omar and Yazan) for making my life full of joy and fun.

List of submissions and funding

Publications:

- Lin, S., Carroll, T., Elshenawy, B., Bridgeman, V., Malanchi, I., Banham, A. H., Harris, A. L. (2023). Transcriptome Profiling of Metastatic niche in a Murine Model of Triple-Negative Breast Cancer Lung Metastases. *Molecular oncology, 17*(S1), 1-597. doi:https://doi.org/10.1002/1878-0261.13469 (abstract)
- Sheldon, H., Zhang, W., Bridges, E., Ang, K. H., Lin, S., Masiero, M., Li, D., Handford, P. A., Whiteman, P., Fischer, R., Buffa, F., Vatish, M., Banham, A. H., & Harris, A. L. (2022). ELTD1 is Present in Extracellular Vesicles Derived from Endothelial Cells as a Cleaved Extracellular Domain which Induces In vivo Angiogenesis. *Journal of Extracellular Biology, 1*(8), e52. doi:https://doi.org/10.1002/jex2.52
- Sheldon, H., Alexander, J., Bridges, E., Moreira, L., Reilly, S., Ang, K. H., Wang, D., Lin, S., Haider, S., Banham, A. H., & Harris, A. L. (2021). ELTD1 Activation Induces an Endothelial-EMT Transition to a Myofibroblast Phenotype. *International journal of molecular sciences, 22*(20). doi:10.3390/ijms222011293

Presentations:

- Lin, S., Carroll, T., Badran, B., Bridgeman, V., Malanchi, I., Banham, A. H., & Harris, A. L. Transcriptome Profiling of Metastatic Niche in a Murine Model of Triple-Negative Breast Cancer Lung Metastases. Annual Congress of the European Association for Cancer Research (EACR), Torino, Italy (2023)
- Lin, S., Carroll, T., Badran, B., Bridgeman, V., Malanchi, I., De Val, S., Banham, A. H., & Harris, A. L. Spatial and Temporal Vascular Remodelling in Triple-Negative Breast Cancer Lung Metastases. 22nd International Vascular Biology Meeting (IVBM), Oakland, California, United States of America (2022)
- Lin, S., Carroll, T., Badran, B., AlMesned, F., Bridgeman, V., Malanchi, I., De Val, S., Banham, A. H., & Harris, A. L. Spatial and Temporal Single-cell Transcriptional Analysis of Metastatic Niche Identifies Distinct Cell Populations Enriched in Advanced Lung Metastases. Weatherall Institute of Molecular Medicine (WIMM) Student Presentation Day 2022, WIMM research centre, University of Oxford, Oxford, United Kingdom University of Oxford, Oxford, United Kingdom (2022)
- Lin, S., Bridgeman, V., Malanchi, I., De Val, S., Banham, A. H., Pezzella, F., & Harris, A. L. Investigating the Mechanism of Vascularisation in Lung Metastases. Oncology Annual Student Symposium, University of Oxford, Oxford, United Kingdom (2020)

Posters:

- Lin, S., Carroll, T., AlMesned, F., Bridgeman, V., Ombrato, L., Allen, D., Kersemans, V., Smart, S., Malanchi, I., De Val, S., Banham, A. H., Pezzella, F., & Harris, A. L. Spatial and Temporal Single-Cell Transcriptional Analysis of Metastatic Niche Identifies Distinct Cell Populations. National cancer research institute NCRI, Glasgow, United Kingdom (virtual) (2021)
- Lin, S., Ang, K. H., Sheldon, H., Banham, A. H., & Harris, A. L. The Role of ELTD1 in Angiogenesis. Medical Sciences Division DPhil symposium, University of Oxford, Oxford, United Kingdom (2019)
- Lin, S., Ang, K. H., Sheldon, H., Banham, A. H., & Harris, A. L. The Role of ELTD1 in Angiogenesis and Tumour Metastasis. The Annual Oncology Student Symposium, University of Oxford, Oxford, United Kingdom (2019)

Funding:

- Ministry of Education, Saudi Arabia
- Breast Cancer Research Foundation, United Kingdom

List of Figures

Figure 1-1. Schematic representation of the mechanism of sprouting angiogenesis. In response to VEGF, tip endothelial cells sprout, followed by activated stalk cells forming new blood vessels. EC: endothelial cell; VEGF: vascular endothelial growth factor; VEGFR1/2: vascular endothelial growth factor receptor1/2; DLL4: Delta Like Canonical Notch Ligand 4; ESM1: endothelial Cell Specific Molecule 1; APLN: apelin; JAG1: Jagged1; EFNB2: ephrin B2..... 24

Figure 1-2. Schematic representation of the mechanism of intussusceptive angiogenesis (IA). Hypoxia and macrophages induce IA formation (A). Endothelial cells protrude towards the vessel lumen, followed by the formation of a vascular wall by myofibroblasts, pericytes, and collagen deposition (B), leading to the splitting of one blood vessel into two vessels (C). EC: endothelial cell; TIE2: tyrosine protein kinase receptor 2; ANG1: Angiopoietin-1; EPO: erythropoietin; EPOR: erythropoietin receptor. 27

Figure 1-3. Schematic representation of the mechanism of vasculogenesis. Endothelial progenitor cells (EPCs) are mobilised from bone marrow to blood circulation with sKitL support (soluble KitL). Then, the receptor for advanced glycation end products (RAGE) and Toll-like receptor 2 (TLR2)-expressing endothelial cells (ECs) migrate and adhere to the tumour to form blood vessels through interacting with high-mobility group box 1 (HMGB1). VEGF: vascular endothelial growth factor; TIE2: tyrosine-protein kinase receptor 2; mKitL: membrane-bound KitL; MMP: matrix metallopeptidase. 29

Figure 1-4. Schematic representation of the mechanism of vasculogenic mimicry (VM). Cancer cells with an epithelial–mesenchymal transition (EMT) phenotype can form vessel-like structures. C-X-C chemokine receptor type (CXCR1)-expressing endothelial cells (ECs) attract Interleukin 8 (IL-8)-secreting cancer cells and cancer-associated fibroblasts (CAFs) secrete stromal cell-derived factor 1 (SDF-1) and Transforming growth factor beta (TGFβ) to aid in the formation of VM tubes. Macrophages also aid VM formation through overexpression of cyclooxygenase-2 (COX-2). 31

Figure 1-5. Schematic diagram of pulmonary alveoli along with lung capillaries. Each alveolus contains type I and type II pneumocytes, surfactant fluid, and alveolar macrophages. Some neighbouring alveoli are connected by pores of Kohn. The interstitial space is the area between the alveoli and the capillaries that contain matrices such as collagen, elastic fibres, fibronectin and fibroblasts. The enlarged inset illustrates the basement membranes of the epithelium and the capillary. 35

Figure 1-6. Schematic representation of different histological growth patterns adopted by lung cancer. A: angiogenic growth pattern identified by chaotic and disorganised blood vessels; B: alveolar growth pattern, cancer cells fill the alveoli; C: cuffing growth pattern, cancer cells grow around big blood vessels; D: interstitial growth pattern, where cancer cells grow in lung interstitium (in between the alveoli and capillaries) 36

Figure 1-7. Schematic representation of signalling molecules involved in vessel co-option by cancer in the lung. Overexpression of protease serine 15 (PRSS15) seems to enhance cancer cells' metabolic respiration, aiding in their perivascular invasion. Intrinsic invasive phenotype of cancer cells and matrix-remodelling macrophages found as cellular players contributing to vessel co-option in a preclinical metastatic lung model. Note that the localisation of the overexpressed signalling molecules, whether surface, cytoplasmic, or nuclear expression, as indicated in this diagram. CTSD: cathepsin D; MMP19: Matrix metallopeptidase 19; ANPEP: alanyl aminopeptidase; CA9: carbonic anhydrase 9; PHD3: prolyl hydroxylase dehydrogenase 3; SERPING1: serine proteinase inhibitor (serpin) family G member 1; SPARC: secreted protein acidic and cysteine-rich; GST: glutathione S-transferase; TRAP1: TNF receptor-associated protein1; NCAM: neural cell adhesion molecule; EPHB2: ephrin type-B2 receptor; EPHB3: ephrin type-B3 receptor; VEGF: vascular endothelial growth factor; TIE2: tyrosine-protein kinase receptor 2; ANG2: Angiopoietin-2. 39

Figure 1-8. Schematic representation of signalling molecules involved in vessel co-option by cancer in the liver. Cancer cells invading the pre-existing blood vessels in the liver are characterised by an overexpression of actin-related protein 2 and 3 complex (ARP2/3). Note that the localisation of the overexpressed signalling molecules, whether surface, cytoplasmic, or nuclear expression, as indicated in this diagram. EFHD2: EF-hand domain family member D2; ATP1A1: ATPase Na+/K+ transporting subunit alpha 1; S100A10: S100 calcium binding protein A10; TIMP1: TIMP1 TIMP metallopeptidase inhibitor 1; ALDH1B1: aldehyde dehydrogenase 1 family member B1; ACTB: actin beta; RUNX1: runt related transcription factor-1; ANG1: angiopoietin-1; THBS1: thrombospondin-1; TGFβ1: transforming growth factor beta 1. 41
Figure 1-9. Schematic representation of signalling molecules involved in vessel co-option by cancer in the brain. Glioma cells co-opting pre-existed blood vessels in the brain have an overexpression of EFNB2, WNT, (SPARC), (PI3K). In contrast, co-opted endothelium upregulates glucose transporter 1 (GLUT-1) and phosphoglycolate phosphatase (PGP). It also overexpresses stromal cell-derived factor 1 (SDF-1) and bradykinin (BK) that attract glioma cells by interacting with their receptors, C-X-C chemokine receptor type 4 (CXCR4) and bradykinin 2 receptor (B2R), respectively. ... 46
Figure 1-10. An arterial anastomosis formed (black arrow) within a lung tumour lesion connecting the bronchial artery to the pulmonary artery. ba: an abbreviation for bronchial artery; pa: an abbreviation for pulmonary artery “adapted from “Vascular patterns in primary and secondary pulmonary tumours in the dog,” by A. M. Jonas, C. B. Carrington, 1969, The American journal of pathology, 56(1), 79–95. Copyright Elsevier (1969). 56
Figure 2-1. Validation of successful transduction of E0771 cells with tdTomato-encoding lentiviral vector. A: High transfection efficiency of tdTomato-transfected E0771 tumour cells visualised by imaging tdTomato expression using an inverted fluorescent microscope; B: gating of population of interest using SSC vs FCS density plot; C: gating of singlets and excluding doublets by plotting FSC-H vs FSC-A; D: the strongly tdTomato-positive cells (shown with dark blue box) were FACS-sorted and expanded for in vitro studies. 63
Figure 2-2. Schematic map of lentiviral plasmid vector containing the two cassettes that are co-expressed under mouse PGK promoter including human CD2 (hCD2) and mCherry protein fused to a lipid-soluble tag (sLP-mCherry). Once this construct is transduced into a specific cell line, it can secrete mCherry labelling neighbouring cells. 65
Figure 2-3. All cell lines were free of mycoplasma. The purple box is a copy from the kit that illustrates how to interpret the readings measured using OPTIMA microplate reader (Manufacturer: BMG LABTECH, Model: BMG FLUOstar). 66
Figure 2-4. A confluent layer of primary pleural mesothelial cells characterised by their cobblestone morphology. These cells were collected from 3 mice about 6 months old and reached confluency on day 6. The image was acquired at 10x magnification. 67
Figure 2-5. Representative diagram of transwell proliferation assay. A: depicts control wells, which contain parental E0771 tumour cells in the inserts and no mesothelial cells in the lower compartment and experimental wells, which contain parental E0771 tumour cells in the inserts and pulmonary mesothelial monolayer in the lower compartment; B: depicts cell densities of parental E0771 tumour cells that were seeded in a 96-well plate for generating a reference standard curve. 69
Figure 2-6. Representative diagram of transwell invasion assay. Green box: depicts control wells which contain tdTomato E0771 tumour cells on top of collagen I (invasion barrier) in inserts and no mesothelial cells in the lower compartment; Experimental wells which contain tdTomato E0771 tumour cells on top of collagen I (invasion barrier) in inserts and pulmonary mesothelial monolayer in the lower compartment. 71
Figure 2-7. Diagram illustrating inducible induction of tdTomato reporter expression in Wt1-expressing pleural mesothelial cells in Wt1-CreERT2:tdTomato reporter

mice. Wt1-CreERT2$^{Cre/+}$;tdTomato$^{td/td}$ male mouse crossed with wild type female mouse yielded 50% Cre+ and 50% Cre- progeny. Tamoxifen administration induces tdTomato labelling of Wt1-expressing cells in 50% of offspring expressing Cre recombinase under Wt1(mesothelial marker)-specific promotor. Upon oral gavage of tamoxifen to this model, tamoxifen will bind to its binding domain of oestrogen receptor (ER), causing translocation of Cre recombinase from the cytoplasm into the nucleus, where recombination (excision) of loxP-flanked stop sequence then occurs inducing tdTomato expression. This transgenic line contains Cre sequence under the promoter of a mesothelial marker, Wt1 gene, allowing spatiotemporal Cre-recombination and tdTomato reporter expression to occur only in pleural mesothelial cells. 74
Figure 3-1. E0771 tumour burden in H&E-stained lung sections of three groups of mice sacrificed at different time points following tumour injection. A: 14 days post tumour injection of 5x10^5, tumour cells started to colonize the lungs; B: 25 days post tumour injection of 5x10^5, tumour cells colonized the lungs forming visible metastases, C: 13 days following injection of 1x10^6 cells. 101
Figure 3-2. High transfection efficiency of EGFP-LUC labelled E0771 tumour cells visualized by imaging EGFP expression using an inverted fluorescent microscope...... 102
Figure 3-3. FACS sorting for strongly positive EGFP-LUC labelled E0771 cells. E0771 cells transduced with EGFP-LUC lentivirus were FACs-sorted based on their EGFP expression levels. A: gating of population of interest using SSC vs FCS density plot; B: gating of singlets and excluding doublets by plotting FSC-H vs FSC-A. The strongly EGFP-positive cells (shown with green box) were collected and expanded for in vivo studies. 102
Figure 3-4. Measurement of luminescence showed that EGFP-LUC co-expressing E0771 cells has high luciferase activity compared to the positive control (LUC-infected GL261). RLU: relative luminescence unit (n=1). 103
Figure 3-5. Transduction of E0771 tumour cells with EGFP-Luc-containing FULGW lentiviral vector does not affect the proliferation ability of these cells compared to the parental E0771 cells. Each data set represents the mean ± standard error of the mean (SEM) of three biological replicates (Statistical analysis was performed using the two-tailed unpaired Student's t-test). 103
Figure 3-6. H&E staining of metastatic lung tissue sections revealed the development of parenchymal micrometastases at an early timepoint and subpleural and parenchymal metastases at a late timepoint. 1x10^6 E0771 breast tumour cells were injected intravenously into WT C57BL/6 mice at 6 weeks of age. Metastatic lungs were harvested on day 8 and day 13 following tumour injection. 104
Figure 3-7. E0771 TNBC cells extravasate from lung blood vessels and grow in the intra-alveolar spaces and along visceral pleura. These E0771 tumour-bearing lungs were immunohistochemically stained with the proliferation marker, Ki67 to visualize tumour cells. Arrows: depicts blood vessels; arrowhead: depicts visceral pleura..... 105
Figure 3-8. EGFP-LUC lentiviral-transduced E0771 TNBC cells growing in lung parenchyma as a micrometastases near a blood vessel (yellow arrows). TTF1: thyroid transcription factor 1 which labelled type II pneumocytes; LUC-E0771: are E0771 that were transduced with lentivirus encoding firefly luciferase (LUC) and EGFP demarcated by dashed line. 105
Figure 3-9. EGFP-LUC lentiviral-transduced E0771 TNBC cells progress via compressing lung parenchyma and expanding toward the lung pleura as subpleural metastases (yellow arrow). TTF1: thyroid transcription factor 1 which labelled type II pneumocytes; LUC-E0771: are E0771 that were transduced with lentivirus encoding firefly luciferase (LUC) and EGFP demarcated by dashed line..... 106
Figure 3-10. E0771 tumour lung metastasis switches from non-angiogenic to angiogenic vascularization during invasion toward the subpleural region. A: immunohistochemistry staining of endothelial cells using anti-CD31 antibody demonstrate that E0771 tumour obtains blood supply from both angiogenesis and non-

angiogenic vascularization. Red arrow depicts the vascular switch; B: IHC staining with anti-CD31 antibody demonstrate that vessel co-option switched off (red scale bars) and new blood formation is triggered (black scale bars) helping the tumour to further grow to ~270 µm in size. The lower inset shows the location of the present field in the whole lung section; C: tumour cells observed growing towards the edge of the lung (subpleura) (black arrow). Asterisks represent the hypoxic areas by immunohistochemistry using an anti-CA9 Ab; D: the percentage of angiogenic and vessel co-opting tumours is quantified per mouse lung. Scale bars in A-C = 250µm..... 108

Figure 3-11. IHC labelling of blood vessels using anti-CD31 antibody showed that E0771 tumour model of experimental lung metastasis utilises both angiogenesis and vessel co-option mechanisms of vascularisation. Vessels in panels A, C, and E were labelled using IHC with anti-CD31 antibody to identify ECs. A and B: demonstrate diffuse growth pattern with neo angiogenesis (yellow arrows denote newly formed blood vessels, which are disorganized and functional (filled with red blood cells) at the visceral pleura (arrowheads); C and D: demonstrate tumour co-option of capillaries illustrating the alveolar growth pattern (yellow arrows denote alveoli filled with E0771 tumour cells); E and F: demonstrate tumour vascular co-option with the perivascular cuffing growth pattern (yellow arrows denote E0771 tumour cells around a vessel (asterisks)). Figures B, D, and F are representative illustrations of various vascularisation patterns. 109

Figure 3-12. Enlarged nuclei as E0771 tumour cells progress toward lung pleura forming subpleural metastases. This metastatic lung tissue section was stained with DAPI (cyan) to visualize the nuclei shape. 110

Figure 3-13. Immunofluorescence labelling lung parenchyma with anti-TTF1 antibody (red) and vessels with anti-CD31 antibody (yellow) to differentiate between angiogenic vessels and co-opted vessels recruited by E0771 TNBC cells. TTF1: thyroid transcription factor 1 which labelled type II pneumocytes. DAPI staining of cell nuclei was used to illustrate tumour growth (blue). 111

Figure 3-14. Co-expression of CD31 and KI67 in the new vessels validated angiogenesis mediating the growth of subpleural metastases at an advanced stage. E0771 metastatic lung section were immunofluorescently stained with an endothelial marker (CD31, green) and a nuclear proliferation marker (KI67, red). 111

Figure 3-15. Angiogenic blood vessels in subpleural E0771 metastases induced by E0771 tumour cells that express VE-Cadherin junctions. VE-CAD expression in new vessels in these metastases is a sign of vessel stabilization. Immunofluorescence staining of E0771 metastatic lung section with anti-VE-CAD and Actin Alpha 2, Smooth Muscle (ACTA2) showed lung capillaries and pulmonary artery, respectively. 112

Figure 4-1. Illustration of generating inducible endothelial-specific Eltd1 knockout model (Pdgfb-iCreERT$^{Cre/+}$; Eltd1$^{fl/fl}$) using Cre/loxP system. Pdgfb-iCreERT2$^{Cre/+}$;Eltd1$^{f/fll}$ male mouse crossed with Eltd1$^{fl/fl}$ female mouse yielded 50% Cre+ and 50% Cre- progeny. Tamoxifen administration induces KO of exons 4 and 5 of Eltd1 in 50% of offspring expressing Cre recombinase under Pdgfb (endothelial marker)-specific promotor. Upon intraperitoneal (IP) injection of tamoxifen to this model, tamoxifen will bind to its binding domain of oestrogen receptor (ER) causing translocation of Cre recombinase from the cytoplasm into the nucleus, where recombination (excision) of loxP-flanked Eltd1 gene (exons 4 and 5) then occurs. Pdgfb-iCreERT2 mouse contains PAC clone, where both Cre and enhanced green fluorescent protein (EGFP)-reporter transgenes are inserted under the promoter of an endothelial marker, Pdgfb gene allowing for spatiotemporal Cre-recombination of Eltd1 gene to occur only in endothelial cells..... 117

Figure 4-2. Identification of transgenic mice (Cre-positive) and littermate controls (Cre-negative) by EGFP amplification. Mice 1,5,6,7, and 8 which are negative for EGFP were used as the control group; mice 2,3,4,9, and 10 which are positive for EGFP were used as the experimental (Eltd1 knockout) group. EGFP: Enhanced green fluorescent protein. 118

Figure 4-3. Significant reduction in ELTD1 expression level in 6-week-old Eltd1^{iEC} mice compared to littermate controls after administration of tamoxifen at ~3-weeks old. A: representative kidney section of control mouse; B: representative kidney section of Eltd1^{iEC} mouse, both sections stained with an in house ELTD1 polyclonal Ab; C: significant difference in ELTD1 protein level in the kidneys of Eltd1^{iEC} group (n= 5) compared to littermate controls (n=4). ELTD1 positive signal in 6 fields of view per mouse was quantified using QuPath digital pathology software. Each data set represents the mean ± standard deviation (SD) (Unpaired Student's t-test was used, *: p ≤ .05; **: p ≤ .01; ***: p ≤ 0.001; ****: p ≤ 0.0001). p value =0.0025. 119
Figure 4-4. The alveolar structure and vascular networks of lungs of Eltd1^{iEC} group (B) appear to be unaffected by Eltd1 recombination after tamoxifen administration in comparison to littermate controls (A). Lung tissue sections were stained with anti-CD31 antibody to visualize blood vessels. 119
Figure 4-5. Timeline of induction of Eltd1 deletion followed by development of experimental E0771 lung metastasis model. Mice were divided into Eltd1^{iEC} group and littermate controls based on PCR amplification of EGFP sequence (co-expressed with Cre transgene). Tumour burden in both groups were assessed using non-invasive magnetic resonance imaging (MRI) imaging of lungs of both groups. Metastatic lungs were harvested for histological assessment. 120
Figure 4-6. Segmented MRI images (X plane cross-sectional view) of E0771 lung metastases showed no difference in tumour burden. However, they showed interlobular strands (thickening) in both Eltd1^{iEC} and littermate control groups at day 14 compared to day 9. Green boxes indicate the control group (n=4 mice); pink boxes indicate Eltd1^{iEC} mice (n=5 mice). 121
Figure 4-7. Quantification of lung volume (in mm^3) of control and Eltd1^{iEC} groups. A and B: representative 3D segmentation of mouse lung at day 9 and 14 post-tumour induction (lung masks are shown in blue) illustrating a reduction in lung volume at day 14 (yellow arrows showing hollow spots) compared to day 9 (smooth surface) post induction; C: quantification of average lung volume in mm^3 of control and Eltd1^{iEC} groups at day 9 and 14 post-tumour induction. Each symbol (circle or triangle) represents one mouse (n= 4 for control group and n= 5 for Eltd1^{iEC} group). Each data set represents the mean ± standard deviation (SD) (Two-way ANOVA with Sidak's multiple comparisons test, *: p ≤ .05; **: p ≤ .01; ***: p ≤ 0.001; ****: p ≤ 0.0001). 122
Figure 4-8. Representative H&E sections and quantification of E0771 metastatic area in control and Eltd1^{iEC} groups. Lungs were removed from the mice post-mortem. The lobes were separated then sections of the formalin fixed, and paraffin embedded tissues were H&E stained. A: Control mouse lungs; B: Eltd1^{iEC} mouse lungs. The cell number used was 1x10^6 and the endpoint to sacrifice the mice was on day 16 following tumour injection. The majority of tumour cells localise to the lung surfaces, with some smaller metastases being observed within the lung parenchyma (yellow circles). C: the percentage of E0771 metastatic area in control and Eltd1^{iEC} groups. H&E-stained lung metastases were quantified using Visiopharm digital pathology software as the percentage of the lung area occupied by tumour cells verses normal tissue. Per mouse, an average percentage of the metastatic area of two tissue sections were calculated. Note that these two sections are 36 µm apart; D: the percentage of E0771 parenchymal metastatic area in control and Eltd1^{iEC} groups. CD31-stained lung metastases were quantified using Qupath digital pathology software as the percentage of the lung area occupied by tumour cells verses normal tissue. Each data set represents the mean ± standard deviation (SD), n=4 (Cre-negative control group); n=5 (Cre-positive Eltd1^{iEC} group)) (Unpaired Student's t-test was used, *: p ≤ .05; **: p ≤ .01; ***: p ≤ 0.001; ****: p ≤ 0.0001)..... 123
Figure 4-9. Gross view of E0771 lung metastases exhibited hematologic swathes of intensity on the outer surface in both Eltd1^{iEC} and littermate control groups at the late timepoint (day 14). The green boxes indicate the control group (n=4 mice); the pink boxes indicate Eltd1^{iEC} mice (n=5 mice)..... 123

Figure 4-10. Representative MRI reconstructed images localizing E0771 tumours and blood vessels in mouse lungs. A: reconstructed front view of E0771 metastatic lungs at early (day 9) and late (day14) timepoints scanned with MRI cardio-respiratory (CR)-synchronized balanced Steady-State Free Precession (bSSFP) scan mode that detect only tumours; B: reconstructed front view of E0771 metastatic lungs at early (day 9) and late (day14) timepoints scanned with MRI gradient echo 3D (GE3D) scan mode detecting both tumours and blood vessels. These images are captured from 3D dataset. 124
Figure 4-11. Endothelial-specific deletion of Eltd1 did not significantly reduces the width of E0771 subpleural metastases. Widths of metastases localized at the subpleural were measured using QuPath digital pathology software. A: an overall view of E0771 metastatic lung tissue section of control group with a white dashed line that separates subpleural from parenchymal metastatic growth and a green line depicting the measurement of subpleural metastases width; B: an overall view of E0771 metastatic lung tissue section of Eltd1^{iEC} group with a white dashed line that separates subpleural from parenchymal metastatic growth and a pink line depicting the measurement of subpleural metastases width. Black dashed boxes in A and B presented as enlarged insets showing angiogenic blood vessels. Each symbol (circle or triangle) represents single measurement (260 measurements were taken from n= 4 of Cre- (Eltd1) group and 281 measurements were taken from n=5 of Cre+ (Eltd1^{iEC}) group. Each dataset represents the mean ± standard deviation (SD) (statistical analysis was performed using the two-tailed unpaired parametric Student's t-test, *: p ≤ .05; **: p ≤ .01; ***: p ≤ 0.001; ****: p ≤ 0.0001). p value =0.7110..... 126
Figure 4-12. IHC labelling of the blood vessels of pazopanib- and vehicle-treated E0771 tumour bearing lungs using anti-CD31 antibody. A: timeline of generating a therapeutic E0771 lung metastasis model, where 100 mg/kg of pazopanib was orally administered to pazopanib-treated group on daily basis; B: an overall view of vehicle-treated E0771 metastatic lung tissue section; C: an enlarged inset of one of the subpleural metastases (dashed box in B) and the enlarged inset showing angiogenic vessels (white arrowheads); D: an overall view of pazopanib-treated E0771 metastatic lung tissue section; E: an enlarged inset of one of the subpleural metastases (dashed box in D). The white dashed lines in C and E separate subpleural from parenchymal metastatic growth and the blue and red lines depict the measurement of subpleural metastases widths. Scale bars in B and D = 1mm. Scale bars in C and E = 100µm... 129
Figure 4-13. In comparison to vehicle treatment, pazopanib administration significantly reduces the width of E0771 subpleural metastases indicating an inhibitory effect on tumour angiogenesis. A: widths of metastases localized at the subpleura were measured using QuPath digital pathology software. Each symbol (circle or triangle) represents single measurement (226 measurements were taken from n= 6 of vehicle-treated group and 315 measurements were taken from n=7 of pazopanib-treated group). B: the percentages of the parenchymal metastatic areas were measured using the same software. Each dataset in B represents the mean ± standard deviation (SD) (statistical analysis was performed using the two-tailed unpaired parametric Student's t-test, *: p ≤ .05; **: p ≤ .01; ***: p ≤ 0.001; ****: p ≤ 0.0001), p value =0.0074 for plot A and ns: not significant for plot B. 130
Figure 5-1. Novel mCherry-labelling strategy (developed by our collaborator, Prof. Ilaria Malanchi) enabling spatial isolation and study of metastatic niche stroma. E0771 tumour cells express both human CD2 (hCD2) and mCherry. Intravenous inoculation of these tumour cells into a syngeneic C57BL/6 mouse primarily producing pulmonary metastases which are able then to secrete permeable mCherry that is then taken up by neighbouring lung cells. These labelled cells then can be FACS sorted for transcriptional analysis..... 137
Figure 5-2. Immunofluorescence staining of the in vitro direct and indirect co-cultures to validate the mCherry niche-labelling system. A: immunofluorescence staining of the direct co-culture of labelling E0771 and HUVECs (CD31+, green) confirmed

mCherry (red) being secreted and taken up by HUVECs (CD31+ and mCherry+); B: immunofluorescence staining of the indirect co-culture of HUVECs with conditioned medium by labelling E0771 confirmed HUVECs uptake the mCherry from the conditioned medium. Nuclei were stained with DAPI (blue)..... 139
Figure 5-3. FACS analysis of the in vitro direct and indirect co-cultures to validate the mCherry niche-labelling system. FACS gating strategy to identify mCherry-positive HUVECs in A, B, and C as follows: SSC-A vs. FSC-A density plot to gate population of interest (P1) excluding debris/ FSC-H vs. FSC-A density plot to gate single cells/ DAPI vs. FSC-A density plot excluding dead cells (DAPI+)/ mCherry vs. hCD2-APC/Fire750 density plot to identify E0771 tumour cells (hCD2+ mCherry+), non-labelled (hCD2- mCherry-), and labelled cells (only mCherry+). The labelled population was further analysed for ECs markers (CD31-FITC vs. mCherry). A: FACS sequential gating of only HUVEC culture showing HUVECs being mCherry negative; B: FACS sequential gating of HUVECs co-cultured with mCherry-labelling E0771 validating HUVECs becoming mCherry positive (52%, labelled as mCherry+/CD31+, yellow arrowhead); C: FACS sequential gating of HUVECs incubated with conditioned mCherry-labelling E0771 medium validating HUVECs taking up mCherry from conditioned medium (100%, labelled as mCherry+/CD31+, yellow arrowhead). 140
Figure 5-4. Spatial localisation of mCherry-labelling hCD2 E0771 tumour cells (arrowheads) and metastatic niche cells (arrows) via immunofluorescence staining of E0771 metastatic lung tissue section. The tissue section was stained with markers of tumour cells A: anti-mCherry (magenta); B: anti-hCD2 antibodies (yellow); C: showed merge image with nuclear staining (cyan), DAPI; D: enlarged inset of box 2 in image C depicting metastatic niche cells expressing only mCherry; E: enlarged inset of box 1 in image C depicting mCherry-labelling hCD2 E0771 tumour cells co-expressing human CD2 (hCD2) and mCherry. 142
Figure 5-5. Immunofluorescence labelling of lung parenchyma and vessels using anti-TTF1 and anti-CD31 antibodies showed that E0771 metastatic lungs exhibited parenchymal growth at early timepoint with vessel co-option pattern and subpleural growth at late timepoint inducing angiogenesis. A-C: H&E microscopic and macroscopic views of non-tumour-bearing and E0771 tumour-bearing lungs. A: healthy non-tumour-bearing lungs; B: early phase of metastasis (day 8 post-tumour inoculation), in which tumour cells colonized lung parenchyma with few subpleural micrometastases; C: late phase of metastasis (day 13 post-tumour inoculation), in which tumour cells colonized lung parenchyma and subpleura with angiogenic metastases. D-F: E0771 tumour cells hijack large blood vessels (E) and recruit (co-opt) lung capillaries (D) as a source for nutrients, oxygen, and energy. The dashed lines in D and E with arrowheads mark tumour areas. F: E0771 tumour cells induce angiogenesis in the subpleural region in order to expand. The dashed line in F separates parenchymal tumour growth from subpleural one. The arrow in F indicate co-opting tumour growth and arrowheads in indicate angiogenic blood vessels induced by E0771 tumour cells. Cell nuclei were stained with Hoechst (blue). Scale bars in A-C = 2.5mm and in D-E = 50µm..... 144
Figure 5-6.Illustration of emission spectral overlap of six fluorochromes used in multiparametric FACS analysis of mouse metastatic lung. Solid peaks are the emission spectra, each labelled with the detected fluorochrome; dashed lines depict the excitation spectra of each of these fluorochromes. (This plot was generated using the tool, the Molecular Probes Spectra Viewer: https://www.thermofisher.com/order/fluorescence-spectraviewer#!/). 145
Figure 5-7. Fluorescence compensation (single-color) and fluorescence Minus One (FMO) controls used to correct for fluorescence spillover and set accurate gating of different mouse lung stromal cells. A, B, D, E: are compensation beads stained with individual fluorochrome-conjugated antibodies that targets cell-surface markers showing separate negative and positive peaks for A: Alexa Fluor 405 (Brilliant™ Violet 421) CD45; B: APC/Fire™ 750 human CD2; D: APC VE-Cadherin; E: FITC CD31; C: an

unstained mouse lung tissue mixed with mCherry-labelling E0771 tumour cells (mCherry+) showing negative and positive peaks for mCherry; F : E0771 tumour-bearing lung cells stained with all fluorochromes except DAPI, Brilliant™ Violet 421 CD45, and Brilliant™ Violet 421 TER119; G: E0771 tumour-bearing lung cells stained with all fluorochromes except APC Fire 750 human CD2; H: non-tumour-bearing lung cells stained with all fluorochromes except mCherry, I: E0771 tumour-bearing lung cells stained with all fluorochromes except APC VE-Cadherin; J: E0771 tumour-bearing lung cells stained with all fluorochromes except FITC CD31; K: E0771 tumour-bearing lung cells stained with all fluorochromes except Brilliant™ Violet 421 CD45, and Brilliant™ Violet 421 TER119; L: E0771 tumour-bearing lung cells stained with all fluorochromes except DAPI. 146

Figure 5-8. FACS sequential gating strategy of mouse lungs identified E0771 tumour cells, metastatic niche, and distal (non-labelled) stroma including ECs. A: non-tumour; B: early; C: late-tumour-bearing lungs; A-C: FACS plots as follows: SSC-A vs. FSC-A density plot to gate population of interest (P1) excluding debris, FSC-H vs. FSC-A density plot to gate single cells, Alexa Fluor 405 vs. FSC-A density plot excluding immune cells (CD45+), RBC (TER119+) and dead cells (DAPI+) and grouping these populations into dump channel (grey box), APC/Fire750 hCD2 vs. mCherry density plot to identify E0771 tumour cells (hCD2+ mCherry+), distal normal stroma cells (non-labelled) and metastatic niche stroma cells (only mCherry+), and the latter two populations were further analysed for ECs marker (CD31). 149

Figure 5-9. FACS quantification of cell proportions of E0771 tumour cells, metastatic niche, and distal (non-labelled) stromal cells including ECs. A: cell percentages in non-tumour, early, and late-tumour-bearing lungs; B: E0771 tumour burden as percentages; C: percentages of metastatic niche stroma; D: percentages of metastatic-distal stroma in non-tumour, early, and late-tumour-bearing lungs 151

Figure 5-10. Optimization of tissue preparation and FACS gating to enrich for ECs and avoid FACS sorting of autofluorescent cells. A: unstained mouse lungs exhibit high autofluorescence in DAPI, mCherry, and APC/Fire750 channels that might interfere with FACS sorting, which should be taken into consideration when sorting populations of interest; B: autofluorescent cells were gated out. C: mouse lung cells without removal of immune cells (CD45-positve cells) with blue box indicating that limited CD45-negative population giving rise to a limited number of ECs (CD31-positive cells) (blue peak); D: immunomagnetic depletion of immune cells from lung cell suspension enriches and speeds up FACS sorting of pure ECs with orange box indicating enriched population of non-immune cells giving rise to higher proportion of ECs (orange peak). Histogram shows that compared to unstained lung cell suspension (red peak), CD45+ depleted lung cell suspension (orange peak and line) has higher percentage of ECs than CD45 non-depleted lung cell suspension (blue peak and line). 153

Figure 5-11. Experimental outline and protocol followed for FACS sorting for scRNA-seq of non-immune stromal lung cells. Lungs were harvested from A: healthy mice; B: at early (day 7), and C: late metastatic phases (day 13 following intravenous inoculation of one million mCherry-labelling E0771 tumour cells); D: lungs were then digested using collagenase I and III enzymes and tissue dissociator which was followed by removal of immune cells (CD45+) using immunomagnetic beads; E: stromal cells were FACS sorted from condition A (healthy lungs); F: both mCherry + metastatic niche and mCherry - distal lung stromal cells were FACS sorted from condition B (early timepoint) and C (late timepoint). FACS sorted stromal cells were used for gene expression analysis using scRNA-seq. Note that several lungs were pooled to enrich for niche (mCherry-labelled) cells at early and late metastatic phases, respectively. 156

Figure 5-12. FACS-stained controls and samples that were used for FACS-sorting for scRNA-seq analysis. A: non-tumour-bearing lung cells that were not stained; B:single-stained (compensation) controls, where only cells stained with one fluorescent-conjugated antibody at a time for calculating the compensation; C: Fluorescence Minus One (FMO) controls used to identify the true negative boundary for the fluorochromes:

FITC, APC, Brilliant Violet 421 (BV421), APC Fire 750, mCherry, and DAPI considering the spread of other fluorochromes into each of these channels; D: using FACS sorter, cells were isolated from three samples, which are the three experimental conditions: non-tumour-bearing (healthy), early-, and late-metastatic lung cells for scRNA-seq analysis. Ab: antibody; Compensation beads: commercially available beads; VE-CAD: VE-Cadherin; hCD2: human CD2. 157

Figure 5-13. FACS sequential gating strategy to isolate lung non-immune stromal cells from normal lungs, early, late metastatic lungs for scRNA-seq analysis. A: FACS gating strategy for normal lungs (n=2); B: FACS gating strategy from early metastatic lungs (n=8); C: FACS gating strategy from late metastatic lungs (n=6). FACS gating strategy from top to bottom as follows: SSC-A vs. FSC-A density plot to gate population of interest (P1) excluding debris; FSC-H vs. FSC-A density plot to gate single cells; Alexa Fluor 405 vs. FSC-A density plot excluding immune cells (CD45+), RBC (TER119+) and dead cells (DAPI+) and grouping these populations into dump channel; hCD2-APC/Fire750 vs. mCherry density plot to identify E0771 tumour cells (hCD2+ mCherry+), distal stroma cells (hCD2- mCherry-), and metastatic niche stromal cells (only mCherry+).The latter two populations were further analysed for ECs markers (CD31 and VE-CAD). Note cell numbers that were FACS sorted are illustrated near each population..... 158

Figure 5-14. Quality control (QC) metrics applied for filtering cells. A: cells expressing more than 200 genes (features) and less than 8700 genes were included; B: cells that contain a total sum of counts across all features, i.e., genes of more than 500 counts per cell (library sizes) were included; C: cells with only less than 15% of UMI counts derived from the mitochondrial genes were included; D: QC metrics combining and visualizing detected features, library size, and percentage of mitochondrial genes for the five conditions: non-tumour, early distal, early niche, late distal, and late niche 160

Figure 5-15. Pan-endothelial marker genes were used to subcluster EC population from the main lung stromal population. Dashed black lining depicts endothelial clusters that were subsetted for higher resolution. Endothelial cells spanned into fibroblast cluster (black arrow). Erythroid cluster (white arrowheads) also express endothelial marker genes. The full names of these genes are shown in **The List of Abbreviations Table.**..... 161

Figure 5-16. Vascular cells from healthy lungs, early, and late E0771 metastatic mouse lungs revealed vascular heterogeneity during metastatic development in the lungs. A: unsupervised clustering visualized as Uniform Manifold Approximation and Projection (UMAP) identified 15 clusters that were annotated to 13 cell types across all five conditions. Cell clusters were annotated by manual curation of previous studies and based on the top 50 differentially expressed (DE) marker genes. Five UMAP projection plots of lung vascular clusters splitting all five conditions: B: normal (healthy); C: early distal region (turquoise arrowheads), early niche (cumin arrowheads); D: late distal region (purple arrowheads), and late niche (green arrowheads) conditions of E0771 metastatic lungs, respectively; E and F: relative (percentage) and absolute cellular composition of lung vascular cells across the five conditions. ECs is abbreviated for endothelial cells; SMCs is abbreviated for smooth muscle cells. 163

Figure 5-17. UMAP plots of top five marker genes for EC subtypes from healthy lungs, early, and late E0771 metastatic mouse lungs. A: top five marker genes of capillary type I ECs; B: top five marker genes of capillary type II ECs; C: top five marker genes of antigen-presenting cap II ECs; D: top five marker genes of artery ECs; E: top five marker genes of vein ECs; F: top five marker genes of stressed ECs; G: top five marker genes of proliferating ECs. These top marker genes were identified based on log2 foldchange of 0.25, min.pct of 0.25, and adjusted p-value <0.05. The full names of these genes are shown in **The List of Abbreviations Table.** 164

Figure 5-18. UMAP plots of top five marker genes for vascular subtypes from healthy lungs, early, and late E0771 metastatic mouse lungs. A: top five marker genes of neophalanx/breach/tip ECs; B: top five marker genes of tumour ECs; C: top five marker

genes of ribosomal-related cluster; D: top five marker genes of smooth muscle cells (SMC); E: top five marker genes of megakaryocytes; F: top five marker genes of lymphatic ECs. These top marker genes were identified based on log2 foldchange of 0.25, min.pct of 0.25, and adjusted p-value <0.05. The full names of these genes are shown in **The List of Abbreviations Table.** 165
Figure 5-19. Heatmap depicting gene expression levels of MHC II Ag presentation molecules and IFNγ-regulated genes in different EC subtypes. Instead of using the normalized expression values, Z-scores were computed for every row (representing each gene) and displayed on the heatmap. This approach guarantees that the visualized expression patterns are not overwhelmed by the actual expression values. The full names of these genes are shown in **The List of Abbreviations Table.**..... 167
Figure 5-20. Gene set enrichment analysis (GSEA) of DEGs showed significant downregulation of gene set related to tight junctions, focal adhesion, and actin cytoskeleton in early niche (co-opted) capillary II ECs compared to normal counterpart. NES: normalized enrichment score. 168
Figure 5-21. Heatmap depicting co-opted capillaries in early niche increase the expression of genes regulating OXPHOS and downregulate genes regulating tight junctions (TJs), focal adhesion, and actin cytoskeleton compared to other conditions. A: heatmap depicting cap II ECs in early niche downregulated genes related to TJs, focal adhesion, and acting cytoskeleton; B: heatmap depicting cap I and cap II ECs increased the expression of OXPHOS genes. Z-scores were computed for every row (representing each gene) and displayed on the heatmap. This approach guarantees that the visualized expression patterns are not overwhelmed by the actual expression values. The full names of these genes are shown in **The List of Abbreviations Table.**..... 169
Figure 5-22. Immunofluorescent staining demonstrated reduced protein expression of the tight junction, TJP1 (purple) in the early metastatic niche (co-opting) metastases compared to TJP1 expression in the distal region and non-tumour-bearing lungs. TJP1 expression: A: in the parenchymal region of non-tumour-bearing lungs; B: in the alveolar co-opted region in early (co-opting) metastases; C: in the cuffing co-opted region in early (co-opting) metastases; D: in the distal region in early (co-opting) metastases-containing lungs. B, C, and D were captured from the same tissue section. Enlarged insets in B and C demonstrate TJP1 expression in the intratumoural (1) and niche (2) regions. TJP1: tight junction protein 1. Nuclei were stained with DAPI (blue)..... 171
Figure 5-23. Immunofluorescent staining demonstrated reduced protein expression of the tight junction, TJP1 in the late metastatic niche of angiogenic metastases compared to TJP1 expression in the non-tumour-bearing lungs. TJP1 expression: A: in the parenchymal region of non-tumour-bearing lungs; B: in subpleural (angiogenic) metastases. Enlarged insets in B demonstrate TJP1 expression in the intratumoural (1) and niche (2) regions. TJP1: tight junction protein 1. Nuclei were stained with DAPI (blue). 172
Figure 5-24. Double immunofluorescence staining of early (co-opting) lungs showed an evident reduction in TJP1 signal in the niche and distal vascular ECs compared to non-tumour ECs. TJP1and CD31 expression: A-C: in the parenchymal region of non-tumour-bearing lungs; D-F: in the distal region in early (co-opting) metastases-containing lungs; G-H: in the alveolar co-opted region in early (co-opting) metastases. Note that D-I were captured from the same tissue section. Enlarged insets in G-I demonstrate TJP1 expression in the intratumoural (1) and niche (2) regions. TJP1: tight junction protein 1..... 173
Figure 5-25. Violin plots depicting top genes that are upregulated in co-opted cap I ECs in early niche compared to non-tumour (A-H) and to early distal region (I-K). The full names of these genes are shown in **The List of Abbreviations Table.**..... 176

Figure 5-26. Violin plots depicting top genes that are upregulated in co-opted cap II in early niche compared to non-tumour (A-C) and to early distal region (D-F). The full names of these genes are shown in **The List of Abbreviations Table.** 177
Figure 5-27. Venn diagram demonstrating upregulated DEGs in cap I and cap II (co-opted) ECs in early niche in comparison to non-tumour, early distal, and late niche counterparts. A: pairwise comparisons showing upregulated genes (red nodes labelled with the number of genes that were upregulated in that comparisons and common genes among comparisons) in cap I; B: in cap II ECs in early niche compared to non-tumour (green node), early distal region (magenta node), late niche (cyan node). Yellow boxes in A and B depicts the common upregulated genes in co-opted cap I and cap II ECs in early niche across comparisons. Visualizing tool used is DiVenn ((L. Sun et al., 2019)..... 178
Figure 5-28. Scoring of tissue dissociation (stress response) gene signature across EC subtypes. A: UMAP visualization of tissue dissociation gene signature across EC subtypes with stressed ECs showing highest score; B: dot plot showing average expression of stress response genes across EC subtypes. The full names of these genes are shown in **The List of Abbreviations Table.** 180
Figure 5-29. Quality assessment of stressed ECs in comparison to other EC subtypes and top four distinct genes. UMAP visualizations of A: normalized number of genes per cell; B: normalized number of mRNA transcripts per cell; C: transcripts that mapped to mitochondrial genes per cell across all EC subtypes; Distinct genes differentially highly expressed in stressed ECs (indicated by white arrowheads) including D: Sertad1; E: Csrnp1; F: Sox17; G: Irf1; H: Pim3; I: Hes1. The full names of these genes are shown in **The List of Abbreviations Table.** 181
Figure 5-30. Angiogenic ECs predicted to arise from cap I and II ECs. A: EC differentiation trajectory analysis using Monocle predicts cap I (yellow arrowhead) and cap II ECs (white arrowhead) to differentiate into neophalanx/breach/tip ECs (black arrow). Light grey circle indicates the root (starting) node; B: annotation for EC subclusters (excluding SMCs, Megakaryocytes, and ribosomal-related cells); C: UMAP projection plot of scRNA-seq merging all five conditions: healthy, early distal, early niche, late distal, and late niche ECs of early metastases and late metastases, respectively; D: Monocle trajectory analysis separates ECs into two partitions indicating two distinct trajectories: trajectory 1 includes all ECs and trajectory 2 includes lymphatic ECs..... 183
Figure 5-31. Heatmap depicting cap I and neophalanx-breach-tip ECs increased the expression of genes regulating glycolysis/gluconeogenesis pathway compared to non-tumour counterparts. A: heatmap depicting expression of glycolysis/gluconeogenesis pathway in neophalanx-breach-tip ECs across five conditions; B: heatmap depicting expression of glycolysis/gluconeogenesis pathway in cap I ECs across five conditions. Z-scores were computed for every row (representing each gene) and displayed on the heatmap. This approach guarantees that the visualized expression patterns are not overwhelmed by the actual expression values. The full names of these genes are shown in **The List of Abbreviations Table.**..... 184
Figure 5-32. Dot plot depicting the expression levels of lipid-regulated genes across different EC subtypes across the five conditions: normal (healthy), early distal, early niche, late distal, and late niche of early and late metastatic lungs, respectively. In order to detect variation in lowly expressed genes, this dot plot was generated with 30% of scale truncation. Thus, any gene expressed in 30% of cells or higher in a cluster have the same dot size. The full names of these genes are shown in **The List of Abbreviations Table.**..... 185
Figure 5-33. Different EC subtypes exhibited heterogenous expression of lipid-regulated genes across the five conditions: normal (healthy), early distal, early niche, late distal, and late niche of early and late metastatic lungs. Violin plots in: A-E: depicting significantly upregulated genes in cap I ECs; F: depicting significantly downregulated gene in stressed ECs; G & H: depicting significantly downregulated

genes in cap II ECs; I & J: depicting significantly downregulated genes in arteries across specified conditions as indicated in **Table5-5**. Differential expression analysis in pairwise-comparison fashion was performed using a non-parametric Wilcoxon (Mann-Whitney) test. Data points represent mRNA counts. P values were corrected using the false discovery rate (FDR) (Benjamini-Hochberg) procedure with a threshold of FDR < 0.05. (*: p ≤ .05; **: p ≤ .01; ***: p ≤ 0.001; ****: p ≤ 0.0001). The full names of these genes are shown in **The List of Abbreviations Table.** 187

Figure 5-34. Neophalanx/breach/tip ECs upregulated specific lipid-regulated genes in late distal region in comparison to late niche. A-F: violin plots depicting significantly upregulated genes in these ECs (Srebf1, Gpihbp1, Cd36, Lpl, Elovl5) in the late distal region, (Plin2) in both late niche and late distal regions compared to specified conditions. Differential expression analysis in pairwise-comparison fashion was performed using a non-parametric Wilcoxon (Mann-Whitney) test. Data points represent mRNA counts. P values were corrected using the false discovery rate (FDR) (Benjamini-Hochberg) procedure with a threshold of FDR < 0.05. (*: p ≤ .05; **: p ≤ .01; ***: p ≤ 0.001; ****: p ≤ 0.0001). The full names of these genes are shown in **The List of Abbreviations Table.** 188

Figure 5-35.Remodelling of lipid metabolism in different EC subtypes in response to early and late E0771 metastatic growth. A:upregulated lipid genes **(listed in Figure 5-33)** in different EC subtypes, including capillary type I, capillary type II, arteries, stressed ECs, and neophalanx/breach/tip ECs across the four conditions: early distal, early niche, late distal, and late niche of early and late metastatic lungs, respectively; B: each EC subtype is shape-coded; C: each condition is color-coded. The text in red depicts the enzymes involved. Text highlighted in yellow depicts disrupted genes in the EC subtype in the specified condition. Abbreviations of disrupted genes are shown in **The List of Abbreviations Table.** 189

Figure 5-36. Raman signatures (tissue fingerprints) revealed an increase of saturated lipid in early metastatic lungs and an increase of unsaturated lipid in late metastatic lungs in comparison to normal (non-tumour) lungs. Inset 1 depicts enlarged view of Raman peak intensities for non-tumour, early, and late metastatic lungs at 1655 cm-1 band representing unsaturated lipid. Inset 2 depicts enlarged view of Raman peak intensities for non-tumour, early, and late metastatic lungs at 1850 cm-1 band representing saturated lipid. Each line depicts average Raman spectrum acquired from 3 fields of view (three technical replicates) (scanned area of 50µm x 50µm) per mouse per condition. Spectral peaks were stacked for comparison purpose..... 191

Figure 5-37. Heatmap visualization of Raman spectra revealed a spatial increase of saturated lipid in early metastatic lungs and a spatial increase of unsaturated lipid in late metastatic lungs in comparison to normal (non-tumour) lung. A: heatmap of Raman spectra of representative field of view of normal lung section showing heterogenous Raman intensities of saturated lipid across the section. Inset 1 shows high and inset 2 shows low levels of saturated lipid; B and C: heatmaps of Raman spectra of representative field of views showing increased saturated lipid in early metastatic lungs compared to normal lungs (B) and increased unsaturated lipid in late metastatic lungs compared to normal lungs (C). 192

Figure 5-38. The congruency of EC subtypes in primary and metastatic lung tumours. Short-term sunitinib means treatment administered for 10 days; long-term sunitinib means treatment administered for 25 days. EC composition of primary LLC lung tumour model from (Goveia et al., 2020); EC composition of RENCA lung metastases from (Teuwen et al., 2021). EC: endothelial cells; TEC: tumour ECs; LLC: Lewis Lung Carcinoma cells; RENCA: renal adenocarcinoma. 196

Figure 6-1. Principal components (PCs) and clustering resolution selected for further downstream analysis of scRNA-seq data. A: Elbow plot plotting standard deviation of principal components. An elbow (black arrow) was observed to be around PC20; therefore, the first 20 PCs were suggested to contain the majority of variance; B:

clustering tree grouping cells that are similar across different clustering resolutions. A clustering resolution of 0.5 was selected for further analysis. 211
Figure 6-2. Non-immune stromal cells from healthy lungs, early, and late E0771 metastatic mouse lungs revealed stromal heterogeneity during metastatic development in the lungs. A: unsupervised clustering visualized as Uniform Manifold Approximation and Projection (UMAP) identified 21 clusters that were annotated to 17 cell types across all five conditions. Cell clusters were annotated by manual curation of previous studies and based on the top 50 differentially expressed (DE) marker genes. Five UMAP projection plots of lung stromal clusters splitting all five conditions: B: normal (healthy); C: early distal region (turquoise arrowheads), early niche (cumin arrowheads); D: late distal region (purple arrowheads), and late niche (green arrowheads) conditions of E0771 metastatic lungs, respectively; E and F: relative (percentage) and absolute cellular composition of lung stromal cells across the five conditions with white arrowheads depicting the enrichment of mature mesothelium in early niche and cancer-associated mesenchymal cells (CAMCs) in late niche. ECs: endothelial cells; SMCs: smooth muscle cells; EBF1: early B-cell factor 1. 212
Figure 6-3. UMAP plots of top five marker genes for EC subtypes from healthy, early, and late E0771 metastatic mouse lungs. A: top five marker genes of capillary type I ECs; B: top five marker genes of capillary type II ECs; C: top five marker genes of veins; D: top five marker genes of stressed ECs; E: top five marker genes of neophalanx/breach/tip ECs; F: top five marker genes of SMCs/pericytes. These top marker genes were identified based on log2 foldchange of 0.25, min.pct of 0.25, and adjusted p-value <0.05. The full names of these genes are shown in **The List of Abbreviations Table.** 213
Figure 6-4. UMAP plots of top five marker genes for fibroblast and mesothelial subtypes from healthy, early, and late E0771 metastatic mouse lungs. A: top five marker genes of mesothelial cells; B: top five marker genes of cancer-associated mesenchymal cells (CAMCs); C: top five marker genes of interstitial fibroblasts; D: top five marker genes of lipofibroblasts; E: top five marker genes of early B cell transcription factor 1 (EBF) positive fibroblasts; F: top five marker genes of myofibroblasts. These top marker genes were identified based on log2 foldchange of 0.25, min.pct of 0.25, and adjusted p-value <0.05. The full names of these genes are shown in **The List of Abbreviations Table.** 214
Figure 6-5. UMAP plots of top marker genes for epithelial subtypes and erythroid cells from healthy, early, and late E0771 metastatic mouse lungs. A: top five marker genes of ciliated epithelial cells; B: top five marker genes of pneumocytes type II; C: top five marker genes of erythroid cells; D: top three marker genes of E0771 tumour cells. These top marker genes were identified based on log2 foldchange of 0.25, min.pct of 0.25, and adjusted p-value <0.05. The full names of these genes are shown in **The List of Abbreviations Table.** 215
Figure 6-6. A cell cluster in scRNA-seq data was identified as E0771 tumour cells as they expressed genes inserted in the lentiviral vector, they transduced with mCherry and human CD2. A: expression of mCherry; B: expression of human CD2 in E0771 tumour cluster (white arrowheads) visualized in UMAP plots. 216
Figure 6-7. Erythroid cluster showed expression of erythroid cell marker genes. The full names of these genes are shown in **The List of Abbreviations Table.** 217
Figure 6-8. Cell-cell communication network in E0771 metastatic lungs. A: Heatmap depicting the total number of potential ligand–receptor pairs among lung cell types predicted by CellPhoneDB. CAMCs showed strongest interactions with other cell subtypes; B: circle plot showing the total number of interactions among different cell types. The source represents the cell contributing the ligand to the interaction, while the target contributes the receptor. Circle size is proportional to the number of cells in the identified cell type class, and the width of the line is proportional to the number of significant ligand–receptor pairs (the communication score) contributing to the

communication between two interacting cell types. ECs: endothelial cells; SMCs: smooth muscle cells; CAMCs: cancer-associated mesenchymal cells 219
Figure 6-9. Alluvial plots depicting outgoing signalling patterns of secreting (sender) lung cell types and E0771 tumour cells predicted using CellChat. The thickness of the flow depicts the strength of the cell groups contributing to the inferred patterns (plot on the left side) and the strength of signalling molecules contributing to the inferred patterns (plot on the right side). The height of each pattern represents the number of cell groups each pattern entails (plot on the left side) and represents the number of signalling molecules each pattern entails (plot on the right side). 221
Figure 6-10. Alluvial plots depicting incoming signalling patterns of receiver lung cell types and E0771 tumour cells predicted using CellChat. The thickness of the flow depicts the strength of the cell groups contributing to the inferred patterns (plot on the left side) and the strength of signalling molecules contributing to the inferred patterns. The height of each pattern represents the number of cell groups each pattern entails (plot on the left side) and represents the number of signalling molecules each pattern entails (plot on the right side). 222
Figure 6-11. SEMA6, SEMA3, JAM, and non-canonical WNT signalling pathways are predicted to be activated in the lung stroma of E0771 metastases. A, C, E, G: the columns in the heatmaps depict lung stromal and E0771 tumour cells, and the rows depict if the cell is signalling as sender, receiver, mediator, or influencer. These heatmaps are color-coded according to the relative importance of each cell subtype based on the computed four network centrality measures of the SEMA6, SEMA3, JAM, and non-canonical WNT (ncWNT) signalling networks, respectively with evident senders and receivers indicated with white arrowheads and black arrows, respectively; B, D, F, H: bar plots showing the relative contribution of each ligand-receptor pair to the SEMA6, SEMA3, JAM, and ncWNT signalling pathways with significant pairs indicated with yellow arrowheads. The relative contribution is calculated as the ratio of the total communication probability of the inferred network of each ligand-receptor pair to that of a particular signalling pathway. The full names of these genes are shown in **The List of Abbreviations Table.** 225
Figure 6-12. CCL, CD39, and NECTIN signalling pathways are predicted to be activated in the lung stroma and tumour cells of E0771 metastases. A, C, E: the columns in the heatmaps depict lung stromal and E0771 tumour cells, and the rows depict if the cell is signalling as sender, receiver, mediator, or influencer. These heatmaps are colour-coded according to the relative importance of each cell subtype based on the computed four network centrality measures of the CCL, CD39, and NECTIN signalling networks, respectively with evident senders and receivers indicated with white arrowheads and black arrows, respectively; B, D, F: bar plots showing the relative contribution of each ligand-receptor pair of the Ccl, CD39, and NECTIN signalling pathways with significant pairs indicated with yellow arrowheads. The relative contribution is calculated as the ratio of the total communication probability of the inferred network of each ligand-receptor pair to that of a particular signalling pathway. The full names of these genes are shown in **The List of Abbreviations Table.** 227
Figure 6-13. Angiogenesis is limited in the late distal region of subpleural metastases via the THBS1 – CD36 signalling pair. A: the columns in the heatmap depict lung stromal and E0771 tumour cells, and the rows depict if the cell is signalling as sender, receiver, mediator, or influencer. This heatmap is colour-coded according to the relative importance of each cell subtype based on the computed four network centrality measures of the THBS signalling network with evident sender and receiver indicated with white arrowhead and black arrow, respectively; B: bar plot showing the relative contribution of each ligand-receptor pair to the THBS signalling pathway with significant pair indicated with yellow arrowhead. The relative contribution is calculated as the ratio of the total communication probability of the inferred network of each ligand-receptor pair to that of the Thbs signalling pathway; C: violin plot depicting the expression distribution of Thbs1 across the subtypes of lung stromal cells in the late distal region,

with myofibroblasts expressing the highest level of Thbs1; D: violin plot depicting the expression distribution of Cd36 across the subtypes of lung stromal cells in the late distal region, with cap I ECs expressing the highest level of Cd36. The full names of these genes are shown in **The List of Abbreviations Table.**..... 228
Figure 6-14. Different angiogenic signalling pathways are predicted to drive the development of late (angiogenic) metastases. A, C, E, G: the columns in the heatmaps depict lung stromal and E0771 tumour cells, and the rows depict if the cell is signalling as sender, receiver, mediator, or influencer. These heatmaps are colour-coded according to the relative importance of each cell subtype based on the computed four network centrality measures of the EPHB, APELIN, CXCL, and CALCR signalling networks, respectively with evident senders and receivers indicated with white arrowheads and black arrows, respectively; B, D, F, H: bar plots showing the relative contribution of each ligand-receptor pair of the EPHB, APELIN, CXCL, and CALCR signalling pathways with significant pairs indicated with yellow arrowheads. The relative contribution is calculated as the ratio of the total communication probability of the inferred network of each ligand-receptor pair to that of a particular signalling pathway. The full names of these genes are shown in **The List of Abbreviations Table.**..... 230
Figure 6-15. Cell-cell communication analysis showed that cancer-associated mesenchymal cells (CAMCs) are the main supplier of pro-angiogenic growth factor VEGFA. A: the columns in the heatmap depict lung stromal and E0771 tumour cells and the rows depict if the cell is signalling as sender, receiver, mediator, or influencer. This heatmap is colour-coded according to the relative importance of each cell subtype based on the computed four network centrality measures of the VEGF signalling network. This heatmap shows CAMCs as the primary cell subtype (sender, white arrowhead) that express Vegfa and cap I ECs as the primary receiver that express the receptor (black arrow); B: bar plot showing the relative contribution of each ligand-receptor pair to the VEGF signalling pathway, with VEGFA-VEGFR2 pair being the dominant contributor with significant pair indicated with yellow arrowhead. The relative contribution is calculated as the ratio of the total communication probability of the inferred network of each ligand-receptor pair to that of the VEGF signalling pathway; C: UMAP visualisation showing hypoxia-responsive CAMCs highly expressing Vegfa; D: violin plot depicting the expression distribution of Vegfa across the subtypes of lung stromal cells in the late niche, with CAMCs expressing the highest level of Vegfa; E: violin plot depicting the expression distribution of Vegfr2 across the subtypes of lung stromal cells in the late niche, with cap I ECs expressing highest level of Vegfr2. The full names of these genes are shown in **The List of Abbreviations Table.** 232
Figure 6-16. The growth factors and cytokines predicted to be secreted by E0771 tumour cells, some of which are reported to mediate EMT of mesothelial cells. A, C, E, G: the columns in the heatmaps depict lung stromal and E0771 tumour cells, and the rows depict if the cell is signalling as sender, receiver, mediator, or influencer. These heatmaps are colour-coded according to the relative importance of each cell subtype based on the computed four network centrality measures of the TGFβ, TNF, EGF, and PDGF signalling networks, respectively with evident senders and receivers indicated with white arrowheads and black arrows, respectively; B, D, F, H: bar plots showing the relative contribution of each ligand-receptor pair to of the TGFβ, TNF, EGF, and PDGF signalling pathways with significant pairs indicated with yellow arrowheads. The relative contribution is calculated as the ratio of the total communication probability of the inferred network of each ligand-receptor pair to that of a particular signalling pathway. The full names of these genes are shown in **The List of Abbreviations Table.**..... 233
Figure 7-1. Pan-mesothelial marker genes were used to subcluster the mesothelial and CAMCs populations from the main lung stromal population. Dashed black lines depict mesothelial and CAMC clusters subdivided for higher resolution analysis. The full names of these genes are shown in **The List of Abbreviations Table.**..... 240
Figure 7-2. Mesenchymal cells from healthy lungs, early, and late E0771 metastatic mouse lungs revealed mesenchymal heterogeneity at early and late metastatic

tumour growth in the lungs. A: unsupervised clustering visualized as Uniform Manifold Approximation and Projection (UMAP) identified four clusters annotated to four cell types across all five conditions. Cell clusters were annotated by manual curating of genes identified by previous studies and based on the top 50 differentially expressed (DE) marker genes. Five UMAP projection plots of lung mesenchymal clusters splitting all five conditions: B: normal (healthy in purple); C early distal region (fuchsia arrowheads), early niche (green arrowheads); D: late distal region (cumin arrowheads), and late niche (turquoise arrowheads) conditions of E0771 metastatic lungs, respectively; E and F: relative (percentage) and absolute cellular composition of lung mesenchymal cells across the five conditions. B-D are colour-coded differently from the rest of the figure. (figure changed modifying meso to CAMCs)..... 242

Figure 7-3. UMAP plots of top five marker genes for mesothelial subtypes from healthy, early, and late E0771 metastatic mouse lungs. A: top five marker genes of mature mesothelium; B-D: top five marker genes of cancer-associated mesenchymal cells (CAMCs), where B: proliferating mesothelium; C: inflammatory fibroblast-like mesothelium; D: hypoxia-responsive perivascular mesothelium. These top marker genes were identified based on log2 foldchange of 0.25, min.pct of 0.25, and adjusted p-value <0.05. The full names of these genes are shown in **The List of Abbreviations Table.** 243

Figure 7-4. A subcluster of hypoxia-responsive perivascular cells highly express hypoxia signature genes. A: UMAP visualization of hypoxia gene signature across mesenchymal subtypes with hypoxia-responsive cluster showing highest score; B-D: UMAP visualization of this subcluster (white arrowheads) upregulating the expression of hypoxia genes such as Hilpda, Slc2a1 (Glut1), and Car9 (Ca-9). The full names of these genes are shown in **The List of Abbreviations Table.** 245

Figure 7-5 . Immunofluorescence staining using anti-WT1 (red) and anti-CD31 (green) antibodies revealed that WT1 is expressed in pleural mesothelial cells in non-tumour-bearing lungs and E0771 tumour cells in E0771 metastatic lungs. A and B: pleural mesothelial cells in normal lungs express WT1, and the cells look thin and elongated in shape; C and D: WT1 is expressed in E0771 tumour cells and the metastatic niche of subpleural metastases; E and F: WT1 is expressed in E0771 tumour cells and the metastatic niche of parenchymal metastases. Nuclei were counterstained with DAPI (blue). 247

Figure 7-6. WT1 and MSLN exhibited expression in E0771 tumour cells and pleural mesothelial cells, and cytokeratin 5/6 staining was used to discriminate between these two populations. A, E: serial sections of non-tumour-bearing lung, where pleural mesothelium expressed MSLN and WT1. Both MSLN and WT1 were expressed in serial sections of B, F: parenchyma metastases; C, D, G, and H: subpleural metastases, respectively. Small and large subpleural metastases showed intact pleural mesothelial monolayer (dashed lines in C, D, G, H. I: overall view of one lung lobe stained with cytokeratin 5/6; J: zoomed inset depicting distinct expression of cytokeratin 5/6 in mesothelial cells with negative expression in E0771 tumour cells. Scale bars in A-H = 100 µm, in I = 500 µm, and in J = 50 µm. The full names of these genes are shown in **The List of Abbreviations Table.** 248

Figure 7-7. VVG staining revealed that the integrity of the pleural mesothelial cells (cell layer covering the lung tissue, dark blue) is intact in micrometastases and late (angiogenic) metastases. Non-tumour (A), early (B), and late (C) metastatic tissue sections were stained with the elastic stain (Verhoeff-Van Gieson (VVG)) to label the elastic fibres that are usually produced by pleural mesothelial cells. 250

Figure 7-8. Primary pleural mesothelial cells promote E0771 tumour cell proliferation (bidirectional signalling using transwell setting) and invasion. A: CYQUANT cell proliferation assay of transwell indirect co-culture, where E0771 tumour cells were seeded in upper inserts and mesothelial cells were seeded in the lower chamber in the indirect co-culture group and no mesothelial cells in the control group; B: invasion assay with same experimental settings as in (A) but coating upper inserts with a matrix

(collagen I) layer that served as an invasion barrier; C: representative fields of view for control group, where almost no invasion occurred (blue box) and indirect co-culture group, showing high numbers of E0771 tumour cells invaded into the lower side of the insert through collagen I layer (red box). Each data point (circle or triangle) represents an average of 3-4 replicate wells per group (n= 3 independent experiments for the control group and n= 3 independent experiments for the indirect co-culture group). Each data set represents the mean ± standard error of the mean (SEM) (Unpaired Student's t-test was used, *: p ≤ .05; **: p ≤ .01; ***: p ≤ 0.001; ****: p ≤ 0.0001). 252

Figure 7-9. Cancer-associated mesenchymal cells (CAMCs) subtypes are predicted to arise from mature mesothelium. A: mesothelial differentiation trajectory analysis using Monocle predicts mature mesothelium differentiates into three CAMC subtypes with a trajectory loop (black arrow) between inflammatory-like and hypoxia-responsive perivascular mesothelial cells. The white circle indicates the root (starting) node starting from mature mesothelium (white arrowhead); B: annotation for mesothelial subclusters; C: UMAP projection plot of scRNA-seq merging all five conditions: healthy, early distal, early niche, late distal, and late niche ECs of early metastases and late metastases, respectively; D: Monocle trajectory analysis separates mesothelial cells into two partitions indicating two distinct trajectories; E: heatmap visualizing high expression of Hif-1-regulated genes in hypoxia-responsive perivascular mesenchymal cells compared to other subtypes. The full names of these genes are shown in **The List of Abbreviations Table.** 254

Figure 7-10. Gene set enrichment analysis (GSEA) of DEGs showed significant upregulation (yellow bars) of gene sets related to inflammatory pathways in early niche mature mesothelium compared to the distal region of the same lungs (B) and normal lungs (A). Upregulated gene sets related to the IFNγ pathway are depicted by white arrowheads and related to the cytokine pathway by black arrows. C: heatmap visualizing high expression of Ifnγ and cytokine genes in mature mesothelium. NES: normalized enrichment score. The full names of these genes are shown in **The List of Abbreviations Table.** 256

Figure 7-11. Gene set enrichment analysis (GSEA) of DEGs showed significant upregulation (yellow bars) of gene sets related to Epithelial–mesenchymal transition (EMT) process, Tnfα pathway (white arrowheads), and angiogenesis (black arrows) in cancer-associated mesenchymal cells (CAMCs) subtypes of the late niche compared to the distal region of the same lung (B) and normal lungs (A). NES: normalized enrichment score. 257

Figure 7-12. Cancer-associated mesenchymal cells (CAMCs) upregulated the expression of mesenchymal markers with a cluster that is highly proliferative. A-C: expression of mesenchymal markers: including Fn1, Cdh2 (Ncad), and Timp3; D-F: CAMCs downregulated the expression of mesothelial markers: Upk3b, Krt18, and Krt19; G-I: cell cycle scoring of mesothelial cells showing a subcluster that is highly proliferative in S and G2M phases (white arrowheads). The full names of these genes are shown in **The List of Abbreviations Table.** 258

Figure 7-13. Diagram illustrating inducible induction of tdTomato reporter expression in WT1-expressing pleural mesothelial cells in Wt1-CreERT2;tdTomato reporter mice. Wt1-CreERT2$^{Cre/+}$;tdTomatotd$^{td/td}$ male mouse crossed with Wt1-CreERT2$^{+/+}$;tdTomato$^{td/td}$ female mouse yielded 50% Cre+ and 50% Cre- progeny. Tamoxifen administration induced tdTomato labelling of WT1-expressing cells in 50% of offspring expressing Cre recombinase under Wt1(mesothelial marker)-specific promotor. Upon oral gavage of tamoxifen to this model, tamoxifen bound to its binding domain of oestrogen receptor (ER), causing translocation of Cre recombinase from the cytoplasm into the nucleus, where recombination (excision) of loxP-flanked stop sequence then occurs inducing tdTomato expression. This transgenic line contained the Cre sequence under the promoter of a mesothelial marker, the Wt1 gene allowing spatiotemporal Cre-recombination and tdTomato reporter expression to occur only in pleural mesothelial cells. 259

Figure 7-14. Identification of transgenic mice (Cre-positive) and littermate controls (Cre-negative) by Cre amplification. Mice 1, 2, and 3 are positive for Cre were used as the experimental (mice with WT1-expressing cells labelled with tdTomato reporter) group.; mice 4 and 5, are negative for Cre. 260
Figure 7-15. Tamoxifen administration induced efficient tdTomato reporter expression in pleural mesothelium of the lungs of Wt1-CreERT2;tdTomato reporter mice. Nuclei were counterstained with DAPI (blue). A: whole left lobe showing endogenous tdTomato signal (magenta); B: whole left lobe stained with WT1 antibody validating the expression of WT1 (yellow) in pleural mesothelial layer; C: whole left lobe merging DAPI, WT1, tdTomato channels in one image; D: enlarged views of insets (white boxes) in A-C showing co-expression of tdTomato and WT1 in the lung visceral pleura, which is indicative of efficient Cre activity and reporter induction via tamoxifen. 261
Figure 7-16. Timeline of induction of reporter expression in Wt1-CreERT2;tdTomato reporter mice followed by the development of experimental E0771 lung metastasis model. Tamoxifen was administered via oral gavage to the Cre positive mice at indicated timepoints. Then, E0771 tumour cells were injected intravenously 2-3 weeks following tamoxifen administration. Metastatic lungs were harvested on days 13-16 for histological assessment. 262
Figure 7-17. Some WT1-derived tdTomato+ pleural mesothelial cells co-expressed tdTomato (magenta) and ACTA2 (yellow) in the subpleural region of the late metastatic niche. Nuclei were counterstained with DAPI (blue). A: non-tumour-bearing lungs showed that WT1-derived mesothelial cells located at the subpleural region; B: lung parenchyma region from E0771 metastatic lung section showed expression of ACTA2 in pulmonary artery only; C and D: pleural mesothelial cells detected in the late niche of the subpleural metastases with partial co-expression of tdTomato and ACTA2 (white arrowheads, inset 2). White arrows depict tdTomato+ cells that are negative for ACTA2 expression (inset 1). 263
Figure 7-18. Interstitial fibroblasts upregulated the expression of cancer-associated mesenchymal cells (CAMCs) markers: Fn1 (A), Tagln (B), and Saa3 (C). The full names of these genes are shown in **The List of Abbreviations Table.** 264
Figure 7-19. A few WT1-derived tdTomato+ pleural mesothelial cells co-expressed tdTomato (magenta) and FN1 (yellow) in the subpleural region of the late metastatic niche. Nuclei were counterstained with DAPI (blue). A and B: pleural mesothelial cells detected in the late niche of the subpleural metastases partially co-expressed tdTomato and FN1 (white arrowheads, inset 2). White arrows depict tdTomato+ cells that are negative for FN1 expression (inset 1); C and D: parenchymal metastases showing high expression of FN1; E and F: distal (non-tumour) lung parenchyma from the same E0771 metastatic lung section showing high expression of FN1 indicating E0771 tumour cells being able to condition the whole lung inducing secretion of FN1 matrix. 266
Figure 7-20. Violin plots depicting high expression of Fn1 in mature mesothelial cells, EBF1-positive fibroblasts, and lipofibroblasts in the early niche (A) and only in lipofibroblasts in the early distal region (B) of E0771 metastatic lungs. The full name of this gene is shown in **The List of Abbreviations Table.** 267
Figure 7-21. Violin plot depicting high expression of Fn1 in lipofibroblasts in the non-tumour lungs. The full name of this gene is shown in **The List of Abbreviations Table.** 267
Figure 7-22. Violin plots depicting high expression of Fn1 in cancer-associated mesenchymal cells (CAMCs) and interstitial fibroblasts in the late niche (A) and only in lipofibroblasts in the late distal region (B) of E0771 metastatic lungs. The full name of this gene is shown in **The List of Abbreviations Table.** 268
Figure 7-23. Wt1-derived tdTomato+ pleural mesothelial cells co-expressed tdTomato (magenta) and SAA3 (yellow) in the subpleural region of the late metastatic niche. Nuclei were counterstained with DAPI (blue). A and B: pleural mesothelial cells detected in the late niche of the subpleural metastases co-expressed tdTomato and SAA3 (white

arrowheads, inset 2). White arrows depict tdTomato+ cells that are negative for SAA3 expression (inset 1); C and D: parenchymal metastases from the same section showing high expression of SAA3; E and F: distal (non-tumour) lung parenchyma from the same E0771 metastatic lung section showing low expression of SAA3 indicating SAA3 being expressed in the metastatic niche only. 269
Figure 7-24. Violin plot depicting low expression of Saa3 across lung stromal cells in the non-tumour-bearing lungs. The full name of this gene is shown in **The List of Abbreviations Table.** 270
Figure 7-25. Violin plots depicting low expression of Saa3 across lung stromal cells and E0771 tumour cells in the early niche (A) and early distal region (B) of E0771 metastatic lungs. The full name of this gene is shown in **The List of Abbreviations Table.** 270
Figure 7-26. Violin plots depicting high expression of Saa3 in cancer-associated mesenchymal cells (CAMCs) and interstitial fibroblasts in the late niche (A) and low expression in the early distal region (B) of E0771 metastatic lungs. The full name of this gene is shown in **The List of Abbreviations Table.** 271
Figure 7-27.Immunofluorescence labelling of Wt1-derived tdTomato+ mesothelial monolayer (red) using anti-Msln antibody (yellow) revealed that cells from this monolayer migrated inward, infiltrating the subpleural (angiogenic) metastases. A: Msln signal in non-tumour-bearing lungs; B: Msln signal in subpleural metastases; C: Msln signal in subpleural metastases with many migratory Wt1-derived tdTomato+ mesothelial cells. Nuclei were counterstained with DAPI (blue). Remove tdTomato label from non-tumour lungs 273
Figure 8-1. Schematic diagram summarising the transcriptional changes occurring in the early (parenchymal/vessel co-opting) E0771 metastases (B and C) in comparison to non-tumour-bearing lungs (A). B: E0771 tumour cells grow in an alveolar growth pattern, filling the alveoli and co-opting lung vessels; C: in response to tumour colonisation, capillaries ECs in the metastatic niche and distal regions increased their OXPHOS metabolism**.** Co-opted capillary type II downregulated their tight junctions and actin cytoskeleton genes. Mature mesothelial cells were increased in the early niche, and upregulated inflammatory genes, including Il6st and Ifit3. A subset of capillary type II changed its expression profile upregulating MHC class II Ag-presenting and IFN response genes in early niche and distal regions. 282
Figure 8-2. Schematic diagram summarising the transcriptional changes occurring in the late (angiogenic and vessel co-opting) E0771 metastases (A and B) in comparison to non-tumour-bearing lungs (Figure 8-1A). A: in addition to their vessel co-opting growth inside the lung parenchyma, E0771 tumours expand and develop subpleural metastases inducing angiogenesis to sustain their progression; B: three CAMC populations, including proliferating, inflammatory-like, and hypoxia-responsive perivascular CAMCs were enriched in the late niche with an upregulation of Mki67, Saa3, and Tagln and Ca9, respectively. Hypoxia-responsive perivascular CAMCs were identified as the major source of Vegfa that mediated angiogenesis by predicted binding to the receptor Vegfr2, which was upregulated in capillary type I ECs. To meet this high proliferative demand, angiogenic (neophalanx/breach/tip and capillary type I ECs in the late niche upregulated their glycolysis metabolism. Few pleural mesothelial cells found to migrate into the intratumoural region and partially contribute to the development of subpleural metastases. Stressed ECs with high expression of Cd36, Pim3 and Cdkn1a emerged in the distal region of late-stage metastasis. 286
Figure 8-3. Gross view and FACS analysis of E0771 vessel co-opting (parenchymal) and angiogenic (subpleural) metastases. Angiogenic metastases showed angiogenic vessels at macroscopic level (yellow arrows). C57BL/6 mouse were injected with mCherry-labelling hCD2 E0771 tumour cells and lungs were harvested 13 days post-tumour injection. A and B: gross view of tumour-bearing lung lobe before and after microdissection of subpleural metastases (white arrow) from parenchymal ones (white arrowhead); C-E: hCD2-APC/Fire750 density plot to identify E0771 tumour cells (hCD2+

mCherry+) from lung stromal cells (non-labelled (hCD2- mCherry-) and labelled cells (only mCherry+). C: FACS analysis of non-tumour-bearing lungs; D and E: FACS analysis of vessel co-opting metastases-containing lung parenchyma (D) and angiogenic metastases (E)..... 288

List of Tables

Table 1-1. Molecular subtypes of breast cancer along with the recommended treatment. Breast cancer has four molecular subtypes defined by the following markers: human epidermal growth factor receptor 2 (HER2), oestrogen receptor (ER), progesterone receptor (PgR), and Ki-67 proliferation marker. 4
Table 1-2. Upregulated genes that mediate vessel co-option in primary and metastatic lung tumours. 40
Table 1-3. Upregulated genes that mediate vessel co-option in liver metastases. 44
Table 1-4. Differentially expressed genes that mediate vessel co-option in brain tumours. 49
Table 2-1. PCR forward and reverse primers were used for genotyping Pdgfb-iCreERT2; Eltd1^{fl} mice and Wt1-CreERT2;tdTomato reporter mice before tamoxifen administration. 76
Table 2-2. PCR cycling conditions for genotyping Pdgfb-iCreERT2; Eltd1^{fl} mice and Wt1-CreERT2;tdTomato reporter mice. 76
Table 2-3. Antibodies used for chromogenic immunohistochemistry (IHC) and immunofluorescence (IF) staining of mouse tissue sections. RT: room temperature 86
Table 2-4. Conditions and endpoints of murine lungs harvested for Raman metabolic profiling of stromal cells. 87
Table 2-5. Conditions and endpoints of murine lungs harvested for FACS sorting and scRNA-seq experiment. Note that healthy lungs were injected with PBS in the same manner as tumour intravenous injection to determine any effects caused by vehicle control upon comparison. 91
Table 2-6. List of FACS antibodies used for staining mouse lungs (healthy/metastatic). 93
Table 3-1. Different E0771 cell numbers injected intravenously and different endpoints for generating E0771 tumour-bearing lungs extracted from literature. 100
Table 5-1. Percentages of stromal cell types in healthy, early, late tumour-bearing mouse lungs from FACS plots. One million mCherry-labelling hCD2 E0771 tumour cells were inoculated in metastatic conditions where lungs were harvested at day 8 (in case of early timepoint) and at day 13 (in case of late timepoint). 150
Table 5-2. Steps in lung tissue digestion for FACS staining and sorting of lung stroma that required optimisation. There are two populations of interest for FACS sorting: metastatic niche and distal lung stroma. hCD2: human CD2; VE-CAD: VE-Cadherin 154
Table 5-3. Murine lung samples were used for FACS sorting of healthy and metastatic niche stromal cells for scRNA-seq analysis. Orange and green text indicates cells that were sorted from the same animals. ECs: endothelial cells. 159
Table 5-4. Differentially expressed genes (DEGs) and references of literature studies used to annotate cell types of mouse lung vasculature. The full names of these genes are shown in **The List of Abbreviations Table.** 166
Table 5-5. Upregulated and downregulated lipid-regulated genes across different EC subtypes. Pairwise comparisons were performed using a non-parametric Wilcoxon (Mann-Whitney) test. Below genes are significantly upregulated or downregulated in specific EC subtype in particular condition compared to non-tumour counterpart, unless otherwise stated between brackets against (versus (vs.)) specific condition). Genes were considered significantly upregulated or downregulated based on the threshold of

Benjamini-Hochberg adjusted p values < 0.05. Conditions matched the colours in the violin plots in **Figure 5-32.** 186
Table 5-6. Experimental details of three murine tumour models were used to isolate ECs for cell composition and transcriptional analysis. The purple column provides details from (Goveia et al., 2020); the yellow column provides details from (Teuwen et al., 2021). EC: endothelial cells; NECs: normal ECs; TEC: tumour ECs. 194
Table 5-7. EC subtypes in three murine tumour models. The purple column provides details from (Goveia et al., 2020); the yellow column provides details from (Teuwen et al., 2021). EC: endothelial cells; IFN: Interferon. Black boxes indicate the absence of a specific EC subtype in a specific tumour model. 195
Table 6-1. Differentially expressed genes (DEGs) and references of literature studies used to annotate cell types of mouse lung stroma. The full names of these genes are shown in **The List of Abbreviations Table.** 216
Table 7-1. Differentially expressed genes (DEGs) and references of literature studies used to annotate cell types of mouse lung mesenchymal cells. CAMCs: cancer-associated mesenchymal cells. The full names of these genes are shown in **The List of Abbreviations Table.** 244

List of abbreviations

Abbreviation	Description
AAT	Anti-angiogenic therapy
ACTB	Actin beta
ADGRL4	ADhesion G protein-coupled Receptors L4
ALDH1	Aldehyde dehydrogenase 1
ALDH1B1	Aldehyde dehydrogenase 1 family member B1
ANG1	Angiopoietin 1
ANG2	Angiopoietin 2
ANPEP	Alanyl aminopeptidase
AR	Anoikis resistant
ARP2/3	Actin related protein 2/3
ATP1A1	ATPase Na+/K+ transporting subunit alpha 1
BC	Breast cancer
BMDCS	Bone marrow-derived myeloid cells
BRCA	BReast CAncer genes
CAF	Cancer-associated fibroblasts
CDH1/E-CAD	E-Cadherin
CRC	Colorectal cancer
CRCLM	Colorectal cancer liver metastases
CTSD	Cathepsin D
DCIS	Ductal carcinoma in situ
DDR1	Discoidin domain receptor tyrosine kinase 1
ECS	Endothelial cells
ELTD1	Epidermal growth factor, Latrophilin and seven Transmembrane Domain
EPCAM	Epithelial cell adhesion molecule
EPCS	Endothelial progenitor cells
EPHA2	Erythropoietin-producing hepatocellular receptor A2
EFHD2	EF-hand domain family member D2
EFNB2	Ephrin B2
ER	Estrogen receptor
ESA	Epithelial specific antigen
FASN	Fatty acid synthase
FGFR2	Fibroblast growth factor receptor 2
FN1	Fibronectin 1
FOXP2	Forkhead-box P2
HCC	Hepatocellular carcinoma
HER2	Human epidermal growth factor receptor 2
HES2	Hyaluronan synthase 2
HEVS	High endothelial venules
IDC	Infiltrating ductal carcinoma
IHC	Immunohistochemistry
IFN	Interferon

KO	Knockout
LGL2	Lethal Giant Larvae Homolog 2
LHRH	Luteinising hormone releasing hormone
L1CAM	L1 cell adhesion molecule
LOX	Lysyl oxidase
LRG5	Leucine-rich repeat–containing G protein–coupled receptor 5
MHCII	Major histocompatibility complex
MIRNAS	MicroRNAs
MMP19	Matrix metallopeptidase 19
MRI	Magnetic resonance imaging
MSI1	Musashi homolog 1
NSCLC	Human non-small cell lung cancer
OS	Osteosarcoma
PD-L1	Programmed death-ligand
PGR	Progesterone receptor
PIK3CA	Phosphatidylinositol-4,5-Bisphosphate 3-Kinase Catalytic Subunit Alpha
PI3K	Phosphoinositide 3-kinase
POSTN	Periostin
PRODH	Proline dehydrogenase
ROBO1	Roundabout homolog 1
RUNX1	Runt related transcription factor-1
SERPING1	Serine proteinase inhibitor (serpin) family G member 1
SOX2	SRY-box transcription factor 2
S100A10	S100 calcium binding protein A10
SPARC	Secreted protein acidic and cysteine rich
STAT3	Signal transducer and activator of transcription 3
TF	Transcription factor
TGFB1	Transforming growth factor beta 1
TGFBRII	TGFβ1 receptor II
THBS1/TSP1	Thrombospondin-1
TIMP1	TIMP metallopeptidase inhibitor 1
TLR3	Toll-like receptor 3
TNBC	Triple-negative breast cancer
TNC	Tenascin-C
TNM	Tumour, node, metastasis (TNM) system
TME	Tumour microenvironment
TM4SF1	Transmembrane 4 L six family member 1
VEGFR1/FLT1	Vascular endothelial growth factor receptor 1/ Fms-Like Tyrosine Kinase 1
VEGFR2	Vascular endothelial growth factor receptor
ZEB1	Zinc Finger E-Box Binding Homeobox 1
ZEB2	Zinc Finger E-Box Binding Homeobox 2
ZO-1/TJP1	Zonula occludens 1/ Tight junction protein 1
ACTA2	Actin Alpha 2, Smooth Muscle
CAR9/CA9	Carbonic Anhydrase 9

CAVIN2	Caveolae associated protein 2
CENPF	Centromere protein F
CDH2/NCAD	Cadherin 2/ N-Cadherin
CLEC3B	C-type lectin domain family 3 member B
HILPDA	Hypoxia Inducible Lipid Droplet Associated
HIST1H2AE	Histone Cluster 1, H2ae
HMGB2	High mobility group box 2
KRT18	Keratin 18
KRT19	Keratin 19
MSLN	Mesothelin
PCLAF	PCNA clamp associated factor
PLXNA4	Plexin-A4
SAA3	Serum amyloid A 3
SAA1	Serum amyloid A 1
SLC2A1/GLUT1	Solute Carrier Family 2 Member 1/ Glucose Transporter Type 1
TAGLN	Transgelin
TIMP3	Tissue Inhibitor of Metalloproteinases 3
TNC	Tenascin C
TOP2A	DNA topoisomerase II alpha
UPK3B	Uroplakin IIIb
UPK1B	Uroplakin Ib
WT1	Wilms Tumour 1
TNF-A	T tumour necrosis factor alpha-like
CXCL	C-X-C motif chemokine ligand
SLPI	Secretory leukocyte peptidase inhibitor
SFRP1	Secreted frizzled related protein 1
NDRG1	N-myc downstream regulated 1
INHBA	Inhibin subunit beta A
FST	Follistatin
CK5/6	Cytokeratin5/6
ADM	Adrenomedullin
LDHA	Lactate dehydrogenase A
ENO1	Enolase 1
HMOX1	Heme oxygenase 1
STAT1	Signal transducer and activator of transcription 1
CAV1	Caveolin 1
LY6E	Lymphocyte antigen 6 family member E
PSMB10	Proteasome 20S subunit beta 10
IFIT3	Interferon induced protein with tetratricopeptide repeats 3
IL6ST	Interleukin 6 cytokine family signal transducer
IRGM1	Immunity-related GTPase family M member 1
CDH2/N-CAD	Cadherin 2/ N-Cadherin
TIMP3	TIMP metallopeptidase inhibitor 3
TAGLN	Transgelin

TNFRSF1	TNF receptor superfamily member 1A
TGFBR	Transforming growth factor beta receptor
IL10	Interleukin 10
HIST1H2A	Histone cluster 1, H2a
COL1A1	Collagen type I alpha 1 chain
COL3A1	Collagen type III alpha 1 chain
SERPING1	Serpin family G member 1
BGN	Biglycan
FSTL1	Follistatin like 1
COL13A1	Collagen type XIII alpha 1 chain
MACF1	Microtubule actin crosslinking factor 1
G0S2	G0/G1 switch 2
TCF21	Transcription factor 21
GYG	Glycogenin
PI16	Peptidase inhibitor 16
SERPINF1	Serpin family F member 1
SCARA5	Scavenger receptor class A member 5
EBF1	EBF transcription factor 1
HHIP	Hedgehog interacting protein
ASPN	Asporin
MUSTN1	Musculoskeletal, embryonic nuclear protein 1
ENNP2	Ectonucleotide pyrophosphatase/phosphodiesterase 2
WNT5A	Wnt family member 5A
DCN	Decorin
RARRES2	Retinoic acid receptor responder 2
SEC14L3	SEC14 like lipid binding 3
CCDC153	Coiled-coil domain containing 153
TPPP3	Tubulin polymerization promoting protein family member 3
SFTPC	Surfactant protein C
SFTPA1	Surfactant protein A1
SFTPB	Surfactant protein B
EGF	Epidermal growth factor
FGF	Fibroblast growth factor 2
IGF	Insulin-like growth factor 1
VEGFA	Vascular endothelial growth factor A
CSF	Colony stimulating factor
ANGPT	Angiopoietin 2
NCAM	Neural cell adhesion molecule 1
NCWNT	Non-canonical Wnt
CDH5	Cadherin 5
JAM	Junctional adhesion molecule
OCLN	Occludin
EPHB	Ephrin Type-B Receptor 4
ESAM	Endothelial cell-specific adhesion molecule

PTPRM	Protein tyrosine phosphatase receptor type M
TNFSF10/TRAIL	TNF superfamily member 10/ TNF-related apoptosis inducing ligand
PDGF	Platelet derived growth factor
PLXNA4	Plexin A4
PLXND1	Plexin D1
ITGAV	Integrin subunit alpha V
ITGB1	Integrin subunit beta 1
FZD	Frizzled
ACKR	Atypical chemokine receptor 2
MCAM	Melanoma cell adhesion molecule
PVR	Poliovirus Receptor
ENTPD1	Ectonucleoside triphosphate diphosphohydrolase 1
ADORA2B	Adenosine A2b receptor
APLN	Apelin
APLNR	Apelin receptor
CXCR4	C-X-C motif chemokine receptor 4
CALCRL	Calcitonin receptor like receptor
ADM	Adrenomedullin
VEGFR2/KDR	Vascular Endothelial Growth Factor Receptor 2/Kinase insert domain receptor
PDGFA	Platelet derived growth factor subunit A
PDGFRA	Platelet derived growth factor receptor alpha
EGFR	Epidermal growth factor receptor
ACVR1B	Activin A receptor type 1B
HBEGF	Heparin binding EGF like growth factor
AREG	Amphiregulin
TTF1	Transcription termination factor 1
CYP4B1	Cytochrome P450 family 4 subfamily B member 1
PLVAP	Plasmalemma vesicle associated protein
AMIGO2	Adhesion molecule with Ig like domain 2
BMX	BMX non-receptor tyrosine kinase
GJA5	Gap junction protein alpha 5
UCP2	Uncoupling protein 2
IFITM3	Interferon induced transmembrane protein 3
FOXF1	Forkhead box F1
UBE2C	Ubiquitin conjugating enzyme E2 C
CD300LG	CD300 molecule like family member g
RPL	Ribosomal protein L3
PDGFRB	Platelet derived growth factor receptor beta
ALOX12	Arachidonate 12-lipoxygenase, 12S type
PLEK	Pleckstrin
PPBP	Pro-platelet basic protein
NRGN	Neurogranin
KLF	KLF transcription factor
ACOT7	Acyl-CoA thioesterase 7
ACOX1	Acyl-CoA Oxidase 1

ACOX3	Acyl-CoA Oxidase 3
ACTA2	Actin alpha 2
ACTB	Actin Beta
AKT	Serine/Threonine Kinase 1
ALDH18A1	Aldehyde Dehydrogenase 18 Family Member A1
ALDOA	Aldolase A
APOE	Apolipoprotein E
ASPN	Asporin
ATF3	Activating transcription factor 3
ATP13A3	ATPase 13A3
BRK1	BRICK1 subunit of SCAR/WAVE actin nucleating complex
BT2	Butyrophilin Subfamily 2
CAR4	Carbonic anhydrase 4
CAV2	Caveolin 2
CBR2	Carbonyl reductase 2
CCDC153	Coiled-coil domain containing 153
CCL21A	CC motif chemokine ligand 21
CD81	Cluster of differentiation 81
CDH5	Cadherin 5
CDKN1A	Cyclin-dependent kinase inhibitor 1a
CD34	Cluster of differentiation 34
CD36	Cluster of differentiation 36
CD74	Cluster of differentiation 74
CEBPD	CCAAT enhancer binding protein delta
CEBPB	CCAAT enhancer binding protein beta
CENPF	Centromere protein F
CFB	Complement factor B
CHCHD10	Coiled-coil-helix-coiled-coil-helix domain containing 10
CIITA	Class II major histocompatibility complex transactivator
CLDN5	Claudin 5
CLEC14A	C-type lectin domain containing 14A
CLEC3B	C-type lectin domain family 3 member B
COL4A1	Collagen type IV alpha 1 chain
COL4A2	Collagen type IV alpha 2 chain
COL1A1	Collagen type I alpha 1 chain
COX4I2	Cytochrome c oxidase subunit 4I2
CP	Ceruloplasmin
CRIP1	Cysteine-rich protein 1
CSRNP1	Cysteine and serine-rich nuclear protein 1
CTLA2A	Cytotoxic T lymphocyte-associated protein 2 alpha
C3	Complement component C3
CTNNA1	Catenin alpha-1
CXCL10	CXC motif chemokine ligand 10
CXCL12	CXCL10 CXC motif chemokine ligand 12
CYP1A1	Cytochrome P450 family 1 subfamily A member 1

CYTL1	Cytokine like 1
DCN	Decorin
DLEU2	Deleted in lymphocytic leukemia 2
DNAJA1	DnaJ heat shock protein family (Hsp40) member A1
DNAJB1	DnaJ heat shock protein family (Hsp40) member B1
DUSP1	Dual specificity phosphatase 1
EDNRB	Endothelin receptor type B
ECM1	Extracellular matrix protein 1
EGR1	Early growth response 1
ELN	Elastin
ELOVL5	Elongase of Very-Long Fatty Acid 5
EMP2	Epithelial membrane protein 2
ENO1	Enolase 1
EPOR	Erythropoietin receptor
FABP4	Fatty acid binding protein 4
FABP5	Fatty acid binding protein 5
FADS1	Fatty acid desaturase 1
FADS2	Fatty acid desaturase 2
FIBIN	Fin Bud Initiation Factor Homolog
FN1	Fibronectin 1
FOS	FBJ osteosarcoma oncogene
FOSB	FBJ osteosarcoma oncogene B
FTH1	Ferritin heavy chain 1
FTL1	Ferritin light polypeptide 1
GAPDH	Glyceraldehyde-3-phosphate dehydrogenase
GATA1	Globin Transcription Factor 1
GBP4	Guanylate binding protein 4
GBP7	Guanylate binding protein 7
GLP1R	Glucagon-like peptide 1 receptor
GPIHBP1	Glycosylphosphatidylinositol-anchored high-density lipoprotein–binding protein 1
GPI1	Glucose-6-phosphate isomerase
GSN	Gelsolin
GSTP1	Glutathione S-transferase pi 1
GUCY1A1	Guanylate cyclase 1, soluble, alpha 1
HBA-A1	Haemoglobin alpha, adult chain 1
HBA-A2	Haemoglobin alpha, adult chain 2
HBA-X	Hemoglobin X
HBB-BH1	Haemoglobin Z, beta-like embryonic chain
HBB-Y	Hemoglobin Y
HES1	Hairy and enhancer of split-1
HHIP	Hedgehog interacting protein
HIST1H2AE	Histone Cluster 1 H2A Family Member E
HMCN1	Hemicentin 1
HMGB2	High mobility group box 2

HPGD	Hydroxyprostaglandin dehydrogenase
HSD17B12	Hydroxysteroid 17β dehydrogenase 12
HSPA8	Heat shock protein family A (Hsp70) member 8
HSPA1A	Heat shock protein family A (Hsp70) member 1A
HSPA1B	Heat shock protein family A (Hsp70) member 1B
HSPB1	Heat shock protein family B (small) member 1
HSPE1	Heat shock protein family E (Hsp10) member 1
HSPH1	Heat shock protein family H (Hsp110) member 1
HSP90AA1	Heat shock protein 90 alpha family class A member 1
HSP90AB1	Heat shock protein 90 alpha family class B member 1
H2-AA	Histocompatibility 2, class II antigen A, alpha
H2-AB1	Histocompatibility 2, class II antigen A, beta 1
H2-DMA	Histocompatibility 2, class II, locus DMa
H2-DMB1	Histocompatibility 2, class II, locus Mb1
H2-D1	Histocompatibility 2, D region locus 1
H2-EB1	Histocompatibility 2, class II antigen E beta
H2-K1	Histocompatibility 2, K1, K region
H2-M3	Histocompatibility 2, M region locus 3
H2-Q7	Histocompatibility 2, Q region locus 7
ID3	Inhibitor of DNA binding 3
IER3	Immediate early response 3
IER2	Immediate early response 2
IFI47	Interferon-gamma inducible protein 47
IFNAR1	Interferon alpha and beta receptor subunit 1
IFNAR2	Interferon alpha and beta receptor subunit 2
IFNGR1	Interferon-gamma receptor 1
IFNGR2	Interferon-gamma receptor 2
IGFBP	Insulin-like growth factor binding protein
IGTP	Interferon-gamma induced GTPase
IFI44	Interferon-induced protein 44
IFIT3	Interferon-induced protein 3
INHBB	Inhibin subunit beta B
INMT	Indolethylamine N-methyltransferase
IRF1	Interferon regulatory factor 1
IRF7	Interferon regulatory factor 7
ISG15	Interferon-stimulated
ITGA1	Integrin subunit alpha 1
ITM2B	Integral membrane protein 2B
JUN	Jun proto-oncogene, AP-1 transcription factor subunit
JUNB	Junb proto-oncogene, AP-1 transcription factor subunit
JUND	Jund proto-oncogene, AP-1 transcription factor subunit
KDR	Kinase insert domain receptor
KIT	KIT proto-oncogene, receptor tyrosine kinase
KITL	Kit ligand
LDHA	Lactate dehydrogenase A

IIGP1	Interferon inducible GTPase 1
LPL	Lipoprotein lipase
LTBP4	Latent transforming growth factor beta binding protein 4
LYVE1	Lymphatic vessel endothelial hyaluronan receptor 1
LYZ2	Lysozyme 2
MACF1	Microtubule actin crosslinking factor 1
MAF	MAF bZIP transcription factor
MALAT1	Metastasis-associated lung adenocarcinoma transcript 1
MEST	Mesoderm specific transcript
MFAP4	Microfibril-associated protein 4
MGLL	Monoglyceride lipase
MGP	Matrix Gla protein
MKI67	Marker of proliferation Ki-67
MMP9	Matrix metalloproteinase 9
MT.ATP6	ATP synthase F0 subunit
MT1	Metallothionein 1
MT.CO1	Cytochrome c oxidase I
MT.CO2	Cytochrome c oxidase II
MT.CYTB	Cytochrome b
MT.ND5	NADH dehydrogenase subunit 5
MT.ND4	NADH dehydrogenase subunit 4
MT.ND4L	NADH dehydrogenase subunit 4L
MT.ND3	NADH dehydrogenase subunit 3
MUSTN1	Musculoskeletal, embryonic nuclear protein 1
MYH9	Myosin heavy chain 9
NFKBIA	NFKB inhibitor alpha
NPNT	Nephronectin
NR4A1	Nuclear receptor subfamily 4 group A member 1
NRGN	Neurogranin
NRP2	Neuropilin 2
PCDH1	Protocadherin 1
PDE5A	Phosphodiesterase 5A
PDZD2	PDZ domain containing 2
PECAM1/CD31	Platelet endothelial cell adhesion molecule 1
PF4	Platelet factor 4
PFKFB3	6-phosphofructo-2-kinase/fructose-2,6-biphosphatase 3
PGK1	Phosphoglycerate kinase 1
PI16	peptidase inhibitor 16
PIM3	Proto-oncogene, serine/threonine kinase
PI3K	Phosphoinositide 3-kinases
PKM	Pyruvate Kinase M1/2
PLIN2	Perilipin 2
PLTP	Phospholipid transfer protein
POSTN	Periostin

PPARA	Peroxisome proliferator-activated receptor alpha
PPARG	Peroxisome proliferator-activated receptor gamma
PPBP	Pro-platelet basic protein
PPP1R15A	Protein phosphatase 1 regulatory subunit 15A
PROX1	Prospero homeobox 1
PRSS23	Prss23
PRX	Periaxin
PTPRB	Protein tyrosine phosphatase receptor type B
RAP1B	RAP1B, member of RAS oncogene family
RARRES2	Retinoic acid receptor responder 2
RDX	Radixin
RGS2	Regulator of G protein signalling 2
RHEB	Ras homolog, mTORC1 binding
RHOA	Ras homolog family member A
RPS29	Ribosomal protein S29
RPS12	Ribosomal protein S12
RSAD2	Radical S-adenosyl methionine domain containing 2
SAA3	Serum amyloid A 3
SAMD5	Sterile alpha motif domain containing 5
SAP18	Sin3A-associated protein 18
SCGB1A1	Secretoglobin family 1A member 1
SCP2	Sterol carrier protein 2
SEC14L3	SEC14-like lipid binding 3
SEMA	Sema domain, immunoglobulin domain (Ig), short basic domain, secreted, (semaphorin)
SERPIN2	Serine protease inhibitor 2
SERTAD1	SERTA domain containing 1
SFTPA1	Surfactant protein A1
SFTPB	Surfactant protein B
SFTPC	Surfactant protein C
SLC6A2	Solute carrier family 6 member 2
SLPI	Secretory leukocyte peptidase inhibitor
SOCS3	SUPPRESSOR of cytokine signaling 3
S100A4	S100 calcium-binding protein A4
S100A6	S100 calcium-binding protein A6
SOX17	SRY (sex determining region Y)-box transcription factor 17
SPARC	Secreted protein acidic and cysteine-rich
SPARCL1	Secreted protein acidic and cysteine-rich like 1
SREBF1	Sterol regulatory element binding transcription factor 1
SRGN	Serglycin
SQLE	Squalene monooxygenase
TAGLN	Transgelin
TIMP1	TIMP metallopeptidase inhibitor 1
TJP1/ ZO-1	Tight junction protein 1/ Zona occludens 1
TOP2A	DNA topoisomerase II alpha

TPT1	Tumour protein, translationally-controlled 1
TMEM252	Transmembrane protein 252
TMSB4X	Thymosin beta 4 X-linked
TMSB10	Thymosin beta 10
TPI1	Triosephosphate isomerase 1
TPPP3	Tubulin polymerisation promoting protein family member 3
TRA2A	Transformer 2 alpha homolog
TRP53I11	Transformation related protein 53 inducible protein 11
TSC22D1	TSC22 domain family member 1
TSC22D3	TSC22 domain family member 3
TTF1	Transcription termination factor 1
UBC	Ubc
UPK3B	Uroplakin 3B
VCAM1	Vascular cell adhesion molecule 1
VE-CAD	VE-Cadherin
VWF	Von Willebrand factor
ZFP36	ZFP36 ring finger protein

Table of Contents

Chapter 1: Introduction 1

1.1 Breast Cancer 2
1.1.1 Symptoms and diagnosis of breast cancer. 2
1.1.2 Stages, grades, and molecular subtypes of breast cancer. 2
1.1.3 Treatment of breast cancer. 5

1.2 Cancer Metastasis 8

1.3 Insights and key players in (pre-) metastatic niche formation and progression in the lungs 9
1.3.1 Recruitment of BMDCs for priming the lungs (metastatic organ) 10
1.3.2 Formation of pre-metastatic niche triggered by tumour-derived or stromal-derived EVs 11
1.3.3 The role of matrix deposition and stiffness in (pre-) metastatic niche formation 13
1.3.4 Metabolic dysregulation of the metastatic niche 14
1.3.5 Development of an immunosuppressive metastatic niche 15
1.3.6 Epithelial-mesenchymal transition (EMT) and mesenchymal-to-epithelial transition (MET) in metastatic dissemination and progression 18
1.3.7 Stemness of disseminated tumour cells (DTCs) (Stemness and plasticity of metastatic breast cancer) 19
1.3.8 Therapeutic strategies to target the metastatic niche 20

1.4 Vascular remodelling in metastasis 22

1.5 Mechanisms of Tumour Vascularisation 24
1.5.1 Neoangiogenesis (sprouting angiogenesis). 24
1.5.2 Intussusceptive angiogenesis (IA). 27
1.5.3 Vasculogenesis 29
1.5.4 Vasculogenic mimicry (VM) 31
1.5.5 Vessel co-option in cancer. 34

1.6 Vessel co-option signalling in common organs. 35
1.6.1 Mechanisms of tumour co-option of lung capillaries. 35
1.6.2 Mechanisms of tumour co-option of liver vessels. 41
1.6.3 Mechanisms of tumour co-option of brain vessels. 46

1.7 Current understanding of vascular switch between angiogenesis and vessel co-option 50

1.8 Insights into crucial players mediating tumour response to anti-angiogenic therapies 53
1.8.1 Vessel co-opting tumours exhibit intrinsic and acquired resistance to anti-angiogenic therapies 53
1.8.2 A single tumour cell line can vascularise using multiple methods 54
1.8.3 Contribution of the pulmonary and bronchial circulation to heterogeneous vascularisation in lung tumours 55
1.8.4 The maturity of tumour vessels can mediate tumour response to anti-angiogenic therapies 56
1.8.5 The potential role of immune cells in tumour response to anti-angiogenic therapies ... 58

1.9 Thesis Aims 60

Chapter 2: Materials and Methods 62

2.1 Cell lines and primary cells 62
2.1.1 HUVECs 62
2.1.2 Parental E0771 tumour cell line 62
2.1.3 The tdTomato transduced E0771 tumour cell 62
2.1.4 The EGFP-LUC transduced E0771 tumour cell 63
2.1.5 The mCherry-labelling hCD2 transduced E0771 tumour cell 65

2.1.6 Mycoplasma testing 66
2.1.7 Isolation of primary pleural mesothelial cells 66

2.2 In vitro assays 68
2.2.1 Transwell proliferation assay (indirect co-culture) 68
2.2.2 Transwell invasion assays (indirect co-culture) 69
2.2.3 Direct co-culture assay 71
2.2.4 Indirect co-culture assay 71

2.3 Transgenic mice model and mouse strains 73
2.3.1 Mice breeding and maintenance 73
2.3.2 Mouse strains: 73
2.3.2.1 Inducible endothelial cell-specific Eltd1 knockout mice 73
2.3.2.2 Inducible Wt1-CreERT2; tdTomato reporter mice 74
2.3.3 Tamoxifen preparation and administration 75
2.3.4 Genotyping 75
2.3.5 Generation of murine experimental lung metastases model 77
2.3.6 Generation of experimental lung metastasis therapy model 77

2.4 Histological analysis: 78
2.4.1 Formalin Fixed Paraffin Embedded (FFPE) murine tissues 78
2.4.1.1 Tissue fixation, paraffin tissue processing and embedding 78
2.4.1.2 Tissue deparaffinisation, rehydration and antigen retrieval 78
2.4.1.3 Haematoxylin and eosin (H&E) staining of tissue sections 79
2.4.1.4 VVG Elastic staining of tissue sections 79
2.4.1.5 Immunohistochemistry staining 80
2.4.1.6 Immunofluorescence staining of FFPE sections 80
2.4.2 Frozen Murine sections (cryosections) 81
2.4.2.1 Tissue preparation 81
2.4.2.2 Immunofluorescence staining of frozen sections (cryosections) 81
2.4.3 Quantification and statistical analysis 87
2.4.4 Tissue preparation for Raman spectroscopy 87

2.5 MRI imaging and image analysis 89

2.6 Tissue preparation for single-cell RNA sequencing (scRNA-seq): 91
2.6.1 Digestion of murine lungs and depletion of CD45-positive cells 91
2.6.2 FACS staining, FACS panel design, and FACS cell sorting of lung stromal cells 92
2.6.3 Cell preparation and scRNA-sequencing: 93

2.7 Bioinformatics analysis 95
2.7.1 Pathway Enrichment Analysis 96
2.7.2 Cell-cell communication inference analysis 97

2.8 Statistical analysis 98

Chapter 3: Generation and characterization of a syngeneic murine triple-negative breast cancer lung metastasis model 99

3.1 Introduction 99

3.2 Optimisation of E0771 cell number and growth time for tumour model 99

3.3 Metastatic growth pattern in the E0771 breast cancer lung metastasis model 101
3.3.1 Lentiviral transduction of parental E0771 tumour cells to generate EGFP LUC-labelled E0771 tumour cells 101
3.3.2 Establishing the growth pattern of E0771 tumour cells 104

3.4 Lung metastases of E0771 tumour-bearing mice exhibit both angiogenic and non-angiogenic vascular patterns (vessel co-option) 107

3.5 Histological discrimination of angiogenic and non-angiogenic blood vessels recruited by E0771 TNBC in the lungs *110*

3.6 Discussion *113*

Chapter 4: Genetic and pharmacological targeting of angiogenic blood vessels in the E0771 lung metastasis model **116**

4.1 Introduction *116*

4.2 Investigating the effect of inducible deletion of the endothelial angiogenic gene, Eltd1 on the in vivo growth of E0771 subpleural metastases *116*

4.2.1 Validation of *Eltd1* deletion 117

4.2.2 Deletion of an angiogenic gene *Eltd1* did not affect tumour burden or reduce the thickness of subpleural metastases 120

4.3 Investigating the effect of the anti-angiogenic drug pazopanib on E0771 subpleural metastases *127*

4.3.1 Pharmacological inhibition of angiogenic ECs in the E0771 lung metastases model reduces the thickness of subpleural metastases 127

4.4 Discussion *131*

Chapter 5: Single-cell transcriptional analysis of metastatic niche lung endothelium using mCherry niche-labelling technology **136**

5.1 Introduction *136*

5.2 In vitro validation of mCherry niche-labelling system *138*

5.2.1 Niche-labelling validation via direct co-culture of non-labelled HUVECs with mCherry-labelling hCD2 E0771 cells 138

5.2.2 Niche-labelling validation via indirect co-culture of non-labelled HUVECs in medium conditioned by mCherry-labelling hCD2 E0771 cells 138

5.3 In-vivo validation of mCherry niche-labelling system *141*

5.3.1 Spatial identification of metastatic niche cells in lungs of mCherry-labelling hCD2 E0771 tumour-bearing mice 141

5.3.2 FACS gating strategy for spatial isolation of metastatic niche stroma (hCD2-mCherry+) 143

5.4 Temporal and spatial single-cell transcriptome analysis of healthy, niche (mCherry+), and distal stroma during metastases evolution *155*

5.4.1 Investigating the endothelial phenotype in early and late E0771 lung metastasis 161

5.4.1.1 EC remodelling in early (co-opting) E0771 metastases 167

5.4.1.2 Transcriptomic gene signature of co-opted capillaries in the early metastatic niche 174

5.4.1.3 EC remodelling in late metastatic lungs 179

5.4.1.4 Remodelling of lipid metabolism in different EC subtypes in early and late E0771 niches 185

5.4.2 Preliminary investigation of metabolic profiles of non-tumour, early, and late metastatic lung stroma using Raman spectroscopy 190

5.4.3 The composition of EC subtypes in different mouse lung tumour models 193

5.5 Discussion *197*

Chapter 6: Investigating the single-cell transcriptome and cell signalling between metastatic niche lung stromal cells and E0771 tumour cells **208**

6.1 Introduction *208*

6.2 Heterogeneity in stromal cells driving the evolution from E0771 micrometastases to established metastases *209*

6.3 Molecular interactions between tumour and lung stromal cells mediating E0771 metastatic growth 218
6.3.1 The predicted intercellular communications occurring in E0771 metastases 223
6.4 Discussion 234

Chapter 7: Investigating the role of metastatic niche mesothelial and mesenchymal cells in metastatic progression 239

7.1 Introduction 239
7.2 Identification of cancer-associated mesenchymal subtypes in the late metastatic niche 240
7.3 Histological evaluation of mesothelial cells in E0771 metastatic lungs 246
7.3.1 Validation of the spatial localisation of mesothelial cells and spatial discrimination from tumour cells 246
7.3.2 Examination of surface pleural mesothelial layer disruption during the invasion of metastatic E0771 breast cancer 249
7.4 In vitro study of the effect of pulmonary mesothelial cells on metastatic E0771 breast cancer cells 251
7.5 Investigating the origin and pathways enriched in cancer-associated mesenchymal cells 253
7.6 In vivo lineage tracing the origin of cancer-associated mesenchymal cells enriched in the late metastatic niche 259
7.6.1 Tamoxifen induction of tdTomato expression in WT1-expressing cells in healthy lungs 260
7.6.2 Generation of an *in vivo* Wt1-CreERT2 tdTomato reporter metastasis model 262
7.6.3 Partial contribution of pleural mesothelial cells to the development of subpleural angiogenic metastases 263
7.7 Discussion 274

Chapter 8: Final Discussion 278

References 290

Appendices 321

Chapter 1: Introduction

Graphical abstract

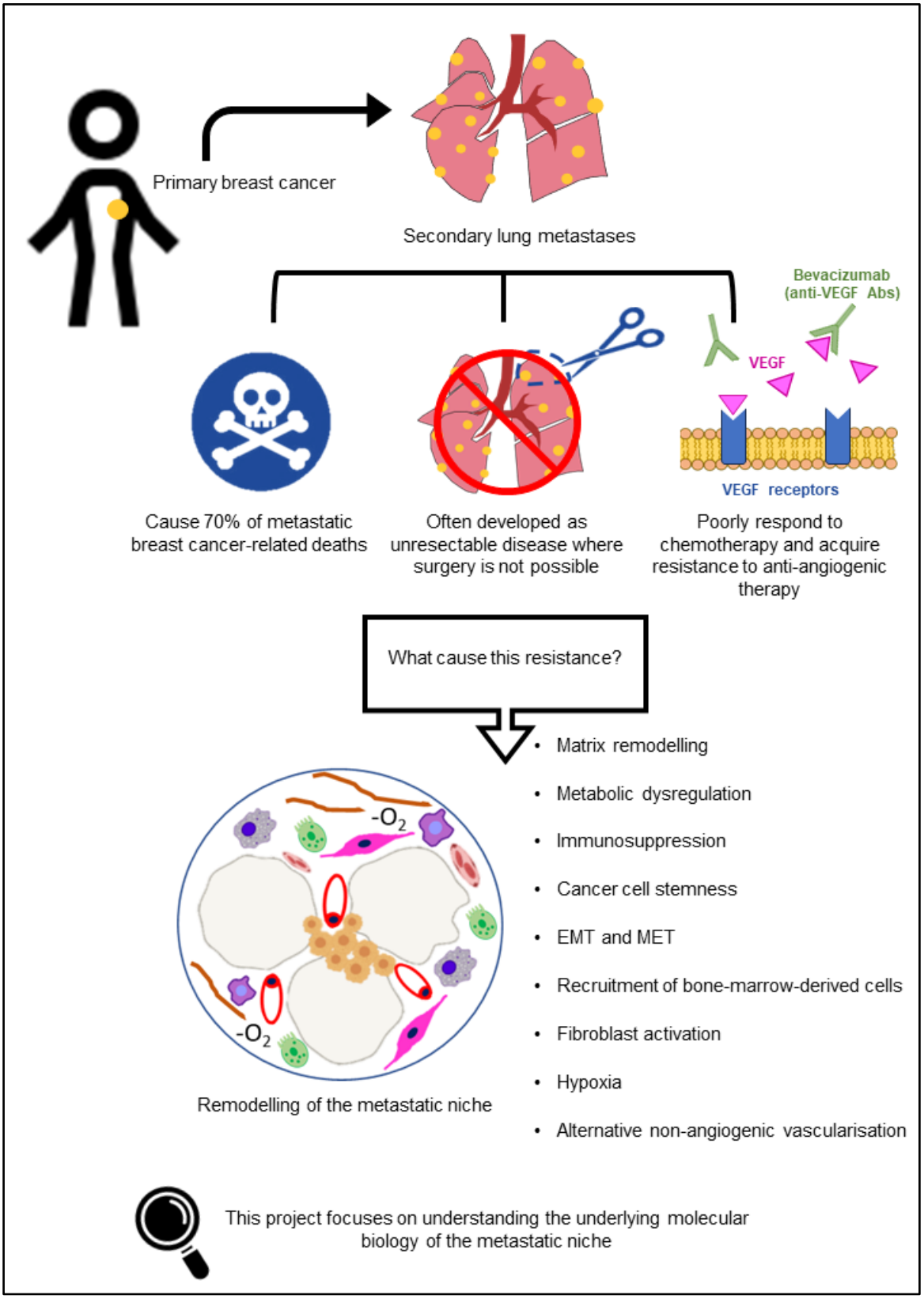

1.1 Breast Cancer

Breast cancer is the most common cancer in females and the second most frequent cause of cancer-related deaths in females worldwide (Bray et al., 2018). Globally, the estimated number of women with breast cancer in 2020 was 2.3 million, and 685,000 breast cancer-related deaths were recorded (World Health Organization, 2023).

1.1.1 Symptoms and diagnosis of breast cancer.

Breast cancer is manifested as a lump or mass in the breast, occasionally accompanied by swelling of lymph nodes in the armpit (Waks & Winer, 2019). Moreover, signs of breast cancer include changes in the shape or colour of the skin, changes in the size of the breast, nipple retraction, or nipple discharge (Senkus et al., 2015; Waks & Winer, 2019). Upon regular breast cancer screening, or if any symptoms of breast cancer appear, triple tests are used to diagnose this cancer (Harbeck et al., 2019). These tests include clinical examination of the breasts and the axillary lymph nodes, mammography or ultrasonography, and needle biopsy (Harbeck et al., 2019). In addition, patient history and menopausal status are considered for assessment (Senkus et al., 2015). Needle biopsy is usually only performed if breast cancer is suspected from the mammogram, with the tissue biopsy microscopically examined by a pathologist (Harbeck et al., 2019). Magnetic resonance imaging (MRI) can also be used to diagnose breast cancer where the routine screening tests are inconclusive or to diagnose hereditary or lobular breast cancers (Harbeck et al., 2019).

1.1.2 Stages, grades, and molecular subtypes of breast cancer.

Tests to determine the grade and stage of breast cancer include examination of the histopathology and investigating the extent of breast cancer spread and metastasis (Harbeck et al., 2019; Malhotra et al., 2010). Based on the invasiveness, breast cancer is classified as *in situ* (non-invasive) or infiltrating (invasive) breast cancer (Malhotra et al., 2010). Histologically, both *in situ* and invasive breast carcinoma are further divided into ductal and lobular carcinoma (Malhotra et al., 2010). Infiltrating ductal carcinoma is the most common breast cancer, accounting for 70-80% (Harbeck et al., 2019; Malhotra et al., 2010).

Treatment plans for patients with breast cancer require information regarding molecular subtype, histological grade (the morphology of cancer cells under a microscope), pathological stage (whether breast cancer has spread), tumour size and number, and involvement of lymph nodes (Harbeck et al., 2019). The Elston- and Ellis-modified Scarff–Bloom–Richardson grading system classifies invasive breast cancers into three histological grades: grade I, grade II, and grade III (Elston & Ellis, 1991). This grading system is generated by the sum score of the following: 1- scoring cancer cells with tubular shape (differentiated cells), 2- scoring the nuclear pleomorphism, and 3- scoring the mitosis at the tumour periphery (Elston & Ellis, 1991). The grade of the tumour is associated with the patient's prognosis, with a higher grade predicting a worse outcome (Elston & Ellis, 1991). The Tumour, Node, Metastasis (TNM) system, published by the American Joint Committee on Cancer (AJCC) and the Union for International Cancer Control (UICC), instead classifies breast cancer into five stages, 0, I, II, III, or IV (Harbeck et al., 2019; Senkus et al., 2015). TNM staging includes an assessment of the size of the primary tumour (T), the number of affected lymph nodes (N), and whether the cancer has metastasised into distant sites or not (M) (Senkus et al., 2015).

According to distinctive gene expression profiles, breast cancer can also be divided into four molecular subtypes: luminal A, luminal B, human epidermal growth factor receptor 2 (HER2)-overexpressed, and triple receptor negative **(Table 1-1)** (Hu et al., 2006; Perou et al., 2000; Sørlie et al., 2001). Most of the triple receptor-negative subtype has a particularly poor prognosis and is basal-like (Masuda et al., 2013; Rakha et al., 2009). As shown in **Table 1-1**, molecular testing of *HER2* expression, and immunohistochemistry (IHC) analysis of oestrogen receptor, progesterone receptor, HER2, and the proliferation marker Ki-67 can help identify the molecular subtype of breast cancer (Coates et al., 2015). It can also discriminate patients for better treatment strategies (Coates et al., 2015). In addition to molecular subtypes, biomarkers such as the immune inhibitory ligand CD274 (PD-L1), *BRCA* and *PI3K* catalytic subunit (PIK3CA) mutations are approved for tailoring treatment decisions when treating breast cancer (Harbeck et al., 2019).

Table 1-1. Molecular subtypes of breast cancer along with the recommended treatment. *Breast cancer has four molecular subtypes defined by the following markers: human epidermal growth factor receptor 2 (HER2), oestrogen receptor (ER), progesterone receptor (PgR), and Ki-67 proliferation marker.*

Molecular subtype	HER2: +/-	ER: +/-	PgR: high/low	Ki-67: high/low	Percentage of breast cancer cases	Systemic therapy, either in neoadjuvant or adjuvant approaches
Luminal A	-	+	High	Low	50-60% (Yersal & Barutca, 2014)	- Endocrine therapy (tamoxifen and aromatase inhibitors) - Chemotherapy - Ovarian suppression
Luminal B: first subclass	-	+	Either	high	15-20% (Yersal & Barutca, 2014)	
Luminal B: second subclass	+	+	Either	Either		
HER2-overexpressed	+	Either	Either	High (Nishimura et al., 2010)	15-20% (Yersal & Barutca, 2014)	- Trastuzumab targeted therapy - Chemotherapy - Trastuzumab conjugated with emtansine (T-DM1)
Triple-negative/basal-like	-	-	-	High (Nishimura et al., 2010)	15-20% (Masuda et al., 2013)	- Chemotherapy - Platinum - Capecitabine

1.1.3 Treatment of breast cancer.

In the case of local breast cancer with no metastasis, surgical removal of the cancer tissue and axillary lymph nodes is performed, followed by localised radiotherapy (Senkus et al., 2015). Depending on the molecular subtype, systemic therapy **(summarised in Table 1-1)** is given either prior to or post-surgery. In this instance, these therapies are termed neoadjuvant therapy or adjuvant therapy, respectively (Senkus et al., 2015).

According to menopausal status, patients with hormone receptor-positive breast cancer usually take specific endocrine therapies, which can block the oestrogen receptor's ability to bind oestrogen or inhibit the production of oestrogen **(Table 1-1)** (Suijkerbuijk et al., 2016; Waks & Winer, 2019). In pre- and post-menopausal patients, tamoxifen hormonal therapy is given, as this drug binds to oestrogen receptors expressed on cancer cells, inhibiting their oestrogen binding and therefore reducing cancer growth (Waks & Winer, 2019). The risk of cancer recurrence upon tamoxifen administration within five years is reduced by 50% (Early Breast Cancer Trialists' Collaborative Group et al., 2011). Aromatase inhibitors, another hormonal therapy for post-menopausal early and metastatic patients, have a different mechanism of action (Rugo et al., 2016; Smith & Dowsett, 2003). These drugs inhibit the action of the enzyme aromatase, which can convert androgen into oestrogen, reducing the amount of circulating oestrogen (Rugo et al., 2016; Smith & Dowsett, 2003). For pre-menopausal patients with local or advanced hormone receptor-positive breast cancer, tamoxifen or an aromatase inhibitor combined with an ovarian ablation drug known as luteinising hormone-releasing hormone is recommended (Francis et al., 2018; Rugo et al., 2016). This treatment strategy improved disease-free and overall survival at eight years for breast cancer patients with localised tumours (Francis et al., 2018; Rugo et al., 2016).

Compared to no chemotherapy, high-risk hormone receptor-positive breast cancer patients benefit from endocrine therapy and adjuvant chemotherapy (Early Breast Cancer Trialists' Collaborative Group et al., 2012). Examples of recommended chemotherapy agents include CDK4/6 inhibitors (palbociclib, ribociclib and abemaciclib) and mechanistic target of

rapamycin (mTOR) inhibitors (everolimus) (Harbeck et al., 2019). These drugs hinder cancer proliferation where resistance to endocrine therapy develops and provide chemotherapy in case of visceral crisis (Harbeck et al., 2019).

HER2-positive breast cancer patients are recommended to take the monoclonal anti-HER2 antibody Trastuzumab (Herceptin), which blocks receptor signalling **(Table 1-1)** (Brenner & Adams, 1999). Trastuzumab can be given to early and locally advanced HER2-positive breast cancer in a neoadjuvant setting along with pertuzumab and docetaxel, or in an adjuvant setting along with pertuzumab (another monoclonal antibody that inhibits HER2 dimerisation) and chemotherapy for one year (Gianni et al., 2016; Von Minckwitz et al., 2017). However, if HER2-positive patients have no tumour metastasis to the regional lymph nodes, it is recommended that they take the standard therapy, trastuzumab and paclitaxel (Tolaney et al., 2017). For those who do not achieve a pathological complete response after receiving neoadjuvant chemotherapy plus trastuzumab, the phase 3 KATHERINE trial showed that taking trastuzumab conjugated with the microtubule inhibitor, emtansine (T-DM1) significantly improved invasive disease–free survival and caused a 50% reduction in the number of deaths in comparison to patients who received trastuzumab only (Von Minckwitz et al., 2019).

Patients with triple-negative breast cancer (TNBC) are not suitable for hormonal therapy and primarily receive chemotherapy composed of an anthracycline and a taxane given using the neoadjuvant approach (Telli, 2016; Waks & Winer, 2019). Adding platinum-based chemotherapy to the neoadjuvant chemotherapy for patients with TNBC reported a higher pathological complete response **(Table 1-1)** (Hahnen et al., 2017). In cases where TNBC patients do not attain a pathological complete response, administering capecitabine as an adjuvant therapy increases disease-free and overall survival (Masuda et al., 2017). If patients have advanced TNBC with germline *BRCA* mutation, a PARP inhibitor (olaparib or talazoparib) is recommended (Litton et al., 2018; Robson et al., 2017). Additionally, advanced TNBC patients with positive expression of PD-L1 on ≥1% of the infiltrating immune cells can receive

nab-paclitaxel and atezolizumab, which is reported to significantly increase progression-free survival (Schmid et al., 2018).

1.2 Cancer Metastasis

Cancer metastasis occurs when tumour cells disseminate from the primary tumour site and invade secondary organs (Obenauf & Massagué, 2015). Death caused by cancer metastasis accounts for 90% of cancer deaths (Valastyan & Weinberg, 2011). The lung, brain, liver and bone are the most frequent organs where metastasis occurs (Obenauf & Massagué, 2015). In 1889, the surgeon Stephen Paget proposed the “seed and soil” principle as a mechanism of metastasis, in which cancer cells dissociate from the primary organ exemplifying the seeds circulate within the body and become non-randomly planted in the microenvironment “soil” of secondary tissues (Paget, 1889).

For tumours to metastasise, cancer cells undergo a complicated process known as the metastatic cascade (Valastyan & Weinberg, 2011). First, tumour cells detach from the initial site and break down the surrounding extracellular matrix (Valastyan & Weinberg, 2011). Then they intravasate blood or lymphatic vessels and migrate in the circulatory system as a single or cluster of tumour cells (Peter & Katarina, 2003). In the circulation, platelets, immune cells such as macrophages, and stromal cells reinforce and coat these circulating tumour cells, forming an embolism (Duda et al., 2010; Gay & Felding-Habermann, 2011; Smith & Kang, 2013). It has been found that only 1.5% of circulating cancer cells manage to survive and metastasise (Fidler, 1970). Depending on the type of the tumour, tumour cell plasticity, the diameter of blood vessels, mechanical force (blood flow), and the microenvironment of distant organs, these surviving tumour cells are trapped in vascular beds or areas with low blood flow and extravasate into the secondary loci (Follain et al., 2018; Valastyan & Weinberg, 2011). Once lodged, these cancer cells start to form a micrometastases (Valastyan & Weinberg, 2011). At this stage, individual cancer cells and micrometastases either undergo dormancy or proliferate to develop a macrometastasis, where a microenvironment that is compatible with the primary site is already established (Valastyan & Weinberg, 2011).

Different types of cancers preferentially metastasise to specific organs, a phenomenon known as metastasis tropism (Obenauf & Massagué, 2015). Malignancies originating from

breast, colorectal, pancreatic, renal cancers, and melanoma have been reported to frequently metastasise to the lungs (Stella et al., 2019). Indeed, lung metastasis is responsible for around 70% of breast cancer metastases-related deaths (Jin et al., 2018). Even when treated with chemotherapy, hormonal therapy, and/or targeted therapy, patients with breast cancer lung metastasis still have a poor prognosis (Jin et al., 2018). For example, a recent study by Xiao and colleagues showed that patients with breast cancer lung metastases have a median survival of only 21 months and that TNBC patients have more lung metastases and a shorter survival time of 11 months (Xiao et al., 2018). TNBC, as described above, lacks oestrogen receptors, progesterone receptors, and overexpression of HER2 receptors, and represents approximately 20% of breast cancers (Wahba & El-Hadaad, 2015). TNBC is an aggressive cancer associated with poor prognosis (Reis-Filho & Tutt, 2008). Not only is this subtype associated with more metastases in the lung, but treating it is challenging in clinical practice owing to its heterogeneity (Lee & Djamgoz, 2018; Lehmann et al., 2016). TNBC can further be categorised into four subgroups: basal-like 1; basal-like 2; luminal androgen receptor (LAR); and mesenchymal (M) (Lee & Djamgoz, 2018; Lehmann et al., 2016).

1.3 Insights and key players in (pre-) metastatic niche formation and progression in the lungs

Colonisation of the lung by circulating cancer cells is a complicated process that requires communication between cancer cells with the lung parenchymal (the stromal) microenvironment encompassing cellular and non-cellular components (Valastyan & Weinberg, 2011). The crosstalk can occur both at the site of metastasis (known as the metastatic niche), and prior to metastatic colonisation through endocrine signalling from the primary cancer cells, leading to the development of the pre-metastatic niche (Maru, 2015). To establish pre-metastatic niches, primary cancer cells recruit a variety of cells via secreting growth factors, cytokines, extracellular matrix protein (ECM) proteins, and exosomes, aiming to convert the secondary organ microenvironment into a welcoming place for cancer cells (Descot & Oskarsson, 2013). The pre-metastatic and metastatic niches induce changes and remodelling in the microenvironment of lung parenchyma (Maru, 2015). These changes, which

will be described in more detail below, include but are not limited to the mobilisation of bone marrow-derived cells (BMDCs) to the lung, deposition and stiffness of ECM, metabolic reprogramming, recruitment of immune cells, remodelling of niche vasculature, and enhancement of tumour cells stemness and plasticity (Celia-Terrassa & Kang, 2018).

Hypoxia has been found to provoke primary cancer cells to secrete and respond to a variety of signalling molecules such as cytokines, growth factors and extracellular vesicles (EVs) (Altorki et al., 2019; Chafe et al., 2015; Psaila & Lyden, 2009). These molecules provoke both endothelial cells and myeloid cells to express the inflammatory cytokines S100A8 and S100A9 in the lung, which in turn recruit macrophages and primary tumour cells into the lung (Hiratsuka et al., 2006). Aberrant expression of transforming growth factor beta (TGFβ) in breast cancer has also been shown to stimulate expression of vascular endothelial growth factor A (VEGFA) and angiopoietin-2 (ANGPT2/ANG2) in addition to S100A8 and S100A9, leading to an increase in vascular permeability and subsequently enhanced seeding of tumour cells in the lung (Ye et al., 2015).

1.3.1 Recruitment of BMDCs for priming the lungs (metastatic organ)

Under the influence of molecules derived from the primary tumour, bone marrow-derived myeloid cells prime the distant microenvironment and transform it into a pre-metastatic niche (Chafe et al., 2015; Kaplan et al., 2005). In a preclinical mouse model, upregulated expression of the hypoxia marker carbonic anhydrase 9 (CA9) in 4T1 TNBC metastatic breast cells was shown to induce recruitment of myeloid-derived suppressor cells (MDSC) to the lungs forming the metastatic niche (Chafe et al., 2015). Lungs of mice bearing hypoxic human breast cancer cells (HIF-1-expressing MDA-MB-231 and MDA-MB-435) recruited more BMDCs than lungs of mice bearing HIF-1-knockdown counterpart cancer cells (Wong et al., 2011). In other metastasis models of B16 melanoma and Lewis lung carcinoma (LLC)-bearing mice, tumour induced-BMDCs expressing VEGFR1+ also home to the lungs, forming pre-metastatic clusters and increasing metastasis propensity (Kaplan et al., 2005). At these secondary sites, these VEGFR1+ BMDCs express VLA-4 (integrin α4β1, a fibronectin

receptor), which binds to fibronectin allowing for matrix metalloproteinase 9 (MMP) 9 and Inhibitor of DNA Binding 3 (ID3) production (Kaplan et al., 2005). MMP9 and ID3 remodel the lungs into an adhesive environment and destroy the basement membrane to facilitate the mobilisation of metastatic tumour cells (Kaplan et al., 2005). In the preclinical metastatic melanoma mouse model, 4T1 breast cancer and human melanoma cells were found to overexpress the protease receptor Tissue Factor (also known as coagulation factor III or CD142), which promotes platelet clot formation around arrested tumour cells in the lungs. These tumour-associated clots attract myeloid cells to the metastatic site, which in turn enhances tumour survival and assists in forming the pre-metastatic niche (Gil-Bernabé et al., 2012). Breast cancer cells and lung stroma were found to secrete the Chemokine Ligand 2 (CCL2), which induces preferential recruitment of inflammatory monocytes and differentiation into metastasis-associated macrophages (MAMs) in the lungs. These monocytes enhanced metastatic seeding, VEGFA-mediated tumour extravasation, and expansion of pulmonary metastases (Qian et al., 2011). Unlike non-metastatic primary mammary carcinoma cells, metastatic breast cancer cells (including 66c14, 4T1, MMTV-PyMT, and human MDA-MB-231) can trigger the mobilisation of granulocytes from the bone marrow to distant organs via granulocyte-colony stimulating factor (G-CSF). These granulocytes thereafter upregulate the expression and secretion of the chemoattractant, BV8, in pre-metastatic lungs, which chemoattract more of these cells, which in turn produce pro-metastatic molecules such as MMP9, S100A8, and S100A9. In the pre-metastatic phase, granulocyte-secreted Bv8 is also reported to enhance the migration of metastatic cells toward the lungs (Kowanetz et al., 2010).

1.3.2 Formation of pre-metastatic niche triggered by tumour-derived or stromal-derived EVs

EVs secreted from tumour cells have been found to remodel lung stromal cells, including endothelial cells (ECs), epithelial cells, and fibroblasts (Liu et al., 2016; Mao et al., 2020; Zeng et al., 2018). Exosomes (a type of EV) containing microRNAs (miRNAs) such as miR-25-3p and miR-105 are secreted from colorectal cancer (CRC) and MDA-MB-231

metastatic breast cancer cells, and have been found to induce pre-metastatic formation via disrupting vascular permeability and induction of angiogenesis (Zeng et al., 2018; Zhou et al., 2014). CRC-derived miR-25-3p-EVs have also been shown to mediate the regulation of permeability and angiogenesis through silencing *KLF2* and *KLF4* in HUVECs (Zeng et al., 2018).

Lung cancer-derived exosomes can also activate lung epithelium through potential binding to Toll-like receptor 3 (TLR3), which induces the secretion of chemokines and thus, recruitment of neutrophils that facilitate the formation of a hospitable metastatic microenvironment and metastatic colonisation (Liu et al., 2016). Hepatocellular carcinoma (HCC) has also been found to trigger the formation of a pre-metastatic niche through nidogen 1 (NID1)-enriched EVs (NID1-EVs). These NID1-EVs increase pulmonary endothelial permeability and stimulate lung fibroblasts to secrete soluble tumour necrosis factor receptor 1 (TNFR1), which can increase hepatoblast colonisation in the lungs (Mao et al., 2020). Both NID1 and TNFR1 levels can correlate with tumour stage in HCC patients, suggesting their potential as diagnostic biomarkers (Mao et al., 2020). In another study, highly metastatic HCC cell lines were shown to secrete miR-1247-3p-enriched EVs able to promote β1-integrin–NF-κB signalling, thus activating lung fibroblasts into cancer-associated fibroblasts (CAFs) that produced pro-inflammatory molecules. miR-1247-3p-enriched EVs were also found to facilitate metastasis of HCC to the lungs, with levels higher in the serum of HCC patients with lung metastasis (Fang et al., 2018).

Tumour-derived EVs can also influence the creation of the pre-metastatic niche by affecting the migration of BMDCs to the lungs (Kong et al., 2019). Murine breast cancer cells were shown to secrete exosomes able to create an immunosuppressive niche in the lungs by recruiting BMDCs and inhibiting the proliferation of T cells and the cytotoxicity of NK cells (Wen et al., 2016). EVs not only secreted from tumour cells but also released from stromal cells may mediate pre-metastatic niche formation. EVs secreted from CAFs of human salivary adenoid cystic carcinoma tumour tissues were also found to be taken up by lung fibroblasts.

These EVs-activated lung fibroblasts then induced pre-metastatic formation and subsequent salivary adenoid lung metastasis through high expression of the periostin (POSTN) matrix (Kong et al., 2019). Tumour and stromal-derived EVs regulated lung niche formation by affecting lung stroma and BMDCs recruitment, representing a therapeutic target for cancer therapy (Vader et al., 2014).

1.3.3 The role of matrix deposition and stiffness in (pre-) metastatic niche formation

Another way in which tumour-derived molecules influence the formation of the pre-metastatic niche is via ECM remodelling (Joyce et al., 2011; Thordur et al., 2011). The ECM influences cell motility, morphogenesis, differentiation, and fate (Bonnans et al., 2014). Remodelling of ECM substantially contributes to almost every step in the metastatic cascade (Maru, 2015). For instance, the matrix component tenascin-C (TNC), produced by metastatic breast cancer cells and lung fibroblasts, can prepare a suitable niche for metastatic colonisation (Joyce et al., 2011; Thordur et al., 2011). Further, a deposited matrix in the metastatic lung has been shown to be produced by both tumour cells and lung stromal cells (Maru, 2015). EVs derived from human TNBC SUM159 primary tumours can also induce lung fibroblasts to upregulate ECM proteins (periostin and fibronectin (FN1)) and produce soluble growth factors and chemokines in the pre-metastatic lungs (Medeiros et al., 2020). Overexpression of p38MAPK (MAPK14) in lung fibroblasts at the periphery of tumour lesions can also reprogram these fibroblasts into CAFs. These CAFs can deposit high levels of an ECM component known as hyaluronan, which interacts with CD44 expressed by tumour cells) and subsequently activate KRAS-driven lung tumorigenesis (Brichkina et al., 2016). Experiments targeting p38, the enzyme responsible for hyaluronan synthesis (HAS2), or TGFβ activation in these CAFs, demonstrated that deposition and crosslinking of collagen and hyaluronan were crucial for ECM remodelling in the cancer niche (Brichkina et al., 2016). In addition to ECM production, crosslinking within the metastatic niche can increase the stiffness of the stroma, supporting metastatic outgrowth (Erler et al., 2009). For example, in a HIF-1-modulating context, metastatic breast cancer cells can secrete lysyl oxidase (LOX) under

hypoxia. This enzyme can catalyse collagen crosslinking, recruit BMDCs, and stiffen ECM in the metastatic niche, thereby priming the lungs for metastatic growth (Erler et al., 2009). Stiff ECM in the metastatic lung niche was observed to mediate breast cancer progression by increasing the mechano-transduction signalling of integrin, focal adhesion, and phosphoinositide 3-kinases (PI3Ks) pathways (Levental et al., 2009).

1.3.4 Metabolic dysregulation of the metastatic niche

Metastatic cancer cells reprogram their metabolism in order to succeed in adapting and colonising distal organs (Bergers & Fendt, 2021). In breast cancer, different molecular subtypes can manifest distinct metabolic phenotypes (Lehuédé et al., 2016). For instance, oestrogen receptor–positive breast cancers adopt an oxidative phosphorylation (OXPHOS) process, whereas TNBCs rely on a Warburg-like phenotype (aerobic glycolysis) for energy production (Lehuédé et al., 2016). EVs secreted from TNBCs (e.g. MDA-MB-231 breast cancer) contain high levels of miR-122A miRNA, which can reduce both the intracellular glucose level and glucose utilisation by niche cells, allowing it to be allocated to cancer cells as an energy resource for metastatic colonisation and expansion (Fong et al., 2015).

Many different breast cancer models have been found to rely on the metabolite pyruvate for ECM modification (collagen hydroxylation and stability) for effective growth. In the presence of pyruvate, and through the alanine aminotransferase (ALT) reaction, these breast cancer cells produce α-ketoglutarate. This substrate metabolically activates prolyl-4-hydroxylase (P4HA), activating collagen remodelling. *In vivo* targeting pyruvate, either through genetic and pharmacological inhibition of monocarboxylate transporter 2 (MCT2) (which prevents pyruvate uptake) and ALT2 (which inhibits the conversion of pyruvate to alanine), was found to reduce collagen hydroxylation markedly, and resulting in impaired metastatic growth in the lung metastatic niche (Elia et al., 2019). Breast cancer cells also showed differential metabolite proline dehydrogenase (Prodh) expression in both human and mouse primary and metastatic sites. Inhibiting Prodh significantly reduced pulmonary metastasis (Elia et al., 2017).

Not only can breast cancer cells rewire their metabolism, but CAFs can also alter their glucose metabolism to facilitate breast cancer progression (Becker et al., 2020). Hypoxia can induce epigenetic reprogramming of fibroblasts, producing CAFs with a pro-glycolytic phenotype (Becker et al., 2020). In an *in vitro* culture setting with stromal cells, CAFs were found to fuel MDA-MB-231 TNBC cells with lipids by increasing the expression and activity of FASN. The FASN enzyme catalysed the production of more fatty acids (FAs), which were transported to cancer cells via the transmembrane fatty acids transporter proteins 1 (FATP1) (Lopes-Coelho et al., 2018). Through *in vitro* exposure to fatty acids (palmitic (C16) and oleic (C18) acids), CAFs-conditioned medium and *in vivo* inoculation with CAFs, MDA-MB-231 cells showed a significant increase in the proliferation and *in vivo* tumour growth (Lopes-Coelho et al., 2018).

Taken together, the above studies have demonstrated that cancer cells can reprogram their own metabolism, and the surrounding stromal cells to obtain energy, suppress their apoptosis, and remodel ECM to facilitate the formation of metastases.

1.3.5 Development of an immunosuppressive metastatic niche

The immune system has been observed to function as a double-edged sword throughout cancer metastasis (Blomberg et al., 2018). On one side, $CD8^+$ T lymphocytes and natural killer (NK) cells have an anti-tumour activity (Janssen et al., 2017). For example, in orthotopic and metastatic murine Lewis lung carcinoma models, NK cells residing in the lung have an immune surveillance effect on the growth of primary lung cancer and lung metastasis (Yamamoto et al., 2018). In another study, IFNγ mediated lung resident NK cells also showed an anti-metastasis effect on B16 melanoma growth in the lung (Takeda et al., 2011). Additionally, during early cancer dissemination, CD8+ T cells secrete cytotoxic cytokines such as IFNγ and TNFα to prolong the dormancy of latent tumour cells in the lung by arresting their cell cycle (Eyles et al., 2010).

Conversely, immune cells can enhance cancer growth and metastasis in response to tumour-induced cytokines, creating an immunosuppressive microenvironment (Kitamura et

al., 2015). Another way for primary tumour cells to form a pre-metastatic niche is via the establishment of an immunosuppressive microenvironment. This environment suppresses cells that usually contribute to immunosurveillance (such as CD8+ T cells, NK cells, and non-classical “patrolling” monocytes) and hence mediate tumour progression (Chiossone et al., 2018; Hanna et al., 2015; Joseph et al., 2021; Liu & Cao, 2016). An example of immunosuppressive cells are tumour-associated macrophages (TAMs), a differentiated version of myeloid cells that emerge intratumorally under the stimulation of the M2-polarizing Cytokines IL10 and TGFβ (Mosser & Edwards, 2008). M2-like TAMs (distinguished from other types of macrophages by low expression LY6C and major histocompatibility complex (MHC) II)) can selectively overexpress macrophage receptors with collagenous structure (MARCO). Antibody (Ab)-mediated targeting of MARCO receptors has demonstrated a significant increase in infiltrating CD4+/CD8+ T cell and M1-like TAMs and a significant reduction in 4T1 TNBC primary and metastatic tumour growth (Georgoudaki et al., 2016). Further, in a spontaneous metastatic model, macrophages as tumour-promoting cells facilitate the adhesion and migration of mammary 4T1 cells over the ECM by producing secreted cysteine protein SPARC (Sangaletti et al., 2008). They also facilitate the adhesion of metastatic breast cancer cells to the stroma, and foster metastasis to the lung and liver through secreting CCL18 (Chen et al., 2011). In addition to macrophages recruited from circulation (Qian et al., 2011), tissue-resident macrophages (such as alveolar macrophages (AMs)) also create an immunosuppressive niche for primary breast cancer cells to metastasise the lungs. These AMs increased in number in pre-metastatic lungs of 4T1-tumour-bearing mice and suppress cytolytic CD4+ T cells (Th1), and downregulate MHCII on both tumour cells and dendritic cells (Sharma et al., 2015). Murine 4T1 tumour-bearing mice were also shown to employ B cells (tumour-evoked regulatory B cells) to suppress anti-tumour immunity and inhibit CD8+ T-cell proliferation. Upon TGFβ-mediated conversion of resting CD4+ T cells to FOXP3+ T regulatory cells, these B cells enable 4T1 tumour cells to escape the immune system and promote 4T1 tumours to metastasise to the lungs (Olkhanud et al., 2011). B cells can also activate (educate) MDSCs, modulating the suppression of CD4+ and CD8+ T cells. B cell

activated MDSCs can exert pro-metastatic and immunosuppressive activities via the production of reactive oxygen species (ROS) and upregulation of metabolic genes: NADPH oxidase (NOX2), nitric oxide synthase (iNOS), and arginase 1 (Arg-1) genes (Bodogai et al., 2015). Alternatively, CD4+ T lymphocytes indirectly affect breast cancer intravasation and invasion of the lung through activation of M2 macrophages, which induce pro-metastatic epidermal growth factor receptor signalling (Denardo et al., 2009). Interestingly, a recent study has shown that the frequency of T-cell responses to tumour antigens can be a more sensitive indicator of early lung metastasis than PET-CT imaging, an observation that could potentially facilitate early detection, effective adjuvant therapy, and improved survival rates (Fear et al., 2019).

Resident T cells in the lungs also support niche formation and metastatic growth by expressing the oxygen-sensing prolyl-hydroxylase (PHD). PHD can generate an immunosuppressive niche for circulating tumour cells by limiting Th1 differentiation, enhancing the differentiation of CD4+ regulatory T (Treg) cells, and impeding CD8+ T cell cytotoxic response (Clever et al., 2016). Neutrophils also contribute to lung metastasis through overexpression of pro-metastatic factors such as CXCR 4 and 7, MMP12 and 13, Interleukin (IL) 6, and TGFβ (Yu et al., 2017). A study by Wu and colleagues showed that the absence of type I interferons triggered neutrophil recruitment from BM infiltrating the lungs through the CXCL/CXCR cytokine signalling axis. These neutrophils subsequently became pro-metastatic and were able to help 4T1 TNBC and primary LLC lung cells to extravasate the lungs (Wu et al., 2015). Additionally, in a spontaneous breast cancer metastasis model, T cells-expressing IL-17A increased the number of neutrophils in the circulation, suppressing effector CD8+ T cells and enhancing pulmonary metastasis formation (Coffelt et al., 2015).

In conclusion, it is clear that cancer cell interactions with immunosuppressive cells can modulate the generation of the metastatic niche, providing potential therapeutic opportunities to reduce metastasis.

1.3.6 Epithelial-mesenchymal transition (EMT) and mesenchymal-to-epithelial transition (MET) in metastatic dissemination and progression

EMT and MET are two reversible processes induced in tumour cells that contribute to cancer metastasis (Jolly et al., 2017). Cancer cells facilitate their detachment and mobilisation from the primary site to secondary organs by acquiring an EMT phenotype, where they become mesenchymal-like, lose cell-cell junctions, become less adhesive, and are more migratory (Huang et al., 2022b). Once cancer cells arrive at the secondary sites, they acquire a MET phenotype with epithelial and proliferative characteristics to achieve the final steps of metastasis colonising the lungs (Yao et al., 2011).

In breast and colorectal cancer cells, EMT of cancer cells has been reported to enhance metastasis to other organs by overexpressing the transcription factor ZEB1, with ZEB1 subsequently inhibiting the expression of the epithelial cell polarity marker, LGL2 (Spaderna et al., 2008). EMT is also reported to drive breast cancer metastasis to the lungs through high expression of TWIST1. TWIST1 can confer an EMT phenotype to these breast cancer cells by reducing the expression of E-cadherin and increasing cell motility (Yang et al., 2004). Targeting TWIST1 in mammary gland tumour cells reduced their intravasation from the primary site and reduced lung metastases (Xu et al., 2017; Yang et al., 2004). SNAIL is another diver of EMT that induces colorectal cancer cell metastasis to the lungs. It mediated EMT by promoting colorectal cancer cells to secrete CXCL2, which chemoattracted M2 macrophages to infiltrate the lungs (Bao et al., 2022).

For metastatic tumour cells to progress and successfully form lung metastases, they are thought to undergo MET and transdifferentiate into a more epithelial-like phenotype (Dykxhoorn et al., 2009; Oltean et al., 2006). For instance, rat prostate AT3 tumour cells have been found to induce MET as they colonise the lungs through alternative splicing of fibroblast growth factor receptor 2 (FGFR2) transcripts (Oltean et al., 2006). Similarly, highly metastatic breast tumour cells, *e.g.* murine 4T1 TNBC cells with epithelial phenotype, can overexpress miR-20, mediating cells to undergo MET and metastasise to the lungs (Dykxhoorn et al.,

2009). Breast cancer cells in a spontaneous murine model initiated metastatic niche formation by enhancing the recruitment of bone marrow-derived myeloid progenitor cells to the lungs. These progenitor cells produced versican, which induces tumour cells to undergo MET and therefore increases their proliferation and accelerating the formation of lung macrometastases (Gao et al., 2012).

Several studies have found that tumour cells metastasise via an induction of EMT followed by MET (Aokage et al., 2011; Ouzounova et al., 2017). However, other studies have conversely reported that EMT can occur in response to therapy as a mechanism of resistance, suggesting that targeting EMT in tumour cells could be beneficial in restoring chemosensitivity of tumour cells (Fischer et al., 2015; Kajiyama et al., 2007). Indeed, several small molecule drugs have been shown to overcome drug resistance via inhibiting EMT pathway (Du & Shim, 2016)

1.3.7 Stemness of disseminated tumour cells (DTCs) (Stemness and plasticity of metastatic breast cancer)

Cancer stem cells (CSCs) are a subset of cancer cells with stem-like characteristics, and are believed to be the cancer cells that survive in the circulation and metastasise to distant sites (Ingangi et al., 2019). Breast cancer stem cells (BCSCs) are distinguished from non-tumorigenic cells by surface markers, with epithelial-specific antigen (ESA) and CD44 expressed along with low/absent expression of CD24 (Al-Hajj et al., 2003). Other surface markers associated with BCSCs are CD133, aldehyde dehydrogenase-1 (ALDH-1), CXCR4, CXCL1, HMGCS1, and integrin beta-3 (β3) /CD61 (Ginestier et al., 2007; Lawson et al., 2009; Vaillant et al., 2008; Won Jun et al., 2016). CSCs are self-renewing (giving rise to more stem cells) while they can also differentiate and proliferate into mature tumour cells, leading to tumour growth and progression (Saeg & Anbalagan, 2018). Signalling crosstalk between CSCs and the metastatic niche has been found to promote CSCs to form metastases (Shiozawa et al., 2013). For example, contact communication between breast cancer cells and mesenchymal stem/stromal cells upregulates miR-199a, conferring stem-like

characteristics to these cancer cells and promoting lung colonisation. Consequently, high levels of miR-199a are associated with poor survival in clinical breast cancer (Cuiffo et al., 2014). Dormant breast cancer cells can also be reactivated into BCSCs via the transmembrane protein TM4SF1, which binds to the collagen receptor tyrosine kinase, DDR1 and increases the expression of pluripotency factors SOX2 and NANOG. TM4SF1-induced BCSCs can also activate the transcription factor STAT3 signalling, thus promoting metastasis to the lungs, brain, and bone (Gao et al., 2016).

CSCs can activate autonomous signalling and secrete TNC matrix, supporting the stemness of breast cancer cells. Cancer-derived TNC maintains the stemness of CSCs and initiates the formation of lung micrometastases through upregulation of the RNA-binding protein MSI1 and the GPCR, LGR5 (Oskarsson et al., 2011). BCSCs can also colonise lungs by increasing the expression of epithelial splicing regulatory protein 1 (ESRP1). This autonomous ESRP1 mechanism controls the stemness of BCSCs and protects them from oxidative stress via regulating both the alternative splicing of CD44 (Yae et al., 2012).

These studies therefore show how CSCs communicate with the metastatic niche to foster metastatic colonisation, implicating their potential as a therapeutic target to prevent forming established metastases.

1.3.8 Therapeutic strategies to target the metastatic niche

The tumour microenvironment has been shown to enhance tumour survival, proliferation, metastasis, and even resistance to therapy (Bremnes et al., 2011). Currently, metastatic disease is treated with chemotherapy, targeted therapy and immunotherapy (Ganesh & Massagué, 2021). Although significant progress has been made recently using immune checkpoint inhibition, only a minority of patients (with immunogenic tumours) can benefit from this therapy (Ganesh & Massagué, 2021). Further, recent studies have shown that responders to immunotherapies can also develop acquired resistance, illustrating the need to find new targets for metastatic disease (Fairfax et al., 2020; Schoenfeld & Hellmann, 2020; Valpione et al., 2020).

Several studies, including the ones discussed above, have highlighted new potential targets for metastatic disease. Such potential molecular and cellular targets can be found in processes like ECM remodelling, metabolic reprogramming, cancer invasion and plasticity, immunosuppression, and tumour blood vessels (Celia-Terrassa & Kang, 2018; Ganesh & Massagué, 2021).

Targeting miR-122 secreted by metastatic breast cancer has been shown to have anti-metastasis potential, with anti-miR-122 antisense oligonucleotides significantly reducing metastases in the brain and lungs and restoring glucose utilisation by niche cells (Fong et al., 2015). Type I interferon signalling can also have an anti-metastatic effect in the preclinical 4T1 TNBC model, polarising neutrophils toward an N1 anti-tumorigenic phenotype and limiting neutrophil mobilisation and extravasation to metastatic organs (Wu et al., 2015). Therefore, it has been suggested that interferon could be used as a therapeutic molecule to prevent cancer metastasis (Wu et al., 2015). PHD, an oxygen-sensing molecule found to have a pro-metastatic effect through establishing an immunosuppressive niche, can also be targeted to limit primary and metastatic tumour growth in a preclinical setting (Clever et al., 2016). Lung-resident alveolar macrophages, which quench the anti-tumour T-cell response, also represent a potential target to enhance the immune response to metastatic breast cancer cells. Targeting these alveolar macrophages via intranasal administration of clodronate liposomes (phagocytised by these cells) in a complement receptor (C5AR)-deficient mice (C5AR mediates self-renewal capability of alveolar macrophages) markedly reduced lung metastases and increased IFNγ–producing CD4+ T cells (Sharma et al., 2015). M2-like TAMs have been targeted in preclinical colon carcinoma (MC38) and melanoma (B16) models using anti-MARCO Abs, resulting in an enhanced response to immune checkpoint therapy using anti-CTLA4 Abs. Consequently, human TNBC samples highly enriched with MARCO-overexpressing M2-like TAMs representing a potential therapeutic target (Georgoudaki et al., 2016).

One of the challenges is that solid evidence about the molecular mechanisms in the metastatic niche is unavailable, owing to the lack of *in vitro* and *in vivo* models that can recapitulate the (pre-) metastatic niche. While the above studies have provided insights about metastatic niche formation, accurate isolation of tumour or stromal cells in the metastatic niche for transcriptional analysis has not been possible. Additionally, the lack of clinical samples of metastatic cancers with defined niche hinders studies in this area. Thus, there is a need for a new model that enables comprehensive analysis of the (pre-) metastatic niche. This would potentially reveal the molecular signalling involved, identify prognostic factors and biomarkers of metastatic niche, and help find new therapeutic targets for metastatic cancers.

1.4 Vascular remodelling in metastasis

Remodelling of the vascular bed often occurs prior to tumour cell colonisation of secondary sites (Hirakawa et al., 2007; Kaplan et al., 2005). For instance, the growth factor receptor VEGFR1/FLT1 expressed by bone marrow-derived haematopoietic progenitor cells, can contribute to the formation of the pre-metastatic vascular niche, and thereafter the development of vascularised micrometastases in the lung (Kaplan et al., 2005). Supporting this, anti-FLT1 peptide was shown to reduce tumour angiogenesis and, subsequently, tumour cells metastasising through the circulation (Bae et al., 2005). Prior to metastasis into sentinel lymph nodes (SLNs), morphologic changes in the vasculature of SLNs and enhanced proliferation rates of endothelial cells in high endothelial venules (HEVs) were also observed (Qian et al., 2006). The endothelial growth factor VEGFC produced by tumour cells was found to play a crucial role in enhancing tumour lymphangiogenesis and metastasis to SLNs and other organs (Hirakawa et al., 2007). In a VEGFC-overexpressing chemically-induced skin carcinogenesis mouse model, VEGFC facilitated tumours to enter the lymphatic circulatory system and metastasise in the lungs (Hirakawa et al., 2007). Blocking the VEGFR3 expressed by lymphatic endothelial cells with an anti-VEGFR3 antibody treatment markedly decreased metastasis of tumour to these organs (Roberts et al., 2006).

Tumour cells have been shown to remodel the vasculature at the primary site and facilitate their intravasation into the metastatic organ (Tavora et al., 2020). For instance, tumour-derived dsRNA was found to induce an upregulation of SLIT2 in primary tumour ECs through binding to endothelial TLR3 (Tavora et al., 2020). Upregulated endothelial SLIT2 binds to its receptor, ROBO1 on tumour cells, enhancing lung metastasis by facilitating tumour migration and intravasation (Tavora et al., 2020). Exosomes secreted by cancer cells also form the vascular niche (Osaki & Okada, 2019). *In vitro* and *in vivo* experiments reported that exosomes-containing miR-105, secreted by metastatic breast cancer cells, MDA-MB-231, promote metastasis by acting on the endothelial barrier, where it reduces endothelial expression of tight junctions such as zonula occludens 1 (ZO1) and occludins and induces vascular permeability (Zhou et al., 2014). The tumour vasculature is also remodelled during tumour progression from micrometastases to macrometastases (Gao et al., 2008). For example, tumour cells can induce the expression of the transcription factor ID1 in bone marrow-derived endothelial progenitor cells (EPCs), which subsequently activates the angiogenic switch and initiates neovascularisation, leading to metastatic progression (Gao et al., 2008).

1.5 Mechanisms of Tumour Vascularisation

1.5.1 Neoangiogenesis (sprouting angiogenesis).

Tumour angiogenesis (also referred to as neovascularisation) is triggered by pro-angiogenic stimuli secreted from cancer cells (Folkman, 1971). As tumours expand, they require oxygen and nutrients, thus a hypoxic environment is generated to trigger angiogenesis that could provide a sustainable blood supply (Ziyad & Iruela-Arispe, 2011). This hypoxic microenvironment enables cancers to grow beyond 2 mm^3 and metastasise (Lars et al., 1995; Ziyad & Iruela-Arispe, 2011).

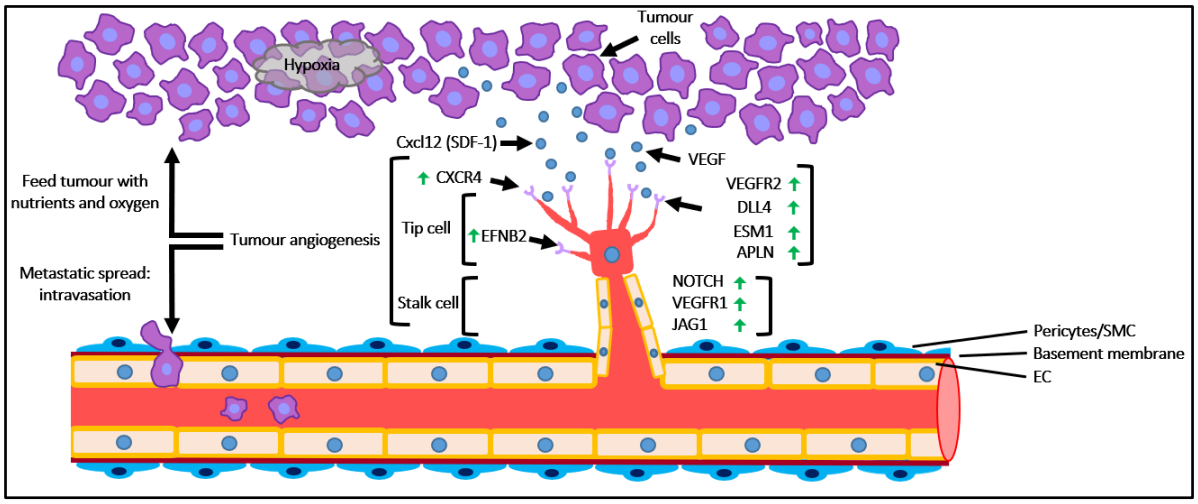

Figure 1-1. Schematic representation of the mechanism of sprouting angiogenesis. *In response to VEGF, tip endothelial cells sprout, followed by activated stalk cells forming new blood vessels. EC: endothelial cell; VEGF: vascular endothelial growth factor; VEGFR1/2: vascular endothelial growth factor receptor1/2; DLL4: Delta Like Canonical Notch Ligand 4; ESM1: endothelial Cell Specific Molecule 1; APLN: apelin; JAG1: Jagged1; EFNB2: ephrin B2.*

Hypoxia induces cancer cells to secrete growth factors such as VEGFA, which binds to its receptor VEGFR2 expressed on the sprouts and thus increases both vascular permeability and angiogenesis **(**Figure 1-1**) (Carmeliet & Jain, 2011; Ziyad & Iruela-Arispe, 2011)**. Tumour angiogenesis is also induced through the chemokine receptor/ligand CXCR4-CXCL12 axis, which can upregulate the levels of VEGFA through the PI3K/AKT pathway (Carmeliet & Jain, 2011; Liang et al., 2007). Angiogenic EC-specific ESM1 is another regulator of tumour angiogenesis, increasing VEGFA bioavailability and vascular permeability (Rocha et al., 2014), whilst APLN-APLNR signalling also regulates tumour angiogenesis (Liu et al., 2015). Notably, both ESM1 and APLN are markers of tip cells **(**Figure 1-1**)** (Liu et al., 2015; Rocha et al., 2014).

Tumour vascular tip cells are found at the leading edge of the angiogenic sprout, and express high levels of Notch ligands delta-like 4 (DLL4) and Jagged1 (JAG1), which bind to the Notch receptors expressed on neighbouring stalk ECs **(Figure 1 1)** (Benedito et al., 2009; Kofler et al., 2011; Kuhnert et al., 2011). The specification of ECs into tip and stalk cells mainly occurs by translocation of cleaved Notch into the nucleus, with Notch intracellular domain (NICD) stimulating the transcription of Notch target genes such as *HEY-1* and *HEY-2* and *HES-1* (Blanco & Gerhardt, 2013). Activated NOTCH signalling subsequently results in the downregulation of DLL4 and VEGFR2 and upregulation of VEGFR1, maintaining the EC as a stalk cell and preventing it from becoming a tip cell (Blanco & Gerhardt, 2013). Tip cells function as the leading endothelial cells at the front of the sprouts, sensing the surrounding microenvironment with their long filopodial protrusions directing their sprouts (Blanco & Gerhardt, 2013). Ephrin-B2 (EFNB2) is also expressed in tumour blood vessels at the tip cell filopodia to guide the sprouting via VEGFR2 internalisation **(Figure 1-1)** (Sawamiphak et al., 2010). Tip cells migrate through tissue via secreting proteases, breaking down the basement membrane and ECM in the tissue (Zuazo-Gaztelu & Casanovas, 2018).

Stalk endothelial cells have high proliferative ability and follow the tip cell, supporting lumen formation, building the endothelial barrier by connecting them with tight junctions, and depositing the basement membrane (Zuazo-Gaztelu & Casanovas, 2018). Stalk cells are characterised by enhanced Notch signalling, which also makes these cells insensitive to VEGFA signalling by reducing the expression of VEGFR2 (Liu et al., 2014).

After vascular network formation, angiogenesis is switched off and the vasculature becomes quiescent (Blanco & Gerhardt, 2013). Tip cells fuse together (a process known as anastomosis), and the vessel becomes perfused, initiating vessel stabilisation and maturation (Zuazo-Gaztelu & Casanovas, 2018). ANGPT1/ANG1 expressed by perivascular cells (e.g., pericytes and smooth muscle cells) contribute to vessel maturation (Augustin et al., 2009). Another co-receptor bound by VEGFA is Neuropilin-1 (NRP1) (Ziyad & Iruela-Arispe, 2011). NRP1 contributes to tumour angiogenesis by enhancing the migration of endothelial cells and pericytes, promoting sprout formation and stabilising the newly formed blood vessels (Pan et

al., 2007b). Combined treatment of the non-small-cell lung cancer xenograft model with anti-VEGFA and anti-NRP1 monoclonal antibodies, showed a substantial reduction of tumour volume, which was ascribed to the significantly reduced vascular density and loss of pericytes associated with the tumour endothelium (Pan et al., 2007a).

Another pro-angiogenic pathway involved in tumour angiogenesis and metastasis is EPHA2-EFNA1 interaction in endothelial and cancer cells (Pasquale, 2010). *In vitro* and *in vivo* orthotopic models of metastatic mammary cancer cells lacking EFNA1 revealed that this ligand mediates the expression of VEGFA and binds to EPHA2 receptors on endothelial cells, inducing their migratory ability (Brantley-Sieders et al., 2006). Migration of endothelial cells during tumour angiogenesis is also mediated by interaction between endothelial ROBO receptor with SLIT2-expressing tumour cells, activating PI-3K pathway (Wang et al., 2003).

Tumour angiogenesis was once considered the sole route providing the vasculature required to support tumour growth and progression (Folkman, 1971). However, this concept has changed over time, and different vascularisation mechanisms used during cancer growth have emerged (Bridgeman et al., 2017; Burri et al., 2004; Cannell et al., 2023). In particular, these are thought to contribute to the resistance seen to anti-angiogenic therapies (Bridgeman et al., 2017; Burri et al., 2004; Cannell et al., 2023). These mechanisms include intussusceptive angiogenesis (Burri et al., 2004), vasculogenic mimicry (Cannell et al., 2023), and vessel co-option (Bridgeman et al., 2017).

1.5.2 Intussusceptive angiogenesis (IA).

Intussusceptive angiogenesis (IA) is the formation of transvascular endothelial pillars in the lumen of a single vessel that enables it to split into two vessels without the need for endothelial cell proliferation (Burri et al., 2004). This phenomenon was first described in postnatal rat lung imaged by scanning electron microscopy (SEM) back in 1986 (Caduff et al., 1986). It is found to occur in lung parenchyma where blood vessels are denser relative to the ones near the pleura, and is induced by blood flow, hydrostatic pressure, and/or shear stress (Caduff et al., 1986; De Spiegelaere et al., 2012). Patan and his colleagues first observed that IA occurs in tumours using a human colon adenocarcinoma xenograft model (Patan et al., 1996). IA has also been observed in human glioma (Nico et al., 2010), hepatocellular carcinoma (Heindryckx et al., 2010), mammary tumours (Djonov et al., 2001), melanoma (Ribatti et al., 2005), and lymphoma (Crivellato et al., 2003).

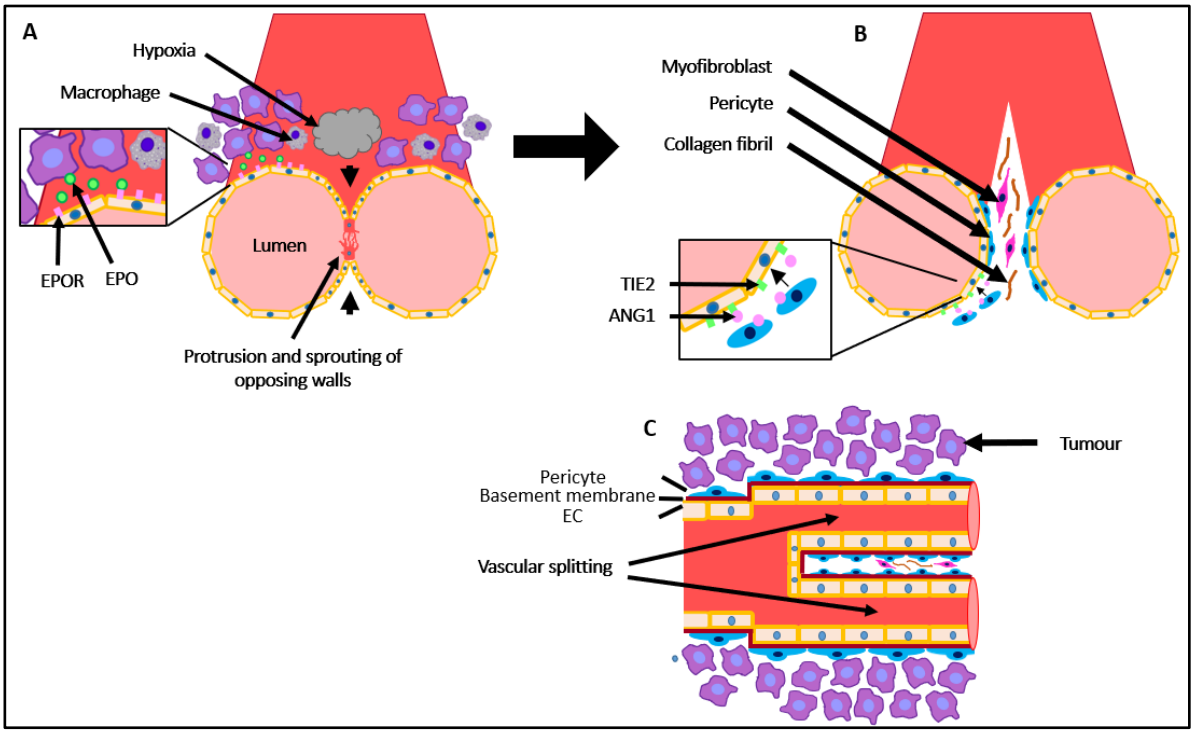

Figure 1-2. Schematic representation of the mechanism of intussusceptive angiogenesis (IA). *Hypoxia and macrophages induce IA formation (A). Endothelial cells protrude towards the vessel lumen, followed by the formation of a vascular wall by myofibroblasts, pericytes, and collagen deposition (B), leading to the splitting of one blood vessel into two vessels (C). EC: endothelial cell; TIE2: tyrosine protein kinase receptor 2; ANG1: Angiopoietin-1; EPO: erythropoietin; EPOR: erythropoietin receptor.*

The morphogenesis of IA is generally divided into four phases (Burri et al., 2004). Endothelial cells first emerge into the lumen of the capillaries and adhere to the facing

projected endothelial cells **(Figure 1-2A)** (Burri et al., 2004). Endothelial junctions are then remodelled, and myofibroblasts create a wall via matrix deposition, which is followed by pericytes coating this wall specifically at the endothelial junctions **(Figure 1-2B)** (Kurz et al., 2003). Lastly, a mature pillar is formed, separating the lumen into two compartments by collagen fibrils and inter-endothelial junctions **(Figure 1-2C)** (Burri et al., 2004).

The molecular regulation of IA is poorly understood due to the difficulty of capturing and modelling this process (De Spiegelaere et al., 2012). However, the growth factors VEGFA, FGF, and platelet-derived growth factor subunit-B (PDGFB) are all reported to contribute to IA during the vascular development of avian lung (Makanya et al., 2007). Additionally, TIE2/ANG1 is a positive regulator and TIE1 a negative regulator of intussusceptive microvascular growth (IMG) during embryonic angiogenesis through promoting EC migration and mobilisation of mural cells **(Figure 1-2B)** (Patan, 1998). Hypoxia can also influence IA: microvessels (except venules) of adult mouse retina exposed to hypoxia for three weeks exhibited ongoing angiogenesis and signs of IA, including an increase in the diameter of vessels and the number of vascular loops (Taylor et al., 2010). In response to hypoxia, erythropoietin (EPO) overexpression by cancer cells and signalling is activated by the HIF transcription factor **(Figure 1-2A)** (Su et al., 2019), with EPO functioning as an angiogenic molecule regulating IA vascularisation (Crivellato et al., 2004; Nico et al., 2011). In addition to the involvement of tumour cells, macrophages are also reported to contribute to IA (Kurz et al., 2003).

1.5.3 Vasculogenesis

Vasculogenesis is defined as the *de novo* formation of early vascular plexuses during embryogenesis or pathological conditions such as tissue ischemia and tumour growth through the recruitment of endothelial progenitor cells (EPCs) from bone marrow (Asahara et al., 1999; Brown, 2014) (Asahara et al., 1999; Brown, 2014; Zuazo-Gaztelu & Casanovas, 2018). Irradiation therapy of tumours inhibits angiogenesis, but can upregulates HIF1α, encouraging some irradiated tumours to regrow using vasculogenesis through stromal cell-derived factor 1 (SDF-1) or CXCL12/CXCR4 chemokine signalling (Ahn & Brown, 2008; Zuazo-Gaztelu & Casanovas, 2018). Vasculogenesis of CXCR4-expressing tumours by SDF1-secreting EPCs can occur in both primary and metastatic tumours (Asahara et al., 1999; Jin et al., 2012; Zuazo-Gaztelu & Casanovas, 2018). First VEGFA and other angiogenic factors secreted from tumour cells activate the production of MMP9 from BM-derived cells (Heissig et al., 2002). This enzyme cleaves the membrane Kit ligand releasing its active soluble form, which provokes differentiation, mobilisation, release into the circulation, and homing of EPCs and stem cells to developing tumours and metastatic sites **(Figure 1-3)** (Heissig et al., 2002; Jin et al., 2012). These EPCs then adhere, transmigrate, and extravasate to reach and associate

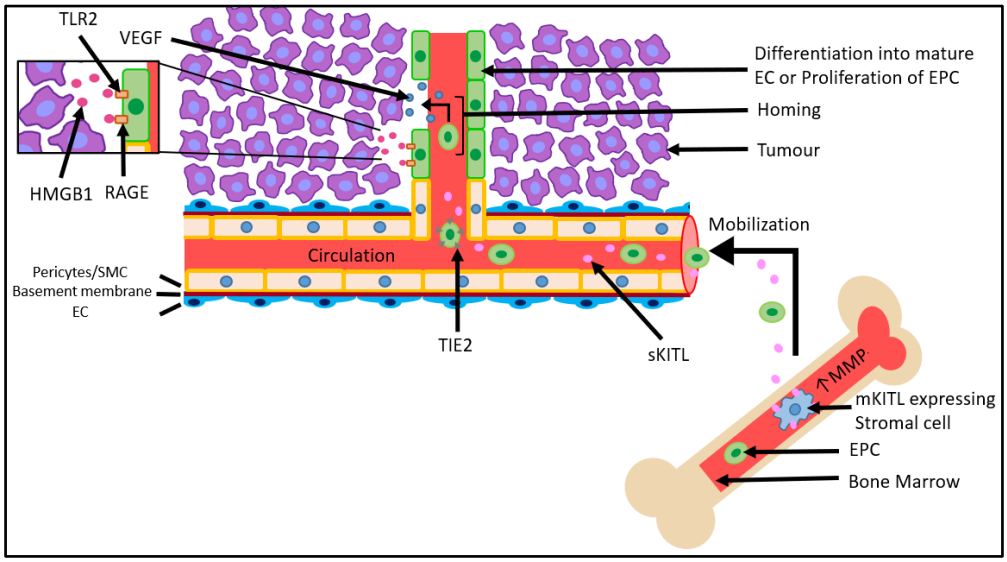

Figure 1-3. Schematic representation of the mechanism of vasculogenesis. *Endothelial progenitor cells (EPCs) are mobilised from bone marrow to blood circulation with sKitL support (soluble KitL). Then, the receptor for advanced glycation end products (RAGE) and Toll-like receptor 2 (TLR2)-expressing endothelial cells (ECs) migrate and adhere to the tumour to form blood vessels through interacting with high-mobility group box 1 (HMGB1). VEGF: vascular endothelial growth factor; TIE2: tyrosine-protein kinase receptor 2; mKitL: membrane-bound KitL; MMP: matrix metallopeptidase.*

with the newly formed tumour blood vessels (to proliferate or differentiate into mature ECs) and to the mature endothelial monolayer **(Figure 1-3)** (Chavakis et al., 2007).

FGF can also mediate the angiogenic role of bone marrow-derived stromal cells (BMSCs) in the formation of tubular structures *in vitro* and tumour neovascularisation *in vivo* (Annabi et al., 2004). Transplantation of wild-type (WT) bone marrow or VEGF-mobilized stem cells into ID-lacking tumour-bearing mice ($Id1^{+/-}Id3^{-/-}$) demonstrates that ID transcription factors govern migration and association of hematopoietic and circulating endothelial precursor cells (CEPs) into tumour neovessels (Lyden et al., 2001). The adhesion and migration of EPCs to tumour tissues is also mediated by crosstalk between their surface proteins, β1 and β2 integrins, RAGE (receptor for advanced glycation end products), TLR2, and P-selectin glycoprotein ligand 1 (PSGL1) with intercellular adhesion molecule (ICAM)-1, fibronectin, (ligands for integrins), high-mobility group box 1 (HMGB1) (ligands for RAGE and TLR2), and E- and P-selectin **(Figure 1-3)** (Chavakis et al., 2007; Vajkoczy et al., 2003). Blood samples collected from human breast cancer patients have revealed that these migrating EPCs highly express TIE2 receptors (Asahara et al., 1999; Sussman et al., 2003).

Therapeutically, the mobilisation and differentiation of EPCs are reported to be abrogated by endostatin, which functions as an anti-angiogenic therapy (Capillo et al., 2003). In addition, targeting both VEGFR1 and VEGFR2 impaired EPCs incorporation into tumour sprouts (Lyden et al., 2001). The vital role of EPC in tumour vascularisation and growth makes it a potential target for cancer treatment (Hillen & Griffioen, 2007).

1.5.4 Vasculogenic mimicry (VM)

Vasculogenic mimicry (VM) was first detected in primary human intraocular and metastatic cutaneous melanomas (Maniotis et al., 1999). In these cases, invasive tumour cells adopt a pluripotent embryonic-like phenotype, mimicking endothelial cells by forming matrix-rich tubular and perfusing networks that can nurture tumours, as evidenced by the absence of necrosis (Liu et al., 2011; Maniotis et al., 1999). VM networks were found to conduct fluid and are detected by staining with periodic acid-Schiff (PAS) and laminin (Maniotis et al., 2002).

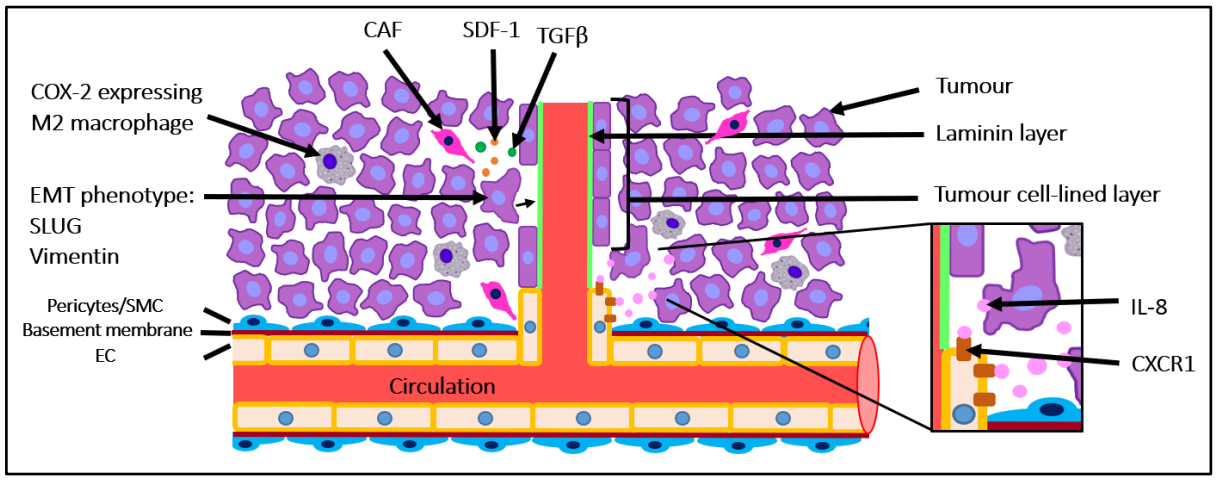

Figure 1-4. Schematic representation of the mechanism of vasculogenic mimicry (VM). *Cancer cells with an epithelial–mesenchymal transition (EMT) phenotype can form vessel-like structures. C-X-C chemokine receptor type (CXCR1)-expressing endothelial cells (ECs) attract Interleukin 8 (IL-8)-secreting cancer cells and cancer-associated fibroblasts (CAFs) secrete stromal cell-derived factor 1 (SDF-1) and Transforming growth factor beta (TGFβ) to aid in the formation of VM tubes. Macrophages also aid VM formation through overexpression of cyclooxygenase-2 (COX-2).*

Studies conducted on different types of tumours reveal that various cell types are involved (Luo et al., 2020). For example, in melanoma VM, vascular conduits formed by tumour cells are characterised by an upregulation in the expression of EC markers (e.g. TIE1, CD144), epithelial cell markers (e.g. Keratin 8), and stem cell markers (e.g. CD34) (Hendrix et al., 2003; Hendrix et al., 2001; Maniotis et al., 1999). These aggressive melanoma tumour cells also express high levels of EPHA2 receptors, matrix remodelling markers, and hypoxia markers, maintaining the tumour vasculature and promoting tumour adhesion, migration, proliferation, and progression (Hendrix et al., 2003; Hess et al., 2001; Seftor et al., 2001; Vartanian et al., 2013).

Regarding the relationship between VM and tumour metastasis, VM is observed to be more prominent in patients with highly metastatic hepatocellular carcinoma and is associated with shorter survival periods (Sun et al., 2006). Analysis of markers has demonstrated characteristics of EMT and CSC phenotypes in the cells involved in the formation of VM **(Figure 1-4**) (Chen et al., 2017; Sun et al., 2013; Sun et al., 2010; Zhao et al., 2018). A study using tissue samples collected from NSCLC patients demonstrated an association between VM, expression of EMT markers SLUG and vimentin **(Figure 1-4)**, and metastasis of NSCLC to distant sites (Song et al., 2018). In colon cancer, various models have shown that VM is formed through overexpression of WNT3a and β-catenin, activating canonical WNT signalling (Qi et al., 2015). Alternatively, VM can be induced in ovarian cancer through upregulation of Wnt5a, which activates the non-canonical WNT signalling pathway (Qi et al., 2014).

The formation of VM is not only attributed to tumour cells but also to the tumour microenvironment (Luo et al., 2020). Brain endothelial cells contribute to this phenotype via the expression of CXCR1, attracting IL-8-secreting glioma cells (**Figure 1-4)** (Sharma et al., 2018). M2 macrophages increase the expression of cyclooxygenase-2 (COX-2), with subsequent activation of the prostaglandin PGE2/EP1/PK pathway in GBM cells supporting VM formation **(Figure 1-4)** (Rong et al., 2016). CAFs are also implicated in VM formation, potentially via CCN2 expression or their production of the growth factors, TGFβ and SDF1 **(Figure 1-4)** (Hutchenreuther et al., 2018; Yang et al., 2016).

Many studies have shown that treating tumours with anti-angiogenic drugs targeting sprouting angiogenesis has only modest efficacy and/or that responsive tumours subsequently acquire resistance, implicating alternative mechanisms supporting tumour regrowth, including VM (Zarrin et al., 2017). For instance, the treatment of TNBC with an anti-angiogenic drug sunitinib generates a hypoxic environment, tumour cells form VM and regrow via overexpressing TWIST1 and CD133 (Zhang et al., 2014). Equally, treatment of orthotopic intracranially xenografted glioblastomas (GBMs) with bevacizumab found that glioma stem cells (GSCs) use autophagy-mediated VM formation as a method of resistance to anti-angiogenic therapy (Wu et al., 2017). Consequently, emerging evidence indicates that VM

may be one of the reasons behind the disappointing response to anti-angiogenic therapies and could be therefore potentially targeted in tumours that display resistance to anti-angiogenic therapies (Sun et al., 2013; Zhang et al., 2014).

1.5.5 Vessel co-option in cancer.

In 1996, Pezzella and his team observed that primary and metastatic lung cancers grew without any sign of new sprouting blood vessels. Instead, they appeared to utilise pre-existing blood vessels, which grew around them, a phenomenon later termed ‘vessel co-option’ (Pezzella et al., 1996; Pezzella et al., 1997). In vessel co-option, tumour cells hijack their host's pre-existing blood vessels to migrate and colonise highly vascularised organs, including the lungs, brain, and liver (Donnem et al., 2018). Both solid tumours and leukaemia have been shown to co-opt host vessels in primary or secondary tumours (Donnem et al., 2018; Kuczynski et al., 2019). Tumours co-opting host vessels also exhibit distinct histological growth patterns depending on the organ in which they grow (Kuczynski et al., 2019).

1.6 Vessel co-option signalling in common organs.

1.6.1 Mechanisms of tumour co-option of lung capillaries.

Single-cell RNA sequencing (scRNA-seq) of human lungs identified 58 distinct cell types. Mainly composed of epithelial subtypes such as alveolar cells and airway cells; endothelial subtypes including arteries, veins, capillaries (aerocytes and general), lymphatic and bronchial; stromal subtypes including vascular smooth muscle (SM) cells, bronchial SM, alveolar, adventitial fibroblasts, lipofibroblasts, myofibroblasts, fibromyocytes, pericytes, mesothelial cells; and immune cell subtypes including monocytes, granulocytes, lymphocytes, platelets **(Figure 1-5)** (Travaglini et al., 2020).

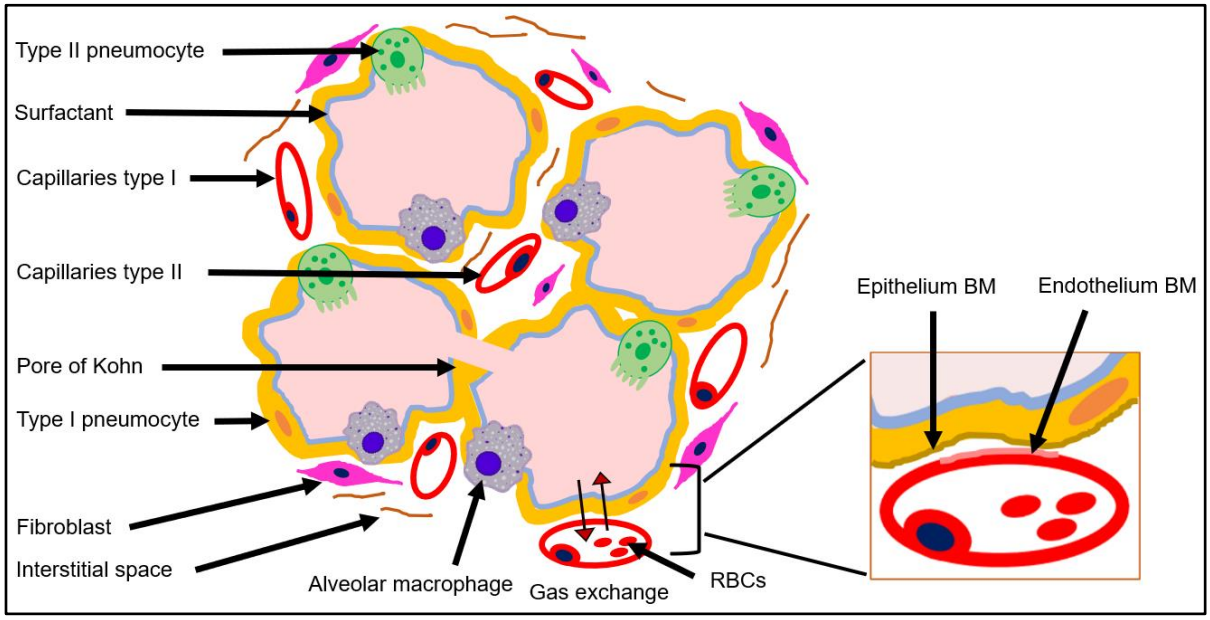

Figure 1-5. Schematic diagram of pulmonary alveoli along with lung capillaries. *Each alveolus contains type I and type II pneumocytes, surfactant fluid, and alveolar macrophages. Some neighbouring alveoli are connected by pores of Kohn. The interstitial space is the area between the alveoli and the capillaries that contain matrices such as collagen, elastic fibres, fibronectin and fibroblasts. The enlarged inset illustrates the basement membranes of the epithelium and the capillary.*

The alveoli are mainly lined by the epithelium and capillaries type I and II **(Figure 1-5)** (Vila Ellis et al., 2020). Capillary type I ECs are large and porous in shape and mainly mediate gas exchange, while capillary type II ECs are smaller in size and are reported to have a role in endothelial maintenance and repair (Gillich et al., 2020; Vila Ellis et al., 2020).

In the lung, tumours usually grow using three different angiogenic patterns (diffuse, basal, and papillary) in which there is destruction of normal parenchyma and generation of angiogenesis **(Figure 1-6A)** (Passalidou et al., 2002; Pezzella et al., 1996; Sardari Nia et al., 2008). There is also a fourth pattern in which the tumour grows by filling the alveolar spaces and exploiting pre-existing normal vessels (Bridgeman et al., 2017; Donnem et al., 2013; Offersen et al., 2001; Passalidou et al., 2002; Pezzella et al., 1996; Pezzella et al., 1997; Sardari Nia et al., 2008; Yousem, 2009). This may be advantageous: a three-dimensional (3D) reconstruction of clinical tissue sections of NSCLC found that non-angiogenic NSCLC vascularisation preserves normal lung structures compared to angiogenic NSCLC vascularisation as the latter showed dilated disorganised vessels within the deposited stroma (Adighibe et al., 2006).

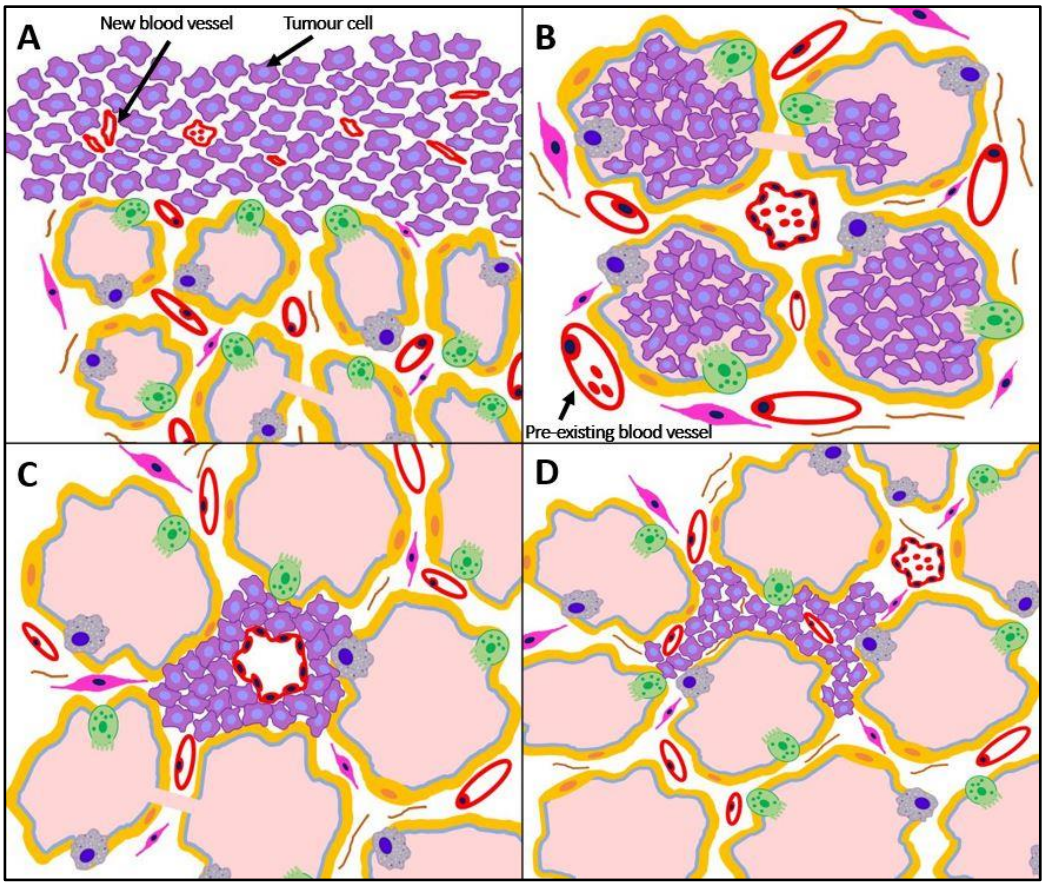

Figure 1-6. Schematic representation of different histological growth patterns adopted by lung cancer. *A: angiogenic growth pattern identified by chaotic and disorganised blood vessels; B: alveolar growth pattern, cancer cells fill the alveoli; C: cuffing growth pattern, cancer cells grow around big blood vessels; D: interstitial growth pattern, where cancer cells grow in lung interstitium (in between the alveoli and capillaries)*

Tumour cells co-opt vessels in the lung through multiple histological growth patterns, including alveolar, lepidic, interstitial, and cuffing patterns (Kuczynski et al., 2019; Sardari Nia et al., 2008). In alveolar tumour growth, tumour cells occupy the airspaces while keeping the alveolar walls intact **(Figure 1-6B)** (Sardari Nia et al., 2008). In the lepidic pattern, tumour cells line the alveoli in place of pneumocytes (Kuczynski et al., 2019). Tumour cells can also grow in the pulmonary interstitium (the space between epithelium and endothelial cells) and obtain blood supply from the vessels lying there, exhibiting an interstitial growth pattern. However, this pattern is reserved for metastatic cells **(Figure 1-6D)** (Kuczynski et al., 2019). Lastly, tumour cells co-opting vessels can also grow in the shape of cuffs, where they encircle large vessels **(Figure 1-6C)** (Kuczynski et al., 2019).

An early study in 1990 demonstrated that after stripping the epithelium that lines the alveoli, human primary lung tumours grow in the alveoli alongside the basement membrane (BM) and tend to invade from one alveolus to another through openings in the alveolar septum, known as, pores of Kohn **(Figure 1-5)** (Pääkkö et al., 1990). This observation has also been reported in preclinical lung metastasis models using different cancer cell lines, demonstrating that tumour cells can adhere to the BM surrounding the alveoli after dividing it into two BM, one attached to the endothelium and the other attached to the airway epithelium **(Figure 1-5, enlarged inset)** (Szabo et al., 2015). In the centre of big lesions, the co-opted vessels detach from the BM. Although they remain able to feed tumours, the proliferation rate of the endothelium is increased, and the stripped epithelium and the BM fragmentise and vanish, while at the interface between the non-malignant alveolar structures and tumour lesions, the BM remains intact (Pääkkö et al., 1990; Szabo et al., 2015).

Bridgeman and her colleagues explicitly demonstrated that the vascular phenotype and heterogeneous growth patterns of tumours in preclinical models are tumour model-dependent (Bridgeman et al., 2017; Szabo et al., 2015). Alveolar co-option by tumours was found to present in 50% of NSCLC patients and up to 25% of patients with advanced NSCLC (Kuczynski et al., 2019). In secondary organs such as breast, colon, and kidney lung

metastases, a high percentage of tumour cells hijack pre-existing blood vessels (about 62-98%) (Bridgeman et al., 2017).

It is still not clear how lung tumours choose whether to obtain their blood supply from pre-existing blood vessels or through inducing the formation of new ones, although this may be related to different signalling pathways. Microarray analysis of resected human tissue samples from angiogenic and non-angiogenic NSCLC revealed heterogeneity in gene expression patterns (Hu et al., 2005). The non-angiogenic NSCLC showed upregulation of genes associated with mitochondrial metabolism, cell cycle, and mRNA transcription, implicating the ability of cells to adapt to hypoxia by elevating mitochondrial respiration **(Figure 1-7)** (Hu et al., 2005). Alternatively, in the angiogenic NSCLC, upregulated genes were associated with angiogenesis, membrane vesicles, adhesion (*integrins* and *collagen VII*), inflammation-related pathways, and apoptosis (Hu et al., 2005). Following this microarray study, immunohistochemical analysis also revealed high levels of the following proteins: TNF receptor-associated protein 1 (TRAP1), CA9, PHD3, ephrin type-B receptor (EPHB) 2, EPHB3, neural cell adhesion molecule (NCAM), junction-mediating and regulatory protein (JMY), glutathione S-transferase (GST), and P53 along with higher P53 mutations in non-angiogenic NSCLC tumour section **(Figure 1-7) (Table 1-2)** (Adighibe et al., 2016). In contrast, angiogenic NSCLC tumour sections were found to highly express HIF1, PHD2, PHD3, CXCR4, BCL2 interacting protein 3 (BNIP3), peptidase inhibitor 3 (PI3), Epidermal growth factor (EGF), FOS, thrombospondin-1 (THBS1/TSP-1), DLL4, and STAT3 (Adighibe et al., 2016).

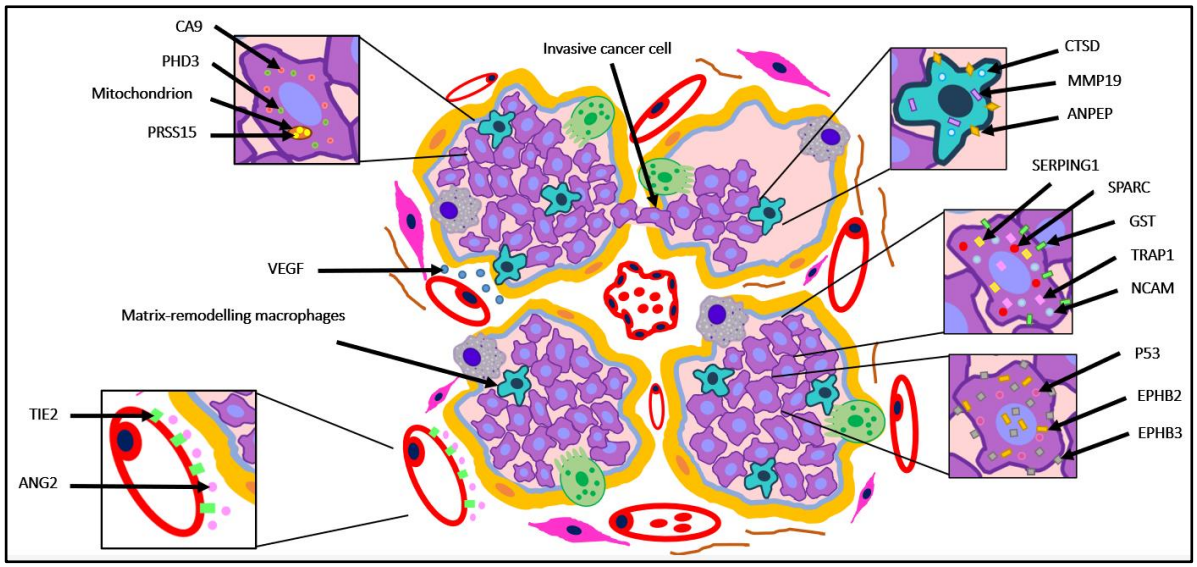

Figure 1-7. Schematic representation of signalling molecules involved in vessel co-option by cancer in the lung*. Overexpression of protease serine 15 (PRSS15) seems to enhance cancer cells' metabolic respiration, aiding in their perivascular invasion. Intrinsic invasive phenotype of cancer cells and matrix-remodelling macrophages found as cellular players contributing to vessel co-option in a preclinical metastatic lung model. Note that the localisation of the overexpressed signalling molecules, whether surface, cytoplasmic, or nuclear expression, as indicated in this diagram. CTSD: cathepsin D; MMP19: Matrix metallopeptidase 19; ANPEP: alanyl aminopeptidase; CA9: carbonic anhydrase 9; PHD3: prolyl hydroxylase dehydrogenase 3; SERPING1: serine proteinase inhibitor (serpin) family G member 1; SPARC: secreted protein acidic and cysteine-rich; GST: glutathione S-transferase; TRAP1: TNF receptor-associated protein1; NCAM: neural cell adhesion molecule; EPHB2: ephrin type-B2 receptor; EPHB3: ephrin type-B3 receptor; VEGF: vascular endothelial growth factor; TIE2: tyrosine-protein kinase receptor 2; ANG2: Angiopoietin-2.*

In the preclinical models of mouse primary LLC lung metastasis, rat C6 gliomas and rat implanted mammary adenocarcinoma, tumour co-opted endothelium initially showed high expression of ANG2 (Holash et al., 1999). High levels of tyrosine kinase 2 (TIE2) receptors at the tumour periphery coordinated with these vessels to facilitate vascular regression and regulate tumour progression, either through endothelium disruption and regression or by inducing proliferation of endothelial cells and neo-angiogenesis in the presence of elevated levels of VEGFA released by tumour cells **(Figure 1-7)** (Holash et al., 1999).

Recent single-cell transcriptional analysis of gene expression in tumour co-opted vascular ECs (induced by treatment of murine renal adenocarcinoma (RENCA) metastatic lung model with an anti-angiogenic therapy) revealed that co-opted ECs and pericytes are similar to healthy counterparts in their gene expression profiles (Teuwen et al., 2021). Instead, cancer cells and matrix-remodelling macrophages were identified as the key players driving vessel co-option in this model (Teuwen et al., 2021). In addition, they found that anti-angiogenic therapy-resistant (co-opting) metastases produced additional three phenotypes of

cancer cells compared to untreated (angiogenic) lung metastases. Based on their gene expression profiles, these cancer subclusters were identified as transitioning cancer cells, hypoxic cancer cells and invasive cancer cells (highly expressing *Serping1* and *Sparc*) **(Figure 1-7) (Table 1-2)** (Teuwen et al., 2021). In the same model, macrophages manifested different phenotypes in angiogenic and co-opting lung metastases. In the untreated angiogenic metastases, macrophages expressed genes related to M2-like phenotype. In contrast, the treated metastases (with vessel co-option) had M1-like macrophages (highly expressing pro-inflammatory, antigen-presentation machinery), matrix-remodelling, and hypoxia-regulated macrophages **(Figure 1-7) (Table 1-2).** These subtypes of macrophages showed distinct spatial localisations in relation to co-opted vessels, implicating them in multiple roles during vessel co-option (Teuwen et al., 2021).

Consequently, as summarised in **(Figure 1-7) (Table 1-2)**, the signalling pathways of vessel co-option in the lung appear to be driven by cancer cells, although a better understanding of the tumour endothelium could still further our understanding of cancer progression. Interestingly, Mitzner and Wagner (2004) suggested that in a diffusion-limited environment, primary and secondary lung tumours grow bigger and vascularise in a manner that may recapitulate lung growth following pneumonectomy (Mitzner & Wagner, 2004). Therefore, although the molecular determinants and morphologic changes of tumour vascularisation are understudied, the idea that it might follow the same fundamental principle of vascularisation of lung regeneration post-pneumonectomy could significantly advance our understanding of lung tumour progression and treatment (Mitzner & Wagner, 2004).

Table 1-2. Upregulated genes that mediate vessel co-option in primary and metastatic lung tumours.

Type of vessel co-opting tumour	Cell type	Upregulated genes or pathways (shown in literature)
Murine renal (RENCA) lung metastases (gene expression was analysed using scRNA-seq technology) (Teuwen et al., 2021)	Transitioning cancer cells	*Ppp1ra5a, Klf4, Ddit3*
	Hypoxic cancer cells	*Ldha, Hlgd1a, Gapdh*

	Invasive cancer cells	*Sparc, Pdpn*
	M1-like macrophages	Pro-inflammatory genes: *Il-1β, Il-6* Ag-presentation machinery genes: *Cd74, Cd80* Ifnγ response genes: *Irf4, Irf5*
	Matrix-remodelling macrophages	*Mmp19, Anpep, Ctsd*
	Hypoxia-regulated macrophages	*Mif, Ndrg1, Slc2a1*
Human non-angiogenic NSCLC tumour section (Adighibe et al., 2016).	Tumour areas	TRAP1, CA9, PHD3, EPHB2, EPHB3, NCAM, JMY, GST, P53

1.6.2 Mechanisms of tumour co-option of liver vessels.

In 2001, Vermeulen et al. observed that liver metastases can grow with three different histological patterns: desmoplastic, pushing and replacement. While the first two patterns were associated with angiogenesis, in the third, replacement, the tumour cells were replacing the hepatocytes and growing in the absence of angiogenesis (Vermeulen et al., 2001).

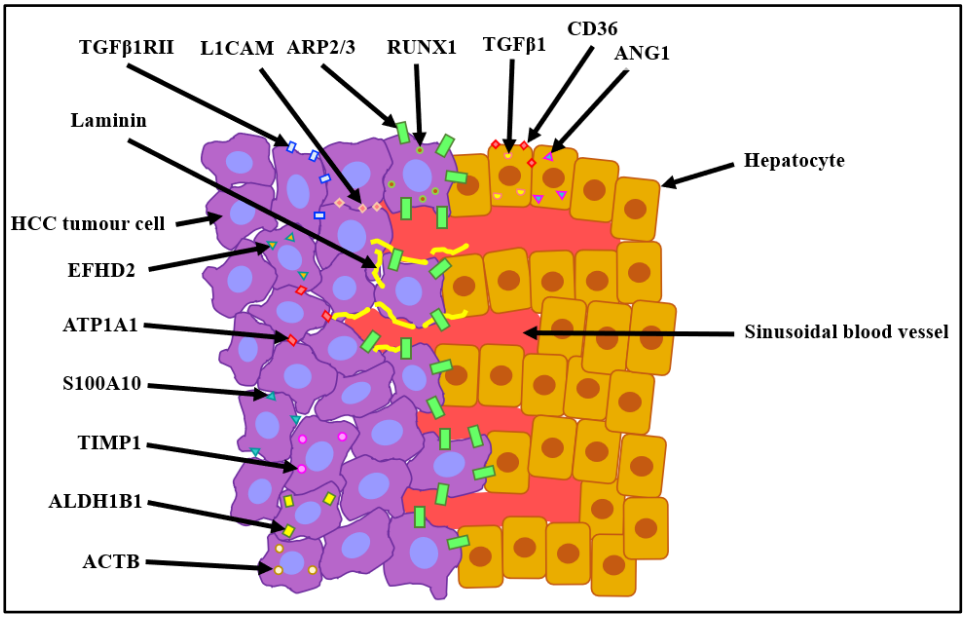

Figure 1-8. Schematic representation of signalling molecules involved in vessel co-option by cancer in the liver*. Cancer cells invading the pre-existing blood vessels in the liver are characterised by an overexpression of actin-related protein 2 and 3 complex (ARP2/3). Note that the localisation of the overexpressed signalling molecules, whether surface, cytoplasmic, or nuclear expression, as indicated in this diagram. EFHD2: EF-hand domain family member D2; ATP1A1: ATPase Na+/K+ transporting subunit alpha 1; S100A10: S100 calcium binding protein A10; TIMP1: TIMP1 TIMP metallopeptidase inhibitor 1; ALDH1B1: aldehyde dehydrogenase 1 family member B1; ACTB: actin beta; RUNX1: runt related transcription factor-1; ANG1: angiopoietin-1; THBS1: thrombospondin-1; TGFβ1: transforming growth factor beta 1.*

Interestingly, Nakashima et al. described that HCC (primary liver cancer) grows and vascularises the liver via three growth patterns they called sinusoidal, replacement, and desmoplastic or encapsulated, with the last two being more common in HCC than the first one (Nakashima et al., 1982). In the replacement pattern, HCC tumour cells are incorporated into the portal tracts, which contain hepatic arteries and sinusoidal vessels **(Figure 1-8)** (Nakashima et al., 1982; Nakashima et al., 1995). Small HCC replaces the hepatic plates while preserving the normal liver architecture and is characterised by indistinct non-fibrous boundaries (Nakashima et al., 1995). Histologically, the co-opted vessels are identified at early growth of the tumour, where tumour cells are well differentiated with lower proliferation ability and less aggressiveness (Nakashima et al., 1995). The other pattern of vessel co-option observed is a sinusoidal pattern that is distinguished from the replacement pattern by tumour cells growing inside the sinusoidal vessels, which might be ascribed to tumour cells failing to transmigrate through the endothelium (Kuczynski et al., 2019; Nakashima et al., 1982). However, unlike Vermeulen et al., these authors did not comment on the biology of these tumours in relation to the blood vessels, i.e., about the concept of angiogenic or non-angiogenic tumours (Nakashima et al., 1982; Nakashima et al., 1995).

The desmoplastic, or encapsulated, growth pattern of HCC is angiogenic and enclosed by a layer of fibrotic stroma (Vermeulen et al., 2001). Prior to pathological angiogenesis occurring in HCC, vascular remodelling is observed, where the endothelium lining the sinusoidal vessels becomes capillarised (transdifferentiate into capillaries) (Géraud et al., 2013). This capillarisation at the tumour periphery and tumour nest is demonstrated by losing the endothelial fenestra (pores) and downregulation/loss of liver sinusoidal endothelial cell (LSEC)-specific markers that eventually helps in HCC progression and neovascularisation (Géraud et al., 2013). In addition to the replacement and desmoplastic or encapsulated vascularisation, liver metastases vascularise using a pushing pattern (Stessels et al., 2004; van Dam et al., 2017; Van den Eynden et al., 2012; Vermeulen et al., 2001). In the pushing

pattern, the expansile growth of liver metastases induces angiogenesis and pushes aside the normal liver parenchyma without fibrosis (Stessels et al., 2004; Vermeulen et al., 2001).

Regarding immune involvement in liver tumours, immune cells are increased in liver metastases with the desmoplastic pattern, concentrated at the boundary of a tumour capsule and non-tumour area (van Dam et al., 2018). In contrast, liver metastases with a replacement pattern showed no immune infiltrates (van Dam et al., 2018).

Cancer cells have also been shown to modulate different growth patterns in human breast cancer and colon cancer liver metastases through upregulation of the actin-related protein 2 and 3 complex (ARP2/3). Expression of ARP2/3 by cancer cells can confer active motility, enabling these cells to invade the normal liver parenchyma with a replacement pattern **(Figure 1-8) (Table 1-3)** (Frentzas et al., 2016). Targeting vessel co-option growth via silencing ARP2/3 in metastatic HT29 human colorectal adenocarcinoma cell line significantly abolished the replacement or co-option pattern, and switched the vascularisation into desmoplastic or angiogenic growth (Frentzas et al., 2016). ARP2/3-overexpression in CRCs can be regulated by the transcription factor RUNX1, a pattern associated with the replacement (vessel co-opting) CRCLM tumours **(Figure 1-8) (Table 1-3)** (Rada et al., 2021). Intercellular communication between liver cells (hepatocytes) and CRCs mediated by THBS1/TSP-1-CD36-TGFβ signalling axis can also facilitate this vessel co-option growth pattern in CRCLM tumours **(Figure 1-8) (Table 1-3)** (Rada et al., 2021). In liver metastasis of primary uveal melanoma (UM), melanoma cells exhibit an angiotropic migration activity, migrating extracellularly along the co-opted sinusoidal vessels (Barnhill et al., 2022). These migratory melanoma cells are spatially localised at the invasive front of UM liver metastases, where they distinctively express L1CAM and laminin **(Figure 1-8) (Table 1-3)** (Barnhill et al., 2022).

Spatial transcriptomic analysis of human colorectal cancer liver metastases (CRCLM) revealed that replacement (co-opting) CRCLMs upregulate genes related to WNT signalling, glycolysis/gluconeogenesis and the pentose phosphate pathway (PPP), suggesting these molecular signalling as potential targets to treat CRCLMs with vessel co-option phenotype

(Table 1-3) (Fleischer et al., 2023). Alternatively, in desmoplastic (angiogenic) CRCLMs, an EC subtype annotated as activated-capillary-like (ACL) was identified with upregulated pathways related to EC development, differentiation, and establishment of EC barrier (Fleischer et al., 2023).

In addition to the upregulated genes in co-opting cancer cells, the origin of primary tumours also affects the respective growth patterns of liver metastasis (Stessels et al., 2004). For instance, breast cancer liver metastases more commonly adopted the replacement pattern than colon cancer liver metastases (Stessels et al., 2004). Even in the same type of primary tumour, cancers exhibited heterogeneous growth patterns depending on the anatomical location in the primary organ it metastasises from (Fleischer et al., 2023). For example, rectal primary colon tumours were reported to metastasise to the liver with the replacement pattern, whereas cecum and colon ascendens primary tumours exhibited liver metastases with desmoplastic growth (Fleischer et al., 2023). Interestingly, many studies have also suggested that the different growth patterns and vascularisation mechanisms seen in the metastatic liver resemble how liver tissue responds toward injury (Kuczynski et al., 2019).

Table 1-3. Upregulated genes that mediate vessel co-option in liver metastases.

Type of vessel co-opting tumour	Cell type	Upregulated genes or pathways (shown in literature)
Human colon cancer liver metastases (Fleischer et al., 2023)	Cancer cells	WNT signalling: EPCAM, ACTB, CSNK2A1, CSNK2B, DVL2, DVL3
		CRC marker genes: FABP1, CEACAM5, CLDN3, EPCAM, S100A10
		EMT: EFHD2, ATP1A1, PRSS8
		Invasion and migration: S100A10
		Poor prognosis: TIMP1, EEF1A1
		Glycolysis: ALDH1B1, LDHA
		Antioxidative glutathione metabolism: G6PD, GSR
		The pentose phosphate pathway (PPP): PGLS, PGD, RPIA, PRPS1, PRPS2
Human uveal melanoma liver metastases (Barnhill et al., 2022)	Invasive front of melanoma cells	L1CAM
	At the invasive front in the	Laminin

	basement membrane localised between sinusoidal vessels and angiotropic melanoma cells	
Human colon cancer liver metastases (Rada et al., 2021)	Cancer cells	RUNX1, TGFβ1, THBS1, TGFβRII, RUNX1 target genes: EMT: CDH2, CDH16, SNAI1, SNAI2, VIM/ cell motility: ARPC1b, ARPC2, ARPC3
	Adjacent hepatocytes	CD36, TGFβ1, THBS1
Human colon cancer liver metastases (Ibrahim et al., 2019)	Centre of the tumour region	ANG2
	Adjacent hepatocytes	ANG1
Human breast and colon cancer liver metastases (Frentzas et al., 2016)	Cancer cells	Cancer cell motility and epithelial-mesenchymal transition (EMT): ARP2/3

1.6.3 Mechanisms of tumour co-option of brain vessels.

Vessel co-option is also used by primary and secondary brain tumours (Lyle et al., 2016; Winkler et al., 2009). In the brain, the non-angiogenic vascularisation has preserved normal brain parenchyma and expresses markers of the blood-brain barrier (BBB) **(Figure 1-9)** (Bernsen et al., 2005; Holash et al., 1999).

The growth of tumours in the brain has distinct histological patterns (Caspani et al., 2014; Holash et al., 1999). Glioma cells can grow around the pre-existing BBB vessels with a perivascular growth pattern (Caspani et al., 2014). In low-grade glioma, these cells often diffuse near vessels that are covered with pericytes and glial cells (astrocytes). In contrast, in high-grade glioma, these cells are replaced with cancer cells encircling the vessels in ring-shaped structures (in high-grade glioma) **(Figure 1-9)** (Bernsen et al., 2005; Caspani et al., 2014; Kuczynski et al., 2019; Watkins et al., 2014). In the latter, glioma cells disrupt the astrocyte–vascular coupling, causing an impairment of BBB and release of K^+ causing vasoconstriction (Watkins et al., 2014).

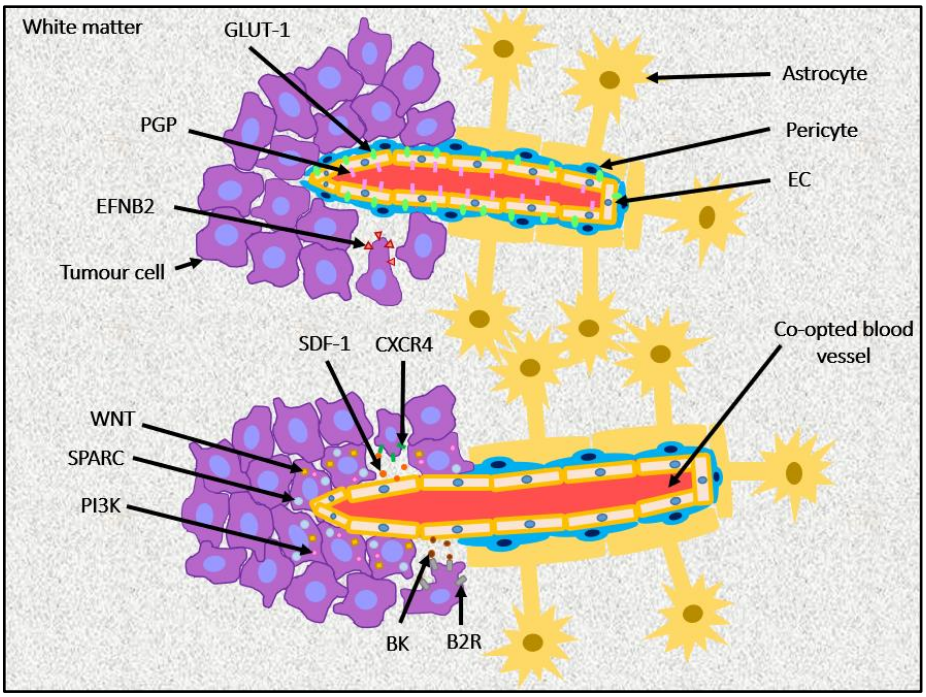

***Figure 1-9. Schematic representation of signalling molecules involved in vessel co-option by cancer in the brain**. Glioma cells co-opting pre-existed blood vessels in the brain have an overexpression of EFNB2, WNT, (SPARC), (PI3K). In contrast, co-opted endothelium upregulates glucose transporter 1 (GLUT-1) and phosphoglycolate phosphatase (PGP). It also overexpresses stromal cell-derived factor 1 (SDF-1) and bradykinin (BK) that attract glioma cells by interacting with their receptors, C-X-C chemokine receptor type 4 (CXCR4) and bradykinin 2 receptor (B2R), respectively.*

An angiogenic pattern is another way for glioma cells to grow in the brain, resembling the growth of lung and liver cancers. In this pattern, new chaotic vessels form in a compact mass of cancer cells separate from the non-malignant brain parenchyma (Holash et al., 1999). Vascularisation patterns in glioma also depend on the cell line (Baker et al., 2014; Holash et al., 1999). For example, mouse GL26 and rat CNS-1 gliomas mainly grow and progress using vessel co-option (Baker et al., 2014), whereas C6 rat glioma cells initially co-opt brain vessels and then compress non-perfusing vessels (Holash et al., 1999; Voutouri et al., 2019). Compression of the vessels causes hypoxia, which in turn induces VEGF and ANG2 production and subsequently induces angiogenesis (Holash et al., 1999; Voutouri et al., 2019).

In addition to the type of cell line used, different gene expression profiles in glioma cells were also found to contribute to angiogenic and vessel co-option phenotypes (Seano & Jain, 2020). Multiple serial passaging of biopsies collected from GBM patients in rats demonstrated that first-generation tumours vascularised via vessel co-option, showing no signs of hypoxia or expression of ANG2, HIF-1α, and VEGF, upregulated the expression of WNT, PI3K, NF-kβ, and SPARC **(Figure 1-9) (Table 1-4),** and expressed stem cell markers such as vimentin and nestin (Sakariassen et al., 2006). In contrast, later-generation tumours (serially passaged) showed many hypoxic regions with an upregulation of CA9, HIF-1α, and VEGF and a high percentage of proliferative endothelial cells inducing the angiogenic phenotype (Sakariassen et al., 2006). GBM cells themselves can orchestrate their invasion pattern either as individual or collective cells, co-opting the brain vasculature depending on their surface expression of oligodendrocyte transcription factor (OLIG2) and WNT7A **(Table 1-4)** (Griveau et al., 2018). These differential vessel co-option patterns were reported to be also controlled by the expression level of the epidermal growth factor receptor variant III (EGFRvIII) in brain tumour neural progenitor cells **(Table 1-4)** (Lindberg et al., 2016).

Stem cell-like or differentiated GBM cells were reported to mediate vessel co-option through differential gene expression (Depner et al., 2016; Krusche et al., 2016). In response to hypoxia (through HIF-1α upregulation), GBM cells can invade and co-opt brain parenchyma

mediating resistance to the bevacizumab (anti-VEGF Abs) by increasing the expression of the EMT repressor ZEB2, which in turns reduced EFNB2 **(Table 1-4)** (Depner et al., 2016). In contrast, a subpopulation of GBM cells, glioblastoma stem-like cells (GSC), overexpress EFNB2 in order to co-opt the pre-existing normal blood vessels **(Figure 1-9) (Table 1-4)** (Krusche et al., 2016).

The bidirectional interaction between glioma cells and vascular and perivascular cells also assists in the non-angiogenic phenotype (Caspani et al., 2014; Montana & Sontheimer, 2011; Yadav et al., 2016). For instance, crosstalk between highly bradykinin 2 receptor (B2R)-expressing glioma cells and bradykinin (BK)-producing vascular endothelial cells can elevate the intracellular level of Ca^{2+} concentration, leading to an increase in directed movement and invasion of glioma cells towards blood vessels **(Figure 1-9) (Table 1-4)** (Montana & Sontheimer, 2011; Seifert & Sontheimer, 2014). SDF1 expressed by brain ECs can also induce CXCR4-overexpressing glioma cells to invade, migrate, and associate with the pre-existing brain vasculature **(Figure 1-9) (Table 1-4)** (Yadav et al., 2016). In this study, inhibiting CXCR4 in glioma cells abrogates their migratory ability *in vitro,* increases the survival of mice, and sensitises glioma cells to radiation therapy *in vivo* (Yadav et al., 2016). Another study using transparent zebrafish and chicken brain metastasis models found that connexin expression in metastatic breast cancer and melanoma cells mediates vessel co-option in the brain (Stoletov et al., 2013). Two-photon and confocal live imaging of brain slice culture demonstrated that GBM cells also interacted with brain pericytes through CD44 and CDC42-overexpressing protrusions, facilitating the fusion of both cell types and thus co-option of brain vessels **(Table 1-4)** (Caspani et al., 2014). Vessel co-option was inhibited upon targeting CDC42 in GBM cells through converting pericytes into phagocytic, macrophage-like cells, contributing to anti-tumour response (Caspani et al., 2014).

In another study, metastatic brain cancer cells were investigated and shown to be protected from lethal stromal cues and co-opted brain capillaries by expressing themselves anti-PA serpins **(Table 1-4)** (Valiente et al., 2014). Secretion of soluble and exosomal L1CAM

by GBM cells supported their binding and motility along the co-opted brain capillaries, proliferation, and invasion **(Table 1-4)** (Pace et al., 2019). Double immunohistochemical staining of human meningioma, astrocytoma, and glioblastoma revealed that co-opting tumour cells exhibit high metabolic activity and high expression of PGP and S100A10 **(Table 1-4)** (Annese et al., 2022). The expression of these genes showed spatial localisation, where in the first two types of brain tumours, genes were highly expressed in the intratumoural area. In contrast, in the latter type, the genes were expressed in the peritumour area (Annese et al., 2022).

Table 1-4. Differentially expressed genes that mediate vessel co-option in brain tumours.

Type of vessel co-opting tumour	Cell type	Upregulated genes or pathways (shown in literature)	Downregulated genes or pathways (shown in literature)
Human meningioma, astrocytoma, and glioblastoma (Annese et al., 2022)	Brain tumour cells	PGP, S100A10	
Glioma (Jung et al., 2021)	Glioma cell	NOTCH1	
Glioblastoma (GBM) (Pace et al., 2019)	GBM cells	L1CAM	
GBM (Griveau et al., 2018)	GBM cells	OLIG2, WN7TA (promoting single-cell co-option)	OLIG2 and WNT7A (promoting collective perivascular co-option)
GBM (Yadav et al., 2016)	Human and murine glioma stem cells	CXCR4	
	Brain ECs	SDF-1	
GBM (Lindberg et al., 2016)	Tumour neural progenitor cells isolated from a model for high-grade astrocytoma developed in mice.	EGFRvIII enhanced collective vessel co-option	EGFRvIII enhanced single-cell vessel co-option
GBM (Depner et al., 2016)	In human G55, LN229 glioblastoma and murine glioma cell	ZEB2	EFNB2
GBM (Krusche et al., 2016)	Glioblastoma stem-like cells	EFNB2	
GBM (Jabouille et al., 2015)	GBM cells	CTGF, MMP-2, s TIMP-2, decorin, THBS1	IRE1
GBM (Caspani et al., 2014)	Human glioblastoma cell lines U87-MG and U373-	CDC42, CD44	

	MG implants into mouse brains and in vitro		
Brain metastases (Valiente et al., 2014)	Metastatic brain cells	Anti-PA serpins such as NS and L1CAM	
Breast cancer brain metastases and melanoma brain metastases (Stoletov et al., 2013)	Metastatic cancer cells	Connexins: Cx43, Cx26	
Glioma (Montana & Sontheimer, 2011)	Glioma cells	B2R	
	ECs	BK	
GBM biopsies that were serially passaged in rats (Sakariassen et al., 2006)		WNT, PI3K, NF-kβ, SPARC	
Gliomatosis cerebri (Bernsen et al., 2005)	Microvessels in tumour-infiltrated area	BBB markers: GLUT-1, PGP	

From the literature review of the molecular signalling of vessel co-option in the lung, liver, and brain, it is conceivable to conclude that this vascular phenotype is organ-specific. At histological level, vessel co-option is not well distinguished from angiogenic vessels. Even at the molecular level, the gene expression changes in intratumoural vessels and stromal cells driving this vascularisation are not well-characterised. In human and mouse models, this non-angiogenic vascularisation found to mediate the response to anti-angiogenic therapies and thus, patient outcomes. The following section discusses key players in tumour vessel co-option mediating response to therapies.

1.7 Current understanding of vascular switch between angiogenesis and vessel co-option

Angiogenic tumours can switch to a non-angiogenic phenotype and vice versa. This change can be primary (in the absence of any treatment) or secondary (after treatment) (Bridgeman et al., 2017; Donnem et al., 2018; Sophia et al., 2016; Vasudev & Reynolds, 2014). Treating many cancers with anti-angiogenic therapy has shown only moderate effectiveness and *de novo* or acquired resistance (Bridgeman et al., 2017; Donnem et al.,

2018; Frentzas et al., 2016; Vasudev & Reynolds, 2014). Potential mechanisms include tumours intrinsically employing alternative non-angiogenic growth, or a switch from an angiogenic mode into a non-angiogenic mode of invasion (co-opting vessels) following treatment (Bridgeman et al., 2017; Sophia et al., 2016; Vasudev & Reynolds, 2014). For example, tumours such as GBM and NSCLC were found to intrinsically obtain their blood supply from the intraparenchymal blood vessels (Baker et al., 2014; Pezzella et al., 1997), while a vascular switch into vessel co-option following anti-angiogenic therapies was observed in preclinical and clinical models of many cancers (Bridgeman et al., 2017; Frentzas et al., 2016; Kuczynski et al., 2016; Lazaris et al., 2018; Leenders et al., 2004).

A study by Kuczynski and colleagues found that targeting VEGFA and PDGF receptors in an orthotopic HCC liver carcinoma mice model with sorafenib resulted in tumour cells acquiring EMT properties, enabling a shift into vessel co-option (Kuczynski et al., 2016). This observed phenotype enabled the acquired resistance illustrated by an absence of reperfusion using contrast-enhanced ultrasound imaging (Kuczynski et al., 2016). Using another anti-angiogenic drug, ZD6474, to target the activity of both VEGFR2 and EGFR tyrosine kinases in a brain metastasis mouse model characterised by a high angiogenic growth also resulted in a switch into metastases with vascular co-option pattern revealed by poor enhancement imaged by contrast-enhanced (CE)-MRI (Leenders et al., 2004). Moreover, blocking VEGFA with bevacizumab in GBM models resulted in a vascular switch, illustrated by a more hypoxic microenvironment resulting in a high anaerobic glycolytic activity of tumour cells (increased lactate level) as a way for metabolic adaptation and enhancing their infiltration towards unaffected brain tissue (Fack et al., 2015; Keunen et al., 2011).

A clinical trial study showed that cediranib, which targets the activity of VEGF receptor tyrosine kinase, inhibited angiogenic growth of recurrent GBM, with tumours alternatively using the pre-existing blood vessels in the brain as evidenced by the expression of normal brain vasculature markers leading to vascular normalisation and a decrease in necrosis (di Tomaso et al., 2011). Similar changes were observed in glioblastoma patients treated with

bevacizumab, which clearly showed non-enhancing infiltrative radiographically and elevated levels of MMP2 and insulin-like growth factor binding protein-2 (IGFBP2) histologically (de Groot et al., 2010). Interestingly, inhibiting a cellular stress sensor signalling molecule, inositol-requiring enzyme 1α (IRE1) increased the expression of anti-angiogenesis genes: the connective tissue growth factor (CTGF), MMP2, tissue inhibitor of metalloproteinases (TIMP)-2, decorin, THBS1 switched glioblastoma from angiogenesis to vessel co-option using an orthotopic xenograft model of human glioma **(Table 1-4)** (Jabouille et al., 2015).

A similar vascular switch was reported in a clinical study of bevacizumab treatment, which observed a switch in the way CRCLMs vascularised, illustrated by a higher percentage of non-angiogenic replacement growth compared to the untreated CRCLMs group (Frentzas et al., 2016). In addition, immunohistochemical analysis of clinical CRCLM sections in another study revealed that the vessels in CRCLM with a replacement growth pattern treated with combination of chemotherapy and bevacizumab showed resistance to therapy demonstrated by minimal decrease in the microvessel density (MVD) compared to CRCLM with desmoplastic patterns that were sensitive to bevacizumab indicated by necrotic areas and the significant drop in proliferating ECs (Lazaris et al., 2018). RUNX1 overexpression has been associated with the resistance of vessel co-opting CRCLMs to chemotherapy and bevacizumab (Rada et al., 2021). Host cells such as hepatocytes can also contribute to vessel co-option either in intrinsic or chemotherapy- and bevacizumab-treated CRCLM lesions by increasing the expression of ANG1 **(Table 1-3)** (Ibrahim et al., 2019). Interestingly, ANG1 knockout mice showed a vascular switch to angiogenic CRCLMs, suggesting ANG1 contributes to vessel co-option (Ibrahim et al., 2019).

Tumours can switch from a non-angiogenic to angiogenic mode as they progress and enlarge in size (Holash et al., 1999). For example, at the periphery of liver metastases from colon, lung, and pancreas cancers, tumours grow along the normal blood vessels into a size of 1 mm in diameter. However, once they progress into macroscopic metastases (exceeding 20 mm in diameter), they switch into an expansive pattern (Terayama et al., 1996).

Conversely, in other cancers such as GBM, lung carcinoma, HCC liver, lung-metastatic renal, breast, colorectal carcinomas, and liver metastatic colorectal carcinomas, both angiogenic and non-angiogenic vascularisation occurs simultaneously in the same organ but spread in different regions (Bridgeman et al., 2017; Kanai et al., 1987; Kåre et al., 2014; Strand et al., 2015; Wesseling et al., 1994). This scenario is not applied in all progressing cancers, as liver metastases from gall bladder/bile duct cancer predominately metastasise using the angiogenic pattern (Terayama et al., 1996).

Identification and assessment of these vascular patterns and the switch from one to another in tumours is suggested to significantly affect patients' survival and response to anti-angiogenic therapies and immunotherapies response (van Dam et al., 2018; van Dam et al., 2017; Vasudev & Reynolds, 2014). However, a major limitation of this approach is the difficulty of resecting tumour specimens both prior to and post-treatment for monitoring treatment response (van Dam et al., 2018; van Dam et al., 2017; Vasudev & Reynolds, 2014).

1.8 Insights into crucial players mediating tumour response to anti-angiogenic therapies

1.8.1 Vessel co-opting tumours exhibit intrinsic and acquired resistance to anti-angiogenic therapies

Vessel co-option is just one of the mechanisms where tumours poorly respond and/or develop resistance to anti-angiogenic drugs (Zarrin et al., 2017). Because anti-angiogenic therapies target newly formed blood vessels in tumours, resistance to these therapies develops partly due to tumours vascularising using non-angiogenic approaches (Vasudev & Reynolds, 2014; Zarrin et al., 2017). Of note, human non-angiogenic CRCLMs treated with bevacizumab are associated with poor overall survival compared to an angiogenic CRCLM group (Frentzas et al., 2016), while CRCLMs with a mixture of replacement (non-angiogenic) and desmoplastic (angiogenic) growth patterns are also associated with worse prognosis than CRCLMs with pure desmoplastic phenotype (Fleischer et al., 2023). Biomarker identification

of CRCLMs with angiogenic or vessel co-option growth patterns would therefore be beneficial in tailoring therapy (Fleischer et al., 2023).

In WNT-overexpressing CRC tumours, CRC progenitor cells grew in a VEGFA-independent manner relying on OXPHOS respiration (Bernier-Latmani et al., 2022). These characteristics conferred an intrinsic resistance of CRC expansion to VEGF blockade, which was shown to be mediated by high expression APLN in crypt ECs (Bernier-Latmani et al., 2022). CRC progenitor expansion induced non-angiogenic growth and APLN-mediated vascular remodelling, subsequently increasing vessel perfusion and niche normoxia (Bernier-Latmani et al., 2022). Intrinsic resistance to therapy was also observed in glioblastoma **(Table 1-4)** (Jung et al., 2021), where differential expression of NOTCH1 in tumour cells mediated intrinsic resistance to chemotherapy and radiotherapy via vessel co-option (high NOTCH1) or formation of tumour microtubes (TMs)-intercellular networks (low NOTCH1) (Jung et al., 2021). Also, in a preclinical model, vessel co-option was developed as a resistance mechanism, and the tumour progressed upon prolonged treatment of the murine RENCA renal lung metastases with the anti-angiogenic drug, sunitinib (Teuwen et al., 2021). Transcriptome analysis of ECs in this preclinical model found that co-opted ECs resembled the transcriptome of healthy ECs, suggesting that targeting co-opted ECs may harm healthy ECs as well, although these observations maybe model-specific (Teuwen et al., 2021). Consequently, further transcriptional studies on co-opted ECs isolated from different preclinical models and human tumours are warranted.

1.8.2 A single tumour cell line can vascularise using multiple methods

Intriguingly, many cancer cell lines grown subcutaneously in the flank of mice (where new angiogenic vessels provide their blood supply) showed sensitivity to anti-angiogenic therapy (Bridgeman et al., 2017). However, the same cell lines administered intravenously developed metastases to the lungs which showed only a modest response or resistance to the same therapy (Bridgeman et al., 2017), potentially influenced by the fact that these cell lines metastasise to the lung using different vascular phenotypes (Bridgeman et al., 2017).

For instance, murine 4T1 breast and C26 colon carcinoma cell lines infiltrated the normal lung parenchyma and heavily utilised tumour vessel co-option, therefore sunitinib treatment did not suppress tumour growth (Bridgeman et al., 2017). Alternatively, the murine RENCA renal carcinoma cell line first colonised the lung via inducing angiogenesis but switched to an alveolar co-option pattern upon sunitinib treatment (Bridgeman et al., 2017; Teuwen et al., 2021). Consequently, resistance to anti-angiogenic therapies can be mediated by non-angiogenic vascularisation and the tumour microenvironment but is not directly related to the cancer cell type involved.

1.8.3 Contribution of the pulmonary and bronchial circulations to heterogeneous vascularisation in lung tumours

Alternative explanation for heterogeneous growth patterns of lung tumours and subsequent modest response to anti-angiogenic therapies could be that the type of blood circulation supplying the pulmonary lesions compromises the efficient delivery of anti-angiogenic therapies (Jonas & Carrington, 1969; Mitzner & Wagner, 2004; Szabo et al., 2015). Primary lung tumours can grow by obtaining their blood supply mainly from bronchial circulation, as evidenced by scans of metastatic human, rat, and mouse lungs (Jonas & Carrington, 1969; Milne & Zerhouni, 1987). Using CT scanning of metastatic human and rat lungs, Milne and Zerhouni demonstrated that lung metastases primarily grow and are nourished via pulmonary blood circulation (Milne & Zerhouni, 1987). Likewise, a mouse model of experimental primary LLC lung metastasis revealed that the pulmonary blood supply nurtures metastatic LLC growth (Savai et al., 2005). However, there is also evidence that some lung tumours are supplied by both bronchial and pulmonary arteries (Jonas & Carrington, 1969). A plausible explanation by this study is that the high proliferation and sprouting ability of the bronchial arteries allow for the expansion of the metastatic nodules, in contrast to pulmonary arteries that seem to support tumour growth towards normal lung parenchyma with arterial anastomoses of both types of arteries shown at the tumour periphery **(Figure 1-10)** (Jonas & Carrington, 1969). This differential vascularisation implicitly explains the mechanism

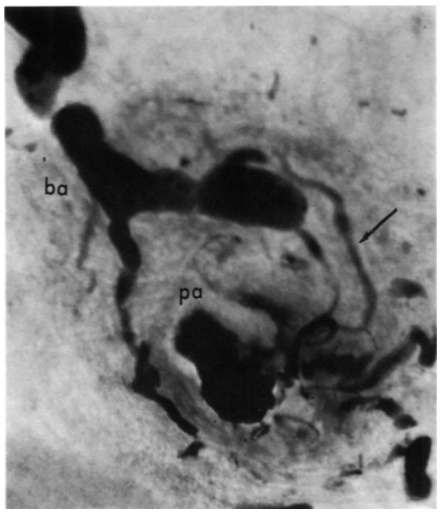

Figure 1-10. An arterial anastomosis formed (black arrow) within a lung tumour lesion connecting the bronchial artery to the pulmonary artery. *ba: an abbreviation for bronchial artery; pa: an abbreviation for pulmonary artery "adapted from "Vascular patterns in primary and secondary pulmonary tumours in the dog," by A. M. Jonas, C. B. Carrington, 1969,* The American journal of pathology, 56*(1), 79–95. Copyright Elsevier (1969).*

of lung tumour vascularisation in relation to the origin of blood supply (Jonas & Carrington, 1969). In support of this study, a later study by Szabo et al. (2015) using experimental rat lung metastases of breast adenocarcinoma cells found that both pulmonary and bronchial arteries ramify secondary lung nodules with tumour size being the key factor (Szabo et al., 2015). Lung nodules of less than 3 mm were found to be nourished by the pulmonary blood supply, whereas nodules of greater than 5 mm were supplied by bronchial circulation (Szabo et al., 2015). The latter showed an increased proliferation rate compared to the nodules ramified with pulmonary arteries, possibly and partly owing to lower oxygen tension in the pulmonary arteries' blood compared to the bronchial arteries' oxygenated blood (Szabo et al., 2015).

1.8.4 The maturity of tumour vessels can mediate tumour response to anti-angiogenic therapies

The heterogeneous maturation status of the blood vessels feeding tumours could also limit the response to anti-angiogenic therapies (Nagy et al., 2009; Ziyad & Iruela-Arispe, 2011). A study by Bergers and colleagues demonstrated that the immature newly formed vessels (devoid of perivascular cells) in the tumour are easily targeted by anti-angiogenic therapies (Bergers et al., 2003). In contrast, the mature ones, covered by perivascular cells, are not easily accessed by these therapies (Bergers et al., 2003). Vessel maturation mainly relies on the interaction between the endothelium and perivascular cells through PDGF-B-PDGF

receptor, S1P1–EDG1, ANG1-TIE2, and TGFβ signalling pathways (Jain, 2003). Thus, targeting these molecules may improve treatment outcomes (Bergers et al., 2003; Coxon et al., 2010; Pietras & Hanahan, 2005; Satoh et al., 2008; Yolla et al., 2020). In preclinical mouse models inoculated with tumour cell lines overexpressing ANG1, there was a reduction in the growth of tumours when the microenvironment contained an abundance of perivascular cells (Satoh et al., 2008). Conversely, in tumour microenvironments containing less perivascular cells, ANG1 overexpressing tumours (such as in human prostate cancer PC3 and murine colon C26) induced tumour angiogenesis (Satoh et al., 2008). Further, pharmacologically targeting both VEGFA and PDGF receptors (expressed on EC and perivascular cells, respectively) in a mouse model of pancreatic β-cell carcinogenesis resulted in more significant anti-tumour and anti-angiogenic effects than either agent alone (Bergers et al., 2003).

A study by Nagy and colleagues identified and morphologically and functionally characterised six types of tumour blood vessels. These were mother vessels (MV), three types of daughter vessels (capillaries, glomeruloid microvascular proliferations (GMPs) and arteriovenous-like vascular malformations), feeding arteries, and draining veins. Further, they were able to induce these vessel types using an *in vivo* ear model injected with adenoviral vectors expressing VEGFA (164) (Ad-VEGFA(164)) (Nagy et al., 2007; Nagy et al., 2008). When investigating their response to anti-angiogenic treatment, this study found that mother vessels and GMPs were hyperpermeable owing to their dependency on VEGFA, and therefore more susceptible to anti-VEGFA therapies (Nagy et al., 2009; Nagy et al., 2007). On the other hand, the other four subtypes are more likely to resist these therapies due to their mature structure (coated with pericytes or smooth muscle cells) and their independence of VEGFA (Nagy et al., 2009; Nagy et al., 2007). The key aspect illustrated by this study is that the response to anti-angiogenic therapies is affected by the timing of treatment, since it indicates that tumours containing newly formed vessels would be more sensitive to anti-VEGFA therapies compared to those containing established vessels (Nagy & Dvorak, 2012). These studies indicate that tumour growth can be inhibited through targeting different subsets of

tumour blood vessels. Thus, understanding the interaction between endothelial cells and perivascular cells in the tumour microenvironment, and finding markers for tumour perivascular cells (so that they can be selectively targeted without affecting the non-tumour perivascular cells) could help to overcome anti-angiogenic drug resistance (Helfrich & Schadendorf, 2011).

1.8.5 The potential role of immune cells in tumour response to anti-angiogenic therapies

Intriguingly, different immune infiltration densities have also been shown to contribute to different vascular patterns in tumours, mediating the response to anti-angiogenic and immune checkpoint therapies (van Dam et al., 2018). For instance, human desmoplastic CRC liver metastases were observed to contain high infiltrates of lymphocytes only at the desmoplastic rim that suppressed anti-tumour immunity and supported angiogenesis, which was not obvious in the replacement CRC liver metastases (van Dam et al., 2018; Vermeulen et al., 2001). Brunner and colleagues identified the types of immune cells surrounding desmoplastic CRC liver metastases as being composed of $CD4^+$ and $CD8^+$ T cells (Brunner et al., 2014). These infiltrated immune cells significantly improved the survival rate of these patients compared to patients with non-capsulated liver metastases (Brunner et al., 2014). Stremitzer et al. have recently found that angiogenic CRC liver metastasis is significantly associated with an immunogenic phenotype where cytotoxic T lymphocytes surround and infiltrate the metastases (Stremitzer et al., 2020). The immunogenic (inflamed) immune phenotype of these angiogenic CRC liver metastases has significantly better clinical outcomes than liver metastases with replacement (vessel co-option) growth pattern, which on the other hand, was significantly correlated with shorter survival (Stremitzer et al., 2020). In patients with angiogenic cancers such as metastatic melanoma and metastatic renal cell carcinoma, this immunosuppressive microenvironment supporting angiogenesis was lifted and anti-tumour cytotoxic $CD8^+$ T cells and macrophages were activated upon treatment with bevacizumab (blocking VEGF) combined with ipilimumab (inhibiting the immune checkpoint, T-lymphocyte-

associated antigen 4 (CTLA-4)) and bevacizumab (anti-CD20) combined with atezolizumab (inhibiting the immune checkpoint, PD-L1), respectively (Hodi et al., 2014; Wallin et al., 2016). In non-angiogenic cancers, for example in liver metastases, the immunosuppression supporting the replacement growth of tumours could be attributed to sinusoidal ECs (SECs) interacting with cytotoxic $CD8^+$ T cells through binding of the upregulated PD-L1 on SECs with PD-1 on T cells inhibiting the immune response and transforming them into tolerised T cells (Diehl et al., 2008). One of the strategies to promote anti-angiogenic and anti-tumour immune responses and to overcome resistance has been suggested by Hamzah and colleagues (2008), they found that targeting the vascular gene, G-protein signalling 5 (Rgs5) in a preclinical tumour model normalised tumour vasculature (an increase in tumour oxygenation and a reduction in vessel permeability) and significantly increased $CD8^+$ and $CD4^+$ T lymphocyte infiltration (Hamzah et al., 2008). Therefore, generating an immune-stimulating environment could enhance the effect of anti-angiogenic therapies.

Several mechanistic insights showed above can modulate the tumour response to anti-angiogenic therapies. Some of these mechanisms include the tumour's intrinsic properties, distinct lung vasculature (containing pulmonary and bronchial circulations), EC-pericytes interaction, maturation status of tumour vessels, and immune infiltration in the tumours.

The above literature review concludes that there is heterogeneity in the mechanisms and types of tumour vascularisation, raising the question of what the signalling molecules and the molecular changes in the endothelium are (in the metastatic niche, micrometastases, and established metastases) operating this complexity. Until now, there is a lack of reliable *in vitro* and *in vivo* models of vessel co-option and metastatic niche illustrating the interaction between cancer cells and the microenvironment, including the vascular component. Finding a model to investigate the molecular mechanisms could provide a comprehensive understanding which could clinically facilitate early detection of co-opted vessels, predict treatment response, and therefore, early targeting tumour growth for better prognosis.

1.9 Thesis Aims

Hypothesis1: we hypothesise that the metastatic niche and distal (uninvolved) vascular endothelial cells change their transcriptome to drive tumour vascularisation and progression. The overall aims of this project were to further understand the transcriptomes of metastatic niche ECs; and to compare the metastatic niche and distal stroma to non-tumour stroma.

In **AIM1**, I will explore the gene expression changes and biomarkers of vessel co-option, and the effect of this phenotype on the outcome of anti-angiogenic therapy

The objectives of Aim 1 are:

- To establish a syngeneic experimental E0771 lung metastasis model via injection of engineered mCherry-secreting E0771 cancer cells into the circulation.
- To characterise E0771 tumour growth and vascularisation in the lung by histological analysis and MRI imaging
- To optimise the spatial isolation of tumour ECs, specifically metastatic niche ECs, using flow cytometry.
- To track the evolution of metastatic-related spatial changes and interrogate gene expression signatures of the metastatic niche labelled endothelium isolated at earlyand late phases of metastasis using 10x Genomics' single-cell RNA-sequencing technique.
- To verify candidate tumour vascular makers identified by single-cell RNA sequencing analysis using immunohistochemistry and immunofluorescence in E0771 lung metastases.

Hypothesis2: we also hypothesise that metastatic niche stromal cells mediate tumour vascularisation through intercellular signalling interactions.

In **AIM2**, I will investigate the molecular cues from the metastatic niche stroma that drive angiogenic and non-angiogenic lung metastases.

The objectives of Aim 2 are:

- To analyse the transcriptome of lung stromal cells isolated from early and late phases of metastasis using 10x Genomics' single-cell RNA-sequencing technique.

- To validate candidate stromal genes that contribute to different patterns of tumour vascularisation.

Investigating these hypotheses will enable us to target the metastatic niche and identify potential targets to inhibit tumour vessel co-option, thus minimise metastatic growth.

Chapter 2: Materials and Methods

2.1 Cell lines and primary cells

2.1.1 HUVECs

Human umbilical vein endothelial cells (HUVEC) were purchased from Lonza and were cultured for up to six passages in EBM-2 Basal Medium (Lonza, CC-3156) and EGM-2 SingleQuots Supplements (Lonza, CC-4176).

2.1.2 Parental E0771 tumour cell line

Parental E0771 cells are a spontaneous metastatic medullary breast adenocarcinoma cell line originally derived from a spontaneous tumour in C57BL/6 mice (Ewens et al., 2005). The E0771 cell line is considered a triple-negative breast adenocarcinoma cell line, with only weak expression of oestrogen receptor alpha (ERα) restricted to the cytoplasm (Le Naour et al., 2020). E0771 cells contain mutations of the *Trp53, Kras, Spen*, and *Tbl1xr1* genes (Yang et al., 2017). It displays high EMT score and is characterised by low expression of claudins (Yang et al., 2017). This cell line was kindly provided by Professor. Ruth Muschel (University of Oxford).

2.1.3 The tdTomato transduced E0771 tumour cell

For *in vitro* experiments, the parental E0771 cell line was transduced with LeGO-iT2 lentiviral vector, which contains tdTomato cassettes (https://www.addgene.org/27343/). Lentiviral transduction was performed where 100,000 E0771 cells were seeded per well in a 12-well plate. The lentivirus (multiplicity of infection (MOI) of 10) was mixed with a transduction medium consisting of RPMI 1640 medium (Gibco, 21875-034), polybrene (6–8μg/ml), and heat-inactivated foetal bovine serum (FBS) and added to the cells. The plate was centrifuged at room temperature (RT) for 1.5 hours at 2000 rpm and then incubated at 37°C in 5% CO2. After 24 hours, the medium was replaced with the lentivirus-free medium. When confluency, the expression of tdTomato in transduced cells was examined under a fluorescent microscope

to confirm the success of lentiviral transduction **(Figure 2-1).** TdTomato E0771 cells, which were strongly positive for tdTomato, were FACS-sorted. Sorted cells were then expanded and frozen at -80°C for *in vitro* experiments **(Figure 2-1).**

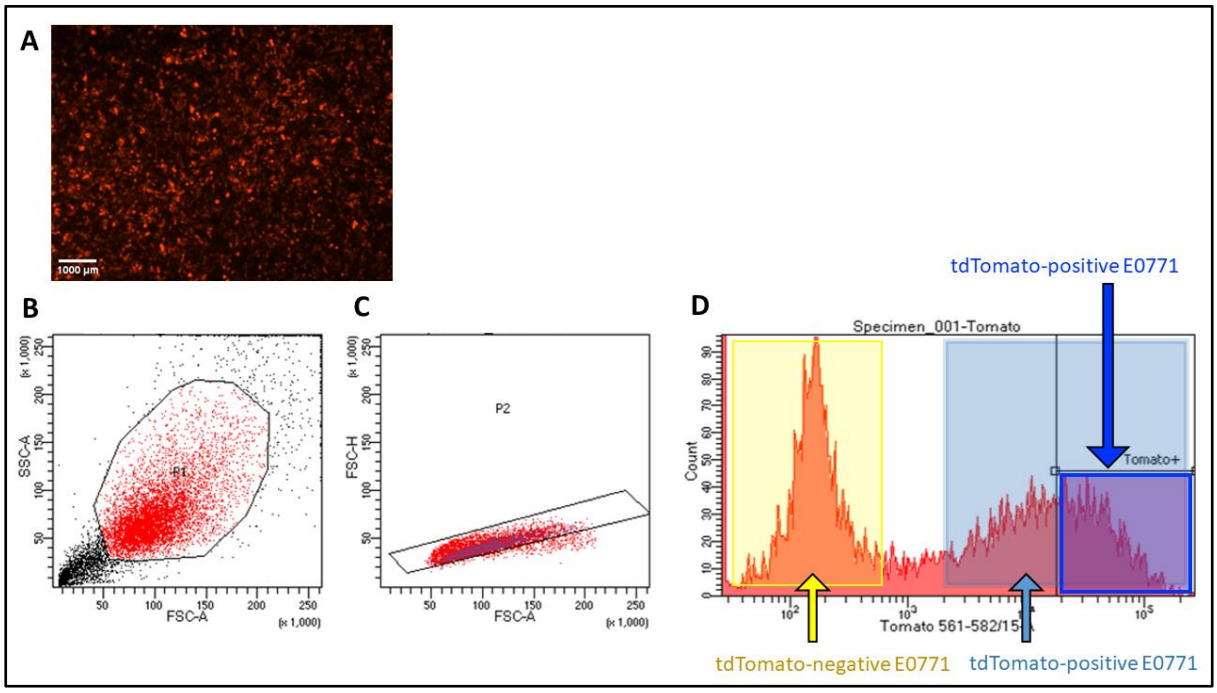

Figure 2-1. Validation of successful transduction of E0771 cells with tdTomato-encoding lentiviral vector. *A: High transfection efficiency of tdTomato-transfected E0771 tumour cells visualised by imaging tdTomato expression using an inverted fluorescent microscope; B: gating of population of interest using SSC vs FCS density plot; C: gating of singlets and excluding doublets by plotting FSC-H vs FSC-A; D: the strongly tdTomato-positive cells (shown with dark blue box) were FACS-sorted and expanded for in vitro studies.*

2.1.4 The EGFP-LUC transduced E0771 tumour cell

In order to fluorescently visualise tumour cells in both *in vitro* and *in vivo* experiments, the parental E0771 cell line was stably transduced with the FUGW lentiviral vector (Brennan et al., 2018), which contains enhanced green fluorescent protein (EGFP) and firefly luciferase (LUC) cassettes (EGFP-LUC E0771). Lentiviral transduction was performed where 100,000 E0771 cells were seeded per well in a 12-well plate. The lentivirus (multiplicity of infection (MOI) of 5) was mixed with a transduction medium consisting of RPMI 1640 medium (Gibco, 21875-034), polybrene (6–8µg/ml), and heat-inactivated foetal bovine serum (FBS) and added to the cells. The plate was centrifuged at room temperature (RT) for 1.5 hours at 2000 rpm and incubated at 37°C. After 24 hours, the medium was replaced with the lentivirus-free medium. When it reached confluency, the expression of EGFP in transduced cells was

examined under a fluorescent microscope to confirm the success of lentiviral transduction. EGFP-LUC E0771 cells strongly positive for EGFP were FACS-sorted, expanded, and frozen at -80°C for *in vivo* experiments. Luciferase enzyme activity of EGFP-LUC transduced E0771 cells was measured using luciferase Assay System (Promega, E1500) and luminescence readings were measured using an OPTIMA microplate reader (Manufacturer: BMG LABTECH, Model: BMG FLUOstar). Also, the proliferation activity of these transduced cells was measured using CellTiter 96® AQueous One Solution Reagent (Promega, G3581).

2.1.5 The mCherry-labelling hCD2 transduced E0771 tumour cell

The mCherry-secreting-human CD2-transduced E0771 cell line (mCherry-labelling hCD2 E0771) was provided by our collaborator, Professor. Illaria Malanchi (The Francis Crick Institute) (Ombrato et al., 2019). Her laboratory generated this by transducing the parental E0771 cell line with the Pentry-CHERRYgw6173 lentiviral vector. This vector contains a secreted fluorescent mCherry protein fused to a lipid-soluble tag (sLP-mCherry) and hCD2 cassettes separated by the internal ribosome entry site (IRES), such that both are co-expressed under the control of the PGK promoter **(Figure 2-2)**. SLP-mCherry is a mCherry fluorescent reporter fused to a soluble peptide (SP) 3 and a modified TAT peptide 4, which facilitates uptake by unlabelled nearby cells in *in vitro* and *in vivo* models, allowing spatial identification of the local cellular environment. Both parental E0771, tdTomato E0771, EGFP-LUC E0771, mCherry-labelling hCD2 E0771 were cultured in Dulbecco's modified Eagle's medium (DMEM) (Gibco, 41966-029) supplemented with 10% heat-inactivated FBS (Gibco, 10500064).

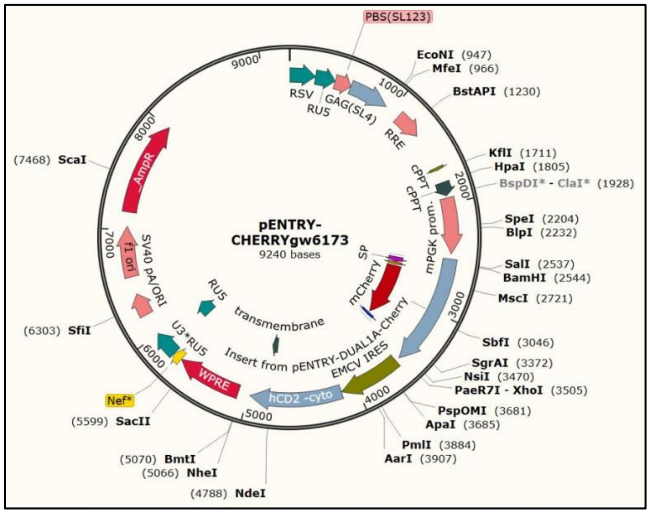

Figure 2-2. Schematic map of lentiviral plasmid vector containing the two cassettes that are co-expressed under mouse PGK promoter including human CD2 (hCD2) and mCherry protein fused to a lipid-soluble tag (sLP-mCherry). *Once this construct is transduced into a specific cell line, it can secrete mCherry labelling neighbouring cells.*

2.1.6 Mycoplasma testing

All the above cell lines tested negative **(Figure 2-3)** for mycoplasma infection every three months using the MycoAlertTM Mycoplasma Detection Kit (Lonza, catalogue number: LT07-318), following the manufacturer's instructions.

Well #	Sample	Reading A	Reading B	Reading B/reading A ratio
A1	Negative control	1610	463	0.288
B1	Positive control	1364	33657	24.675
C1	Parental E0771	634	512	0.808
A1	Negative control	1395	441	0.316
B1	Positive control	1096	33847	30.882
D1	GFP-Luc E0771	574	406	0.707
E1	mCherry-hCD2 E0771	480	369	0.769

10. Interpretation of results

The ratio of Reading B to Reading A is used to determine whether a cell culture is contaminated by mycoplasma.

Ratio	Interpretation
< 0.9	Negative for mycoplasma
0.9 - 1.2	Borderline: quarantine cells & retest in 24 h
> 1.2	Mycoplasma contamination

Figure 2-3. All cell lines were free of mycoplasma. The purple box is a copy from the kit that illustrates how to interpret the readings measured using OPTIMA microplate reader (Manufacturer: BMG LABTECH, Model: BMG FLUOstar).

2.1.7 Isolation of primary pleural mesothelial cells

Primary pleural mesothelial cells were isolated from C57BL/6 mouse lungs following a protocol published by Kawai and colleagues with some modifications (Kawai et al., 2019). Briefly, a pool (three or more) of C57BL/6 mice of approximately six weeks or older were euthanised by cervical dislocation, followed by cutting the inferior vena cava for blood drainage. An incision was made in the diaphragm to release the negative pressure in the chest. The thoracic cavity was washed with 2-3ml cold PBS, and the diaphragm was completely removed. 2-3ml of 0.05%Trypsin-EDTA (Gibco, 25300-096) was pipetted into the thoracic cavity, and mice were placed in a 37°C induction chamber for 20mins to allow for detachment of pleural mesothelial cells with the mouse chest cavity positioned in a 6-well plate in an upright position. Using this established protocol, we could also obtain epicardial cells (mesothelial cells covering the heart). The cell suspension was then collected into a 15ml tube containing DMEM medium supplemented with 20% FBS and centrifuged at 300 x g at 4°C for 8mins. Cells were washed with PBS before resuspending in DMEM medium supplemented

(Gibco, 31966-021) with 20% FBS and 1% penicillin/streptomycin (Lonza, DE17-602E). Cells were then added to each well of a 24-well plate (Corning, 83-3526), which had been previously coated with collagen type I (at 6-10 µg/cm^2) (Sigma-Aldrich, C3867). Cells were left until confluency, then used for functional assays as described. below, including transwell proliferation and invasion assays. These isolated pleural mesothelial cells exhibited cobblestone morphology **(Figure 2-4).**

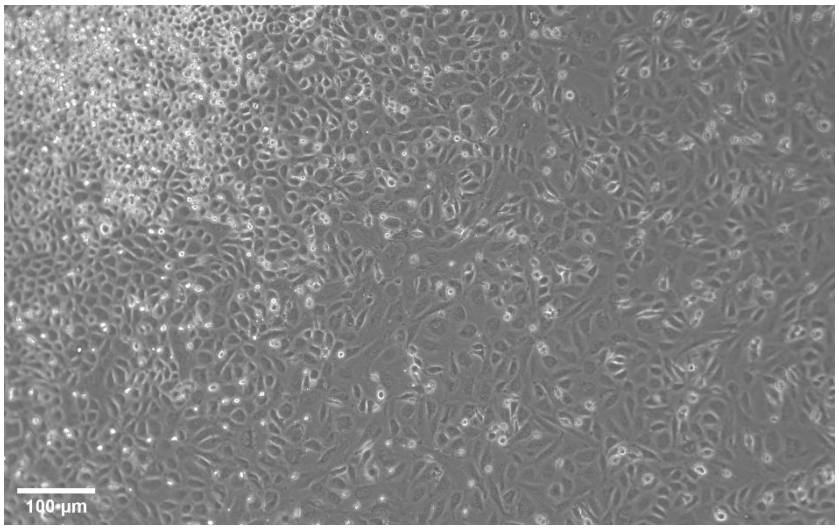

Figure 2-4. A confluent layer of primary pleural mesothelial cells characterised by their cobblestone morphology*. These cells were collected from 3 mice about 6 months old and reached confluency on day 6. The image was acquired at 10x magnification.*

2.2 In vitro assays

2.2.1 Transwell proliferation assay (indirect co-culture)

Parental E0771 tumour cells were cultured until confluency, then trypsinised into single cells for cell counting and seeding of 20,000 E0771 cells per insert (0.4µm sterile pore polycarbonate membrane inserts, Corning, 3415). In experimental wells, these E0771-seeded inserts were transferred into a 24-well plate containing a confluent monolayer of mouse primary pleural mesothelial cells (collected as described above) **(Figure 2-5A).** In control wells, E0771-seeded inserts were instead placed into wells with no mesothelial cells **(Figure 2-5A).** These seeded experimental and control transwells were then incubated for 48 hours with DMEM medium supplemented with 10% FBS in both compartments, allowing for tumour-stromal (mesothelial) crosstalk. Transwell assays were always performed in triplicate, with one mouse donor per replicate. To measure the proliferative ability of E0771 cells either in the presence or absence of the mesothelial monolayer, the CyQUANT Cell Proliferation Assay Kit (Invitrogen, C7026) was used following the manufacturer's instructions. In brief, inserts containing E0771 cells were washed once with PBS, followed by trypsinisation using 0.05%Trypsin-EDTA for 3mins. Trypsinised E0771 cells were transferred into a 96-well plate and pelleted via centrifuging the plate for 5mins at 1200 rpm. Pelleted cells were stored at -80°C. A cell number standard curve was created **(Figure 2-5B)** using different densities of parental E0771 tumour cells and frozen. On the day of measuring cell proliferation, a 96-well plate containing control and experimental wells as well as standard cell numbers, was thawed at RT.

Meanwhile, CyQUANT® GR dye was diluted 80-fold in 1X cell-lysis buffer. CyQUANT® GR dye/cell-lysis buffer was added (200µl per well) and incubated for 5mins in the dark. The fluorescence of the CyQUANT® GR dye was then measured using a CLARIOstar® Plus multi-mode plate reader (serial number 430-0024), which was set up with an excitation filter of 488 nm and an emission filter of 520 nm. Based on the generated standard curve, cell numbers of E0771 tumour cells of both conditions were then estimated from the measured fluorescence readings.

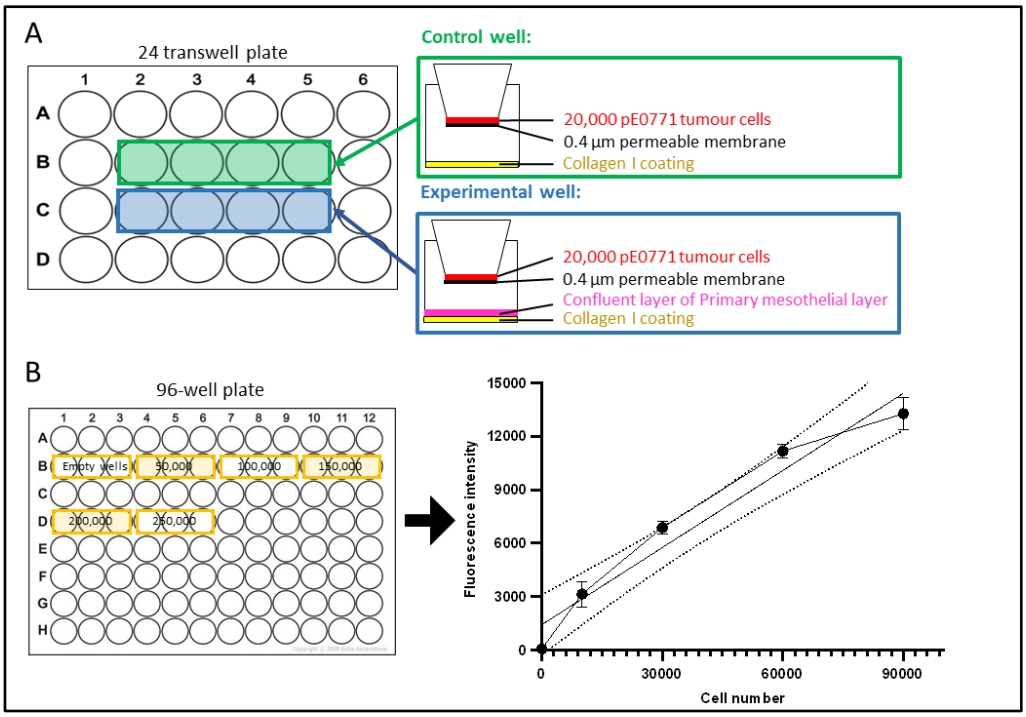

Figure 2-5. Representative diagram of transwell proliferation assay. *A: depicts control wells, which contain parental E0771 tumour cells in the inserts and no mesothelial cells in the lower compartment and experimental wells, which contain parental E0771 tumour cells in the inserts and pulmonary mesothelial monolayer in the lower compartment; B: depicts cell densities of parental E0771 tumour cells that were seeded in a 96-well plate for generating a reference standard curve.*

2.2.2 Transwell invasion assays (indirect co-culture)

Inserts of 8µm pore size (polycarbonate membrane, sterile, VWR, 734-2744) were coated with matrix to act as an invasion barrier) using collagen I (final concentration of 0.2mg/ml). To do this, the collagen I coat was incubated for 3 hours at 37°C, after which the wells were blocked and rinsed once with DMEM medium supplemented with 1% FBS. 100,000 tdTomato E0771 cells were seeded per insert. Prior to indirect co-culture, both confluent E0771 tumour cells and mesothelial cells were serum-starved overnight with DMEM medium

supplemented with 1% FBS to synchronise their cell cycle. In experimental wells, inserts containing E0771 tumour cells were placed in a 24-well plate containing a confluent monolayer of mouse primary pleural mesothelial cells **(Figure 2-6).** In control wells, E0771 tumour-containing inserts were instead incubated in wells with no mesothelial cells **(Figure 2-6)**. This indirect co-culture of tumour and mesothelial cells was incubated in DMEM medium supplemented with 1% FBS in both compartments for 48 hours to allow for tumour-stromal (mesothelial) crosstalk. Inserts were rinsed once with PBS, followed by fixation using 4%PFA for 15mins. Following fixation, cells were washed twice using PBS, and non-invaded cells on the apical side of the inserts were removed using a cotton swab. Cells that had invaded the insert's basolateral side were stained with Cresyl Violet acetate (Sigma, C5042) for 20mins at RT, followed by three washes with distilled water. Filter membranes were detached from inserts using cotton swabs and mounted on glass slides. Each transwell assay was performed in triplicate, with cells from one mouse used per replicate. To measure the invasive ability of E0771 tumour cells either in the presence or absence of mesothelial monolayer, four fields of view were captured per well (total number of wells per condition per replicate is four wells) using a Nikon ECLIPSE Ts2 inverted microscope with 20X magnification. Areas that were occupied by invaded E0771 tumour cells were quantified as a percentage using Fiji (version 1.53q) (Schindelin et al., 2012), with an 'in-house' designed macro (script) for automated measurements **(Appendix A)**. In brief, these macro-converted images were converted from TIF into 8-bit grayscale, followed by adjusting the threshold to create a red pixel overlay (mask). The background was then subtracted to exclude debris, membrane pores, and non-cellular background.

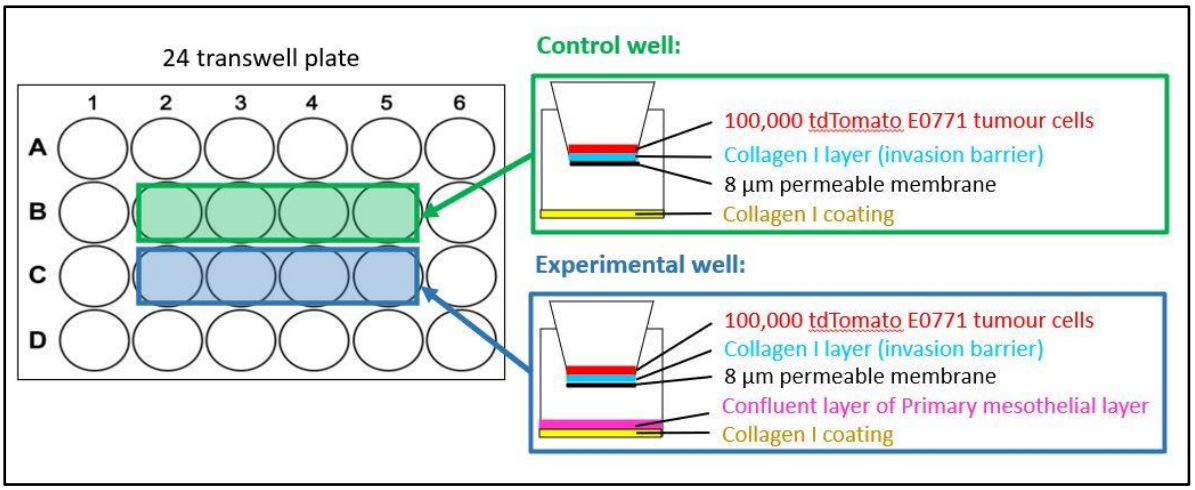

***Figure 2-6. Representative diagram of transwell invasion assay. Green** box: depicts control wells which contain tdTomato E0771 tumour cells on top of collagen I (invasion barrier) in inserts and no mesothelial cells in the lower compartment; Experimental wells which contain tdTomato E0771 tumour cells on top of collagen I (invasion barrier) in inserts and pulmonary mesothelial monolayer in the lower compartment.*

2.2.3 Direct co-culture assay

To validate the labelling ability of mCherry-labelling hCD2 E0771 cell line *in vitro*, HUVECs were directly co-cultured with these cells in a 1:4 ratio. After 48 hours of incubation, cells were trypsinised with 0.05%Trypsin-EDTA and washed twice with 1x PBS solution. The cell suspension was centrifuged at 300 x g for 5mins, and the cell pellet was resuspended in FACS staining buffer (PBS containing 10% FBS) and FACS-stained with FITC-anti-human CD31 (Pecam-1) (Biolegend, 303104)**.** Cells were washed twice with FACS staining buffer and then analysed using Attune Flow Cytometers. FACS data was analysed using FlowJo v10.6.2 software (TreeStar Inc.).

2.2.4 Indirect co-culture assay

Indirect co-culture assay was performed to validate if the mCherry-labelling hCD2 E0771 cells correctly secreted mCherry in the medium, and that the recipient cells can uptake the mCherry. The laboratory that has generated this mCherry labelling tumour cells reported that the *in vitro* labelling efficiency of the conditioned medium is low. First, the mCherry-labelling hCD2 E0771 cell line was cultured to confluency. Then, a fresh DMEM medium supplemented with 10% FBS was added to the confluent layer and incubated for 48 hours to allow the cells to secrete mCherry into the medium. Conditioned medium (CM) was then

collected and centrifuged at 300 × g for 10mins to pellet cells and debris for removal. The supernatant was collected and centrifuged at 2000 × g for 10mins, then, filtered using a 0.22µm pore size filter (Millex, 0369). This CM was added to HUVECs that were seeded the day before and then incubated for 48 hours. HUVECs were then trypsinised with 0.05%Trypsin-EDTA and washed twice with 1x PBS solution. The cell pellet was resuspended in FACS staining buffer and FACS-stained with FITC-anti-human CD31 (Pecam-1) (Biolegend, 303104)**.** HUVECs were washed twice with FACS staining buffer, and then mCherry uptake by HUVECs was analysed using Attune Flow Cytometers. FACS data was analysed using FlowJo v10.6.2 software (TreeStar Inc.).

2.3 Transgenic mice model and mouse strains

2.3.1 Mice breeding and maintenance

Animal breeding, maintenance, and animal procedures were performed by staff from Biomedical Services at the University of Oxford and by myself (PIL license: I984511B0) under specific-pathogen-free conditions following approval by the University of Oxford Animal Welfare and Ethical Review Board and in accordance with the Animals Scientific Procedures Act of 1986 UK under PPL30/3197 and PP1224162.

2.3.2 Mouse strains:

2.3.2.1 Inducible endothelial cell-specific Eltd1 knockout mice

Eltd1-floxed mice were kindly provided by our collaborator, Professor. Peter Carmeliet's laboratory, CCB-KU Leuven Centre for Cancer Biology, Belgium. In these, loxP sites were inserted within the *Adgrl4/Eldt1* gene, such that exons 4 and 5 are excised after exposure to Cre recombinase. The inducible endothelial cell-specific Cre-driver *Pdgfb-iCreERT2* mice were generated by Professor. Marcus Fruttiger's laboratory (University College London, United Kingdom) (Claxton et al., 2008), specifically containing the *Tg(Pdgfb-iCre/ERT2-EGFP)1Frut* allele. The breeding to generate induced EC-specific *Eltd1*-KO mice (*Eltd1*^{iEC}) was carried out previously in our laboratory by Dr. Koon Hwee Ang (Ang, 2019). Firstly, a *Pdgfb-iCreERT2* male mouse was mated with an *Eltd1*$^{fl/fl}$ female mouse producing *Pdgfb-iCreERT2*$^{Cre/+}$*; Eltd1*$^{fl/+}$ offspring (+ indicates wild-type allele). This transgenic mouse was then crossed to an *Eltd1*$^{fl/fl}$ female mouse, eventually generating *Pdgfb-iCreERT2*$^{Cre/+}$*; Eltd1*$^{fl/fl}$ male mice, from which the experimental mice could be bred (again using crosses with *Eltd1*$^{fl/fl}$ females). This breeding results in progeny where 50% were positive for Cre and 50% lacking this transgene, providing the control littermates for tumour models.

2.3.2.2 *Inducible Wt1-CreERT2; tdTomato reporter mice*

Inducible *Wt1-CreERT2*; tdTomato mice were provided by our collaborator, Professor. Nicola Smart's laboratory (University of Oxford, United Kingdom). The *Wt1-CreERT2* mice contained the *Wt1tm2(cre/ERT2)tm2(cre/ERT2)Wtp* allele (Zhou et al., 2008), whilst the tdTomato reporter mice contained the *Gt(ROSA)26Sortm9(CAG-tdTomato)Hze* allele, also known as the Ai9 allele (Madisen et al., 2010). Our transgenic line was generated by crossing *Wt1-CreERT2*$^{Cre/+}$;tdTomato$^{td/+}$ male mouse with R26tdTomato$^{td/td}$ female mice. A male *Wt1-CreERT2*$^{Cre/+}$;tdTomato$^{td/td}$ mouse was then further crossed with either Rosa26tdTomato$^{td/td}$ females (yielding *Wt1-CreERT2*$^{Cre/+}$;tdTomato$^{td/td}$ experimental and *Wt1-CreERT2*$^{+/+}$; tdTomato$^{td/td}$ Cre negative controls) **(see Figure7-13 in Chapter 7),** or with wild type female mice **(Figure 2-7)**, yielding *CreERT2*$^{Cre/+}$;tdTomato$^{td/+}$ and *CreERT2*$^{+/+}$;tdTomato$^{td/+}$ mice for tumour models.

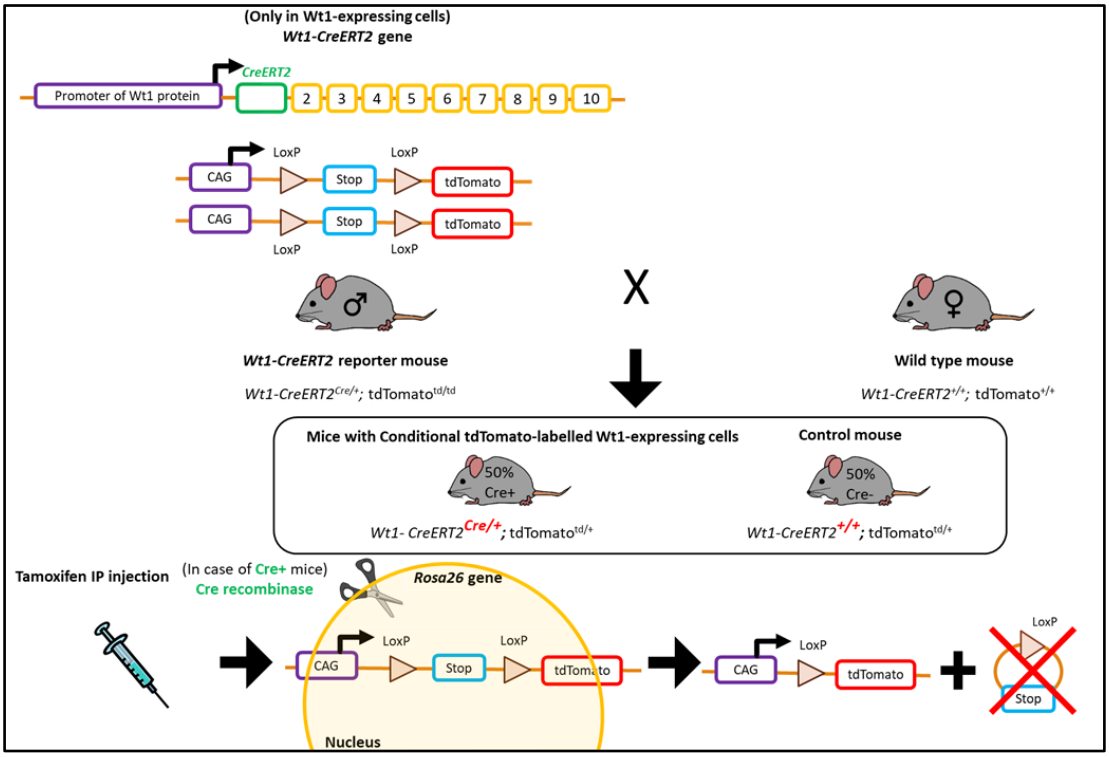

Figure 2-7. Diagram illustrating inducible induction of tdTomato reporter expression in Wt1-expressing pleural mesothelial cells in Wt1-CreERT2:tdTomato reporter mice. *Wt1-CreERT2*$^{Cre/+}$;*tdTomato*$^{td/td}$ *male mouse crossed with wild type female mouse yielded 50% Cre+ and 50% Cre- progeny. Tamoxifen administration induces tdTomato labelling of Wt1-expressing cells in 50% of offspring expressing Cre recombinase under Wt1(mesothelial marker)-specific promotor. Upon oral gavage of tamoxifen to this model, tamoxifen will bind to its binding domain of oestrogen receptor (ER), causing translocation of Cre recombinase from the cytoplasm into the nucleus, where recombination (excision) of loxP-flanked stop sequence then occurs inducing tdTomato expression. This transgenic line contains Cre sequence under the promoter of a mesothelial marker, Wt1 gene, allowing spatiotemporal Cre-recombination and tdTomato reporter expression to occur only in pleural mesothelial cells.*

2.3.3 Tamoxifen preparation and administration

Tamoxifen (T5648, Sigma-Aldrich, St. Louis, MO, USA) was dissolved in 100% ethanol in a sterile and dark environment within a biological safety cabinet, at 100mg/ml stock concentration. This mixture was then wrapped in foil, vortexed several times, and incubated overnight in a shaking incubator (200 rpm, 37˚C). This stock solution was then stored at -20˚C. To prepare a working tamoxifen solution, sunflower seed oil (Sigma, S5007) was added to this ethanol mixture in a ratio of 9:1 and wrapped in aluminium foil to protect from light. This working solution was further incubated for 24 hours in a shaking incubator before injection to dissolve any precipitates (the working solution can be stored at 4˚C for up to one week).

3-5 weeks old *Pdgfb-iCreERT2; Eltd1*^{fl} mice were intraperitoneally (IP) injected with tamoxifen (0.5 mg per mouse weighing 17 grams or below, and 1 mg per mouse weighing above 17 grams) every 24 hours for three consecutive days. Deletion of *Eltd1* using the approach was previously validated by our laboratory (Ang, 2019).

Wt1-CreERT2; tdTomato mice were treated via gavage administration of tamoxifen, with two doses in 4 weeks mice, followed by two doses one week later (0.5 mg per mouse weighing 17 grams or below and 1 mg per mouse weighing above 17 grams).

All mice were monitored for any adverse effects following tamoxifen treatment, and their weights were measured. Where relevant, tamoxifen-treated mice were kept for 2-3 weeks before tumour inoculation to allow tamoxifen and its metabolites to be cleared from the system.

2.3.4 Genotyping

All mice were genotyped from ear notches. DNA was extracted from ear notches using Hot Shot lysis buffer (25mM NaOH/0.2mM EDTA) and incubated for an hour at 98°C to lyse the tissue, then neutralised using neutralisation buffer (40mM Tris-HCl (pH=5.5). Extracted DNA was amplified via polymerase chain reaction (PCR) with *EGFP* and *Cre* forward and reverse primers for *Pdgfb-iCreERT2; Eltd1*^{fl} mice and *Cre* forward and reverse primers for the *Wt1-CreERT2*;*tdTomato* mice **(Table 2-1)**. The PCR reaction mixture was prepared by adding

the following reagents: 12.5µl Go Taq Green Master Mix (Promega, M7113, containing DNA polymerase, dNTPs and dye), 0.5µl 5µm of primers, 6.75µl nuclease-free water, 0.75µl DMSO (*EGFP* primers only) and 4µl extracted DNA. The amplified DNA samples and 1 Kb Plus DNA Ladder (Thermo Fisher Scientific, 10787018) were loaded into a 1% agarose gel (Fisher Scientific, BP1356-500), and a voltage of 145 V was applied to the gel for 25 min.

Table 2-1. PCR forward and reverse primers were used for genotyping Pdgfb-iCreERT2; Eltd1^{fl} mice and Wt1-CreERT2;tdTomato reporter mice before tamoxifen administration.

Transgenic mice	Primer name	Forward or reverse	Primer sequence: oligo sequence (5' to 3')	Annealing temperature	Expected band size
Pdgfb-iCreERT; Eltd1^{fl}	*EGFP*	Forward	CCCATCCTGGTCGAGC	59°C	396 bp
		Reverse	GTTGTACTCCAGCTTGTGCC		
	Cre	Forward	CCAGCCGCCGTCGCAACT	59°C	430 bp
		Reverse	GCCGCCGGGATCACTCTCG		
***Wt1-CreERT2*; tdTomato**	*Cre*	Forward	CATTTGGGCCAGCTAAACAT	60°C	308
		Reverse	ATTCTCCCACCGTCAGTACG		

Table 2-2. PCR cycling conditions for genotyping Pdgfb-iCreERT2; Eltd1^{fl} mice and Wt1-CreERT2;tdTomato reporter mice.

Transgenic mice	Cycling condition			
	Temperature	Duration	Number of cycles	
Pdgfb-iCreERT2;Eltd1^{fl}	94°C	2 mins	Initial denaturation	1 cycle
	94°C	30 sec	Denaturation	35 cycles
	59°C	30 sec	Annealing	
	72°C	1 min	Extension	
	72°C	10 mins	Final extension	1 cycle
	16°C	∞	Final hold	
	Cycling condition			
Inducible *Wt1-CreERT2;* tdTomato reporter mice	94°C	2 mins	Initial denaturation	1 cycle
	94°C	50 sec	Denaturation	10 cycles
	65°C	50 sec	Initial annealing (0.5 °C gradual decrease every cycle)	
	68°C	1min 15 sec	Extension	
	94°C	50 sec	Denaturation	28 cycles
	60°C	50 sec	Annealing	
	72°C	1min 15 sec	Extension	
	72°C	5 mins	Final extension	1 cycle
	16°C	∞	Final hold	

2.3.5 Generation of murine experimental lung metastases model

One million cells (either parental E0771, firefly luciferase-EGFP-transduced E0771, or mCherry-secreting-human CD2-transduced E0771) were intravenously injected into the tail vein of experimental mice (e.g. *Wt1-CreERT2*;*tdTomato)* at 6-7 weeks of age. Tumour-bearing mice were monitored daily. In this experimental mouse model, there were no severe changes in body weight, mobility, posture, or feeding habits. The time frame of sacrificing the mice following tumour induction was empirically predicted to be on day 13-16 (experimental endpoint), a timepoint chosen as mice showed acceptable tolerability. If any tumour-bearing mouse showed established signs of distress, discomfort, paralysis, spontaneous tremors, moribund, or severe weight loss of > 15% (cachexia) prior to this endpoint, they were immediately culled (humane endpoint).

2.3.6 Generation of experimental lung metastasis therapy model

An anti-angiogenic drug, pazopanib (GW786034 HCl) (Stratech, S1035) was prepared by dissolving it in DMSO (final concentration of the pazopanib master mixture of 800mg/ml). The pazopanib master mixture was then mixed sequentially with 30% v/v PEG300, 0.5% v/v Tween 80, and double distilled water (final concentration of 8mg/ml).

One million parental E0771 cells were intravenously injected into the tail vein of wild-type female mice on a C57BL/6 genetic background at approximately 6 weeks of age. These mice were randomly distributed into drug- or vehicle-treated groups and received an oral gavage of pazopanib (anti-angiogenic therapy) at 100 mg/kg, or solvent control (used to dissolve and prepare the drug). The dosing volume per animal was 200µl for the first day of treatment, followed by 120µl for the remaining 5 days. The health and welfare of these mice were monitored daily, as above. The experimental endpoint was day 13 post-tumour inoculation.

2.4 Histological analysis:

2.4.1 Formalin Fixed Paraffin Embedded (FFPE) murine tissues

2.4.1.1 Tissue fixation, paraffin tissue processing and embedding

Harvested mouse lungs were fixed overnight in 4% paraformaldehyde (PFA) (Sigma) at 4°C. PFA was then washed away through a series of PBS washes, and the tissues were then incubated in 70% ethanol until processed using a tissue processor (Tissue-Tek® VIPTM 5 JR.). Following tissue processing (in which the organs were cleared through a series of ethanol and xylene treatments), organs were embedded in paraffin. Tissue blocks were placed in a -20°C freezer prior to sectioning. Tissues were cut into 4µm thickness using a Thermo Scientific™ HM 355S Automatic Microtome (Brand: Thermo Scientific™ 905200STS), collected onto glass slides and dried overnight in a 37°C incubator.

2.4.1.2 Tissue deparaffinisation, rehydration and antigen retrieval

The sections were warmed in a 60°C oven for 10 min, deparaffinised and rehydrated by immersion using the following sequential washes: 2 x 5mins in Histo-Clear II (National Diagnostics, NAT1330) 2 x 3mins in 100% Industrial Methylated Spirit (IMS) (Fisher, M/4450/PB17), 1 x 3mins 70% IMS for 3 min, 1 x 3mins 50% IMS, 1 x 3mins tap water. Next, sections were pre-treated with the antigen retrieval reagent citrate buffer (pH 6.0) (EnVision FLEX Target Retrieval Solution, Low pH (50x) or (Enzo, ADI-950-271-0500), Agilent Technologies, K800521-2) and exposed to high temperature using a pressure cooker for 3mins followed by cooling for 20 min. Sections were then washed 3x with 1X EnVision FLEX wash buffer (stock concentration: 20x) (Dako, DM831, Agilent Technologies, K800721-2). Water-repellent circles were drawn around tissue sections using a pap pen (Vector Laboratories, H-4000). These sections were then ready for either immunohistochemistry or immunofluorescence staining.

2.4.1.3 Haematoxylin and eosin (H&E) staining of tissue sections

Dewaxed and rehydrated sections were stained with Harris's haematoxylin (Sigma-Aldrich, HHS32) for 1 min, rinsed with running tap water, then washed in 1% acid alcohol (1% of hydrochloric acid (HCL) and 70% alcohol) to remove excess dye then returned to running tap water. Slides were then placed into Scott's tap water substitute (20g $MgSO_4$, 2g $NaHCO_3$, 1l water) for 1 min, then returned to running tap water. Slides were then counterstained with Acidified Eosin Y Solution (1 gram Eosin Y disodium salt, Sigma-Aldrich, E6003 in 100ml of 70% ethanol acidified by adding up to 0.5ml of glacial acetic acid per 100ml of stain) for 1min then returned to running tap water. Finally, slides were dehydrated through increasing percentages of IMS, incubated for 2 x 5mins in Histolene clearing agent and then mounted using either DPX mountant (Sigma 06522) or VectaMount™ Permanent Mounting Medium (VWR, 101098-066). Coverslips (VWR International Limited, 631 – 0147) were applied to these tissue sections.

2.4.1.4 VVG Elastic staining of tissue sections

Following tissue deparaffinisation and rehydration (as above), elastic fibres of lung tissue sections were stained using an Elastic (Connective Tissue Stain) kit (Abcam, ab150667) as per the manufacturer's instructions. Lung tissue sections were immersed in an elastic stain solution (Haematoxylin solution, ferric chloride solution, and Lugol's iodine solution) for 15 min, followed by washing under running tap water. Then, sections were dipped 20 times in Differentiating solution and washed under running tap water. Sections were then placed into a sodium thiosulfate solution for 1 min, rinsed with tap water, stained with Van Gieson's solution for 4 min, rinsed in tap water, and then dehydrated through an ethanol series into 100% ethanol. Slides then were mounted using Permanent Mounting Medium (VWR, 101098-066). Coverslips (VWR International Limited, 631 – 0147) were applied to these tissue sections.

2.4.1.5 Immunohistochemistry staining

EnVision FLEX peroxidase-blocking reagent (15 mmol/l) (Dako, SM801, Agilent Technologies) was added on top of dewaxed, rehydrated, heat-mediated antigen retrieval-treated tissue sections for 15mins to block endogenous peroxidase activity. Next, these tissue sections were incubated with normal donkey serum as a second blocking step (5% v/v in PBS). The primary antibody was diluted with EnVision FLEX antibody diluent (Dako, DM830, Agilent Technologies, K800621-2) and added to the sections (refer to **(Table 2-3)** for antibodies details, dilutions, and incubation periods). After primary antibody incubation, tissue sections were washed three times in 1X EnVision FLEX wash buffer. Next, the secondary antibody was added for two-hour incubation at RT (refer to **Table 2-3)**. Secondary antibodies were then removed by washing three times in PBS, followed by incubation (varies depending on the primary antibody used) with the DAB substrate (EnVision FLEX Substrate Working Solution: 1 drop EnVision Flex DAB+ Chromogen (DM827) per 1ml EnVision FLEX Substrate Buffer (SM803), Dako, Agilent Technologies). Next, slides were washed with running tap water and counterstained with Harris's haematoxylin, as described previously. Lastly, slides were rinsed with running tap water and dehydrated, cleared, mounted, and covered with coverslips, as discussed above.

H&E and IHC stained tissue sections were scanned using a NanoZoomer S210 digital slide scanner with the NDP.view2 viewing software (Hamamatsu).

2.4.1.6 Immunofluorescence staining of FFPE sections

Dewaxed, rehydrated, heat-mediated antigen retrieval-treated tissue sections (as detailed above) were blocked for an hour with 5% horse serum (Sigma, H1138). The primary antibody was diluted with EnVision FLEX antibody diluent (Dako, DM830, Agilent Technologies, K800621-2) and then added onto the tissue sections (refer to **(Table 2-3)** for antibody details, dilutions, and incubation periods). After incubation, sections were washed three times using 1X EnVision FLEX wash buffer, after which fluorophore-conjugated secondary antibodies were added for one-hour incubation at RT (refer to **Table 2-3)**. This was

followed by 3 x 1min PBS washes, and then stained sections were mounted using either VectaMount™ Permanent Mounting Medium (VWR, 101098-066) or Vectashield antifade mounting medium with DAPI (Vector Laboratories, H-1200-10). Coverslips (VWR International Limited, 631 – 0147) were applied to these tissue sections, and slides were left overnight at RT.

2.4.2 Frozen Murine sections (cryosections)

2.4.2.1 Tissue preparation

Mice were euthanised as described above under **the Cell lines and primary cells section**. The right ventricle of the heart was then perfused with 3-5ml of cold PBS to clear the lung of RBCs, followed by perfusion of the lungs with 4%PFA. Dissected lungs were washed with PBS, then fixed with 4%PFA at 4°C for 2-3 hours. These fixed lungs were then immersed in 30% sucrose (diluted with PBS) and incubated overnight at 4°C. Next, lungs were immersed in a 1:1 ratio of 30% sucrose: OCT mounting media (VWR, 361603E) overnight at 4°C, followed by overnight incubation in 100% OCT media. Lungs were placed into OCT-containing moulds and on dry ice for 30 min. Once frozen at the desired angle, these samples were then stored in a -80°C freezer ready for cryosectioning. These lung samples were then cryosectioned into 15µm in thickness using Cryostat (Bright Instruments Company, model: OTF5000/LS-001, serial number: 055032805/5627) and collected onto glass slides (VWR, 531-0107) and dried for an hour for tissues to adhere to the slide then stored in a -20 °C freezer.

2.4.2.2 Immunofluorescence staining of frozen sections (cryosections)

Cryosections were dried at RT for 15mins, and then placed into PBS to remove the OCT media. Next, the fixative mixture (4%PFA and 5% methanol-containing PBS) was added to the tissues, followed by three washes with 0.1% Triton X-100. Cryosections were next permeabilised by incubation with a PBS solution containing 0.5% Triton X-100 and three

washes with 0.1% Triton X-100. Water-repellent circles were drawn surrounding cryosections using a pap pen. After that, cyrosections were blocked with a blocking buffer (PBS containing 10% donkey serum, 1% bovine serum albumin (BSA) (Sigma, A9418) and 0.2% Triton X-100) for an hour at RT. Following blocking, cryosections were stained with primary antibody (diluent used was the blocking buffer) (refer to **(Table 2-3)** for antibodies details, dilutions, and incubation periods). Sections were then washed three times with 0.1% Triton X-100. Next, a fluorophore-conjugated secondary antibody was added for an hour incubation at RT (refer **to Table 2-3)**. Excess secondary antibody was removed by three washes in PBS. Nuclei were stained using DAPI (Sigma, D9542, stock concentration of 10mg/ml, final concentration of 0.05 µg/ml) for 15 min, followed by three washes in PBS. Stained cryosections were mounted with a prolong gold antifade reagent (Invitrogen, P36930). Coverslips (VWR International Limited, 631 – 0147) were then applied to these cryosections and slides were left overnight at RT and stored at 4°C ready for imaging.

Primary antibody	Cellular location	Company, host, and clonality	Dilution, incubation time, and temperature	IHC-secondary antibody		IF-secondary antibody			
				Secondary antibody name, company, and host	Dilution and incubation time	Secondary antibody	Company	Host	Dilution and incubation time
Anti-aSMA (Anti-Actin, α-Smooth Muscle - Cy3)	Intracellular	Sigma (C6198) anti-mouse/human/rat/rabbit mouse IgG2a (monoclonal, clone 1A4)	IF: 1:100 for 1hr at RT	-	1 hr at RT	-	-		-
Anti-Carbonic Anhydrase IX (CA9)	Intracellular/ membrane	Absolute antibody (Ab00414-1.1), anti-human/mouse, mouse IgG1 (recombinant monoclonal, clone M75)	Stock concentration=1mg/ml IHC: 1:100 for 1 hr at RT	EnVision FLEX /HRP detection reagent, Dako (SM802), goat anti-mouse/rabbit		-	-		-
Anti-CD31 (Pecam-1)	Membrane	Dianova (DIA-310), anti-mouse/swine, rat IgG2a (monoclonal, clone SZ3)	Stock concentration=0.2mg/ml IHC & IF: 1:20 for 1 hr at RT	Simple stain mouse MAX PO (Rat) Immuno-peroxidase polymer		Alexa Fluor 488 conjugated IgG	Invitrogen (A-21208) anti-rat		Stock concentration= 2mg/ml 1:200 for 1 hr at RT

				Histofine (414311F) Goat anti-rat					
Anti-Cytokeratin 5/6	Intracellular	Invitrogen (PA5-116450), anti-human/mouse/ rat, rabbit IgG (polyclonal)	Stock concentration=1mg/ml IHC: 1:200 for 1 hr at RT	Envision system-HRP labelled polymer, Dako (K4003), goat anti-rabbit		-	-		-
Anti-Eltd1	Intracellular/ membrane	In-house anti-mouse, rabbit F04 (polyclonal)	1:2000 for 1 hr at RT	Envision system-HRP labelled polymer, Dako (K4003), goat anti-rabbit		-	-		-
Anti-fibronectin (Fn1)	Secreted/intracellular	Sigma (F3648), anti-human/mouse, rabbit (polyclonal)	IF: 1:400	-		Alexa Fluor 488 conjugated	Invitrogen(A-21206) anti-rabbit		Stock concentration= 2mg/ml 1:200 for 1 hr at RT
Anti-Ki67	Nuclear	Cell signalling (9129S) Anti-human/mouse/rat, rabbit IgG	IHC & IF: 1:400 for 1 hr at RT	Envision system-HRP labelled polymer,		-	-		-

		(monoclonal, clone D3B5)		Dako (K4003), goat anti-rabbit					
Anti-luciferase	Intracellular	Novus Biologicals (NB100-1677), anti-Photinus pyralis firefly luciferase, goat IgG (polyclonal)	Stock concentration=1mg/ml IF: 1:400 for 1 hr at RT	-		Alexa Fluor 647conjugated	Invitrogen (A-21447) anti-goat		Stock concentration= 2mg/ml 1:200 for 1 hr at RT
Anti-mesothelin (Msln)	Intracellular/ membrane	LSBio (LS-C407883-100), anti-mouse, rabbit (recombinant polyclonal)	Stock concentration=0.5mg/ml IHC: 1:500 for 1 hr at RT	Envision system-HRP labelled polymer, Dako (K4003), goat anti-rabbit		-	-		-
Anti-serum amyloid A3 (Saa3)	Secreted/intracellular	ABclonal (A11948), rabbit IgG (polyclonal)	IF: 1:500	-		Alexa Fluor 488 conjugated	Invitrogen(A-21206) anti-rabbit		Stock concentration= 2mg/ml 1:200 for 1 hr at RT
Anti-tight junction protein 1 (Tjp1/ZO-1)	Intracellular	Invitrogen (40-2200), anti-mouse/human/rat/dog, rabbit IgG (polyclonal)	Stock concentration= 0.25mg/ml IF: 1:100	-		Alexa Fluor 546 conjugated	Invitrogen (A10040) Anti-rabbit		Stock concentration= 2mg/ml 1:200 for 1 hr at RT
Anti-thyroid transcripti	Intracellular	Abcam (ab76013), anti-human/mouse/rat, rabbit IgG	IHC & IF: 1:300	Envision system-HRP labelled		Alexa Fluor 555 conjugated	Invitrogen (A-31572) anti-rabbit		Stock concentration= 2mg/ml

on factor 1 (TTF1)		(recombinant monoclonal, clone EP1584Y])		polymer, Dako (K4003), goat anti-rabbit					1:200 for 1 hr at RT
Anti-VE-Cadherin antibody (VE-CAD)	Intracellular/ membrane	Merck (MABT886), anti-mouse, & bovine, rabbit IgG (monoclonal, clone Vli37)	IF: 1:100	-		Alexa Fluor 488 conjugated	Invitrogen (A-21206) anti-rabbit		Stock concentration= 2mg/ml 1:200 for 1 hr at RT
Anti-Wilms Tumour (Wt1)	Nuclear	Abcam (ab89901), anti-human/mouse, rabbit IgG (recombinant monoclonal, clone CAN-R9(IHC)-56-2)	IHC: 1:300 IF: 1:100 for 1 hr at RT	Envision system-HRP labelled polymer, Dako (K4003), goat anti-rabbit		Alexa Fluor 546 conjugated	Invitrogen (A10040) Anti-rabbit		Stock concentration= 2mg/ml 1:200 for 1 hr at RT

Table 2-3. Antibodies used for chromogenic immunohistochemistry (IHC) and immunofluorescence (IF) staining of mouse tissue sections. RT: room temperature

2.4.3 Quantification and statistical analysis

ELTD1 protein levels were quantified in kidney tissue sections of *Eltd1*^{iEC} (*Pdgfb-iCreERT2* $^{Cre/+}$*; Eltd1*$^{fl/fl}$) and control littermates using QuPath software (version 0.3.1). ELTD1 was measured in 6 fields of view of each kidney section per mouse (avoiding shredded, folded, RBCs, and areas with high DAB background).

Tumour burden in vehicle and pazopanib-treated E0771 metastatic lung tissue sections (4µm in thickness) was quantified using QuPath software (version: 0.3.1).

The width of subpleural metastases in the vehicle and pazopanib-treated E0771 metastatic lung tissue sections, as well as *Eltd1*^{iEC} and control E0771 metastatic lung tissue sections (4µm in thickness) was measured using QuPath software (version: 0.3.1).

2.4.4 Tissue preparation for Raman spectroscopy

One million parental E0771 cells were intravenously injected into the tail vein of 2 wild-type C57BL/6 female mice at approximately 6 weeks of age. Lung lobes were harvested, perfused with PBS solution, and prepared as shown in the table below.

Table 2-4. Conditions and endpoints of murine lungs harvested for Raman metabolic profiling of stromal cells.

Group number	Murine lungs groups	Endpoint	Lung preparation
1	Healthy lungs (control sample)	-	Lung lobes were perfused with 4%PFA, then were embedded in OCT mounting media and stored in a -80°C freezer
2	Early-stage metastatic lungs	Day 7 following tumour inoculation	
3	Late-stage metastatic lungs	Day 13 following tumour inoculation	

Prior to tissue sectioning, special slides were prepared. Aluminium metal-coated slides (1" x 3" x 1.1mm Thick, Deposition Research Laboratory, Inc (DRLI)) were pre-treated with 1ml of Poly-L-lysine solution (Sigma-Aldrich, P4707) for 10mins in a 37°C incubator. After rinsing with PBS, slides were allowed to dry 1-2 hours in the incubator. Frozen lung samples were sectioned 4µm in thickness using a Cryostat (Bright Instruments Company, model:

OTF5000/LS-001, serial number: 055032805/5627), collected onto coated slides and dried for an hour, then stored at -80 °C.

In collaboration with Dr. Jiabao Xu (Professor. Wei Huang's laboratory), Raman microscopy was used to spatially measure the metabolic profile of stromal cells in non-tumour-bearing, early and late metastatic-bearing lungs. Lung endothelial cells were labelled with anti-CD31 antibody prior to Raman measurement. For this, OCT was first removed from the sections by washing the slides in PBS for 15 min, and water-repellent circles were drawn surrounding tissue sections using pap pen. Sections were fixed using 4%PFA for 15mins, followed by three washes with PBS, then blocked for an hour with 5% donkey serum. Finally, the sectioned tissue was incubated overnight with the primary antibody (anti-CD31 antibody, Dianova (DIA-310), 1:20 dilution) diluted with the blocking solution at 4°C. Sections were then washed three times with PBS, followed by staining with secondary antibody (Alexa Fluor 647 conjugated donkey anti-rat IgG, Invitrogen, A78947, 1:400 dilution) for an hour at RT. Sectioned were washed three times with PBS, immersed in PBS and imaged using Confocal Raman micro-spectroscopy (LabRAM HR Evolution, Horiba Scientific, UK) equipped with an integrated microscope (BX41, Olympus) and a motorised XYZ stage. The Raman scattering was excited with a 532-nm neodymium-doped yttrium aluminium garnet laser (Ventus, Laser Quantum, Manchester, UK). A water immersion objective with a magnification of 60x was used to detect and acquire Raman spectra.

2.5 MRI imaging and image analysis

In collaboration with Dr. Sean Smart and Dr. Veerle Kersemans (at the Oncology preclinical imaging facility at the University of Oxford), MRI imaging was acquired at day 9 and day 14 post-E0771 tumour injection, using a small-build MRI. Briefly, mice were anaesthetised by isoflurane (1–4%). The temperature of mice was monitored using an optical rectal probe (OTP-M, Opsens Inc, Quebec, Canada) connected via a fibre-optic extension to an AccuSense Signal Conditioner (ACS-P4-N-62SC, Opsens Inc) that maintains the animal temperature at 37˚C. Real-time prospective cardio-respiratory gating and dynamic reacquisition was applied via measurement of the respiration and electrocardiogram (ECG) signals. MRI scans were run on anesthetised mice while maintaining the respiration rate at 40–60 breaths per minute. MRI imaging was conducted on a 7.0T 210mm horizontal bore VNMRS preclinical imaging system equipped with a 120mm bore gradient insert (Varian Inc., CA) and 100mm long 25mm ID quadrature birdcage coil (Rapid Biomedical GmbH, Germany). Two different T_2*-weighted sequences were used. Contrast imaging was used to visualise metastases in white (brighter than the liver) and normal lung tissue in black, using a spin echo technique known as high-resolution balanced Steady-State Free Precession (bSSFP) scanning. Dynamic contrast-enhanced imaging was used to visualise tumours as well as the vasculature using a 3D FLASH (single gradient echo 3D (GE3D)) scan mode. The scan parameters for cardio-respiratory (CR)-synchronised bSSFP scan were TR 2.8ms, TE 1.4ms, RF hard pulse 16μs, FA 30˚, FOV 51.2×25.6×25.6 mm3, matrix 256×128×128, and N = 32 k-lines per R-wave to give a single 3D data set with 200μm isotropic resolution in less than 2.5min. The gradient echo scans operated with 16 microseconds 5-degree square/TE 1.226ms/TR 3.2ms/192kHz receiver bandwidth/1.22ms crusher duration/12.8 G/cm3 axis crusher strength/RF spoiling/Cardiac and respiratory gating, with steady-state maintenance and dynamic reacquisition of respiration-corrupted data/256x128x128 pixels/voxels/54x27x27 mm field of view/25 mm diameter birdcage coil. Of note, these scans operated at least 32 times faster than any commercial or reported alternative.

Semi-automatic segmentation (using active contour methods) and threshold-based segmentation of MRI lung images were reconstructed by Dr. Danny Allen (at the Oncology preclinical imaging facility at the University of Oxford) using ITK-SNAP software generating 3D masks. The air space of the lung (lung volume) and manual segmentation in three orthogonal views (X, Y, and Z) were performed for both *Eltd1*^{iEC} and control littermates. The scans acquired from the same mouse at the two-timepoints were registered as 3D segmentations using a rigid body registration (volumetric alignment) and an iterative closest point algorithm.

2.6 Tissue preparation for single-cell RNA sequencing (scRNA-seq):

2.6.1 Digestion of murine lungs and depletion of CD45-positive cells

Mice were euthanised as described above in **the Cell lines and primary cells section**. The right ventricle of the heart was then perfused with 3-5ml of cold PBS to clear red blood cells (RBCs) from the lungs. Healthy and metastatic lungs were harvested at the experimental endpoints indicated in **(Table 2-5)** for FACS sorting and scRNA-seq.

Table 2-5. Conditions and endpoints of murine lungs harvested for FACS sorting and scRNA-seq experiment. *Note that healthy lungs were injected with PBS in the same manner as tumour intravenous injection to determine any effects caused by vehicle control upon comparison.*

Group number	Murine lungs groups	Condition	Endpoint
1	Healthy lungs (control sample)	Non-tumour-bearing lungs, where mice injected with PBS	Day 7 following PBS injection
2	Early-stage metastatic lungs	Tumour-bearing lungs, where mice injected with mCherry-labelling hCD2 E0771 tumour cells	Day 7 following tumour inoculation
3	Late-stage metastatic lungs	Tumour-bearing lungs, where mice injected with mCherry-labelling hCD2 E0771 tumour cells	Day 13 following tumour inoculation

Harvested lungs were washed with cold PBS and placed in a biosafety cabinet. The lungs were then cut into smaller pieces in a petri dish and transferred into gentleMACS™ C tubes (Miltenyi Biotec, 130-093-237) containing a digestion mixture (0.1% collagenase I (Worthington) and 0.1% collagenase III (Worthington) dissolved in PBS). This mixture was physically dissociated into single-cell suspensions by gentleMACS™ Dissociator (Miltenyi Biotec, 130-093-235) using the mouse_lung_01 program. After physical dissociation, tubes containing lung cell suspensions were incubated in a MACSmix Tube Rotator (Miltenyi Biotec, 130-090-753) inside a 37°C incubator for 30 min. Following enzymatic digestion of the lungs, the cell suspension was further homogenised by the dissociator using the mouse_lung_02 program (following this step, the tube containing cell suspension always kept on ice). The digestion was terminated by adding MACS buffer (PBS containing 0.5% FBS and 2mM EDTA),

followed by centrifugation at 300 x g for 3 min. Cell pellets were then resuspended in MACS buffer and filtered using a 70µm cell strainer (Corning, 352350). Filtered cell suspensions were washed once with MACS buffer, centrifuged, and then 1X RBC lysis buffer (Biolegand, 420301) was added and incubated for 1min to lyse RBCs. PBS was added to stop the lysis reaction, the tubes were centrifuged, and the supernatant was discarded. To enrich for lung non-immune stromal cells, CD45+ cells were depleted using MACS microbeads technology per the manufacturer's instructions. Briefly, a mixture of 1:10 of microbeads conjugated to rat anti-mouse CD45 antibody (Miltenyi Biotec, 130-052-301, clone 30F11.1) and MACS-buffer containing 10^7 cells was prepared and incubated at 4°C for 15 min. Following the binding of microbeads to CD45+ cells, removal of this population was achieved by loading cell-microbeads mixture into MACS LD columns (Miltenyi Biotec, 130-042-901), which was attached to MACS QuadroMACS magnetic separator (Miltenyi Biotec, 130-091-051). CD45+ cells were retained in the column, while lung stromal cells and E0771 tumour cells passed through the column.

2.6.2 FACS staining, FACS panel design, and FACS cell sorting of lung stromal cells

The CD45- flow-through, containing lung non-immune stromal cells and E0771 tumour cells, was collected, centrifuged at 300 x g for 5 min, and stained using FACS antibodies listed in **(Table 2-6)**. FACS staining buffer (PBS containing 10% FBS and DNase I recombinant (final concentration: 100 U/l) (Roche, 04716728001) was used for diluting FACS antibodies and for washing cells following FACS staining. Cells were resuspended in 1ml of FACS staining buffer and DAPI (Sigma, D9542, stock concentration of 10mg/ml, final concentration of 0.05 µg/ml) was added prior to FACS sorting. Compensation (single-color) and fluorescence Minus One (FMO) controls were used to compensate for fluorescence spillover and accurately sort the population of interest. The viability of cells was 80% and above. Following proper FACS gating, five stromal subsets were sorted **(see Table5-3 in Chapter 5)** on either a BD FACSAria III Cell Sorter (BD Biosciences) or a FACSAria Fusion Cell Sorter (BD Life Sciences, San Jose,

CA, 95131, USA) with a 100µm nozzle. Cells were sorted into PBS containing 0.04% BSA (400 µg/ml) (New England BioLabs, B9000S, 20mg/ml) to prevent loss or aggregation of cells. Next, FACS-sorted cells were centrifuged at 300 x g for 5mins and resuspended in ~46µl of PBS containing 0.04% BSA. FACS data was analysed using FlowJo v10.6.2 software (TreeStar Inc.).

Table 2-6. List of FACS antibodies used for staining mouse lungs (healthy/metastatic).

FACS antibody	Company	Catalogue number	Host and isotype	Clonality	Clone	Dilution and incubation time
FITC-anti-mouse CD31 (Pecam-1)	Biolegend	102405	Rat IgG2a, κ	Monoclonal	390	1:100 for 30mins
APC-anti-mouse CD144 (VE-cadherin)	Biolegend	138012	Rat IgG1, κ	Monoclonal	BV13	1:100 for 30mins
Brilliant Violet 421-anti-mouse CD45	Biolegend	103133	Rat IgG2b, κ	Monoclonal	30-F11	1:100 for 30mins
Brilliant Violet 421-anti-mouse Erythroid Cells	Biolegend	116233	Rat IgG2b, κ	Monoclonal	TER-119	1:100 for 30mins
APC/Fire 750-anti-human CD2	Biolegend	300226	Mouse IgG1, κ	Monoclonal	RPA-2.10	1:100 for 30mins

2.6.3 Cell preparation and scRNA-sequencing:

FACS-sorted single-cell suspensions were prepared and sequenced by the MRC Weatherall Institute of Molecular Medicine (MRC WIMM) Single Cell Genomics Facility (Dr. Neil Ashely), using the droplet-based 10X Genomics Chromium (10X) platform. The Chromium Next GEM Single Cell 3' Reagent Kit (10x Genomics, v3.1 Chemistry) was used per the manufacturer's instructions. Briefly, this kit provided Gel Beads-in-emulsion (GEMs) generation and barcoding, cDNA amplification, and 3' gene expression library construction of FACS-sorted single-cell suspensions**.** The quantity and quality of cDNA were examined post-cDNA amplification using Agilent TapeStation.

The barcoded libraries were sequenced by the Novogene sequencing service on Illumina Novaseq 6000 system. FASTQ files containing both raw sequence data and quality

scores, project reports, and quality control reports were provided by Novogene company. A custom reference package (combining the mouse reference genome (mm10), mCherry, and human CD2 reference genome sequences (FASTA file) and gene annotations (GTF file)) were created by Dr Thomas Caroll using cellranger mkref command. Next, the Cell Ranger pipeline (10x Genomics, version 5.0.0.) (cellranger count and cellranger aggr (with no normalisation) commands) was used to align RNA-seq reads and generate feature-barcode matrices.

2.7 Bioinformatics analysis

The Cell Ranger pipeline output matrices were read, and the Seurat object was created (version 4.1.1) using the Rstudio programming language (version 4.2.0). It is important to mention that the Cell Ranger analysis pipelines generated five separate outputs (matrices) for the five experimental conditions (five samples). Rstudio programming language was then used to merge these five datasets without applying scRNA-seq data integration and batch effect correction. Cells were then filtered based on the quality control (QC) metrics demonstrated in **(see Figure5-14 in Chapter 5)**. QC metrics were applied to exclude empty droplets, low-quality cells, and doublets. Gene expression measurements for each cell were normalised, highly variable features were selected, and data was scaled using SCTransform (Hafemeister & Satija, 2019). Dimensional reduction was performed on the merged scRNA dataset using principal components analysis (PCA). Principal components (PCs) were ranked in an Elbow plot based on the percentage of variance explained by each PC. The dimensionality of the data was determined from this plot by selecting the number of PCs that capture most of the variation in the data to be included in downstream analysis. The first 20 PCs were included in the downstream analysis.

Cells were clustered using ***FindNeighbors()*** and ***FindClusters()*** functions. A clustering tree was performed using the **clustree()** function to generate a cluster hierarchy for a range of resolutions (Zappia & Oshlack, 2018). The optimal clustering resolution was selected after inspecting cluster composition and marker genes at a certain resolution. Cells were then grouped in a low-dimensional space using the dimensional reduction algorithm, Uniform Manifold Approximation and Projection (UMAP). The function ***RunUMAP()*** was used to visualise and partition the clusters based on similarity in gene expression (McInnes et al., 2018). Compared to all other clusters, the differentially expressed genes per cluster were identified by running the function ***FindAllMarkers()***. The threshold used was as follows: logfc.threshold = 0.25 and mins.pct = 0.25 parameters, followed by filtration for adjusted p-value < 0.05.

The clusters were annotated based on each cluster's top 50 differentially expressed genes (DEGs) along with manual curation of several publications **(see Table5-4 in Chapter 5 and Table6-1 in Chapter 6)**. EC population was identified based on the expression of pan-EC marker genes and subdivided into a separate Seurat object for higher resolution of clusters **(see Figure5-15 in Chapter 5).** Based on the expression of the pan-mesothelial marker genes, mature mesothelium and CAMCs were also subdivided into a separate Seurat object **(see Figure7-1 in Chapter 7).** All the above analysis was re-run on the EC and mesenchymal subclusters. For the EC subcluster, a clustering resolution 0.5 was selected, giving rise to 15 cell clusters annotated into 13 cell subtypes. For the mesenchymal subcluster, a clustering resolution of 0.1 was selected, giving rise to 5 cell clusters annotated into four cell subtypes with the removal of the fifth cluster that was believed to be contamination from the parent EC cluster.

To visualise the data, the following Seurat functions were used: ***DimPlot(), FeaturePlot(),*** and ***SCpubr do_DimPlot()*** and ***do_FeaturePlot()*** functions. Shiny app interactive interface was generated using the ShinyCell R package to easily explore and visualize the scRNA-seq data as a heatmap, UMAP and violin plots (Ouyang et al., 2021).

2.7.1 Pathway Enrichment Analysis

Gene set enrichment analysis (GSEA) was implemented using Fast Gene Set Enrichment Analysis (fgsea v1.16.0) in R (Subramanian et al., 2005). Briefly, for a given contrast, differential expression results were calculated using ***FindMarkers()*** from the Seurat package (with mins.pct = 0.05 and logfc.threshold = 0.1, but otherwise default parameters), and the "avg_log2FC" metric for each gene was used as the test statistic for GSEA. fgsea was implemented using the ***fgseaMultilevel()*** function (minSize = 10, maxSize = 1000, eps = 0). The top 10 most significantly upregulated and downregulated pathways were selected for visualisation. Single-cell pseudotime trajectories of EC and mesenchymal populations were constructed using the Monocle3 R package (Trapnell et al., 2014).

2.7.2 Cell-cell communication inference analysis

To calculate the total number of ligand–receptor pairs among all cell subtypes identified in the lungs across all conditions, CellPhoneDB analysis was performed using the scRNA-seq data (Efremova et al., 2020). The ligand-receptor pairs that belong to specific signalling pathways were studied among all cell subtypes identified in the lungs across all conditions using the CellChat tool (Jin et al., 2021). The overall incoming and outgoing cell signalling patterns were determined by CellChat, with parameter k = 2 to specify the modelling of 2 signalling patterns, which were visualised as alluvial plots. After cell-cell communication analysis using CellChat with default arguments, the CellChatShiny interface was used to visualise the strength of cell-cell communication signalling between specific cell types for each signalling pathway as heatmaps. The CellChatShiny interface was also used to visualise the cell subtypes as primary senders, receivers, mediators, and influencers in the intercellular communication networks as bar plots.

Bioinformatic analysis of the scRNA-seq experiment was performed by myself with assistance from three collaborating bioinformaticians, details are summarised as follows:

- **Dr. Thomas Carroll** (Ludwig Institute for Cancer Research, Nuffield Department of Medicine, University of Oxford, United Kingdom) converted the raw sequencing data into readable FASTQ files. He then aligned the reads to a custom mouse reference genome, generating output files containing a count matrix. He also performed the pathway enrichment analysis (GSEA), single-cell trajectory analysis, and cell-cell communication analysis.
- **Dr. Fahad AlMesned** (Bioinformatics Section, National Institute of Neurological Disorders and Stroke, National Institutes of Health, Bethesda, MD 20892, USA) conducted differential gene expression analysis.
- **Badran Elshenawy (**Department of Oncology, University of Oxford, Oxford, United Kingdom) generated the clustering tree (to select the resolution that gave a stable number of cell clusters). He also generated the stacked composition plots and

visualised the data as UMAP plots, violin plots, and heatmaps. He performed differential expression analysis, signature scoring, and created Shiny-based web application (visualisation tool of scRNA-seq data)

- I have inserted the matrix files into the Rstudio programming tool and generated the Seurat object. QC, data normalisation, dimensional reduction clustering, cluster annotation, data visualisation as UMAP & violin plots, and differential expression analysis were performed on the Seurat object.

2.8 Statistical analysis

GraphPad Prism 9.3.1 was used for statistical analysis. A two-tailed Student's t-test was used to assess the statistical significance between the means of two groups. Analysis of Variance (ANOVA) was used to assess the statistical significance among the means of several groups. P-values of less than 0.05 were considered significant.

Chapter 3: Generation and characterization of a syngeneic murine triple-negative breast cancer lung metastasis model

3.1 Introduction

Compared to other subtypes, triple negative breast cancer (TNBC) tumours are found to preferentially metastasize to the lungs (Lachapelle & Foulkes, 2011; Soh et al., 2020). Metastatic disease is generally incurable and is the leading cause of mortality for TNBC patients. Consequently, the spread of breast cancer cells to distant organs such as the lungs represents a substantial clinical concern (Neophytou et al., 2018). Standard treatment of metastatic TNBC consists of chemotherapy, and for PD-L1+ TNBC tumours, a combination of chemotherapy and immunotherapy is used (Won & Spruck, 2020). Metastatic TNBC tends to acquire resistance to systemic therapies (Rakha & Chan, 2011). The complexity of the tumour microenvironment (TME) in TNBC appears to modulate the responses to therapy, but this can be challenging to study. This chapter describes the generation of an *in vivo* experimental TNBC metastasis mouse model with an immunohistochemical assessment of tumour growth patterns and vascular phenotype during the evolution of micrometastatic to macrometastatic lesions.

3.2 Optimisation of E0771 cell number and growth time for tumour model

Introducing the E0771 triple negative breast adenocarcinoma cell line into an immunocompetent mouse is one approach to generating TNBC metastases in a lung microenvironment (stroma). To develop this experimental lung metastasis model, I first examined the literature, finding several studies which injected a range of E0771 cell numbers ($1.5x10^5$-$1x10^6$ cells) and harvested the lungs at different time points (day 14-day 26) **(Table 3-1)**. To obtain sufficient tumour burden for my model, I therefore empirically tested this range of cell numbers and time points. To do this, C57BL/6 mice were injected intravenously via the tail vein with either $5x10^5$ (first and second groups) or $1x10^6$ (third

group) parental E0771 breast cancer cells (syngeneic model) and at the indicated time points. lungs were removed, sectioned, and H&E stained to assess tumour burden **(Figure 3-1)**. The first group, injected with $5x10^5$ E0771 cells, were sacrificed 14 days post-tumour injection and showed no metastases, but signs of tumour cells starting to colonize the lung were detectable **(Figure 3-1A)**. The second group, also injected with $5x10^5$ E0771 cells but sacrificed later at day 25 following injection, showed a small number of macro- and micro-metastases **(Figure 3-1B)**. The third group, injected with $1x10^6$ E0771 cells, were sacrificed 13-16 days after injection, showed a larger number of micro- and macro-metastases, although the mice tolerated this tumour burden without loss of conditioning or other welfare concerns **(Figure 3-1C)**. Consequently, the protocol used in the third group ($1x10^6$ E0771 cells, collection after 13-16 days) was selected for subsequent experiments representing a late stage of metastasis.

Table 3-1. Different E0771 cell numbers injected intravenously and different endpoints for generating E0771 tumour-bearing lungs extracted from literature.

E0771 cell number	**Endpoint for assessing tumour burden**	**Reference**
$1.5x10^5$	On day 22-26	(Green et al., 2017)
$2x10^5$ or $4x10^5$	On day 21	(Bottos et al., 2016)
$5x10^5$	On day 21	(Collier, 2017)
$5x10^5$	On day 21	(Burikhanov et al., 2017)
$1x10^6$	On day 7-14	(Kitamura et al., 2018)
$1x10^6$	On day 14	(Vandereyken et al., 2017)

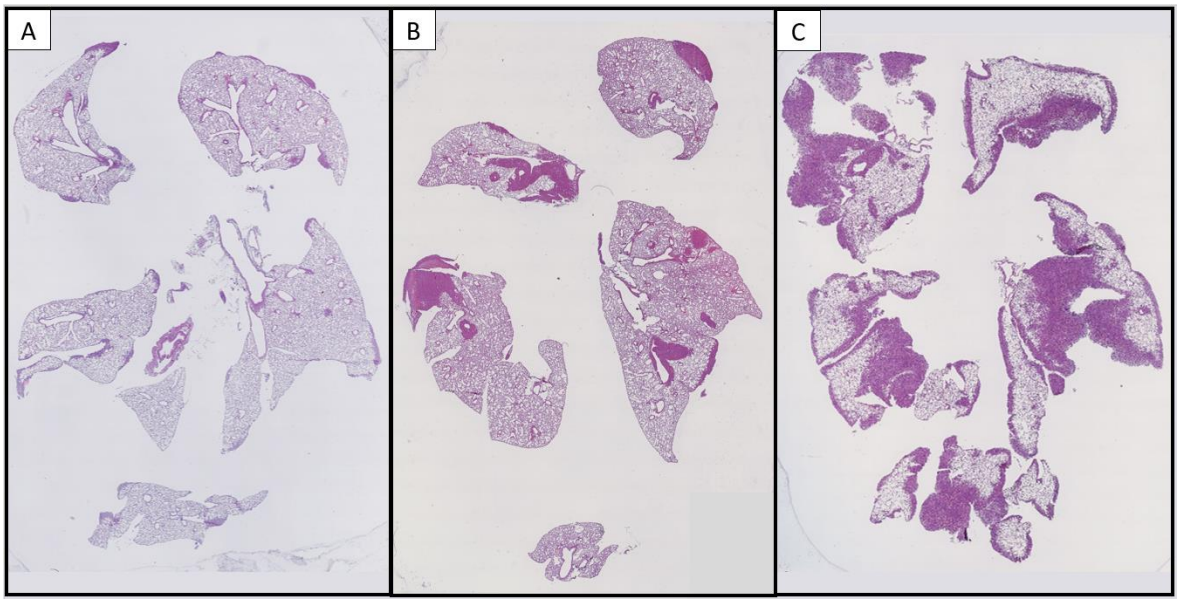

Figure 3-1. E0771 tumour burden in H&E-stained lung sections of three groups of mice sacrificed at different time points following tumour injection. *A: 14 days post tumour injection of 5x10^5, tumour cells started to colonize the lungs; B: 25 days post tumour injection of 5x10^5, tumour cells colonized the lungs forming visible metastases, C: 13 days following injection of 1x10^6 cells.*

3.3 Metastatic growth pattern in the E0771 breast cancer lung metastasis model

3.3.1 Lentiviral transduction of parental E0771 tumour cells to generate EGFP LUC-labelled E0771 tumour cells

To visualize tumour growth patterns along with blood vessels, the E0771 breast adenocarcinoma cell line was transduced with a double cassette lentivirus (Brennan et al., 2018) encoding firefly luciferase (LUC) and enhanced green fluorescent protein (EGFP). Transfection of E0771 tumour cells with EGFP and LUC-encoding lentiviral vector was validated by imaging on inverted fluorescent microscope **(Figure 3-2).** For *in vivo* studies, fluorescence-activated cell sorting (FACS) sorting of strongly EGFP-LUC co-expressing E0771 cells was performed using EGFP as a surface marker **(Figure 3-3).** The activity of luciferase of these sorted cells was then tested *in vitro* by measuring the luminescence of cells **(Figure 3-4).** Using an *in vitro* proliferation assay, no difference in proliferation was found between EGFP-LUC labelled E0771 cells and parental E0771 cells based on a two-tailed unpaired Student's t-test, p = 0.785 **(Figure 3-5).**

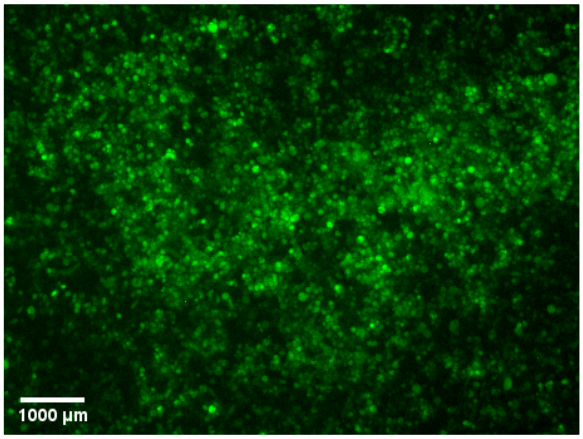

Figure 3-2. High transfection efficiency of EGFP-LUC labelled E0771 tumour cells visualized by imaging EGFP expression using an inverted fluorescent microscope.

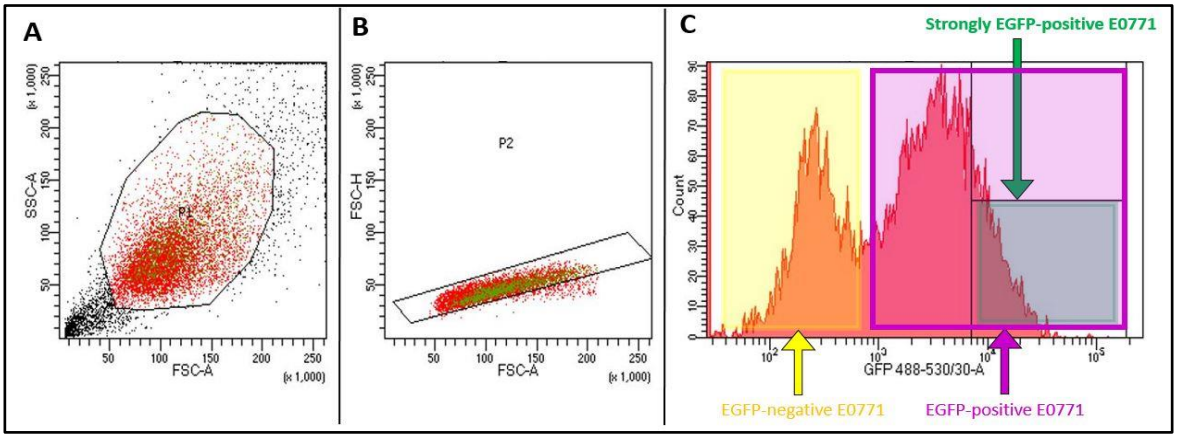

Figure 3-3. FACS sorting for strongly positive EGFP-LUC labelled E0771 cells. E0771 cells transduced with EGFP-LUC lentivirus were FACs-sorted based on their EGFP expression levels. A*: gating of population of interest using SSC vs FCS density plot; B: gating of singlets and excluding doublets by plotting FSC-H vs FSC-A. The strongly EGFP-positive cells (shown with green box) were collected and expanded for in vivo studies.*

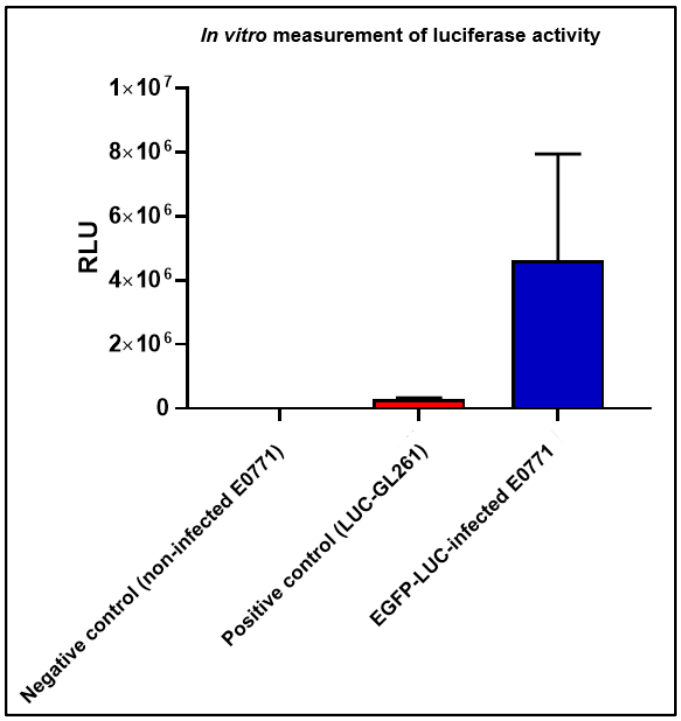

Figure 3-4. Measurement of luminescence showed that EGFP-LUC co-expressing E0771 cells has high luciferase activity compared to the positive control (LUC-infected GL261). *RLU: relative luminescence unit (n=1).*

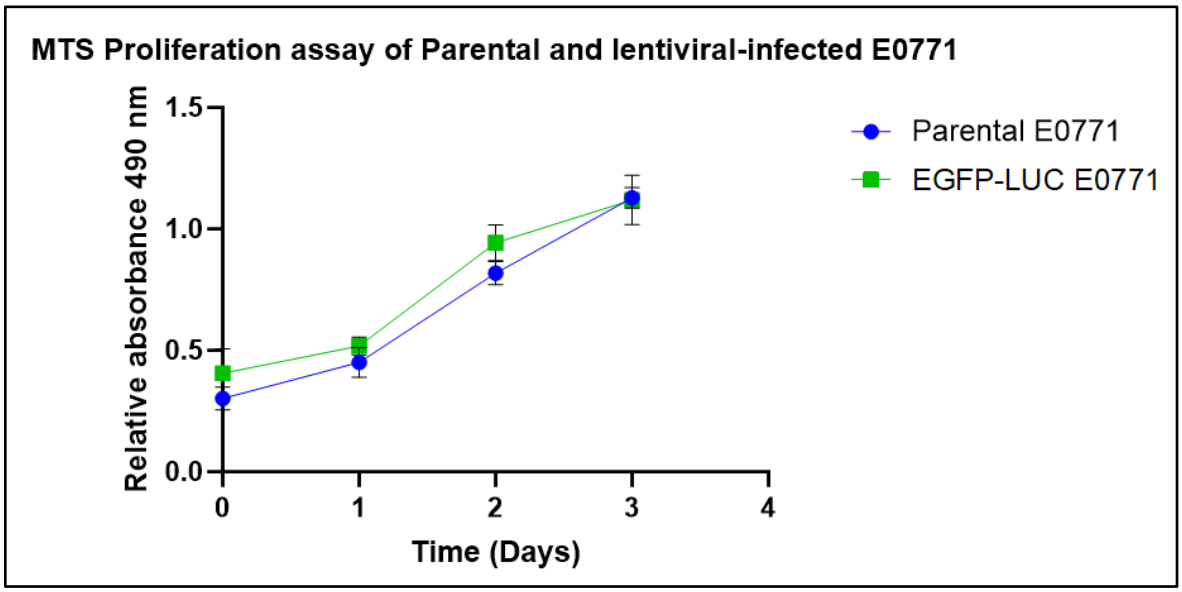

Figure 3-5. Transduction of E0771 tumour cells with EGFP-Luc-containing FULGW lentiviral vector does not affect the proliferation ability of these cells compared to the parental E0771 cells*. Each data set represents the mean ± standard error of the mean (SEM) of three biological replicates (Statistical analysis was performed using the two-tailed unpaired Student's t-test).*

3.3.2 Establishing the growth pattern of E0771 tumour cells

H&E staining of E0771 metastatic lungs (injected with $1x10^6$ cells and sacrificed 8 and 13 days post tumour injection) showed that the E0771 TNBC cells colonize the lung parenchyma at the early metastatic phase **(Figure 3-6A).** Immunohistochemical labelling showed these tumour cells have high proliferative capacity (KI67+) and appear to extravasate from lung blood vessels and occupy the alveoli **(Figure 3-7).** During tumour progression, the E0771 cells grew toward the pleura forming subpleural metastases **(Figure 3-6B)**. Immunofluorescence tagging of endothelial cells and E0771 tumour cells using anti-CD31 and anti-luciferase (LUC) antibodies validated the metastatic growth patterns of E0771 TNBC cells in the lungs **(Figure 3-8, Figure 3-9)**

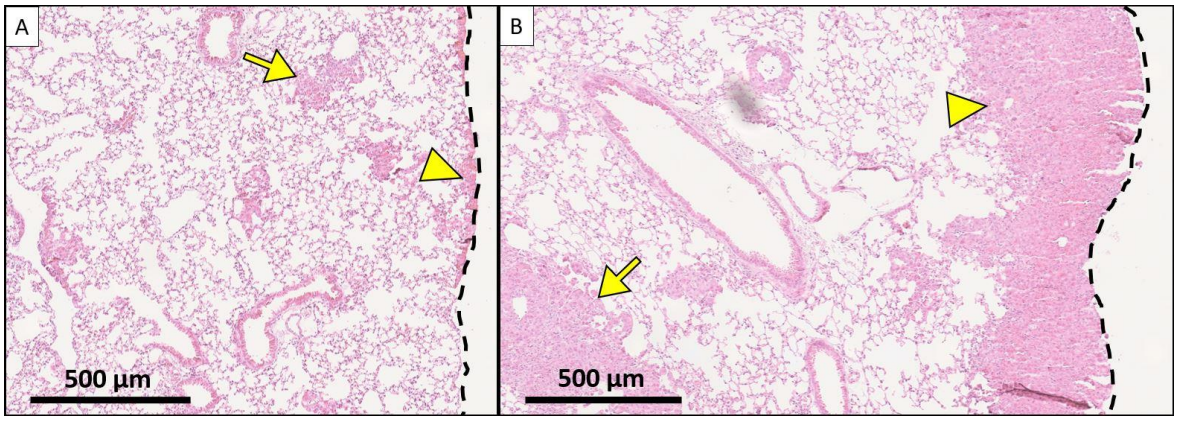

Figure 3-6. H&E staining of metastatic lung tissue sections revealed the development of parenchymal micrometastases at an early timepoint and subpleural and parenchymal metastases at a late timepoint. *$1x10^6$ E0771 breast tumour cells were injected intravenously into WT C57BL/6 mice at 6 weeks of age. Metastatic lungs were harvested on day 8 and day 13 following tumour injection.*

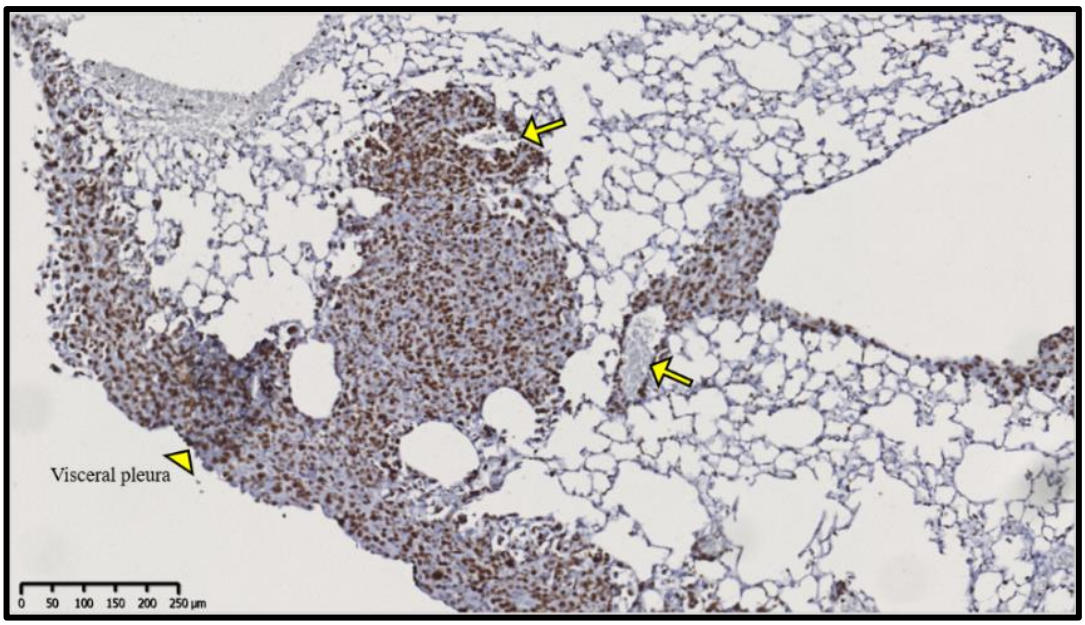

Figure 3-7. E0771 TNBC cells extravasate from lung blood vessels and grow in the intra-alveolar spaces and along visceral pleura. *These E0771 tumour-bearing lungs were immunohistochemically stained with the proliferation marker, Ki67 to visualize tumour cells. Arrows: depicts blood vessels; arrowhead: depicts visceral pleura.*

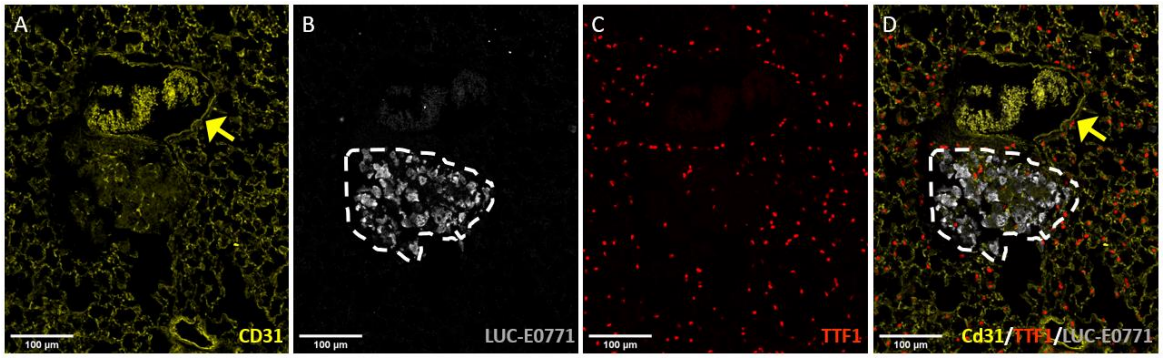

Figure 3-8. EGFP-LUC lentiviral-transduced E0771 TNBC cells growing in lung parenchyma as a micrometastases near a blood vessel (yellow arrows). *TTF1: thyroid transcription factor 1 which labelled type II pneumocytes; LUC-E0771: are E0771 that were transduced with lentivirus encoding firefly luciferase (LUC) and EGFP demarcated by dashed line.*

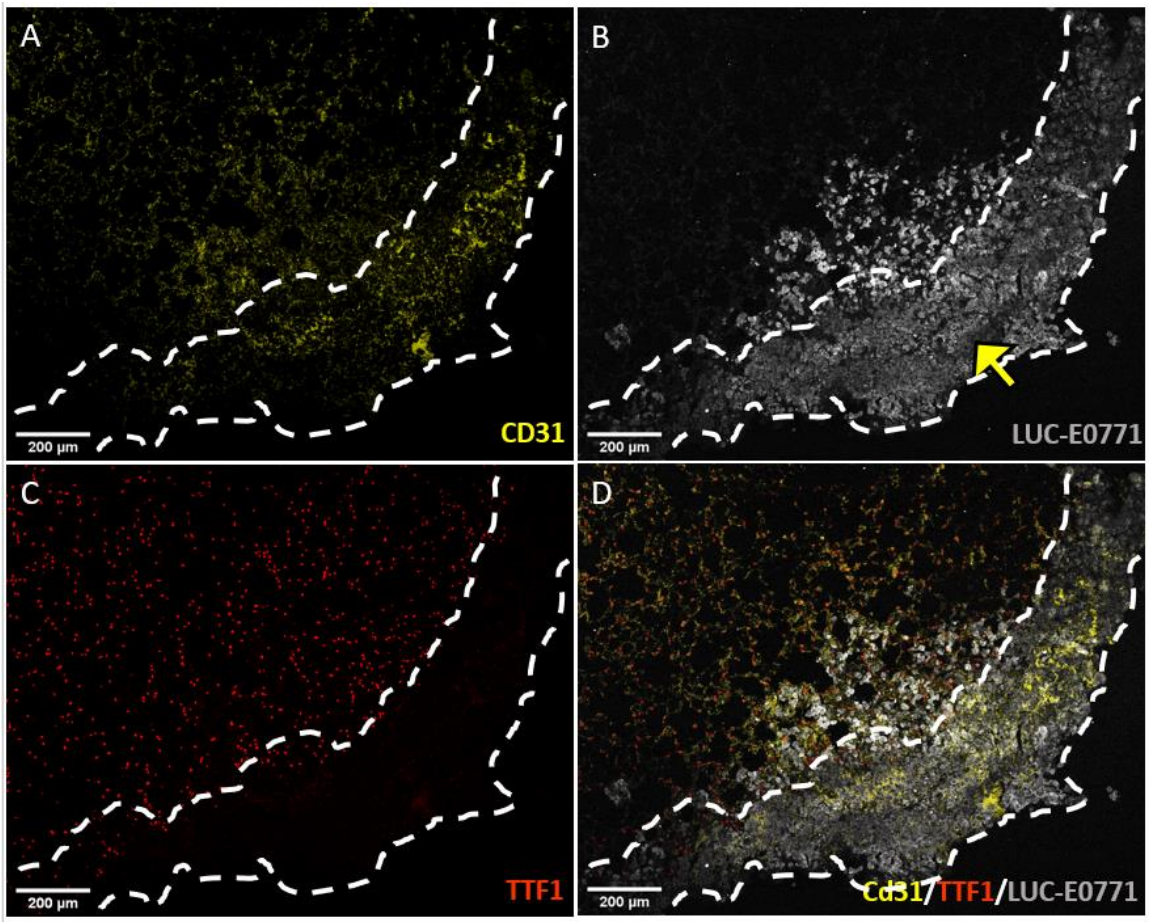

Figure 3-9. EGFP-LUC lentiviral-transduced E0771 TNBC cells progress via compressing lung parenchyma and expanding toward the lung pleura as subpleural metastases (yellow arrow). *TTF1: thyroid transcription factor 1 which labelled type II pneumocytes; LUC-E0771: are E0771 that were transduced with lentivirus encoding firefly luciferase (LUC) and EGFP demarcated by dashed line.*

3.4 Lung metastases of E0771 tumour-bearing mice exhibit both angiogenic and non-angiogenic vascular patterns (vessel co-option)

Histological evaluation of the lung metastases demonstrated that E0771 is a metastatic and highly destructive cell line. An antibody against the pan-endothelial marker CD31/PECAM (anti-platelet endothelial cell adhesion molecule) was used to mark blood vessels in the tumour-bearing lungs **(Figure 3-10A,B, Figure 3-11).** The mechanism of E0771 tumour vascularization in the lungs, visualised by CD31 staining of the vessels and quantified, demonstrated a mixture of both neo-angiogenic and non-angiogenic (vessel co-option) patterns of tumour vessel acquisition had been used **(Figure 3-10A,C).** The co-opted vessels were pre-existing vessels with either alveolar or cuffing tumour growth patterns **(Figure 3-11B,D),** while blood vessels that were newly formed via angiogenesis had chaotic irregular structures of different sizes, giving a diffuse pattern of tumour growth **(Figure 3-11A).** Consequently, it appears that in this E0771 lung metastasis model, E0771 metastases initially co-opt lung parenchyma showing alveolar and cuffing patterns to enable growth up to ~300 μm in size **(Figure 3-10B).** Once tumours expand towards the lung pleura, a switch into neo-angiogenesis to generate new blood vessels appears to be activated, as this is where the more angiogenic blood vessels where found **(Figure 3-11A)**. The nuclei of cancer cells during tumour expansion also appeared altered, with some enlarging in shape **(Figure 3-12)**, becoming hypoxic (Ca-9 staining identified hypoxia areas), and these are likely to be non-viable **(Figure 3-10D).**

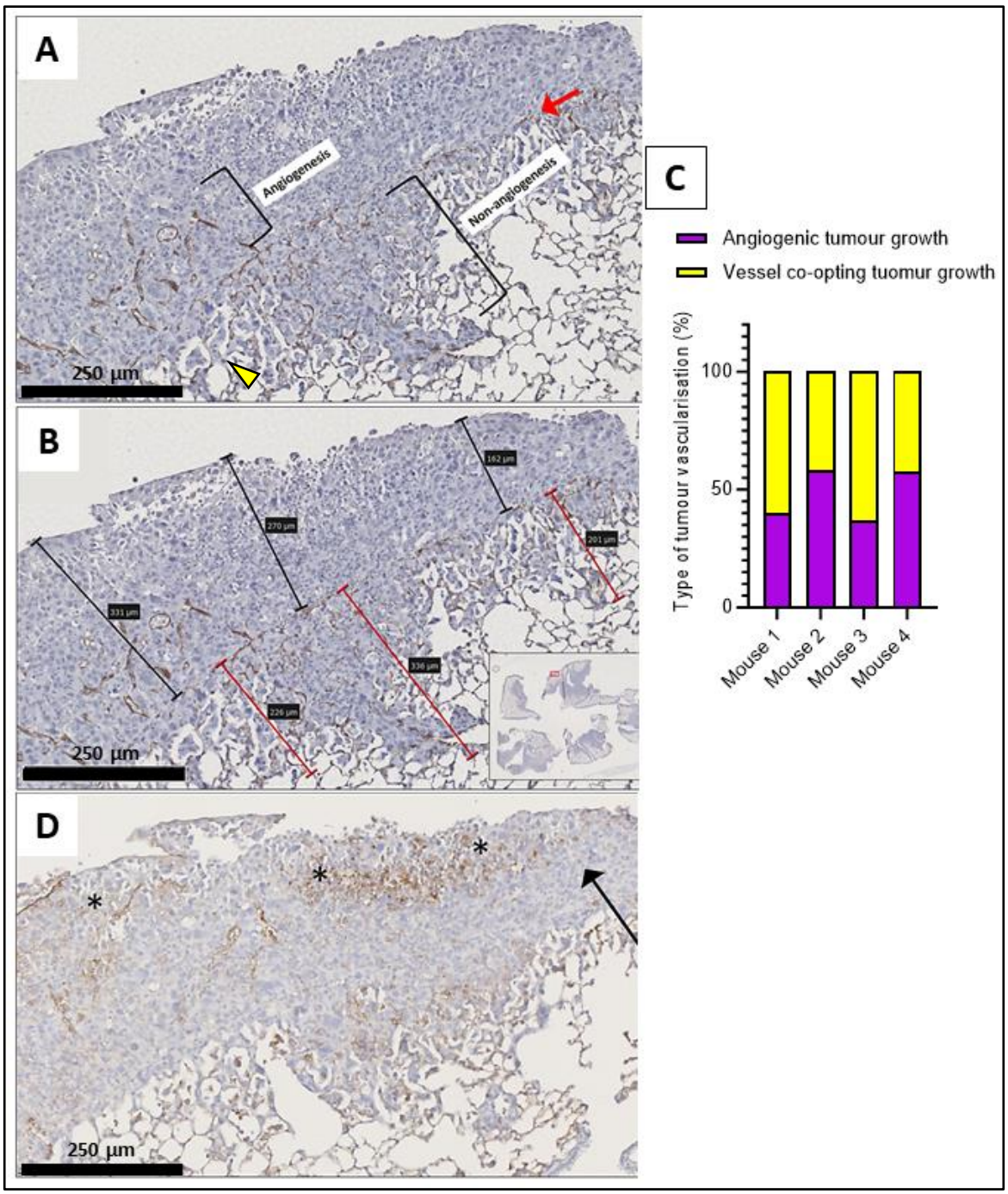

Figure 3-10. E0771 tumour lung metastasis switches from non-angiogenic to angiogenic vascularization during invasion toward the subpleural region. *A: immunohistochemistry staining of endothelial cells using anti-CD31 antibody demonstrate that E0771 tumour obtains blood supply from both angiogenesis and non-angiogenic vascularization. Red arrow depicts the vascular switch and yellow arrowhead depicts an interstitial growth pattern; B: IHC staining with anti-CD31 antibody demonstrate that vessel co-option switched off (red scale bars) and new blood formation is triggered (black scale bars) helping the tumour to further grow to ~270 µm in size. The lower inset shows the location of the present field in the whole lung section; C: the percentages of angiogenic and vessel co-opting tumours were quantified per mouse lung; D: tumour cells observed growing towards the edge of the lung (subpleura) (black arrow). Asterisks represent the hypoxic areas by immunohistochemistry using an anti-CA9 Ab; Scale bars in A-C = 250µm.*

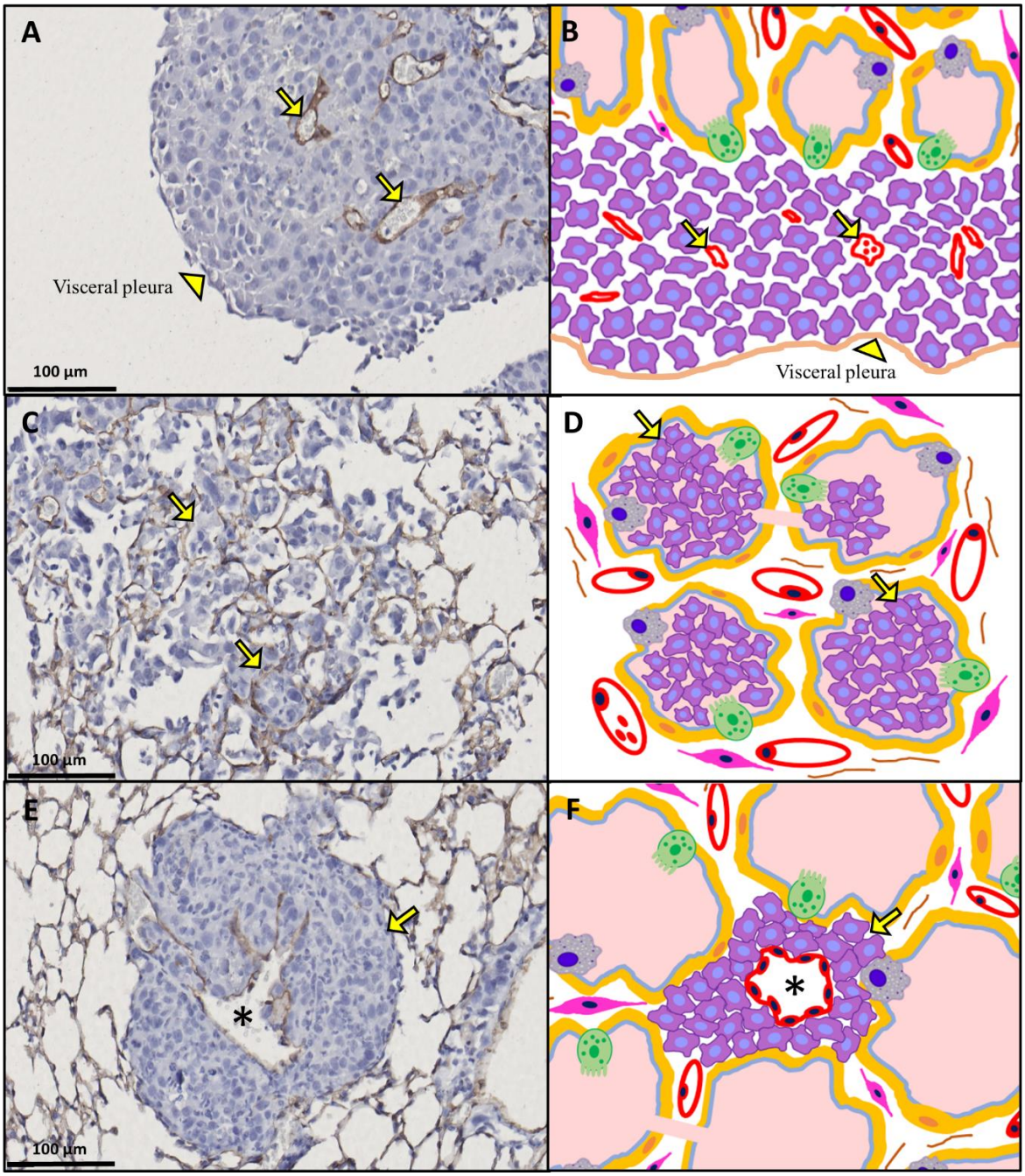

Figure 3-11. IHC labelling of blood vessels using anti-CD31 antibody showed that E0771 tumour model of experimental lung metastasis utilises both angiogenesis and vessel co-option mechanisms of vascularisation*. Vessels in panels A, C, and E were labelled using IHC with anti-CD31 antibody to identify ECs. A and B: demonstrate diffuse growth pattern with neo angiogenesis (yellow arrows denote newly formed blood vessels, which are disorganized and functional (filled with red blood cells) at the visceral pleura (arrowheads); C and D: demonstrate tumour co-option of capillaries illustrating the alveolar growth pattern (yellow arrows denote alveoli filled with E0771 tumour cells); E and F: demonstrate tumour vascular co-option with the perivascular cuffing growth pattern (yellow arrows denote E0771 tumour cells around a vessel (asterisks)). Figures B, D, and F are representative illustrations of various vascularisation patterns.*

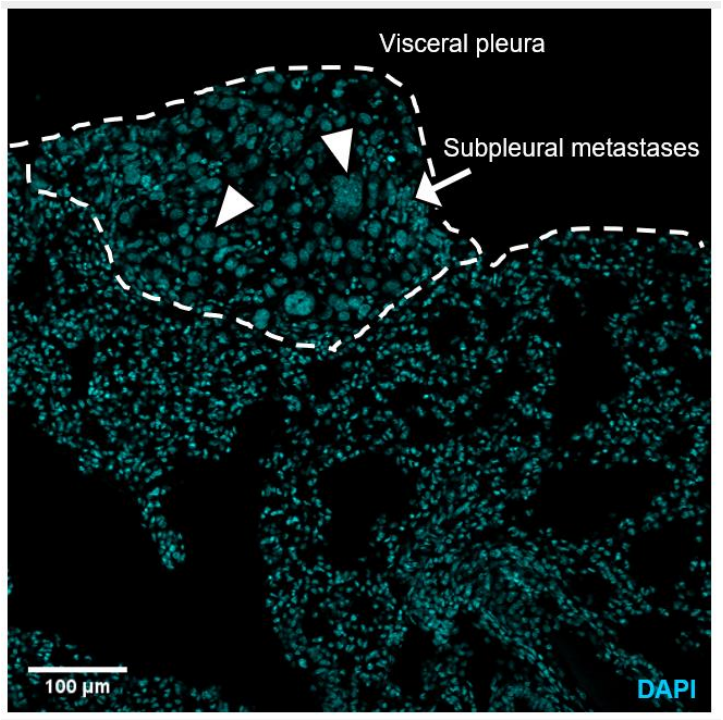

Figure 3-12. Enlarged nuclei as E0771 tumour cells progress toward lung pleura forming subpleural metastases. This metastatic lung tissue section was stained with DAPI (cyan) to visualize the nuclei shape.

3.5 Histological discrimination of angiogenic and non-angiogenic blood vessels recruited by E0771 TNBC in the lungs

To validate the heterogeneity in blood vessels adopted by E0771 TNBC cells for growth and progression in the lungs, E0771-bearing lung tissue sections were immunofluorescently stained with an anti-CD31 antibody and an antibody against thyroid transcription factor 1 (TTF1). TTF1 labels lung parenchyma, including alveoli and intertwined capillaries, and therefore enables the identification of co-opted capillaries **(Figure 3-13).** Another method to discriminate between vessel growth types was by co-staining for CD31 alongside the proliferation marker KI67. This identifies the actively proliferating angiogenic vessels (positive for both CD31 and Ki67) (Figure 3-14)**.** These observations suggested that the parenchymal metastases are supplied by co-opted vessels, and subpleural metastases are supplied by angiogenic vessels. Next, we asked if these angiogenic vessels in metastases express VE-Cadherin (VE-CAD) which is found in stabilized junctions and is associated with decreased vascular permeability. E0771-bearing

lung tissue sections with subpleural metastases were stained with vascular endothelial cadherin VE-CAD. We found that the newly formed vessels also express VE-CAD **(Figure 3-15).**

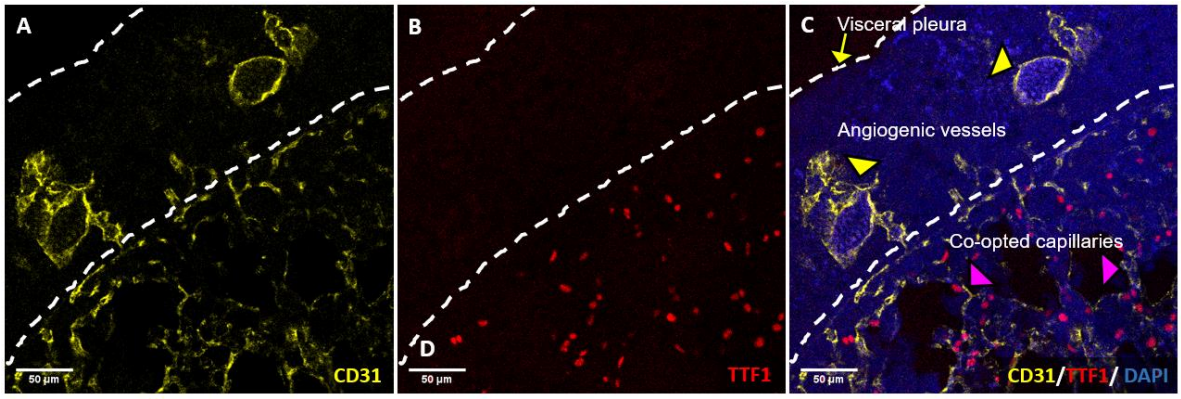

Figure 3-13. Immunofluorescence labelling lung parenchyma with anti-TTF1 antibody (red) and vessels with anti-CD31 antibody (yellow) to differentiate between angiogenic vessels and co-opted vessels recruited by E0771 TNBC cells. *TTF1: thyroid transcription factor 1 which labelled type II pneumocytes. DAPI staining of cell nuclei was used to illustrate tumour growth (blue).*

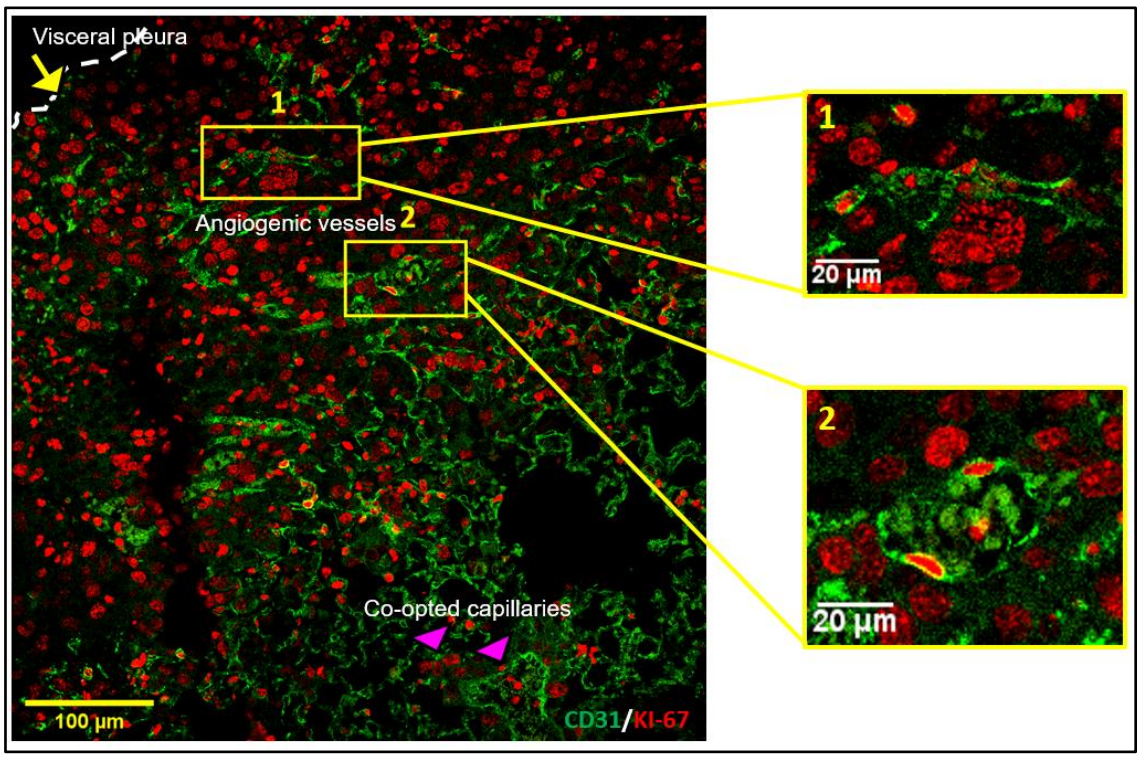

Figure 3-14. Co-expression of CD31 and KI67 in the new vessels validated angiogenesis mediating the growth of subpleural metastases at an advanced stage. *E0771 metastatic lung section were immunofluorescently stained with an endothelial marker (CD31, green) and a nuclear proliferation marker (KI67, red).*

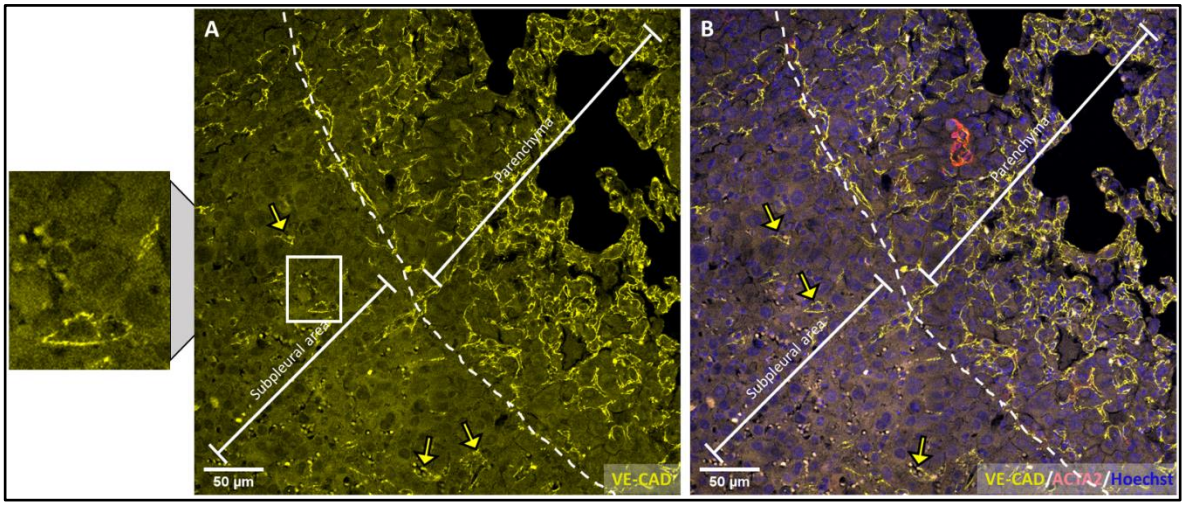

Figure 3-15. Angiogenic blood vessels in subpleural E0771 metastases induced by E0771 tumour cells that express VE-Cadherin junctions. *VE-CAD expression in new vessels in these metastases is a sign of vessel stabilization. Immunofluorescence staining of E0771 metastatic lung section with anti-VE-CAD and Actin Alpha 2, Smooth Muscle (ACTA2) showed lung capillaries and pulmonary artery, respectively.*

3.6 Discussion

Here, I have developed an experimental model with which I can study homing and progression of circulating metastatic TNBC cells in the lung. An experimental metastasis model where tumour cells were injected through the circulation allows us to mimic tumour metastasis in the absence of primary tumour. In this model, the late stages of the metastatic cascade (arrest and extravasation of tumour cells and remodelling of the local microenvironment) can be investigated. Intravenous-delivered metastasis model was used in this project rather than allowing for the metastasis to occur naturally from a primary breast tumour as our lung metastases developed in a short time and avoided compromising the animal's welfare.

As shown by my results, E0771 TNBC cells are an aggressive cell line. Injecting one million cells through the tail vein enabled E0771 tumour cells to home to the lungs forming a sufficient tumour burden within only two weeks (day 13-16 post-tumour injection). Using this experimental lung metastasis model, I observed that E0771 tumours appeared to colonize the lungs initially by primarily using the pre-existing blood vessels (vessel co-option, with both alveolar and cuff growth patterns observed). Upon further progression, E0771 tumour cells continued to grow expanding outside the lung parenchyma, *i.e.*, by growing in the subpleural location. Tumours growing in this location cannot exploit pre-existing blood vessels and hypoxic areas of oxygen deprivation were detected. My observations indicate that this hypoxic microenvironment may induce the formation of new blood vessels. This process is commonly termed the vascular switch, that we observed to occur specifically at the pleural edges of the lungs when the availability of normal lung vessels ceases.

Angiogenic vessels found in the advanced pleural stage of metastasis express the adherens junction marker VE-Cadherin, implicating it in the vascular stability and integrity of these growing vessels (Cavallaro et al., 2006). Although VE-Cadherin is ubiquitously

expressed in resting and growing vessels, Liao and colleagues identified a novel anti-VE-Cadherin antibody (E4G10) that selectively targets and binds angiogenic vessels (Liao et al., 2002). This selective binding of the E4G10 Ab was explained by the epitopes of VE-Cadherin junctions being loose and accessible in the newly formed vessels suggesting the anti-angiogenic therapeutic potential of targeting these junctions in tumours (Liao et al., 2002).

Another murine TNBC cell line, 4T1 (2×10^5 cells injected via tail vein injection and lungs harvested on day 10 post-injection) was previously described to only use vessel co-option in alveolar and interstitial growth patterns as it generated lung metastases (Bridgeman et al., 2017). Other tumours of different origins, such as the C26 murine colorectal carcinoma cell line (2×10^5 cells were injected and lungs harvested on day 10 post-injection) also exhibited vessel co-option (Bridgeman et al., 2017). Alternatively, RENCA renal cell carcinoma (2×10^5 injected and lungs harvested on day 21 post-injection) primarily utilized angiogenesis to generate the required vascular network, with a pushing growth pattern excluding lung parenchyma (Bridgeman et al., 2017; Teuwen et al., 2021). However, in addition to different cell types, each of these experiments used differing cell numbers and lung harvest schedules. Therefore, both cell number and the differing metastatic efficiency of tumour cell lines (4T1/C26/RENCA/E0771) may be determinant factors in the way these metastases recruit a tumour vascular network.

The limitation of this *in vivo* model is that E0771 tumour cells were administered through the tail vein. A more relevant study to mimic metastasis development from a primary tumour in human would include using spontaneous (orthotopic) model, where E0771 tumour cells are injected into mammary fat pad. This would enable assessing early stages of metastasis including intravasation and vascular patterns as primary tumour cells change at the molecular level when metastasize, which might lead to different vascularisation compared to IV-inoculated tumour cells. Since orthotopic model take longer time in order to metastasise to the lungs and using MRI imaging to assess tumour burden and visualise

vascular phenotypes in the metastatic lungs was considered as a high-cost tool, generating the orthotopic model of Eltd1 lacking transgenic mice were not pursued.

However, the results shown here indicate that my E0771 experimental lung metastasis model combines both non-angiogenic (vessel co-option) and angiogenic tumour vascularization in a single model in a temporal and spatial manner. In human cancers, several primary and secondar cancers **(as discussed in the Introduction Chapter)** exhibited both types of vascularization (Bridgeman et al., 2017; Kanai et al., 1987; Kåre et al., 2014; Strand et al., 2015; Wesseling et al., 1994). Thus, this E0771 metastasis model may mimic tumour vascularisation of human cancers and is therefore a useful tool with which to investigate transcriptional changes of heterogeneous mechanisms of vascularisation as well as the cellular composition of the lung stroma that remodels the lungs and supports the formation of non-angiogenic (parenchymal) and angiogenic (subpleural) metastases.

Chapter 4: Genetic and pharmacological targeting of angiogenic blood vessels in the E0771 lung metastasis model

4.1 Introduction

Our hypothesis is that subpleural metastases in the developed E0771 model are supported by angiogenic blood vessels not pre-existing vessels. In this chapter, I have used the experimental E0771 lung metastasis model **(described in the first Results chapter)** to investigate the vascular response to two different approaches to inhibiting angiogenesis. Specifically, I examined the response of E0771 TNBC metastases after genetic ablation of the angiogenic-associated gene *Eltd1* (*E*pidermal growth factor, *L*atrophilin and seven *T*ransmembrane *D*omain 1, also known as *Adgrl4, Ad*hesion *G* Protein-Coupled *R*eceptor *L4*), and after treatment with the tyrosine kinase inhibitor pazopanib, an established anti-angiogenic therapy (Ji et al., 2018). This chapter aimed to investigate whether the growth of E0771 TNBC metastatic tumours was reduced, whether they developed resistance mechanisms, and whether alternative mechanisms of vascularization were exploited after inhibition of angiogenesis.

4.2 Investigating the effect of inducible deletion of the endothelial angiogenic gene, *Eltd1* on the *in vivo* growth of E0771 subpleural metastases

Our laboratory has previously used a bioinformatics approach to identify *ELTD1* as a part of a core tumour angiogenesis signature common to multiple cancer types (Masiero et al., 2013). A vascular endothelial-specific *Eltd1* knockout mouse model (*Pdgfb-iCreERT2*$^{Cre/+}$;*Eldt1*$^{fl/fl}$ abbreviated to *Eltd1*^{iEC} here) **(Figure 4-1)**, previously generated by our laboratory, was used here in combination with the E0771 lung metastasis model described in **Chapter 3.** Using this transgenic mouse model, I aimed to validate the vascular phenotype observed in the *in vivo* E0771 metastasis model in wild-type mice and then to

study E0771 tumour behaviour upon loss of *Eltd1* and subsequent reduction in angiogenesis.

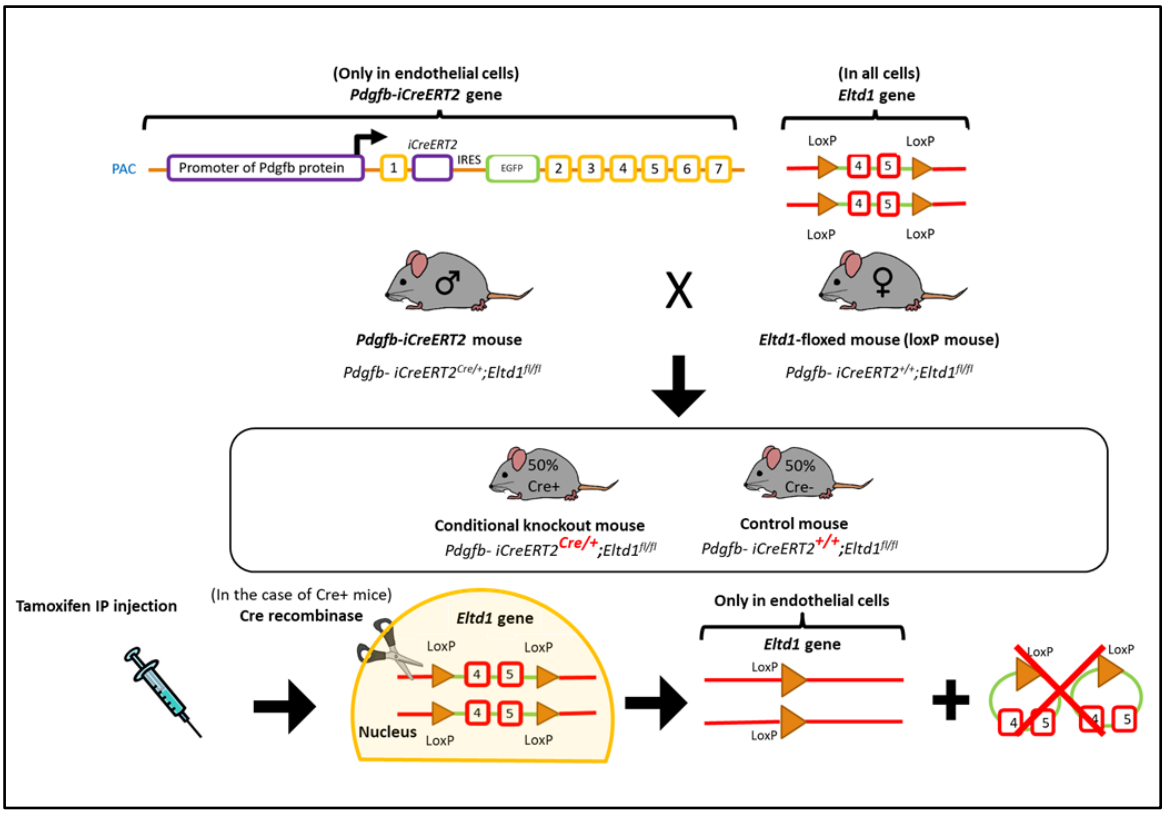

Figure 4-1. Illustration of generating inducible endothelial-specific Eltd1 knockout model (Pdgfb-iCreERT$^{Cre/+}$; Eltd1$^{fl/fl}$) using Cre/loxP system. *Pdgfb-iCreERT2$^{Cre/+}$;Eltd1$^{f/fl}$ male mouse crossed with Eltd1$^{fl/fl}$ female mouse yielded 50% Cre+ and 50% Cre- progeny. Tamoxifen administration induces KO of exons 4 and 5 of Eltd1 in 50% of offspring expressing Cre recombinase under Pdgfb (endothelial marker)-specific promotor. Upon intraperitoneal (IP) injection of tamoxifen to this model, tamoxifen will bind to its binding domain of oestrogen receptor (ER) causing translocation of Cre recombinase from the cytoplasm into the nucleus, where recombination (excision) of loxP-flanked Eltd1 gene (exons 4 and 5) then occurs. Pdgfb-iCreERT2 mouse contains PAC clone, where both Cre and enhanced green fluorescent protein (EGFP)-reporter transgenes are inserted under the promoter of an endothelial marker, Pdgfb gene allowing for spatiotemporal Cre-recombination of Eltd1 gene to occur only in endothelial cells.*

4.2.1 Validation of *Eltd1* deletion

Ear notches were collected from the experimental mice for genotyping, identifying *Cre*-positive (*Eltd1*^{iEC} induced EC-specific knockout) and *Cre*-negative mice (*Pdgfb-Cre*$^{-/-}$; *Eltd1*$^{fl/fl}$, referred throughout the thesis as littermate controls) **(Figure 4-2).** Next, 3-week-old mice were injected with tamoxifen to induce Cre-mediated *Eltd1* deletion. Tissues were harvested when the mice were 6 weeks old to study *Eltd1* deletion, the timepoint at which we will later injecting this model with E0771 tumour cells. Validating ELTD1 protein loss in the lungs (the organ of interest) of 6-week-old mice at the protein level was not possible

due to the high background staining generated by an 'in-house' ELTD1 rabbit polyclonal antibody. Therefore, instead I quantified the ELTD1 protein levels by IHC evaluation in kidneys (another highly vascularised organ that has previously been used to validate *Eltd1* knockout by tamoxifen) using the same antibody. Both qualitative and quantitative analysis of this ELTD1 staining demonstrated a significant reduction in ELTD1 expression level in *Eltd1*^{iEC} mice compared to littermate controls **(Figure 4-3).**

I also investigated the gross morphology of *Eltd1*^{iEC} lungs after tamoxifen administration. This analysis found that CD31-positive vessels in the lungs of these unchallenged *Eltd1*^{iEC} mice (physiological condition) were intact with similar pulmonary physiology compared to littermate control group **(Figure 4-4)**, suggesting that ELTD1 is dispensable in quiescent normal state of ECs. Consequently, this model was deemed a suitable transgenic tool to explore the effect of endothelial-specific ablation of the angiogenic *Eltd1* gene on tumour progression.

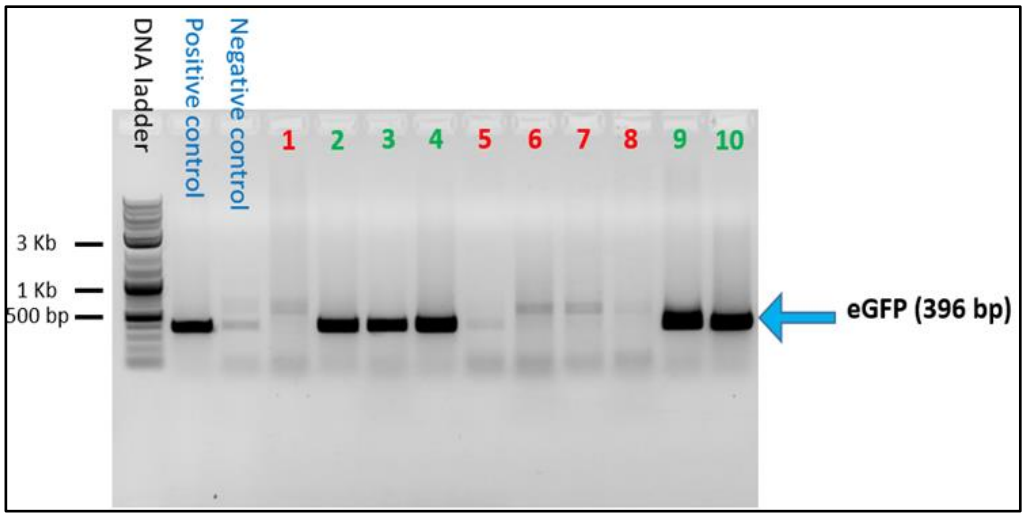

Figure 4-2. Identification of transgenic mice (Cre-positive) and littermate controls (Cre-negative) by EGFP amplification. *Mice 1,5,6,7, and 8 which are negative for EGFP were used as the control group; mice 2,3,4,9, and 10 which are positive for EGFP were used as the experimental (Eltd1 knockout) group. EGFP: Enhanced green fluorescent protein.*

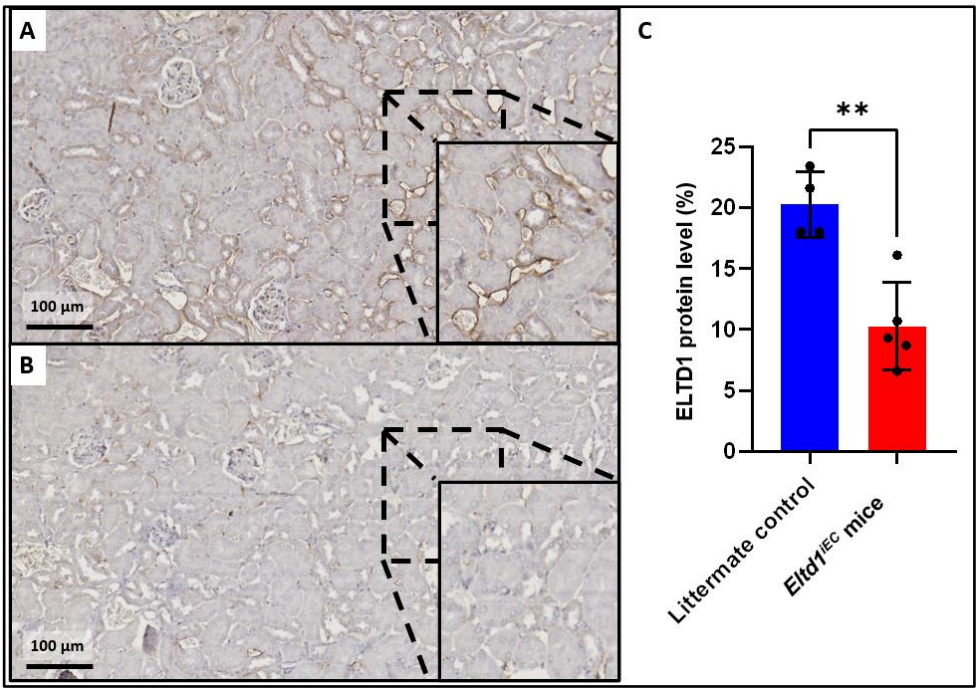

Figure 4-3. Significant reduction in ELTD1 expression level in 6-week-old Eltd1^{iEC} mice compared to littermate controls after administration of tamoxifen at ~3-weeks old. *A: representative kidney section of control mouse; B: representative kidney section of Eltd1^{iEC} mouse, both sections stained with an in house ELTD1 polyclonal Ab; C: significant difference in ELTD1 protein level in the kidneys of Eltd1^{iEC} group (n= 5) compared to littermate controls (n=4). ELTD1 positive signal in 6 fields of view per mouse was quantified using QuPath digital pathology software. Each data set represents the mean ± standard deviation (SD) (Unpaired Student's t-test was used, *: p ≤ .05; **: p ≤ .01; ***: p ≤ 0.001; ****: p ≤ 0.0001). p value =0.0025.*

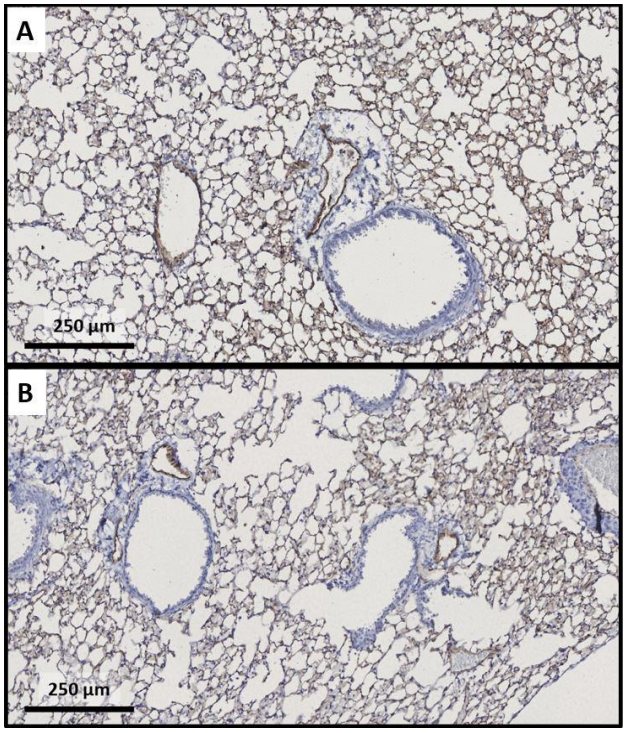

Figure 4-4. The alveolar structure and vascular networks of lungs of Eltd1^{iEC} group (B) appear to be unaffected by Eltd1 recombination after tamoxifen administration in comparison to littermate controls (A). *Lung tissue sections were stained with anti-CD31 antibody to visualize blood vessels.*

To stimulate TNBS metastasis, 1x10^6 of EGFP-LUC labelled E0771 breast tumour cells were injected intravenously into both control and *Eltd1*^{iEC} mice **(Figure 4-5).** My previous results indicate that established lung metastases would be formed in wild type mice by day 13-16.

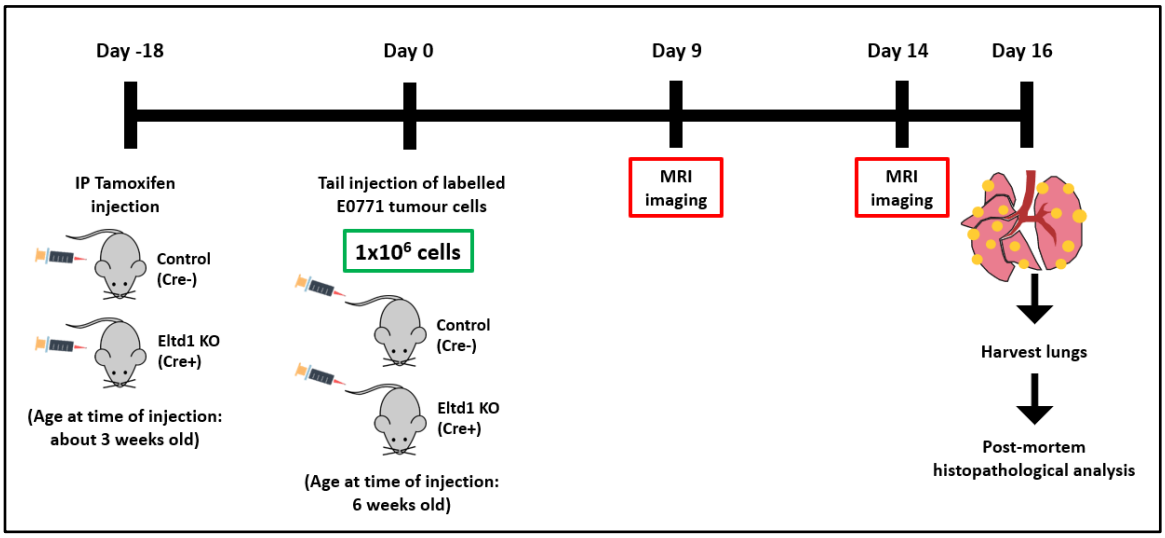

Figure 4-5. Timeline of induction of Eltd1 deletion followed by development of experimental E0771 lung metastasis model. *Mice were divided into Eltd1*^{iEC} *group and littermate controls based on PCR amplification of EGFP sequence (co-expressed with Cre transgene). Tumour burden in both groups were assessed using non-invasive magnetic resonance imaging (MRI) imaging of lungs of both groups. Metastatic lungs were harvested for histological assessment.*

4.2.2 Deletion of an angiogenic gene *Eltd1* did not affect tumour burden or reduce the thickness of subpleural metastases

We hypothesise that E0771 metastatic growth decrease upon *Eltd1* deletion. To identify the location and assess lung metastases burden of *Eltd1*^{iEC} and littermate control mice, non-invasive *in vivo* magnetic resonance imaging (MRI) was used at both day 9 and day 14 following tumour injection. In addition, I also conducted post-mortem histological analysis on tissues harvested on day 16.

MRI scans are the traditional tool used for detection, staging, and defining the extent of invasion of lung tumours (Salzer, 2012). Dr Sean Smart (at the Oncology pre-clinical imaging facility at the University of Oxford) and his team have developed MRI approaches to monitor the development of metastasis and visualize lung blood vessels using two image acquisition modes: cardio-respiratory (CR)-synchronized balanced Steady-State Free Precession (bSSFP) and gradient echo 3D (GE3D) sequences. Reconstruction of MRI

bSSFP images of E0771-bearing lungs at early and late stage of metastases in 2D **(Figure 4-6)** and 3D **(Figure 4-7A,B)** visualizations uncovered unique 'grey strands' like structures and thickened septal lines at day 14 compared to day 9 (different MRI plane cross-sectional views of the lungs are provided in **Appendix B**). Comparing images to the H&E-stained lung sections **(Figure 4-8A, B)**, these strands were found to be tumour cells spreading at the lung edges (subpleura) between the lobes (fissures) of the lungs. Bright contrasts appeared also in the outer rim of the lungs on day 14 post-tumour injection indicating the presence of subpleural metastases **(Figure 4-6B)** which matched the gross view of post-mortem images of the lungs **(Figure 4-9),** whereas MRI GE3D images visualized blood vessels in the lungs as well as metastases **(Figure 4-10).**

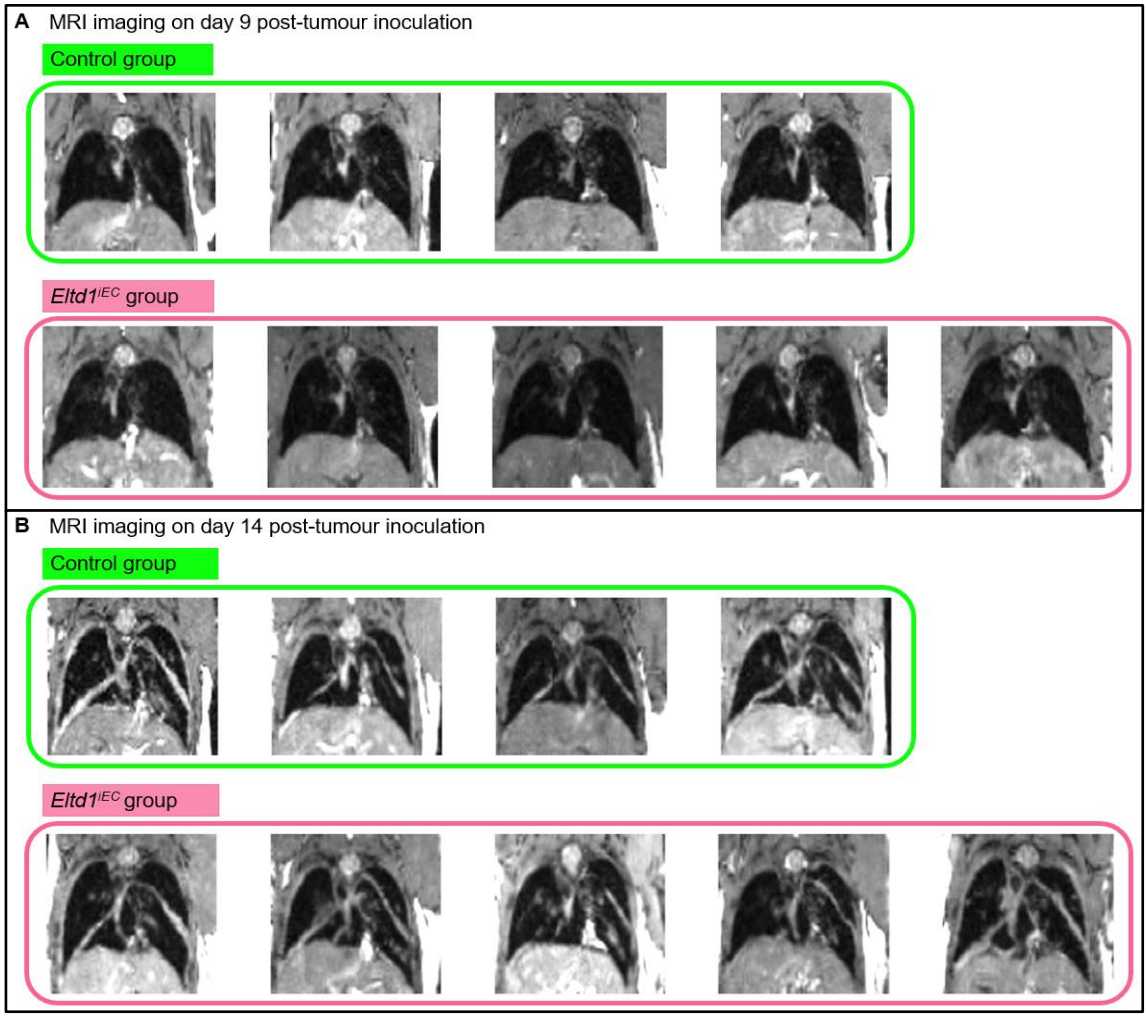

Figure 4-6. Segmented MRI images (X plane cross-sectional view) of E0771 lung metastases showed no difference in tumour burden. *However, they showed interlobular strands (thickening) in both Eltd1^{iEC} and littermate control groups at day 14 compared to day 9. Green boxes indicate the control group (n=4 mice); pink boxes indicate Eltd1^{iEC} mice (n=5 mice).*

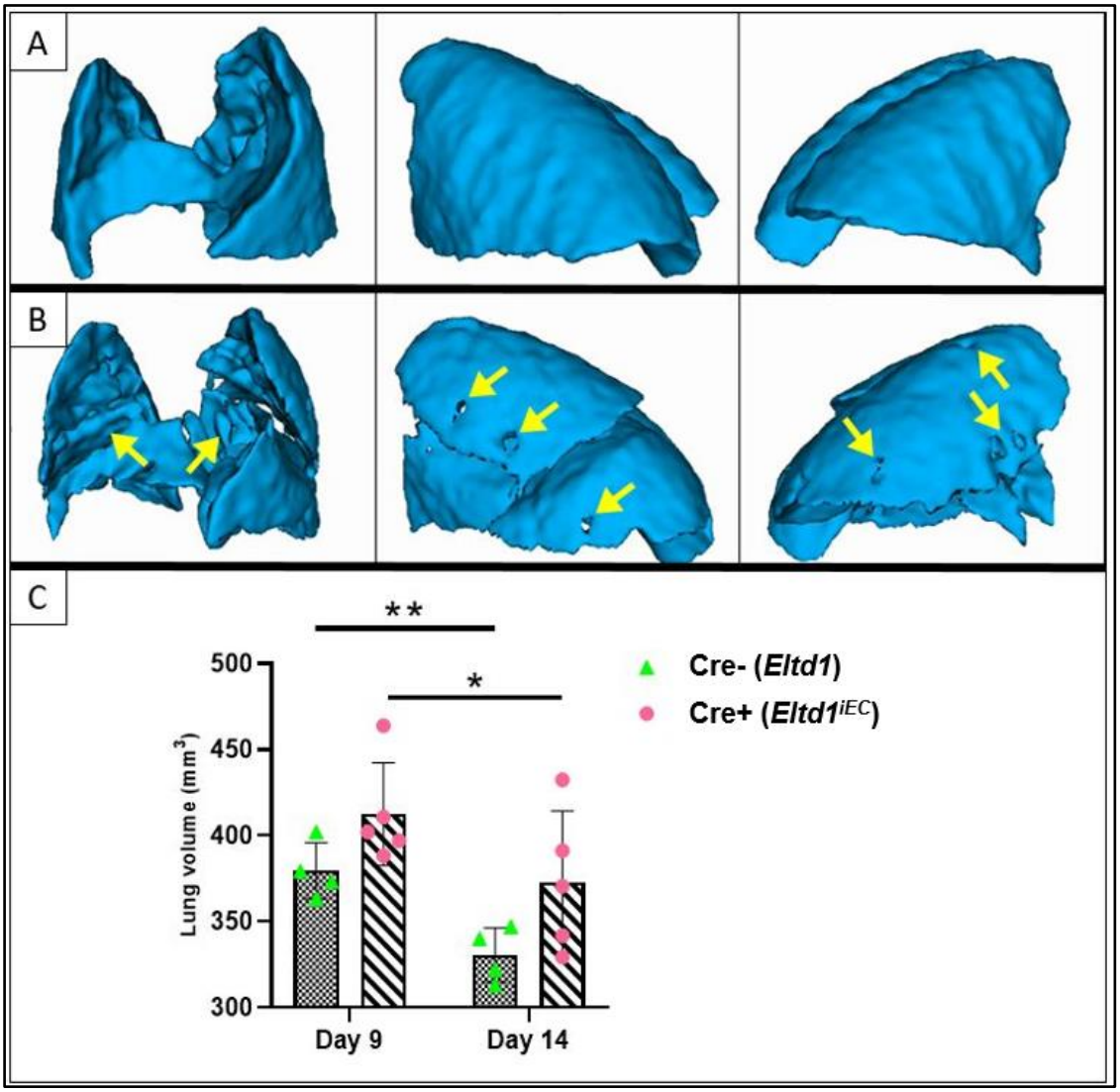

Figure 4-7. Quantification of lung volume (in mm³) of control and $Eltd1^{iEC}$ groups. *A and B: representative 3D segmentation of mouse lung at day 9 and 14 post-tumour induction (lung masks are shown in blue) illustrating a reduction in lung volume at day 14 (yellow arrows showing hollow spots) compared to day 9 (smooth surface) post induction; C: quantification of the average lung volume in mm³ of control and $Eltd1^{iEC}$ groups at day 9 and 14 post-tumour induction. Each symbol (circle or triangle) represents one mouse (n= 4 for control group and n= 5 for $Eltd1^{iEC}$ group). Each data set represents the mean ± standard deviation (SD) (Two-way ANOVA with Sidak's multiple comparisons test, *: p ≤ .05; **: p ≤ .01; ***: p ≤ 0.001; ****: p ≤ 0.0001).*

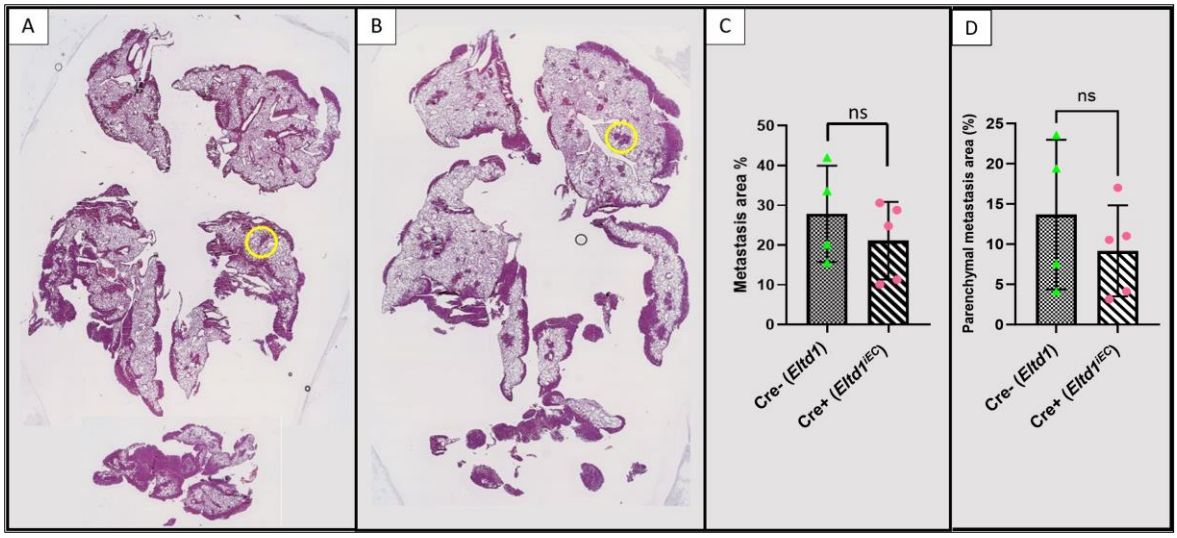

Figure 4-8. Representative H&E sections and quantification of E0771 metastatic area in control and Eltd1^{iEC} groups. *Lungs were removed from the mice post-mortem. The lobes were separated then sections of the formalin fixed, and paraffin embedded tissues were H&E stained. A: Control mouse lungs; B: Eltd1^{iEC} mouse lungs. The cell number used was 1x10^{6} and the endpoint to sacrifice the mice was on day 16 following tumour injection. The majority of tumour cells localise to the lung surfaces, with some smaller metastases being observed within the lung parenchyma (yellow circles). C: the percentage of E0771 metastatic area in control and Eltd1^{iEC} groups. H&E-stained lung metastases were quantified using Visiopharm digital pathology software as the percentage of the lung area occupied by tumour cells verses normal tissue. Per mouse, an average percentage of the metastatic area of two tissue sections were calculated. Note that these two sections are 36 µm apart; D: the percentage of E0771 parenchymal metastatic area in control and Eltd1^{iEC} groups. CD31-stained lung metastases were quantified using Qupath digital pathology software as the percentage of the lung area occupied by tumour cells verses normal tissue. Each data set represents the mean ± standard deviation (SD), n=4 (Cre-negative control group); n=5 (Cre-positive Eltd1^{iEC} group)) (Unpaired Student's t-test was used, *: p ≤ .05; **: p ≤ .01; ***: p ≤ 0.001; ****: p ≤ 0.0001, ns: not significant).*

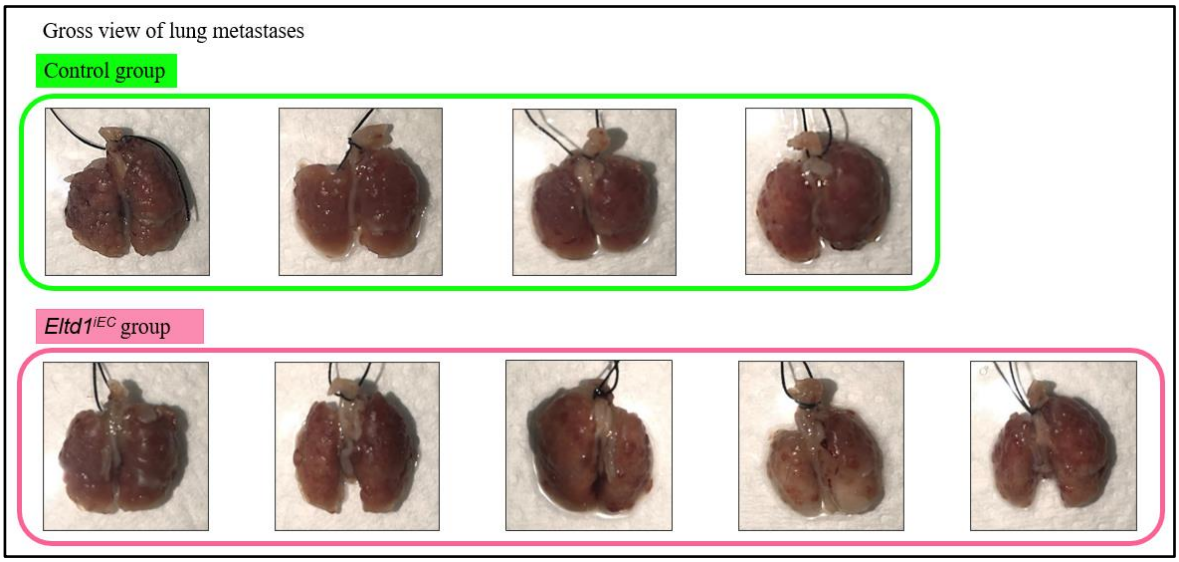

Figure 4-9. Gross view of E0771 lung metastases exhibited hematologic swathes of intensity on the outer surface in both Eltd1^{iEC} and littermate control groups at the late timepoint (day 14). *The green boxes indicate the control group (n=4 mice); the pink boxes indicate Eltd1^{iEC} mice (n=5 mice).*

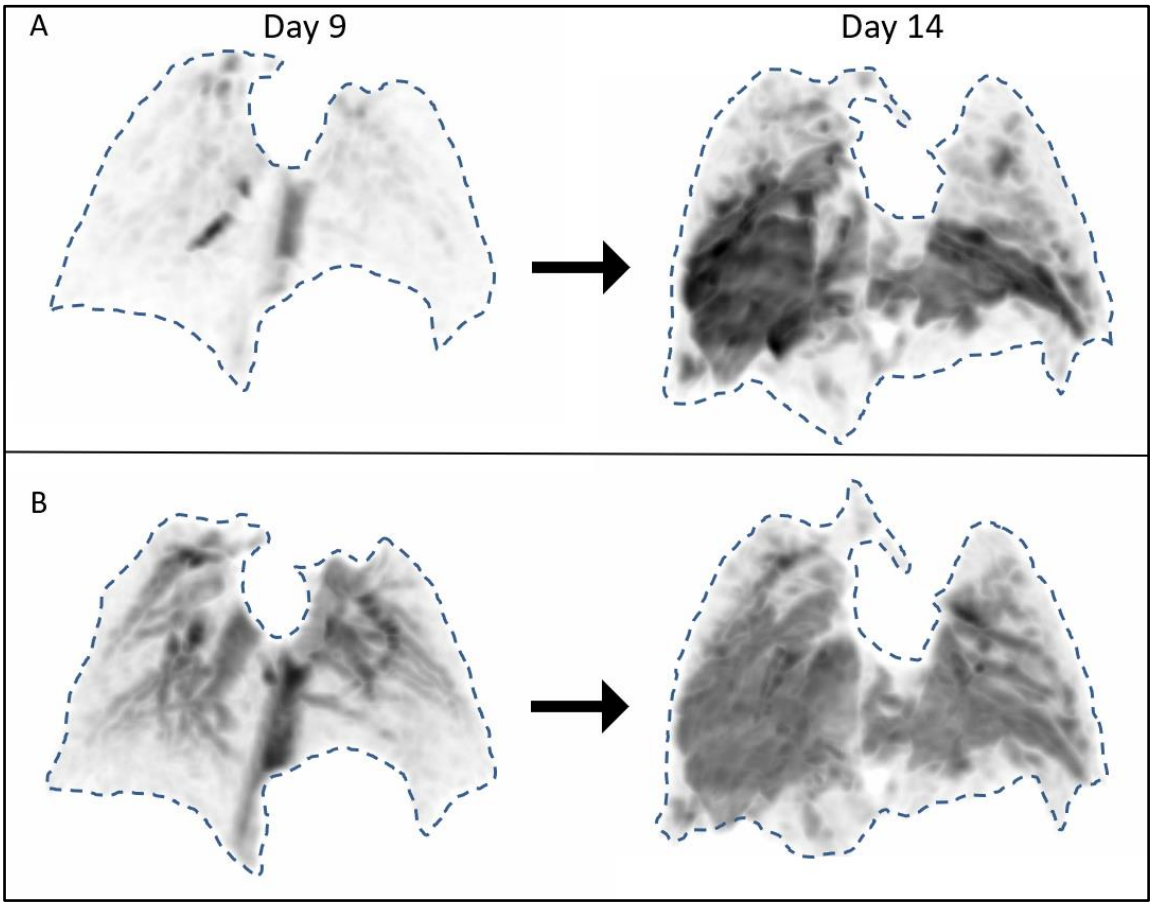

Figure 4-10. Representative MRI reconstructed images localizing E0771 tumours and blood vessels in mouse lungs. *A: reconstructed front view of E0771 metastatic lungs at early (day 9) and late (day14) timepoints scanned with MRI cardio-respiratory (CR)-synchronized balanced Steady-State Free Precession (bSSFP) scan mode that detect only tumours; B: reconstructed front view of E0771 metastatic lungs at early (day 9) and late (day14) timepoints scanned with MRI gradient echo 3D (GE3D) scan mode detecting both tumours and blood vessels. These images are captured from 3D dataset.*

Previous study showed that other types of lung tumours develop as discrete and compact tumours that can be quantified (Gomes et al., 2019). Unfortunately, it was not possible to use the MRI images to quantify tumour burden in the E0771 lung metastasis model due to the unusual strand-like pattern of distribution. The air space of the lung parenchyma was reconstructed as a 3D mask and quantified instead to assess tumour burden **(Figure 4-7).** Quantification of lung volume (air spaces occupied by normal lung parenchyma subtracting the space occupied by the tumour) showed that the genotype (control versus *Eltd1*^{iEC} group) had no significant effect on lung volume **(Figure 4-7C).** However, in comparison to an early timepoint (day 9) of tumour development (control group= 379.56 mm^3 ± 16.36 and *Eltd1*^{iEC} group= 412.39 mm^3 ± 29.91) MRI monitoring showed that the E0771 tumour significantly and invasively outgrew and reduced the lung

volume by day 14 in both groups (in the control group, the lung volume was 330.62 mm^3 ± 15.68, ρ = .007; whilst in the *Eltd1*^{iEC} group it was 373.09 mm^3 ± 41.08, p = 0.012) **(Figure 4-7C).**

Mice lungs sacrificed on day 16 post-tumour injection showed both macro- and micro-metastases **(Figure 4-8A, B)**. Analysis of H&E- and CD31-stained lungs supported the conclusions from the MRI scanning, finding there was no significant difference in either the total tumour burden **(Figure 4-8C)** nor in the parenchymal metastatic area (both expressed as metastasis area %) between the *Eltd1*^{iEC} group and littermate controls **(Figure 4-8D).**

While I detected no difference in overall tumour burden between control and *Eltd1*^{iEC} groups, I also investigated whether *Eltd1* deletion in ECs led to a reduction in subpleural angiogenic metastases. This analysis found that the width of subpleural metastases was comparable in both the control and *Eltd1*^{iEC} groups **(Figure 4-11C).** Further**,** an examination of the subpleural metastases found that both groups contain comparable numbers of angiogenic vessels **(Figure 4-11A, B).** However, a larger sample size is needed to validate this finding, but the cost of the MRI experiment prevented this during the current study.

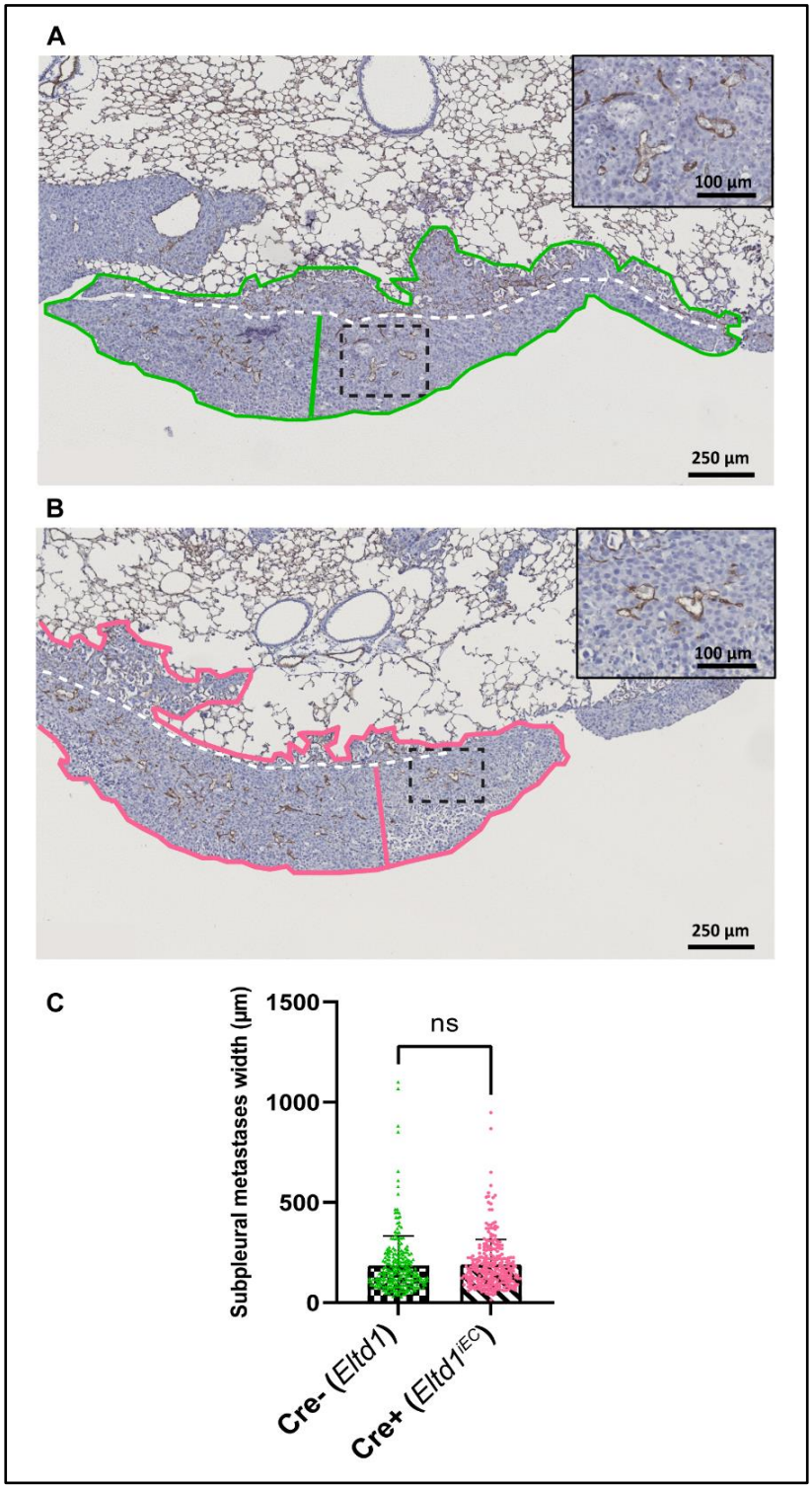

Figure 4-11. Endothelial-specific deletion of Eltd1 did not significantly reduces the width of E0771 subpleural metastases. *Widths of metastases localized at the subpleura were measured using QuPath digital pathology software. A: an overall view of E0771 metastatic lung tissue section of control group with a white dashed line that separates subpleural from parenchymal metastatic growth and a green line depicting the measurement of subpleural metastases width; B: an overall view of E0771 metastatic lung tissue section of* $Eltd1^{iEC}$ *group with a white dashed line that separates subpleural from parenchymal metastatic growth and a pink line depicting the measurement of subpleural metastases width. Black dashed boxes in A and B presented as enlarged insets showing angiogenic blood vessels. Each symbol (circle or triangle) represents single measurement (260 measurements were taken from n= 4 of Cre- (Eltd1) group and 281 measurements were taken from n=5 of Cre+ (*$Eltd1^{iEC}$*) group. Each dataset represents the mean ± standard deviation (SD) (statistical analysis was performed using the two-tailed unpaired parametric Student's t-test, *: p ≤ .05; **: p ≤ .01; ***: p ≤ 0.001; ****: p ≤ 0.0001). p value =0.7110.*

4.3 Investigating the effect of the anti-angiogenic drug pazopanib on E0771 subpleural metastases

Targeting VEGF using bevacizumab has proven to be ineffective in treating metastatic breast cancer and did not improve survival, thus revoked by US FDA in 2011 (Pfister et al., 2015). Mutant p53 TNBC cancer cell lines have been shown to upregulate the expression of VEGFR2 (Pfister et al., 2015). The TNBC cell line we use, E0771 tumour cells is p53 mutated and is also reported to express VEGF, VEGFR1 and VEGFR2 (Gu et al., 2009). Thus, we hypothesise that angiogenesis occurring in the E0771 subpleural metastases is mediated by VEGF-VEGFR signalling. I therefore used a VEGFR2-targeted therapy, the tyrosine kinase inhibitor pazopanib hydrochloride (Votrient, made by GlaxoSmithKline), to target tumour angiogenesis in my *in vivo* E0771 metastasis model and to study E0771 tumour response after inhibition of angiogenesis. Pazopanib is an anti-angiogenic therapy that mainly inhibits the intracellular tyrosine kinase of vascular endothelial growth factor receptors (VEGFR1 and 2), making VEGF receptors insensitive to secreted VEGFA. This drug also inhibits VEGFR3, interleukin-2 receptor-inducible T-cell kinase (ITK), leukocyte-specific protein tyrosine kinase (LCK), platelet-derived growth factor receptors (PDGFR-α and −β), stem cell factor receptor (c-KIT), transmembrane glycoprotein receptor tyrosine kinase (c-FMS), and fibroblast growth factor receptors (FGFR-1 and -3) (Chellappan et al., 2017).

4.3.1 Pharmacological inhibition of angiogenic ECs in the E0771 lung metastases model reduces the thickness of subpleural metastases

Here I aimed to determine whether blocking angiogenesis using pazopanib prevents the development of metastases in my E0771 TNBC model. Pazopanib was orally administered to E0771 metastatic-bearing mice from day 7 post-tumour induction (as defined by the day of E0771 cell injection) **(Figure 4-12A).** This timepoint was chosen as it

is prior the development of subpleural metastases, which prominently feature angiogenic-like growth **(see Chapter 3).** At 13 days after tumour injection, the width of subpleural metastases (where active angiogenesis had previously been observed) was measured in post-mortem lung tissue sections. This can be used as an indication of the inhibitory effect of pazopanib on the angiogenesis induced by E0771 TNBC cells. This analysis found that the width of subpleural metastases was significantly reduced in the pazopanib-treated group compared to the vehicle group (the average width of subpleural metastases in the vehicle group was 91.35 µm ± 67.28; whilst in the pazopanib-treated group it was 77.23 µm ± 54.58 (p= 0.007)) **(Figure 4-12B-E, Figure 4-13B).** This finding suggests that non-angiogenic vascularization (vessel co-option) may have been adopted by metastatic E0771 breast cancer cells after treatment with pazopanib. This could potentially then make pazopanib less effective at eliminating tumour growth, despite the reduction in the width of subpleural metastases. This finding was evidenced by the burden of parenchymal (vessel co-opting) metastases, which was not affected by pazopanib therapy **(Figure 4-13B).**

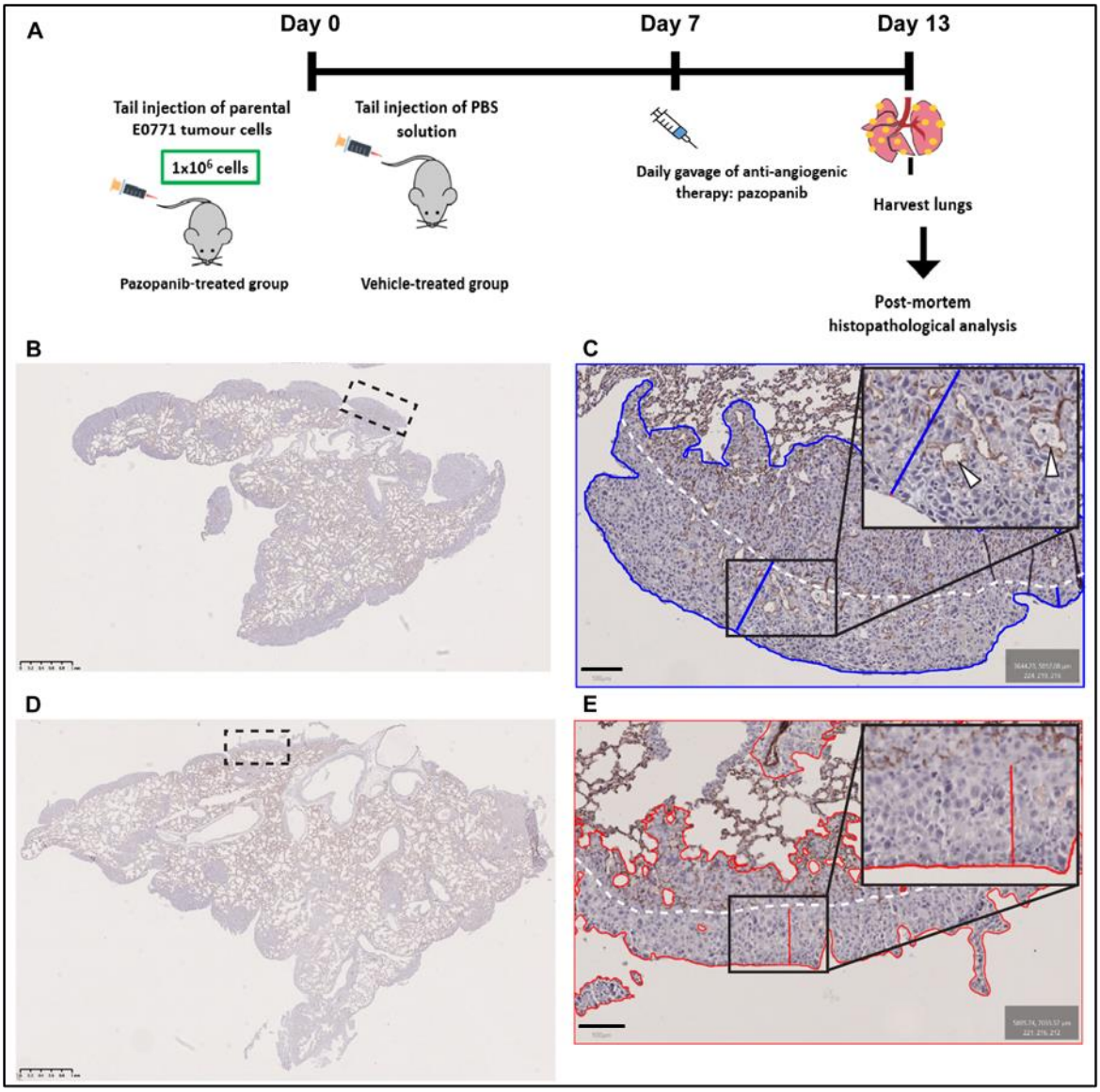

Figure 4-12. IHC labelling of the blood vessels of pazopanib- and vehicle-treated E0771 tumour bearing lungs using anti-CD31 antibody. *A: timeline of generating a therapeutic E0771 lung metastasis model, where 100 mg/kg of pazopanib was orally administered to pazopanib-treated group on daily basis; B: an overall view of vehicle-treated E0771 metastatic lung tissue section; C: an enlarged inset of one of the subpleural metastases (dashed box in B) and the enlarged inset showing angiogenic vessels (white arrowheads); D: an overall view of pazopanib-treated E0771 metastatic lung tissue; E: an enlarged inset of one of the subpleural metastases (dashed box in D). The white dashed lines in C and E separate subpleural from parenchymal metastatic growth and the blue and red lines depict the measurement of subpleural metastases widths. Scale bars in B and D = 1mm. Scale bars in C and E = 100µm.*

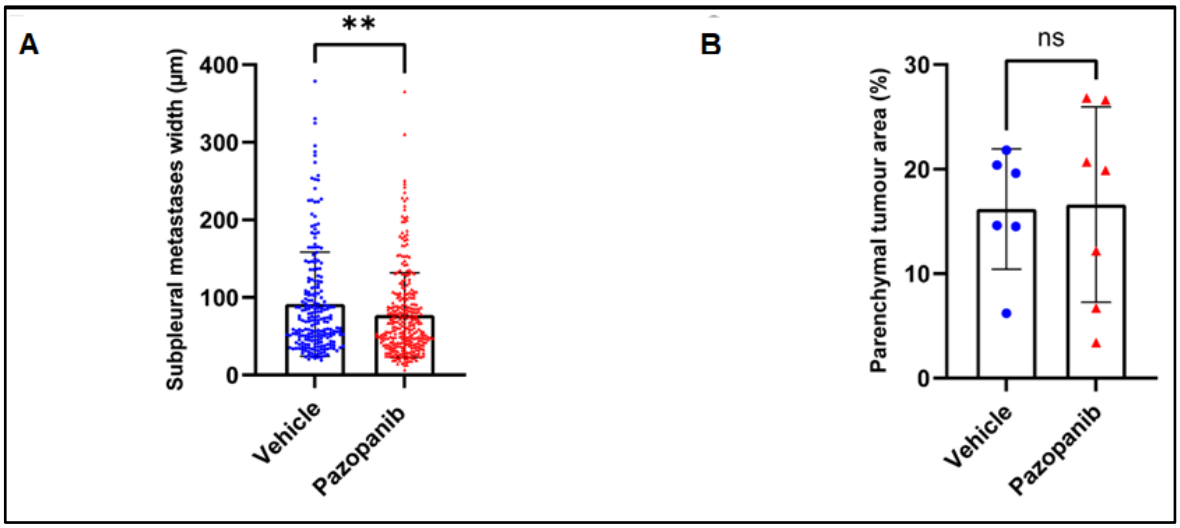

Figure 4-13. In comparison to vehicle treatment, pazopanib administration significantly reduces the width of E0771 subpleural metastases indicating an inhibitory effect on tumour angiogenesis*. A: widths of metastases localized at the subpleura were measured using QuPath digital pathology software. Each symbol (circle or triangle) represents single measurement (226 measurements were taken from n= 6 of vehicle-treated group and 315 measurements were taken from n=7 of pazopanib-treated group). B: the percentages of the parenchymal metastatic areas were measured using the same software. Each dataset in B represents the mean ± standard deviation (SD) (statistical analysis was performed using the two-tailed unpaired parametric Student's t-test, *: p ≤ .05; **: p ≤ .01; ***: p ≤ 0.001; ****: p ≤ 0.0001), p value =0.0074 for plot A and ns: not significant for plot B.*

4.4 Discussion

In **Chapter 3**, histological analysis of the vasculature of *in vivo* E0771 metastasis model was characterised as being vessel co-optive at an early stage and angiogenic and co-optive at a late stage of metastasis. In this chapter, I aimed to study E0771 TNBC tumour behaviour upon *in vivo* targeting the angiogenesis, hypothesising that angiogenesis would be necessary to support the subpleural metastases. Angiogenesis was targeted genetically via an *in vivo* induction of deletion of an angiogenic gene, *Eltd1* in ECs and targeted pharmacologically via administration of the anti-angiogenic drug, pazopanib.

The ELTD1 receptor has previously been shown to contribute to physiological and tumour angiogenesis by promoting the tip cell phenotype (a feature of sprouting angiogenesis) (Masiero et al., 2013). Supporting this, syngeneic tumour xenografts grown in an *Eltd1*^{iEC} mice have a significant reduction in microvascular density (MVD) (an angiogenic marker) compared to littermate controls (Ang, 2019). Here, we used the same endothelial-specific *Eltd1* knockout mice (*Eltd1*^{iEC}) to investigate E0771 tumour progression and vascularization after loss of *Eltd1*. Surprisingly, both MRI and post-mortem quantification of metastatic foci in lung tissue found no difference between both groups in terms of the E0771 tumour colonising the lungs. However, there is some precedent for these observations. In particular, loss of ELTD1 was also reported to not affect orthotopic glioma growth (Huang et al., 2022a). In that case, deletion of *Eltd1* (using a constitutive KO model) after treatment of murine glioma models with PD-1 blockade immunotherapy was found to improve vessel perfusion and recruit cytotoxic T cells (Huang et al., 2022a).

Of note, I found little difference in E0771 tumour angiogenesis between *Eltd1*^{iEC} and control groups when assessed by measuring the widths of subpleural metastases, and both groups had the presence of angiogenic vessels in these subpleural metastases. These findings could be influenced by a number of factors including:

1. Disturbing only the *Eltd1* gene in ECs might not be sufficient to inhibit tumour angiogenesis as it may switch to be driven by an alternative angiogenic mechanism. Previous studies reported that several cancers increase the secretion of pro-angiogenic factors following treatment with anti-angiogenic therapies. For instance, patients with rectal cancer showed an increase of placental growth factor (PlGF) in their plasma after receiving anti-VEGF Ab (bevacizumab) (Willett et al., 2005). In a preclinical model, immunodeficient pancreatic islet cell carcinogenesis model, tumours developed resistance to anti-VEGFR2 Ab (DC101) and induce VEGF-independent angiogenesis via FGF whilst on treatment (Casanovas et al., 2005).
2. Other G-protein-coupled receptors (GPCRs) might compensate for the loss of *Eltd1* contributing to tumour angiogenesis. This possible explanation is supported by a previous study which found that double knockout (DKO) of *Gpr116* and *Eltd1* in mice showed vascular defects in the heart and kidneys, whereas single deletion of either GPCR showed no effect (Lu et al., 2017).
3. *Eltd1* deletion may have been induced in only the fraction of ECs that express *Pdgfb-iCreERT2,* which could dilute the effect of inhibiting tumour angiogenesis and reducing subpleural tumour growth.
4. The absence of the effect of *Eltd1* on angiogenesis and metastatic growth relies on the efficiency of *Eltd1* deletion in Pdgfb-expressing ECs upon tamoxifen administration. However, immunohistochemical staining of mice kidneys illustrated a significant reduction of ELTD1 protein level in *Eltd1*^{iEC} compared to control groups, suggesting this may not be a major contributor.

The small sample size of this study (n=4 for the control group and n=5 for *Eltd1*^{iEC} group) yields relatively low statistical power. Therefore, caution must be applied to interpreting the results, as the findings might not reflect a true effect of the contribution of endothelial *Eltd1* deficiency on tumour burden (which could be either reduction or increase in normal air space) and angiogenesis. G power analysis has been performed to calculate the required sample

size for high power that could detect a genuine effect of genotype on tumour burden if a significant difference exists. This analysis revealed that ten mice per genotype would be required to increase the statistical power for genotype correlation to differences in tumour burden. Hence, a larger sample size is required to conclusively determine the absence of a small but significant effect.

While targeting angiogenesis in the E0771 metastasis mouse model via *in vivo* genetic ablation of an angiogenic gene *Eltd1* showed no reduction in the development of subpleural (angiogenic) metastases, alternative experiments may be needed to fully investigate the role of ELTD1 in tumour growth. For example, potential future studies would be to investigate the effect of *Eltd1* deletion on established metastases instead. Further, instead of targeting the GPCR receptor (ELTD1), further research could be conducted to identify the ELTD1 ligand, and to develop pharmacological inhibitors and/or antibodies that block its function. This would enable ELTD1 targeting in an established ELTD1+ tumour vasculature that is more relevant to the intended clinical setting.

The MRI screening found no significant effect of genotype on air space and the level of tumour burden as a function of time, with both groups showing a significant reduction in normal alveolar air space on day 14 following tumour induction compared to the earlier timepoint. This observation was more evident in MRI 3D segmentation of the air space, which demonstrated perforated surfaces indicating more E0771 tumour cells hijack lung parenchyma and fill the alveoli deriving supply from the pre-existed capillaries surrounding these alveoli (non-angiogenic vessel co-option). In regards to air space quantification of metastatic lungs by MRI imaging, the effect of peritumoral oedema (accumulation of fluid) is a potential concern because pulmonary oedema is identified as a condensed matter during MRI scanning that could displace and reduce the air space governing a technical artefact when it comes to estimating tumour burden in the lung using MRI. In addition, the metastatic lungs of both groups subjected to MRI not only showed discrete metastases but also revealed a distinct invasive pattern of E0771 tumour growth that has not been reported before in the literature

using the same imaging tool (Gomes et al., 2019). MRI scanning of the lungs detected bright threads in between the lobes, which was validated in H&E-stained sections to be angiogenic subpleural E0771 metastases covering the borders of the lung lobes. These two vascular phenotypes observed in MRI scanning corroborate with the immunohistochemical analysis observed in **Chapter 3.** Overall, the MRI bSSFP acquisition mode enabled visualization of parenchymal and subpleural metastases. In addition to visualizing metastases, MRI acquisition using GE3D sequence revealed the major lung vessels which has potential translational benefits of monitoring vascular remodelling by tumour growth and monitoring vessel response recruited by tumour to therapy. The absence of MRI imaging of healthy lungs failed to confirm the bright structures present at the early timepoint (day 9) post-tumour induction and resolve vasculature. However, these bright structures are thought to be tumours as the MRI signal became more prominent and brighter at a later timepoint and parenchymal metastases started to emerge even earlier on day 7 and 8 in post-mortem H&E staining.

Targeting VEGFR receptors via pazopanib delayed the development of subpleural metastases and demonstrated a significant reduction in the thickness of these angiogenic metastases with fewer angiogenic vessels being observed. The reduction in the growth of angiogenic metastases illustrates that tyrosine kinase signalling is a key regulator for cancer progression and angiogenesis in the E0771 model. Further, these results also indicate that E0771 TNBC tumours induces tyrosine kinase-dependent angiogenesis, potentially via VEGFR1 or VEGFR2. Supporting this, the tumour burden within areas predominantly using vessel co-option (parenchymal metastases), rather than angiogenesis, was comparable in vehicle- and pazopanib-treated groups. Therefore, these findings suggest that pazopanib can be effective at treating TNBC lung metastasis when administered as a preventive drug prior development of angiogenic metastases. Also, the reduction in subpleural metastases and angiogenic vessels in this *in vivo* model validated my MRI imaging findings at a functional level. Identification of cell types and mechanisms that upregulate expression of VEGF receptors and/or potentially other pazopanib substrates in the E0771 TNBC metastatic

microenvironment could help to tailor anti-angiogenic therapy and circumvent drug resistance. The limitation of this *in vivo* study is that pazopanib effect on E0771 tumour cell proliferation, migration, and invasion was not studied in an *in vitro* setting. My results show that pharmacological targeting angiogenesis using pazopanib significantly reduces the expansion of subpleural metastases in an *in vivo* model. It should be noted that the findings from this murine *in vivo* model also suffer from the limitation that it could be an artificial model that does not represent human cancers (specifically the subpleural metastases, which is not common in human). However, combining both angiogenesis and non-angiogenesis in a single tumour model is biologically relevant, and human patients with lung metastases of different primary tumours have been shown to exhibit both types of tumour vascular growth (Bridgeman et al., 2017). Further, the E0771 metastasis model is particularly valuable as an experimental tool to interrogate the response of the stromal niche (including the heterogenous vascular niche) to E0771 growth at the transcriptional level. This avenue of investigation will therefore be pursued in the next chapter.

Chapter 5: Single-cell transcriptional analysis of metastatic niche lung endothelium using mCherry niche-labelling technology

5.1 Introduction

In the previous chapter, I investigated the spatiotemporal vascular phenotypes seen by the *in vivo* E0771 metastasis model. This analysis found that intravenously inoculated E0771 breast tumour cells initially appeared to primarily co-opt pre-existing blood vessels (non-angiogenesis) to form parenchymal metastases. These then sustained themselves throughout expansion by inducing the formation of new blood vessels (angiogenesis), likely to meet their high metabolic demand while developing subpleural metastases and remaining non-angiogenic inside lung parenchyma (distinct anatomical sites)

Remodelling of the stroma (which includes the vascular beds of the lungs) by tumour cells is a key stage in metastatic niche formation and secondary tumour expansion and progression (Maru, 2015). Studies have shown that distant primary tumours are able to provoke vascular permeability and ECM degradation through the release of enzymes such as MMP9 in pre-metastatic and metastatic lung stroma, subsequently enhancing tumour cell survival and lung metastasis (Hiratsuka et al., 2002). However, the transcriptional profile of the metastatic niche endothelium and surrounding non-immune stroma are uncharacterised due to the inherent difficulty in spatially isolating them for single-cell transcriptome sequencing (scRNA-seq). This technical challenge impedes advances in understanding the molecular and cellular changes during metastasis and limits effective therapeutic intervention in the metastatic setting.

Professor Ilaria Malanchi's team at the Francis Crick Institute have recently developed a genetically engineered mCherry-secreting E0771 tumour cell line (Ombrato et al., 2019). Here, I collaborated with their team in order to use these cells to label and isolate the metastatic niche stromal cells adjacent to tumour cells. This allowed me to explore the

molecular changes and signalling pathways in the metastatic niche stroma that drive vascular co-opting and angiogenic metastasis. In addition, I also wanted to investigate markers of the vascular co-option and angiogenesis phenotypes using this system.

The mCherry-secreting E0771 tumour cell line was generated from the parental syngeneic murine E0771 cells by genetic engineering via lentiviral transduction, so that it to stably co-expressed the cell surface human CD2 (hCD2) and a secreted mCherry protein fused to a lipid-soluble tag, a transactivator of transcription (TATk) peptide (sLP-mCherry) that is cell permeable **(Figure 5-1, Figure 2-1 in Chapter 2).** These mCherry niche-labelling E0771 tumour cells (referred to here as mCherry-labelling hCD2 E0771) were injected intravenously into C57/BL6 mice to generate an experimental lung metastasis syngeneic mouse model **(Figure 5-1)**. As shown in **Figure 5-1**, these mCherry-labelling hCD2 E0771 tumour cells were able to secrete the mCherry to nearby metastatic niche cells (which were consequently $hCD2^{-}$ $mCherry^{+}$), permitting them to be spatially isolated via fluorescence-activated cell sorting (FACS) flow cytometry. These cells can then be used for transcriptomics.

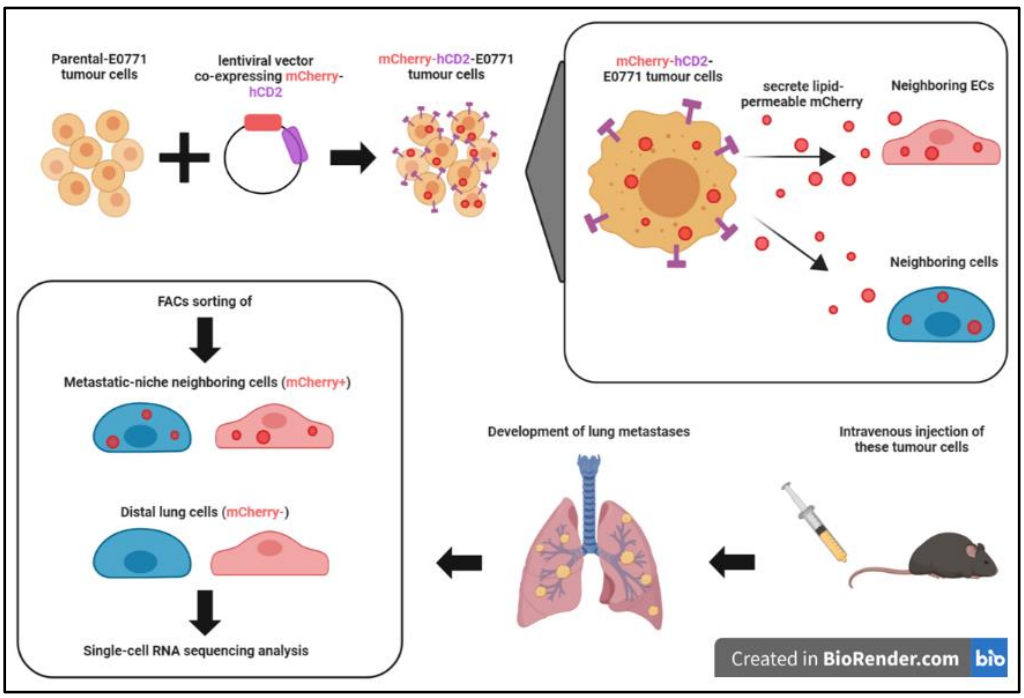

Figure 5-1. Novel mCherry-labelling strategy (developed by our collaborator, Prof. Ilaria Malanchi) enabling spatial isolation and study of metastatic niche stroma. *E0771 tumour cells express both human CD2 (hCD2) and mCherry. Intravenous inoculation of these tumour cells into a syngeneic C57BL/6 mouse primarily producing pulmonary metastases which are able then to secrete permeable mCherry that is then taken up by neighbouring lung cells. These labelled cells then can be FACS sorted for transcriptional analysis.*

5.2 *In vitro* validation of mCherry niche-labelling system

The functionality of the mCherry niche-labelling system was validated *in vitro* and *in vivo* in a previous publication by the laboratory that generated it (Ombrato et al., 2019). However, prior to commencing the transcriptional studies, I validated the functionality of this system in an *in vitro* setting via histological and FACS analysis of direct and indirect co-culture.

5.2.1 Niche-labelling validation via direct co-culture of non-labelled HUVECs with mCherry-labelling hCD2 E0771 cells

To validate *in vitro*, mCherry-labelling hCD2 E0771 cells were co-cultured with non-labelled HUVECs at a 1:2 ratio, incubating the cells for 48 hours. Following this, I used immunofluorescence staining with anti-mCherry antibodies to confirm that the mCherry-labelling hCD2 E0771 tumour cells secreted and labelled the nearby HUVECs, which took up the label **(Figure 5-2A).** Further, flow cytometric analysis (FACS) of this co-culture also demonstrated that mCherry was released and entering HUVECs, when compared to HUVECs in culture alone **(Figure 5-3A, B, yellow arrowheads)**.

5.2.2 Niche-labelling validation via indirect co-culture of non-labelled HUVECs in medium conditioned by mCherry-labelling hCD2 E0771 cells

Next, I incubated non-labelled HUVECs in a medium conditioned by mCherry-labelling hCD2 E0771 cells, again validating via immunofluorescence staining that mCherry had been taken up by the HUVECs **(Figure 5-2B)**. FACS analysis of this indirect culture showed similar findings where HUVECs were labelled with mCherry compared to only HUVECs culture **(Figure 5-3A, C, yellow arrowheads).**

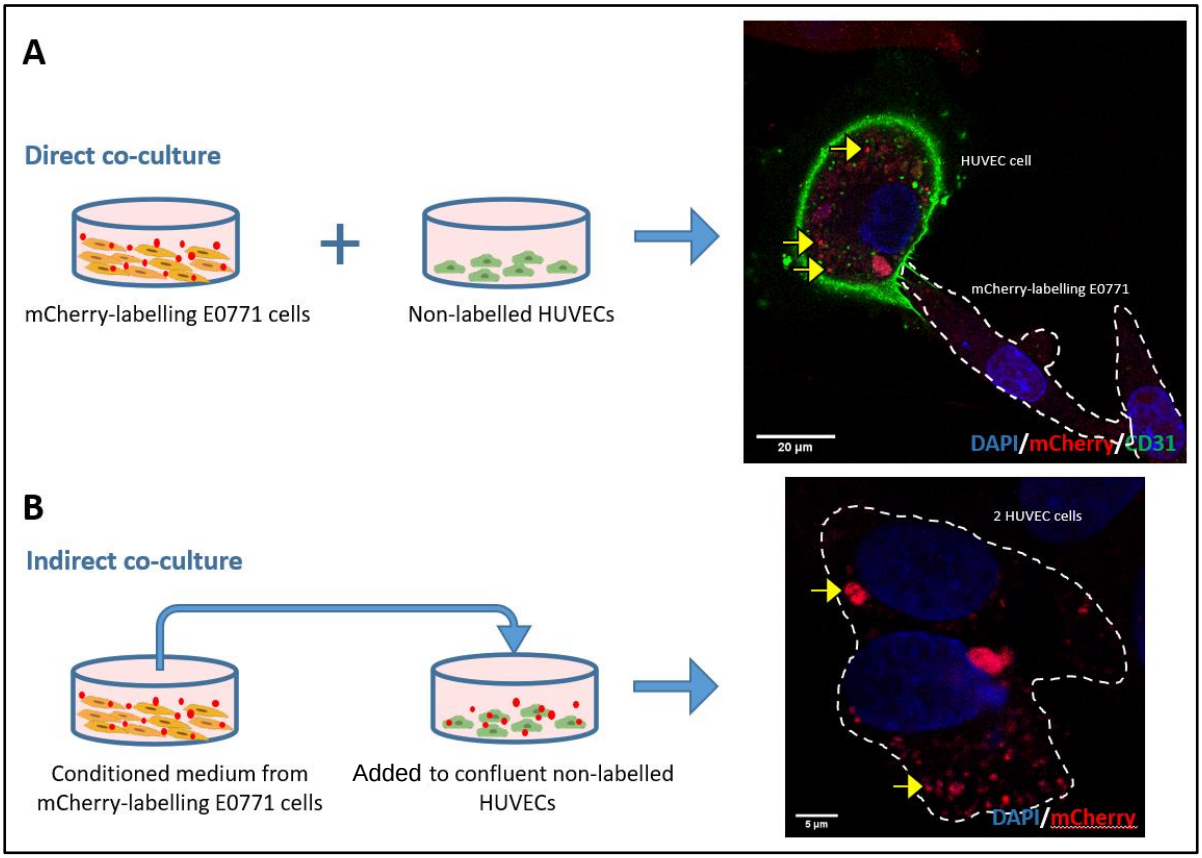

Figure 5-2. Immunofluorescence staining of the in vitro direct and indirect co-cultures to validate the mCherry niche-labelling system*. A: immunofluorescence staining of the direct co-culture of labelling E0771 and HUVECs (CD31+, green) confirmed mCherry (red) being secreted and taken up by HUVECs (CD31+ and mCherry+); B: immunofluorescence staining of the indirect co-culture of HUVECs with conditioned medium by labelling E0771 confirmed HUVECs uptake the mCherry from the conditioned medium. Nuclei were stained with DAPI (blue).*

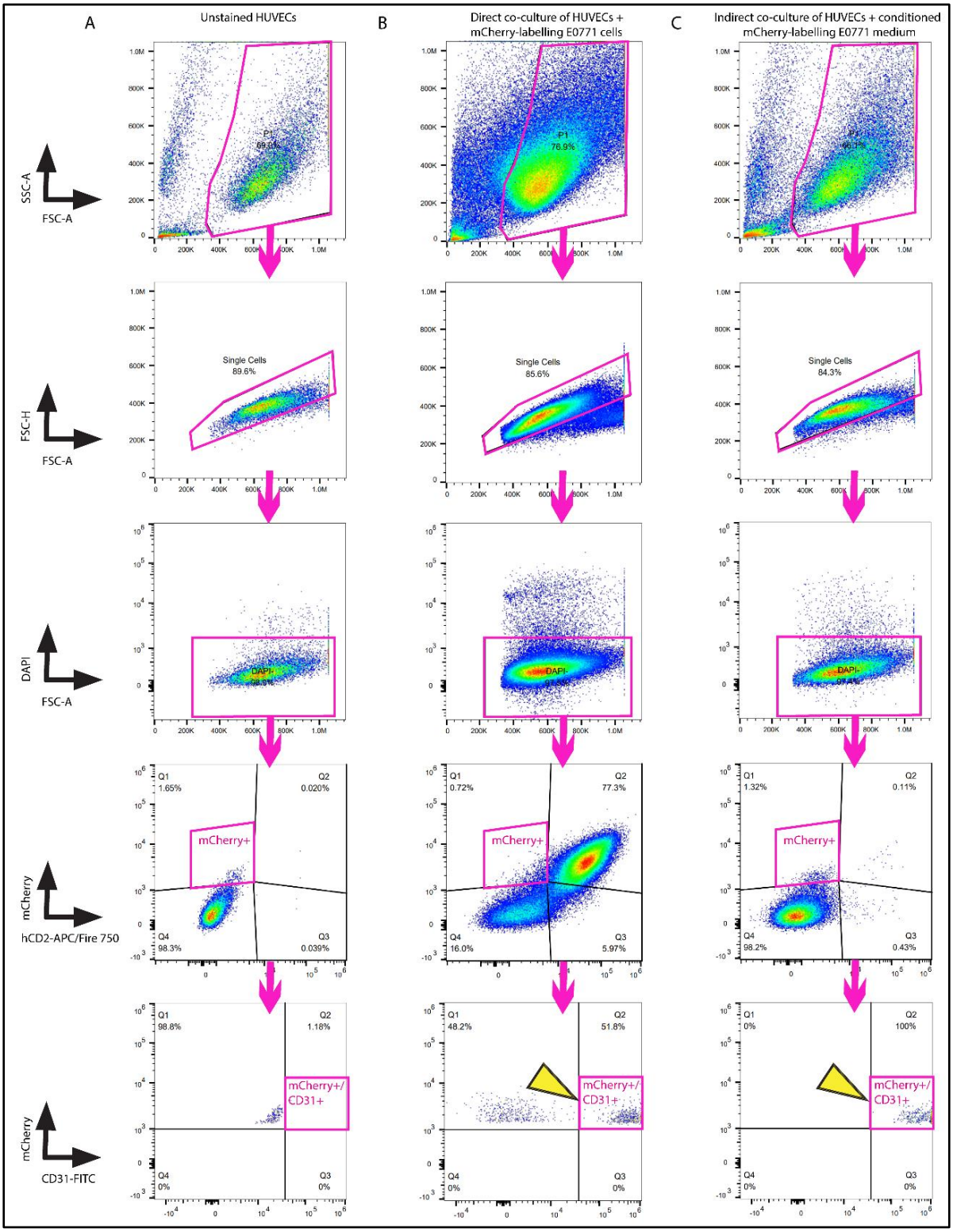

Figure 5-3. FACS analysis of the in vitro direct and indirect co-cultures to validate the mCherry niche-labelling system. *FACS gating strategy to identify mCherry-positive HUVECs in A, B, and C as follows: SSC-A vs. FSC-A density plot to gate population of interest (P1) excluding debris/ FSC-H vs. FSC-A density plot to gate single cells/ DAPI vs. FSC-A density plot excluding dead cells (DAPI+)/ mCherry vs. hCD2-APC/Fire750 density plot to identify E0771 tumour cells (hCD2+ mCherry+), non-labelled (hCD2- mCherry-), and labelled cells (only mCherry+). The labelled population was further analysed for ECs markers (CD31-FITC vs. mCherry). A: FACS sequential gating of only HUVEC culture showing HUVECs being mCherry negative; B: FACS sequential gating of HUVECs co-cultured with mCherry-labelling E0771 validating HUVECs becoming mCherry positive (52%, labelled as mCherry+/CD31+, yellow arrowhead); C: FACS sequential gating of HUVECs incubated with conditioned mCherry-labelling E0771 medium validating HUVECs taking up mCherry from conditioned medium (100%, labelled as mCherry+/CD31+, yellow arrowhead).*

5.3 *In-vivo* validation of mCherry niche-labelling system

Next, the functionality of this system was validated in my *in-vivo* tumour model via histological and FACS analysis of mCherry-labelling hCD2 E0771-bearing mouse lungs as illustrated below.

5.3.1 Spatial identification of metastatic niche cells in lungs of mCherry-labelling hCD2 E0771 tumour-bearing mice

One million mCherry-labelling hCD2 E0771 tumour cells were delivered intravenously through tail vein injection to obtain lung metastases. Metastatic lungs were harvested on day 13 following tumour inoculation and sectioned for histological analysis. Immunofluorescence staining of lung sections with anti-mCherry and anti-hCD2 antibodies validated the spatial localisation of mCherry-labelling hCD2 E0771 tumour cells **(Figure 5-4A, B, C, E)**. The *in vivo* labelling ability of these genetically engineered E0771 tumour cells to the mouse lung stroma near metastases was also validated by detecting cells that were only positive for mCherry. These mCherry+ cells were therefore designated the metastatic niche cells and are marked with mCherry signal taken up after secretion from nearby mCherry-labelling tumour cells (**Figure 5-4A, B, C, D) (Appendix D1)**.

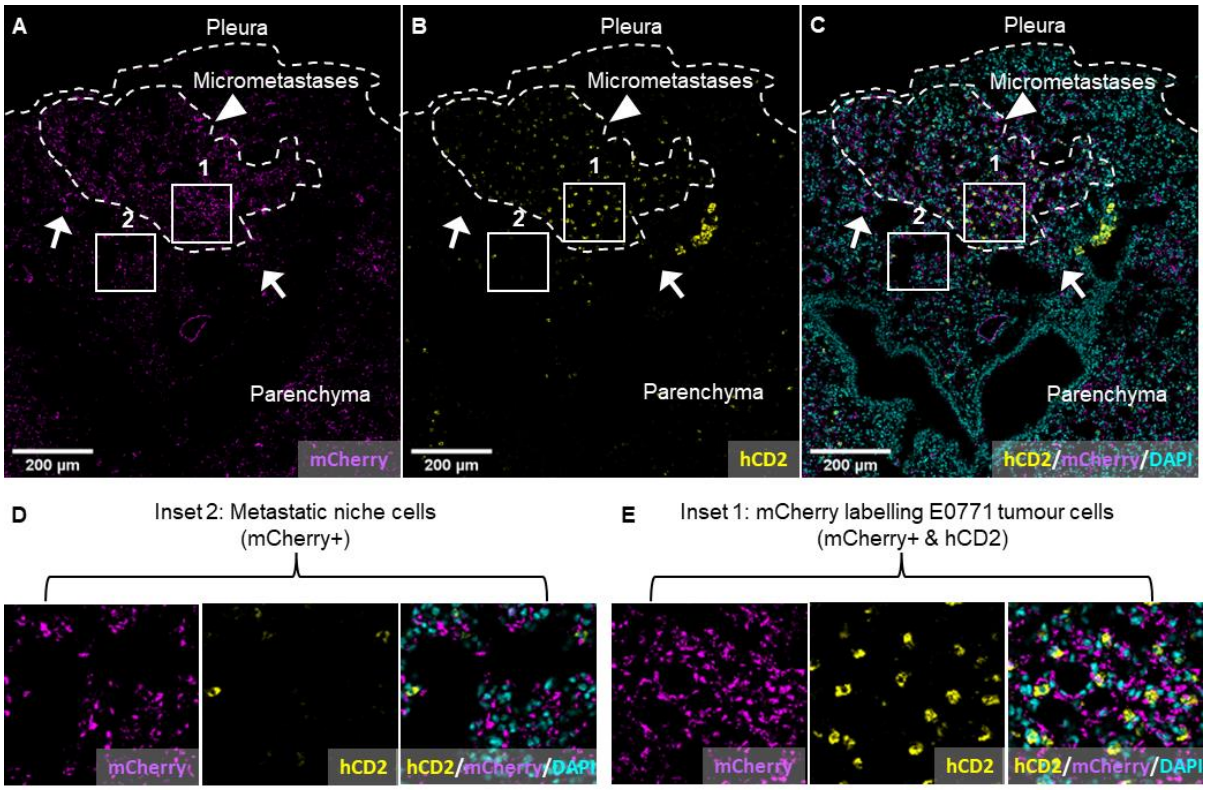

Figure 5-4. Spatial localisation of mCherry-labelling hCD2 E0771 tumour cells (arrowheads) and metastatic niche cells (arrows) via immunofluorescence staining of E0771 metastatic lung tissue section. *The tissue section was stained with markers of tumour cells A: anti-mCherry (magenta); B: anti-hCD2 antibodies (yellow); C: showed merge image with nuclear staining (cyan), DAPI; D: enlarged inset of box 2 in image C depicting metastatic niche cells expressing only mCherry; E: enlarged inset of box 1 in image C depicting mCherry-labelling hCD2 E0771 tumour cells co-expressing human CD2 (hCD2) and mCherry.*

5.3.2 FACS gating strategy for spatial isolation of metastatic niche stroma (hCD2- mCherry+)

A pilot experiment was initially conducted to (i) test if the protocol of lung tissue digestion using collagenase enzymes works on metastatic lungs and yields our cell types of interest with high viability (mCherry+ metastatic niche lung and mCherry- distal stromal cells; (ii) to apply a FACS antibody panel developed in collaboration with Dr. Luigi Ombrato and Dr. Victoria Bridgeman (Professor Malanchi's laboratory); and (iii) to set all FACS gates in order to identify the percentage of the two populations of interest at early and late timepoints of metastatic growth *in vivo*. Three mice per group for healthy, early-tumour-and late-tumour-bearing lung mice were harvested, digested, and stained for FACS analysis.

The macroscopic and microscopic metastases were visible at early (day 8) and late (day 13) timepoints following tumour injection **(Figure 5-5A-C).** As shown in **Chapter 3**, harvesting metastatic lungs on day 8 following tumour inoculation mainly resulted in tumour cells that co-opted lung parenchyma, with a few surface metastases revealed by immunofluorescence staining of the lung parenchyma and the vasculature using anti-TTF1 and CD31 antibodies **(Figure 5-5B, D, E)**. Hence, days 7-9 were a suitable timepoint for harvesting lung metastases with a predominantly vessel co-option phenotype **(Figure 5-5B, D, E)**. Conversely, metastatic lungs harvested at the late timepoint (day 13) exhibited a higher tumour burden with established metastases that contained angiogenic-like vessels in addition to parenchymal metastases **(Figure 5-5C, F)**.

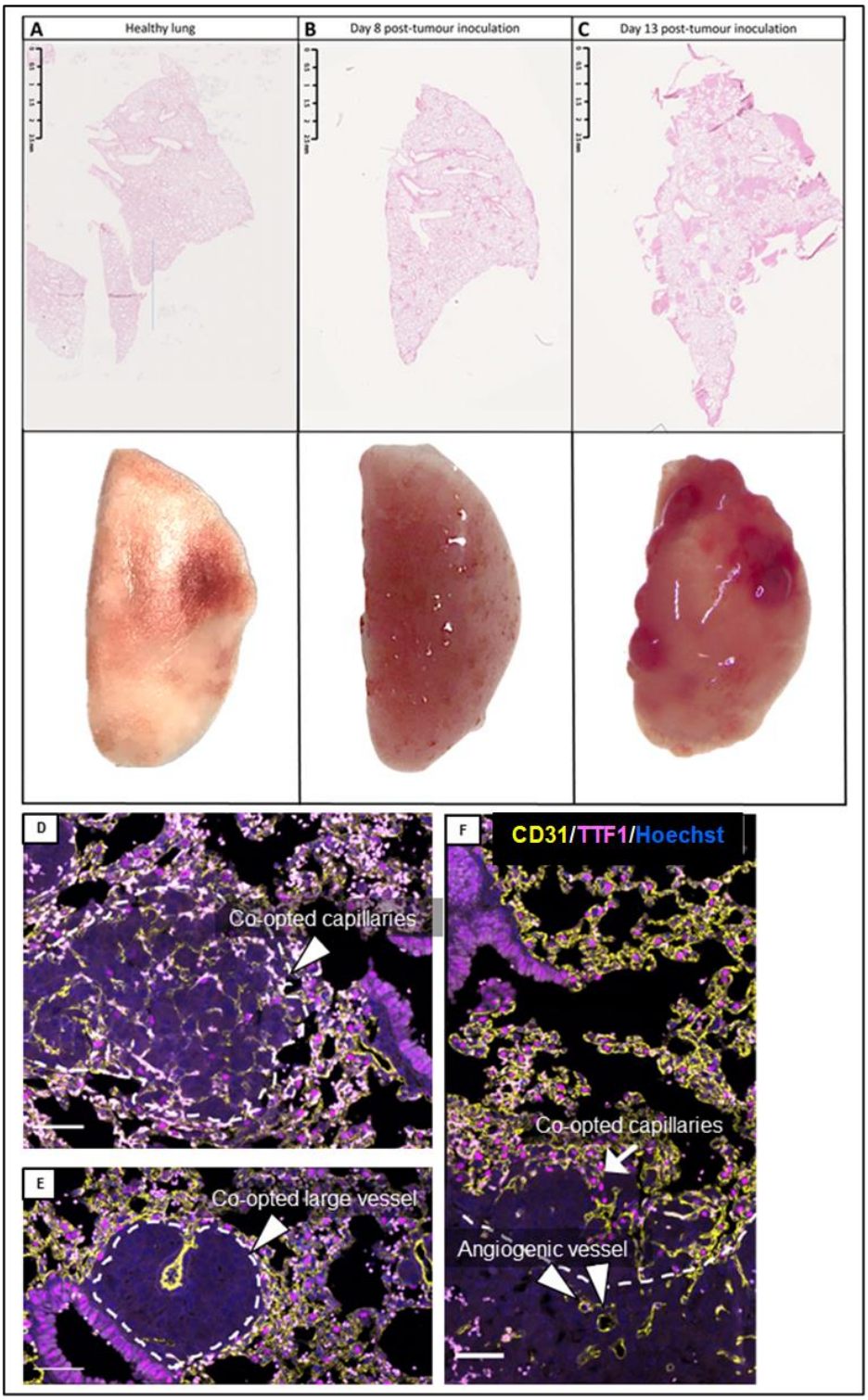

Figure 5-5. Immunofluorescence labelling of lung parenchyma and vessels using anti-TTF1 and anti-CD31 antibodies showed that E0771 metastatic lungs exhibited parenchymal growth at early timepoint with vessel co-option pattern and subpleural growth at late timepoint inducing angiogenesis. *A-C: H&E microscopic and macroscopic views of non-tumour-bearing and E0771 tumour-bearing lungs. A: healthy non-tumour-bearing lungs; B: early phase of metastasis (day 8 post-tumour inoculation), in which tumour cells colonized lung parenchyma with few subpleural micrometastases; C: late phase of metastasis (day 13 post-tumour inoculation), in which tumour cells colonized lung parenchyma and subpleura with angiogenic metastases. D-F: E0771 tumour cells hijack large blood vessels (E) and recruit (co-opt) lung capillaries (D) as a source for nutrients, oxygen, and energy. The dashed lines in D and E with arrowheads mark tumour areas. F: E0771 tumour cells induce angiogenesis in the subpleural region in order to expand. The dashed line in F separates parenchymal tumour growth from subpleural one. The arrow in F indicate co-opting tumour growth and arrowheads in indicate angiogenic blood vessels induced by E0771 tumour cells. Cell nuclei were stained with Hoechst (blue). Scale bars in A-C = 2.5mm and in D-E = 50µm.*

I used multiple fluorochromes in FACS analysis of mouse lungs; thus, emission spectral overlap is inevitable **(Figure 5-6).** Also, fluorescence compensation is required to obtain actual staining of the cell markers used. Compensation (single-colour) controls have been used to subtract the spillover of each fluorophore into other channels **(Figure 5-7).** Compensation beads were used for fluorochrome-conjugated antibodies that target cell-surface markers, including FITC anti-CD31, APC anti-VE-CAD (VE-cadherin (CD144)), APC/Fire™ 750 anti-human CD2 (hCD2), and Brilliant Violet 421 (BV421) anti-CD45 and anti-TER-119 antibodies **(Figure 5-7A-E)**. Whereas for intracellular cell markers such as mCherry, mCherry positive and negative cell populations have been used to apply compensation **(Figure 5-7C)**. FMO controls were also used to set a gating boundary considering the spread of other fluorophores into the missing fluorophore **(Figure 5-7F-L)**. Note that APC anti-VE-CAD was later added to the antibody panel as an additional endothelial marker.

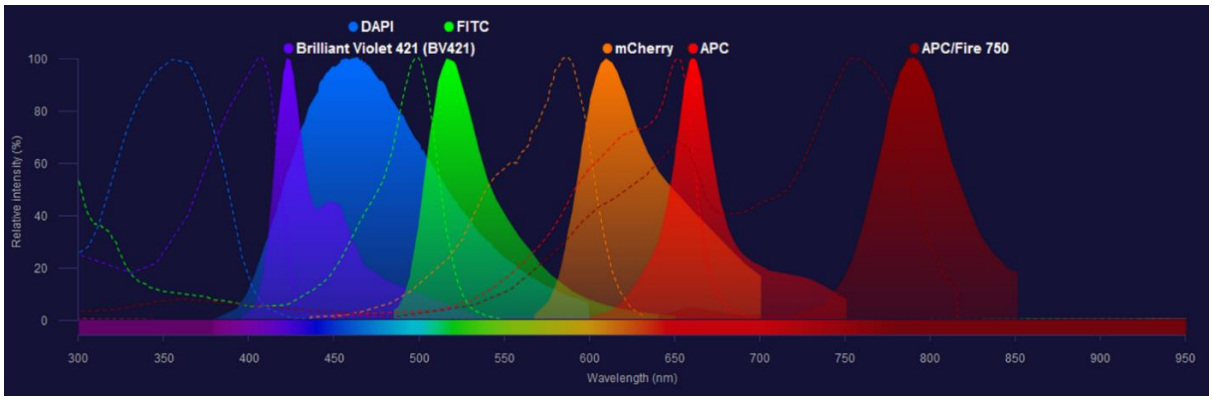

Figure 5-6.Illustration of emission spectral overlap of six fluorochromes used in multiparametric FACS analysis of mouse metastatic lung. *Solid peaks are the emission spectra, each labelled with the detected fluorochrome; dashed lines depict the excitation spectra of each of these fluorochromes. (This plot was generated using the tool, the Molecular Probes Spectra Viewer: https://www.thermofisher.com/order/fluorescence-spectraviewer#!/).*

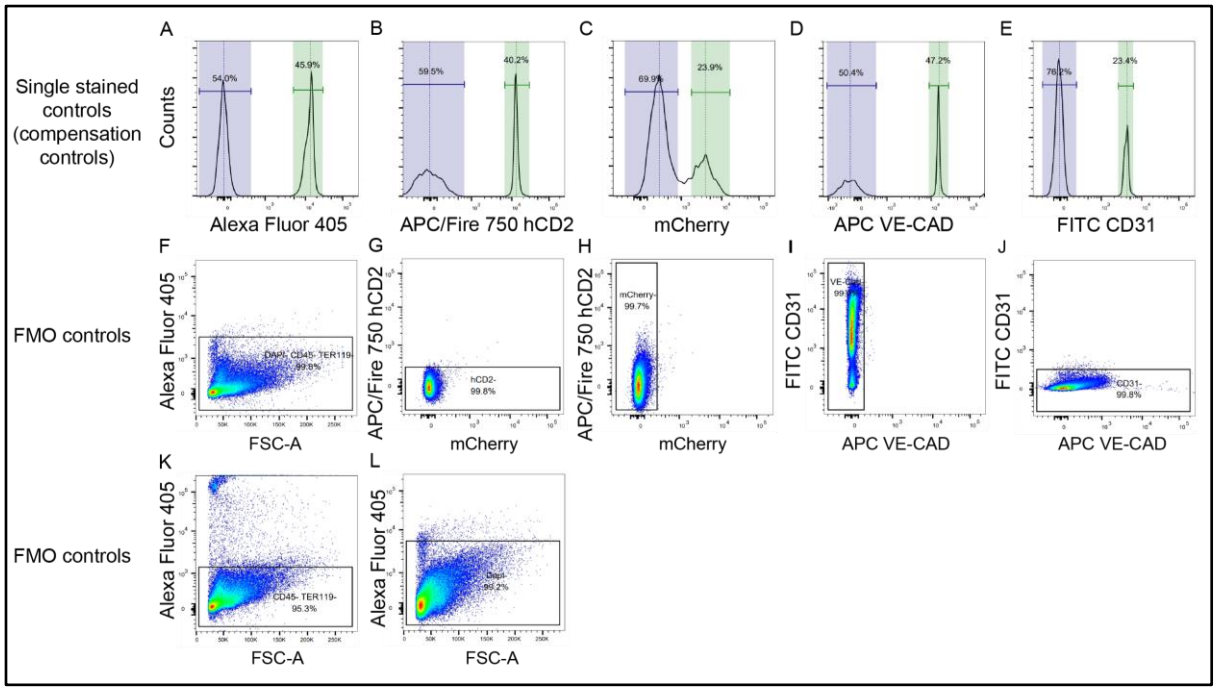

Figure 5-7. Fluorescence compensation (single-color) and fluorescence Minus One (FMO) controls used to correct for fluorescence spillover and set accurate gating of different mouse lung stromal cells*. A, B, D, E: are compensation beads stained with individual fluorochrome-conjugated antibodies that targets cell-surface markers showing separate negative and positive peaks for A: Alexa Fluor 405 (Brilliant™ Violet 421) CD45; B: APC/Fire™ 750 human CD2; D: APC VE-Cadherin; E: FITC CD31; C: an unstained mouse lung tissue mixed with mCherry-labelling E0771 tumour cells (mCherry+) showing negative and positive peaks for mCherry; F : E0771 tumour-bearing lung cells stained with all fluorochromes except DAPI, Brilliant™ Violet 421 CD45, and Brilliant™ Violet 421 TER119; G: E0771 tumour-bearing lung cells stained with all fluorochromes except APC Fire 750 human CD2; H: non-tumour-bearing lung cells stained with all fluorochromes except mCherry, I: E0771 tumour-bearing lung cells stained with all fluorochromes except APC VE-Cadherin; J: E0771 tumour-bearing lung cells stained with all fluorochromes except FITC CD31; K: E0771 tumour-bearing lung cells stained with all fluorochromes except Brilliant™ Violet 421 CD45, and Brilliant™ Violet 421 TER119; L: E0771 tumour-bearing lung cells stained with all fluorochromes except DAPI.*

Mouse lung cell suspensions were stained using DAPI (viability marker), anti-CD45 Ab (immune cell marker), anti-TER-119 Ab (RBC marker), anti-hCD2 Ab (mCherry-labelling E0771 tumour cell marker) (note that E0771 tumour cells endogenously express mCherry), and anti-CD31 Abs (endothelial cell marker). To set a sequential gating strategy to identify stromal cells and ECs from non-tumour and metastatic lungs, stained cell suspension was analysed using FACS technology where the population of interest was gated (named P1), and doublets were gated out **(Figure 5-8, 1st,2nd rows).** Dead cells, immune cells, and RBCs were also excluded and grouped into a single channel known as the dump channel (grouping all these three populations labelled with a similar fluorochrome (Alexa Fluor 405)) **(Figure 5-8, 3rd row).** Non-CD45, non-RBCs, and viable cells were then plotted using a dual-parameter dot

plot of markers of mCherry-labelling E0771 tumour cells (mCherry versus APC/Fire™ 750 human CD2 **(Figure 5-8, 4th row)**. This dot plot identifies three populations, including E0771 tumour cells (hCD2^{+} mCherry^{+}), distal lung cells (hCD2^{-} mCherry^{-}), and metastatic niche cells (hCD2^{-} mCherry^{+}). Niche and distal lung cells were further analysed for the endothelial marker expression CD31 **(Figure 5-8, 5th,6th rows) (Appendix C1, C2, C3)**.

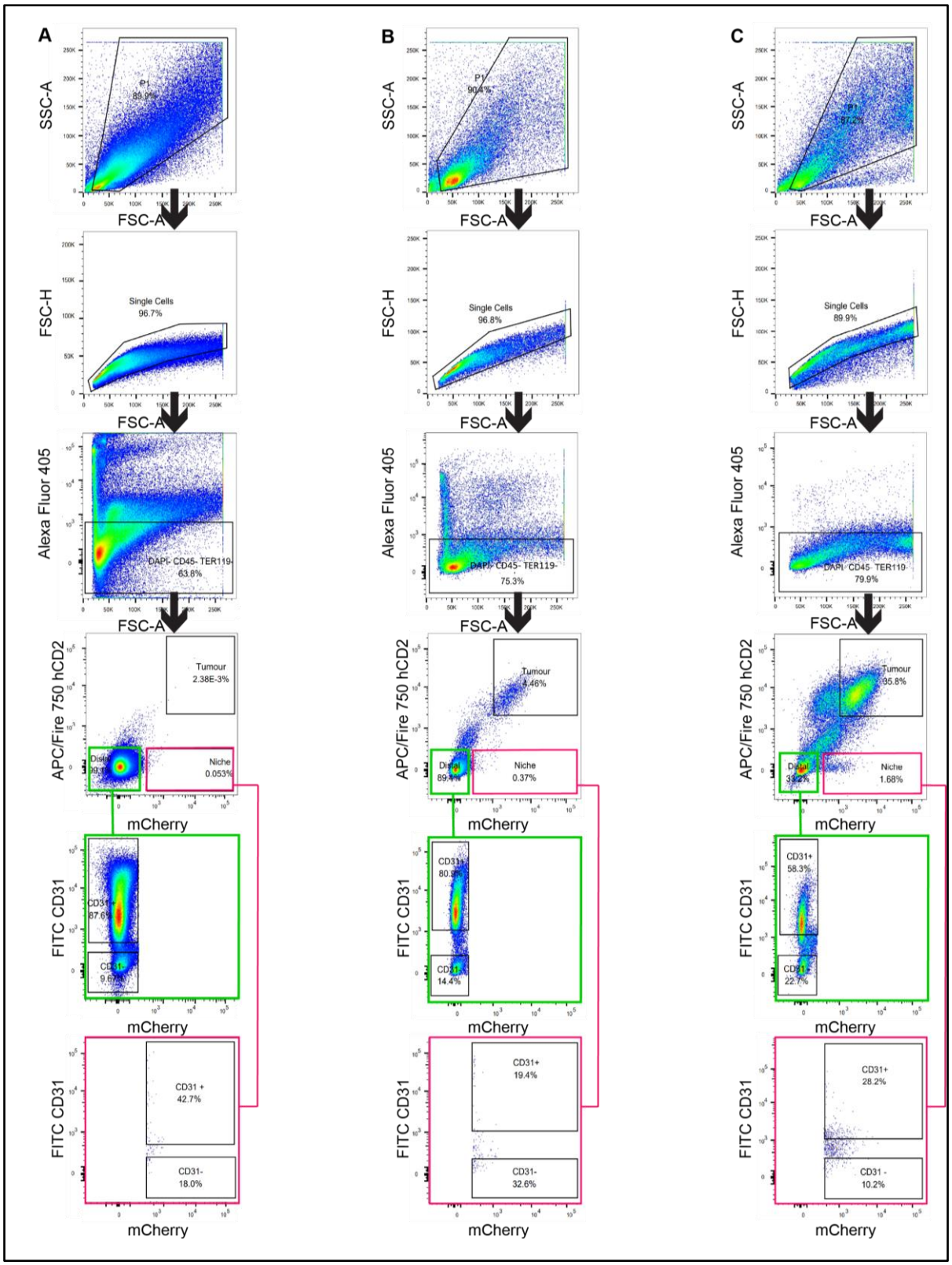

Figure 5-8. FACS sequential gating strategy of mouse lungs identified E0771 tumour cells, metastatic niche, and distal (non-labelled) stroma including ECs. *A: non-tumour; B: early; C: late-tumour-bearing lungs; A-C: FACS plots as follows: SSC-A vs. FSC-A density plot to gate population of interest (P1) excluding debris, FSC-H vs. FSC-A density plot to gate single cells, Alexa Fluor 405 vs. FSC-A density plot excluding immune cells (CD45+), RBC (TER119+) and dead cells (DAPI+) and grouping these populations into dump channel (grey box), APC/Fire750 hCD2 vs. mCherry density plot to identify E0771 tumour cells (hCD2+ mCherry+), distal normal stroma cells (non-labelled) and metastatic niche stroma cells (only mCherry+), and the latter two populations were further analysed for ECs marker (CD31). Note that a small population in the APC/Fire750 hCD2 vs. mCherry density plot in C is only positive for hCD2 as mCherry is lipid bilayer-permeable and can exit the niche labelling E0771 tumour cells.*

Using the mCherry labelling system with the above FACS gating strategy enabled tumour burden, niche, and distal stroma to be quantified as cell percentages **(Table 5-1).** As shown in **(Figure 5-9A, B, D)**, tumour burden increased from 0% in healthy lungs to 6% (early timepoint) and then 31% (late timepoint post-tumour injection), replacing the distal stroma (mCherry-) from 99% to 85% to 34% during the development of lung metastases. mCherry+ metastatic niche stroma cells increased to represent about 2% of cells in late metastatic lungs **(Figure 5-9C) (Table 5-1).** Within the late metastatic niche stroma, approximately 23% of cells were ECs **(Table 5-1).**

Table 5-1. Percentages of stromal cell types in healthy, early, late tumour-bearing mouse lungs from FACS plots. *One million mCherry-labelling hCD2 E0771 tumour cells were inoculated in metastatic conditions where lungs were harvested at day 8 (in case of early timepoint) and at day 13 (in case of late timepoint).*

Non-tumour-bearing mice	**Mouse 1**	**Mouse 2**	**Mouse 3**	**Mean**
E0771 tumour cell percentages of live lung cells (mCherry+ and hCD2+)	0.002	0.040	0.003	0.015
Metastatic-distal percentages of live lung cells (mCherry-)	99.100	97.500	99.100	98.567
Metastatic-distal-EC percentages of mCherry- distal cells (mCherry-/CD31+)	87.600	83.200	85.900	85.567
metastatic niche percentages of live lung cells (mCherry+)	0.050	0.150	0.048	0.083
Early tumour-bearing mice (day 8 following tumour inoculation)	**Mouse 1**	**Mouse 2**	**Mouse 3**	**Mean**
E0771 tumour cell percentages of live lung cells (mCherry+ and hCD2+)	4.460	10.800	4.010	6.423
Metastatic-distal percentages of live lung cells (mCherry-)	89.400	76.800	88.700	84.967
Metastatic-distal-EC percentages of mCherry- distal cells (mCherry-/CD31+)	80.900	85.100	80.700	82.233
metastatic niche percentages of live lung cells (mCherry+)	0.370	0.780	0.710	0.620
Late tumour-bearing mice (day 13 following tumour inoculation)	**Mouse 1**	**Mouse 2**	**Mouse 3**	**Mean**
E0771 tumour cell percentages of live lung cells (mCherry+ and hCD2+)	35.800	20.300	36.900	31.000
Metastatic-distal percentages of live lung cells (mCherry-)	33.200	42.000	27.800	34.333
Metastatic-distal-EC percentages of mCherry- distal cells (mCherry-/CD31+)	58.300	36.900	44.500	46.567
metastatic niche percentages of live lung cells (mCherry+)	1.680	2.160	2.400	2.080
metastatic niche-EC percentages % of mCherry+ niche cells (mCherry+/CD31+)	28.200	19.500	20.100	22.600

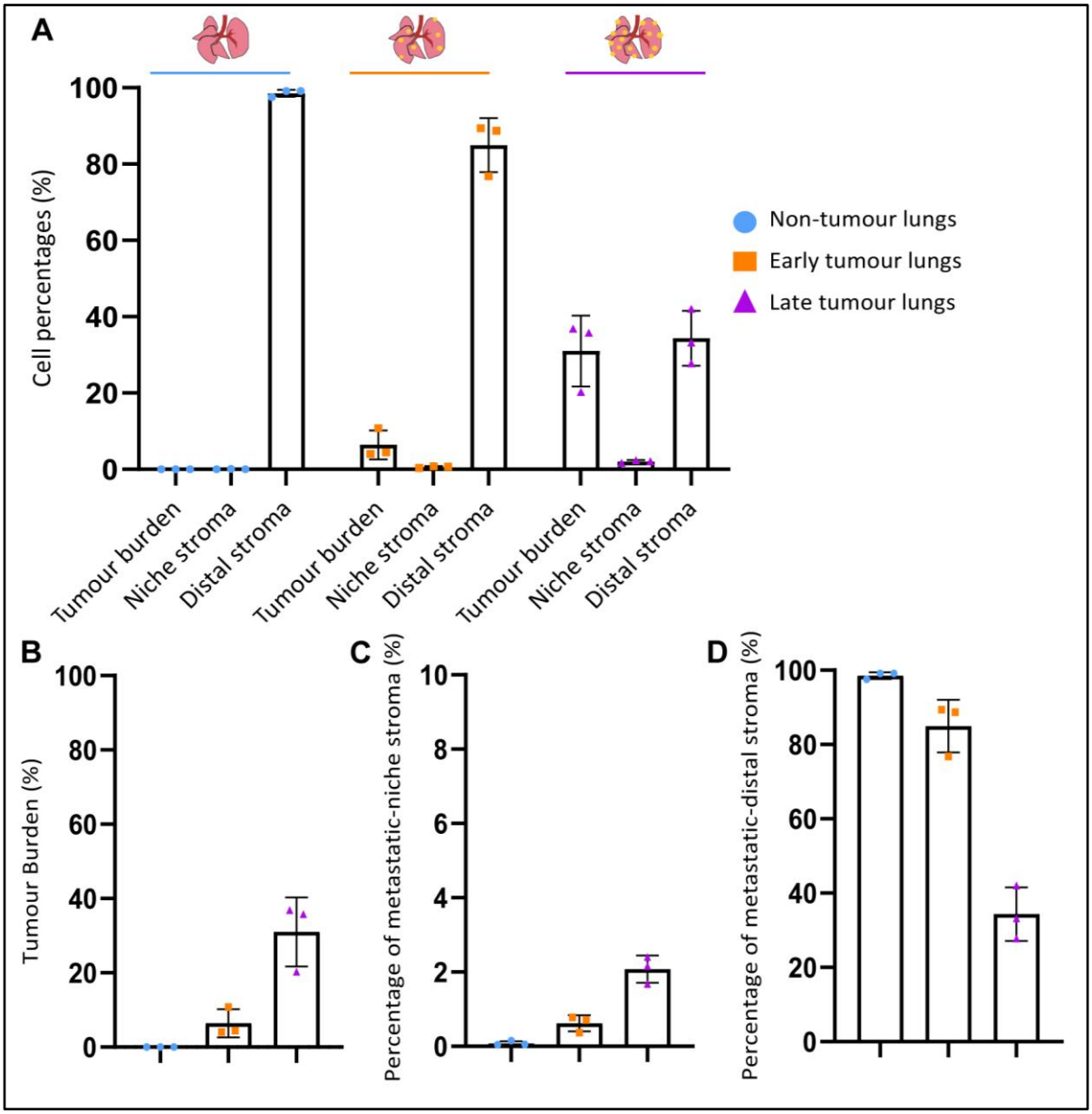

Figure 5-9. FACS quantification of cell proportions of E0771 tumour cells, metastatic niche, and distal (non-labelled) stromal cells including ECs. *A: cell percentages in non-tumour, early, and late-tumour-bearing lungs; B: E0771 tumour burden as percentages; C: percentages of metastatic niche stroma; D: percentages of metastatic-distal stroma in non-tumour, early, and late-tumour-bearing lungs*

To accurately FACS sort my cell population of interest and avoid sorting a false positive population, I also analysed unstained non-tumour-bearing lungs. Mouse lung cells exhibited a strong autofluorescence that overlapped with other fluorophores: DAPI, mCherry, and APC/Fire 750 **(Figure 5-10A)**. This autofluorescence was minimised during FACS sorting of viable cells (DAPI -) by confining the gating **(Figure 5-10B)**.

To enrich metastatic niche ECs for comprehensive transcriptional profiling and to accelerate FACS sorting of this population with high purity, I carried out MACS magnetic depletion of immune (CD45+) cells from metastatic lungs and used FACS for EC isolation. As shown in **Figure 5-10C, D,** the removal of CD45+ cells yielded highly pure and enriched ECs, accelerating the sorting time of this population. metastatic niche ECs were also enriched by pooling several metastatic lungs.

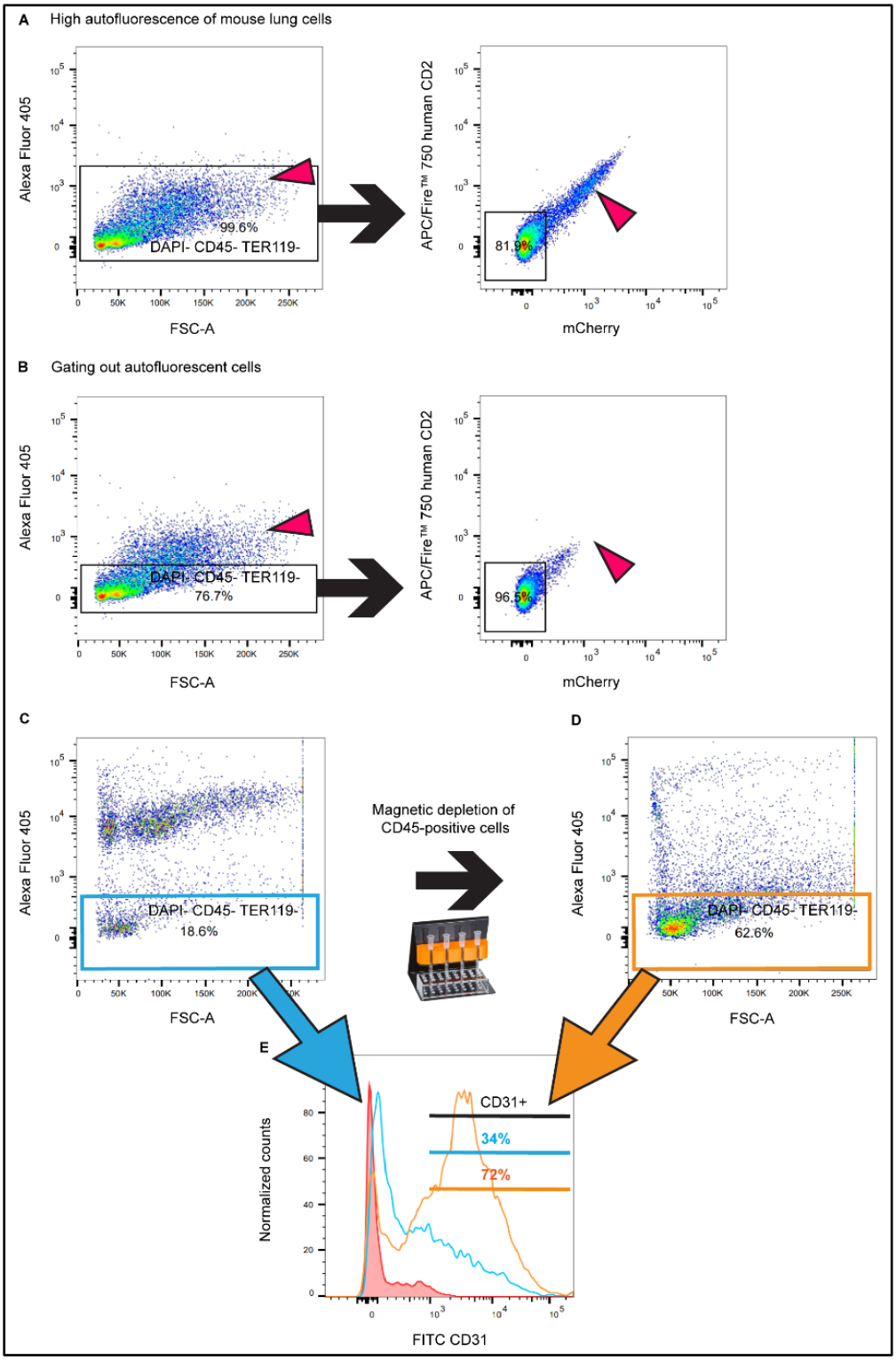

Figure 5-10. Optimization of tissue preparation and FACS gating to enrich for ECs and avoid FACS sorting of autofluorescent cells*. A: unstained mouse lungs exhibit high autofluorescence in DAPI, mCherry, and APC/Fire750 channels that might interfere with FACS sorting, which should be taken into consideration when sorting populations of interest; B: autofluorescent cells were gated out. C: mouse lung cells without removal of immune cells (CD45-positve cells) with blue box indicating that limited CD45-negative population giving rise to a limited number of ECs (CD31-positive cells) (blue peak); D: immunomagnetic depletion of immune cells from lung cell suspension enriches and speeds up FACS sorting of pure ECs with orange box indicating enriched population of non-immune cells giving rise to higher proportion of ECs (orange peak). Histogram shows that compared to unstained lung cell suspension (red peak), CD45+ depleted lung cell suspension (orange peak and line) has higher percentage of ECs than CD45 non-depleted lung cell suspension (blue peak and line).*

Table 5-2 describes the steps used for lung tissue digestion, FACS staining, and sorting that require optimisation to enrich for metastatic niche ECs and obtain highly pure and viable lung stromal cells, including ECs.

Table 5-2. Steps in lung tissue digestion for FACS staining and sorting of lung stroma that required optimisation*. There are two populations of interest for FACS sorting: metastatic niche and distal lung stroma. hCD2: human CD2; VE-CAD: VE-Cadherin*

Steps requiring optimisation	Technical solution
1- mCherry-labelling hCD2 E0771-bearing metastatic lung express mCherry, therefore, unable to check for the lung autofluorescence using FACS	Use unstained, non-tumour-bearing lung cells to check for autofluorescence.
2- Lung metastases are haemorrhagic (containing high numbers of RBCs)	Use RBC lysis buffer
3- Cell suspensions are viscous, containing clumps that interfere with isolating stromal cells	Use DNase I Solution
4- The time of tissue digestion and FACS sorting is long (4 hours or longer)	Use tissue dissociator (time-saving and reproducible method)
5- Metastatic lungs are highly infiltrated with immune cells	Depletion of immune cells using MACS antibodies-coupled magnetic beads (to enrich ECs with high purity and accelerate FACS sorting of ECs)
6- Fluorescence compensation was not applied because there is no single-colour compensation control for hCD2 since E0771 tumour cells are positive for both mCherry and hCD2	Use compensation beads
7- Very few metastatic niche ECs that are positive for CD31 and VE-CAD	Pool multiple lungs together to enrich for this population and IHC stain metastatic lung section to check if metastatic niche ECs are positive for CD31 and VE-CAD

5.4 Temporal and spatial single-cell transcriptome analysis of healthy, niche (mCherry+), and distal stroma during metastases evolution

After optimising the protocol for lung tissue preparation and the FACS gating strategy, I investigated changes in the gene expression profile of lung non-immune stromal cells during cancer metastatic evolution using the *in vivo* E0771 experimental metastatic model and state-of-the-art scRNA-seq. Using the described niche-labelling system (Ombrato et al., 2019), this aim was achieved via isolating stromal cells from healthy, early (day 7) and late (day 13) mCherry-labelling hCD2 E0771 tumour-bearing lungs **(Figure 5-11,Figure 5-12)**. Based on the expression of mCherry, two populations: lung distal (mCherry-/hCD2-) and lung metastatic niche stromal cells (mCherry+/hCD2-) were spatially isolated from early and late metastatic lungs using FACS **(Figure 5-13) (Table 5-3)**. To further characterise lung metastasis-mediated vascular remodelling and identify potential markers of early vessel co-option and late tumour angiogenesis, lung endothelial cells (CD31+ and CD31+ and VE-Cadherin+ EC populations) were also isolated and added to stromal cells to be sequenced **(Figure 5-11) (Table 5-3).** The number of cells sorted per condition is illustrated in **(Figure 5-13) (Table 5-3).**

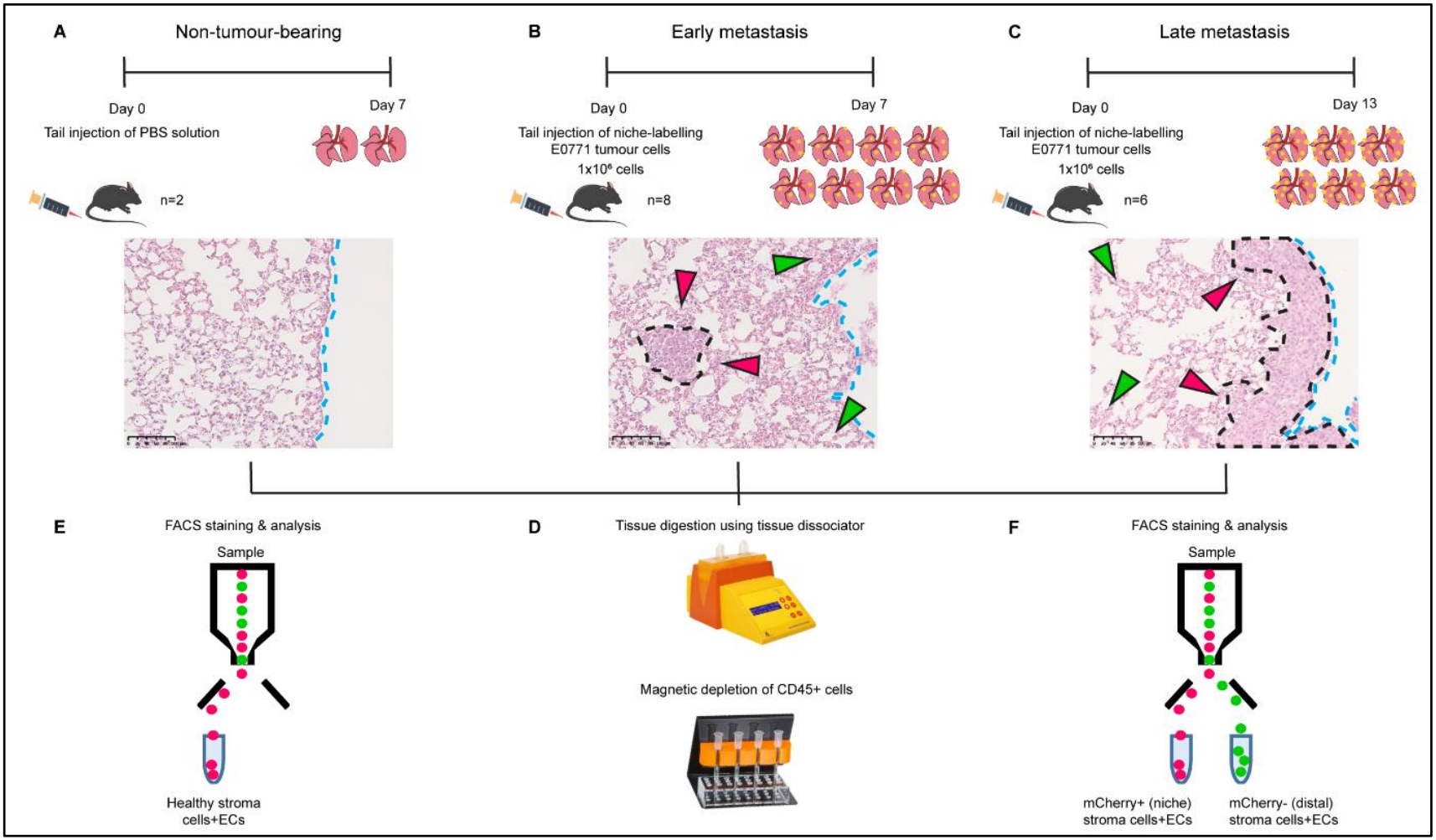

Figure 5-11. Experimental outline and protocol followed for FACS sorting for scRNA-seq of non-immune stromal lung cells. *Lungs were harvested from A: healthy mice; B: at early (day 7), and C: late metastatic phases (day 13 following intravenous inoculation of one million mCherry-labelling E0771 tumour cells); D: lungs were then digested using collagenase I and III enzymes and tissue dissociator which was followed by removal of immune cells (CD45+) using immunomagnetic beads; E: stromal cells were FACS sorted from condition A (healthy lungs); F: both mCherry + metastatic niche and mCherry - distal lung stromal cells were FACS sorted from condition B (early timepoint) and C (late timepoint). FACS sorted stromal cells were used for gene expression analysis using scRNA-seq. Note that several lungs were pooled to enrich for niche (mCherry-labelled) cells at early and late metastatic phases, respectively.*

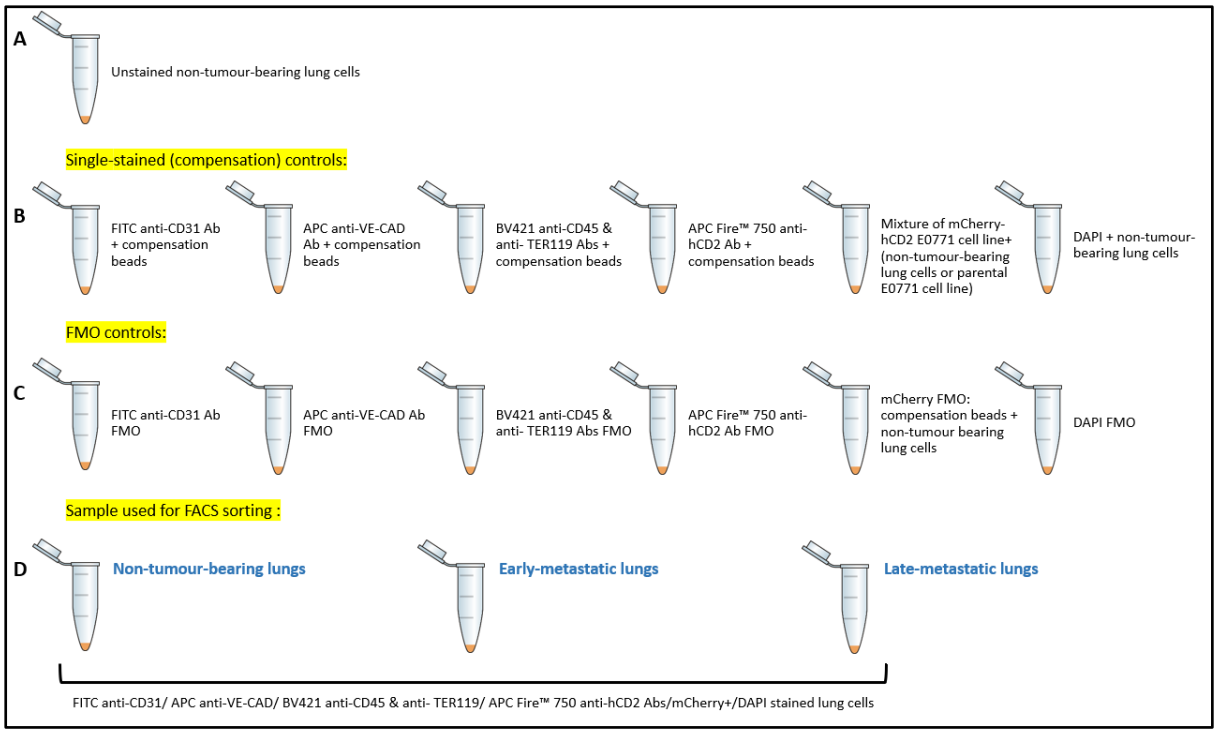

Figure 5-12. FACS-stained controls and samples that were used for FACS-sorting for scRNA-seq analysis. *A: non-tumour-bearing lung cells that were not stained; B:single-stained (compensation) controls, where only cells stained with one fluorescent-conjugated antibody at a time for calculating the compensation; C: Fluorescence Minus One (FMO) controls used to identify the true negative boundary for the fluorochromes: FITC, APC, Brilliant Violet 421 (BV421), APC Fire 750, mCherry, and DAPI considering the spread of other fluorochromes into each of these channels; D: using FACS sorter, cells were isolated from three samples, which are the three experimental conditions: non-tumour-bearing (healthy), early-, and late-metastatic lung cells for scRNA-seq analysis. Ab: antibody; Compensation beads: commercially available beads; VE-CAD: VE-Cadherin; hCD2: human CD2.*

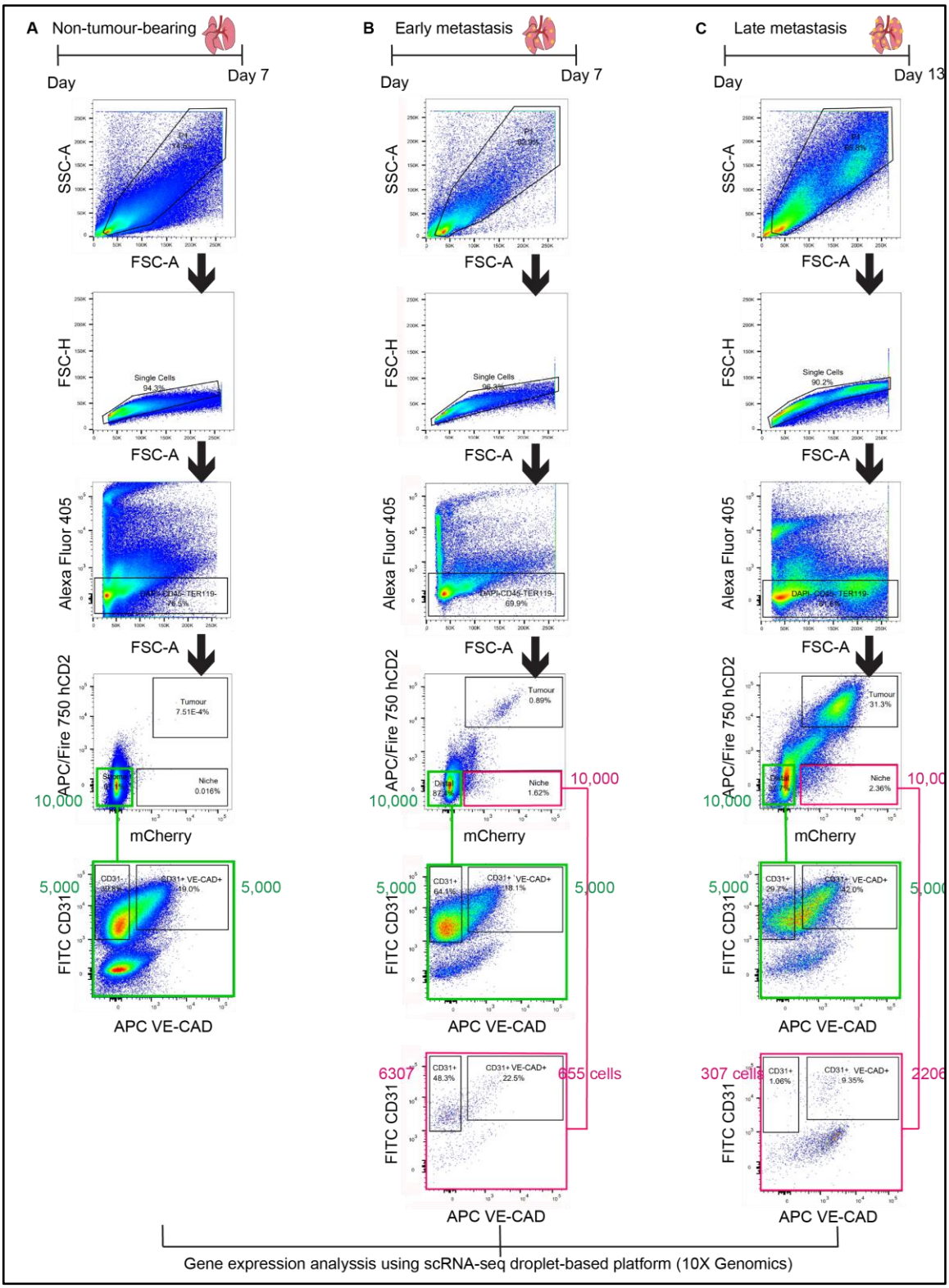

Figure 5-13. FACS sequential gating strategy to isolate lung non-immune stromal cells from normal lungs, early, late metastatic lungs for scRNA-seq analysis. *A: FACS gating strategy for normal lungs (n=2); B: FACS gating strategy from early metastatic lungs (n=8); C: FACS gating strategy from late metastatic lungs (n=6). FACS gating strategy from top to bottom as follows: SSC-A vs. FSC-A density plot to gate population of interest (P1) excluding debris; FSC-H vs. FSC-A density plot to gate single cells; Alexa Fluor 405 vs. FSC-A density plot excluding immune cells (CD45+), RBC (TER119+) and dead cells (DAPI+) and grouping these populations into dump channel; hCD2-APC/Fire750 vs. mCherry density plot to identify E0771 tumour cells (hCD2+ mCherry+), distal stroma cells (hCD2- mCherry-), and metastatic niche stromal cells (only mCherry+).The latter two populations were further analysed for ECs markers (CD31 and VE-CAD). Note cell numbers that were FACS sorted are illustrated near each population.*

Table 5-3. Murine lung samples were used for FACS sorting of healthy and metastatic niche stromal cells for scRNA-seq analysis*. Orange and green text indicates cells that were sorted from the same animals. ECs: endothelial cells.*

Sample number	Murine lungs samples	Labelled or not by mCherry-labelling E0771 cells (indicative of metastatic niche)	FACS sorter used	Cell type sorted	Cell density sorted per cell type	Total cell density sorted	Number of pooled lungs
1	Healthy lungs (control sample)	Non-tumour-bearing lungs, therefore mCherry negative	BD FACSAria III Cell Sorter (BD Biosciences)	Healthy stromal cells	10,000	20,000	2 lungs
				Healthy ECs	10,000		
2	Early-stage metastatic lungs	mCherry negative	FACSAria Fusion Cell Sorter (BD Life Sciences, San Jose, CA, 95131, USA)	Distal stromal cells	10,000	20,000	**4 lungs**
				Distal ECs	10,000		
3		mCherry positive		metastatic niche stromal cells	10,000	16,962	**4 lungs** + 4 lungs
				metastatic niche ECs	6,962		
4	Late-stage metastatic lungs	mCherry negative		Distal stromal cells	10,000	20,000	**3 lungs**
				Distal ECs	10,000		
5		mCherry positive		metastatic niche stromal cells	10,000	12,513	**3 lungs** + 3 lungs
				metastatic niche ECs	2,513		

In summary, cells were isolated from five experimental conditions as follows: non-immune stromal cells from non-tumour-bearing lungs, distal region and niche from early (day 7), and distal region and niche from late (day 13 following E0771 tumour inoculation) metastatic lungs **(Table 5-3).** These FACS-sorted lung stromal cells were sequenced using a single-cell RNA-seq (scRNA-seq) droplet-based platform, the 10X Genomics Chromium system. The scRNA-seq data of sequenced lung stromal cells across these five groups was

processed, and quality control metrics were applied for filtering cells. Cells were filtered based on the following quality control (QC) metrics: (i) exclude cells expressing below 200 genes (represents low-quality cells or empty droplets) or above 8700 genes (represents cell doublets or multiplets); (ii) include cells that contain more than 500 counts per cell (library sizes); (iii) include cells with only less than 15% of UMI counts derived from the mitochondrial genes (more than 15% is indicative of low-quality or dying cells) **(Figure 5-14A-D).** Variation due to technical noise was removed from scRNA data via normalisation using negative binomial regression, R package sctransform (Hafemeister & Satija, 2019)

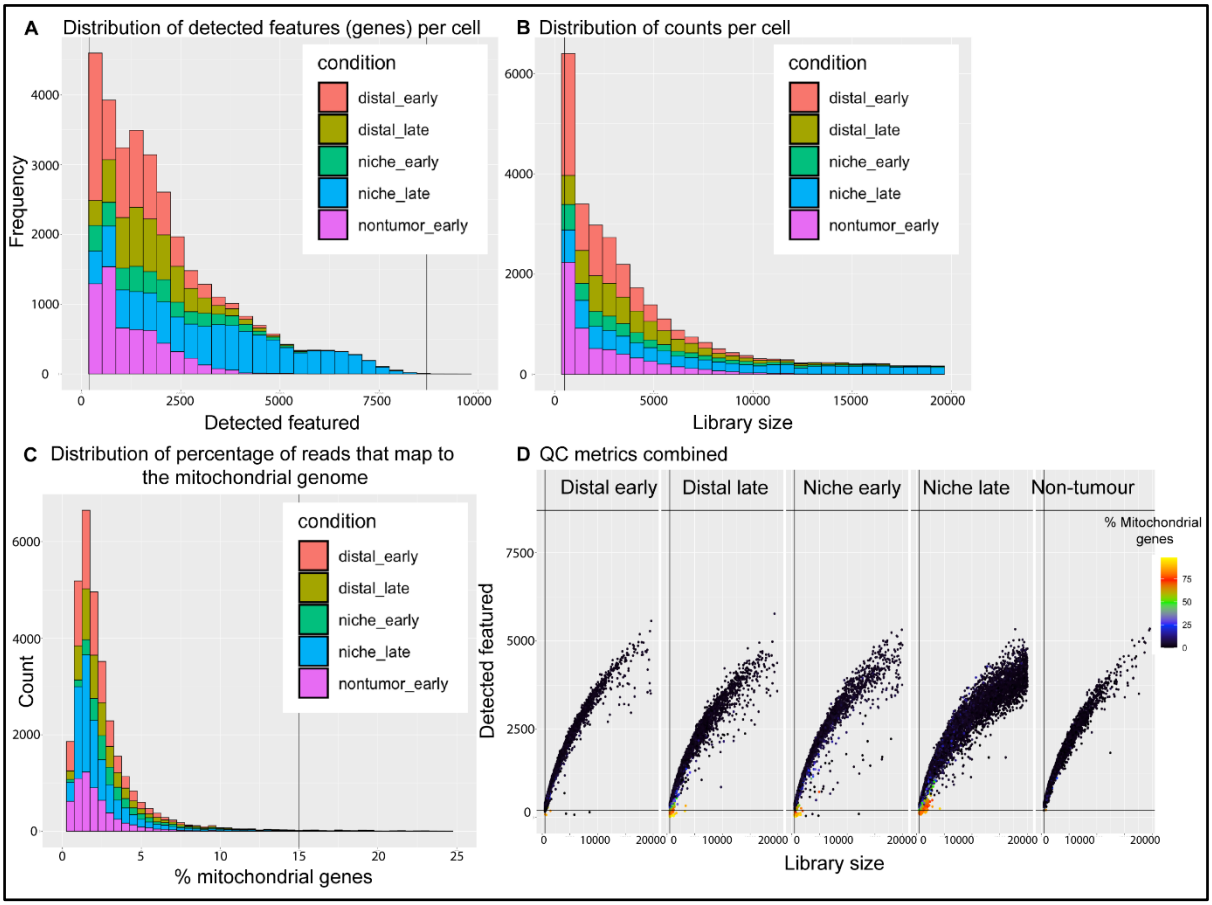

Figure 5-14. Quality control (QC) metrics applied for filtering cells*. A: cells expressing more than 200 genes (features) and less than 8700 genes were included; B: cells that contain a total sum of counts across all features, i.e., genes of more than 500 counts per cell (library sizes) were included; C: cells with only less than 15% of UMI counts derived from the mitochondrial genes were included; D: QC metrics combining and visualizing detected features, library size, and percentage of mitochondrial genes for the five conditions: non-tumour, early distal, early niche, late distal, and late niche*

To further study the transcriptional changes in the EC compartment and to identify distinct cell subpopulations across normal, early-, and late-metastatic conditions, the vascular (mainly EC) population (15,282 cells containing 13,816 ECs) was subclustered from the main stromal population based on pan-marker genes (*Pecam1* (*Cd31), Cadherin 5 (Cdh5 or VE-Cad), Claudin 5 (Cldn5*)) **(Figure 5-15) (Supplementary TableS1).** Besides high expression of fibroblast marker genes, fibroblast subtypes were observed to co-express EC marker genes, but to a lesser extent. It could be that EC subtypes span EC cluster boundaries into the fibroblast population. However, these cells were annotated as fibroblasts, as we relied on the top marker genes for annotating cell subtypes.

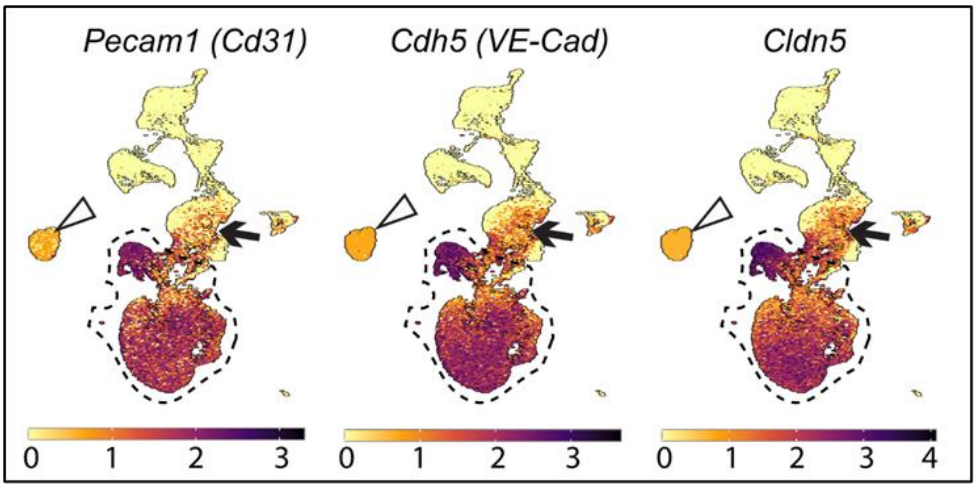

Figure 5-15. Pan-endothelial marker genes were used to subcluster EC population from the main lung stromal population*. Dashed black lining depicts endothelial clusters that were subsetted for higher resolution. Endothelial cells spanned into fibroblast cluster (black arrow). Erythroid cluster (white arrowheads) also express endothelial marker genes. The full names of these genes are shown in* ***The List of Abbreviations Table.***

5.4.1 Investigating the endothelial phenotype in early and late E0771 lung metastasis

The five scRNA-seq datasets representing EC populations from non-tumour, early, and late timepoints were merged to identify common EC subtypes across these conditions. Dimensionality reduction was performed on the merged scRNA dataset using PCA, and the first 20 PCs were included in downstream analysis. Generating a clustering tree (graph structure), a clustering resolution of 0.5 was selected, giving rise to 13 cell subtypes **(Figure**

5-16A). Unsupervised clustering (using computational tools developed for automated identification of cell types), clustered cells based on similarity in expressed genes within the EC population. The cell subtypes were visualised by dimensional reduction using the uniform manifold approximation and projection (UMAP) method and unsupervised clustering **(Figure 5-16A)**. Most of the cell subtypes detected were ECs. These clusters of lung vascular cells across the five conditions were annotated as follows: capillary type I (cap I) ECs; capillary type II (cap II) ECs; interferon (IFN) antigen (Ag)-presenting cap II ECs, vein ECs; artery ECs; stressed ECs; proliferating ECs; neophalanx/breach/tip ECs; tumour ECs; ribosomal-related ECs; lymphatic ECs; smooth muscle cells (SMC)/myofibroblasts; and megakaryocytes **(Figure 5-16A-F)**. EC subtypes were annotated based on the top 50 differentially expressed genes (DEGs) in each cluster and manual curation using gene sets in relevant publications **(listed in Table 5-4) (Supplementary TableS2).** The top five marker genes of each annotated vascular cluster are visualised by UMAP plots **(Figure 5-17) (Figure 5-18).** Sequenced lung cells across the five conditions were mainly comprised of cap I and II ECs **(Figure 5-16A)**. Cap I were distinct from cap II ECs by differential expression of *Emp2, Igfbp7, Ednrb, Car4,* and *Fibin.* Whereas cap II ECs differentially expressed *Hmcn1, Glp1r, Ptprb, Itga1,* and *Kit* **(Figure 5-16A, B).**

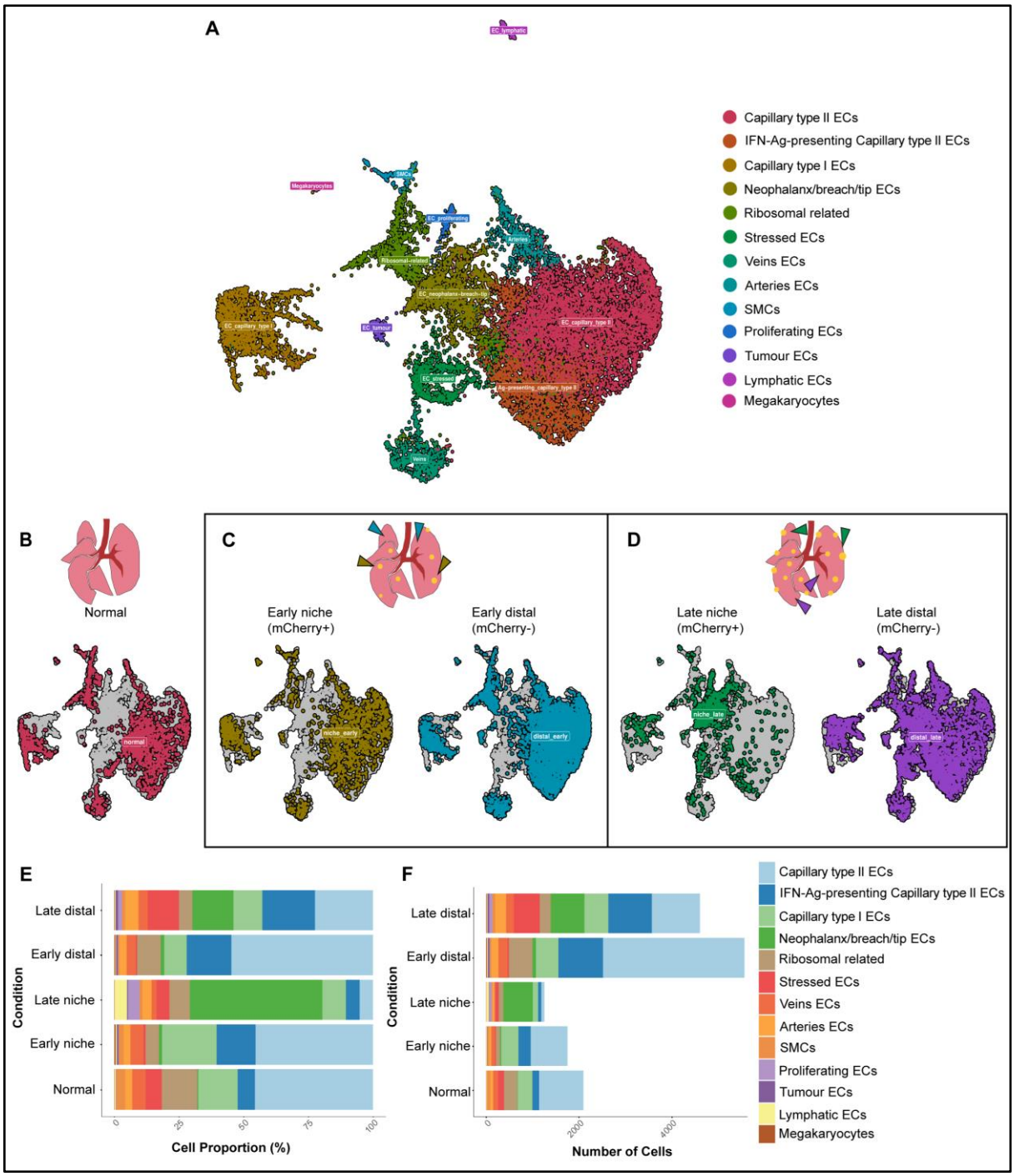

Figure 5-16. Vascular cells from healthy lungs, early, and late E0771 metastatic mouse lungs revealed vascular heterogeneity during metastatic development in the lungs. *A: unsupervised clustering visualized as Uniform Manifold Approximation and Projection (UMAP) identified 15 clusters that were annotated to 13 cell types across all five conditions. Cell clusters were annotated by manual curation of previous studies and based on the top 50 differentially expressed (DE) marker genes. Five UMAP projection plots of lung vascular clusters splitting all five conditions: B: normal (healthy); C: early distal region (turquoise arrowheads), early niche (cumin arrowheads); D: late distal region (purple arrowheads), and late niche (green arrowheads) conditions of E0771 metastatic lungs, respectively; E and F: relative (percentage) and absolute cellular composition of lung vascular cells across the five conditions. ECs is abbreviated for endothelial cells; SMCs is abbreviated for smooth muscle cells.*

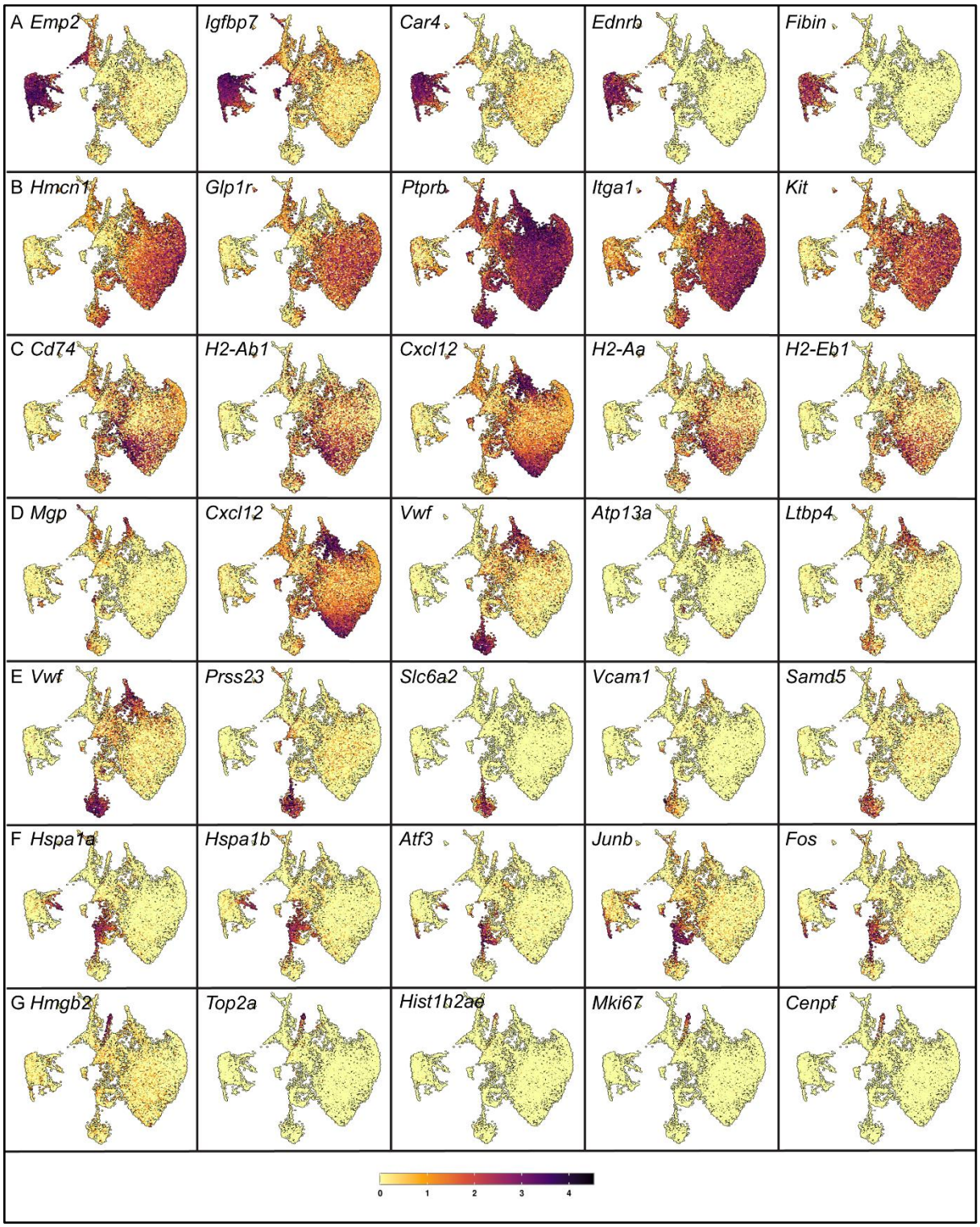

Figure 5-17. UMAP plots of top five marker genes for EC subtypes from healthy lungs, early, and late E0771 metastatic mouse lungs. *A: top five marker genes of capillary type I ECs; B: top five marker genes of capillary type II ECs; C: top five marker genes of antigen-presenting cap II ECs; D: top five marker genes of artery ECs; E: top five marker genes of vein ECs; F: top five marker genes of stressed ECs; G: top five marker genes of proliferating ECs. These top marker genes were identified based on log2 foldchange of 0.25, min.pct of 0.25, and adjusted p-value <0.05. The full names of these genes are shown in* ***The List of Abbreviations Table.***

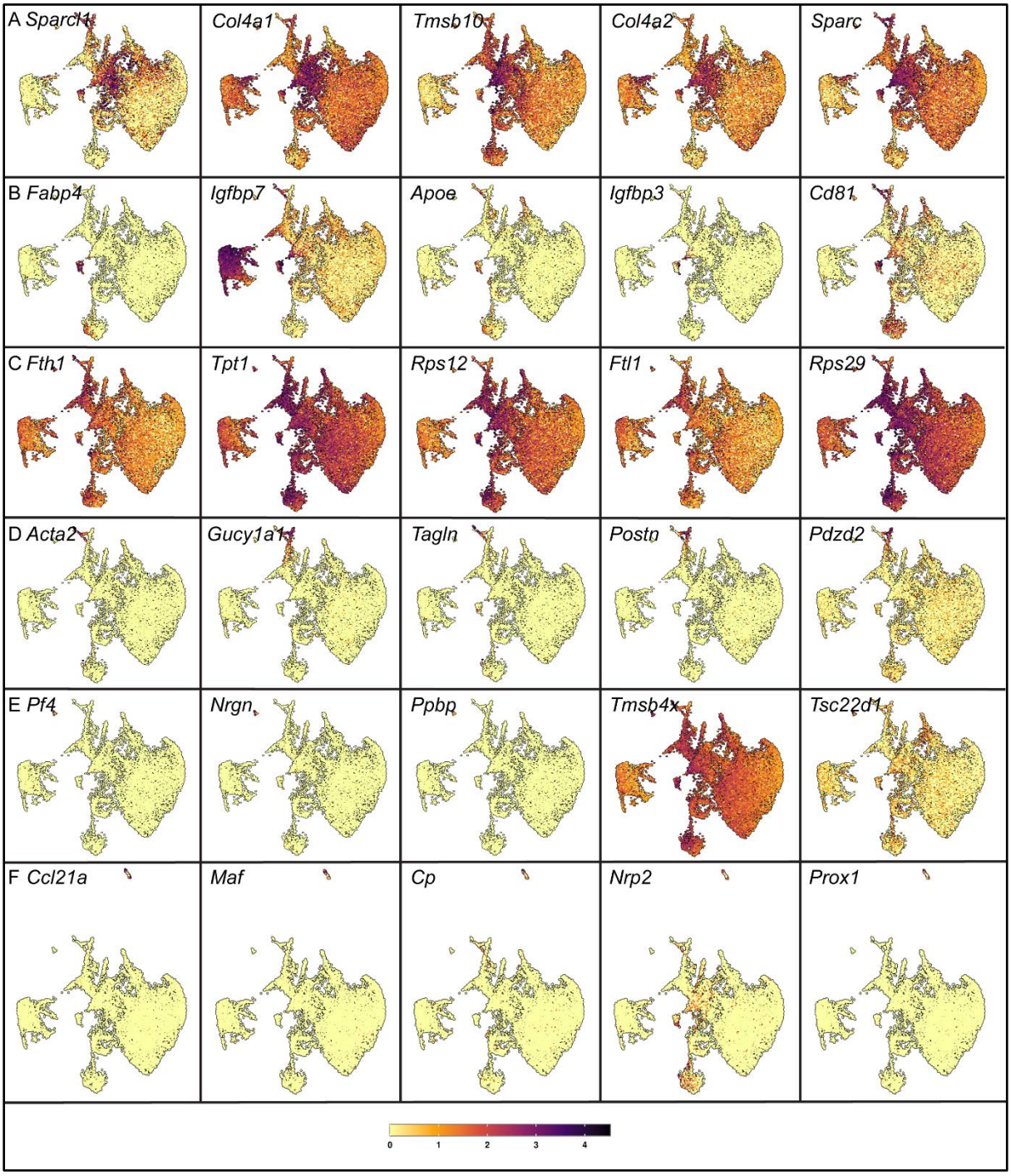

Figure 5-18. UMAP plots of top five marker genes for vascular subtypes from healthy lungs, early, and late E0771 metastatic mouse lungs. *A: top five marker genes of neophalanx/breach/tip ECs; B: top five marker genes of tumour ECs; C: top five marker genes of ribosomal-related cluster; D: top five marker genes of smooth muscle cells (SMC); E: top five marker genes of megakaryocytes; F: top five marker genes of lymphatic ECs. These top marker genes were identified based on log2 foldchange of 0.25, min.pct of 0.25, and adjusted p-value <0.05. The full names of these genes are shown in* ***The List of Abbreviations Table.***

Table 5-4. Differentially expressed genes (DEGs) and references of literature studies used to annotate cell types of mouse lung vasculature*. The full names of these genes are shown in* **The List of Abbreviations Table.**

Annotated cell type	DEGs		Reference
Vascular population			
Capillary type I ECs	*Emp2, Car4, Fibin, Cyp4b1*		(Gillich et al., 2020; Goveia et al., 2020)
Capillary type II ECs	*Plvap*		(Gillich et al., 2020; Vila Ellis et al., 2020)
	Sema3c, Hmcn1, Clec14a		(Gillich et al., 2020; Goveia et al., 2020)
IFN-Ag-presenting Capillary type II ECs	MHC-II antigen presentation marker genes:	*CD74, H2-Ab1, H2-Eb1,*	(Wolf et al., 2018)
		H2-DMa, H2-DMb1	(Goveia et al., 2020; Roewe et al., 2020)
	Capillary type II ECs marker genes: *Sema3c, Pltp, Hmcn1*		(Gillich et al., 2020; Goveia et al., 2020)
Veins	*Vwf, Slc6a2, Amigo2*		
Arteries	*Atp13a3, Ltbp4, Gja5, Bmx*		
Lymphatic ECs	*Maf, Prox1*		
	Ccl21a		(Goveia et al., 2020)
Stressed ECs	Stressed-induced marker genes: *Ucp2, Dusp1, Ifitm3*		(Zhao et al., 2020)
	EC marker genes: *Klf4, Klf2, Foxf1*		(Goveia et al., 2020)
Proliferating ECs	*Top2a, Mki67, Ube2c*		(Goveia et al., 2020)
Tumour ECs	*Fabp4, Cd300lg, Fabp5*		
Neophalanx/breach/tip ECs	Neophalanx ECs marker genes: *Sparcl1, S100a6*		
	Breach ECs marker genes: *Col4a1, Col4a2*		
	Tip ECs marker genes: *Tmsb10, Sparc, Trp53i11*		
Ribosomal-related cells	*Rpl3, Rpl7a*		
SMCs or pericytes	SMCs marker genes: *Cox4i2, Postn, Pdgfrb, Tagln, Acta2, Myh9*		(Angelidis et al., 2019)
	Pericytes marker genes: *Cox4i2, Postn, Pdgfrb, Acta2, Myh9*		(Liu et al., 2021; Teuwen et al., 2021)
Megakaryocytes	*Ppbp, Nrgn, Plek, Alox12*		(Angelidis et al., 2019)

5.4.1.1 EC remodelling in early (co-opting) E0771 metastases

A recent study by Goveia and colleagues found that tumour and peritumoural capillaries from patients with human non-small cell lung cancer (NSCLC) highly express genes related to MHC-II-mediated antigen (Ag) presentation (Goveia et al., 2020). I also found this EC subtype, and consequently investigated at what stage of metastatic development, temporally and spatially, they were enriched. Compared to healthy lung ECs, there was an increase in IFN-Ag-presenting cap II ECs in the early metastatic-distal region and early niche **(Figure 5-16E, F).** These overexpress the MHC class II antigen-processing machinery and IFNγ-regulated genes such *as Ifngr1, H2-Q7, Gbp4, Gbp7, Ifi47,* and *Igtp* **(Figure 5-19).** IFN-Ag-presenting cap II ECs were combined with cap II ECs for subsequent differential expression analysis and Gene set enrichment analysis (GSEA).

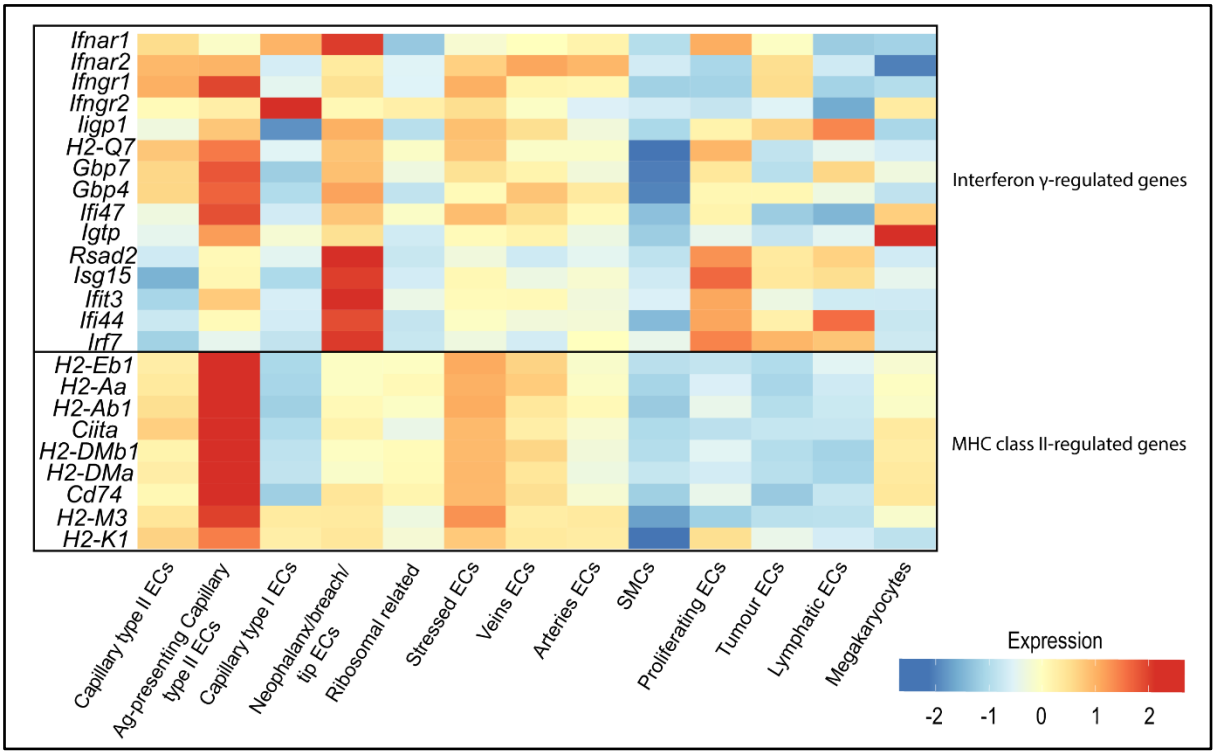

Figure 5-19. Heatmap depicting gene expression levels of MHC II Ag presentation molecules and IFNγ-regulated genes in different EC subtypes. *Instead of using the normalized expression values, Z-scores were computed for every row (representing each gene) and displayed on the heatmap. This approach guarantees that the visualized expression patterns are not overwhelmed by the actual expression values. The full names of these genes are shown in* ***The List of Abbreviations Table.***

GSEA also showed a significant reduction of gene sets related to tight junctions (TJs), focal adhesion, and regulation of actin cytoskeleton in early niche cap II ECs compared to their normal counterpart **(Figure 5-20, Figure 5-21A).** The downregulation of genes related to the actin cytoskeleton and TJs, and upregulation of *Ifnγ*-response genes, specifically in co-opted cap II ECs, suggest a potential link whereby IFNγ increases the permeability of these vessels permitting extravasation and colonisation of E0771 BC in the lungs **(Figure 5-19, Figure 5-21A).** The vascular endothelial growth factor A, *Vegfa* was also upregulated in early niche cap II ECs mediating vascular hyperpermeability.

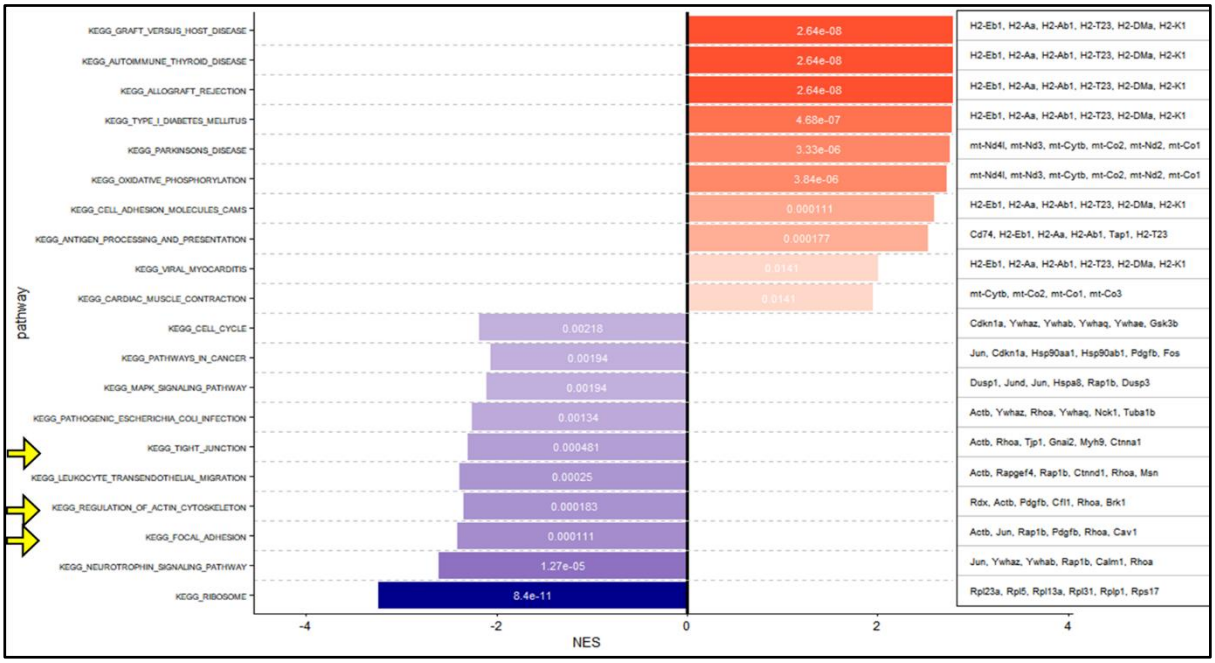

Figure 5-20. Gene set enrichment analysis (GSEA) of DEGs showed significant downregulation of gene set related to tight junctions, focal adhesion, and actin cytoskeleton in early niche (co-opted) capillary II ECs compared to normal counterpart. *NES: normalized enrichment score.*

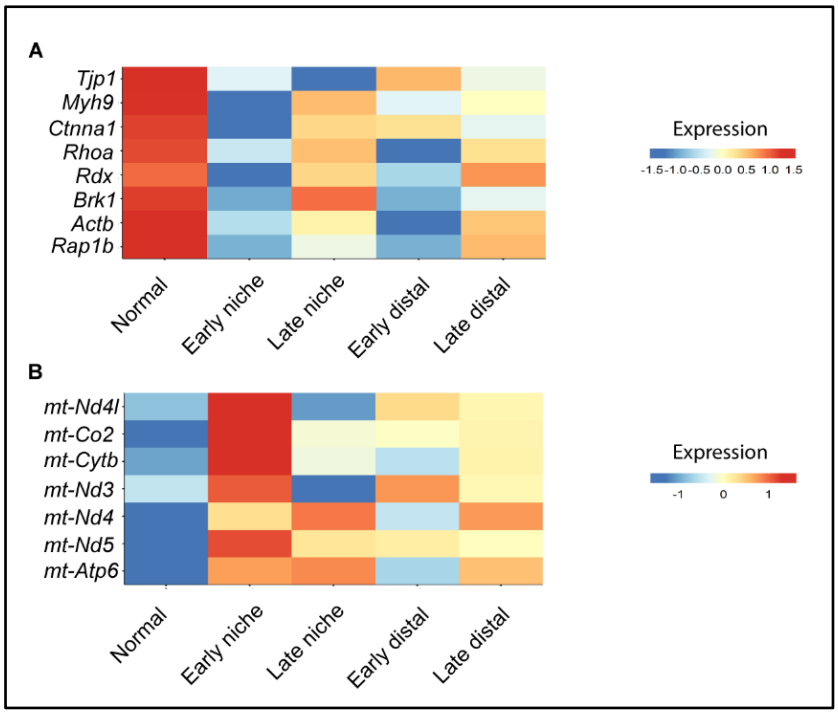

Figure 5-21. Heatmap depicting co-opted capillaries in early niche increase the expression of genes regulating OXPHOS and downregulate genes regulating tight junctions (TJs), focal adhesion, and actin cytoskeleton compared to other conditions. *A: heatmap depicting cap II ECs in early niche downregulated genes related to TJs, focal adhesion, and acting cytoskeleton; B: heatmap depicting cap I and cap II ECs increased the expression of OXPHOS genes. Z-scores were computed for every row (representing each gene) and displayed on the heatmap. This approach guarantees that the visualized expression patterns are not overwhelmed by the actual expression values. The full names of these genes are shown in* ***The List of Abbreviations Table.***

In order to validate the findings in scRNA-seq data, immunofluorescence staining of early (co-opting) and late metastatic lungs with the TJ marker, TJP1 junctional protein was performed. The TJP1 signal was reduced in both lungs containing early metastases and late metastases (niche and distal regions) compared to non-tumour lungs **(Figure 5-22, Figure 5-23)**. This reduction could potentially facilitate alveolar and cuffing (vessel co-opting) growth of E0771 tumours, which was correlated with its transcript expression in the scRNA-seq data **(Figure 5-22A-C, Figure 5-21A) (Appendix D2)**. TJP1 signal was also reduced in the distal regions of early metastases and in the intratumoural regions of late metastases when compared to non-tumour lungs **(Figure 5-22, Figure 5-23).** To confirm the reduction of TJP1 signal in the vascular endothelial cells of early and late metastases and was not due to fewer vessels, double immunofluorescence staining using anti-CD31 and anti-TJP1 antibodies was performed **(Figure 5-24)**. TJP1 signal confirmed to be reduced in the endothelial compartment

(CD31+ cells) of early metastases (niche and distal regions) when compared to non-tumour ECs **(Figure 5-24)**.

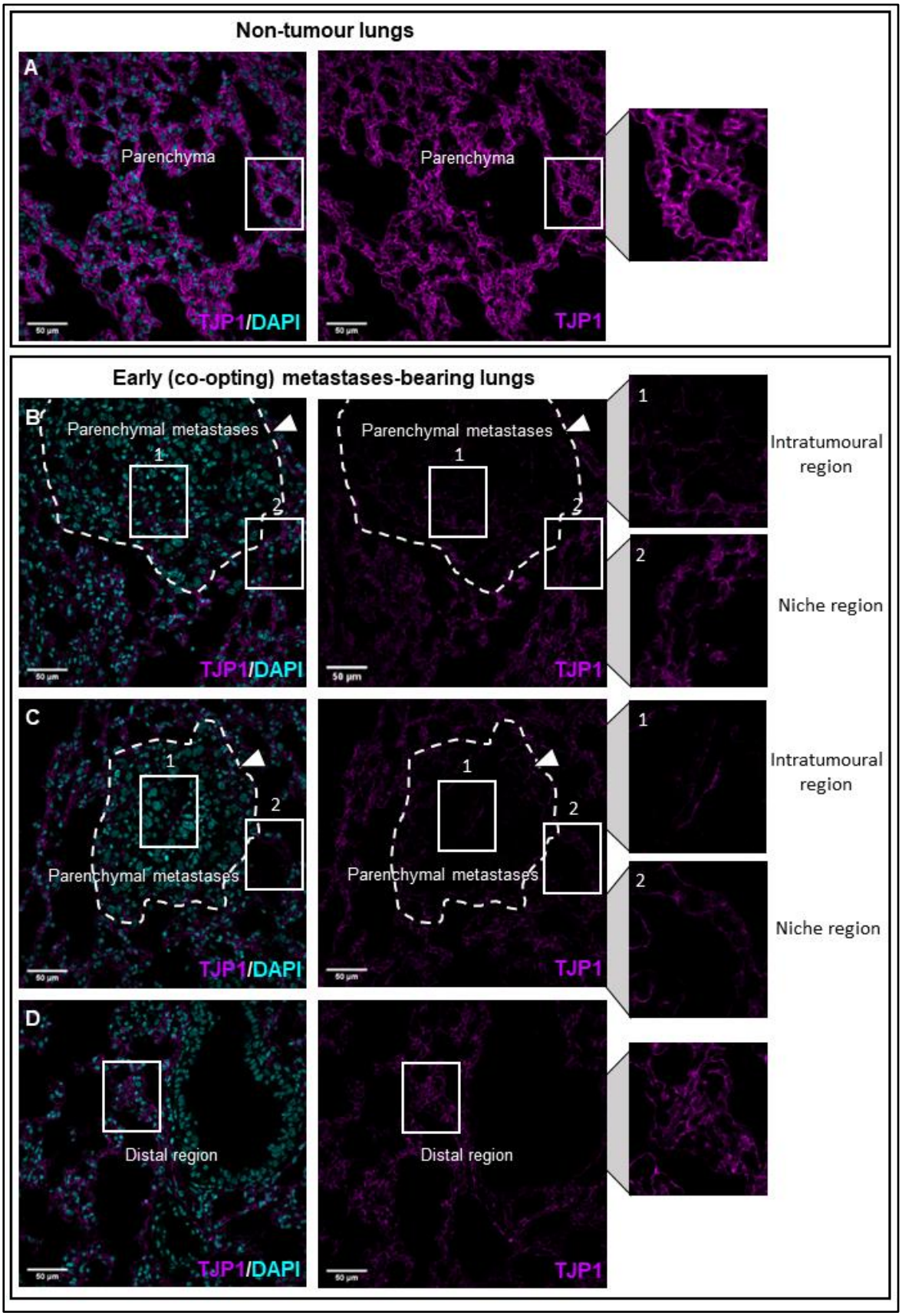

Figure 5-22. Immunofluorescent staining demonstrated reduced protein expression of the tight junction, TJP1 (purple) in the early metastatic niche (co-opting) metastases compared to TJP1 expression in the distal region and non-tumour-bearing lungs*. TJP1 expression: A: in the parenchymal region of non-tumour-bearing lungs; B: in the alveolar co-opted region in early (co-opting) metastases; C: in the cuffing co-opted region in early (co-opting) metastases; D: in the distal region in early (co-opting) metastases-containing lungs. B, C, and D were captured from the same tissue section. Enlarged insets in B and C demonstrate TJP1 expression in the intratumoural (1) and niche (2) regions. TJP1: tight junction protein 1. Nuclei were stained with DAPI (blue).*

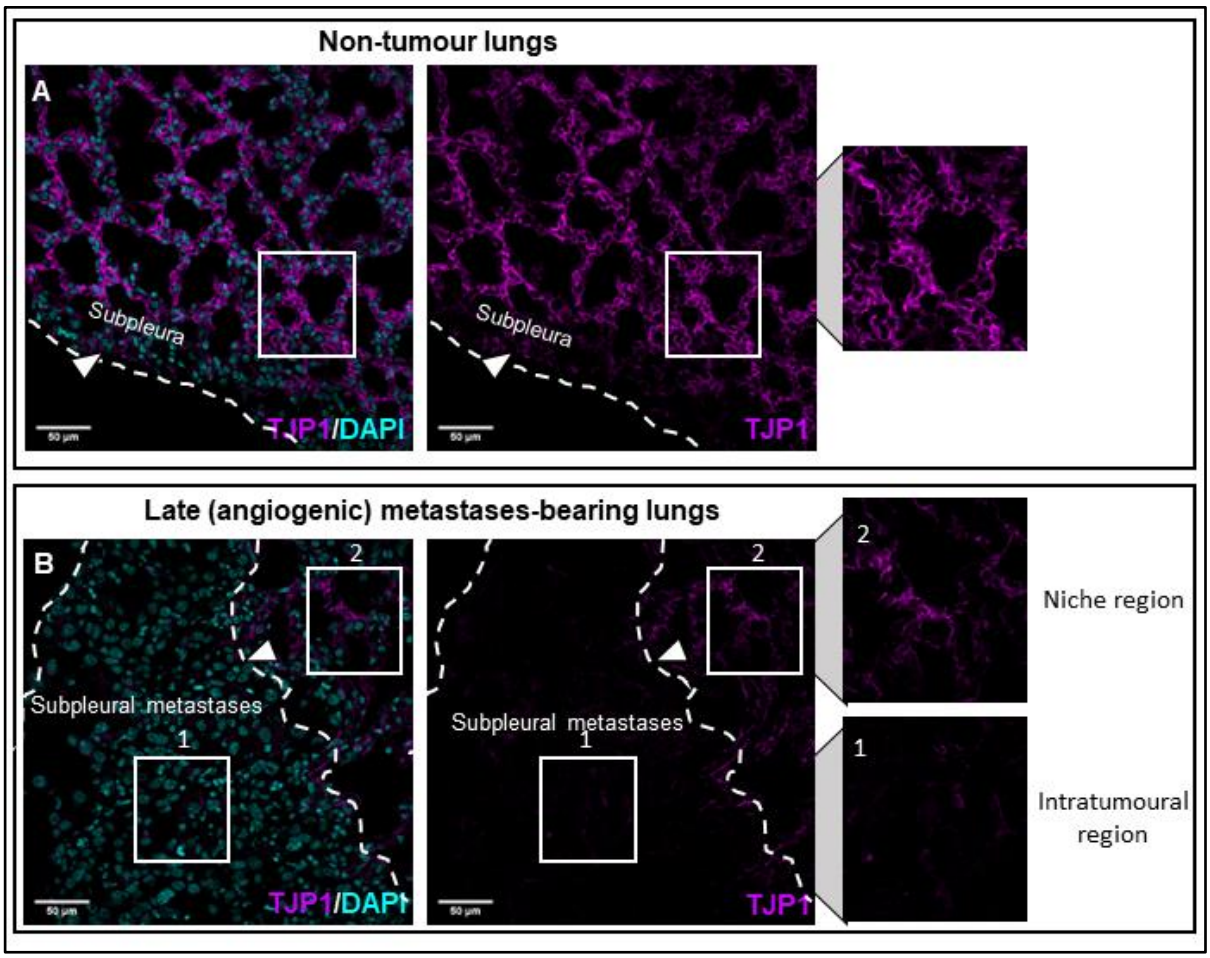

Figure 5-23. Immunofluorescent staining demonstrated reduced protein expression of the tight junction, TJP1 in the late metastatic niche of angiogenic metastases compared to TJP1 expression in the non-tumour-bearing lungs*. TJP1 expression: A: in the parenchymal region of non-tumour-bearing lungs; B: in subpleural (angiogenic) metastases. Enlarged insets in B demonstrate TJP1 expression in the intratumoural (1) and niche (2) regions. TJP1: tight junction protein 1. Nuclei were stained with DAPI (blue).*

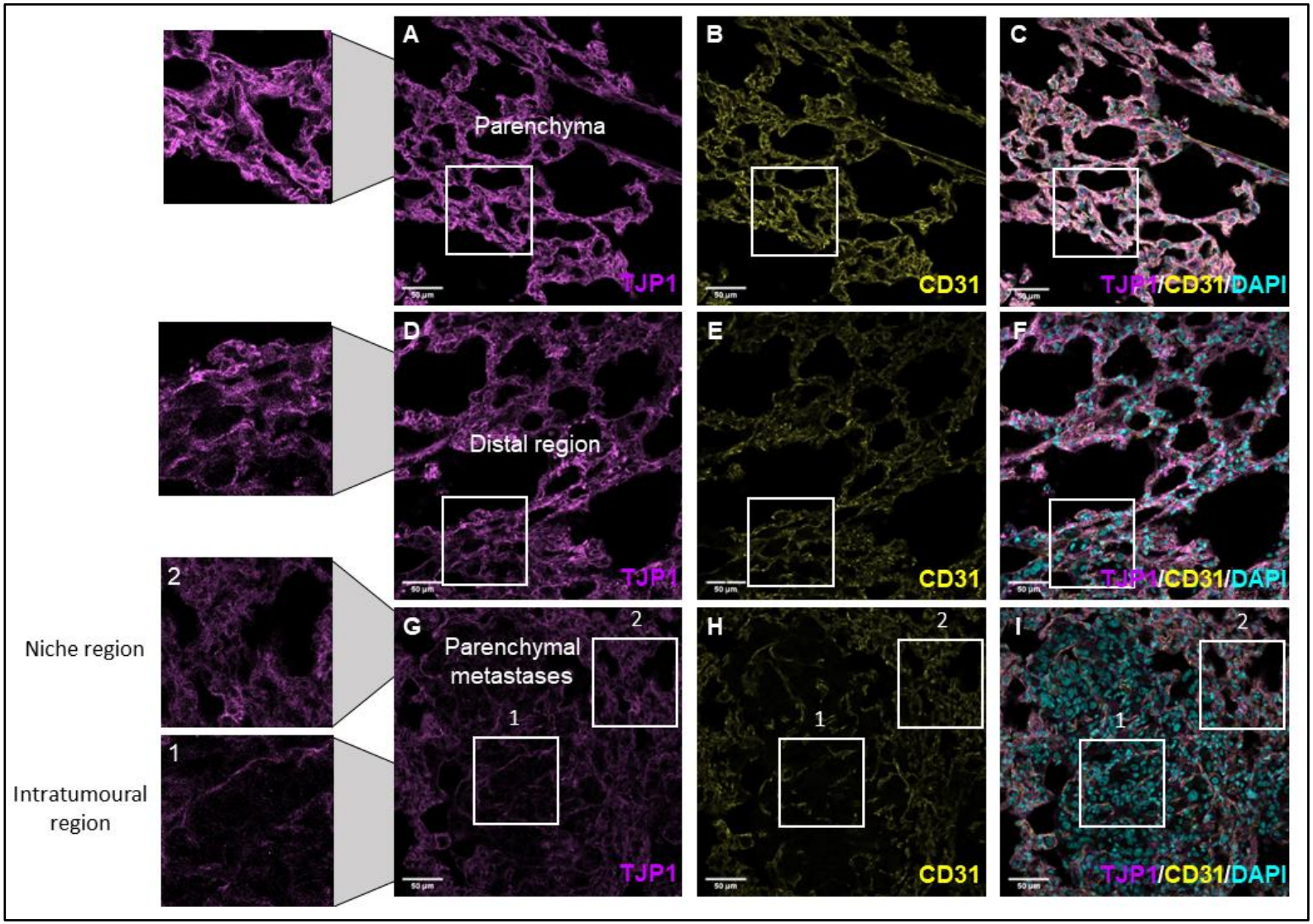

Figure 5-24. Double immunofluorescence staining of early (co-opting) lungs showed an evident reduction in TJP1 signal in the niche and distal vascular ECs compared to non-tumour ECs*. TJP1and CD31 expression: A-C: in the parenchymal region of non-tumour-bearing lungs; D-F: in the distal region in early (co-opting) metastases-containing lungs; G-H: in the alveolar co-opted region in early (co-opting) metastases. Note that D-I were captured from the same tissue section. Enlarged insets in G-I demonstrate TJP1 expression in the intratumoural (1) and niche (2) regions. TJP1: tight junction protein 1.*

As the oxygenation status of co-opting versus angiogenic metastasis differs, I next investigated metabolic pathway components that were altered in the early and late metastatic lungs (distal and niche) compared to non-tumour-bearing lungs via GSEA analysis. In comparison to the non-tumour compartment, microvessel ECs, including cap I and cap II ECs, in both early niche and early distal regions upregulated pathways related to oxidative phosphorylation (OXPHOS) **(Figure 5-20, Figure 5-21B) (Appendix E1, E2).**

5.4.1.2 Transcriptomic gene signature of co-opted capillaries in the early metastatic niche

As capillaries constitute the major EC populations in the lungs, I investigated gene changes in the cap I and cap II ECs (Ag-presenting cap II combined with cap II ECs) in the early niche compared to non-tumour and distal counterparts. Differential expression analysis of cap I and II ECs was performed across the five conditions (non-tumour, early niche, late niche, early distal, late distal) as pair comparisons with log fold change threshold = 0.25 and the focus in this thesis was on the differentially upregulated genes **(Appendix F) (downregulated genes in Supplementary TableS6)**. Gene expression of cap I ECs (representing co-opted vessels) in the early niche was compared to: cap I ECs in non-tumour, early distal, and late niche separately (as pairwise comparisons). This resulted in 59, 31, and 266 differentially upregulated genes, respectively **(Appendix F1, F2, F3).** Unique upregulated genes in cap I ECs in the early niche compared to the non-tumour counterpart are listed in **Appendix F1,** and include *Gstp1, Sap18, Dleu2, Mest, Pcdh1, Igfbp7, Id3,* and *Prx* **(Figure 5-25A-H).** Compared to the distal region, cap I ECs in the early niche differentially upregulated the expression of several genes **(Appendix F2),** including *Klf2, Tsc22d3* and *Rheb* **(Figure 5-25I-K)**. Nine genes were commonly differentially upregulated in the cap I ECs of the early niche compared to all other counterparts **(Figure 5-27A, B).**

Whereas cap II (co-opted) ECs in the early niche, when compared to: cap II ECs in non-tumour, early distal, and late niche separately (as pairwise comparisons), resulted in 48,

19, and 154 differentially upregulated genes, respectively **(Appendix F4, F5, F6).** Unique upregulated genes in cap II ECs from the early niche compared to non-tumour counterpart **(Appendix F4)** include *Gbp4, Malat1*, and *Tra2a* **(Figure 5-26A-C).** Compared to the distal region, cap II ECs in the early niche also upregulated the expression of several genes **(Appendix F5)**, including *Klf2, Mgp,* and *Cav2* **(Figure 5-26D-F)**. In general, cap II ECs of the early niche commonly upregulated eight genes compared to other counterparts **(Figure 5-27C, D)**. Most of which are consistent with GSEA analysis that showed upregulated OXPHOS in cap II ECs isolated from early niche **(Figure 5-20).**

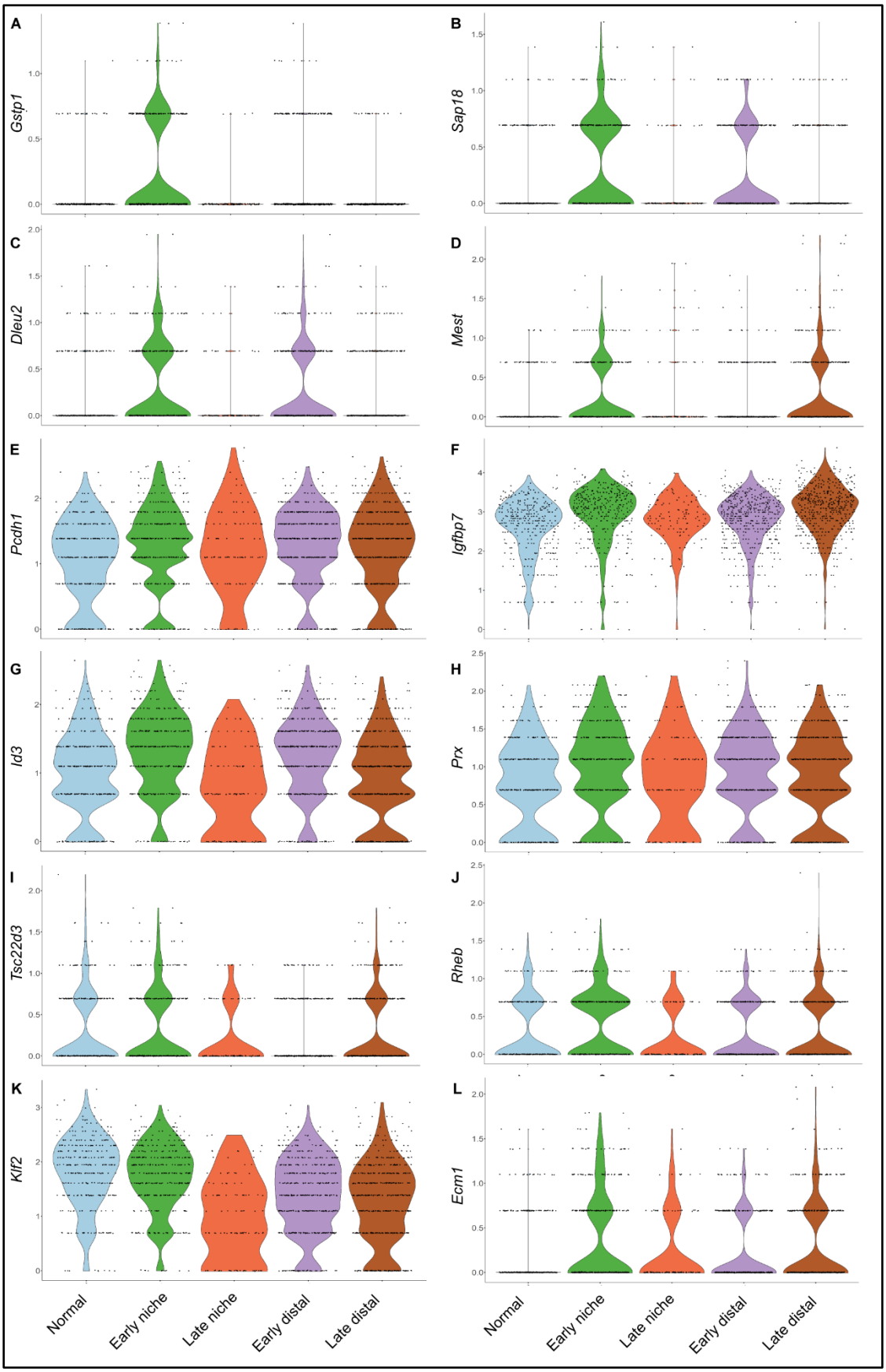

Figure 5-25. Violin plots depicting top genes that are upregulated in co-opted cap I ECs in early niche compared to non-tumour (A-H) and to early distal region (I-K). *The full names of these genes are shown in* ***The List of Abbreviations Table.***

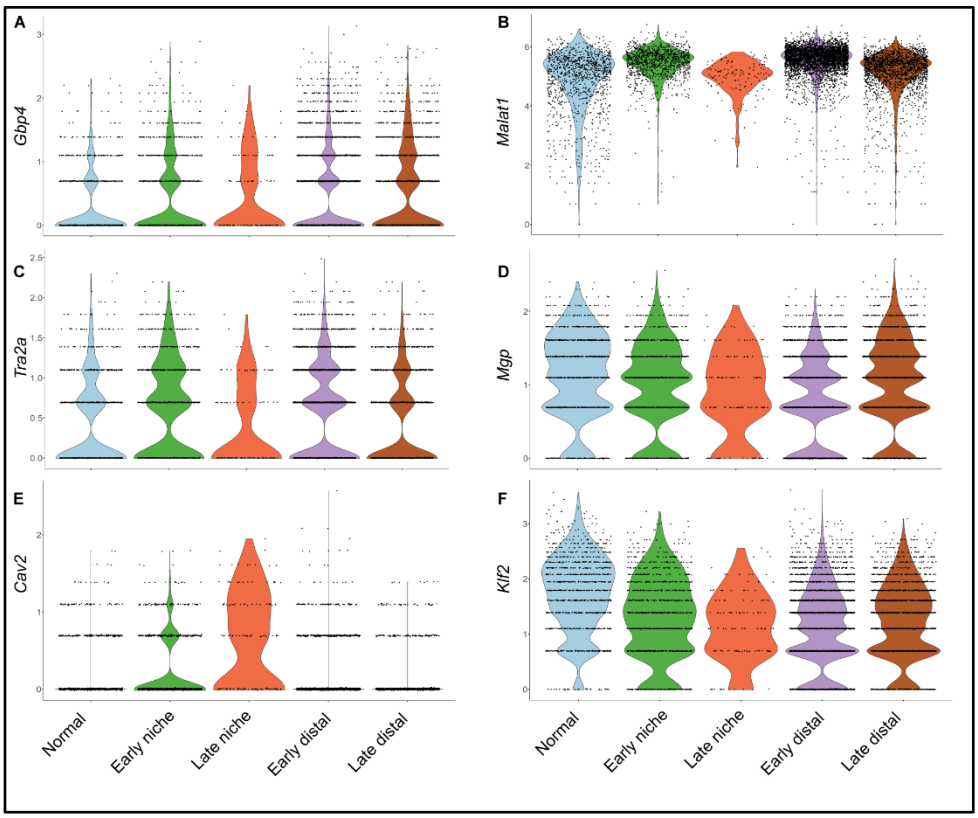

Figure 5-26. Violin plots depicting top genes that are upregulated in co-opted cap II in early niche compared to non-tumour (A-C) and to early distal region (D-F). *The full names of these genes are shown in* ***The List of Abbreviations Table.***

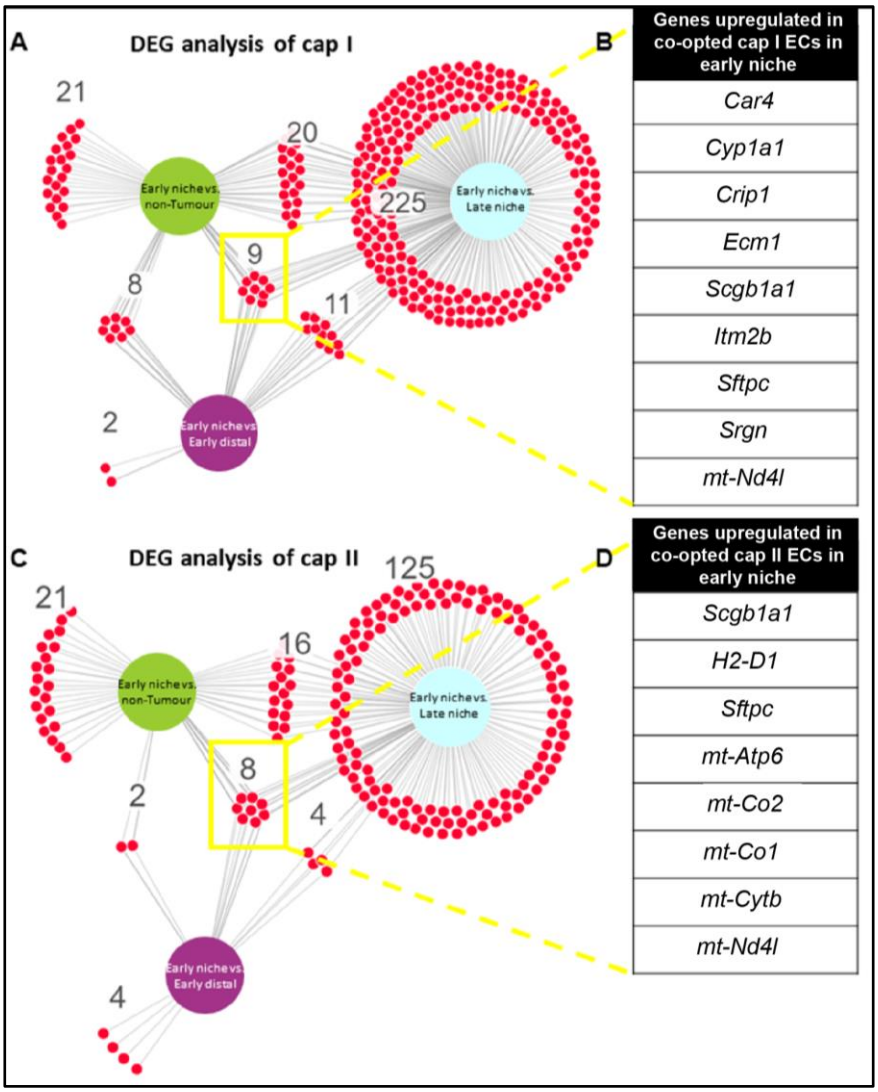

Figure 5-27. Venn diagram demonstrating upregulated DEGs in cap I and cap II (co-opted) ECs in early niche in comparison to non-tumour, early distal, and late niche counterparts*. A: pairwise comparisons showing upregulated genes (red nodes labelled with the number of genes that were upregulated in that comparisons and common genes among comparisons) in cap I; B: in cap II ECs in early niche compared to non-tumour (green node), early distal region (magenta node), late niche (cyan node). Yellow boxes in A and B depicts the common upregulated genes in co-opted cap I and cap II ECs in early niche across comparisons. Visualizing tool used is DiVenn ((Sun et al., 2019)*

All these upregulated genes have been reported in the literature (references detailed in the **Discussion section**) to regulate EC response in different disease contexts in different ways. However, in the early metastatic context of our study, these upregulated genes represent the differential transcriptome signature of co-opted capillaries type I and II **(Appendix F).**

5.4.1.3 EC remodelling in late metastatic lungs

In addition to their abundance in the early metastases, IFN-Ag-presenting cap II ECs persisted during the late metastatic stage but only in distal regions **(Figure 5-16E, F)**. During late metastasis, a subset of ECs develops a stress-adapted response, annotated as stressed ECs **(Figure 5-16E, F)**. Stressed ECs were found to highly express genes described in the literature to be induced by tissue dissociation (van den Brink et al., 2017) **(Figure 5-28)**. This tissue dissociation gene signature is also a conserved stress-adapted response that can be triggered by biological stimuli *in vivo,* such as metastatic niche remodelling by metastatic tumour cells in our study, but this is not a definitive cause. It is important to note that a stressed EC cluster enriched in late distal condition probably indicates a real biological response, not a technical artefact (due to tissue preparation or digestion enzymes used), as cells in all conditions were exposed to the same tissue preparation protocol but at different timepoints. To investigate this further, I assessed the quality of this cluster in comparison to other EC subtypes **(Figure 5-29A-C).** Stressed ECs expressed a comparable number of transcripts compared to other clusters **(Figure 5-29A, B)**. Also, the stressed ECs cluster was not dying cells as they did not express a high percentage of transcripts mapping to mitochondrial genes **(Figure 5-29C)**. Other than stress-adapted response genes, stressed ECs also upregulated some published marker genes of postcapillary veins, cap I, cap II, veins, breach ECs, neophalanx ECs, and Tip ECs (Goveia et al., 2020) **(Supplementary TableS2).** This population also highly expressed unique genes: IFN-response genes (*Irf1*), and genes involved in inhibition of apoptosis (*Sertad1*), inhibition of cell cycle (*Cdkn1a*), transcription factor (TF) regulation (*Sox17* and *Hes1*), and proto-oncogene enhancing cell proliferation and survival (*Pim3*) **(Figure 5-29D-I)** (Garbicz et al., 2020; Hu et al., 2019; Sunitha et al., 2019; Yang et al., 2013).

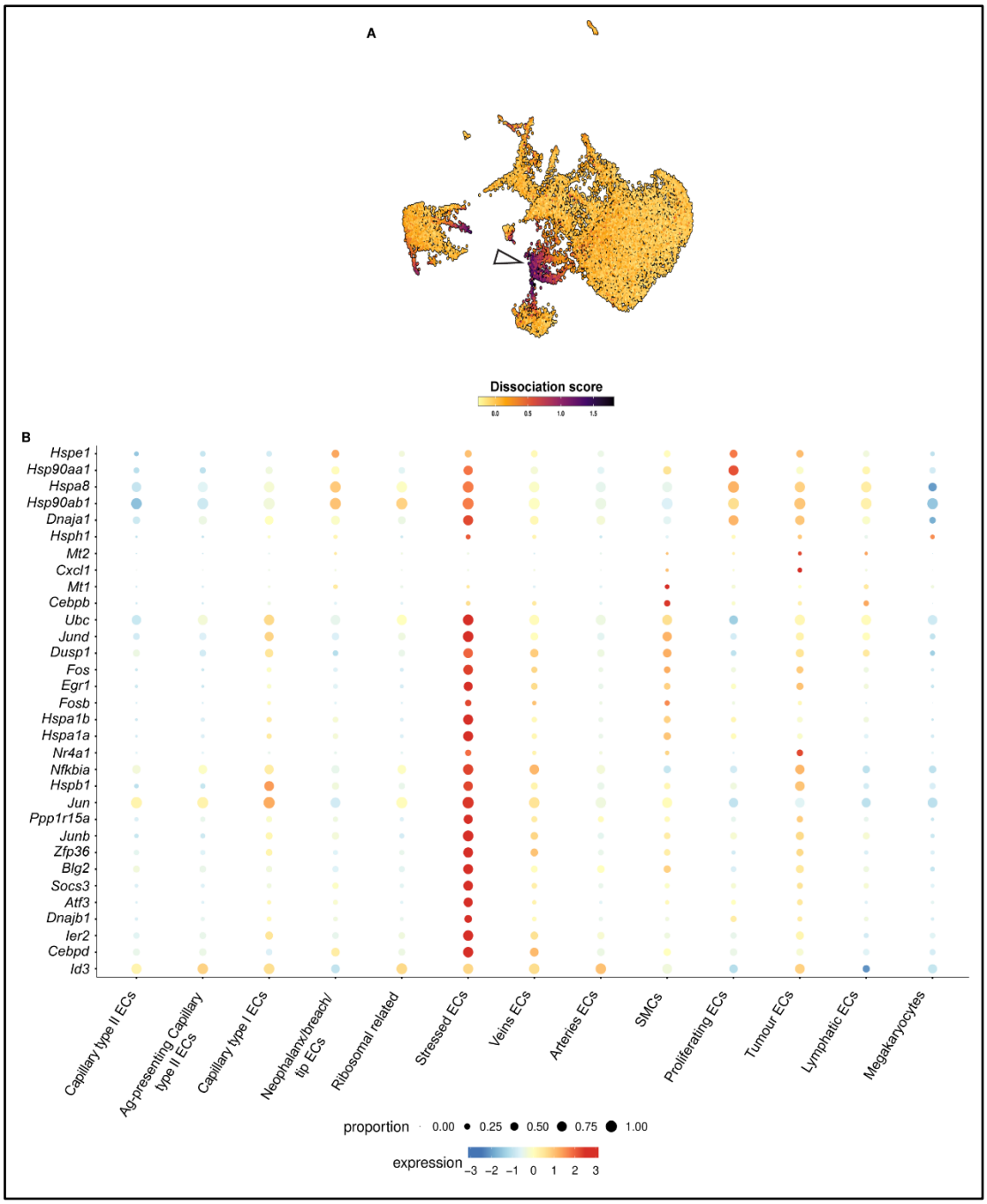

Figure 5-28. Scoring of tissue dissociation (stress response) gene signature across EC subtypes. *A: UMAP visualization of tissue dissociation gene signature across EC subtypes with stressed ECs showing highest score; B: dot plot showing average expression of stress response genes across EC subtypes. The full names of these genes are shown in* ***The List of Abbreviations Table.***

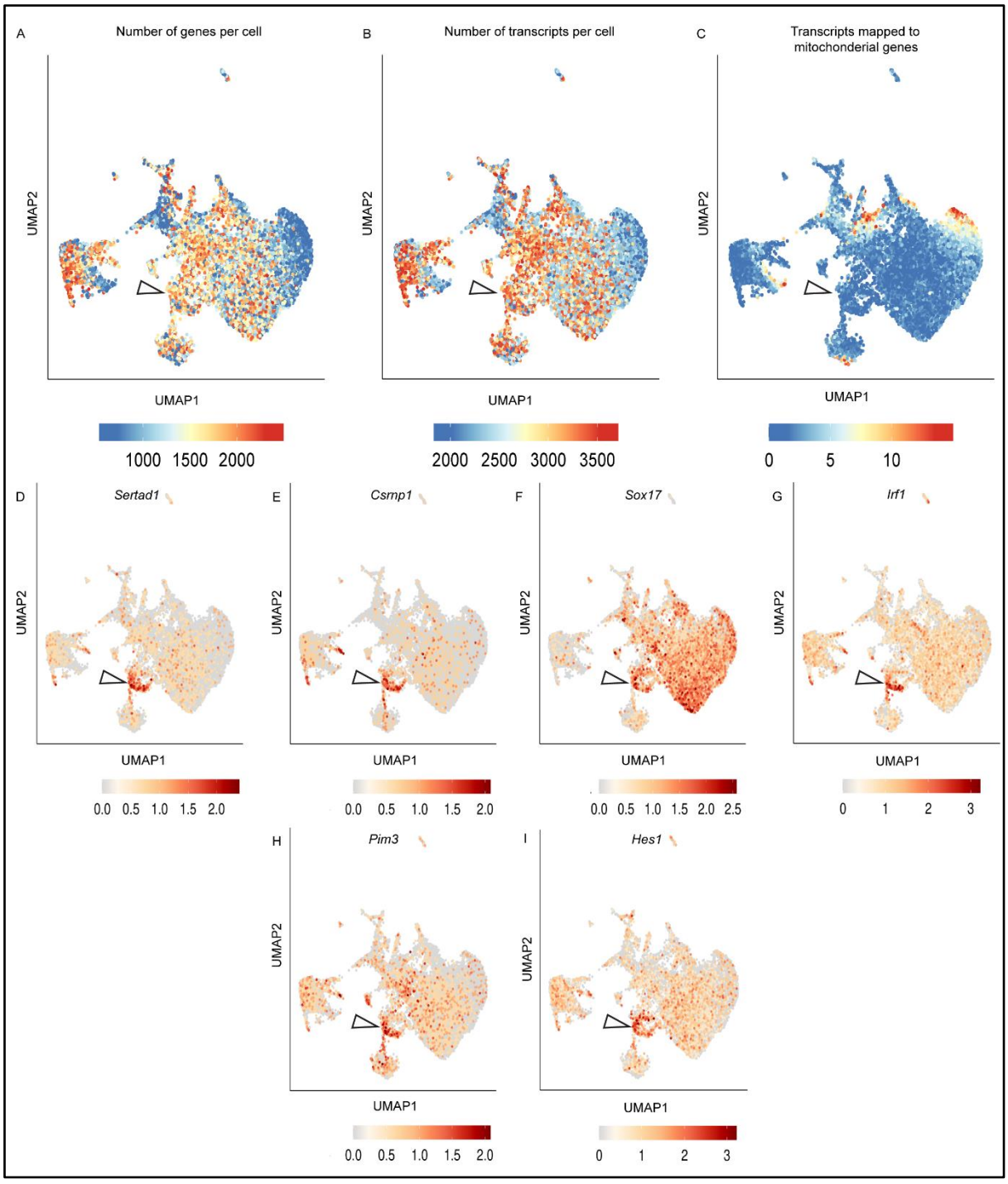

Figure 5-29. Quality assessment of stressed ECs in comparison to other EC subtypes and top four distinct genes. *UMAP visualizations of A: normalized number of genes per cell; B: normalized number of mRNA transcripts per cell; C: transcripts that mapped to mitochondrial genes per cell across all EC subtypes; Distinct genes differentially highly expressed in stressed ECs (indicated by white arrowheads) including D: Sertad1; E: Csrnp1; F: Sox17; G: Irf1; H: Pim3; I: Hes1. The full names of these genes are shown in* ***The List of Abbreviations Table.***

Lymphatic ECs prominently emerge in the late niche area, highly expressing *Ccl21a, Maf, Cp, Nrp2,* and *Prox1* **(Figure 5-16E,F, Figure 5-18F)**. This is likely to provide a route for cancer to metastasise through tumour lymphangiogenesis.

Interestingly, proliferating ECs, expressing proliferation genes such as *Hmgb2, Top2a, Hist1h2ae, Mki67,* and *Cenpf,* started to emerge in the late niche, possibly linked to E0771 tumour cells inducing the formation of new blood vessels **(Figure 5-16E, F, Figure 5-17G).** ScRNA-seq of ECs of niche and distal areas of late metastasis-bearing lungs also detected an enrichment of neophalanx/breach/tip ECs, indicating that angiogenic vessels support E0771 progression to form established metastases **(Figure 5-16E, F)**. This finding agrees with my earlier histology findings which identified an angiogenic vasculature at this stage. The genes that were highly expressed in this angiogenic cluster include tip marker genes such as *Trp53i11, Tmsb10,* and *Sparc*; breach EC marker genes, *Col4a1, Col4a2, Pkm,* and *Inhbb*; and neophalanx EC marker genes, *Sparcl1, S100a6* and *Cd34* (Goveia et al., 2020) **(Supplementary TableS2).**

To investigate the origin of the neophalanx/breach/tip ECs that emerge late in E0771 breast cancer metastasis, I performed single-cell trajectory analysis using the Monocle3 R package (Trapnell et al., 2014). This pseudotime analysis of EC subclusters predicted differentiation of neophalanx/breach/tip ECs from either cap I or cap II ECs in the late-metastatic niche **(Figure 5-30)**.

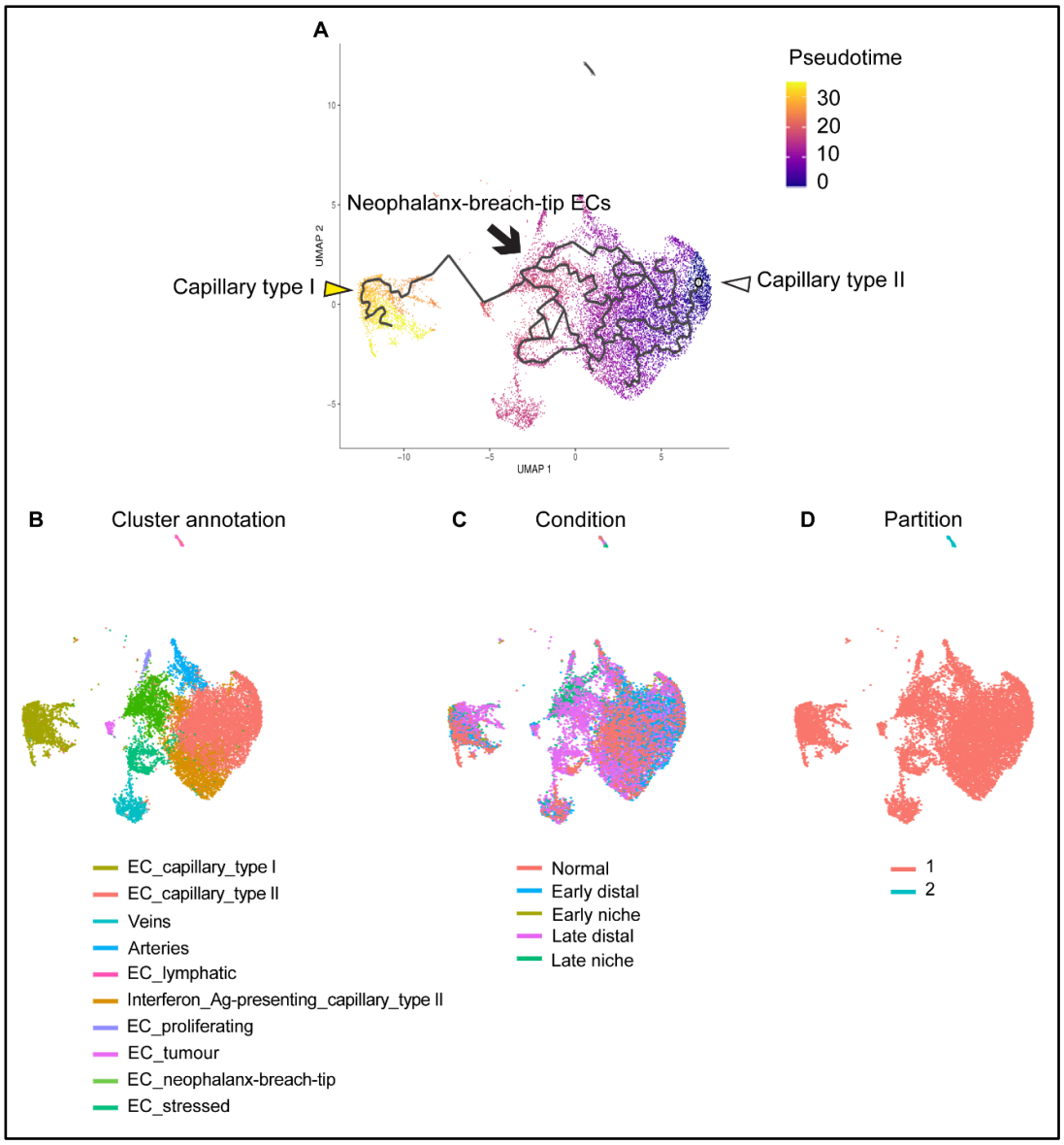

Figure 5-30. Angiogenic ECs predicted to arise from cap I and II ECs. A: EC differentiation trajectory analysis using Monocle predicts cap I (yellow arrowhead) and cap II ECs (white arrowhead) to differentiate into neophalanx/breach/tip ECs (black arrow). *Light grey circle indicates the root (starting) node; B: annotation for EC subclusters (excluding SMCs, Megakaryocytes, and ribosomal-related cells); C: UMAP projection plot of scRNA-seq merging all five conditions: healthy, early distal, early niche, late distal, and late niche ECs of early metastases and late metastases, respectively; D: Monocle trajectory analysis separates ECs into two partitions indicating two distinct trajectories: trajectory 1 includes all ECs and trajectory 2 includes lymphatic ECs.*

Large vessels such as arteries and veins located in the late distal region and late niche upregulated OXPHOS compared to non-tumour compartments **(Appendix E3, E4).** Also, neophalanx/breach/tip ECs in angiogenic metastases upregulated OXPHOS as an energy source **(Appendix E5).**

In contrast to OXPHOS being used by cap I ECs in early metastases, in late niche of E0771 metastases I found that cap I and neophalanx/breach/tip ECs upregulated gene sets for enzymes related to the glycolysis/gluconeogenesis pathway. These EC subsets also upregulated glycolytic enzymes such as *Gapdh, Gpi1, Aldoa, Ldha, Tpi1, Pgk1, Eno1,* and *Pkm* **(Figure 5-31).** This upregulation in glycolysis is consistent with a vascular switch driven by hypoxia, in which E0771 tumour cells may induce angiogenesis at a late stage due to demanding high energy levels.

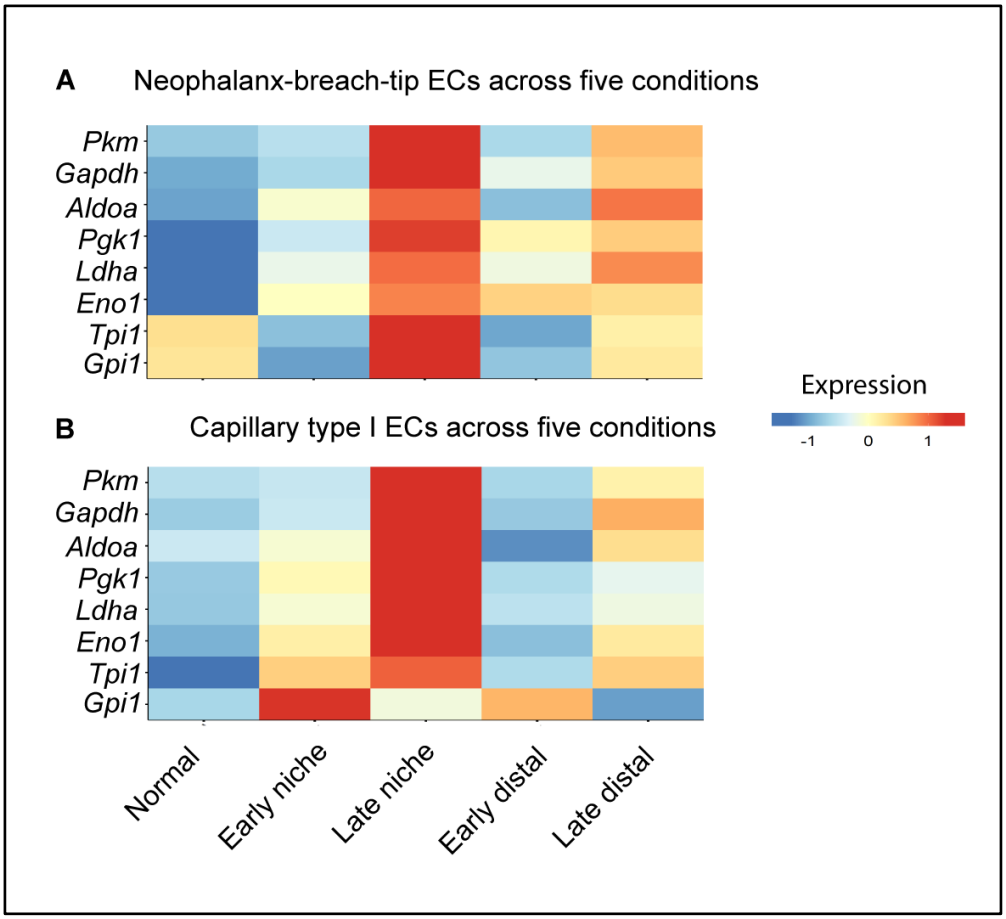

Figure 5-31. Heatmap depicting cap I and neophalanx-breach-tip ECs increased the expression of genes regulating glycolysis/gluconeogenesis pathway compared to non-tumour counterparts. *A: heatmap depicting expression of glycolysis/gluconeogenesis pathway in neophalanx-breach-tip ECs across five conditions; B: heatmap depicting expression of glycolysis/gluconeogenesis pathway in cap I ECs across five conditions. Z-scores were computed for every row (representing each gene) and displayed on the heatmap. This approach guarantees that the visualized expression patterns are not overwhelmed by the actual expression values. The full names of these genes are shown in* ***The List of Abbreviations Table.***

5.4.1.4 Remodelling of lipid metabolism in different EC subtypes in early and late E0771 niches

Lipid metabolism is reported to reprogram cancer cells, contributing to cancer growth, metastasis, and response to therapy (Bacci et al., 2021). However, lipid reprogramming in the tumour microenvironment (TME) is poorly understood. Therefore, I manually extracted lipid-regulated genes (Fatehi-Hassanabad & Chan, 2005; Nagarajan et al., 2021; Wang et al., 2020) and performed differential expression analysis using a non-parametric Wilcoxon (Mann-Whitney) test. E0771 tumour cells were found to induce heterogeneous lipid metabolic rewiring in different EC subtypes in early versus late metastases, potentially in order to provide fatty acids as a substrate for energy, or to act as building blocks for cell membrane formation and macromolecule synthesis **(Figure 5-32, Figure 5-33, Figure 5-34, Figure 5-35) (Table 5-5).**

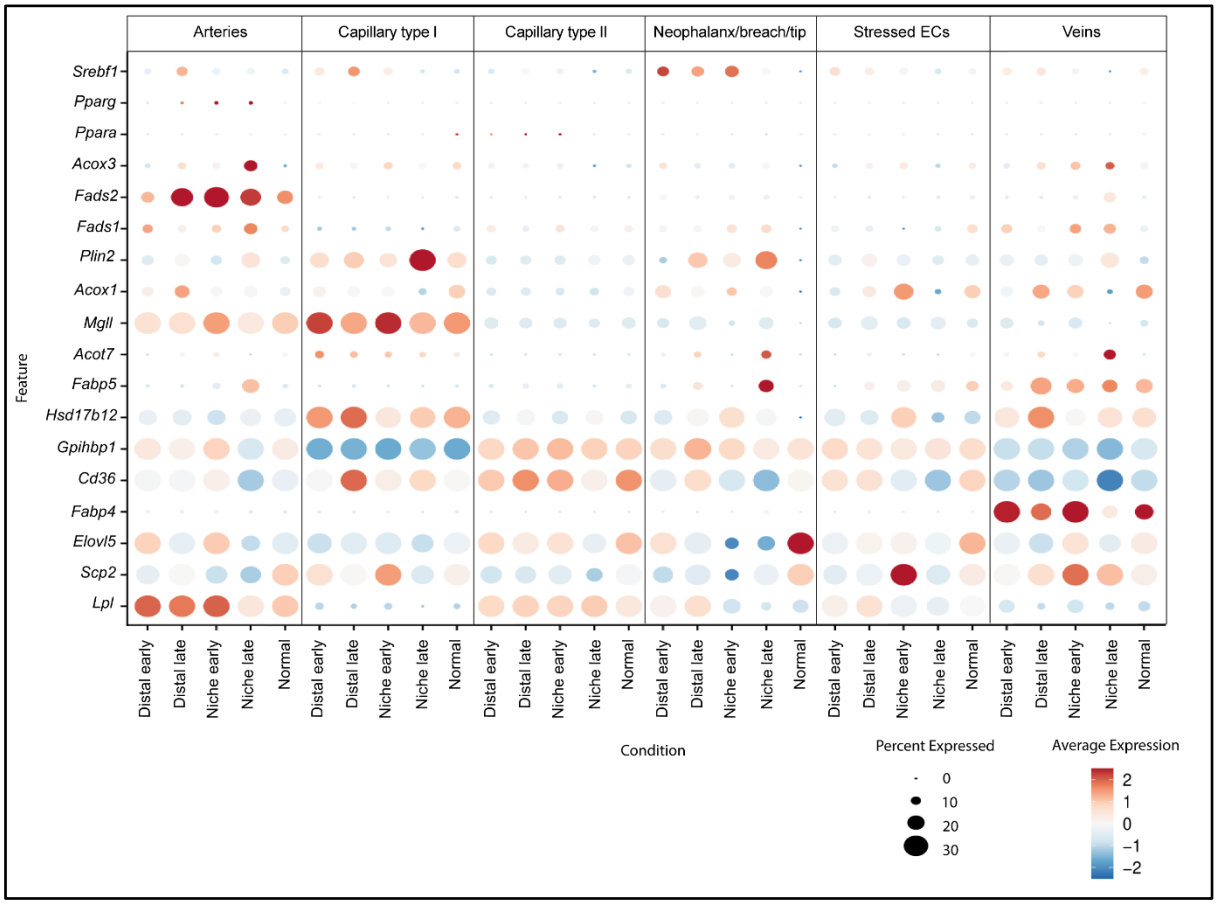

Figure 5-32. Dot plot depicting the expression levels of lipid-regulated genes across different EC subtypes across the five conditions: normal (healthy), early distal, early niche, late distal, and late niche of early and late metastatic lungs, respectively. *In order to detect variation in lowly expressed genes, this dot plot was generated with 30% of scale truncation. Thus, any gene expressed in 30% of cells or higher in a cluster have the same dot size. The full names of these genes are shown in* ***The List of Abbreviations Table.***

Table 5-5. Upregulated and downregulated lipid-regulated genes across different EC subtypes. *Pairwise comparisons were performed using a non-parametric Wilcoxon (Mann-Whitney) test. Below genes are significantly upregulated or downregulated in specific EC subtype in particular condition compared to non-tumour counterpart, unless otherwise stated between brackets against (versus (vs.)) specific condition). Genes were considered significantly upregulated or downregulated based on the threshold of Benjamini-Hochberg adjusted p values < 0.05. Conditions matched the colours in the violin plots in* ***Figure 5-32.***

EC subtype	Upregulated genes	Downregulated genes
Capillary type I	*Mgll* (early niche & early distal) *C36* (late distal vs. late niche & non-tumour) *Scp2* (early niche) *Hsd17d12* (late distal vs. early niche) *Srebf1* (late distal & early distal)	
Capillary type II		*C36* (late niche & early distal) *Elovl5* (late niche & late distal)
Arteries		*Gpihbp1, Cd36* (late niche vs. early niche)
Stressed ECs		*C36* (late niche vs. non-tumour & late distal)
Neophalanx/breach/tip ECs	*Srebf1, Gpihbp1, Cd36, Lpl, Elovl5* (late distal vs. late niche) *Plin2* (late niche & late distal)	

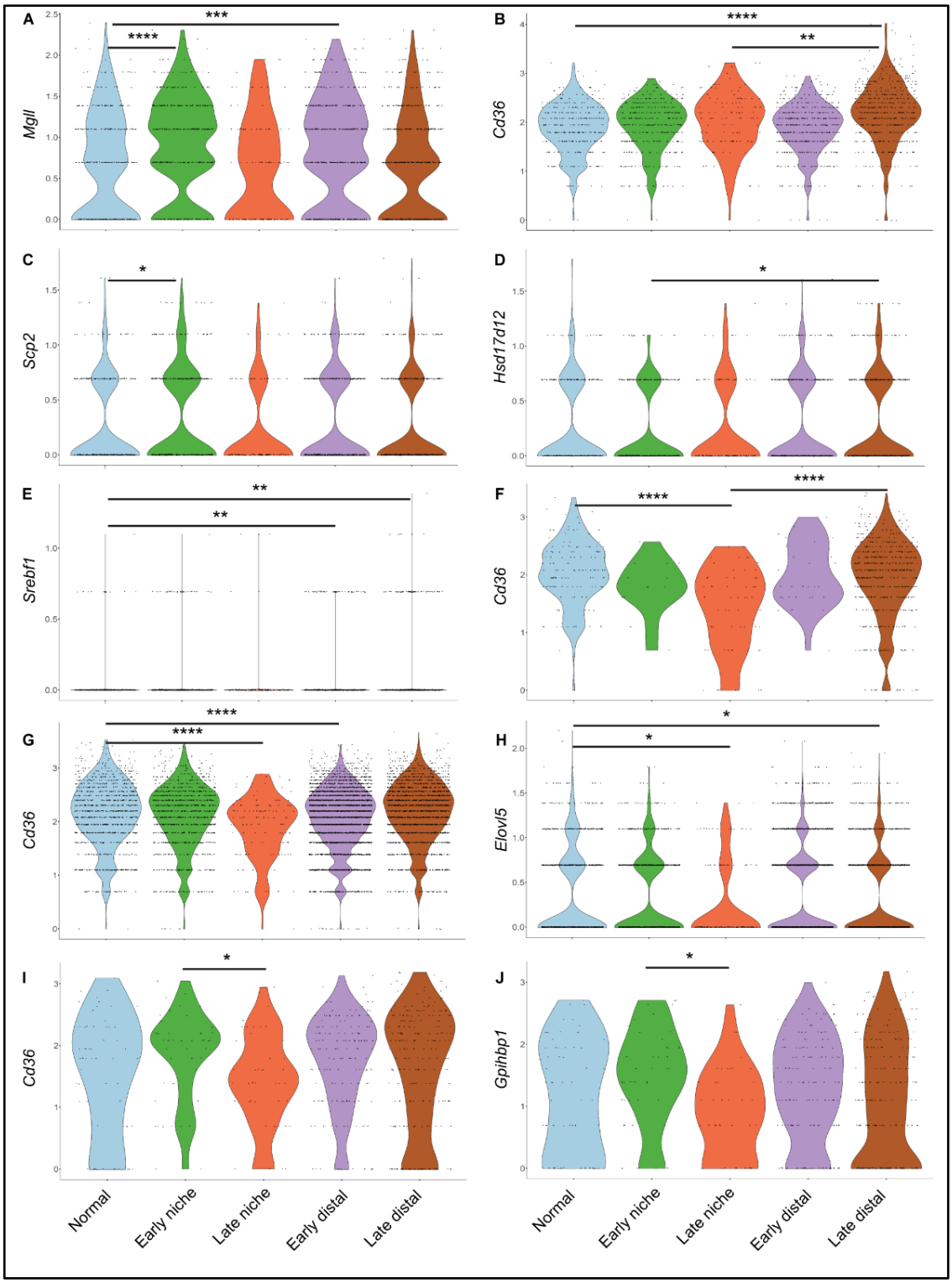

Figure 5-33. Different EC subtypes exhibited heterogenous expression of lipid-regulated genes across the five conditions: normal (healthy), early distal, early niche, late distal, and late niche of early and late metastatic lungs. *Violin plots in: A-E: depicting significantly upregulated genes in cap I ECs; F: depicting significantly downregulated gene in stressed ECs; G & H: depicting significantly downregulated genes in cap II ECs; I & J: depicting significantly downregulated genes in arteries across specified conditions as indicated in* ***Table5-5****. Differential expression analysis in pairwise-comparison fashion was performed using a non-parametric Wilcoxon (Mann-Whitney) test. Data points represent mRNA counts. P values were corrected using the false discovery rate (FDR) (Benjamini-Hochberg) procedure with a threshold of FDR < 0.05. (*: p ≤ .05; **: p ≤ .01; ***: p ≤ 0.001; ****: p ≤ 0.0001). The full names of these genes are shown in* ***The List of Abbreviations Table.***

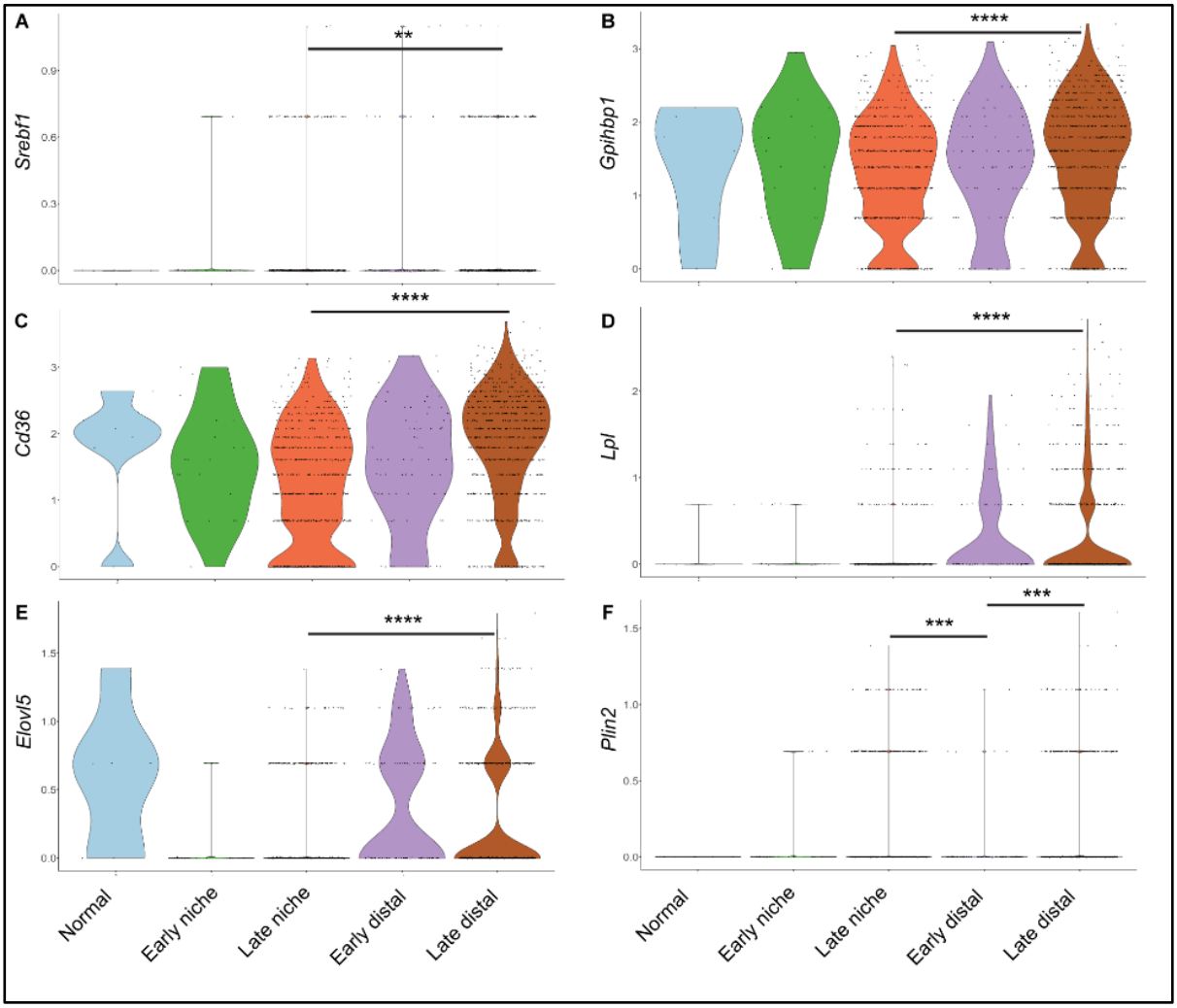

Figure 5-34. Neophalanx/breach/tip ECs upregulated specific lipid-regulated genes in late distal region in comparison to late niche. *A-F: violin plots depicting significantly upregulated genes in these ECs (Srebf1, Gpihbp1, Cd36, Lpl, Elovl5) in the late distal region, (Plin2) in both late niche and late distal regions compared to specified conditions. Differential expression analysis in pairwise-comparison fashion was performed using a non-parametric Wilcoxon (Mann-Whitney) test. Data points represent mRNA counts. P values were corrected using the false discovery rate (FDR) (Benjamini-Hochberg) procedure with a threshold of FDR < 0.05. (*: p ≤ .05; **: p ≤ .01; ***: p ≤ 0.001; ****: p ≤ 0.0001). The full names of these genes are shown in* ***The List of Abbreviations Table.***

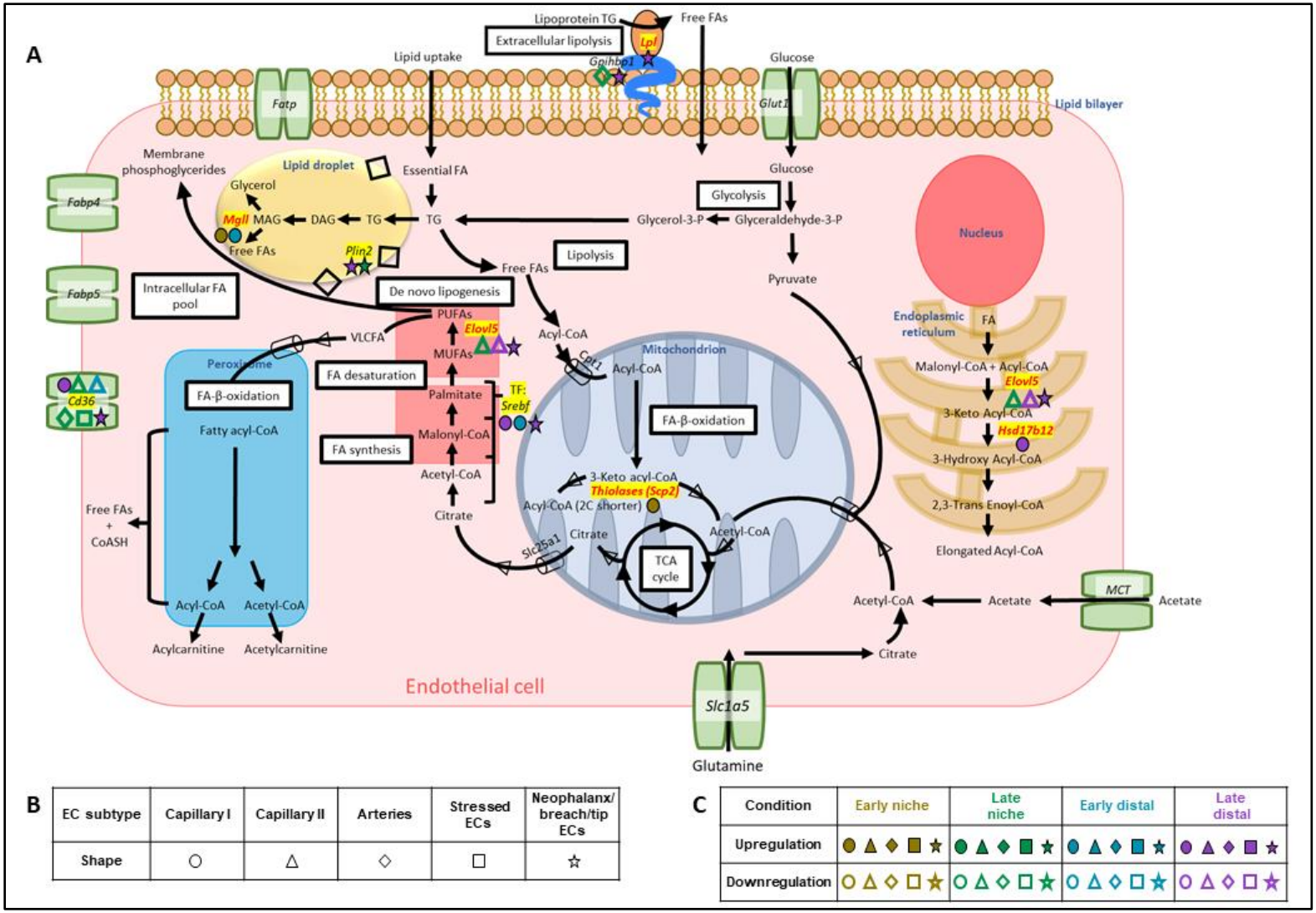

Figure 5-35.Remodelling of lipid metabolism in different EC subtypes in response to early and late E0771 metastatic growth. *A:upregulated lipid genes* ***(listed in Figure 5-33)*** *in different EC subtypes, including capillary type I, capillary type II, arteries, stressed ECs, and neophalanx/breach/tip ECs across the four conditions: early distal, early niche, late distal, and late niche of early and late metastatic lungs, respectively; B: each EC subtype is shape-coded; C: each condition is color-coded. The text in red depicts the enzymes involved. Text highlighted in yellow depicts disrupted genes in the EC subtype in the specified condition. Abbreviations of disrupted genes are shown in* ***The List of Abbreviations Table.***

5.4.2 Preliminary investigation of metabolic profiles of non-tumour, early, and late metastatic lung stroma using Raman spectroscopy

Sc-RNA-seq revealed the metabolic remodelling of EC subtypes during the development of metastases. Next, I aimed to study the metabolic changes in metastatic regions using Raman spectroscopy, and to assess whether they correlate with the transcriptomics data, to validate our findings using a different approach. Raman spectroscopy enables the identification of a biomolecular chemical fingerprint of cells and tissues with high spatial resolution (Xu et al., 2021b). ECs in these sections were labelled via immunofluorescence staining of the EC marker CD31; however dissecting Raman spectra of only ECs was challenging. To measure Raman spectra, lung tissue sections were not mounted, leading to tissue autofluorescence, and the fluorescence signal of CD31 was not sharp, requiring manual drawing of CD31+ vessels. Therefore, Raman measurement of the whole region of interest was taken. Raman spectral measurements from non-tumour, early and late metastatic regions were acquired over the molecular fingerprinting spectral range of 300–3100 cm^{-1} **(Figure 5-36).** Levels of saturated and unsaturated lipids were heterogeneous even in the same section **(Figure 5-37A)**. Preliminary Raman profiling and quantification demonstrated that with the progression of metastasis, unsaturated lipids increased (peaks at 1655 cm^{-1}), showing the highest average Raman spectra in the late niche and then reduced spectra in early niche and non-tumour stroma **(Figure 5-36, inset1**, **Figure 5-37C)**. In regards to saturated lipid (peaks at 2850 cm^{-1}), the highest average Raman intensity was in the early niche, and the lowest average intensity was in the late niche compared to normal lung stroma **(Figure 5-36, inset2, Figure 5-37B)**.

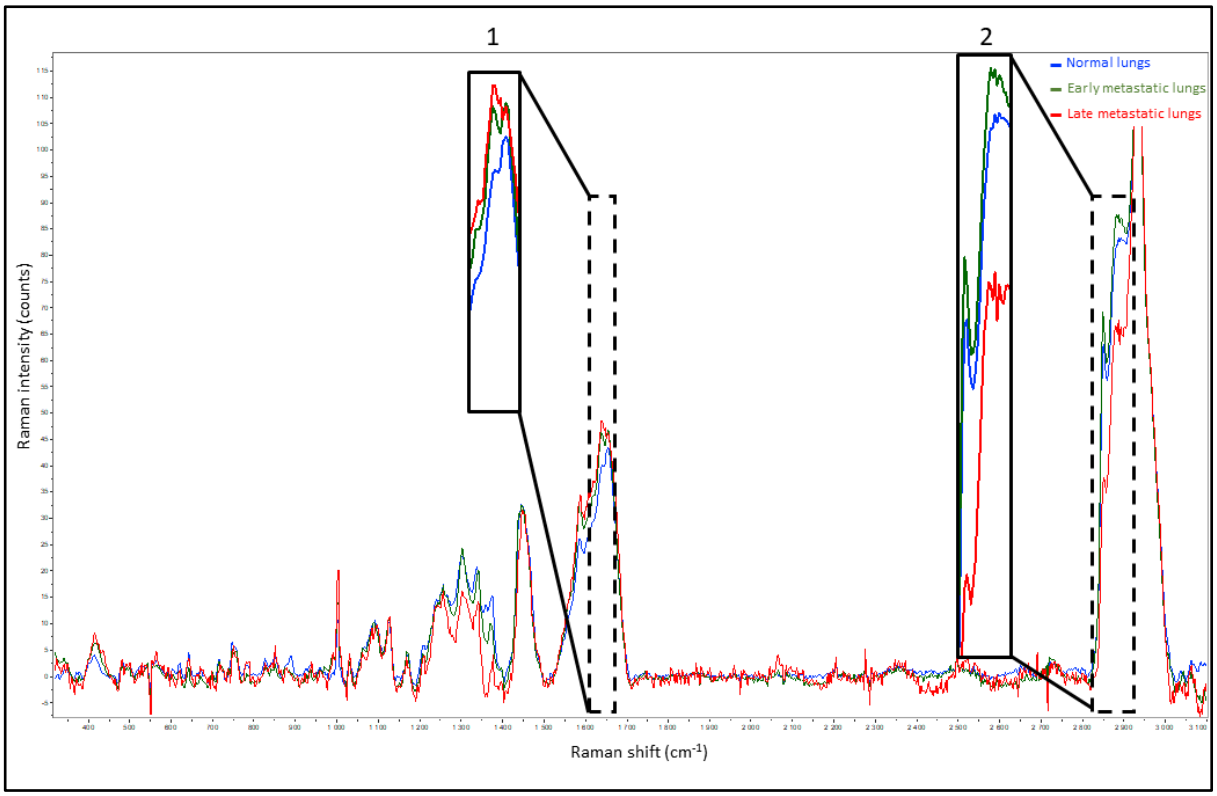

Figure 5-36. Raman signatures (tissue fingerprints) revealed an increase of saturated lipid in early metastatic lungs and an increase of unsaturated lipid in late metastatic lungs in comparison to normal (non-tumour) lungs*. Inset 1 depicts enlarged view of Raman peak intensities for non-tumour, early, and late metastatic lungs at 1655 cm-1 band representing unsaturated lipid. Inset 2 depicts enlarged view of Raman peak intensities for non-tumour, early, and late metastatic lungs at 1850 cm-1 band representing saturated lipid. Each line depicts average Raman spectrum acquired from 3 fields of view (three technical replicates) (scanned area of 50µm x 50µm) per mouse per condition. Spectral peaks were stacked for comparison purpose.*

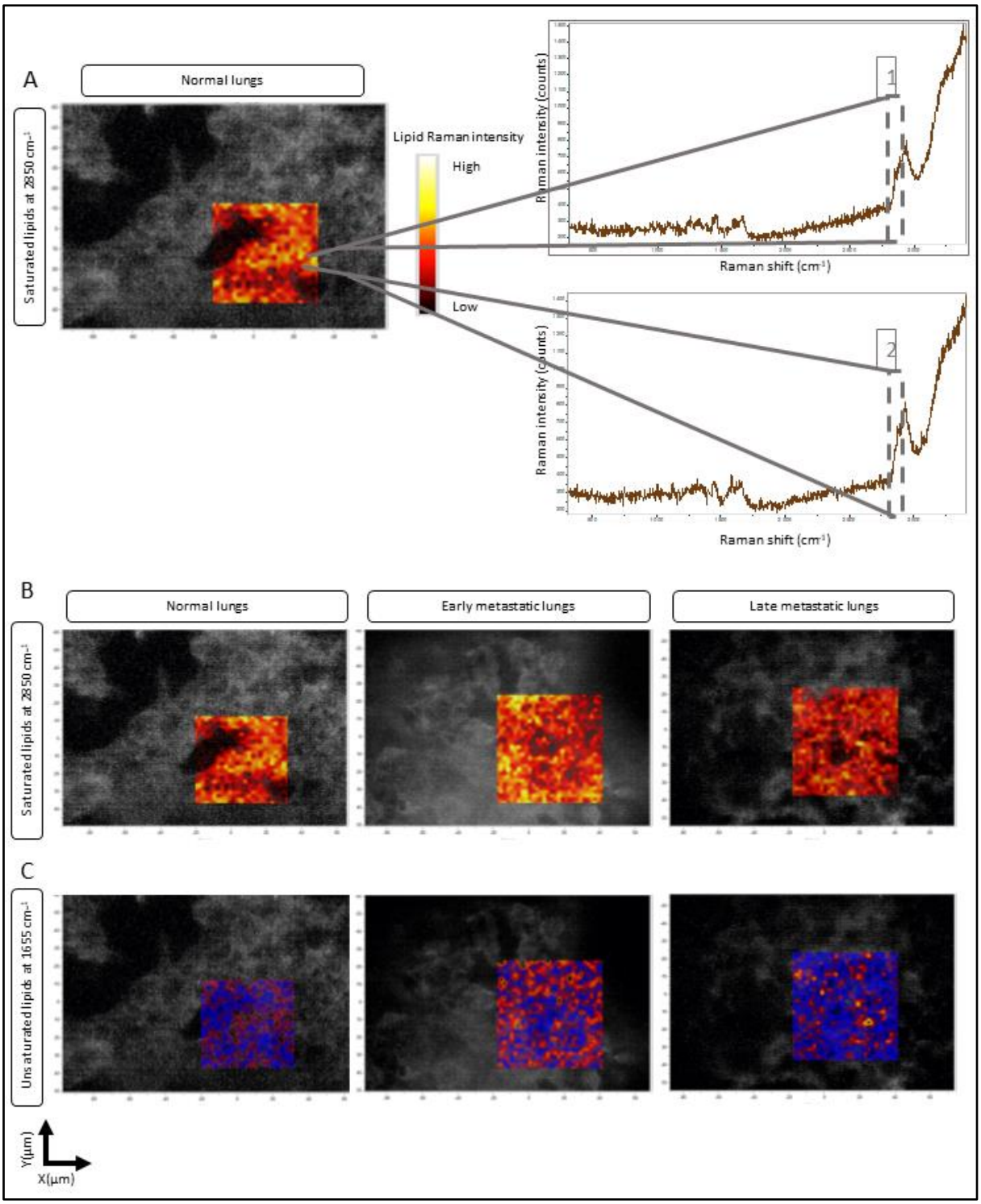

Figure 5-37. Heatmap visualization of Raman spectra revealed a spatial increase of saturated lipid in early metastatic lungs and a spatial increase of unsaturated lipid in late metastatic lungs in comparison to normal (non-tumour) lung. *A: heatmap of Raman spectra of representative field of view of normal lung section showing heterogenous Raman intensities of saturated lipid across the section. Inset 1 shows high and inset 2 shows low levels of saturated lipid; B and C: heatmaps of Raman spectra of representative field of views showing increased saturated lipid in early metastatic lungs compared to normal lungs (B) and increased unsaturated lipid in late metastatic lungs compared to normal lungs (C).*

5.4.3 The composition of EC subtypes in different mouse lung tumour models

After identifying EC subtypes and their transcriptional profiles in the early and late stages of E0771 lung metastases, I next investigated if other tumour types have a similar vascular response. EC subtypes of the E0771 lung metastatic model were compared to two published mouse tumour models: the RENCA lung metastasis model , and the primary Lewis (LLC) lung tumour model (Goveia et al., 2020), visualised as a composition plot **(Figure 5-38) (Table 5-6,**

Table 5-7, Supplementary TableS7).

During early (10 days) growth of RENCA metastases in lungs, EC subtypes were comparable in composition to EC subtypes in non-tumour-bearing lungs, with a slight increase in immature ECs and an emergence of proliferating ECs and TECs (Teuwen et al., 2021). Proliferating ECs increased at the late (21 days) stage of RENCA metastatic development and persisted following short sunitinib treatment (Teuwen et al., 2021). However, they showed sensitivity and were inhibited upon prolonged sunitinib treatment (sunitinib inhibits VEGFRs, PDGFR, and cKIT) (Teuwen et al., 2021). In contrast, the immature EC subtype was less sensitive to prolonged sunitinib treatment in RENCA metastases (therapy administered for 25 days) (Teuwen et al., 2021) **(Figure 5-38).**

In comparison to non-tumour-bearing lungs, LLC metastases were found to contain abundant pre-breach ECs, proliferating ECs, and TECs that persisted but with a reduction in abundance following DC101 and PTK787 treatments (Goveia et al., 2020) **(Figure 5-38)**. In E0771 metastases, specifically in the late niche, proliferating ECs, TECs, and lymphatic ECs emerged **(Figure 5-38)**.

E0771 lung metastasis showed no post-capillary veins, pre-breach, or immature ECs. Post-capillary veins increased in abundance in LLC tumour-bearing lungs following AAT therapies: DC101 (VEGFR2 antibody) and VEGFR tyrosine kinase inhibitor (PTK787) with a

significant reduction in tumour burden (Goveia et al., 2020) **(Figure 5-38)**. In RENCA lung metastases, post-capillary veins emerged and increased following prolonged sunitinib treatment, which coincided with a significant increase in tumour burden (Teuwen et al., 2021) **(Figure 5-38)**.

Cap I and II ECs were less abundant in late E0771 lung metastases and LLC lung tumours than RENCA lung metastases (Goveia et al., 2020) **(Figure 5-38)**. As shown in this chapter, in early E0771 metastases, IFN-Ag-presenting cap II increased and persisted to the late stage but reduced abundance in the late niche. In LLC lung tumours, this EC subtype was sensitive to DC101 and PTK787 therapies (Goveia et al., 2020) **(Figure 5-38)**.

Angiogenic ECs (Neophalanx-breach-tip ECs) were found to support the development of tumours in all three models: late (day13) E0771 metastases, late (day21) RENCA metastases, and primary LLC lung tumours. This EC subtype was sensitive to both DC101 and PTK787 and most sensitive to sunitinib (Goveia et al., 2020) (Teuwen et al., 2021) **(Figure 5-38)**.

In summary, EC subtypes differ in the three tumour models. These also showed individual heterogeneous sensitivity to AATs which target different molecules in the VEGF signalling pathway (Goveia et al., 2020) (Teuwen et al., 2021).

Table 5-6. Experimental details of three murine tumour models were used to isolate ECs for cell composition and transcriptional analysis*. The purple column provides details from (Goveia et al., 2020); the yellow column provides details from (Teuwen et al., 2021). EC: endothelial cells; NECs: normal ECs; TEC: tumour ECs.*

***In vivo* model**	**E0771 lung metastases**	**Primary LLC lung tumour**	**RENCA lung metastases**
Reference	This thesis	(Goveia et al., 2020)	(Teuwen et al., 2021)
Cell line injected	E0771 breast adenocarcinoma cells (1×10^6 cells)	Primary Lewis lung carcinoma (LLC) cells (1×10^6 cells)	Renal cancer cell line (RENCA) cells (2×10^5 cells)
Primary or metastatic	Breast cancer lung metastases	Primary lung tumours	Renal cancer lung metastases
Route of administration	Intravenous into the tail vein	Orthotopically into the parenchyma of the right lung through the rib cage	Intravenous into the tail vein
Mouse background	C57BL6/J mice	C57BL6/J mice	BALB/c mice
Endpoint+Vascularisation phenotype	On day 7 (vessel co-option), on day13	On day 10, it relies on angiogenesis	At day 21, it relies on 70%

	(vessel co-option and angiogenesis)		angiogenesis/30% vessel co-option. At day 21 (treated with 10-day sunitinib), relies on 70% vessel co-option/30% angiogenesis At day 36 (treated with 25-day sunitinib), relies on 75% vessel co-option/25% angiogenesis
Method of EC isolation	Using a niche labelling system (mCherry secreting tumour cells) that enables isolation of distal and niche ECs	Lung tumours were micro-dissected from lung tissue to isolate TECs. Lungs of control (non-tumour bearing) mice were used to isolate normal ECs	60 metastases were micro-dissected, and TECs were isolated. For NECs, control (non-tumour bearing) mice were used
Number of replicates per group	NECs: pooled 2 lungs Early distal ECs: pooled 4 lungs/early niche ECs: pooled 8 lungs Late distal ECs: pooled 3 lungs/late niche ECs: pooled 6 lungs	NECs: 2 replicates TEC: 3 replicates TEC treated with DC101: 3 replicates TEC treated with PTK787: 3 replicates	NECs: pooled 5 lungs TECs: pooled 60 lung metastases from 5 lungs

Table 5-7. EC subtypes in three murine tumour models. *The purple column provides details from (Goveia et al., 2020); the yellow column provides details from (Teuwen et al., 2021). EC: endothelial cells; IFN: Interferon. Black boxes indicate the absence of a specific EC subtype in a specific tumour model.*

EC subtypes in E0771 lung metastases.	**EC subtypes in primary LLC lung tumour**	**EC subtypes in RENCA lung metastases**
Capillary type I ECs	Capillary type I ECs	Capillary type I ECs
Capillary type II ECs	Capillary type II ECs	Capillary type II ECs
IFN-Ag-presenting capillary type II ECs	IFN ECs	
Veins ECs	Veins ECs (includes large vein)	Veins ECs
Arteries ECs	Arteries ECs (includes activated artery)	Arteries ECs
Lymphatic ECs	Lymphatic ECs	Lymphatic ECs
Neophalanx-breach-tip ECs	Neophalanx-breach-tip ECs	Tip ECs
Proliferating ECs	Proliferating ECs	Proliferating ECs
Tumour ECs	Tumour capillary ECs	Tumour capillary ECs
Stressed ECs		
	Post-capillary veins ECs	Post-capillary veins ECs
	Immature ECs	Immature ECs
	Pre-breach ECs	

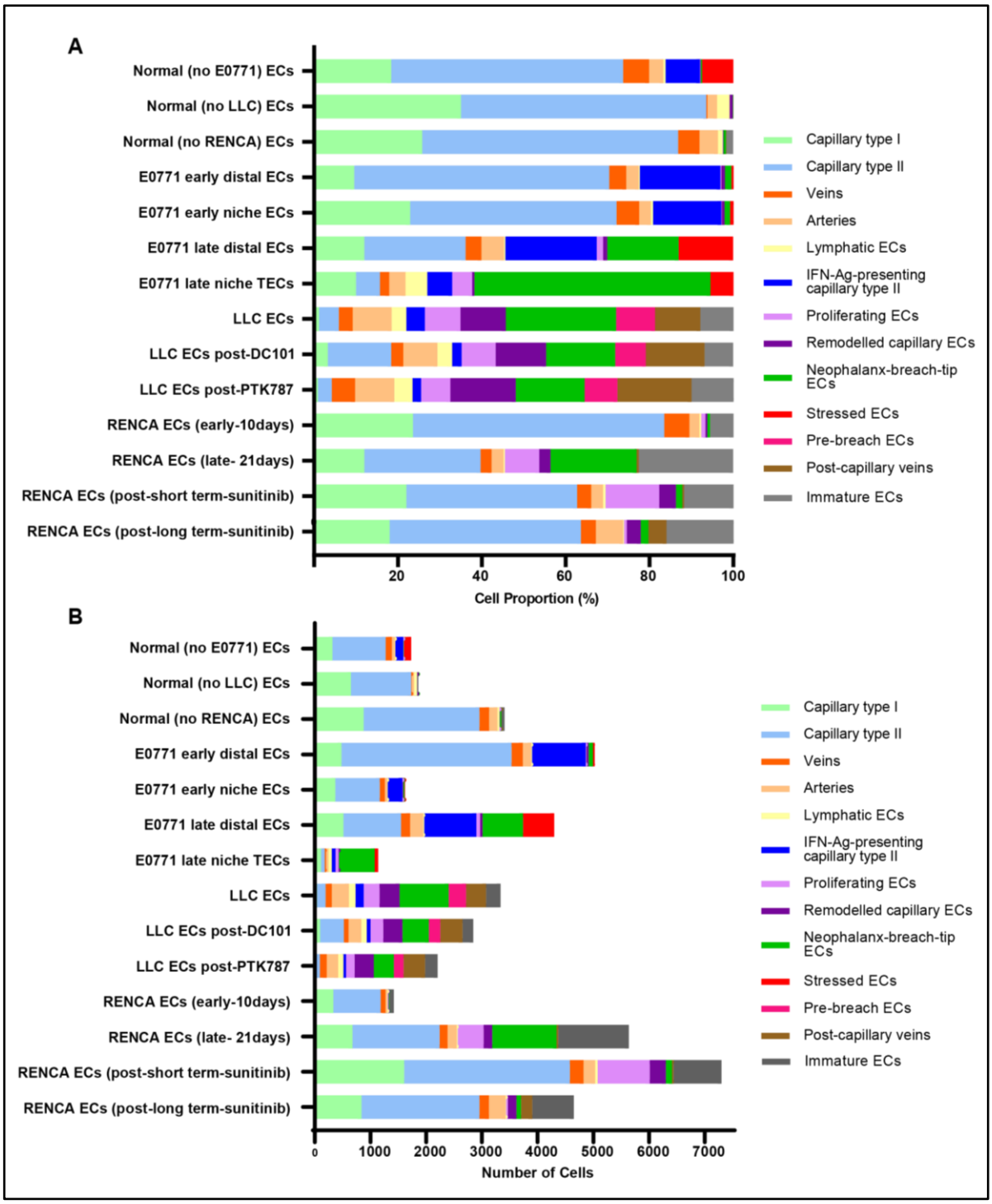

Figure 5-38. The congruency of EC subtypes in primary and metastatic lung tumours. *Short-term sunitinib means treatment administered for 10 days; long-term sunitinib means treatment administered for 25 days. EC composition of primary LLC lung tumour model from (Goveia et al., 2020); EC composition of RENCA lung metastases from (Teuwen et al., 2021). EC: endothelial cells; TEC: tumour ECs; LLC: Lewis Lung Carcinoma cells; RENCA: renal adenocarcinoma.*

5.5 Discussion

Investigating the transcriptomic changes of tumour-co-opted ECs has not yet to be extensively studied. Consequently, here I used an mCherry-labelling system (Ombrato et al., 2019) to spatially study the transcriptional changes of the tumour niche stroma at early and late stages of metastasis compared to distal regions and normal lungs.

A recent study using scRNA-seq of ECs isolated from a RENCA renal adenocarcinoma lung metastasis model found that the co-opted ECs are similar in gene profile to non-tumour ECs (Teuwen et al., 2021). However, this study and previous studies may have failed to capture the transcriptional changes in co-opted tumour ECs due to the difficulty of dissecting these ECs to sufficient purity. However, with the niche-labelling tumour cells (mCherry+), I was able to see that co-opted ECs in the E0771 model exhibited a transcriptional shift when compared to non-tumour ECs, and the genes are even different from the genes expressed in the distal region of the same lungs.

Reduction of EC tight junctions and activation of an immunomodulatory capillaries in early (non-angiogenic) metastases

A study by Jiang and colleagues demonstrated that metastatic breast cancer cells (4T1) injected into the mammary glands (primary site) were able to condition the pre-metastatic niche by downregulating *Tjp1* (*Zo-1*) and occluding junctions, which facilitated the extravasation of intravenous injected tumour cells (Jiang et al., 2016). Here, my data suggest that breast cancer cells (E0771) can also prime the metastatic niche upon their arrival, facilitating extravasation of lung capillaries and forming early metastases. Co-opted lung cap II ECs in the early niche facilitated tumour cell extravasation by significantly downregulating gene sets related to TJs, actin cytoskeleton, and focal adhesion such as *Tjp1*, *Actb*, and *Rap1b* compared to non-tumour cap II, thus increasing vascular permeability**.** This result warrant further investigation via quantification of TJP1 protein level in metastatic niche ECs and non-tumour lung ECs. This finding is consistent with other studies, where computed

Tomography Imaging of the 4T1 breast orthotopic model showed that co-opted vessels were leaky with high permeability (Ghaghada et al., 2011).

A subset of early niche (co-opted) and early distal cap II ECs in my scRNA-seq data was found to regulate the immune response early on via upregulation of the expression of MHC class II antigen-processing machinery and IFNγ-regulated genes**.** A study by (Goveia et al., 2020) also detected that both cap I and cap II ECs in human primary non-small cell lung cancer (NSCLC) upregulated genes involved in MHC-II antigen presentation, suggesting primary and secondary lung tumours induce similar capillaries remodelling responses.

Transcriptional changes of cap I ECs in early (non-angiogenic) metastases

The gene signatures of co-opted cap I and cap II were defined via pairwise differential expression analysis of these EC subtypes in early niche against the non-tumour, distal region, and late niche. Nine and eight DEGs were commonly upregulated in co-opted cap I and cap II, respectively, in early niche (mCherry+) compared to the other conditions. These commonly upregulated genes in co-opted cap I are illustrated in**.** Interestingly, *Car4*, a well-defined marker gene for cap I ECs, was overexpressed in E0771-tumour co-opted cap I ECs in the early niche. In the lungs, this enzyme is reported to localise to the luminal side of alveolar capillary endothelial cells, indicating its crucial role in gas exchange and pH and CO_2 homeostasis (Fleming et al., 1993). The role of the CAR4 enzyme expressed by lung capillaries has not been extensively studied, however previous studies found that this enzyme catalyses the dehydration of bicarbonate (HCO3−) to carbon dioxide (Klocke, 1980; Zhu & Sly, 1990). CAR4's function implicates its potential role in enhancing the respiration of co-opted capillaries, hence supporting early metastatic growth.

Crip1, Ecm1, Itm2b, Cyp1a1, and *Srgn* are other genes detected in the co-opted cap I. A single study reported that *Crip1* knockdown in HUVECs reduces EC migration and the number of branches in a tube formation assay, implicating its potential role in vessel formation (Streef et al., 2023). scRNA-seq showed that *Ecm1* was upregulated mainly in the early niche

and showed almost no expression in the non-tumour cap I. ECM1 is reported to have a role in angiogenesis and triggers EC proliferation, being expressed by human primary and secondary breast cancers (Han et al., 2001). Since *Ecm1* is expressed in the cap I ECs in early metastasis and continues to be expressed at lower abundance in late metastases **(Figure 5-25L),** it exemplifies a potential therapeutic target to block tumour growth from an early timepoint. ITM2B is reported to inhibit lung cancer proliferation by inhibiting PI3K/AKT pathway activation (Zhou et al., 2020). Whereas *Cyp1a1* and *Srgn* represent shear-stress-sensitive genes regulating EC response in atherosclerosis (Ma et al., 2020)

Co-opted cap I ECs also increased the expression of *Gstp1, Sap18, Dleu2, Pcdh1, Igfbp7, Id3,* and *Prx* when compared to non-tumour counterparts, and *Klf2, Tsc22d3* and *Rheb* when compared to the cap I in a distal region. Metabolically, we discovered that co-opted capillaries increased gene sets related to OXPHOS**.** Upregulation of *Gstp1*, could act as anti-oxidant defence system in the co-opted cap I, as it is reported to have an anti-oxidant role in protecting cells against oxidative stress and NO cytotoxicity (Russell & Richardson, 2023). Whereas SAP18 may suppress angiogenesis in the co-opted cap I as its reduction in Kaposi's sarcoma (KS) was found to be associated with the induction of EC migration and angiogenesis (Ding et al., 2019). KLF2, TSD22D3 and RHEB are also reported to have an anti-angiogenic role and to inhibit EC proliferation, respectively (Bhattacharya et al., 2005; Kanda et al., 2020; Xu et al., 2021c). While DLEU2 could contribute to EC survival as its downregulation in lung capillaries in hyperoxia-induced injury induces EC apoptosis (Wu et al., 2021). Other molecules, including PCDH1, IGFBP7, ID3, PRX, and RHEB are reported to regulate the EC barrier and EC junctions (Dilling et al., 2017; Gadomski et al., 2020; Gorbunova et al., 2016; Li et al., 2023; Wang et al., 2018).

Transcriptional changes of cap II ECs in early (non-angiogenic) metastases

Compared to the other conditions. the commonly significantly upregulated genes in niche co-opted cap II (mCherry+) are illustrated in **Figure 5-27.** Most of these genes represent metabolic genes that regulate OXPHOS. Co-opted cap II also increased the expression of

Gbp4, Malat1, Dleu2 and *Tra2a* when compared to non-tumour counterparts, and *Klf2, Mgp* and *Cav2* when compared to the cap II in the distal region. GBP4, MALAT1, KLF2 and CAV2 have been reported to inhibit EC proliferation and angiogenesis (Bhattacharya et al., 2005; Michalik et al., 2014; Razani et al., 2002; Weinländer et al., 2008). While MGP has a vascular protective role as it is found to reduce EC fibrosis by controlling collagen deposition (Kida & Yamaguchi, 2022). *Tra2a* is reported to increase the permeability of the blood-brain barrier by reducing tight junctions of microvascular ECs (Liu et al., 2020b), this mechanism seems to be activated in co-opted cap II in the early niche. The upregulation of *Tra2a* in co-opted cap II was consistent with the TJ reduction revealed by GSEA analysis.

Early niche (co-opted) capillaries differed from non-tumour capillaries

Using a different murine metastasis model (RENCA renal lung metastasis), a recent study found that vessel co-option is regulated by non-vascular cells, including matrix-remodelling macrophages and tumour cells themselves (Teuwen et al., 2021). Combination therapy with AATs and an immune checkpoint inhibitor was suggested to target vascular co-opting cancers (Teuwen et al., 2021). In contrast, using an E0771 breast cancer lung metastasis model, I found that co-opted capillaries showed a different transcriptome from non-tumour ECs. Co-opted capillaries were found to increase the expression of genes that induce vascular permeability, disturb EC junctions, inhibit proliferation and angiogenesis, promote EC survival, and have an anti-oxidant effect protecting these metabolically hyperactive capillaries during early development of E0771 metastases. My findings suggest that early development of lung metastases through vessel co-option can be inhibited via targeting the above upregulated genes. For instance, Norrin/Wnt surrogate antibody that has been shown to reduce permeability and restore EC barrier function in a mouse retinopathy model (Chidiac et al., 2021). Such antibody combined with chemotherapy could reduce spontaneous or therapy-induced co-opting metastatic tumour growth and limit tumour extravasation via restoring endothelial integrity, thus strengthening the EC junctions.

Transcriptional changes and EC subtypes emerged In the late (non-angiogenic and angiogenic) metastases

In late metastases, stressed ECs were most abundant in the late distal region (mCherry-) highly expressed unique genes: S*ertad1, Sox17, Pim3*, *Cdkn1a,* and *Cd36*. *Sertad1, Sox17,* and *Pim3* are reported to regulate the cell cycle, destabilise blood vessels and actin cytoskeleton, and induce angiogenesis, suggesting stressed ECs respond to E0771 tumour cells via conditioning the late distal area for expansion of angiogenic metastases, conversely, limiting excessive angiogenesis by upregulating *Cdkn1a* and *Cd36* in late distal cap I (Garbicz et al., 2020; Hu et al., 2019; Sunitha et al., 2019; Yang et al., 2013).

A neophalanx/breach/tip ECs cluster was detected in E0771 metastases. E0771 tumour cells were found to induce angiogenesis in both metastatic-distal and niche to help in cancer progression. Interestingly, both neophalanx/breach/tip and cap I ECs in the late niche condition upregulated glycolysis genes probably supporting angiogenesis occurring in the subpleural metastases. Recent evidence by (Rohlenova et al., 2020) has identified two metabolic enzymes, ALDH18A1 and SQLE, as potential targets to target tumour angiogenesis by impairing their metabolism. Targeting EC metabolism is a potential therapeutic strategy to reduce metastatic growth as a previous study revealed that genetic and pharmacological *in vivo* inhibition of a glycolytic activator, *Pfkfb3* was found to induce vessel normalisation and adhesion, reduce metastasis, tighten the EC junctions limiting tumour intravasation, and enhance the delivery of chemotherapy (Cantelmo et al., 2016). I investigated the origin of these angiogenic ECs via performing trajectory analysis, which produces branched trajectories inferring cells differentiating (transitioning) to multiple lineages. Single-cell trajectory analysis inferred that the potential origin of angiogenic ECs was either cap I or cap II**.** It is important to bear in mind the possible bias in this analysis, as it requires prior selection of a single EC subtype as the root (start) point of differentiation (cap II was selected as the root of the trajectory) overlooking the potential of other origins which includes cap I. Cap II ECs were selected because, along with cap I ECs, they constitute the primary vascular

network of the lungs. Also, our transcriptional study captures cellular composition throughout metastasis evolution, starting from non-tumour-bearing to early-stage to late-stage metastatic growth, which aided in identifying capillaries as the root ECs.

EC subtypes from early and late metastases exhibited heterogenous lipid metabolic profiles

Different EC subtypes exhibited heterogeneous remodelling in lipid metabolism at early and late stages of metastasis synthesis. Co-opted cap I in the early niche upregulated the expression of *Scp2* (involved in vascular inflammation, intermembrane lipid transfer, regulation of lipid peroxidation, increases cellular fatty acid uptake, and activates oxidation and esterification of straight-chain and branched-chain fatty acids) (Guillou et al., 2010; Xu et al., 2022). *Mgll* expression was also upregulated in cap I in early niche and early distal region (MGLL catalyses the conversion of monoacylglycerides to free fatty acids (FFAs) and glycerol), suggesting their reliance on energy production from FAs (Nomura et al., 2010). Cap I cells in the late niche, and the late distal region also increased the expression of Cd36, which was previously identified for its high affinity for fatty acids (FAs) uptake, its transportation of long-chain fatty acids (LCFAs), and its anti-angiogenic activity suggesting cap I ECs-expressing *Cd36* fuel ECs but limited angiogenesis in the late distal area (Liao et al., 2022; Son et al., 2018).

Cap II ECs downregulated the expression of *Cd36* in the early distal and late niche and *Elovl5* in the late niche and late distal region compared to its non-tumour counterpart. ELOVL5 regulated lipid metabolism by catalysing the first reaction in the fatty acids elongation cycle (Guillou et al., 2010).

Arteries downregulated *Gpihbp1* (involved in lipolytic processing of triglyceride-rich lipoproteins) and *Cd36* in the late niche when compared to co-opted arteries (mCherry+) present in the early niche (Beigneux et al., 2009). GPIHBP1 was previously revealed to be expressed by glioma capillaries providing lipid nutrients to glioma cells through binding to

lipoprotein lipase (LPL), which in turn causes lipolysis of triglyceride-rich lipoproteins (Hu et al., 2019). Although GPIHBP1 is reported in the literature to be only expressed by capillaries, not large vessels (Davies et al., 2010), our scRNA-seq data revealed its expression in veins and arteries but with higher expression observed in capillaries **(Appendix G1).** We found *that Gpihbp1* expression was significantly reduced in the late niche compared to the early niche, reflecting arteries in the late niche being less reliant on GPIHBP1 as a source of nutrients.

In late distal (mCherry-) regions, neophalanx/breach/tip ECs upregulated *Srebf1, Gpihbp1, Cd36, Lpl,* and *Elovl5* compared to late niche**.** SREBF1 is reported to regulate the transcription of genes involved in lipogenesis and enzymes of glycolysis (Fatehi-Hassanabad & Chan, 2005). It is a TF that contributes to synthesising cholesterol and unsaturated fatty acids and induces cancer proliferation by incorporating accumulated lipids (Guo et al., 2014; Horton et al., 2002). These upregulated genes as shown above regulate lipogenesis, reliance on lipid nutrients, anti-angiogenic effect, and lipolysis, reflecting angiogenic ECs in the distal region of advanced metastases rely on FAs as a source of nutrients and energy.

scRNA-seq analysis revealed an upregulation of *Plin2* in neophalanx/breach/tip ECs in late niche and late distal region compared to other conditions. PLIN2 constitutes a structural protein-coating lipid droplet that is reported to be upregulated in several cancers, promoting cell proliferation, and preventing apoptosis and ferroptosis (Heid et al., 1998; Luo et al., 2022). A previous study found that PLIN2 is highly expressed in CD68+ tumour-associated macrophages of oral squamous cell carcinoma (OSCC), specifically in tumour centres and invasive front inducing immunosuppression. Its upregulation was correlated with a higher postoperative metastasis rate and poor survival (He et al., 2022). Our study revealed the spatial expression of upregulated *Plin2*, which was found in late niche ECs (mCherry+), suggesting its potential function in inducing angiogenesis in late metastasis.

Label-free Raman microscopy demonstrated a spatial increase in saturated lipids in early metastatic lungs and a spatial increase in unsaturated lipids in late metastatic lungs compared to non-tumour lungs**.** Unsaturated lipid is linked to protecting cells against saturated lipotoxicity

and ER stress and polarising myeloid cells to M2-like TAMs (Kuo et al., 2017; Williams et al., 2013; Wu et al., 2019). Late metastases are characterised by hypoxia and angiogenesis. We found that the lipid transport receptor, Cd36, regulated angiogenesis in late metastasis in a spatial and EC subtype-specific manner. The upregulation in lipid transport receptors (Cd36) in neophalanx/breach/tip ECs found by transcriptional analysis**,** along with an upregulation of unsaturated lipid found by Raman analysis suggests that angiogenic ECs uptake these unsaturated lipids from an exogenous source through CD36 facilitating membrane synthesis. However, in addition to *Srebf1* and *Hsd17b12, Cd36* was also upregulated in the cap I present in the late distal region**.** CD36 null mice were reported to have bigger tumours with increased angiogenesis compared to wild-type mice, indicating the anti-angiogenic role of Cd36 mediated by binding to thrombospondin-1 (THBS1/TSP-1) (Hale et al., 2012). HSD17B12 is an enzyme that contributes to the elongation of polyunsaturated fatty acids (PUFAs), such as arachidonic acid (Guillou et al., 2010). Arachidonic acid was reported in an *in vitro* culture system to reduce EC migration and adhesion via incorporation into cell membranes, thus reducing EC viscosity (Rossen et al., 2011). Upregulated expression of *Cd36, Hsd17b12,* and *Srebf1* suggests an accumulation of lipids in cap I cells for membrane remodelling with an anti-angiogenic phenotype tightly controlling angiogenesis in the late distal region. Our data is similar to those reported by a recent study by (Geldhof et al., 2022), where they identified lipid processing ECs that highly express CD36 in the periphery of human primary breast cancer tissues. However, the lipid-processing EC detected was cap II ECs, which was found to upregulate the TF, peroxisome proliferator-activated receptor gamma (PPAR-γ or PPARG). Early, hormone receptor-positive/HER2-negative BC patients treated with metformin (which is an indirect activator of PPAR-γ) were found to have increased lipid processing vessels than metformin-untreated patients, and this correlated with long-term clinical benefits (Geldhof et al., 2022). Comparing this study to our findings demonstrated that lipid-processing ECs emerge in primary and metastatic tumours but are regulated by different lipid-regulated genes. The presence of ECs highly expressing lipid-regulated genes in the distal region of metastatic context requires further validation in human metastatic disease.

Slight differences in EC composition among different mouse lung tumour models

Comparing EC subtypes in E0771 lung metastases to published primary LLC lung tumour and RENCA lung metastasis models demonstrated different vascular phenotypes (Goveia et al., 2020; Teuwen et al., 2021)**.** Ag cap II ECs may modulate an immune response during early development of E0771 metastases, and neophalanx-breach-tip ECs, proliferating ECs, and lymphatic ECs modulated the late angiogenic stage of E0771 metastasis. Whereas, in LLC lung tumours, several tumour EC subtypes emerged in comparison to non-tumour lungs, including immature ECs, post-capillary veins, pre-breach ECs, neophalanx-breach-tip ECs, TECs, and proliferating ECs. Upon administration of DC101 and PTK787 AATs, all tumour EC subtypes were reduced except post-capillary veins, which were less sensitive and increased abundance. This subtype upregulated the expression of HEV marker genes (Goveia et al., 2020). In other studies, it is reported that high endothelial venules (HEVs) create an anti-tumour microenvironment enhancing T-cell infiltration and activation (He et al., 2020; Johansson-Percival et al., 2017), which could explain the significant reduction of tumour burden in LLC tumour-bearing lungs following AATs administration. Post-capillary veins have been reported to give rise to immature ECs, tip cells, and neophalanx ECs (Rohlenova et al., 2020). Thus, the increase of post-capillary veins in LLC tumours following AAT treatments could also provide an alternative angiogenic route and serve as a source of angiogenic ECs. In RENCA metastases, emerging tumour EC subtypes include immature ECs, tip cells, TECs and proliferating ECs. The former two EC subtypes were sensitive to short sunitinib treatment, whereas the latter was less sensitive and increased in abundance. Interestingly, post-capillary veins emerge upon prolonged (36 days) sunitinib treatment, which could contribute to vessel co-option that causes persistent RENCA metastatic overgrowth. The emergence of post-capillary veins in primary LLC lung tumours and secondary RENCA metastases following ATT treatments with differential effects on tumour burden could indicate a differential response of post-capillary veins either modulating anti-tumour response and pro-angiogenic response or supporting a vascular switch to vessel co-option (Goveia et al., 2020; Teuwen et al., 2021).

Tip ECs are markedly inhibited in RENCA metastases upon short and long sunitinib treatment, with increased cap I and II that might cause a vascular switch to vessel co-option (Teuwen et al., 2021). Based on the above tumour models, induction of HEVs, targeting co-opted vessels, or combination therapy of AAT and immune checkpoint inhibitors represent potential therapeutic strategies for targeting early and late metastatic disease.

Limitation of the study

In tumour-bearing lungs, upon the arrival of genetically engineered mCherry-labelling hCD2 E0771 tumour cells in the lungs, they release mCherry to label nearby metastatic niches (the lung stroma). FACS analysis showed that some lung cells in non-tumour lungs were autofluorescent and overlapped with the mCherry signal. This means that mCherry positive niche cells FACS-sorted for scRNA-seq experiment also contained autofluorescent cells. To limit sorting of autofluorescent cells, FACS gating was narrowed. Although distinguishing mCherry signal from autofluorescence was not possible, the percentage of autofluorescent cells was very small (0.083%) in the non-tumour lung cells.

To summarise, this chapter illustrates the distinct transcriptomic and metabolic signatures of EC subtypes in early (co-opted ECs) and late (both co-opted and angiogenic ECs) metastases. In early (non-angiogenic) metastases, capillaries reduced their tight junctions, increased their OXPHOS metabolism, and activated a subset of capillaries to express IFN and MHC II genes. Whereas late (non-angiogenic and angiogenic) metastases increased the glycolysis metabolism of pre-existed capillaries, induced the formation of angiogenic ECs in both late niche and distal regions, and switched the transcriptome of a subset of ECs in the late distal region into stressed ECs. Our E0771 model and previous models demonstrated that different tumour origins, whether primary or metastatic or early or late stage, could contribute to the EC subtypes that emerged in these tumour models and human lung tumours (Geldhof et al., 2022; Goveia et al., 2020; Rohlenova et al., 2020; Teuwen et al., 2021). These EC subtypes were of: 1) different maturation statuses some of which were co-opted and pre-existing, others with actively proliferating EC, 2) have different

metabolic signatures, 3) some mediate immune response, all of which contribute to pathogenesis, response to therapy, and should be considered when targeting tumour growth and metastatic progression. Our findings and previous studies warrant further investigation into targeting EC metabolism to inhibit tumour vascularisation, growth, metastasis, and orthogonal validation in human primary and metastatic tumours.

Chapter 6: Investigating the single-cell transcriptome and cell signalling between metastatic niche lung stromal cells and E0771 tumour cells

6.1 Introduction

In the previous chapter, I investigate the distinct vascular EC composition, and the transcriptional and metabolic changes, that occur in ECs during E0771 metastases, comparing early (vessel co-opting) and late (angiogenic plus vessel co-opting) metastatic stages. In this chapter, I am now interested in exploring the molecular changes and the instructive signalling that occur in the metastatic niche stroma neighbouring metastatic E0771 breast cancer cells, and therefore involved in driving co-opting and angiogenic metastases. To investigate this, gene expression analysis of scRNA-seq data of lung non-immune stromal cells of non-tumour, early (niche and distal), and late (niche and distal) metastatic E0771 lungs was conducted (utilizing the data from the scRNA-seq discussed in the previous chapter). In particular, here I focus on analysis of cell-cell communication, investigating overall lung stromal cells and E0771 tumour cells from all timepoints.

6.2 Heterogeneity in non-immune stromal cells driving the evolution from E0771 micrometastases to established metastases

To identify non-immune stromal subtypes across all five experimental conditions, the five scRNA-seq datasets of non-tumour, early, and late time points were merged. Dimensionality reduction was performed on the merged scRNA dataset using principal components analysis (PCA), and the first 20 PCs were included in the downstream analysis **(Figure 6-1A).** Generating a clustering tree (graph structure), a clustering resolution of 0.5 was stable and selected, which gave rise to 21 clusters that were annotated into 17 cell subtypes **(Figure 6-1A, Figure 6-2A).** An unsupervised clustering of lung cells was performed. One cluster (annotated as a low-quality cluster) was removed prior to further analysis due to a lack of unique genes, a low number of detected genes, and a high expression of ribosomal genes **(Supplementary TableS3)**. The cell clusters were visualized by the UMAP method **(Figure 6-2A)**. These lung clusters across the five conditions comprise 30,525 lung cells **(Supplementary TableS4)**. They were annotated based on the top 50 differentially expressed genes in each cluster along with manual curation using gene sets in several publications **(Table 6-1) (Supplementary TableS5).** The annotation was as follows: vascular cells (mainly ECs) including capillary type I and type II ECs, vein ECs, stressed ECs, neophalanx/breach/tip ECs, SMCs/pericytes **(Figure 6-3)**; mesothelial cells and fibroblasts including mature mesothelial cells, cancer-associated mesenchymal cells (CAMCs), EBF1-positive fibroblasts, interstitial fibroblasts, lipofibroblasts, myofibroblasts **(Figure 6-4)**; epithelial cells including type II pneumocytes, ciliated epithelial cells, E0771 tumour cells; and erythroid cells **(Figure 6-5).** The top five marker genes of each annotated cluster were identified and visualized by UMAP plots **(Figure 6-3, Figure 6-4, Figure 6-5)** based on the following thresholds: (i) log2 fold change of 0.25 and above; (ii) percentage of cells where the gene is detected in a particular cluster (min.pct) of 0.25 and above; and (iii) adjusted p-value of less than 0.05 **(Supplementary TableS5)**.

scRNA-seq data showed that the composition of lung stromal cells changed during the development of metastases. In early-metastatic lungs, mature mesothelium and ciliated epithelial cells increased in number in the niche areas (mCherry+) compared to normal lungs. In contrast, erythroid cells were abundant in distal areas (mCherry-) of early metastases **(Figure 6-2E, F).** On the other hand, in late-metastatic lungs, neophalanx/breach/tip ECs and CAMCs were enriched in the niche (mCherry+) whereas stressed ECs were increased in distal areas (mCherry-) compared to normal stroma **(Figure 6-2E, F)**. Due to the characteristic of tumour cells being adhesive, they adhered to stromal cells during FACS sorting and sequencing. Indeed, scRNA-seq data detected a cluster annotated as E0771 tumour cells only in the late niche **(Figure 6-6).** They were confirmed to be E0771 tumour cells based on the expression of both *mCherry* and *hCD2* (both genes were part of the lentiviral vector E0771 tumour cells transduced with) **(Figure 6-6, Figure 2-1 in Chapter 2)**. Overall, fibroblast subpopulations were found to be reduced in both early and late metastatic lungs in comparison to normal stroma, except EBF1-positive fibroblasts increased in the early niche and interstitial fibroblasts that persist in the late niche but to a lesser abundance **(Figure 6-2E, F)**.

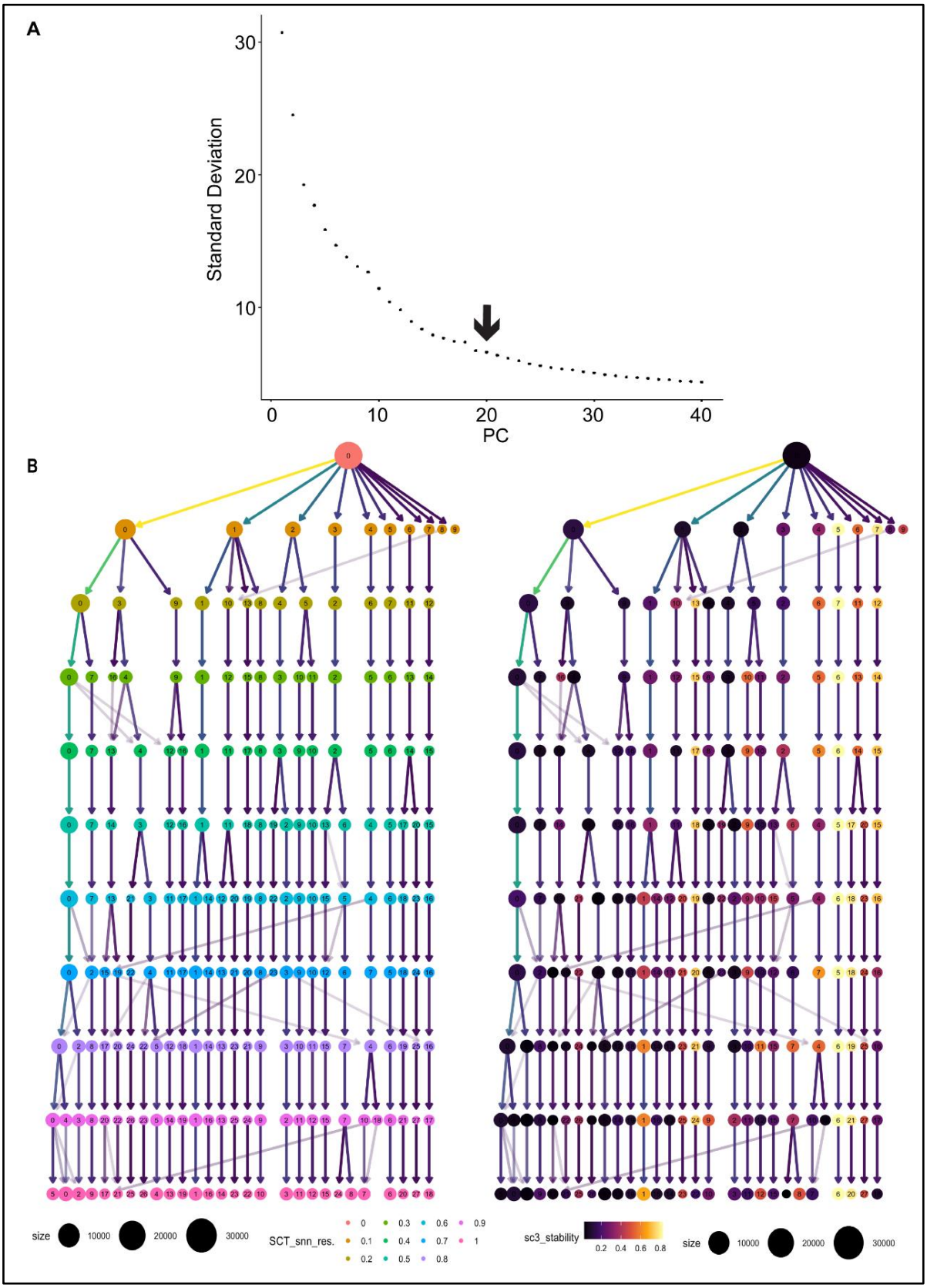

Figure 6-1. Principal components (PCs) and clustering resolution selected for further downstream analysis of scRNA-seq data. *A: Elbow plot plotting standard deviation of principal components. An elbow (black arrow) was observed to be around PC20; therefore, the first 20 PCs were suggested to contain the majority of variance; B: clustering tree grouping cells that are similar across different clustering resolutions. A clustering resolution of 0.5 was selected for further analysis.*

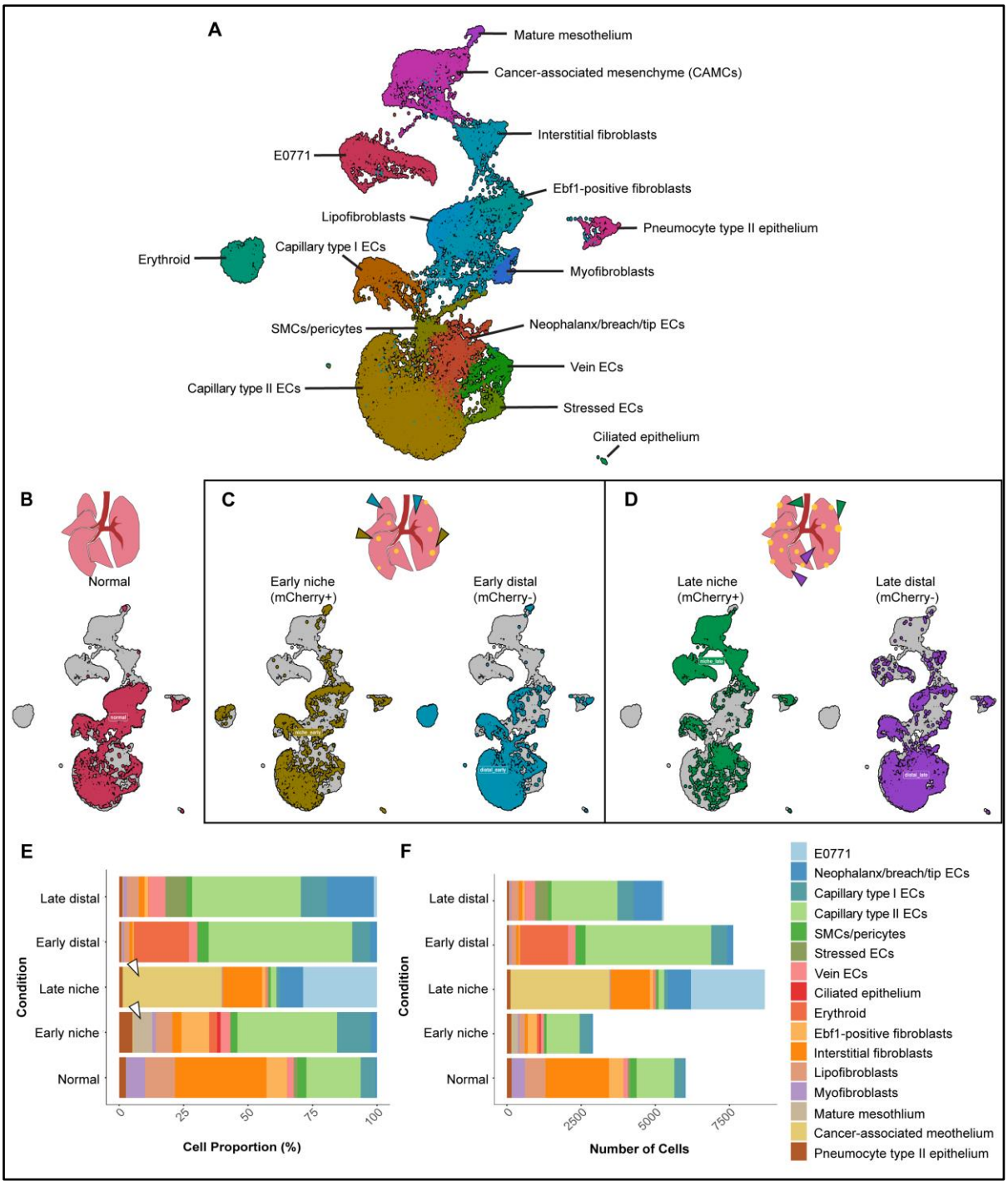

Figure 6-2. Non-immune stromal cells from healthy lungs, early, and late E0771 metastatic mouse lungs revealed stromal heterogeneity during metastatic development in the lungs*. A: unsupervised clustering visualized as Uniform Manifold Approximation and Projection (UMAP) identified 21 clusters that were annotated to 17 cell types across all five conditions. Cell clusters were annotated by manual curation of previous studies and based on the top 50 differentially expressed (DE) marker genes. Five UMAP projection plots of lung stromal clusters splitting all five conditions: B: normal (healthy); C: early distal region (turquoise arrowheads), early niche (cumin arrowheads); D: late distal region (purple arrowheads), and late niche (green arrowheads) conditions of E0771 metastatic lungs, respectively; E and F: relative (percentage) and absolute cellular composition of lung stromal cells across the five conditions with white arrowheads depicting the enrichment of mature mesothelium in early niche and cancer-associated mesenchymal cells (CAMCs) in late niche. ECs: endothelial cells; SMCs: smooth muscle cells; EBF1: early B-cell factor 1.*

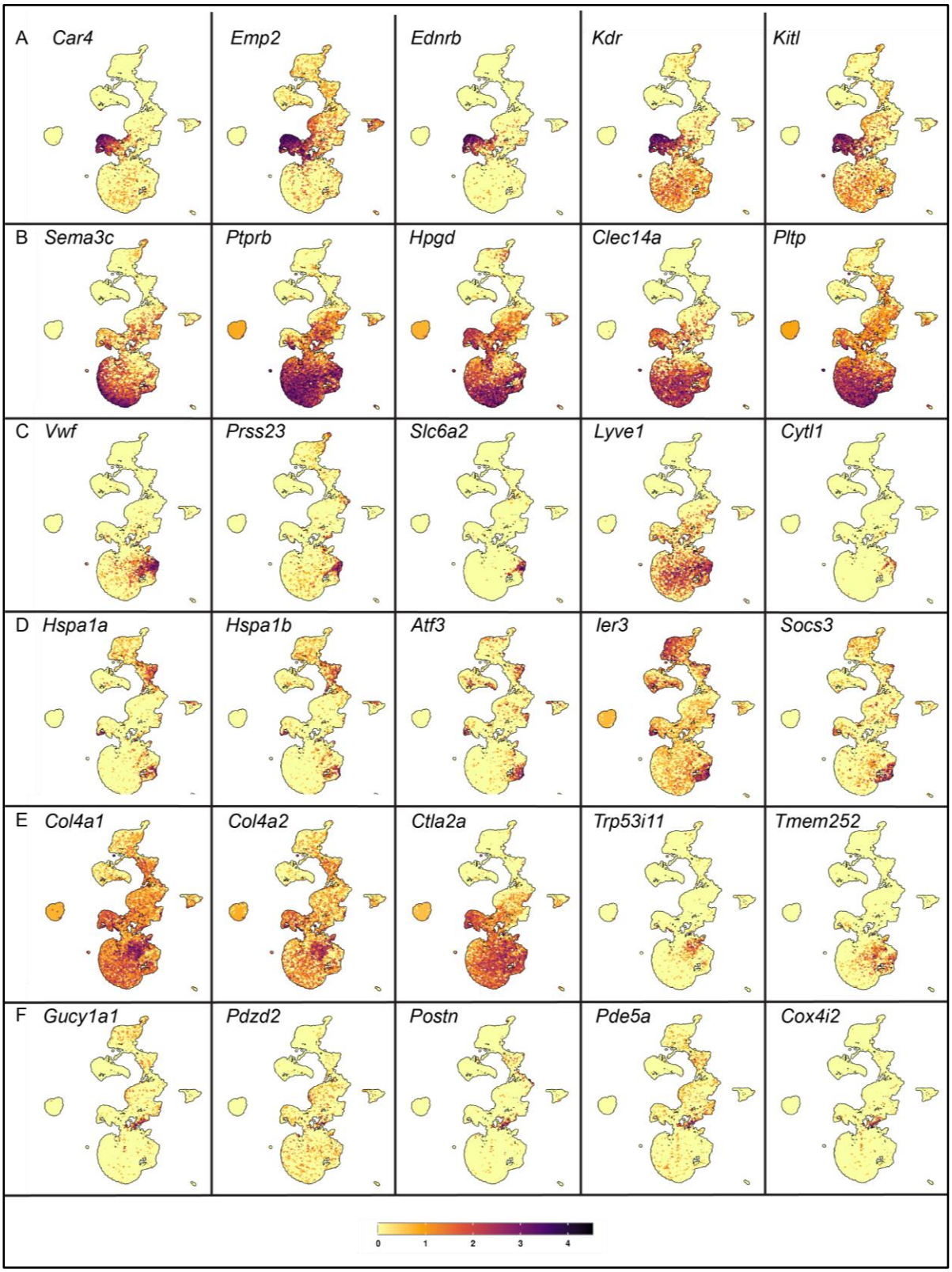

Figure 6-3. UMAP plots of top five marker genes for EC subtypes from healthy, early, and late E0771 metastatic mouse lungs. *A: top five marker genes of capillary type I ECs; B: top five marker genes of capillary type II ECs; C: top five marker genes of veins; D: top five marker genes of stressed ECs; E: top five marker genes of neophalanx/breach/tip ECs; F: top five marker genes of SMCs/pericytes. These top marker genes were identified based on log2 foldchange of 0.25, min.pct of 0.25, and adjusted p-value <0.05. The full names of these genes are shown in* ***The List of Abbreviations Table.***

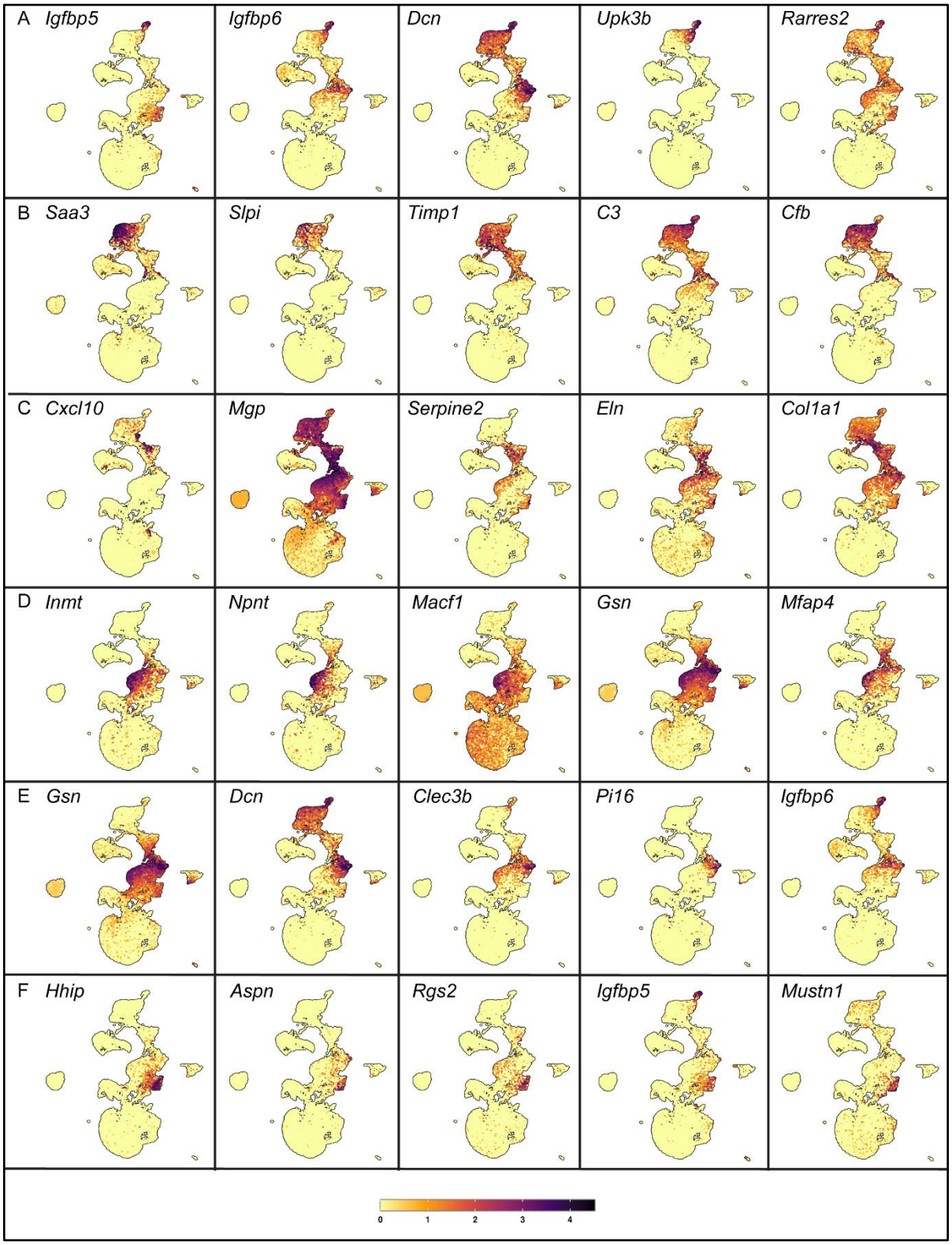

Figure 6-4. UMAP plots of top five marker genes for fibroblast and mesothelial subtypes from healthy, early, and late E0771 metastatic mouse lungs. *A: top five marker genes of mesothelial cells; B: top five marker genes of cancer-associated mesenchymal cells (CAMCs); C: top five marker genes of interstitial fibroblasts; D: top five marker genes of lipofibroblasts; E: top five marker genes of early B cell transcription factor 1 (EBF) positive fibroblasts; F: top five marker genes of myofibroblasts. These top marker genes were identified based on log2 foldchange of 0.25, min.pct of 0.25, and adjusted p-value <0.05. The full names of these genes are shown in* ***The List of Abbreviations Table.***

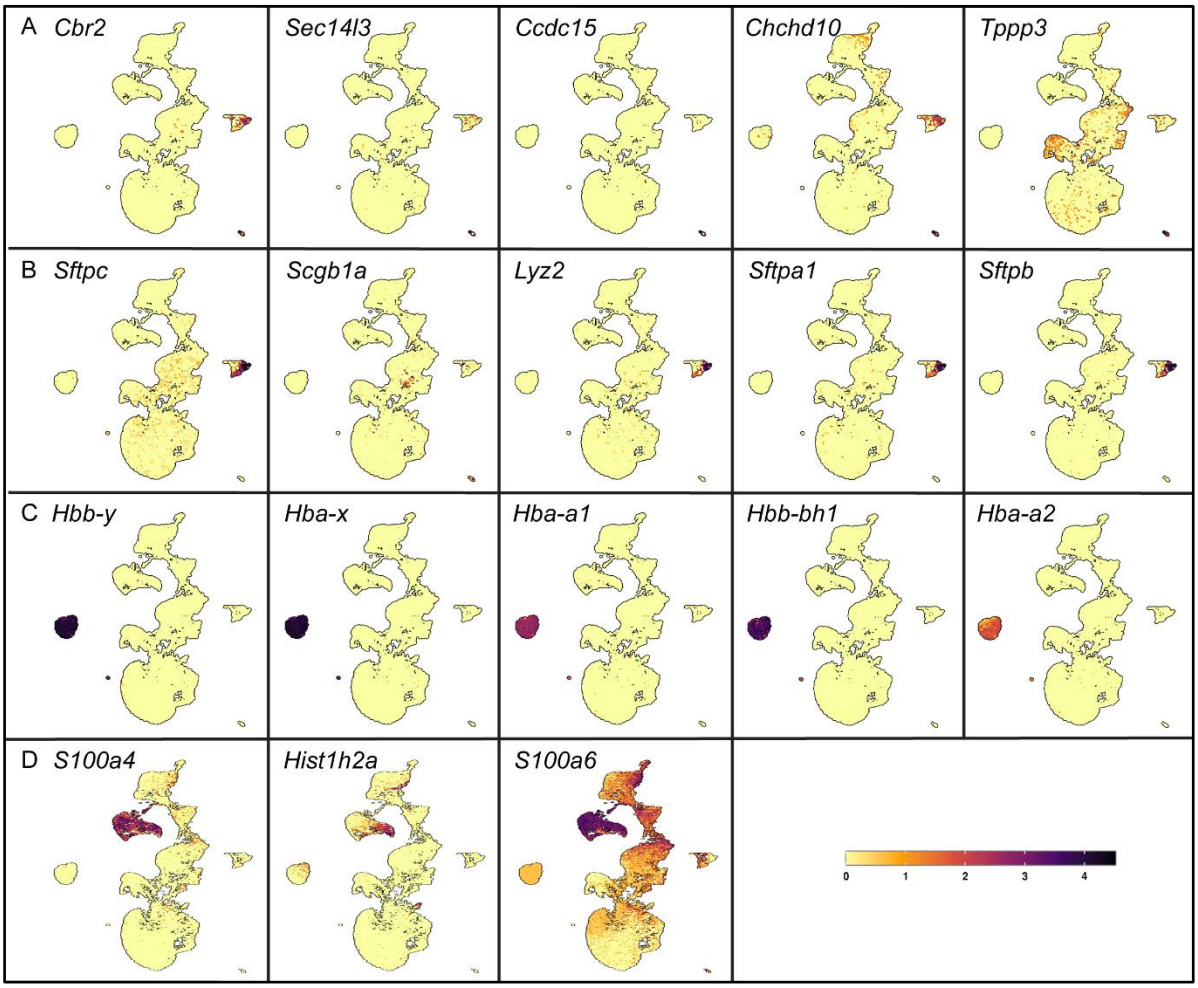

Figure 6-5. UMAP plots of top marker genes for epithelial subtypes and erythroid cells from healthy, early, and late E0771 metastatic mouse lungs*. A: top five marker genes of ciliated epithelial cells; B: top five marker genes of pneumocytes type II; C: top five marker genes of erythroid cells; D: top three marker genes of E0771 tumour cells. These top marker genes were identified based on log2 foldchange of 0.25, min.pct of 0.25, and adjusted p-value <0.05. The full names of these genes are shown in* ***The List of Abbreviations Table.***

Table 6-1. Differentially expressed genes (DEGs) and references of literature studies used to annotate cell types of mouse lung stroma. *The full names of these genes are shown in* ***The List of Abbreviations Table.***

Annotated cell type	DEGs	Reference
Fibroblast population		
Interstitial fibroblasts	*Col1a1, Col3a1, Serping1, Bgn*	(Angelidis et al., 2019)
	Igfpb7, Fst1l	(Liu et al., 2021)
Lipofibroblasts	*Col13a1, Macf1, G0s2, Tcf21, Gyg*	(Liu et al., 2021)
EBF1-positive fibroblasts	*Pi16, Serpinf1, Scara5, Ebf1*	(Liu et al., 2021)
Myofibroblasts	*Hhip, Aspn, Mustn1*	(Xie et al., 2018)
	Hhip, Tagln, Enpp2, Wnt5a	(Liu et al., 2021)
Mesothelial population		
Mature mesothelial cells	*Igfbp5, Igfbp6, Dcn, Upk3b, Rarres2, Msln, Wt1*	(Angelidis et al., 2019; Xie et al., 2018)
	Upk3b, Msln, Wt1	(Liu et al., 2021)
Cancer-associated mesenchymal cells (CAMCs)	*Rarres2, Wt1, Msln, Upk3b*	(Angelidis et al., 2019)
	Fn1	(Kenny et al., 2014; Sakai et al., 2022)
Other cell types		
Ciliated epithelial cells	*Sec14l3, Ccdc153, Tppp3*	(Angelidis et al., 2019)
Pneumocytes type II	*Sftpc, Sftpa1, Sftpb*	
Erythroid cells	*Hba-x, Hbb-bh1, Hbb-y*	(Otsuka et al., 2016)
E0771 tumour cells	Human *CD2* Note: E0771 cells express human *CD2* because they were transduced with mCherry-labelling lentiviral plasmid **(Figure 2-1 in Chapter 2)**	(Ombrato et al., 2019)
	Note: E0771 cells characterized by low to negative expression of: *Cldn1, Cldn3, Cldn4, Cldn7, Cytokeratin5/6, Keratin 8*	(Yang et al., 2017)

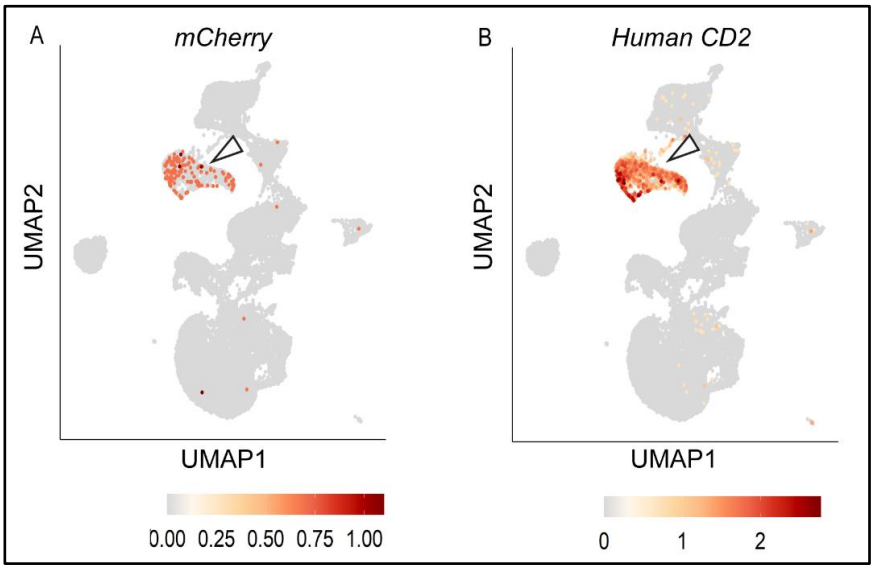

Figure 6-6. A cell cluster in scRNA-seq data was identified as E0771 tumour cells as they expressed genes inserted in the lentiviral vector, they transduced with mCherry and human CD2. *A: expression of mCherry; B: expression of human CD2 in E0771 tumour cluster (white arrowheads) visualized in UMAP plots.*

During tissue preparation for FACS sorting, RBC lysis buffer was used to remove RBCs from cell suspension. The cell suspension was then FACS-stained with anti-TER119 to remove RBCs during FACS sorting of lung stromal cells for scRNA-seq analysis. Although these steps were taken to avoid contaminating the cells subjected to scRNA-seq analysis, a cluster annotated as an erythroid cluster was detected in early metastases and was abundant, specifically in the early distal region. Interestingly, this cluster highly expressed embryonic haemoglobins *Hba-x, Hbb-bh1* and *Hbb-y* **(Figure 6-5C)**. It also co-expressed the erythroid cell development marker genes *Gata1* and *Epor* (Zhao et al., 2006) **(Figure 6-7),** and to a lesser extent also expressed EC marker genes such as *Pecam1, Cdh5*, and *Cldn5* (**Figure 5-15 in Chapter 5, white arrowheads).**

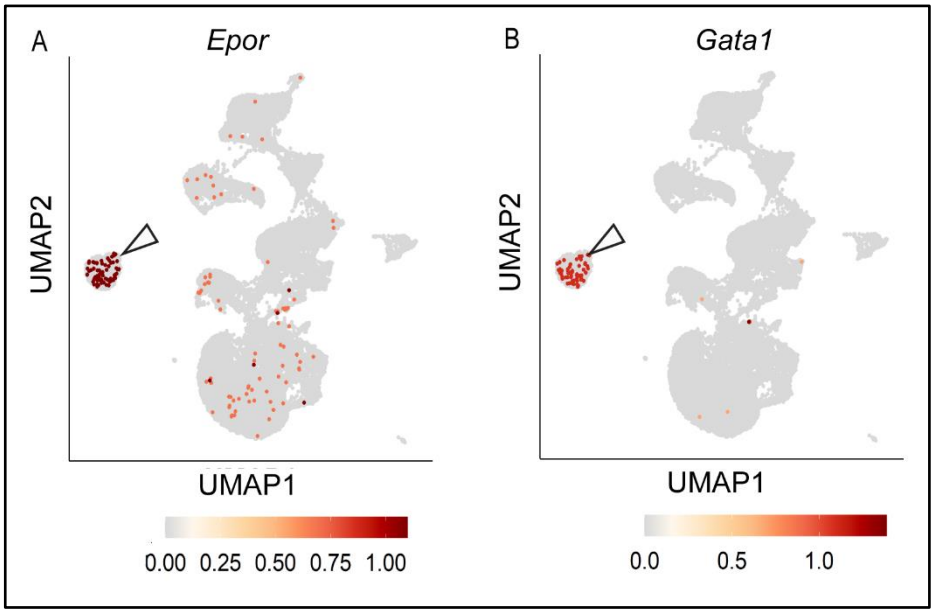

Figure 6-7. Erythroid cluster showed expression of erythroid cell marker genes**. The full names of these genes are shown in **The List of Abbreviations Table.

6.3 Molecular interactions between tumour and lung stromal cells mediating E0771 metastatic growth

My scRNA-seq data revealed stromal heterogeneity of the lungs in response to E0771 tumour colonization and progression. As E0771 tumour cells were detected and sequenced in the scRNA-seq, I investigated the molecular intercellular signalling genes that supported the growth of E0771 metastases. To do this, cell-cell communication analysis was performed on scRNA-seq data of mouse overall lung non-immune stroma (regardless of which condition these cells were coming from) and E0771 tumour cells using CellChat (Jin et al., 2021) and CellPhoneDB (Efremova et al., 2020).

CellphoneDB tool was used to explore the network of cell-to-cell interactions among the cell types identified in our murine E0771 metastatic model. Remarkably, CAMCs showed the most interactions with other cell types, especially with E0771 tumour cells (245 interactions), mature mesothelium (268 interactions), and two fibroblast subtypes (EBF1-positive fibroblasts and lipofibroblasts (232 and 219 interactions, respectively) **(Figure 6-8A).** Comparing the number of inferred interactions among cell types using CellChat revealed that all cell types interact with each other with high outgoing signalling from CAMCs and EBF1-positive fibroblasts **(Figure 6-8B).**

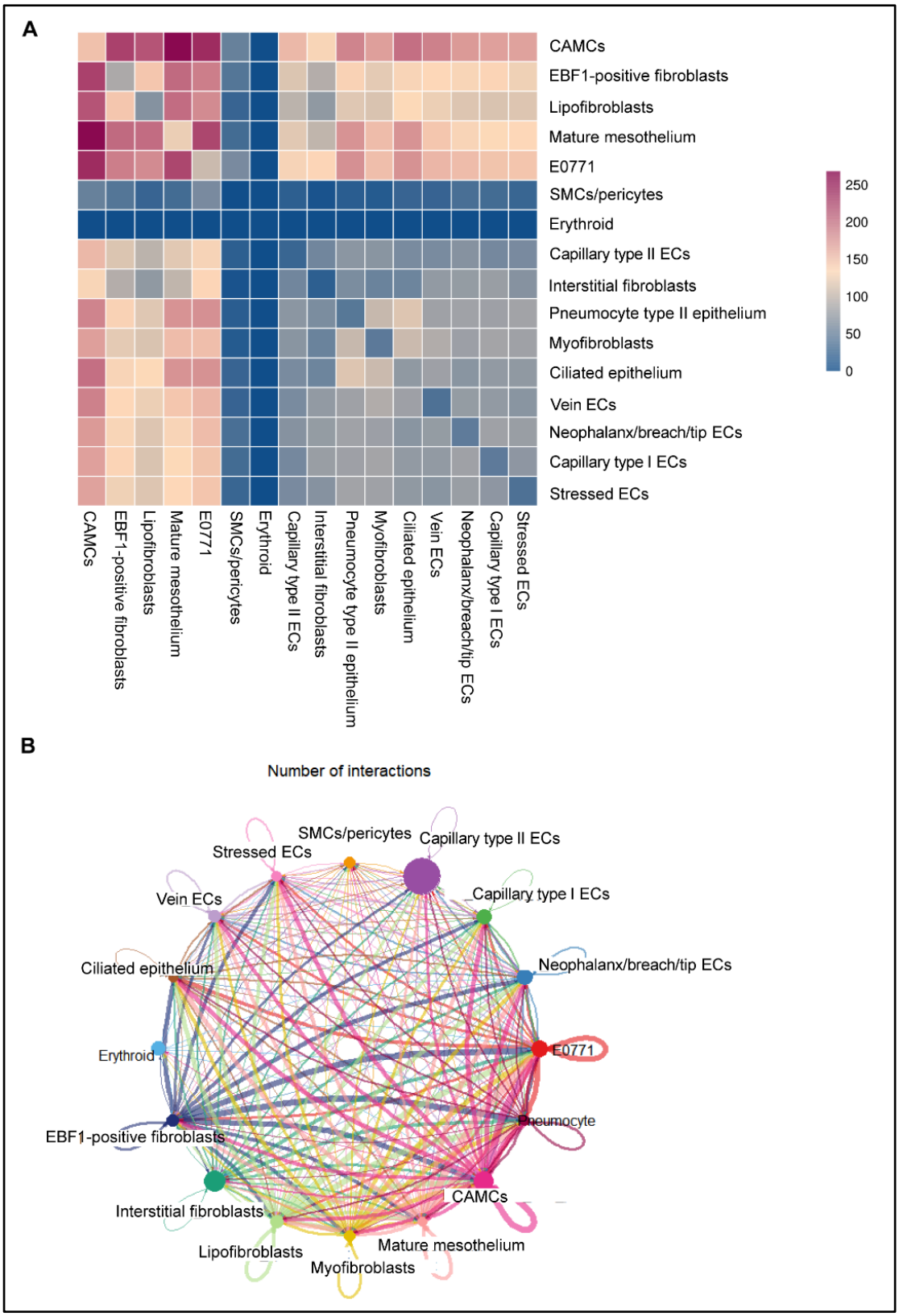

Figure 6-8. Cell-cell communication network in E0771 metastatic lungs. *A: Heatmap depicting the total number of potential ligand–receptor pairs among lung cell types predicted by CellPhoneDB. CAMCs showed strongest interactions with other cell subtypes; B: circle plot showing the total number of interactions among different cell types. The source represents the cell contributing the ligand to the interaction, while the target contributes the receptor. Circle size is proportional to the number of cells in the identified cell type class, and the width of the line is proportional to the number of significant ligand–receptor pairs (the communication score) contributing to the communication between two interacting cell types. ECs: endothelial cells; SMCs: smooth muscle cells; CAMCs: cancer-associated mesenchymal cells*

To investigate the outgoing and incoming signalling molecules of different cell types alongside their function, CellChat pattern recognition inference analysis was performed. This analysis detected two communication patterns; each pattern combined certain cell types that were predicted to have similar signalling pathways **(Figure 6-9).** Pattern one combined fibroblast subsets, mesothelial subsets, ciliated epithelium, erythroid, and E0771 tumour cells expressing genes including: growth factor genes *Egf, Fgf, Igf, Vegf*; pro-inflammatory genes *Ccl, Csf, Tgfb, Tnf*; extracellular matrix genes *collagen, Fn1,* laminin, *Tnc*; angiogenic and EC proliferation genes *Angpt* and *Tweak*; adhesion genes *L1cam* and *Ncam*; semaphorins *Sema4* and *Sema5; Wnt* and *ncWnt* genes (involved in carcinogenesis, immunomodulation, cell migration, cancer cell stemness) (Zhan et al., 2017) **(Figure 6-9)**. Pattern two combined EC subsets and pneumocytes driving outgoing signalling of pathways involving: junctional genes *Cdh5, Jam, Nectin, Ocln*; angiogenic genes *Apelin, Ephb, Esam*; gene markers of progenitor cells such as *Cd34; Cxcl, Kit, Periostin, Ptprm, Sema7* and *Trail,* (involved in inflammation, apoptosis, lymphatic metastasis, lymphangiogenesis, EC migration, and adhesion) **(Figure 6-9)** (de Looff et al., 2019; Jiang et al., 2022; Keklikoglou et al., 2018; Liu et al., 2020a).

With regards to incoming signalling, the CellChat pattern recognition inference analysis detected two incoming communication patterns with signalling pathways similar to the outgoing signalling pathways **(Figure 6-10)**. However, some signalling molecules showed paracrine interactions, with signalling being received by cell types in the other pattern. For instance, *Pdgf and Sema3* are secreted (signal sender-outgoing) by ECs and received (signal receiver-incoming) by cells present in the other pattern **(Figure 6-10).**

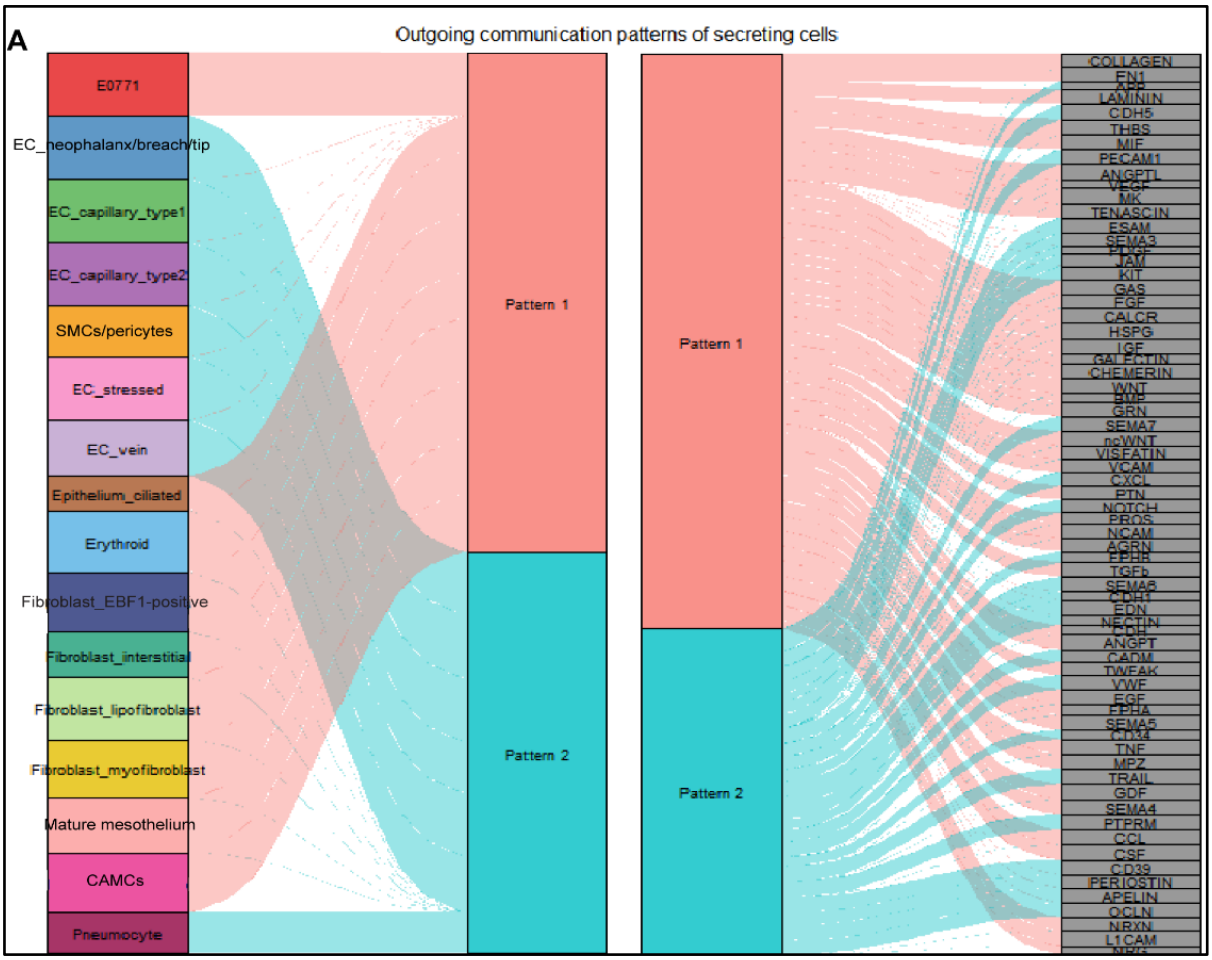

Figure 6-9. Alluvial plots depicting outgoing signalling patterns of secreting (sender) lung cell types and E0771 tumour cells predicted using CellChat. *The thickness of the flow depicts the strength of the cell groups contributing to the inferred patterns (plot on the left side) and the strength of signalling molecules contributing to the inferred patterns (plot on the right side). The height of each pattern represents the number of cell groups each pattern entails (plot on the left side) and represents the number of signalling molecules each pattern entails (plot on the right side).*

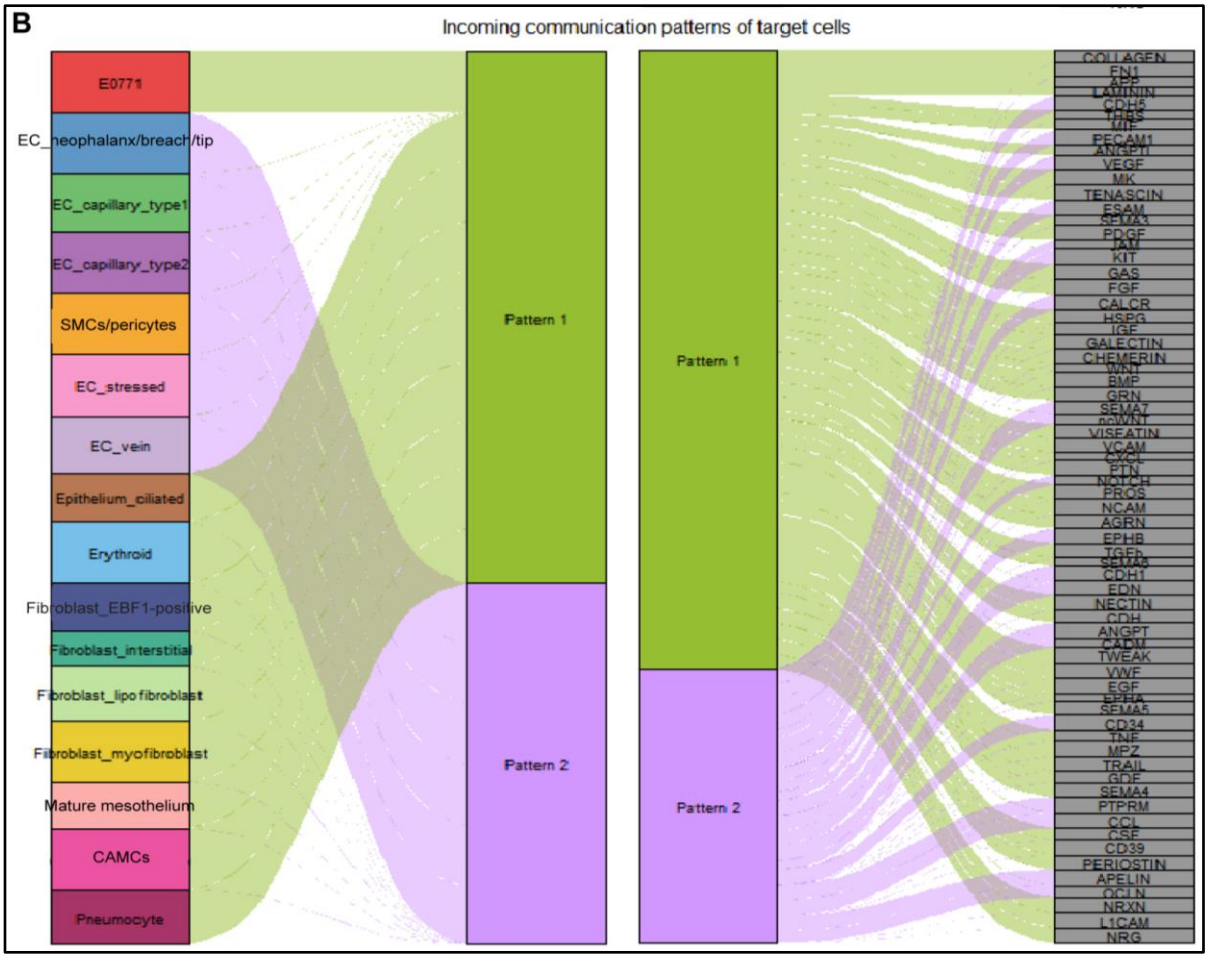

Figure 6-10. Alluvial plots depicting incoming signalling patterns of receiver lung cell types and E0771 tumour cells predicted using CellChat. *The thickness of the flow depicts the strength of the cell groups contributing to the inferred patterns (plot on the left side) and the strength of signalling molecules contributing to the inferred patterns. The height of each pattern represents the number of cell groups each pattern entails (plot on the left side) and represents the number of signalling molecules each pattern entails (plot on the right side).*

We hypothesised that different signalling molecules drive intercellular communication between E0771 tumour cells and non-immune stromal cells and among stromal cells mediating different biological processes. To decipher the complexity of intercellular communication networks, we had a closer look at selected significant signalling pathways individually via CellChat unsupervised analysis. CellChat predicted many cell-cell communication signalling pathways involved in pro-inflammation, immunosuppression, angiogenesis, vascular permeability, cell invasion, adhesion, migration, matrix remodelling, and epithelial–mesenchymal transition (EMT). However, we focused on investigating the crosstalk between E0771 tumour cells, the initial drivers of the whole process, and lung stromal cells that facilitated the development and progression of early (co-opting) and late (co-opting and angiogenic) E0771 metastases. Since this analysis was conducted on the lung stromal cells regardless of metastatic status (*e.g.* control, early and late timepoints), I relied on the cell composition and the expression levels of genes of interest in each condition to infer the signalling pathways.

6.3.1 The predicted intercellular communications occurring in E0771 metastases

The intercellular communications extrapolated below were the evident ones (visualised in heatmaps as dark green) that were predicted to be the main signalling pathways activated. It should be emphasized that the analysis discussed here is based on statistical associations using mRNA sequences; therefore, although I state 'secreted, signalled, interacted, bound', this is an extrapolation from the analysis that has not yet been experimentally validated. This analysis indicates: (i) Cap I ECs are predicted to signal in both autocrine and paracrine manners to mature mesothelial cells in the early niche (considering the latter is only present in the early niche) through *Sema6ac* – *Plxna4* **(Figure 6-11A, B) (Figure 6-2E)**; (ii) Cap II ECs and mature mesothelium are predicted to signal to lipofibroblasts and EC subtypes via *Sema3c* and *Plxnd1* **(Figure 6-11C, D)**; (iii) Vein ECs are predicted to signal in both autocrine and paracrine manners to EC subtypes, mature mesothelium, and CAMCs through *Jam-1*

(F11r) – *Itgb1* and the latter two subtypes through *Jam-1* – *Itgav* **(Figure 6-11E, F)**; and (iv) Myofibroblasts were predicted to activate non-canonical WNT signalling communicating with EC subsets, EBF1-positive fibroblasts, and mature mesothelial cells through *Wnt5a* – *Fzd1, Fzd2,* and *Fzd4* **(Figure 6-11G, H)**.

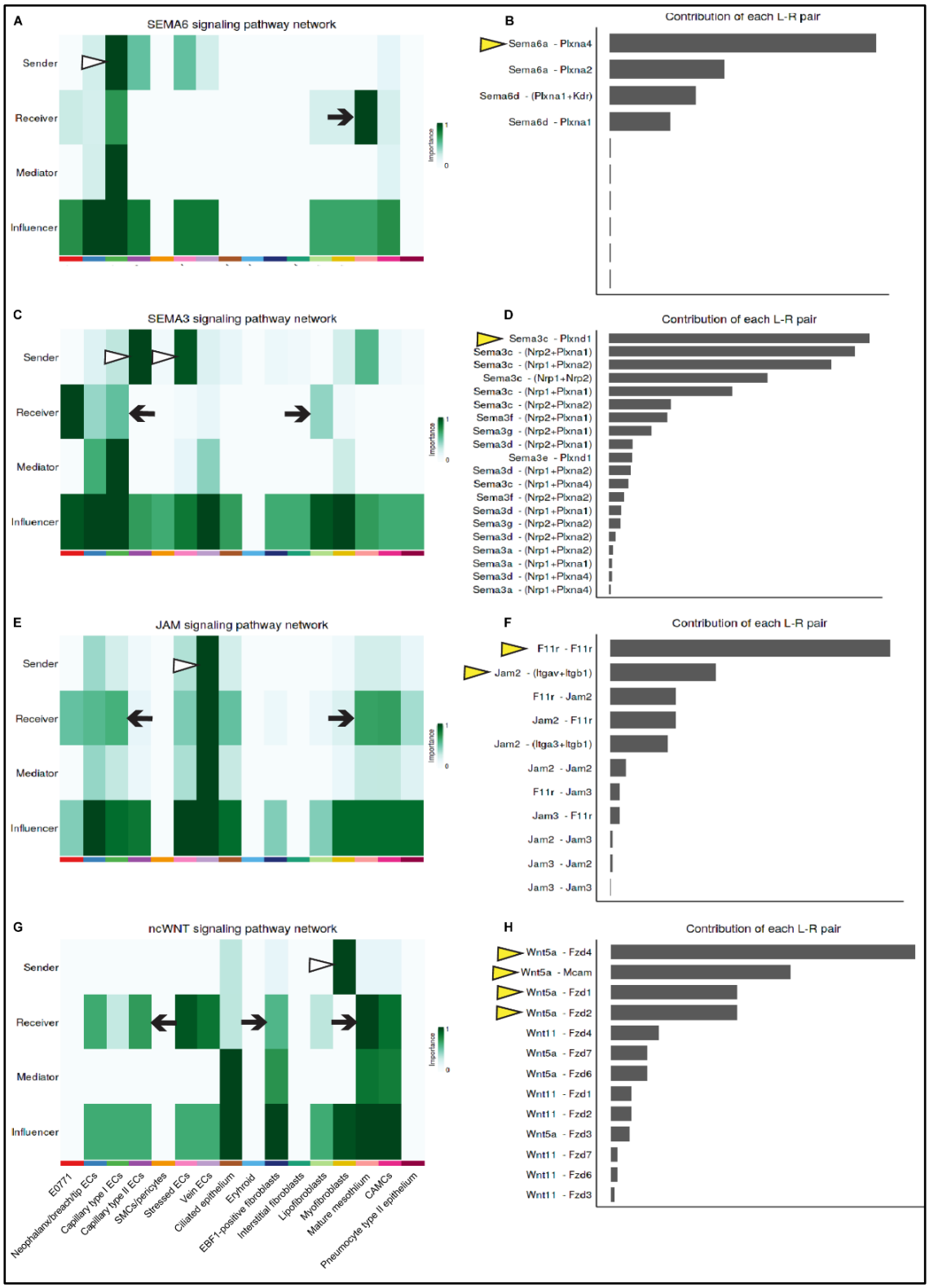

Figure 6-11. SEMA6, SEMA3, JAM, and non-canonical WNT signalling pathways are predicted to be activated in the lung stroma of E0771 metastases*. A, C, E, G: the columns in the heatmaps depict lung stromal and E0771 tumour cells, and the rows depict if the cell is signalling as sender, receiver, mediator, or influencer. These heatmaps are color-coded according to the relative importance of each cell subtype based on the computed four network centrality measures of the SEMA6, SEMA3, JAM, and non-canonical WNT (ncWNT) signalling networks, respectively with evident senders and receivers indicated with white arrowheads and black arrows, respectively; B, D, F, H: bar plots showing the relative contribution of each ligand-receptor pair to the SEMA6, SEMA3, JAM, and ncWNT signalling pathways with significant pairs indicated with yellow arrowheads. The relative contribution is calculated as the ratio of the total communication probability of the inferred network of each ligand-receptor pair to that of a particular signalling pathway. The full names of these genes are shown in* ***The List of***

Since E0771 tumour cells were only detected in late metastases, I was able to investigate their interaction with lung non-immune stroma. My analysis suggests that tumour cells and CAMCs communicate with the cap I ECs through *Ccl2* – *Ackr2* pair **(Figure 6-12A, B).** Notably, myofibroblasts are predicted to interact with neophalanx/breach/tip ECs through *Wnt5a* – *Mcam* pair **(Figure 6-11G, H)**. CellChat communication analysis revealed that ECs found to signal to CAMCs through *Nectin3* – *Nectin2/Pvr* **(Figure 6-12E, F)** and *Entpd1 (Cd39)* – *Adora2b* **(Figure 6-12C, D)**. Exploring the expression level of these genes in my scRNA-seq data, cap I ECs are predicted to communicate with CAMCs via *Nectin3* – *Nectin2*. Cap I ECs also interacted with hypoxia-responsive perivascular CAMCs via *Nectin3* – *Pvr*. Other EC subtypes, such as neophalanx/breach/tip ECs, capillary type II, stressed ECs, veins as well as pneumocytes, also signal to CAMCs and E0771 tumour cells through *Entpd1* – *Adora2b* **(Figure 6-12C, D)**. In the previous chapter, I found that cap I ECs in the late distal region upregulated the expression of *Cd36* (**Figure 5-33F in Chapter 5).** Because the interaction of CD36 and THBS1 (TSP-1) was reported to have an anti-angiogenic effect (Hale et al., 2012), I hypothesised that this interaction would occur in the late distal region. My cell-cell communication analysis verified this interaction, predicting that myofibroblasts may signal to cap I ECs through *Thbs1* – *Cd36* **(Figure 6-13A-D).**

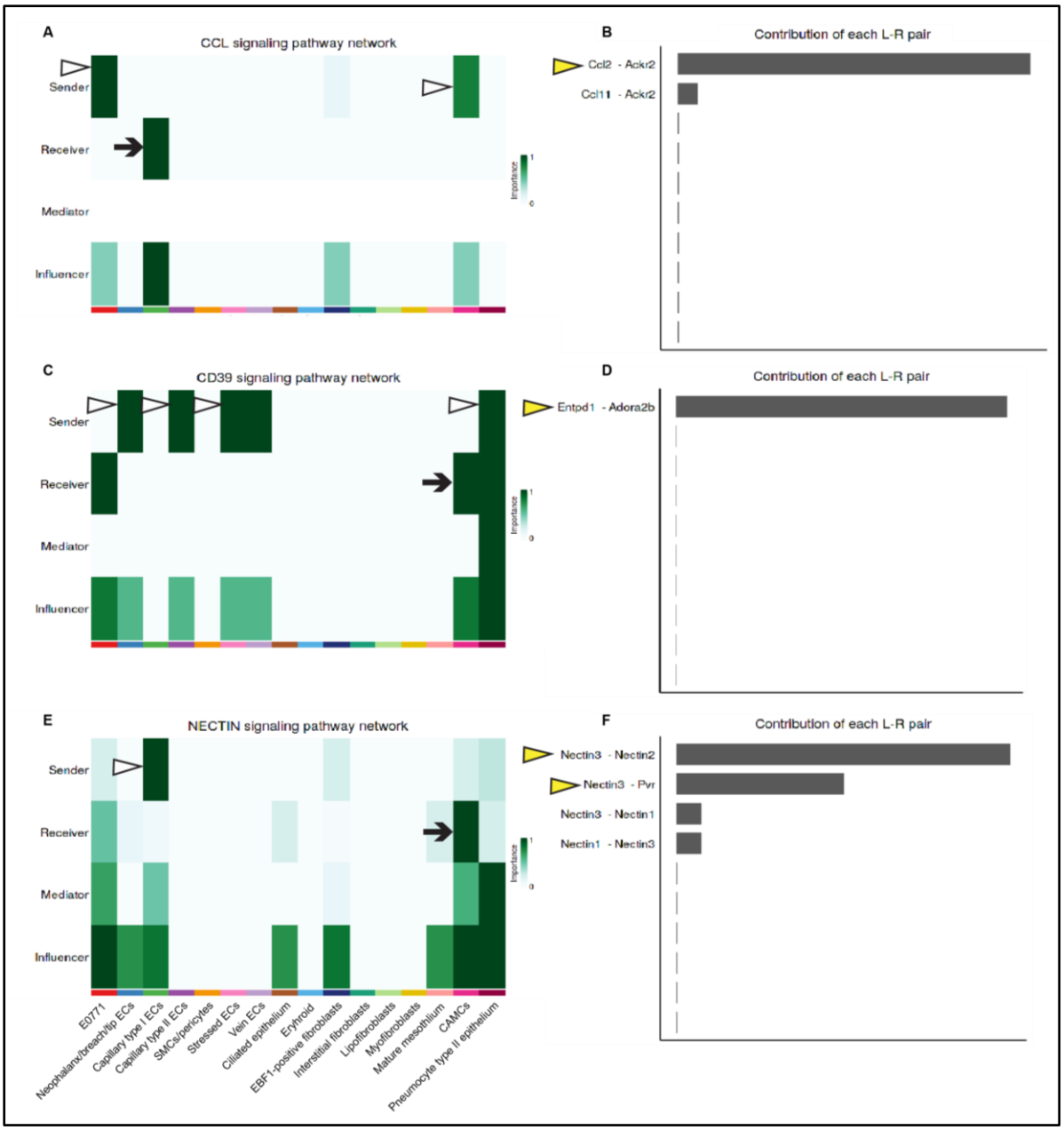

Figure 6-12. CCL, CD39, and NECTIN signalling pathways are predicted to be activated in the lung stroma and tumour cells of E0771 metastases*. A, C, E: the columns in the heatmaps depict lung stromal and E0771 tumour cells, and the rows depict if the cell is signalling as sender, receiver, mediator, or influencer. These heatmaps are colour-coded according to the relative importance of each cell subtype based on the computed four network centrality measures of the CCL, CD39, and NECTIN signalling networks, respectively with evident senders and receivers indicated with white arrowheads and black arrows, respectively; B, D, F: bar plots showing the relative contribution of each ligand-receptor pair of the Ccl, CD39, and NECTIN signalling pathways with significant pairs indicated with yellow arrowheads. The relative contribution is calculated as the ratio of the total communication probability of the inferred network of each ligand-receptor pair to that of a particular signalling pathway. The full names of these genes are shown in* ***The List of Abbreviations Table.***

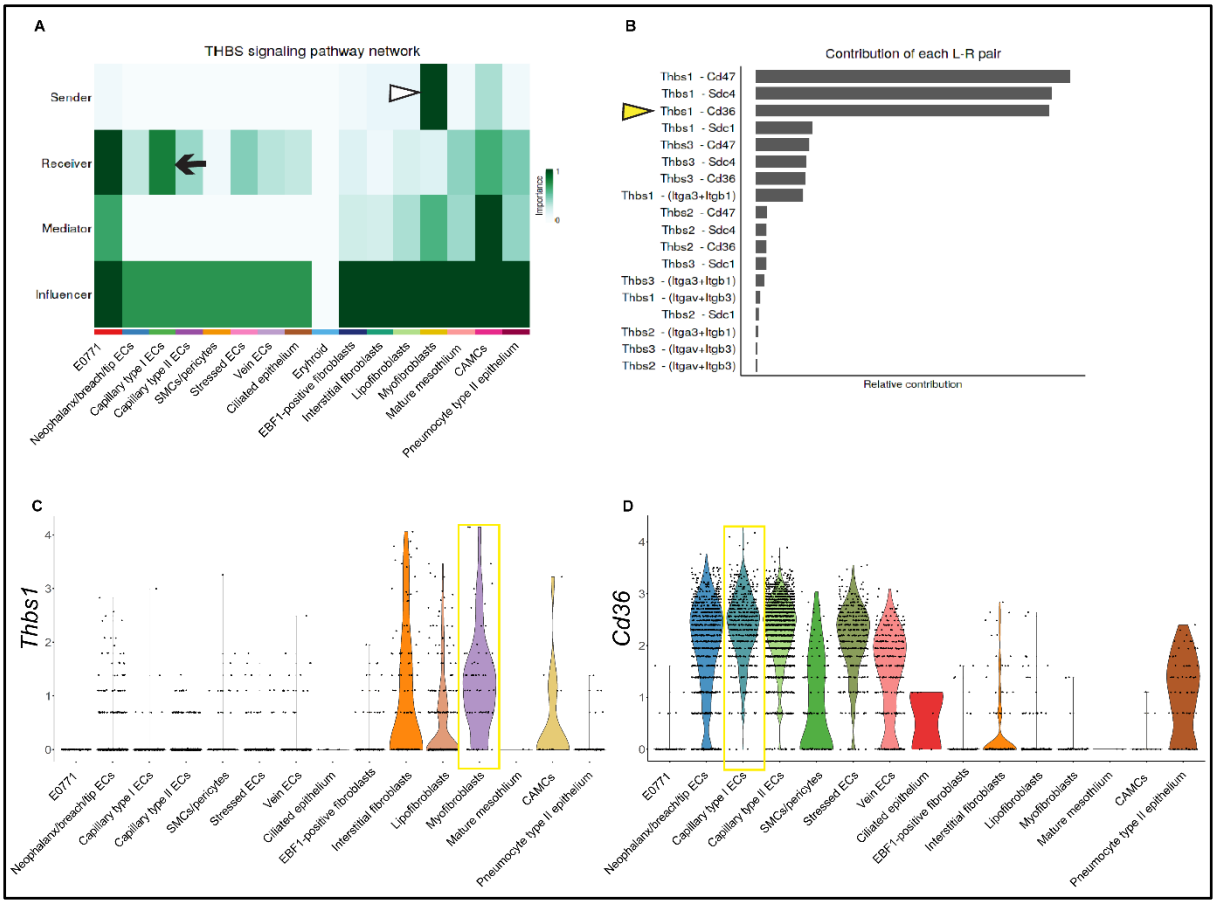

Figure 6-13. Angiogenesis is limited in the late distal region of subpleural metastases via the THBS1 – CD36 signalling pair. *A: the columns in the heatmap depict lung stromal and E0771 tumour cells, and the rows depict if the cell is signalling as sender, receiver, mediator, or influencer. This heatmap is colour-coded according to the relative importance of each cell subtype based on the computed four network centrality measures of the THBS signalling network with evident sender and receiver indicated with white arrowhead and black arrow, respectively; B: bar plot showing the relative contribution of each ligand-receptor pair to the THBS signalling pathway with significant pair indicated with yellow arrowhead. The relative contribution is calculated as the ratio of the total communication probability of the inferred network of each ligand-receptor pair to that of the Thbs signalling pathway; C: violin plot depicting the expression distribution of Thbs1 across the subtypes of lung stromal cells in the late distal region, with myofibroblasts expressing the highest level of Thbs1; D: violin plot depicting the expression distribution of Cd36 across the subtypes of lung stromal cells in the late distal region, with cap I ECs expressing the highest level of Cd36. The full names of these genes are shown in* ***The List of Abbreviations Table.***

The detection of lung non-immune stromal types using scRNA-seq analysis and the mCherry-niche-labelling system **(Figure 6-2)** enabled us to dissect which specific cell types express pro-angiogenic molecules, and to predict what other cell types they signals to. This analysis found that capillaries and stressed ECs signal to neophalanx/breach/tip ECs in both autocrine and paracrine manners through *Efnb1* and *Efnb2 (Ephrin B1* and *B2) – Ephb4* **(Figure 6-14A, B).** Other potential drivers of angiogenesis include: cap I signalling to cap II ECs, stressed, and neophalanx/breach/tip ECs through *Apln (Apelin) – Aplnr (Apelin receptor)* **(Figure 6-14C, D)**; and cap II and stressed ECs signalling to veins through *Cxcl12 – Ackr3,*

and to neophalanx/breach/tip ECs through *Cxcl12* – *Cxcr4* **(Figure 6-14E, F)**. E0771 tumour cells were also found to interact with cap I, cap II, stressed ECs, veins, and neophalanx/breach/tip ECs through *adrenomedullin (Adm)* – *Calcrl* **(Figure 6-14G, H)**.

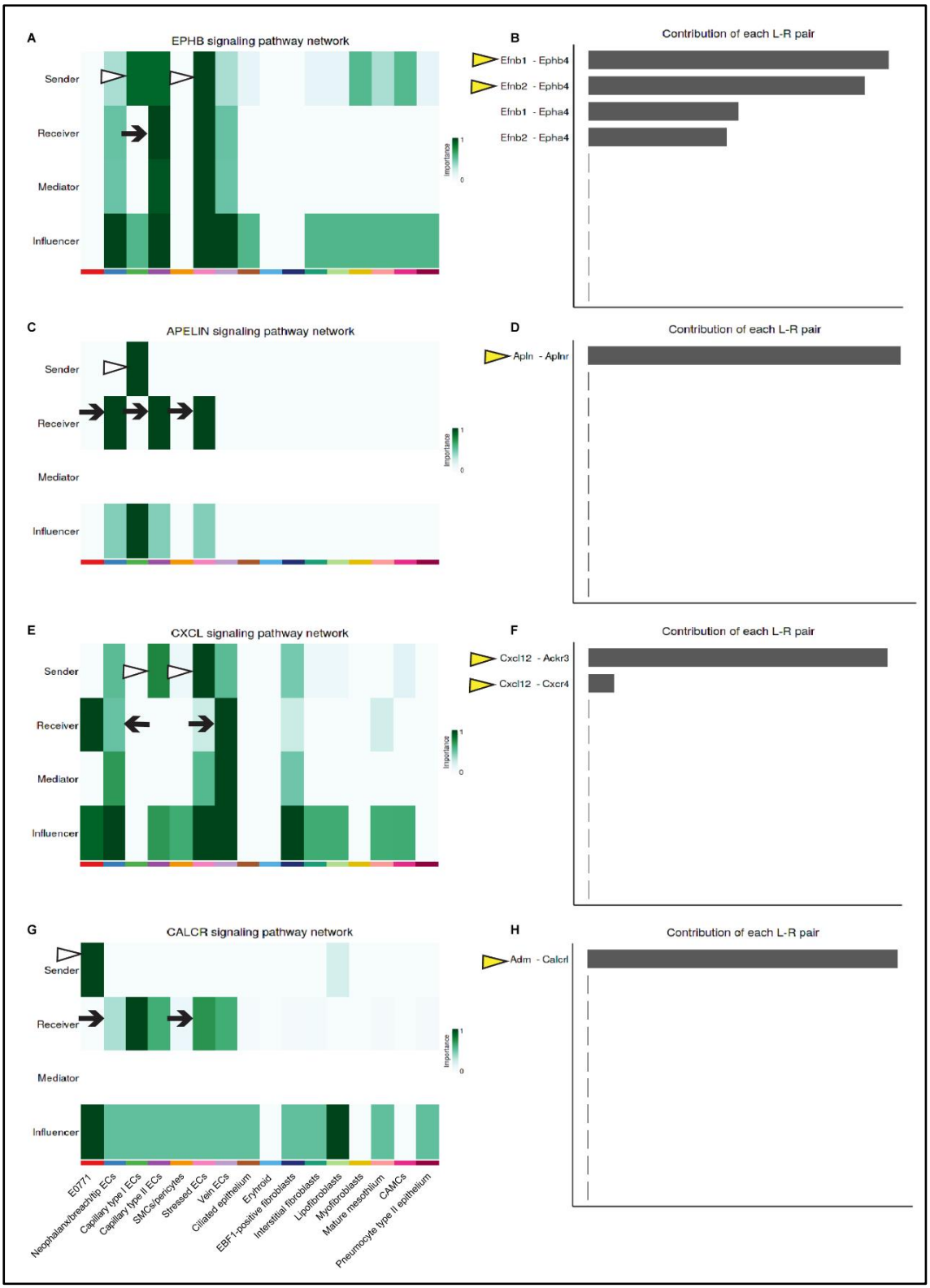

Figure 6-14. Different angiogenic signalling pathways are predicted to drive the development of late (angiogenic) metastases. *A, C, E, G: the columns in the heatmaps depict lung stromal and E0771 tumour cells, and the rows depict if the cell is signalling as sender, receiver, mediator, or influencer. These heatmaps are colour-coded according to the relative importance of each cell subtype based on the computed four network centrality measures of the EPHB, APELIN, CXCL, and CALCR signalling networks, respectively with evident senders and receivers indicated with white arrowheads and black arrows, respectively; B, D, F, H: bar plots showing the relative contribution of each ligand-receptor pair of the EPHB, APELIN, CXCL, and CALCR signalling pathways with significant pairs indicated with yellow arrowheads. The relative contribution is calculated as the ratio of the total communication probability of the inferred network of each ligand-receptor pair to that of a particular signalling pathway. The full names of these genes are shown in* ***The List of Abbreviations Table.***

Angiogenesis in E0771 late metastases is also mediated by the well-recognised *Vegfa* – *Vegfr* signalling pathway **(Figure 6-15A, B).** In comparison to E0771 tumour cells and other stromal cells, the hypoxia-responsive perivascular CAMCs **(Figure 6-15C, D)**, present in the late niche, highly expressed *Vegfa* and predicted as the major sender of *Vegfa* signalling to mainly cap I ECs **(Figure 6-15A)** via *Vegfr2* **(Figure 6-15B, E)**.

E0771 tumour cells communicated with CAMCs enriched in the late niche through the upregulation of several cytokines and growth factors with the following inferred ligand-receptor pairs: *Tgf-β1* – *Tgfbr1+Tgfbr2* (multimeric receptor)/*Acvr1b* **(Figure 6-16A, B),** *Tnf-α* – *Tnfrsf1a* **(Figure 6-16C, D)**, *Hbegf/Areg* – *Egfr* **(Figure 6-16E, F)**, and *Pdgfa* – *Pdgfra* **(Figure 6-16G, H)** mediating the signalling.

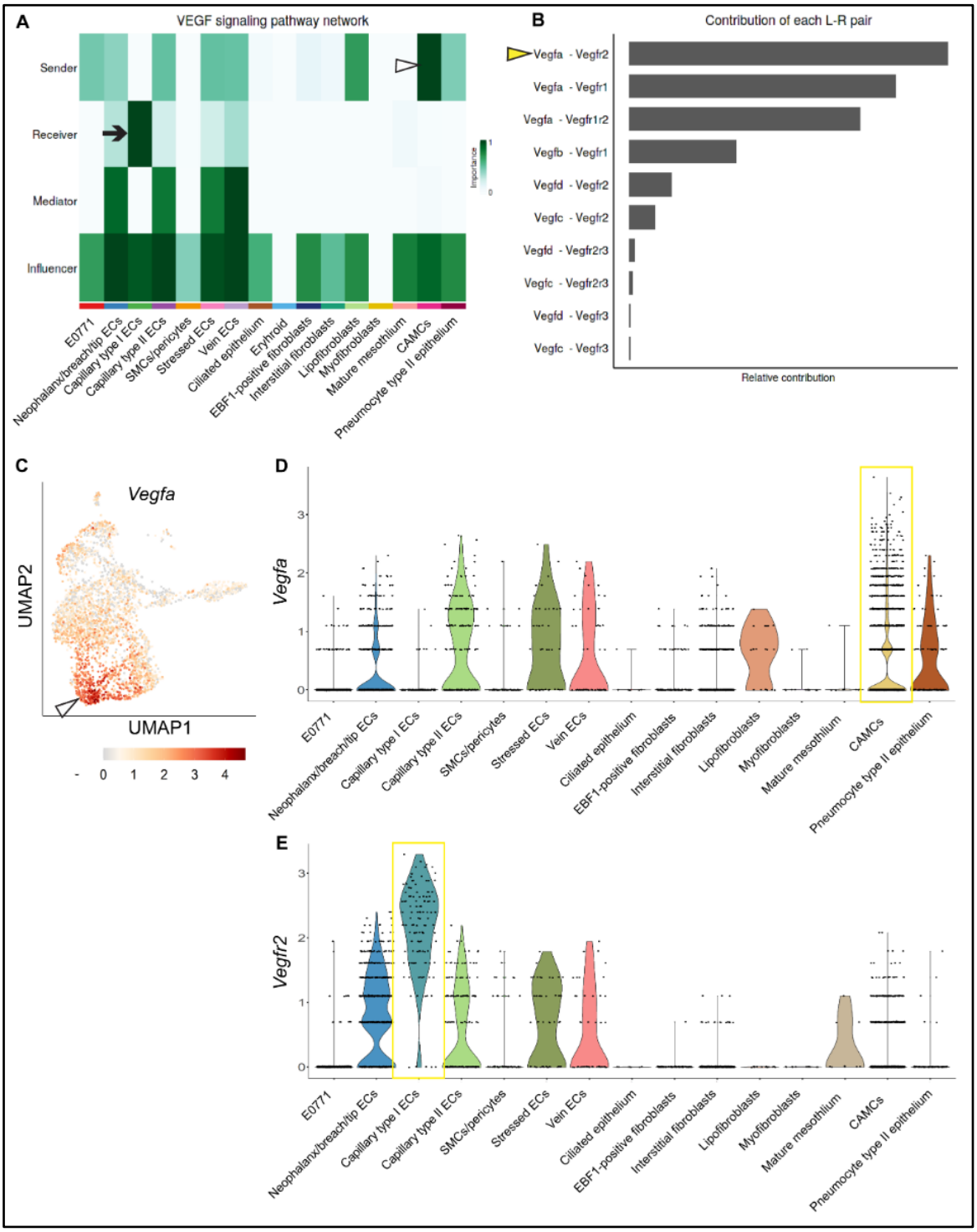

Figure 6-15. Cell-cell communication analysis showed that cancer-associated mesenchymal cells (CAMCs) are the main supplier of pro-angiogenic growth factor VEGFA. *A: the columns in the heatmap depict lung stromal and E0771 tumour cells and the rows depict if the cell is signalling as sender, receiver, mediator, or influencer. This heatmap is colour-coded according to the relative importance of each cell subtype based on the computed four network centrality measures of the VEGF signalling network. This heatmap shows CAMCs as the primary cell subtype (sender, white arrowhead) that express Vegfa and cap I ECs as the primary receiver that express the receptor (black arrow); B: bar plot showing the relative contribution of each ligand-receptor pair to the VEGF signalling pathway, with VEGFA-VEGFR2 pair being the dominant contributor with significant pair indicated with yellow arrowhead. The relative contribution is calculated as the ratio of the total communication probability of the inferred network of each ligand-receptor pair to that of the VEGF signalling pathway; C: UMAP visualisation showing hypoxia-responsive CAMCs highly expressing Vegfa; D: violin plot depicting the expression distribution of Vegfa across the subtypes of lung stromal cells in the late niche, with CAMCs expressing the highest level of Vegfa; E: violin plot depicting the expression distribution of Vegfr2 across the subtypes of lung stromal cells in the late niche, with cap I ECs expressing highest level of Vegfr2. The full names of these genes are shown in* ***The List of Abbreviations Table.***

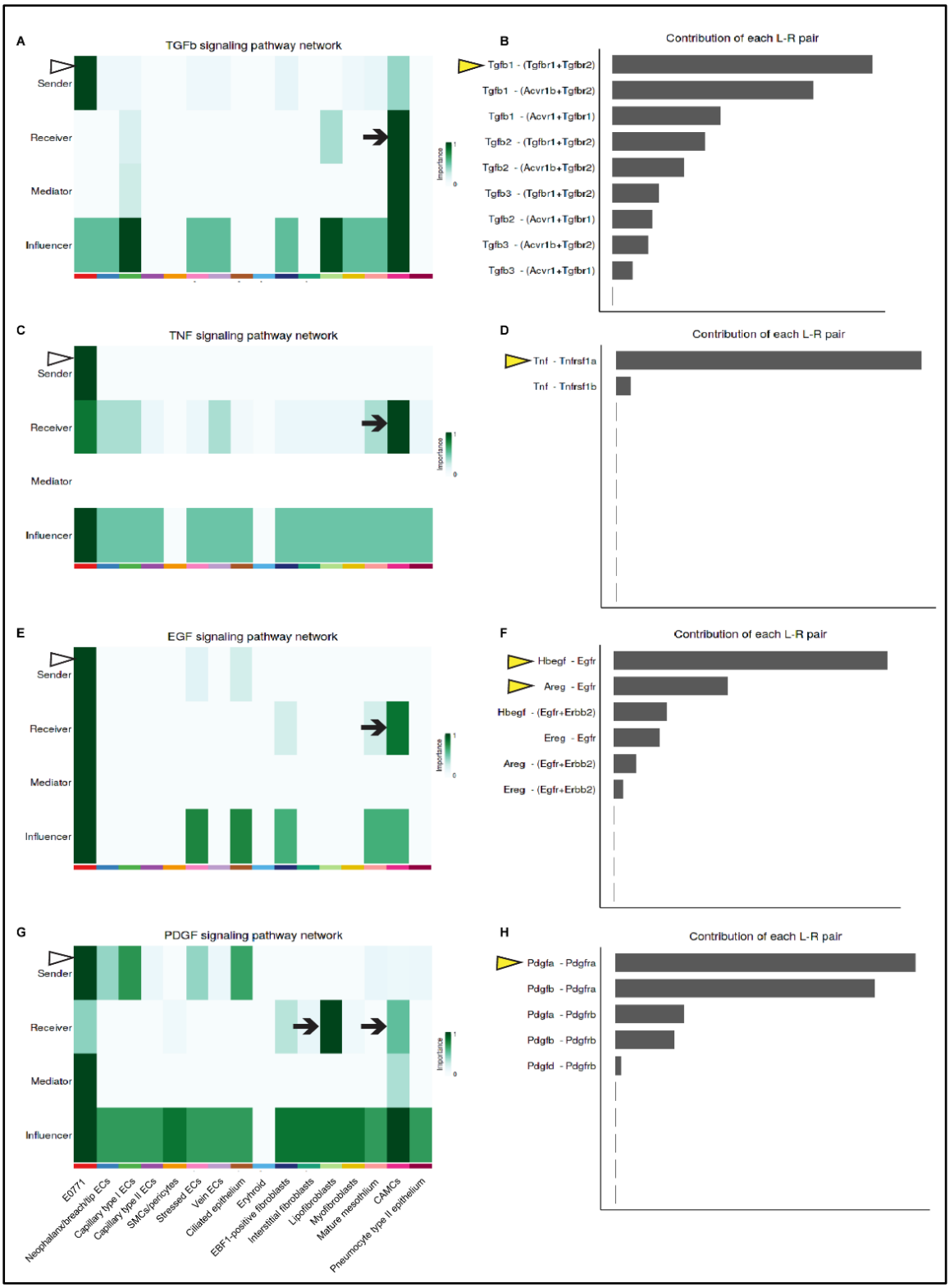

Figure 6-16. The growth factors and cytokines predicted to be secreted by E0771 tumour cells, some of which are reported to mediate EMT of mesothelial cells. *A, C, E, G: the columns in the heatmaps depict lung stromal and E0771 tumour cells, and the rows depict if the cell is signalling as sender, receiver, mediator, or influencer. These heatmaps are colour-coded according to the relative importance of each cell subtype based on the computed four network centrality measures of the TGFβ, TNF, EGF, and PDGF signalling networks, respectively with evident senders and receivers indicated with white arrowheads and black arrows, respectively; B, D, F, H: bar plots showing the relative contribution of each ligand-receptor pair to of the TGFβ, TNF, EGF, and PDGF signalling pathways with significant pairs indicated with yellow arrowheads. The relative contribution is calculated as the ratio of the total communication probability of the inferred network of each ligand-receptor pair to that of a particular signalling pathway. The full names of these genes are shown in* ***The List of Abbreviations Table.***

6.4 Discussion

My scRNA-seq analysis showed the extent of spatial and temporal heterogeneity in lung stromal cells during the development of breast cancer lung metastases. The reduction of fibroblast subtypes (except EBF1-positive fibroblasts) in early and late metastases could indicate those cells were undergoing EMT. This assumption might be addressed in future studies. Additionally, an erythroid cluster was abundant in distal areas of early metastases. This cluster upregulated the expression of both embryonic haemoglobins and erythroid cell development marker genes (Zhao et al., 2006) along with co-expression of EC genes. These results therefore also suggest the potential of endothelial-to-hematopoietic transition (EHT), where hemogenic endothelium (HE) could give rise to erythroid lineage in a metastatic context. This process is known to primarily occur during developmental haematopoiesis in the yolk sac and Aorta-Gonad-Mesonephros (AGM) (Lee et al., 2016; Oatley et al., 2020). Consequently, exploring if this process is activated in metastatic context warrants further investigation.

The lung microenvironment is distinct, comprising vascular cells, pneumocytes, immune cells, mesothelial cells, fibroblasts, and non-cellular components. These components create a complex network of intercellular communication mediated by ligand–receptor complexes that are crucial for the progression of metastasis. However, this signalling remains poorly understood. Here, my inferred analysis of the intercellular communication occurring in E0771 metastases provides insight into the cells involved and the potential signalling pathways that are activated. For example, this found that cap I ECs highly expressed *Sema6a*, which is predicted to signal to mature mesothelium in the early niche through binding to the highly expressed gene *Plxna4*. *In vivo* stromal deletion of *Plxna4* has been reported to impair tumour growth and increase cytotoxic T-cell infiltration (Celus et al., 2022). It also induces tumorigenesis and proliferation (Kigel et al., 2011). Whereas SEMA6A has been reported to maintain the survival of ECs but with an inhibitory effect on EC migration and angiogenesis (Dhanabal et al., 2005; Segarra et al., 2012; Zhou et al., 2011). Since *Plxna4* is highly expressed in mature mesothelial cells that are profoundly increased in the early niche, it is

possible that it mediates early metastatic growth through inducing proliferation and cytotoxic T-cell exclusion, sitting along the pro-survival and anti-angiogenic effect of *Sema6a* in cap I ECs. Another predicted signalling pathway that was highly upregulated in the early niche was the interaction of the Sema3c and Plxnd1 pair between cap II ECs and mature mesothelium and EC subtypes and lipofibroblasts. The SEMA3C – PLXND1 pair has been reported to have an anti-angiogenic effect by decreasing EC migration, breaking down adherens junctions, and causing tip cell apoptosis in retinal angiogenesis (Yang et al., 2015). Mature mesothelium, which is increased in the early niche, could have a similar anti-angiogenic effect on ECs, allowing vessel co-option to occur. At an early stage of E0771 metastasis in the lungs, *Jam1 (F11r)* was found to be upregulated in EC subtypes and mature mesothelium; this is predicted to interact with the integrins *Itgb1* and *Itgav*, which were upregulated in the mesothelial population. JAM1 is reported to mediate cell migration, EMT initiation, cell proliferation, and maintenance of cancer stemness (Czubak-Prowizor et al., 2022). Targeting JAM1 has been reported to reduce adhesion and transendothelial migration of metastatic breast cancer, indicating its role in promoting tumour extravasation (Bednarek et al., 2020). These studies suggest the crucial role of JAM1 junctions in enhancing pro-tumourigenic properties of cancer cells and their transmigration through the EC layer. Another signalling pair, *Wnt5a – Fzd1/Fzd2/Fzd4*, is predicted to occur in myofibroblasts communicating with EC subsets, EBF1-positive fibroblasts, and mature mesothelial cells. WNT5A is highly expressed by cancer-associated fibroblasts (CAFs) and has been found to increase colorectal cancer proliferation and migration (Hirashima et al., 2021). The WNT5A – FZD2 pair are also reported to trigger EMT in hepatocellular carcinomas (Gujral et al., 2014). The high expression of this pair in the lung stroma in our E0771 metastatic model suggest they might contribute to the EMT of mesothelial cells.

Analysis of the intercellular communication pathways during the late stage of E0771 metastasis suggests they may activate immunosuppression, EMT, and angiogenesis. For instance, the *Ccl2 – Ackr2* pair is predicted to be activated in E0771 tumour cells and in

CAMCs signalling to cap I ECs. A previous study reported ACKR2 to have immunosuppressive and pro-metastatic effects, as it scavenges CCL2 and impairs the CCL2-mediated inflammatory function of NK-cell recruitment by limiting the expression of CCR2 on NK cells (Hansell et al., 2018; Woodcock et al., 2017). Similarly, the *Wnt5a* – *Mcam* pair, through being expressed by myofibroblasts and neophalanx/breach/tip ECs, may support angiogenesis in the late niche, as MCAM receptors have been reported to regulate RHOA-dependent cell migration and motility (Ye et al., 2013). Cap I ECs in the late niche are also predicted to communicate with CAMCs through the *Nectin3* – *Nectin2* pair, which could be involved in regulating cell-cell adherens junctions (Devilard et al., 2013). It is also signalled to the hypoxia-responsive perivascular CAMCs through *Nectin3* – *Pvr*. The NECTIN3 – PVR interaction has been previously reported to enhance directional cell migration and oncogenic fibroblast metastasis, suggesting the potential involvement of this interaction in late E0771 metastatic progression (Ikeda et al., 2004). PVR receptors are highly upregulated in several malignancies where they may mediate the immune escape of tumour cells (Gromeier et al., 2000; Masson et al., 2001; Pende et al., 2005). *Pvr* was found to be highly expressed in the lung stroma in a subset of CAMCs in our scRNA-seq data **(Appendix G2)**; thus it represents a potential therapeutic target using oncolytic poliovirus-based therapy to treat tumours and possibly to treat late metastases (Kučan Brlić et al., 2019). Different EC subtypes and pneumocytes are also predicted to interact with CAMCs and E0771 tumour cells through *Entpd1 (Cd39)*–*Adora2b*. ENTPD1, along with CD73, can produce adenosine in TME, which in turn binds to ADORA2B receptors (Wang et al., 2021). ADORA2B receptors are expressed by T cells and tumour cells, where they play anti-inflammatory roles by increasing regulatory T cells, cell proliferation, and angiogenesis (Ehrentraut et al., 2012; Wilkat et al., 2020). The *Entpd1-Adora2b EC*-CAMCs inferred interaction in TME of late E0771 metastases might play a similar role in creating an immunosuppressive tumour microenvironment.

The angiogenesis that occurs during the growth of late (subpleural) E0771n metastases was predicted by my analysis to be, in part, mediated by EC – EC interactions

including *Efnb1* and *Efnb2* (*Ephrin B1 and B2*) – *Ephb4, Apln (Apelin) – Aplnr, Cxcl12 – Ackr3* and *Cxcr4*. Additionally, another angiogenic signalling pathway was predicted to be driven by the *Adm – Calcrl* pair expressed by E0771 tumour cells and EC subtypes respectively. Notably, angiogenesis in the late niche was supported by *Vegfa* expressed by the tumour microenvironment, specifically from the hypoxia-responsive perivascular subtype of CAMCs, which binds to *Vegfr2* expressed by the cap I ECs. These different angiogenic mechanisms occur in the same type of cancer, suggesting that combined therapies that target angiogenic vessels (above new targets for anti-angiogenic therapies) as well as stromal cells that secrete pro-angiogenic factors may be successful. Alternatively, a treatment could potentially modify the junctions of tumour blood vessels *e.g.* targeting angiogenic vessels and JAM-1-overexpressing vessels to limit tumour adhesion and extravasation. Angiogenesis was observed to occur in late metastases, prominently in the late niche (mCherry+) **(Figure 3-15E, F)**. However, at this timepoint it was less abundant in the distal area **(Figure 3-15E, F).** This could have been influenced by the upregulation of the *Thbs1 – Cd36* signalling pair that was predicted to be activated in myofibroblast and cap I ECs, since this has been described in the literature to exert an anti-angiogenic effect (Hale et al., 2012). This signalling crosstalk was recently reported to be activated between co-opting colorectal cancer and niche stroma (hepatocytes), inducing TGFβ1 overexpression and subsequently facilitating ARP2/3-mediated cancer cell invasion and migration in vessel co-opting CRCLM lesions (Rada et al., 2021). This study suggested that this signalling axis could contribute to inducing migration of E0771 cancer cells in our model as cap I ECs in the late distal region were shown to highly express *Tgfβ1* as well **(Appendix G3).**

I acknowledge that these ligand–receptor pairs and signalling pathways inferred using cell-cell communication bioinformatics tools represent predictions and need to be confirmed at the protein level. For example, to validate the molecular mechanisms inferred from scRNA-seq data, qPCR and immunofluorescence staining of E0771 metastatic lung tissue sections

could confirm the spatial and temporal expression levels and map the expression of ligand-receptor pairs to the different cell types predicted in my analysis.

In my experimental model, E0771 cells highly expressed several growth factors inferred to communicate with CAMCs in late metastases. Both TGF-B1 and TNF-A have been shown to induce mesothelial-to-mesenchymal transition (MMT) in metastatic cancer, defining mesothelial cells as the epithelial cells that giving rise to mesenchymal cells (Rynne-Vidal et al., 2017). Consequently, in the next chapter, I investigated whether MMT is activated and mediates late (angiogenic) growth of breast cancer lung metastases.

Chapter 7: Investigating the role of metastatic niche mesothelial and mesenchymal cells in metastatic progression

7.1 Introduction

As shown in the previous chapter, scRNA-seq analysis of E0771 metastatic lung stroma detected mature mesothelial cells in the early niche and cancer-associated mesenchymal cells (CAMCs) in the late niches **(Figure6-2 in Chapter 6, white arrowheads).** Further, my cell-cell communication inference analysis predicted that E0771 tumour cells signalled to CAMCs through TGF-β1 and TNF-α signalling pathways, both of which are known inducers of EMT in cancer (Rynne-Vidal et al., 2017). Based on these findings, I hypothesised that mature mesothelial cells might transdifferentiate into these CAMCs in order to support the advanced growth of E0771 metastases. To test this hypothesis, here I will study the origin of CAMCs via histological analysis, trajectory inference analysis of scRNA-seq data, and the *in vivo* lineage tracing model *Wt1-CreERT2*;tdTomato reporter mice.

7.2 Identification of cancer-associated mesenchymal subtypes in the late metastatic niche

To further study the transcriptional changes in mesenchymal cells, and to identify distinct cell subpopulations across early- and late-metastatic conditions, the mesothelial and CAMC populations (3542 cells) were subclustered from the main lung stromal population based on the pan-mesothelial marker genes (*Wt1, Msln, Upk3b, Upk1b, Krt18, Krt19*) **(Figure 7-1) (Supplementary TableS8).** To do this, the five scRNA seq datasets of the subsetted population (comprising non-tumour, early, and late time points) were merged to identify the subtypes common across these conditions.

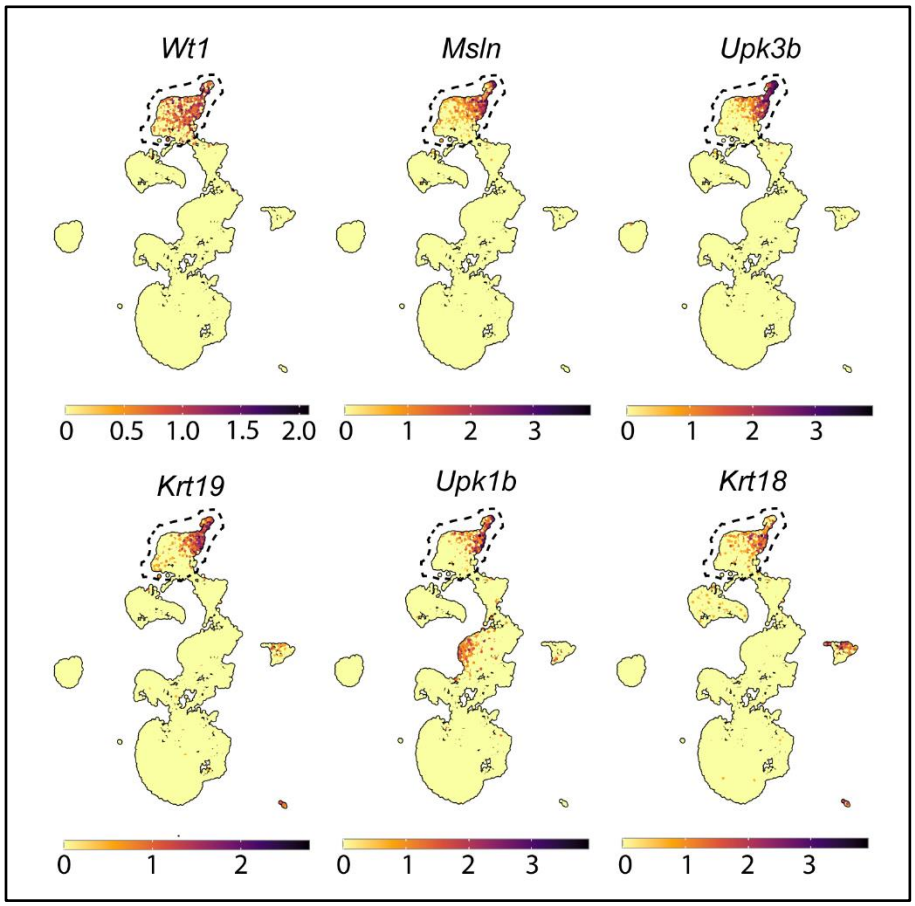

Figure 7-1. Pan-mesothelial marker genes were used to subcluster the mesothelial and CAMCs populations from the main lung stromal population. *Dashed black lines depict mesothelial and CAMC clusters subdivided for higher resolution analysis. The full names of these genes are shown in* ***The List of Abbreviations Table.***

Dimensionality reduction was then performed on the merged scRNA dataset using PCA, and the first 20 PCs were included in the downstream analysis. Further dimensional reduction used the UMAP method, and then unsupervised clustering was performed on this dataset. This detected four subtypes, three of which were not described in the literature and were annotated as CAMCs **(Figure 7-2A)**. These clusters of lung stromal cells were annotated as follows: mature mesothelial cells (MCs); proliferating CAMCs; inflammatory fibroblast-like CAMCs; and hypoxia-responsive perivascular CAMCs**.** Mesothelial and CAMC subtypes were annotated based on the top 50 differentially expressed genes (DEGs) in each cluster, along with manual curation of genes from several publications **(Table 7-1) (Supplementary TableS9).** The top five marker genes of each annotated cluster were visualized by UMAP plots **(Figure 7-3).**

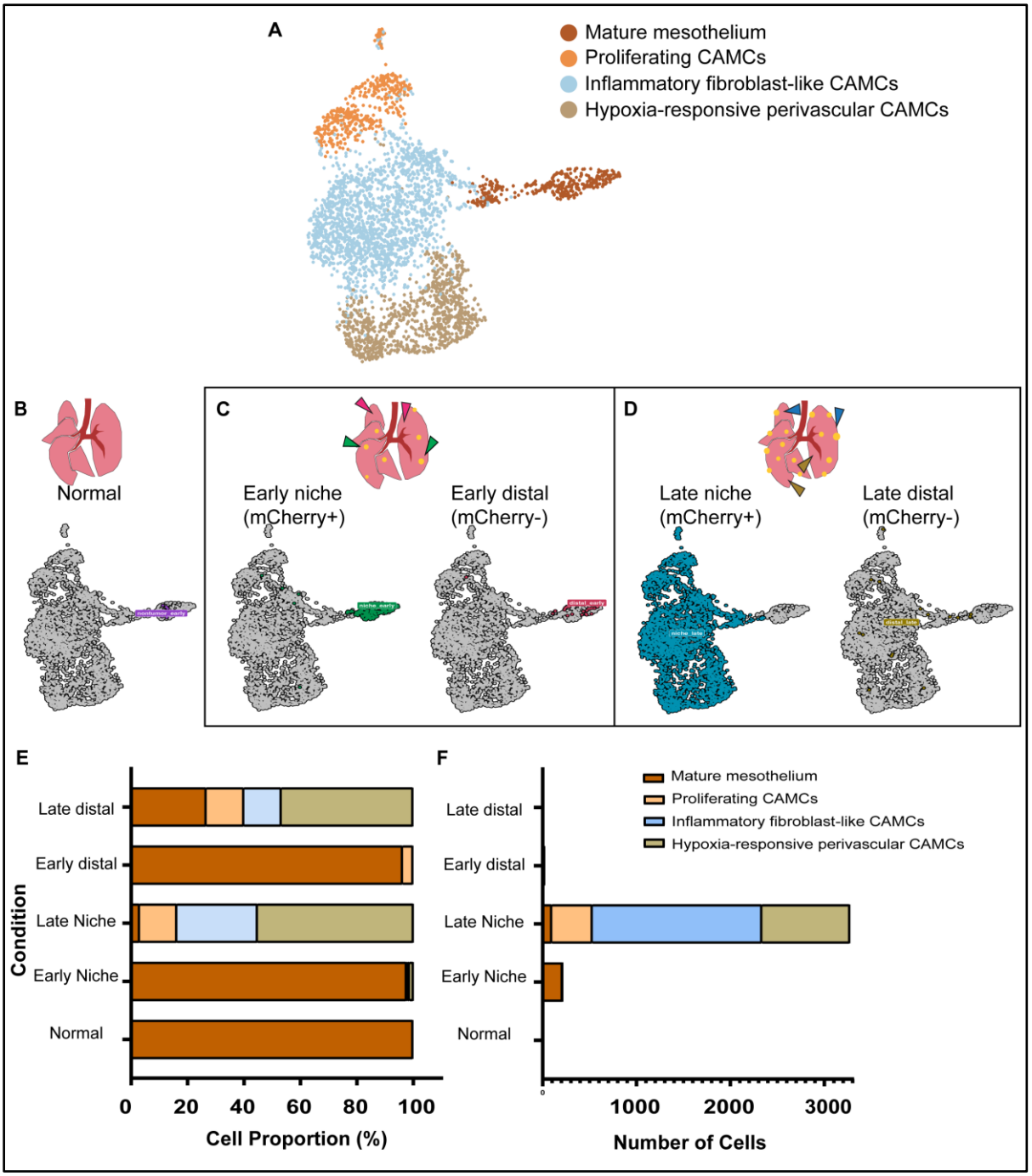

Figure 7-2. Mesenchymal cells from healthy lungs, early, and late E0771 metastatic mouse lungs revealed mesenchymal heterogeneity at early and late metastatic tumour growth in the lungs. *A: unsupervised clustering visualized as Uniform Manifold Approximation and Projection (UMAP) identified four clusters annotated to four cell types across all five conditions. Cell clusters were annotated by manual curating of genes identified by previous studies and based on the top 50 differentially expressed (DE) marker genes. Five UMAP projection plots of lung mesenchymal clusters splitting all five conditions: B: normal (healthy in purple); C early distal region (fuchsia arrowheads), early niche (green arrowheads); D: late distal region (cumin arrowheads), and late niche (turquoise arrowheads) conditions of E0771 metastatic lungs, respectively; E and F: relative (percentage) and absolute cellular composition of lung mesenchymal cells across the five conditions. B-D are colour-coded differently from the rest of the figure.*

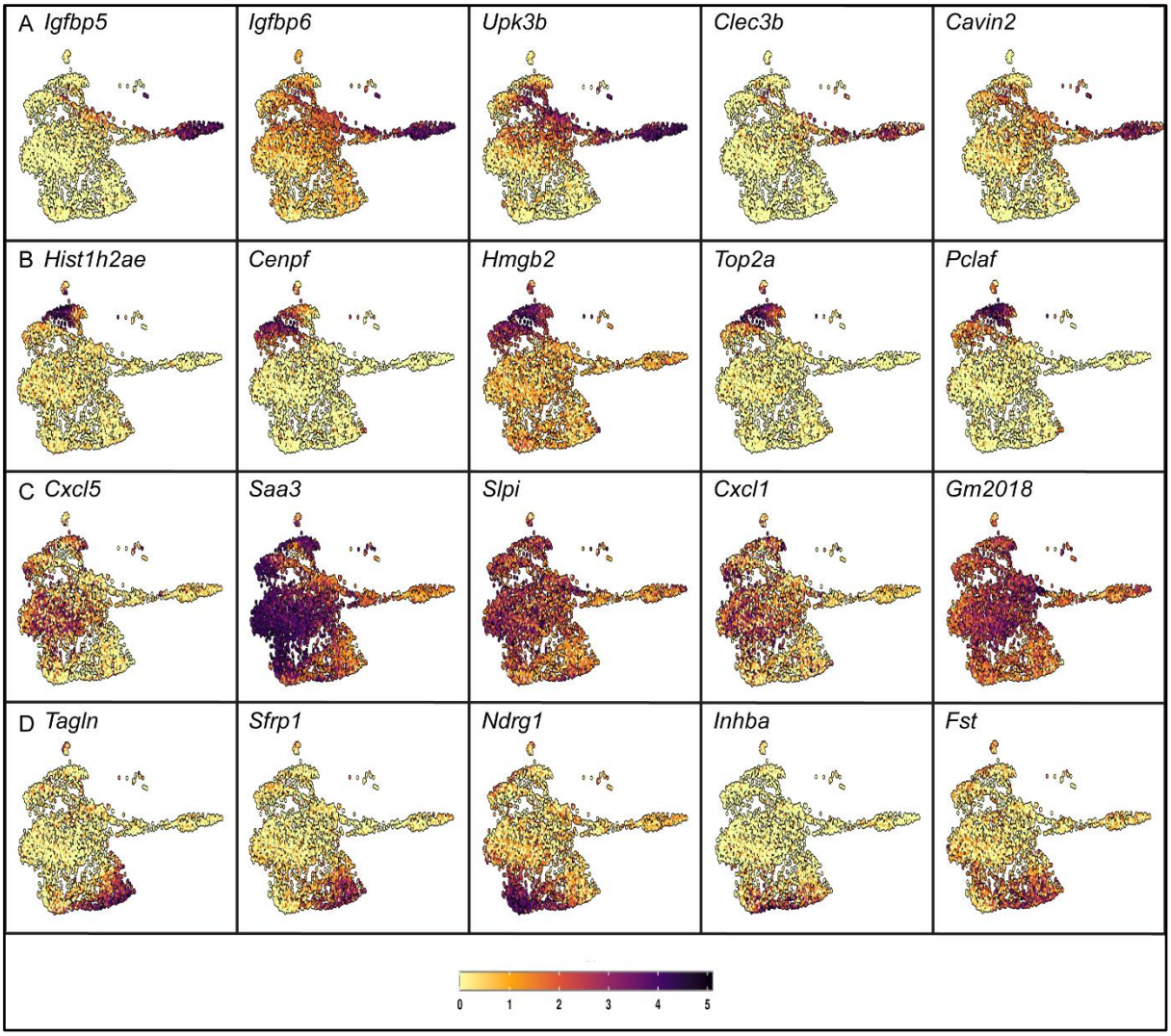

Figure 7-3. UMAP plots of top five marker genes for mesothelial subtypes from healthy, early, and late E0771 metastatic mouse lungs. *A: top five marker genes of mature mesothelium; B-D: top five marker genes of cancer-associated mesenchymal cells (CAMCs), where B: proliferating mesothelium; C: inflammatory fibroblast-like mesothelium; D: hypoxia-responsive perivascular mesothelium. These top marker genes were identified based on log2 foldchange of 0.25, min.pct of 0.25, and adjusted p-value <0.05. The full names of these genes are shown in* ***The List of Abbreviations Table.***

Table 7-1. Differentially expressed genes (DEGs) and references of literature studies used to annotate cell types of mouse lung mesenchymal cells. *CAMCs: cancer-associated mesenchymal cells. The full names of these genes are shown in* ***The List of Abbreviations Table.***

Annotated cell type	DEGs	Reference
Mesenchymal population		
Mature mesothelial cells	*Igfbp5, Igfbp6, Dcn, Upk3b, Rarres2, Msln, Wt1*	(Angelidis et al., 2019; Xie et al., 2018)
	Upk3b, Msln, Wt1	**(Liu et al., 2021)**
Hypoxia-responsive perivascular-like CAMCs	Hypoxia marker genes: *Ndrg1*	(Cangul, 2004)
	Hypoxia marker genes: *Inhba*	(Zheng et al., 2023)
	Perivascular marker genes: *Tagln*	(Chakraborty et al., 2019)
Inflammatory fibroblast-like CAMCs	Fibroblast marker genes: *Col1a2, Mgp*	(Angelidis et al., 2019)
	Inflammatory marker genes: *Saa3, Cxcl1*	(Djurec et al., 2018)
Proliferating CAMCs	Proliferation marker genes: *Top2a, Hmgb2*	(Angelidis et al., 2019)

By evaluating the hypoxia gene signature (generated by Professor Francesca Buffa's laboratory, **(Supplementary TableS10)** within these four cell types, a subset of hypoxia-responsive perivascular CAMCs was found to display the highest hypoxia score **(Figure 7-4A).** This subpopulation upregulated hypoxia signature genes such as *Ndrg1, Hilpda, Slc2a1 (Glut1),* and *Car9 (Ca9)* **(Figure 7-4B-D).** Interestingly, mature MCs were primarily abundant in the early niche, while the proliferating, inflammatory fibroblast-like and hypoxia-responsive perivascular CAMCs were detected in the late niche (mCherry+), indicating their potential roles in late E0771 metastatic progression **(Figure 7-2B-F)**. The increase of these inflammatory mature mesothelial cells in the early niche, where the metastases are primarily found in the lung parenchyma, is surprising as there are no pleural mesothelial cells in the parenchyma. However, the activated inflammation fits with the emergence of immune regulatory (IFN Ag-presenting) capillaries at an early stage of metastasis in both niche and distal regions **(Figure5-16 in Chapter 5)**, suggesting that these cells are priming the lungs for metastatic growth. Future studies could further explore this observation by immunofluorescence staining of early metastases using mesothelial markers.

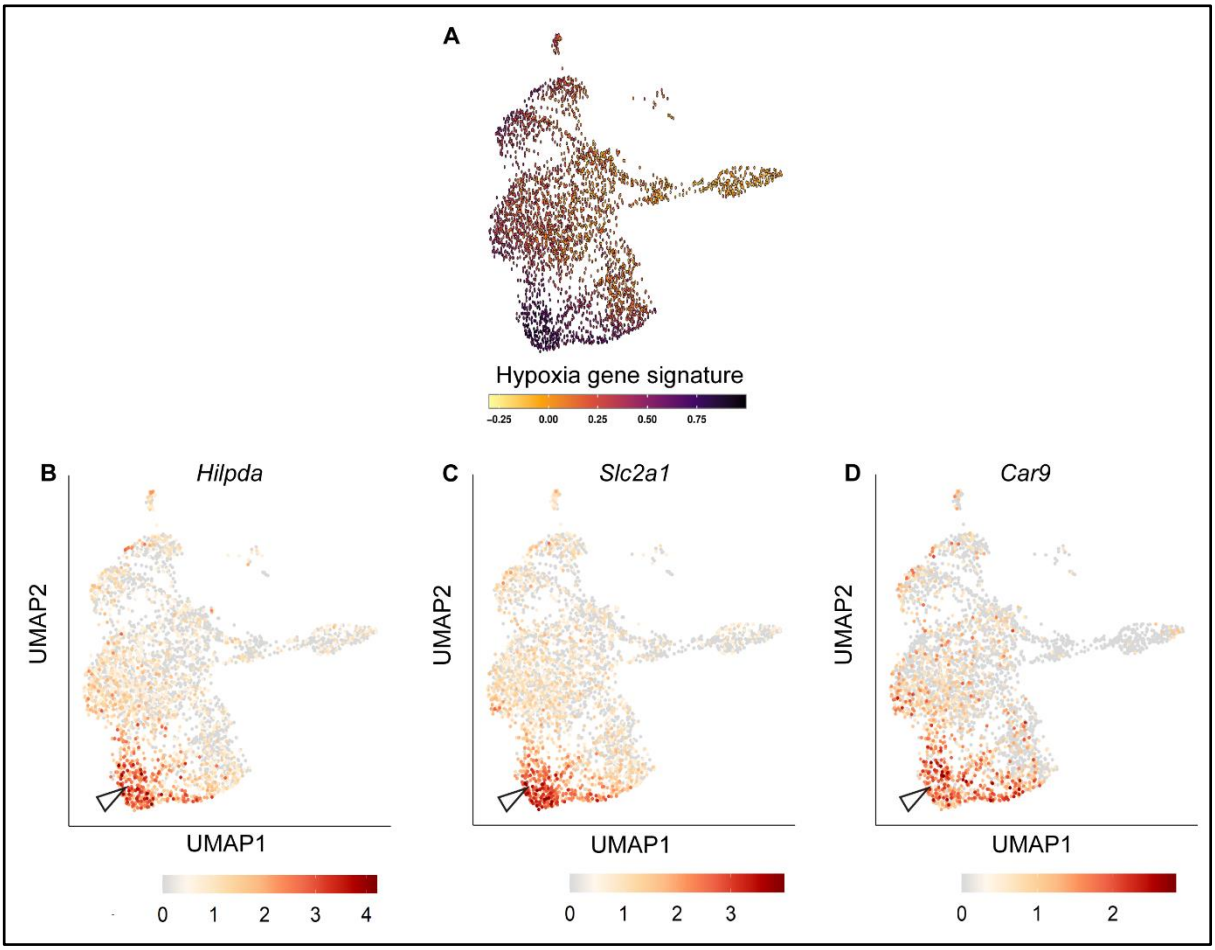

Figure 7-4. A subcluster of hypoxia-responsive perivascular cells highly express hypoxia signature genes. *A: UMAP visualization of hypoxia gene signature across mesenchymal subtypes with hypoxia-responsive cluster showing highest score; B-D: UMAP visualization of this subcluster (white arrowheads) upregulating the expression of hypoxia genes such as Hilpda, Slc2a1 (Glut1), and Car9 (Ca-9). The full names of these genes are shown in* ***The List of Abbreviations Table.***

7.3 Histological evaluation of mesothelial cells in E0771 metastatic lungs

7.3.1 Validation of the spatial localisation of mesothelial cells and spatial discrimination from tumour cells

Two known markers of mesothelial cells, WT1 and MSLN, were selected from the scRNA-seq data, and antibodies against them were used in immunofluorescence analysis of E0771 metastatic lung tissue section in order to validate the increase of mesothelial cells during metastasis. Analysis comparing non-tumour-bearing and E0771 metastatic lung tissue sections revealed different patterns of WT1 expression between the two. In non-tumour-bearing lungs, WT1-expressing cells were elongated in shape and localised at the pleura lining the lung parenchyma **(Figure 7-5A, B, Figure 7-6E).** In contrast, in E0771 metastatic lungs, there were a larger number of WT1-expressing cells in both the parenchymal and subpleural metastases. Staining was presented intratumourally and localised inside nuclei, which were round **(Figure 7-5C-F).**

In addition to acting as a marker gene for mesothelial cells, WT1 is a transcription factor expressed in tumour cells. It has been identified as a tumour suppressor gene *e.g. Wt1* inactivation causes Wilms' tumour; but can also act as an oncogene and is overexpressed in several tumours (Lee & Haber, 2001; Menssen et al., 1995; Oji et al., 2004; Oji et al., 2003). E0771 tumour cells also express WT1 **(Figure 7-5C-F, Figure 7-6F-H)** and other mesothelial markers **(Figure 7-6B-D).** Therefore, to distinguish pleural mesothelial cells from E0771 cells for further investigation, an antibody against cytokeratin 5/6 (CK5/CK6) was used. CK5/CK6 expression is highly indicative of a mesothelial origin for cells (Ordóñez, 1998). In my section analysis, I found that CK5/CK6 reactivity was localised at the subpleural region of late subpleural metastases, with no expression detected in E0771 tumour cells **(Figure 7-6I, J).**

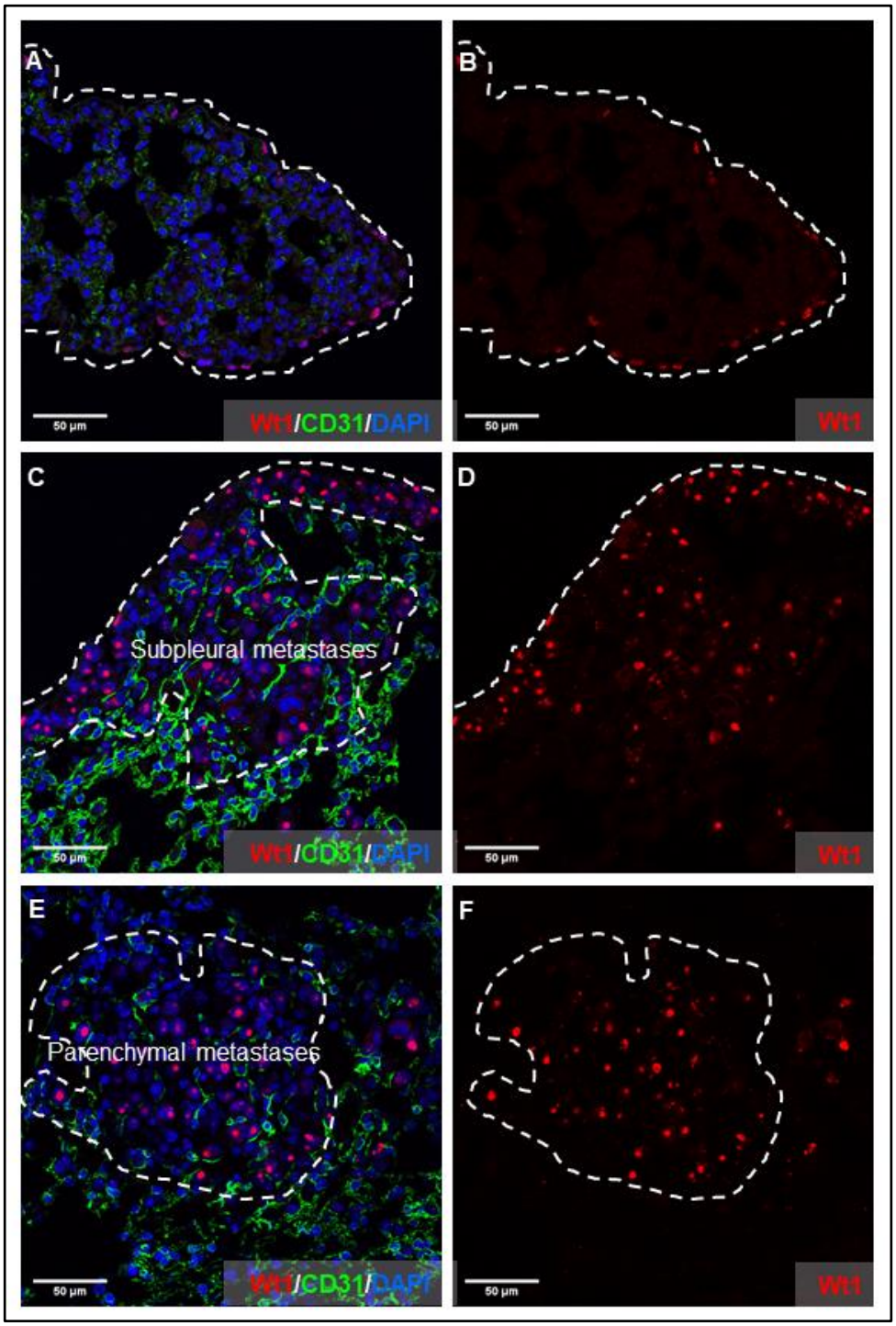

Figure 7-5 . Immunofluorescence staining using anti-WT1 (red) and anti-CD31 (green) antibodies revealed that WT1 is expressed in pleural mesothelial cells in non-tumour-bearing lungs and E0771 tumour cells in E0771 metastatic lungs. *A and B: pleural mesothelial cells in normal lungs express WT1, and the cells look thin and elongated in shape; C and D: WT1 is expressed in E0771 tumour cells and the metastatic niche of subpleural metastases; E and F: WT1 is expressed in E0771 tumour cells and the metastatic niche of parenchymal metastases. Nuclei were counterstained with DAPI (blue).*

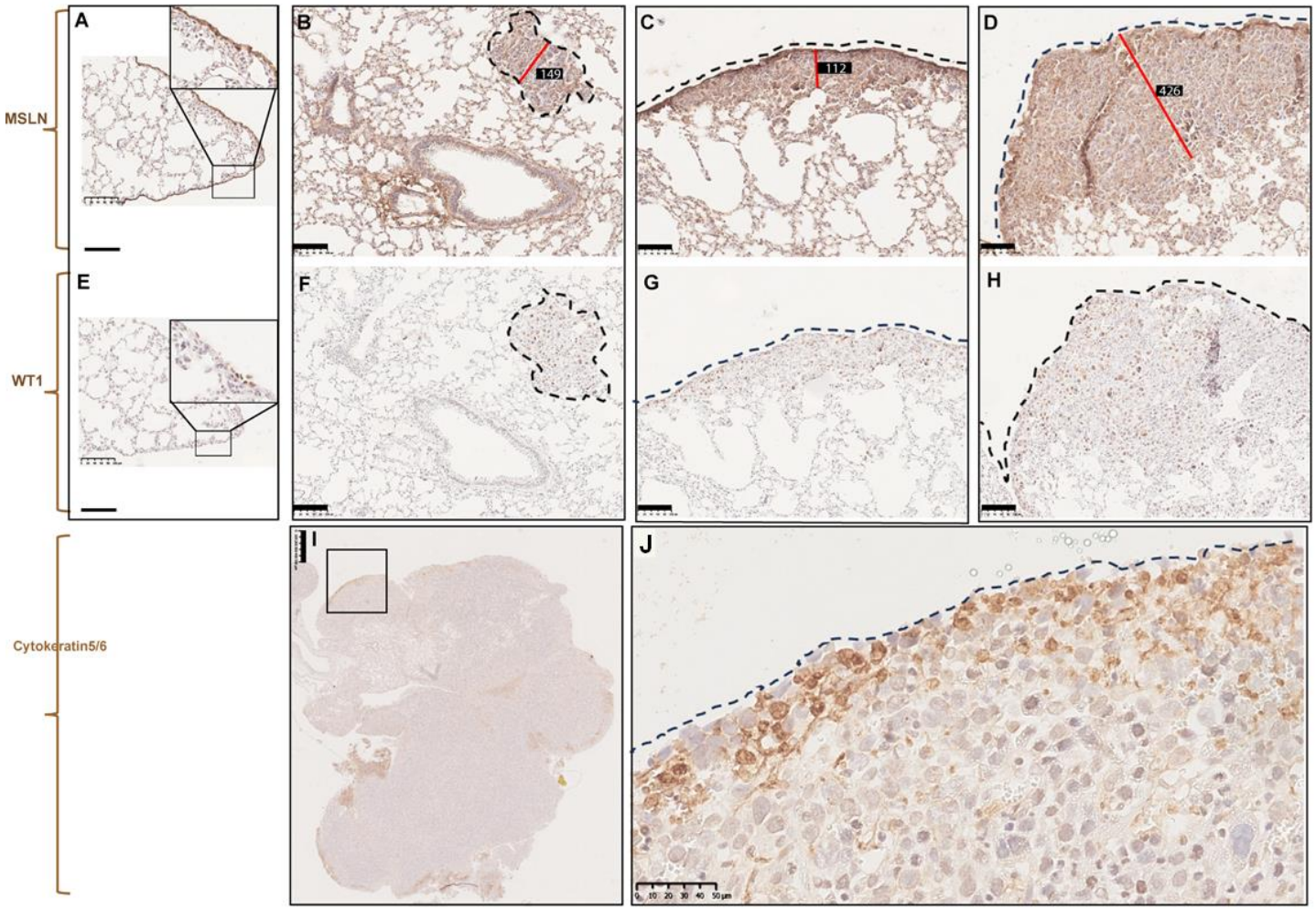

Figure 7-6. WT1 and MSLN exhibited expression in E0771 tumour cells and pleural mesothelial cells, and cytokeratin 5/6 staining was used to discriminate between these two populations. *A, E: serial sections of non-tumour-bearing lung, where pleural mesothelium expressed MSLN and WT1. Both MSLN and WT1 were expressed in serial sections of B, F: parenchyma metastases; C, D, G, and H: subpleural metastases, respectively. Small and large subpleural metastases showed intact pleural mesothelial monolayer (dashed lines in C, D, G, H. I: overall view of one lung lobe stained with cytokeratin 5/6; J: zoomed inset depicting distinct expression of cytokeratin 5/6 in mesothelial cells with negative expression in E0771 tumour cells. Scale bars in A-H = 100 µm, in I = 500 µm, and in J = 50 µm. The full names of these genes are shown in* ***The List of Abbreviations Table.***

7.3.2 Examination of surface pleural mesothelial layer disruption during the invasion of metastatic E0771 breast cancer

Pleural mesothelial cells produce a variety of extracellular matrix proteins including collagen types I, III and IV, elastin, fibronectin and laminin, and the cells are connected by adherens junctions (Mutsaers, 2002). I next investigated whether the integrity of this mesothelial monolayer could be breached by E0771 tumour cells as a mechanism to increase pleural permeability, and whether the tumour cells invaded the visceral pleura. This analysis used Verhoeff-Van Gieson (VVG) staining that label elastic fibres in the tissue. Although VVG stain (dark blue) labels almost the whole lungs (because elastic fibres are ubiquitously expressed (Mecham, 2018)), histological evaluation revealed that E0771 tumour cells grew within the subpleural region underneath the elastic layer without penetrating the surface of the visceral pleura, at both early and late time points **(Figure 7-7)**. VVG staining was correlated with MSLN staining, which found that the pleural mesothelial monolayer was not disrupted by tumour cells at the late time point **(Figure 7-6C, D).** Consequently, I concluded that E0771 tumour cells are not outgrowing the pleural mesothelial layer and thus are not invading beyond the visceral pleura.

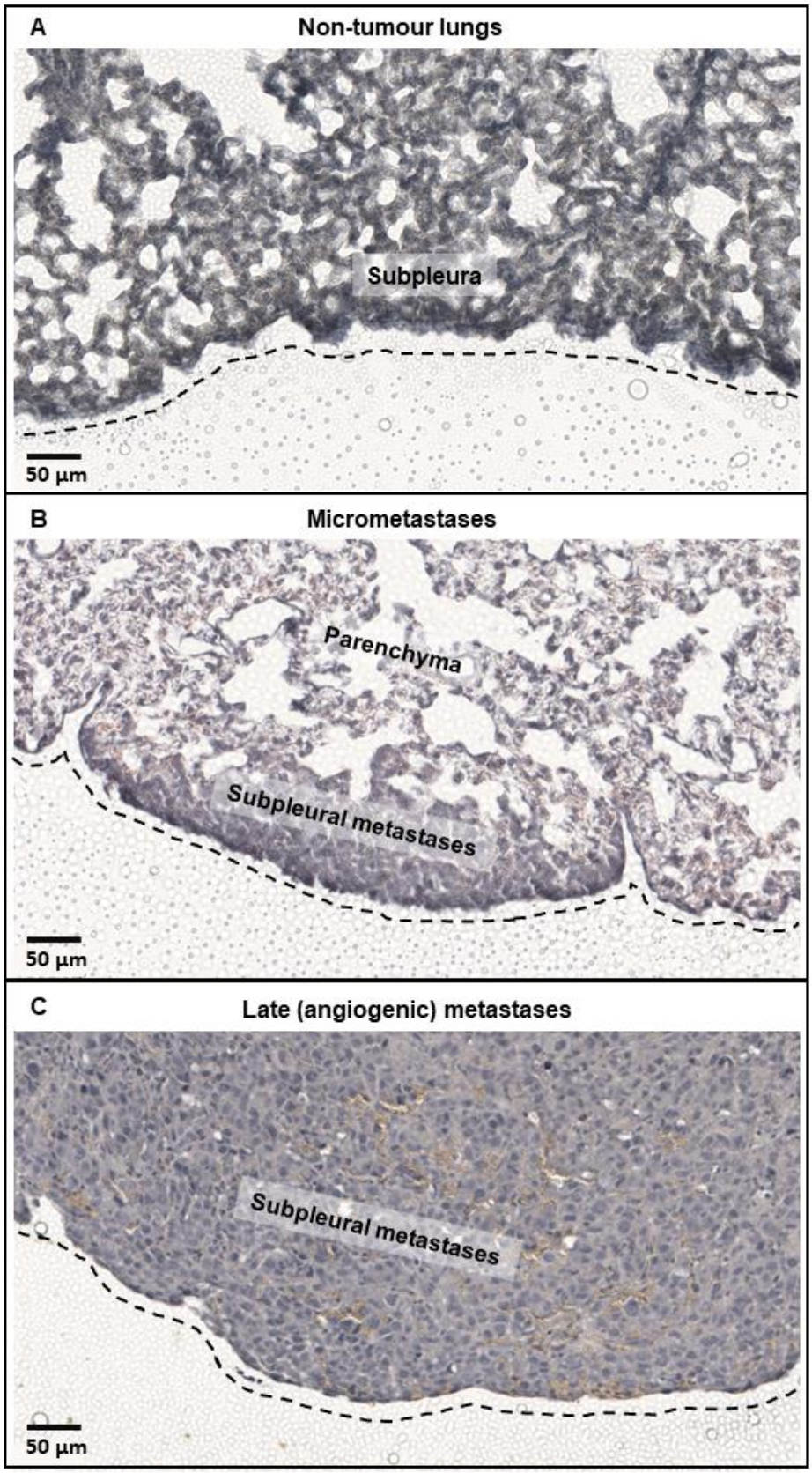

Figure 7-7. VVG staining revealed that the integrity of the pleural mesothelial cells (cell layer covering the lung tissue, dark blue) is intact in micrometastases and late (angiogenic) metastases. *Non-tumour (A), early (B), and late (C) metastatic tissue sections were stained with the elastic stain (Verhoeff-Van Gieson (VVG)) to label the elastic fibres that are usually produced by pleural mesothelial cells.*

7.4 *In vitro* study of the effect of pulmonary mesothelial cells on metastatic E0771 breast cancer cells

After validating and characterising the localisation of pleural mesothelial cells in metastatic E0771 lungs at the histological level, I investigated whether mesothelial cells promote E0771 tumour proliferation and invasion. Primary pleural mesothelial cells were isolated from the thoracic cavity using an established protocol (Kawai et al., 2019). To determine whether close contact was necessary for tumour-mesothelium interaction, a transwell assay (pore size= 0.4 µm) was used. E0771 tumour cells were seeded in the upper inserts and primary mesothelial cells in the lower chamber in an indirect co-culture setting (in shared media). No mesothelial cells were added in the single culture setting. Fluorescence quantification of cell numbers revealed that indirect transwell co-culture with primary mesothelial cells significantly increased the proliferation of E0771 cells when compared to E0771 monoculture (the average number of E0771 in the indirect co-culture= 58381 cells ± 2054; in monoculture= 17838 cells ± 826.8; p <0.0001) **(Figure 7-8A).** These findings suggest that signalling between E0771 tumour cells and pleural mesothelial cells is mediated by soluble factors or exosomes in a transwell setting, where both cell types share the same media.

I next examined whether primary mesothelial cells promoted E0771 tumour cell invasion. Transwell assay was performed, seeding E0771 tumour cells in the upper inserts on top of a collagen I layer (as an invasion barrier), and seeding primary mesothelial cells in the lower chamber, creating an indirect co-culture setting. No mesothelial cells were added in the single culture control. Mesothelial cells were found to significantly enhance E0771 invasion through the matrix monolayer compared to single E0771 culture (% of invaded tumour area in the indirect coculture= 38.03 ± 3.12; in single culture= 12.28 ± 4.24; p = 0.008) **(Figure 7-8B, C).**

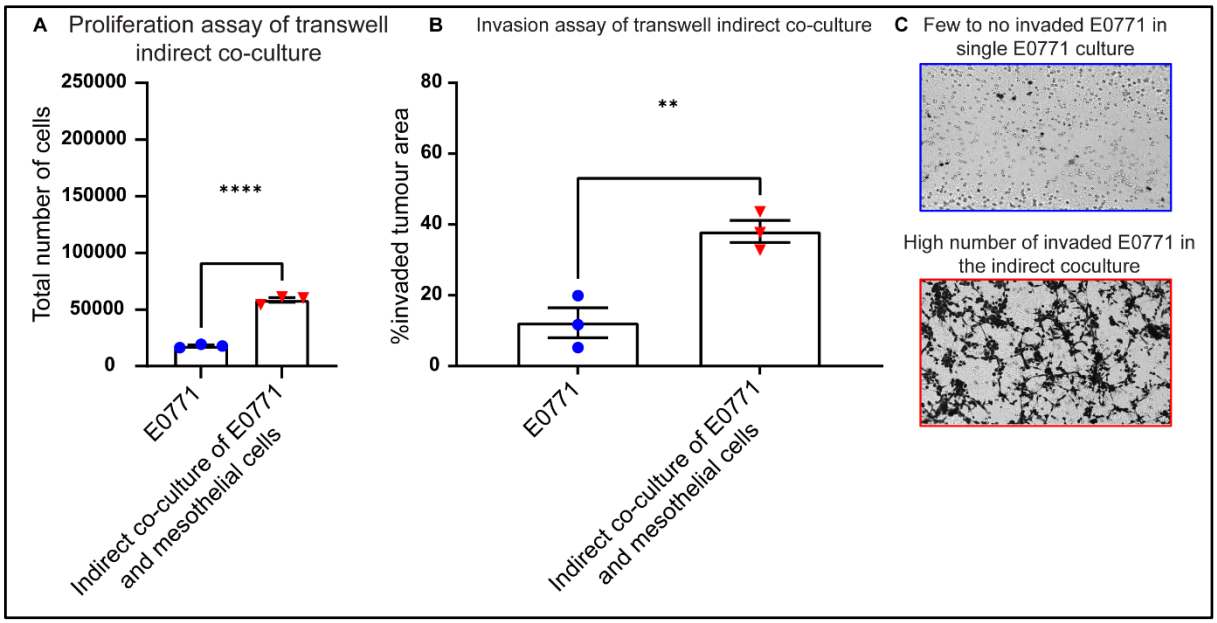

Figure 7-8. Primary pleural mesothelial cells promote E0771 tumour cell proliferation (bidirectional signalling using transwell setting) and invasion. *A: CYQUANT cell proliferation assay of transwell indirect co-culture, where E0771 tumour cells were seeded in upper inserts and mesothelial cells were seeded in the lower chamber in the indirect co-culture group and no mesothelial cells in the control group; B: invasion assay with same experimental settings as in (A) but coating upper inserts with a matrix (collagen I) layer that served as an invasion barrier; C: representative fields of view for control group, where almost no invasion occurred (blue box) and indirect co-culture group, showing high numbers of E0771 tumour cells invaded into the lower side of the insert through collagen I layer (red box). Each data point (circle or triangle) represents an average of 3-4 replicate wells per group (n= 3 independent experiments for the control group and n= 3 independent experiments for the indirect co-culture group). Each data set represents the mean ± standard error of the mean (SEM) (Unpaired Student's t-test was used, *: p ≤ .05; **: p ≤ .01; ***: p ≤ 0.001; ****: p ≤ 0.0001).*

7.5 Investigating the origin and pathways enriched in cancer-associated mesenchymal cells

I next wanted to validate the transition of mesothelial cells into CAMCs in the late niche. Therefore, I further examined scRNA-seq data using a differentiation trajectory reconstruction method, Monocle3 R package and GSEA analysis **(Figure 7-9A-D)**. As tumours evolved from early to late stages of metastasis, mature mesothelium emergence was followed by an increase in CAMCs. Therefore, I was able to track that the trajectory started from the mature mesothelium **(Figure 7-9A, white arrowhead)**. Pseudotime trajectory analysis revealed that the mature mesothelium branched into three trajectory paths indicative of its differentiation toward the three subtypes of CAMCs **(Figure 7-9A).** Interestingly, the trajectory path bifurcated into inflammatory fibroblast-like and hypoxia-responsive perivascular mesenchymal cells forming a loop, suggesting these two mesenchymal subtypes are interchangeable and transiently transform into each other **(Figure 7-9A, black arrow)**.

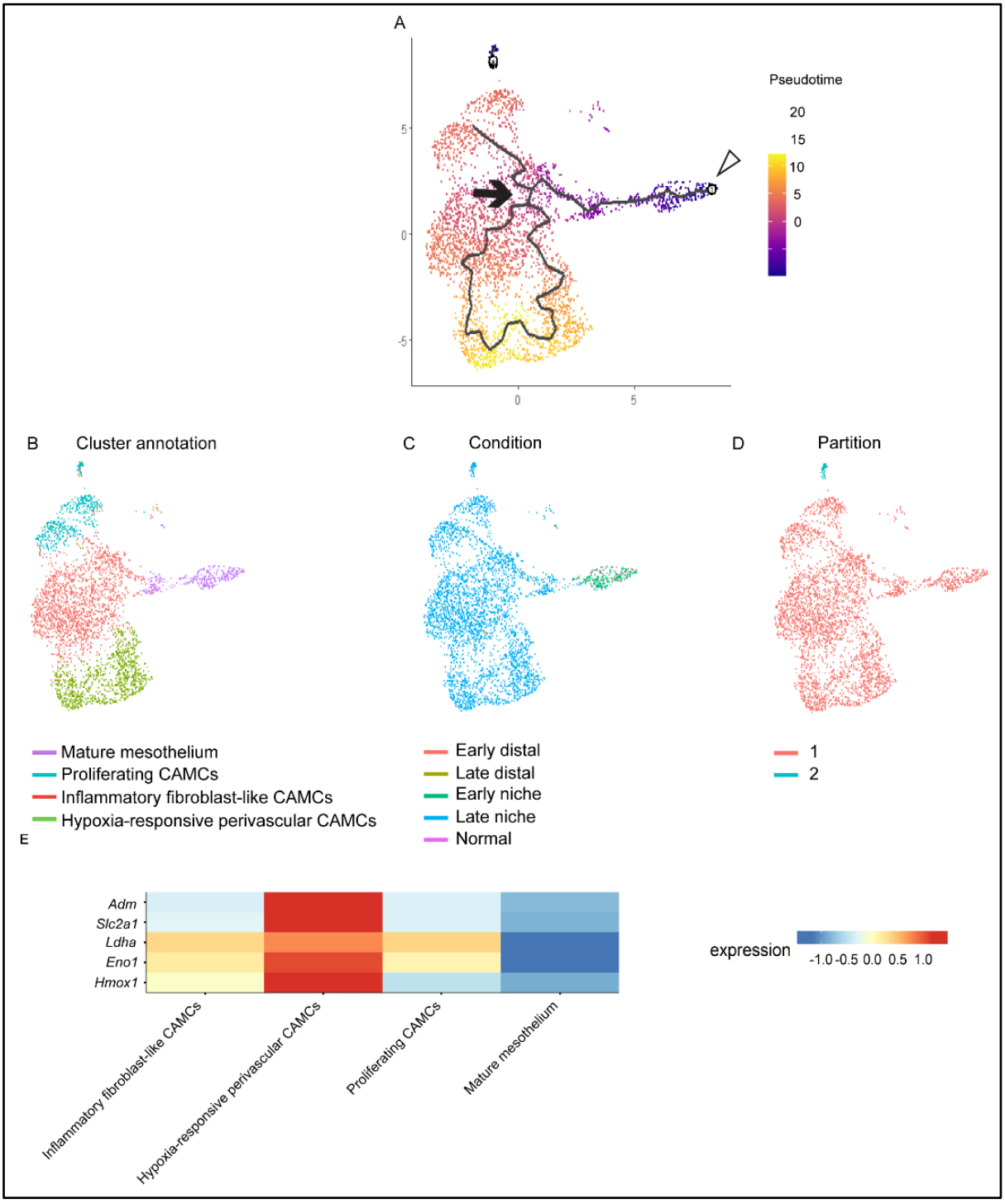

Figure 7-9. Cancer-associated mesenchymal cells (CAMCs) subtypes are predicted to arise from mature mesothelium. *A: mesothelial differentiation trajectory analysis using Monocle predicts mature mesothelium differentiates into three CAMC subtypes with a trajectory loop (black arrow) between inflammatory-like and hypoxia-responsive perivascular mesothelial cells. The white circle indicates the root (starting) node starting from mature mesothelium (white arrowhead); B: annotation for mesothelial subclusters; C: UMAP projection plot of scRNA-seq merging all five conditions: healthy, early distal, early niche, late distal, and late niche ECs of early metastases and late metastases, respectively; D: Monocle trajectory analysis separates mesothelial cells into two partitions indicating two distinct trajectories; E: heatmap visualizing high expression of Hif-1-regulated genes in hypoxia-responsive perivascular mesenchymal cells compared to other subtypes.. The full names of these genes are shown in* ***The List of Abbreviations Table.***

GSEA analysis of mesothelial cells in the early niche identified the upregulation of inflammatory pathways such as IFNγ and cytokine-mediated signalling in comparison to mesothelium either in distal area or in non-tumour-bearing lungs **(Figure 7-10A, B).** Indeed, mature mesothelium in the early niche upregulated Ifnγ-regulated genes (*Stat1, Ly6e, Psmb10, Ifit3*) and cytokine-regulated genes (*Cav1, Il6st, Irgm1*) **(Figure 7-10C).** In contrast, CAMCs (including the three novel aforementioned subtypes) upregulated EMT and gene sets related to active cellular biosynthesis, including translational initiation and cotranslational protein targeting to the membrane **(Figure 7-11A, B).** Upregulated expression of EMT signalling genes such as *Fn1, Cdh2 (N-Cadherin),* and *Timp3* **(Figure 7-12A-C)** is correlated with the predicted trajectory path from quiescent into mesenchymal-like cells (CAMCs: proliferating, inflammatory fibroblast-like, and hypoxia-responsive perivascular) **(Figure 7-9A)**. Gene expression patterns in CAMCs supported the acquisition of a mesenchymal phenotype, as they downregulated mesothelial markers such as *Upk3b, Krt18,* and *Krt19* **(Figure 7-12D-F).** In contrast, the upregulated biosynthetic pathway correlated with the proliferating CAMCs that showed the highest proportion of cells in the G2/M (mitosis) phase **(Figure 7-12H, white arrowhead).**

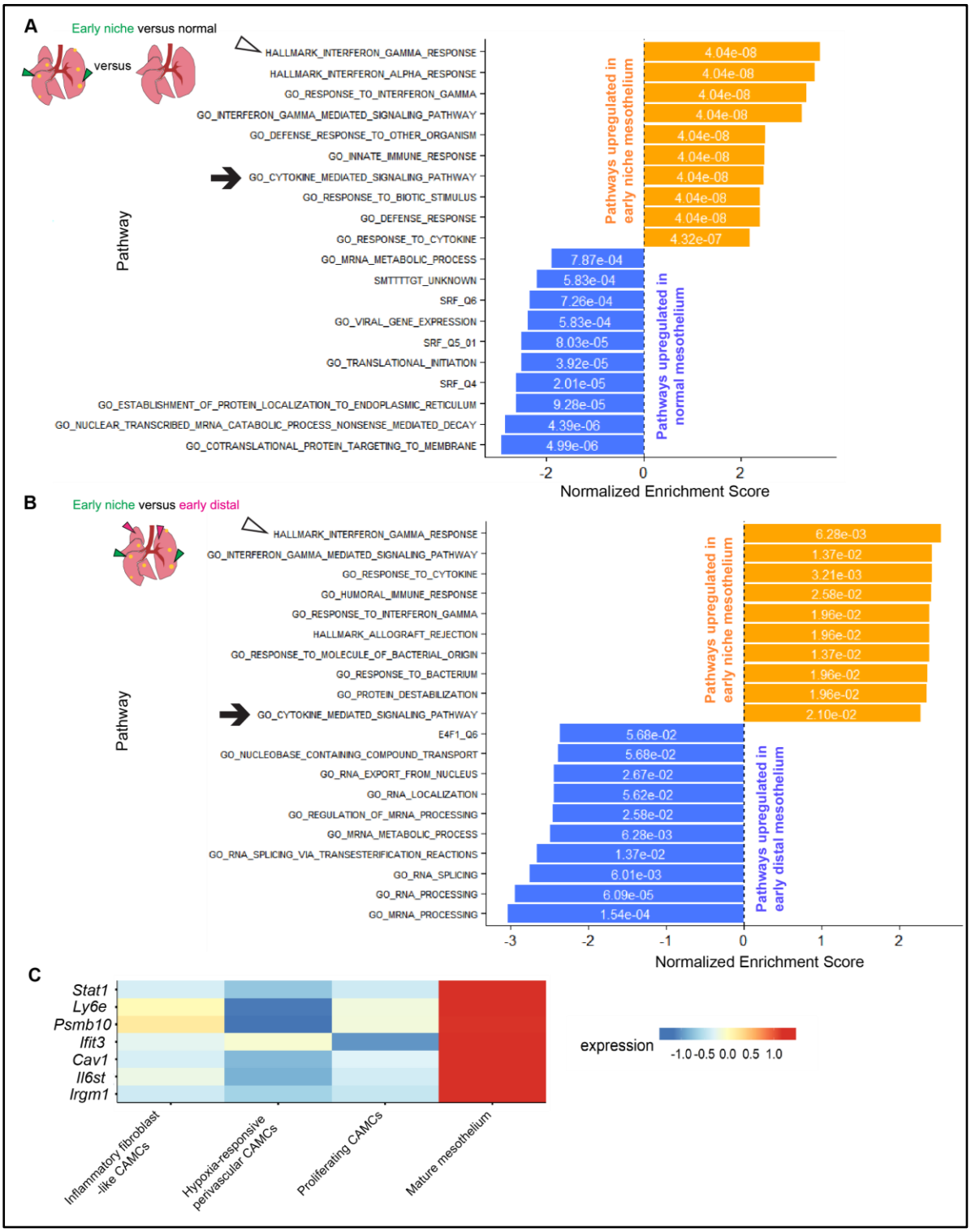

Figure 7-10. Gene set enrichment analysis (GSEA) of DEGs showed significant upregulation (yellow bars) of gene sets related to inflammatory pathways in early niche mature mesothelium compared to the distal region of the same lungs (B) and normal lungs (A). *Upregulated gene sets related to the IFNγ pathway are depicted by white arrowheads and related to the cytokine pathway by black arrows. C: heatmap visualizing high expression of Ifnγ and cytokine genes in mature mesothelium. NES: normalized enrichment score. The full names of these genes are shown in* ***The List of Abbreviations Table.***

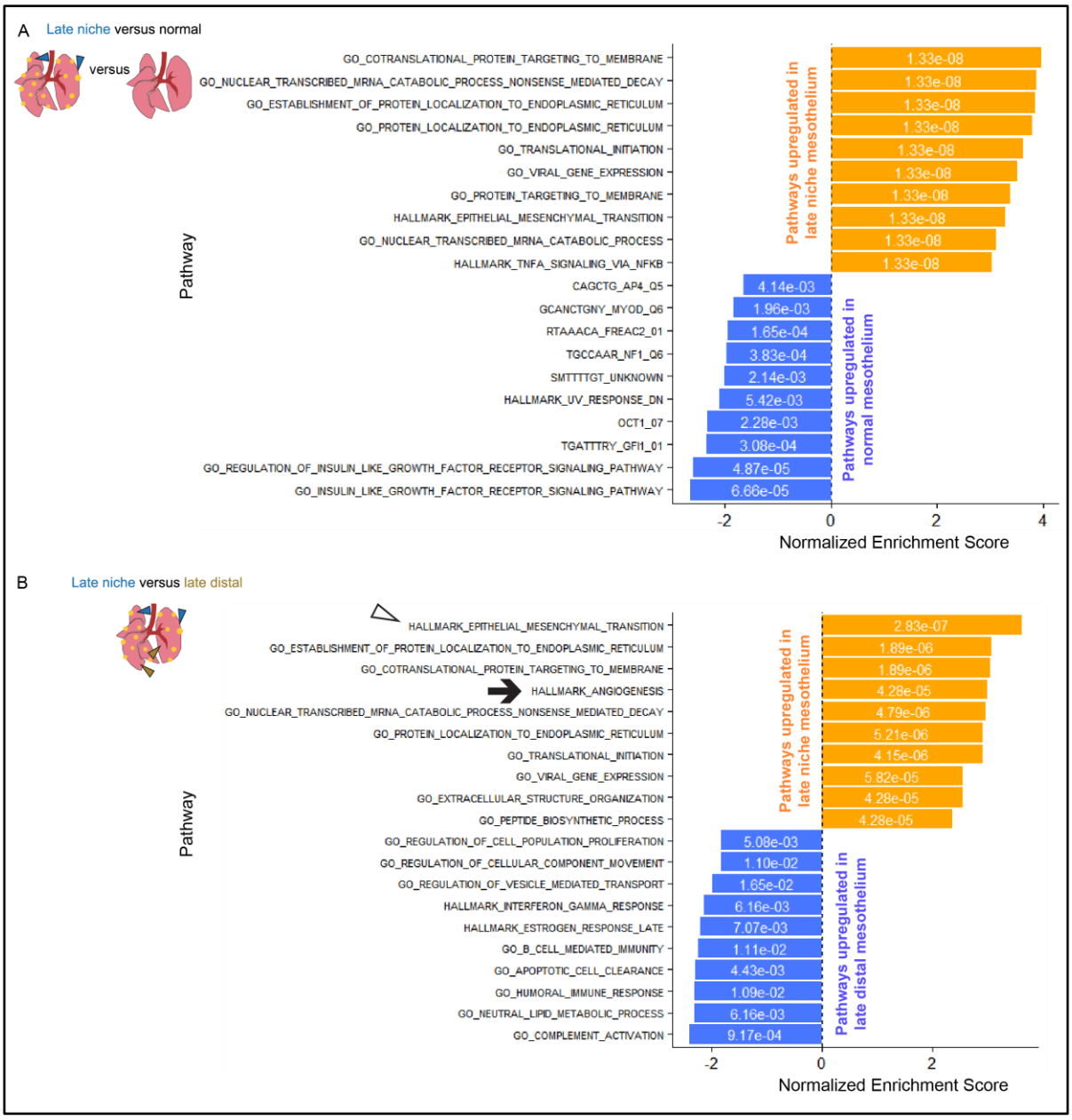

Figure 7-11. Gene set enrichment analysis (GSEA) of DEGs showed significant upregulation (yellow bars) of gene sets related to Epithelial–mesenchymal transition (EMT) process, Tnfα pathway (white arrowheads), and angiogenesis (black arrows) in cancer-associated mesenchymal cells (CAMCs) subtypes of the late niche compared to the distal region of the same lung (B) and normal lungs (A). *NES: normalized enrichment score.*

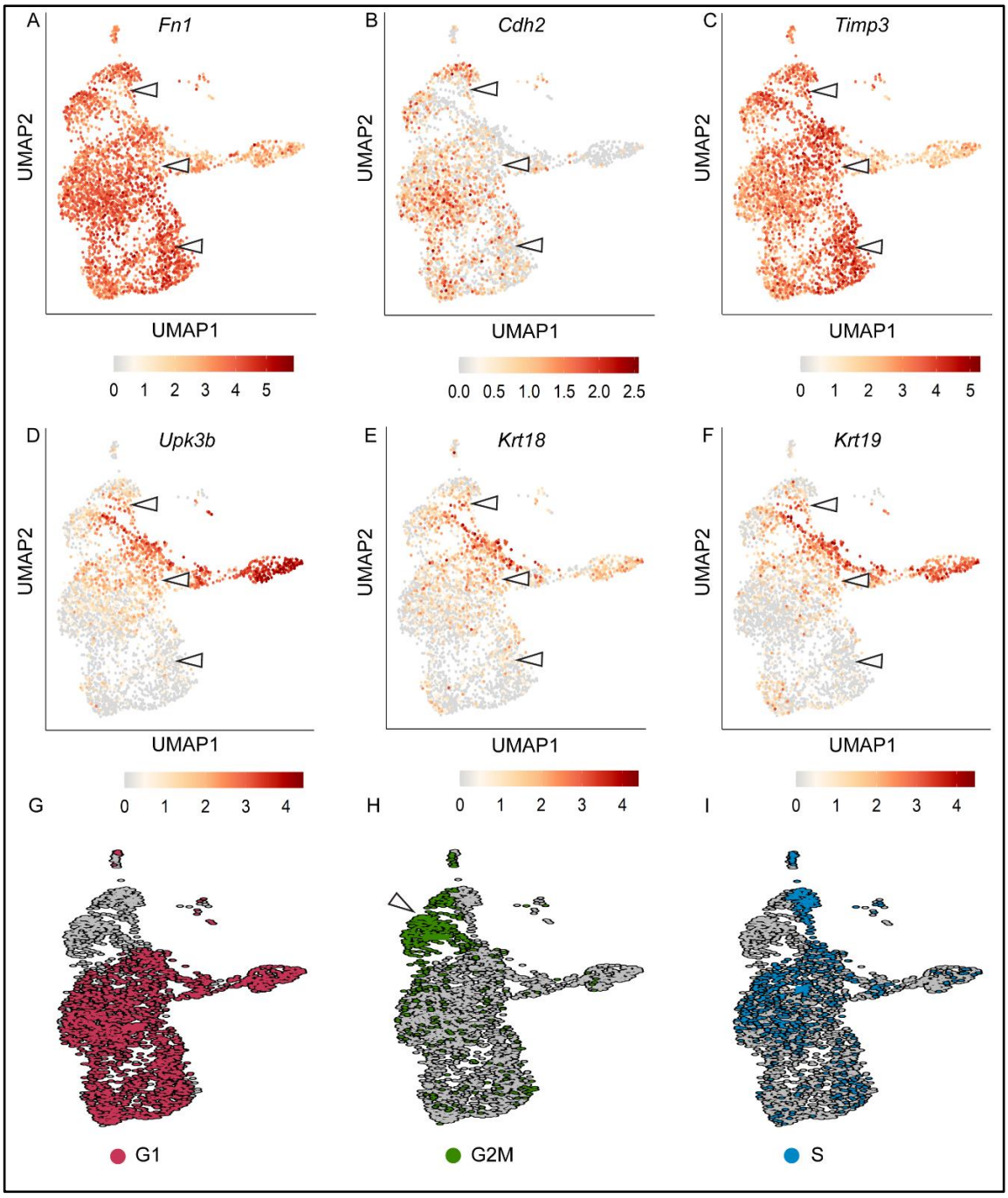

Figure 7-12. Cancer-associated mesenchymal cells (CAMCs) upregulated the expression of mesenchymal markers with a cluster that is highly proliferative. *A-C: expression of mesenchymal markers: including Fn1, Cdh2 (Ncad), and Timp3; D-F: CAMCs downregulated the expression of mesothelial markers: Upk3b, Krt18, and Krt19; G-I: cell cycle scoring of mesothelial cells showing a subcluster that is highly proliferative in S and G2M phases (white arrowheads). The full names of these genes are shown in* ***The List of Abbreviations Table.***

The GSEA pathway analysis found angiogenesis to be one of the top significant pathways in CAMCs of the late niche when compared to normal mature mesothelium **(Figure 7-11B, black arrow).** This finding is consistant with my cell-cell communication analysis that found that *Vegfa* – *Vegfr2* signalling is activated and predicted to be driven by CAMCs – cap I cells **(Figure6-15 in Chapter 6).**

7.6 *In vivo* lineage tracing the origin of cancer-associated mesenchymal cells enriched in the late metastatic niche

My results so far found temporal heterogeneity in mesothelial cells that correlated with an upregulation of the EMT pathway in subpleural metastases **(Figure 7-2B-F, Figure 7-11A,B)** and an increase in mesenchymal marker genes **(Figure 7-12A-C).** Therefore, I next sought to further investigate whether pleural mesothelial cells undergo EMT to differentiate into mesenchymal cells in order to support late E0771 metastatic progression. To do this, I used an *in vivo* lineage tracing model. This took advantage of inducible *Wt1-CreERT2*;tdTomato reporter mice, which enabled me to label and track the cell fate of pleural mesothelial cells in the metastatic context **(Figure 7-13A).** In this transgenic mouse, tamoxifen administration induces Cre activity and subsequent tdTomato reporter expression in WT1-expressing cells **(Figure 7-13B)**.

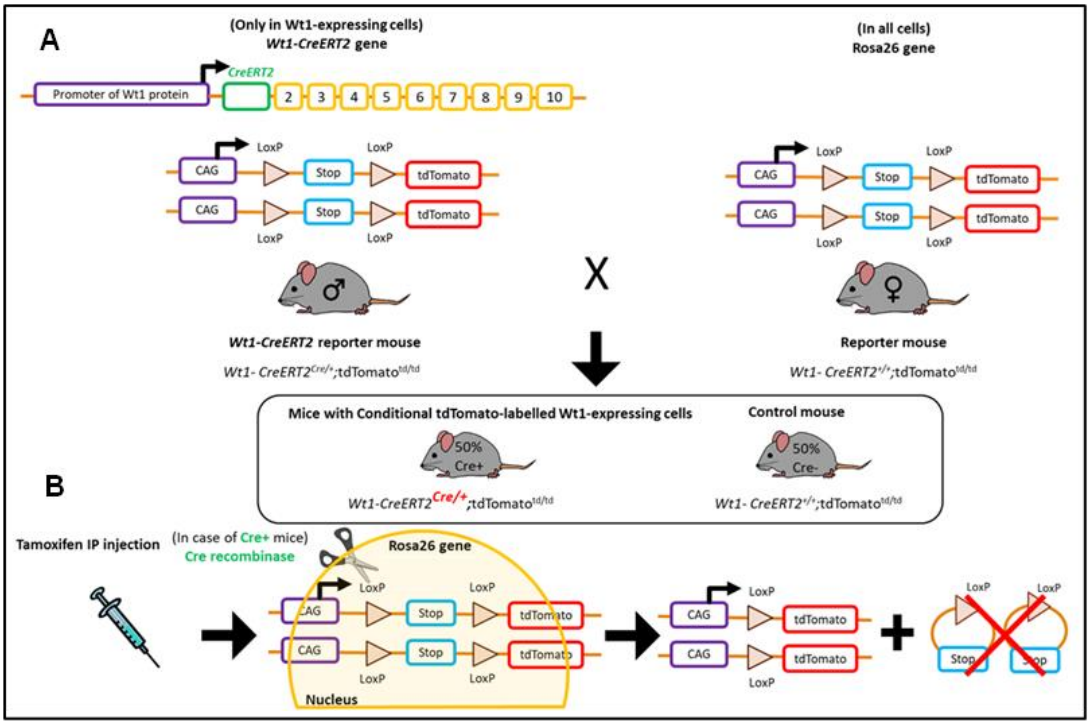

Figure 7-13. Diagram illustrating inducible induction of tdTomato reporter expression in WT1-expressing pleural mesothelial cells in Wt1-CreERT2;tdTomato reporter mice. *Wt1-CreERT2$^{Cre/+}$;tdTomatotd$^{td/td}$ male mouse crossed with Wt1-CreERT2$^{+/+}$;tdTomato$^{td/td}$ female mouse yielded 50% Cre+ and 50% Cre- progeny. Tamoxifen administration induced tdTomato labelling of WT1-expressing cells in 50% of offspring expressing Cre recombinase under Wt1(mesothelial marker)-specific promotor. Upon oral gavage of tamoxifen to this model, tamoxifen bound to its binding domain of oestrogen receptor (ER), causing translocation of Cre recombinase from the cytoplasm into the nucleus, where recombination (excision) of loxP-flanked stop sequence then occurs inducing tdTomato expression. This transgenic line contained the Cre sequence under the promoter of a mesothelial marker, the Wt1 gene allowing spatiotemporal Cre-recombination and tdTomato reporter expression to occur only in pleural mesothelial cells.*

7.6.1 Tamoxifen induction of tdTomato expression in WT1-expressing cells in healthy lungs

WT1 is reported to be expressed in pleural mesothelial cells in the lungs, with no expression reported in the mesenchyme of the lung tissue (Que et al., 2008). This information was used to validate Cre activity and tdTomato expression in our reporter mice by examining dissected lungs under a fluorescent microscope after Cre-reporter activation. First, experimental mice were genotyped to identify *Cre*-positive (mice with WT1-expressing cells labelled with the tdTomato reporter) and *Cre*-negative mice **(Figure** 7-14**),** and tamoxifen was administrated at four and five weeks of age. Both times, tamoxifen was administered for two consecutive days to provide maximal reporter induction in pleural mesothelial cells with minimal welfare issues *in vivo.*

Analysis of the lungs of *Wt1-CreERT2*;tdTomato reporter mice with WT1 antibody showed high co-localisation of the tdTomato Cre reporter and WT1 **(Figure 7-15)**, and verified efficient spatial expression of tdTomato in pleural mesothelial cells **(Figure 7-15A)**.

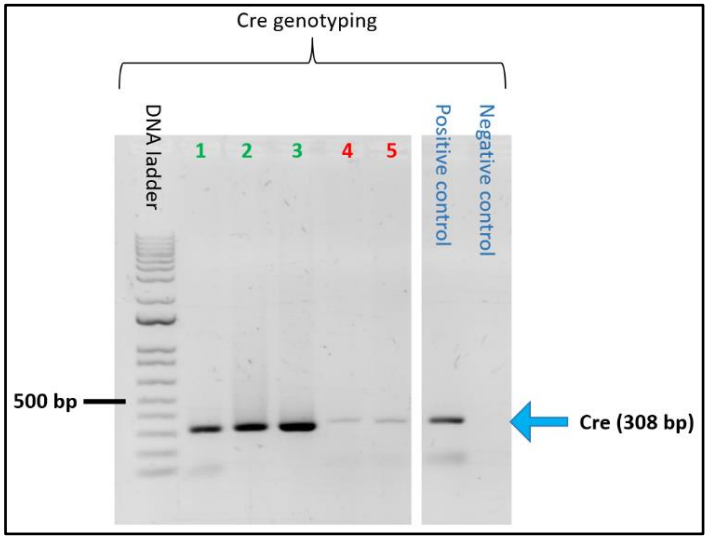

Figure 7-14. Identification of transgenic mice (Cre-positive) and littermate controls (Cre-negative) by Cre amplification. *Mice 1, 2, and 3 are positive for Cre were used as the experimental (mice with WT1-expressing cells labelled with tdTomato reporter) group.; mice 4 and 5, are negative for Cre.*

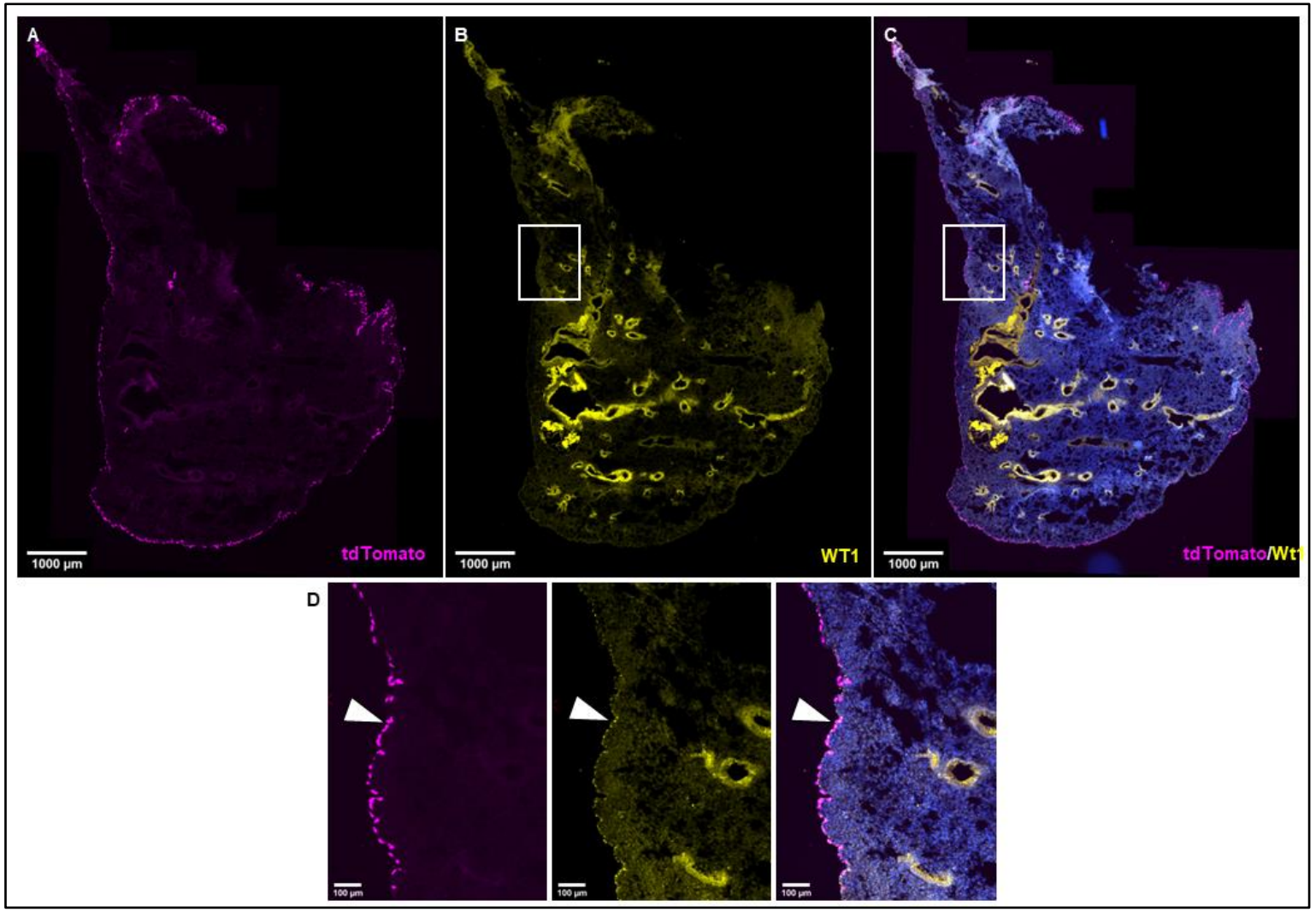

Figure 7-15. Tamoxifen administration induced efficient tdTomato reporter expression in pleural mesothelium of the lungs of Wt1-CreERT2;tdTomato reporter mice. *Nuclei were counterstained with DAPI (blue). A: whole left lobe showing endogenous tdTomato signal (magenta); B: whole left lobe stained with WT1 antibody validating the expression of WT1 (yellow) in pleural mesothelial layer; C: whole left lobe merging DAPI, WT1, tdTomato channels in one image; D: enlarged views of insets (white boxes) in A-C showing co-expression of tdTomato and WT1 in the lung visceral pleura, which is indicative of efficient Cre activity and reporter induction via tamoxifen.*

7.6.2 Generation of an *in vivo* Wt1-CreERT2 tdTomato reporter metastasis model

Following efficient induction of Cre-reporter labelling of pleural mesothelium using tamoxifen, parental E0771 breast tumour cells were injected intravenously. Mice were sacrificed at the experimental endpoint on days 13-16, when established lung metastases were formed **(Figure 7-16).**

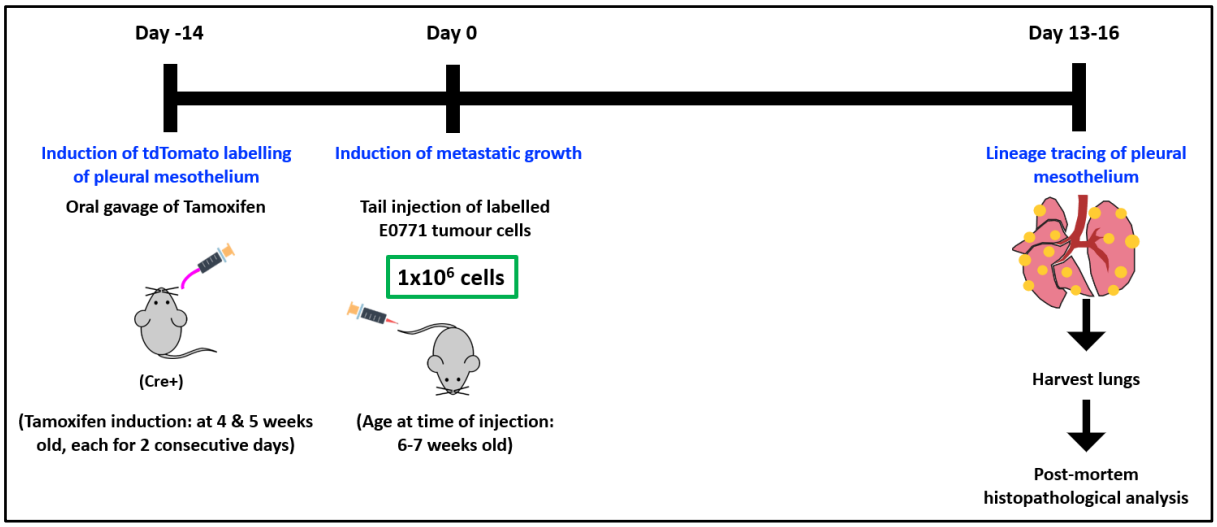

Figure 7-16. Timeline of induction of reporter expression in Wt1-CreERT2;tdTomato reporter mice followed by the development of experimental E0771 lung metastasis model. *Tamoxifen was administered via oral gavage to the Cre positive mice at indicated timepoints. Then, E0771 tumour cells were injected intravenously 2-3 weeks following tamoxifen administration. Metastatic lungs were harvested on days 13-16 for histological assessment.*

7.6.3 Partial contribution of pleural mesothelial cells to the development of subpleural angiogenic metastases

I next investigated the contribution and distribution of pleural mesothelial cells in the *Wt1-CreERT2*;tdTomato reporter E0771 lung metastasis model. Histological examination revealed a few tdTomato+ (therefore WT1Cre-derived) pleural mesothelial cells in the late (subpleural) metastases, just beneath the supleura **(Figure 7-17C, D).** This finding suggests that pleural mesothelial cells are not the primary origin of CAMCs present in the late niche.

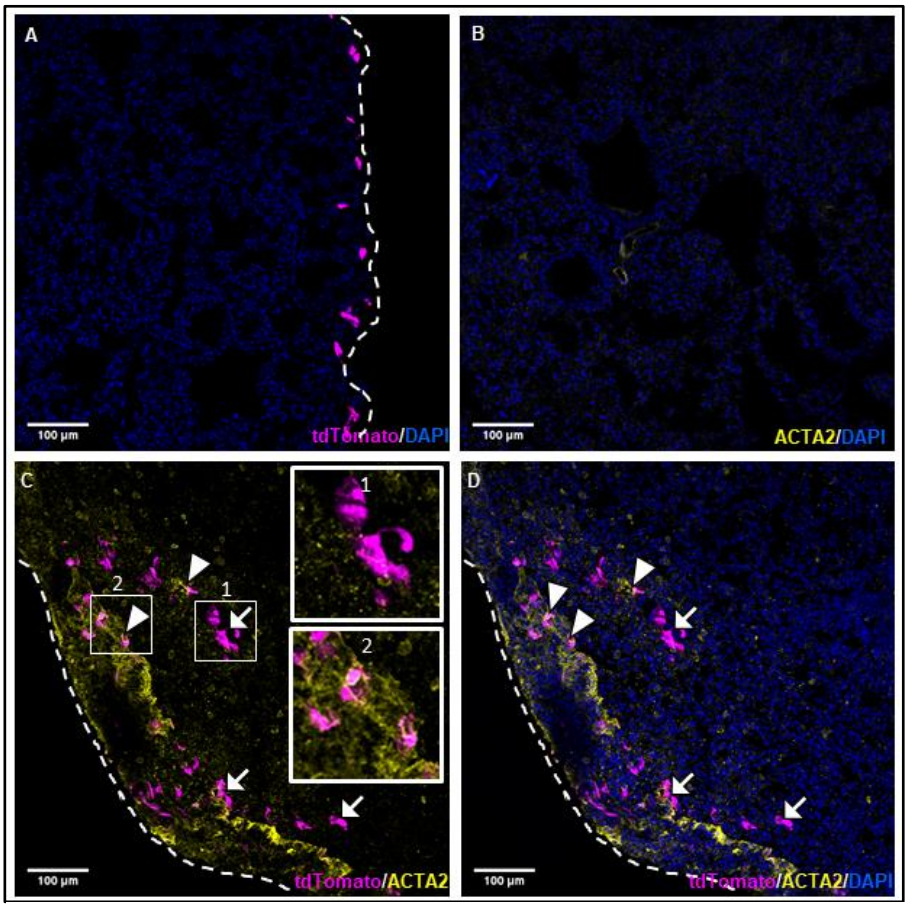

Figure 7-17. Some WT1-derived tdTomato+ pleural mesothelial cells co-expressed tdTomato (magenta) and ACTA2 (yellow) in the subpleural region of the late metastatic niche. *Nuclei were counterstained with DAPI (blue). A: non-tumour-bearing lungs showed that WT1-derived mesothelial cells located at the subpleural region; B: lung parenchyma region from E0771 metastatic lung section showed expression of ACTA2 in pulmonary artery only; C and D: pleural mesothelial cells detected in the late niche of the subpleural metastases with partial co-expression of tdTomato and ACTA2 (white arrowheads, inset 2). White arrows depict tdTomato+ cells that are negative for ACTA2 expression (inset 1).*

This result prompted me to revisit my scRN-seq data. Further analysis found that interstitial fibroblasts also highly express *Fn1,* which is the primary marker of CAMCs detected in the late niche. Additionally, they highly express *Saa3* and *Tagln*, which are also markers of

CAMC subtypes. Consequently, this re-analysis suggests that these fibroblasts might be the source of CAMCs (**Figure 7-18**).

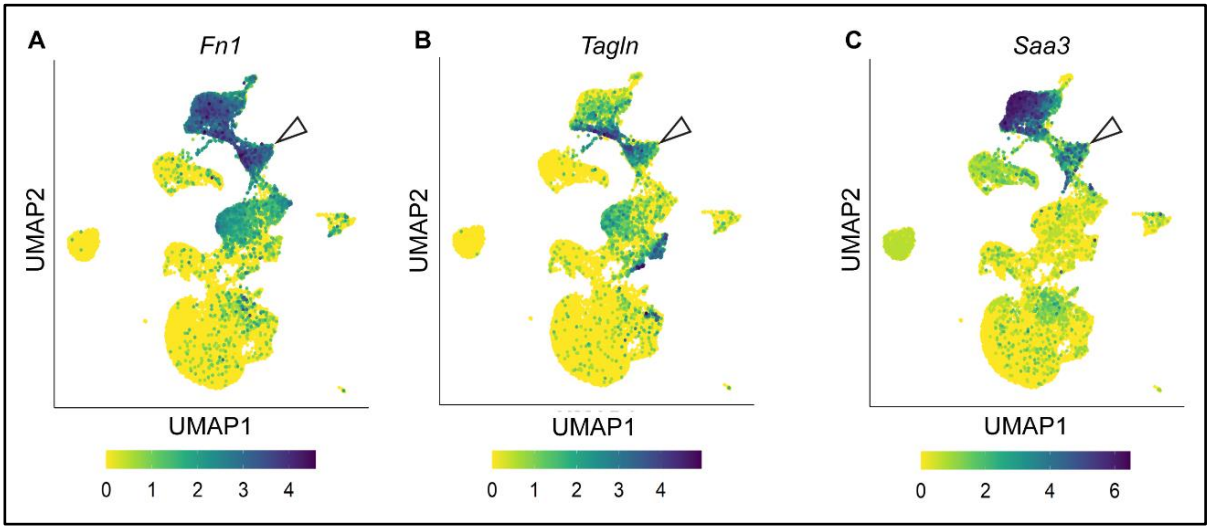

Figure 7-18. Interstitial fibroblasts upregulated the expression of cancer-associated mesenchymal cells (CAMCs) markers: Fn1 (A), Tagln (B), and Saa3 (C). *The full names of these genes are shown in* ***The List of Abbreviations Table.***

Frozen sections from murine lungs were analysed by immunofluorescence staining for co-expression of tdTomato with markers of CAMC subtypes including SAA3, FN1, and ACTA2. Non-tumour-bearing lungs showed an enclosing pleural mesothelial monolayer with preserved tdTomato reporter expression **(Figure 7-17A).** In contrast, some of the WT1-derived mesothelial cells in E0771 metastatic lungs at the late stage (day 13 following tumour injection) co-expressed tdTomato and the classical vascular smooth muscle cell or perivascular cell marker, ACTA2 **(Figure 7-17C, D).** This finding indicates that few pleural mesothelial cells are transdifferentiating to perivascular-like cells in the late metastatic niche, which is consistent with my scRNA-seq data, which detected a cell subtype annotated as hypoxia-responsive perivascular CAMCs **(Figure 7-2).** Other than being expressed in this CAMC subtype, ACTA2 is also expressed in the pulmonary arteries **(Figure 7-17B)**.

Immunofluorescence staining of E0771 metastatic lungs showed some of the WT1-derived tdTomato+ pleural mesothelial cells co-expressed tdTomato and the mesenchymal marker FN1 in subpleural metastases **(Figure 7-19A, B).** This finding is consistent with my scRNA-seq data **(Figure 7-12A).** Parenchymal metastases and distal regions in the same

lungs also expressed FN1, indicating that E0771 tumour cells may condition the whole lungs and induce fibroblast subtypes and mesothelial cells to produce a FN1 matrix **(Figure 7-19C-F).** My scRNA-seq data suggest that tdTomato-negative cells with high FN1 expression may be fibroblast subtypes. Interestingly, compared to non-tumour-bearing lungs **(Figure 7-21),** lipofibroblasts detected in the scRNA-seq data upregulated *Fn1* in the distal region of early and late metastases **(Figure 7-20B, Figure 7-22B)**. Whereas in the early niche, mature mesothelial cells, EBF1-positive fibroblasts, and lipofibrooblasts highly expressed *Fn1* **(Figure 7-20A)**. CAMCs and interstitial fibroblasts were the source of FN1 in the late niche (**Figure 7-22A**).

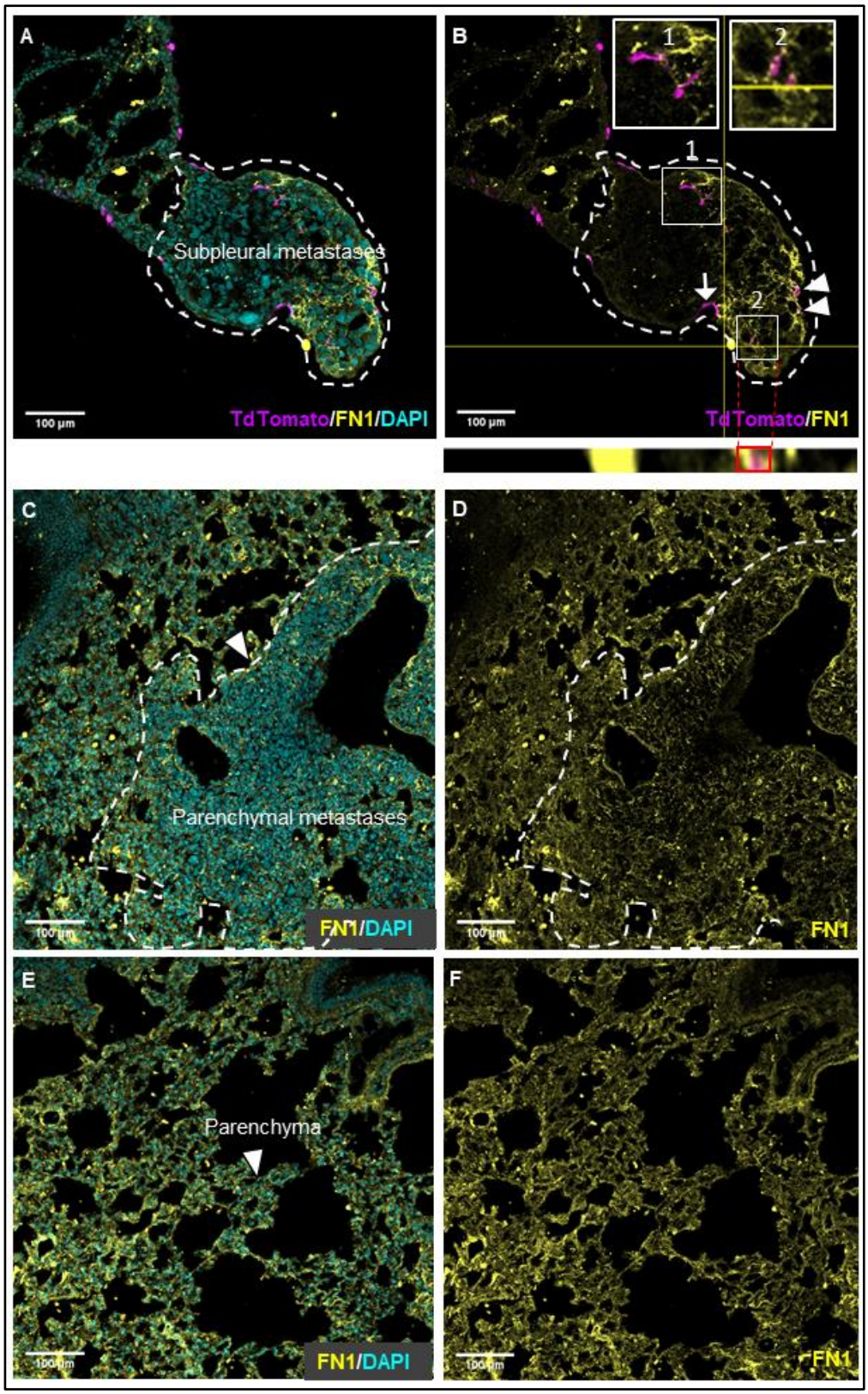

Figure 7-19. A few WT1-derived tdTomato+ pleural mesothelial cells co-expressed tdTomato (magenta) and FN1 (yellow) in the subpleural region of the late metastatic niche. *Nuclei were counterstained with DAPI (blue). A and B: pleural mesothelial cells detected in the late niche of the subpleural metastases partially co-expressed tdTomato and FN1 (white arrowheads, inset 2). White arrows depict tdTomato+ cells that are negative for FN1 expression (inset 1); C and D: parenchymal metastases showing high expression of FN1; E and F: distal (non-tumour) lung parenchyma from the same E0771 metastatic lung section showing high expression of FN1 indicating E0771 tumour cells being able to condition the whole lung inducing secretion of FN1 matrix.*

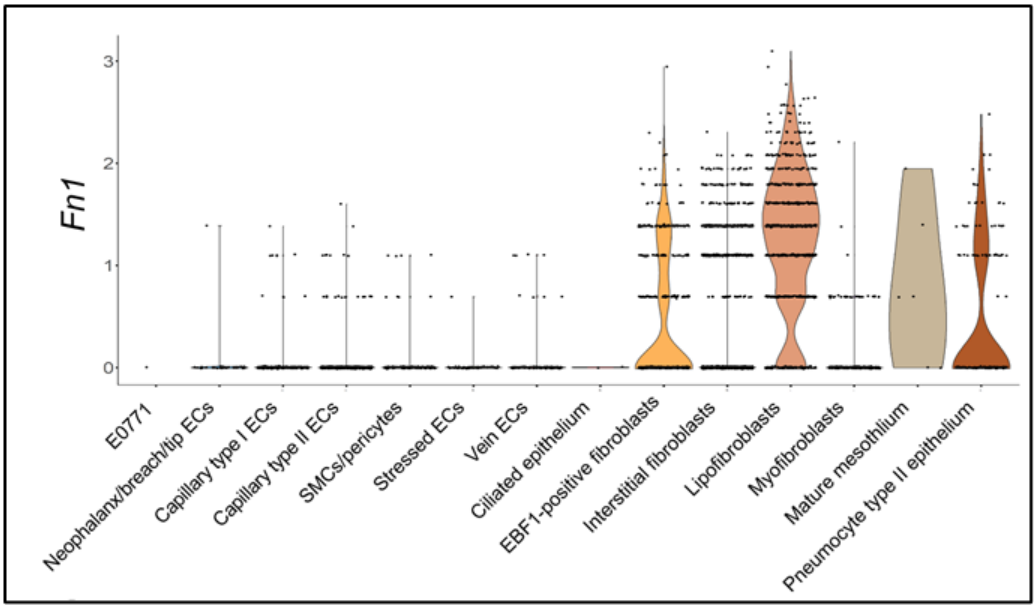

Figure 7-21. Violin plot depicting high expression of Fn1 in lipofibroblasts in the non-tumour lungs. *The full name of this gene is shown in* ***The List of Abbreviations Table.***

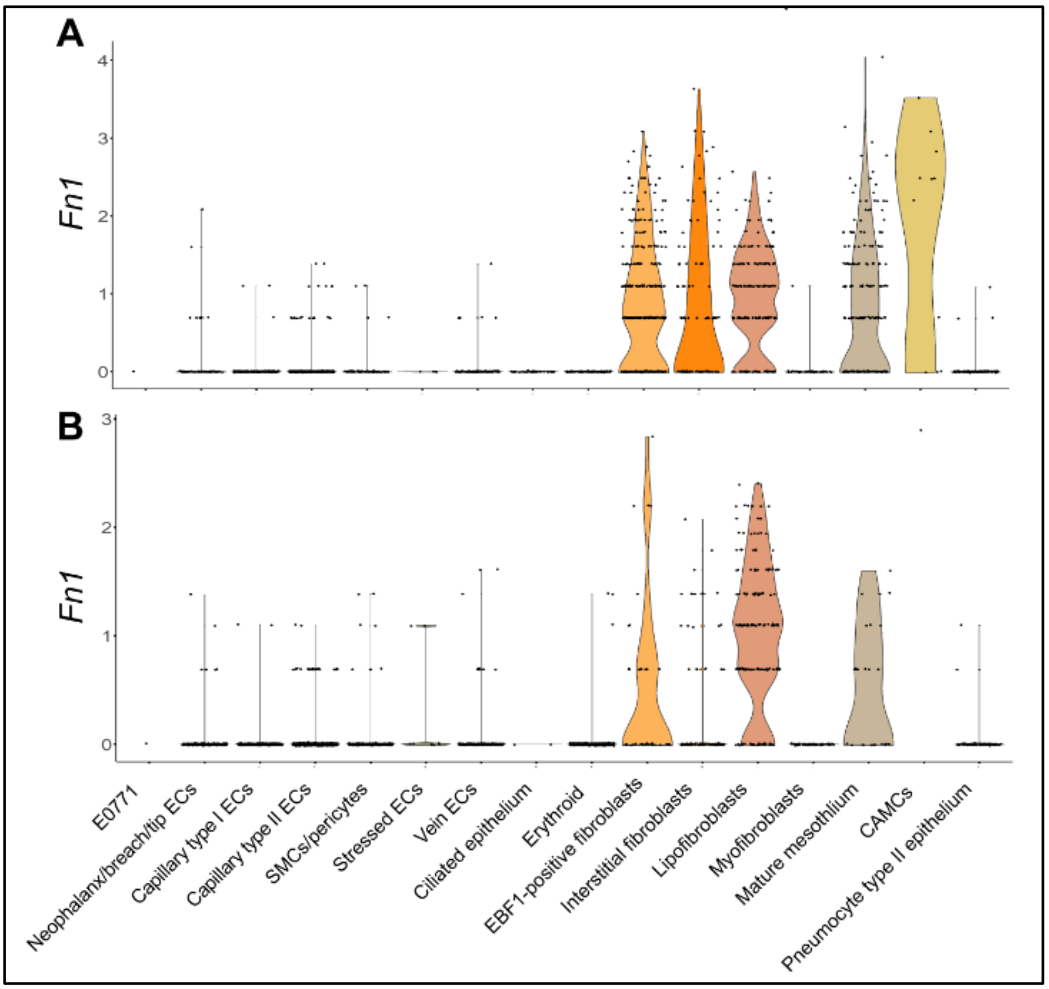

Figure 7-20. Violin plots depicting high expression of Fn1 in mature mesothelial cells, EBF1-positive fibroblasts, and lipofibroblasts in the early niche (A) and only in lipofibroblasts in the early distal region (B) of E0771 metastatic lungs. *The full name of this gene is shown in* ***The List of Abbreviations Table.***

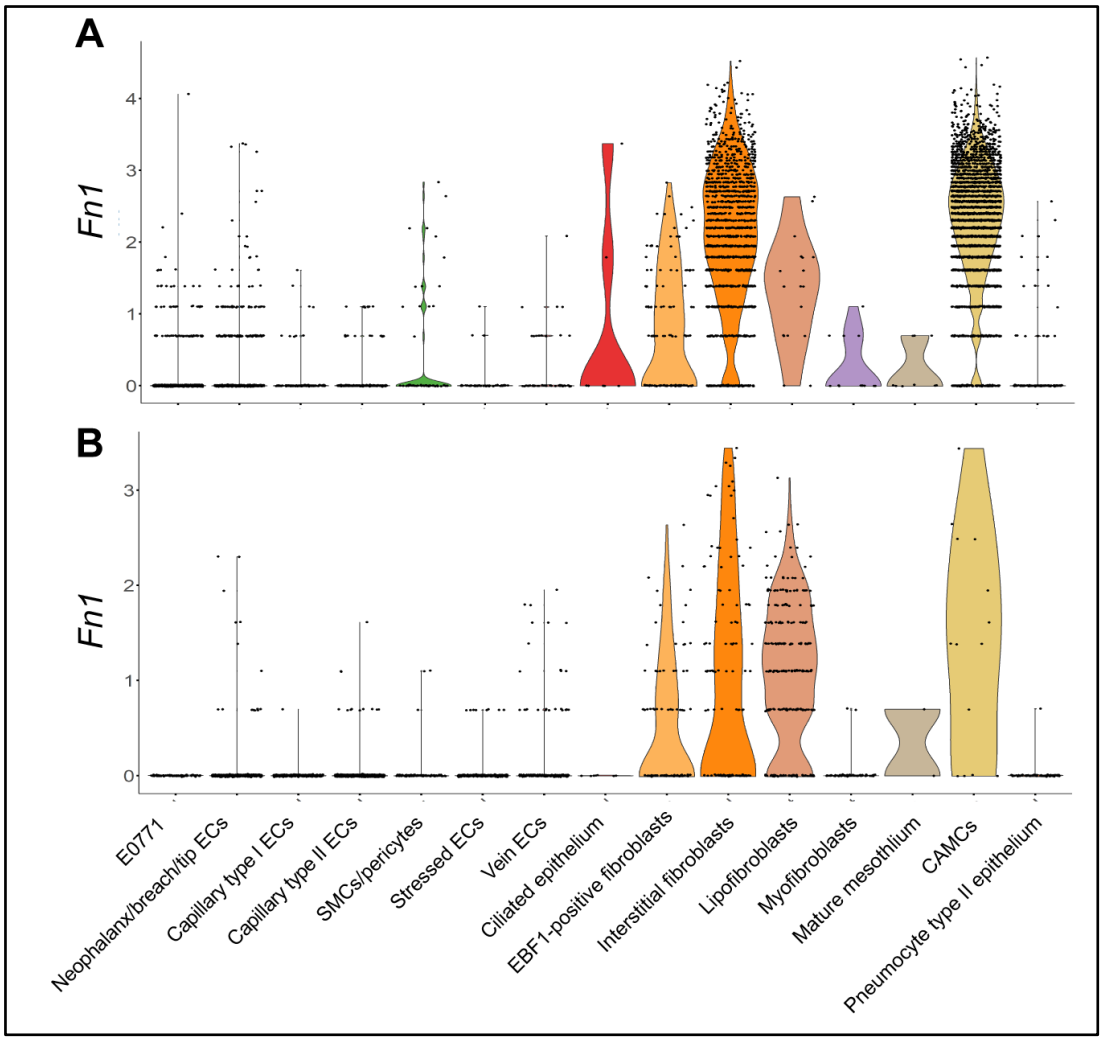

Figure 7-22. Violin plots depicting high expression of Fn1 in cancer-associated mesenchymal cells (CAMCs) and interstitial fibroblasts in the late niche (A) and only in lipofibroblasts in the late distal region (B) of E0771 metastatic lungs. *The full name of this gene is shown in* ***The List of Abbreviations Table.***

WT1-derived tdTomato+ cells in the subpleural metastases in the late niche co-express tdTomato and SAA3 **(Figure 7-23A, B),** agreeing with my scRNA-seq data **(Figure 7-3C).** In comparison to the distal non-tumour region **(Figure 7-23E, F)**, SAA3 was also observed to be differentially upregulated in parenchymal metastases at a late stage of metastasis **(Figure 7-23C, D)**. This finding suggests that SAA3 is expressed in cell types other than mesothelial cells, as WT1-derived tdTomato+ cells are absent in the lung parenchyma. Indeed, my scRNA-seq data suggested that *Saa3* is highly expressed by interstitial fibroblasts in addition to CAMCs when compared to the early stage of metastasis and non-tumour-bearing lungs **(Figure 7-25, Figure 7-24, Figure 7-26).**

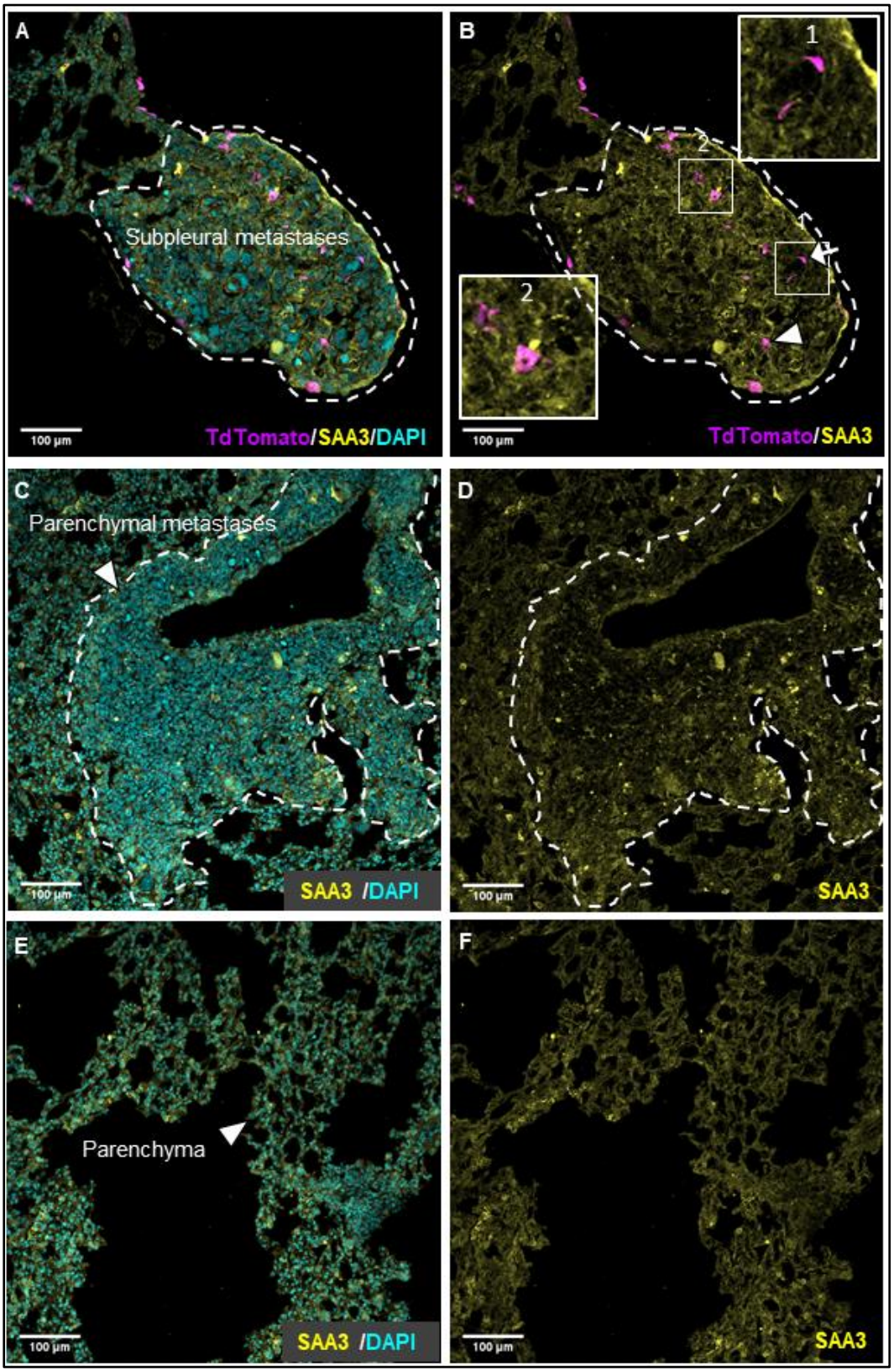

Figure 7-23. Wt1-derived tdTomato+ pleural mesothelial cells co-expressed tdTomato (magenta) and SAA3 (yellow) in the subpleural region of the late metastatic niche. *Nuclei were counterstained with DAPI (blue). A and B: pleural mesothelial cells detected in the late niche of the subpleural metastases co-expressed tdTomato and SAA3 (white arrowheads, inset 2). White arrows depict tdTomato+ cells that are negative for SAA3 expression (inset 1); C and D: parenchymal metastases from the same section showing high expression of SAA3; E and F: distal (non-tumour) lung parenchyma from the same E0771 metastatic lung section showing low expression of SAA3 indicating SAA3 being expressed in the metastatic niche only.*

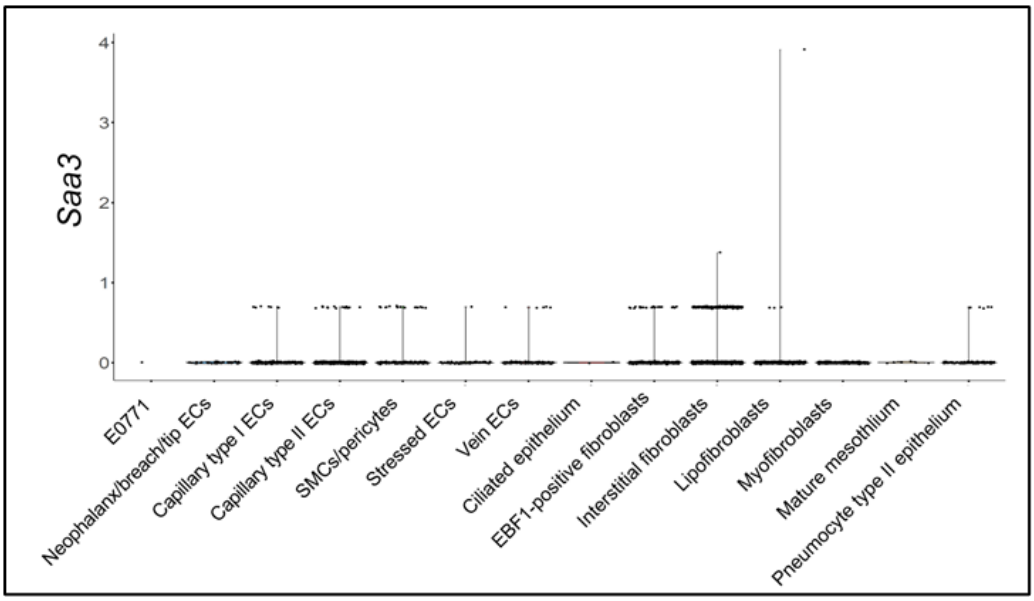

Figure 7-24. Violin plot depicting low expression of Saa3 across lung stromal cells in the non-tumour-bearing lungs. *The full name of this gene is shown in* ***The List of Abbreviations Table.***

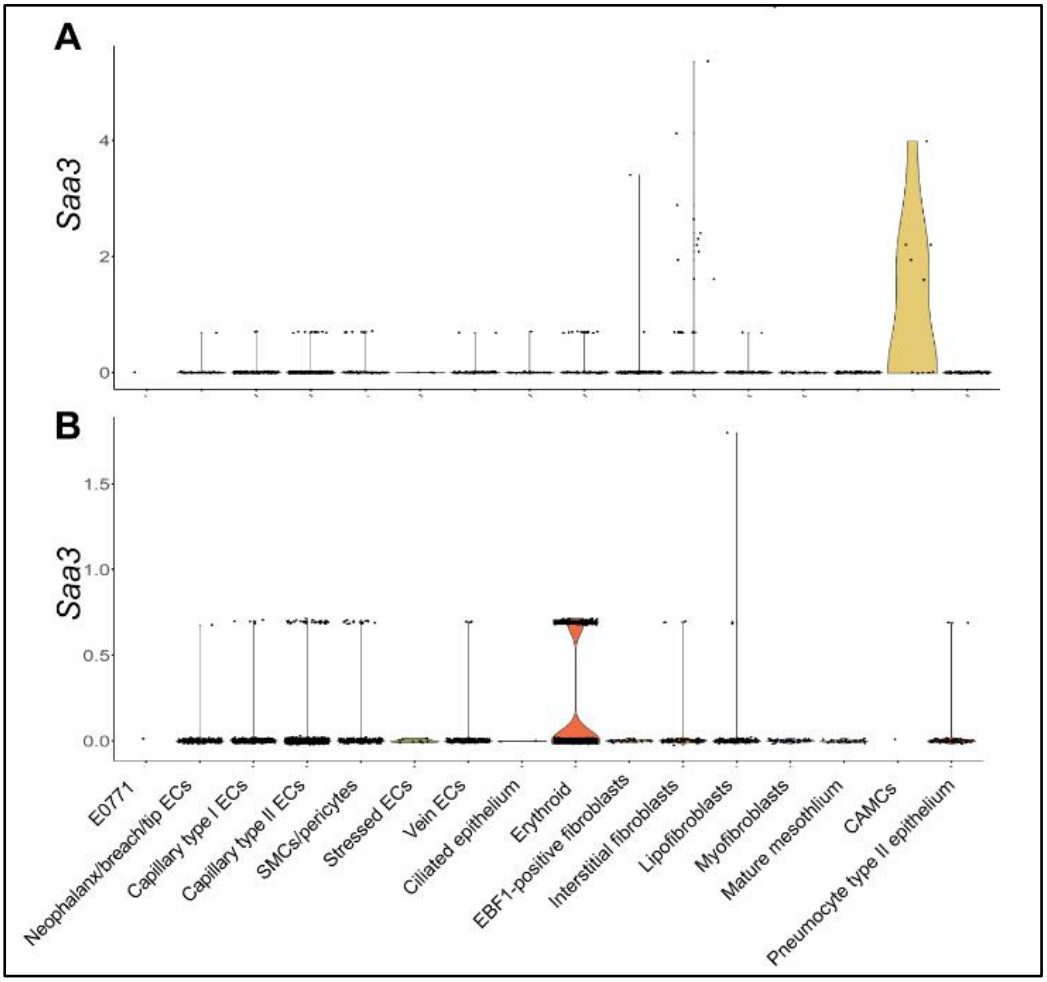

Figure 7-25. Violin plots depicting low expression of Saa3 across lung stromal cells and E0771 tumour cells in the early niche (A) and early distal region (B) of E0771 metastatic lungs. *The full name of this gene is shown in* ***The List of Abbreviations Table.***

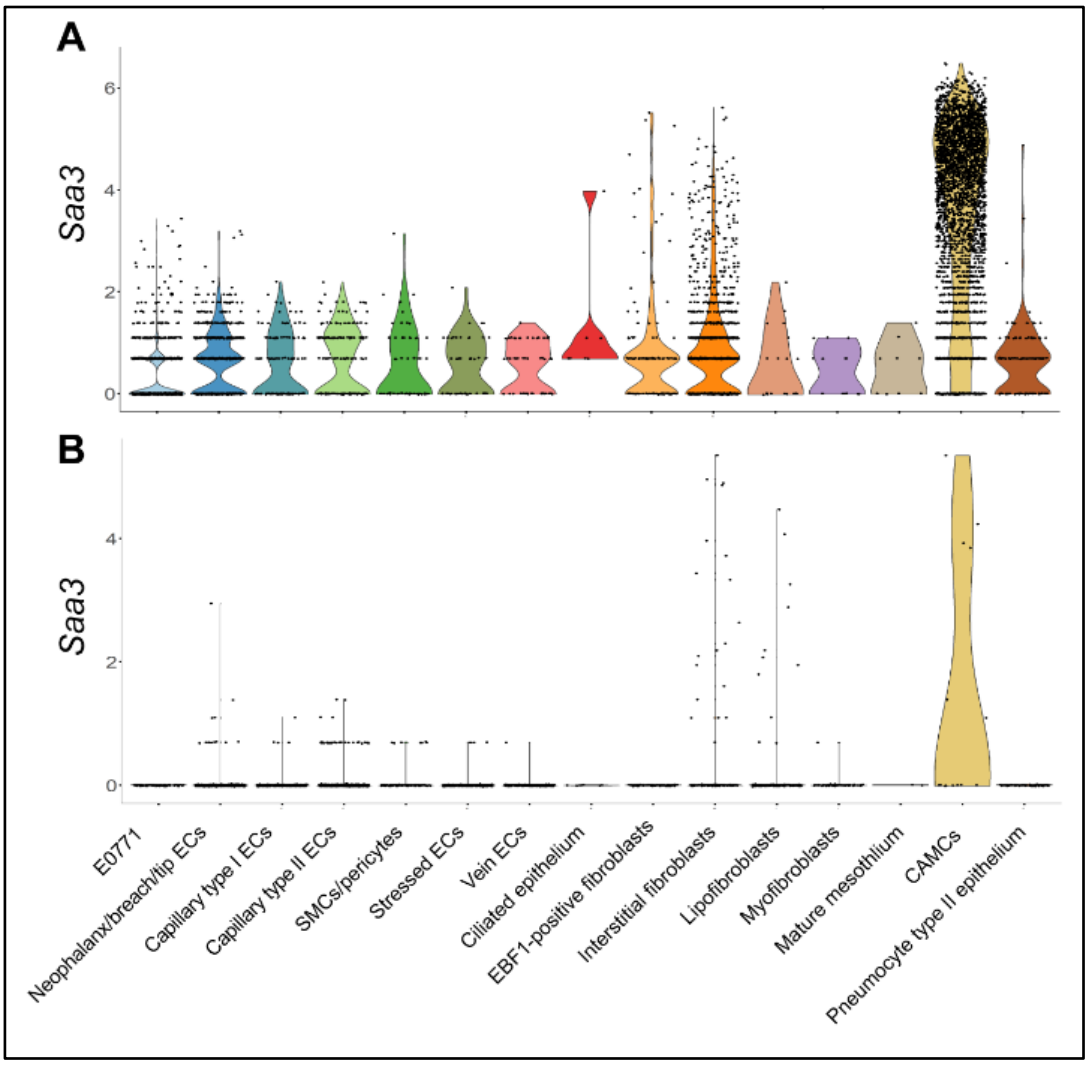

Figure 7-26. Violin plots depicting high expression of Saa3 in cancer-associated mesenchymal cells (CAMCs) and interstitial fibroblasts in the late niche (A) and low expression in the early distal region (B) of E0771 metastatic lungs. *The full name of this gene is shown in* ***The List of Abbreviations Table.***

Next, I investigated whether pleural mesothelial cells migrate inward toward the intratumoural region of subpleural metastases or the tumour cells grow beyond this monolayer. I used an anti-MSLN antibody to label the pleural mesothelial cells in tumour-bearing *Wt1-CreERT2*; tdTomato reporter mice. This immunofluorescent staining found that Wt1-derived tdTomato+ pleural mesothelial cells positive for MSLN enclose the subpleural metastases. This provides some validation for the idea that tumour cells get trapped beneath the mesothelial layer, and that WT1-derived tdTomato+ mesothelial cells ingress inward, infiltrating the subpleural metastases to a limited extent **(Figure 7-27).**

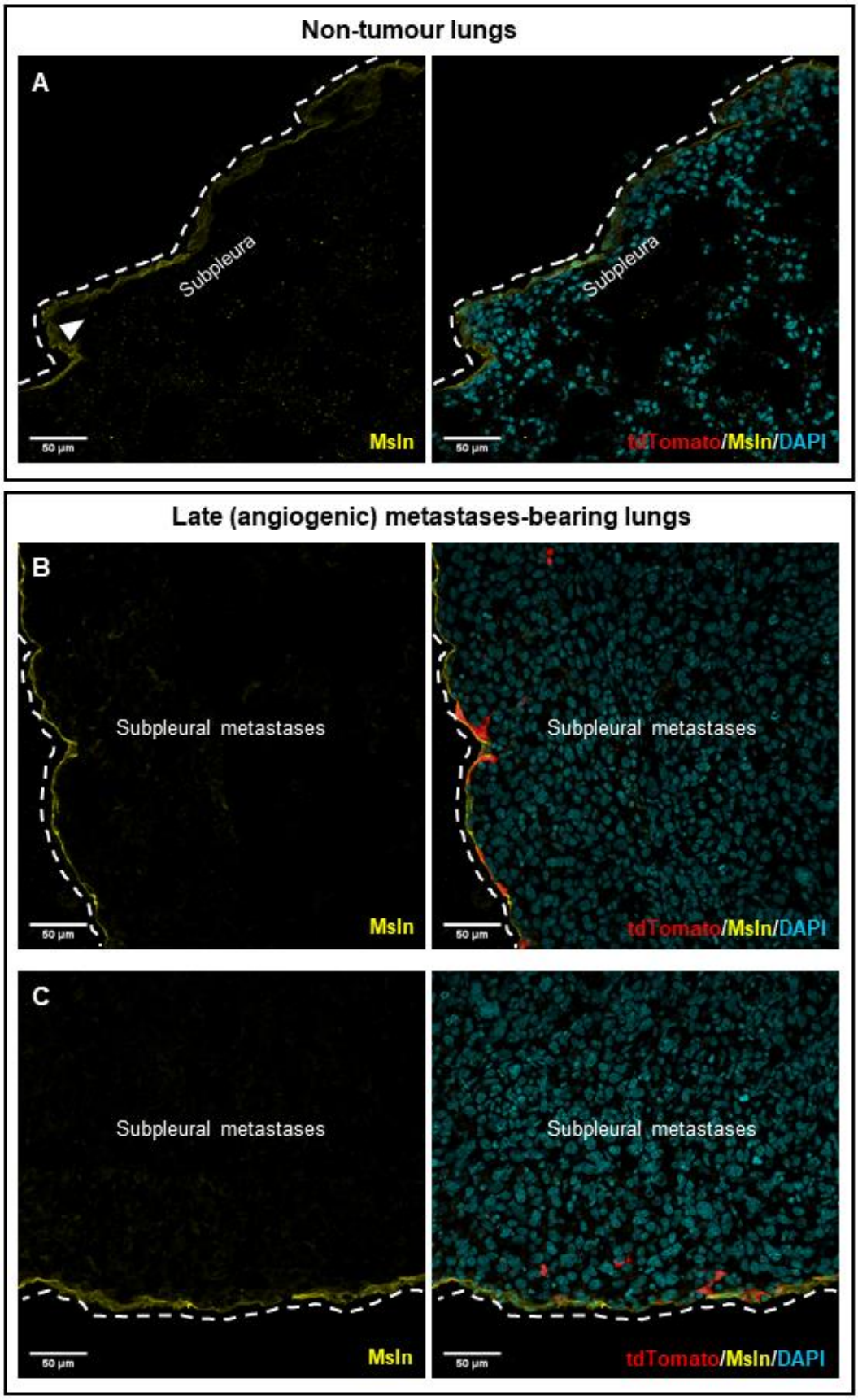

Figure 7-27.Immunofluorescence labelling of Wt1-derived tdTomato+ mesothelial monolayer (red) using anti-Msln antibody (yellow) revealed that cells from this monolayer migrated inward, infiltrating the subpleural (angiogenic) metastases. *A: Msln signal in non-tumour-bearing lungs; B: Msln signal in subpleural metastases; C: Msln signal in subpleural metastases with many migratory Wt1-derived tdTomato+ mesothelial cells. Nuclei were counterstained with DAPI (blue).*

Above Immunofluorescence analysis revealed minor co-expression of the reporter, tdTomato and markers of CAMC subtypes: FN1, ACTA2, and SAA3 at the protein level detected in the late niche.

7.7 Discussion

My scRNA-seq analysis of E0771 metastatic lungs identified a temporal lung response during early and late metastatic growth. At the early timepoint after E0771 injection, the mature mesothelium in the early niche was enriched with inflammatory molecules. Once E0771 tumour progression continued and angiogenic metastases developed, I found that three mesenchymal subtypes (annotated as CAMCs) increased specifically in the late niche (mCherry+). These CAMC subtypes were annotated as proliferating, inflammatory fibroblast-like, and hypoxia-responsive perivascular CAMCs.

Histological staining of non-tumour-bearing lungs using antibodies against mesothelial markers WT1 and MSLN (selected by their expression in the scRNA-seq data) revealed the localisation of these mesothelial cells on the visceral pleura lining the lungs. In contrast, E0771 metastatic lung sections exhibited WT1 and MSLN expression throughout the metastatic areas, indicating that E0771 tumour cells also express WT1 and MSLN. WT1 in the metastatic niche was localised to nuclei with round morphology, which might suggest activation of the WT1 pathway in these cells as its nuclear localisation has been reported to regulate gene transcription and translation (Niksic et al., 2004). Cytokeratin 5/6, which is indicative of mesothelial origin, was used to histologically discriminate between E0771 tumour and mesothelial cells, finding that mesothelial cells were localised superficially in the submesothelial region (Shield & Koivurinne, 2008). Lastly, VVG and MSLN staining in the late metastatic lung indicated that the mesothelial monolayer was not damaged, and that E0771 tumour cells did not invade through the visceral pleura or exhibit a phenotype known in literature as visceral pleural invasion (VPI) (David et al., 2013).

Understanding the molecular crosstalk between tumour cells and mesothelium is worthy of further study. Here, the effects of mesothelial cells on E0771 tumour cells were first pursued *in vitro* using transwell assays. This found that mesothelial cells significantly enhance the proliferation and invasion of E0771 cells. Intercellular signalling between tumour cells and lung stroma was investigated next. Through GSEA and differential expression analysis, mesothelial and mesenchymal cells were found to exhibit a heterogeneous response during the development of early (co-opting) and late (angiogenic) metastases. At an early stage, mesothelial cells demonstrated an inflammatory phenotype, with several interferon and cytokine-related gene sets enriched compared to non-tumour and early distal regions. However, in late metastases, GSEA analysis revealed an upregulation of a gene set related to EMT in CAMCs, compared to non-tumour and distal mesothelium. This finding was consistent with my cell-cell communication analysis, which predicted that E0771 tumour cells signalling to CAMCs through EMT inducers, TNFα – TNFRSF1 and TGFβ – TGFBR1/TGFBR2 pairs. CAMCs were also found to differentially upregulate the expression of mesenchymal markers such as *Fn1*, *Cdh2*, and *Timp3* and downregulate mesothelial markers such as *Upk3b, Krt18*, and *Krt19*. Trajectory inference analysis also predicted the mature mesothelium bifurcating and transdifferentiating to CAMC subtypes with a trajectory loop predicted between fibroblast-like and hypoxia-responsive perivascular CAMCs. This trajectory loop was predicted to occur spatially in the angiogenic metastases, and temporally at the later metastasis stage, which could indicate fluctuations in reoxygenation within the niche microenvironment. It is possible that invasive E0771 growth in the subpleural metastases and formation of tortuous angiogenic vessels (enriched in the late niche, **(Figure5-16 in Chapter 5)**) could result in poor perfusion, and thus could be causing this fluctuation, a phenomenon known as cycling hypoxia (Kimura et al., 1996). In response to this intermittent hypoxia, a subset of CAMCs upregulate the expression of HIF1-regulated transcripts. Cycling hypoxia has been reported to promote tumour invasion, metastasis, and resistance to therapies (Michiels et al., 2016), thus understanding the molecular mechanism of this phenomenon in CAMCs could provide new avenues for targeting cancer.

Mesothelial-to-mesenchymal transition (MMT) is reported to occur during embryonic organ development (Rinkevich et al., 2012). It has also been reported by previous studies to occur in different disease contexts, such as during human peritoneal metastasis of intestinal adenocarcinoma (Gordillo et al., 2020), peritoneal metastases of ovarian cancer (Rynne-Vidal et al., 2017), pancreatic cancer (Huang et al., 2022b), peritoneal metastasis of gastric cancer (Tanaka et al., 2017), idiopathic pulmonary fibrosis (IPF) (Sontake et al., 2018; Zolak et al., 2013), and malignant mesothelioma (Wörthmüller et al., 2018). To validate my scRNA-seq data that suggested a mesothelial origin of the CAMCs, I performed a lineage tracing study using the inducible *Wt1-CreERT2*;tdTomato reporter mouse model. This enabled me to track Wt1-derived mesothelial cells in the metastatic niche. However, subsequent histological analysis revealed few tdTomato+ mesothelial cells, rejecting my hypothesis. Interestingly, at a late stage, there were a few Wt1-derived tdTomato+ mesothelial cells, demonstrating detachment from visceral pleural and ingress into the submesothelial region with restricted capacity. These cells co-expressed tdTomato with FN1, ACTA2, and SAA3, markers for CAMCs, hypoxia-responsive perivascular, and inflammatory fibroblast-like mesothelium, respectively. *Saa3 was* one of the top overexpressed genes in the inflammatory-like CAMC subtype in my scRNA-seq data, an observation validated using immunofluorescence staining of WT1-derived mesothelium. SAA3 is an acute-phase protein mainly expressed by extrahepatic tissues such as macrophages and adipocytes (Uhlar & Whitehead, 1999). SAA3 is reported to be expressed in acute inflammation and some cancers (Chait et al., 2020; Djurec et al., 2018). SAA1, an ortholog of SAA3, is overexpressed in CAFs, promotes tumorigenesis of pancreatic cancer, and correlates with poor survival (Djurec et al., 2018). Further, SAA1 signalling in melanoma can produce neutrophils with an immunosuppressive phenotype capable of suppressing T cell proliferation via this IL-10 signalling (De Santo et al., 2010). It is also overexpressed in lung cancer patients, where it interacts with macrophages to induce the production of MMP9 which enhance lung cancer metastasis (Sung et al., 2011). These studies demonstrate an important role for SAA1/SAA3 in human cancers, therefore warrants further investigation into the molecular mechanism of this inflammatory molecule. Consequently, the

role of murine *Saa3* in my breast cancer lung metastasis model, and its overexpression in CAMCs, could potentially serve as a platform for this analysis.

In conclusion, in this chapter I used my preclinical mouse model of breast cancer lung metastasis to determine that pleural mesothelial cells are not the primary source of the three CAMC subtypes, but they contribute to the growth of subpleural metastases. Potential future work could next investigate whether the interstitial fibroblasts detected in my scRNA-seq data are the potential cell of origin generating these CAMCs, and to identify the receptor SAA3 bind to. Based on the above findings, we propose that targeting the Saa3 signalling molecule could potentially limit the metastatic growth of breast cancer in the lungs. Further studies will be needed to prove this hypothesis experimentally.

Chapter 8: Final Discussion

My research has focused on understanding tumour vascularisation, with a focus on the molecular signalling that occurs at the site of metastasis. Specifically, I aimed to investigate how triple-negative breast cancers acquire access to blood vessels to colonise the lungs as the metastatic site, to study the transcriptomic changes that occur in the tumour vascular ECs at both early and late metastatic timepoints, and to examine the molecular cues from the tumour non-immune stroma that support tumour vascularisation.

Vessel co-option (a non-angiogenic approach to vascular access) mediates resistance to anti-angiogenic therapy in many cancers (Bridgeman et al., 2017; Frentzas et al., 2016). However, vessel co-option has not been extensively studied due to the lack of reliable methods to isolate tumour co-opted vessels of sufficient purity for gene expression analysis, although there have been some very recent transcriptional studies on tumour vessels using scRNA-seq technology e.g. (Goveia et al., 2020; Rohlenova et al., 2020). The vascular endothelial cells in these studies were isolated from manually dissected metastases. To better understand vessel co-option, here I developed an *in vivo* syngeneic murine E0771 TNBC lung metastasis model that used both vessel co-option and angiogenesis to access the vascular system. Using MRI imaging and histological examination approaches, I found that E0771 cancer cells were able to vascularise the lungs via co-opting the pre-existing vessels (parenchymal-vessel co-option) forming micrometastases during the early colonisation of the lungs by the tumour cells. However, as the cells progressed into established (subpleural) metastases, E0771 cells then induced angiogenesis. Characterisation of E0771 tumour growth and vascularisation using *in vivo* MRI revealed its potential use as a diagnostic, a follow-up tools assessing the impact of anti-angiogenic therapy, and to make resectability decisions for clinical lung tumours. Further, the temporal heterogeneity in E0771 vascularisation mechanisms within a single tumour model provide me a model with which to interrogate gene expression changes during both tumour-adopted vessel co-option and angiogenesis vascularisation. Such analysis has the potential to

identify markers for targeting co-opting tumours that could otherwise provide a mechanism of resistance to anti-angiogenic therapy.

To evaluate the response of E0771 lung metastasis model to inhibition of angiogenesis, I took both a pharmacological and genetic disruption of angiogenesis. However, deletion of the angiogenic gene *Eltd1* (*Adgrl4*) in an inducible EC murine model showed no significant impact on reducing the growth of angiogenic E0771 metastases. This finding suggests that other pro-angiogenic GPCRs might act to compensate for the loss of *Eltd1* and mediate angiogenesis upon *Eltd1* inhibition, suggesting that targeting a range of these factors may be required to minimise metastatic tumour growth. As an alternative approach, pazopanib was used to block primarily VEGFR2 receptor-mediated tumour angiogenesis. Targeting angiogenesis in this manner significantly reduced the development of established subpleural metastases. However, there was no significant difference in the burden of parenchymal co-opting metastases between pazopanib- and vehicle-treated groups, suggesting that the intrinsic co-option renders the anti-angiogenic therapy ineffective in reducing their metastatic growth. This finding is consistent with another recent study, which found that RENCA renal lung metastasis switched to use co-opting vessels and expanded upon prolonged treatment with an anti-angiogenic drug, sunitinib, which block angiogenesis via targeting VEGFR2 and PDGFR (Teuwen et al., 2021). Consequently, my model and previous metastasis models both indicate that vessel co-option mediates persistent metastatic growth whilst under treatment with anti-angiogenic therapy.

I next took advantage of scRNA-seq technology combined with a metastatic niche labelling system (Ombrato et al., 2019) in order to interrogate the transcriptional and metabolic changes of the tumour ECs and intercellular communication between cancer and lung non-immune stroma that drive metastatic niche formation during metastatic development **(Figure 8-1, Figure 8-2).** This study found that, in early co-opting metastases, co-opted cap type I and II (niche mCherry+) cells increased their OXPHOS process, generating the high energy levels needed for vessel stabilisation. In metastases that

primarily use vessel co-opting, the co-opted cap II cells became more permeable via downregulating tight junctions and actin cytoskeleton genes, potentially facilitating the extravasation of E0771 tumour cells and the formation of micrometastases **(Figure 8-1)**. Previous analysis using nanoparticle contrast agents and high-resolution computed tomography (CT) imaging depicted co-opted veins as leakier and more permeable, with the authors proposing that this could promote tumour intravasation and migration to distant organs (Ghaghada et al., 2011). However, my findings are the first to experimentally show the increased OXPHOX metabolism at the transcriptional level, and to show hyperpermeability of co-opted microvessels in the metastatic niche of E0771 BC lung metastasis model at gene expression and protein levels. Genes upregulated in co-opted capillaries include those reported in the literature to increase EC survival, inhibit EC proliferation and angiogenesis, and protect cells from oxidative stress. These findings suggest a potential therapeutic strategy to use OXPHOS inhibitors or drugs that can enhance EC barrier integrity to target co-opted ECs, thus alleviating hypoxia and preventing the early development of lung metastases. OXPHOS inhibitors have recently proven their therapeutic potential, where they significantly reduced tumour growth in oestrogen receptor (ER) positive patient–derived xenograft (PDX) model (El-Botty et al., 2023). My results do contrast with those from another model of lung metastasis (RENCA renal metastasis model), which found that tumour-co-opted ECs resembles healthy ECs at both transcriptional and metabolic levels (Teuwen et al., 2021). This inconsistency between the earlier study and ours may be due to the use of metastasis models with tumours of different origins.

In E0771 early lung metastases (in both niche and distal regions), a subset of cap II cells upregulated the expression of both MHC II Ag presentation machinery and IFNγ-regulated genes **(Figure 8-1)**. Similar EC responses emerged in human and murine primary LLC lung tumours (Goveia et al., 2020), suggesting EC's immunomodulatory and inflammatory role toward primary and secondary lung tumours. In the early niche, mature

mesothelium with high expression of inflammatory genes were also abundant. Our findings suggest possible therapeutic implications. Identifying immunoregulatory capillaries and inflammatory mesothelial cells at an early-stage metastasis suggests that pro-inflammation may play a role in tumour vessel co-option. It remains to be determined whether these inflammatory stromal cells, which highly express *Ifnγ* may mediate the response to immune checkpoint blockade treatment in our model, as previous research reported that high IFN expression secreted by reactive T cells upregulates PD-L1 expression and is associated with treatment response (Hoekstra et al., 2020; Thibaut et al., 2020).

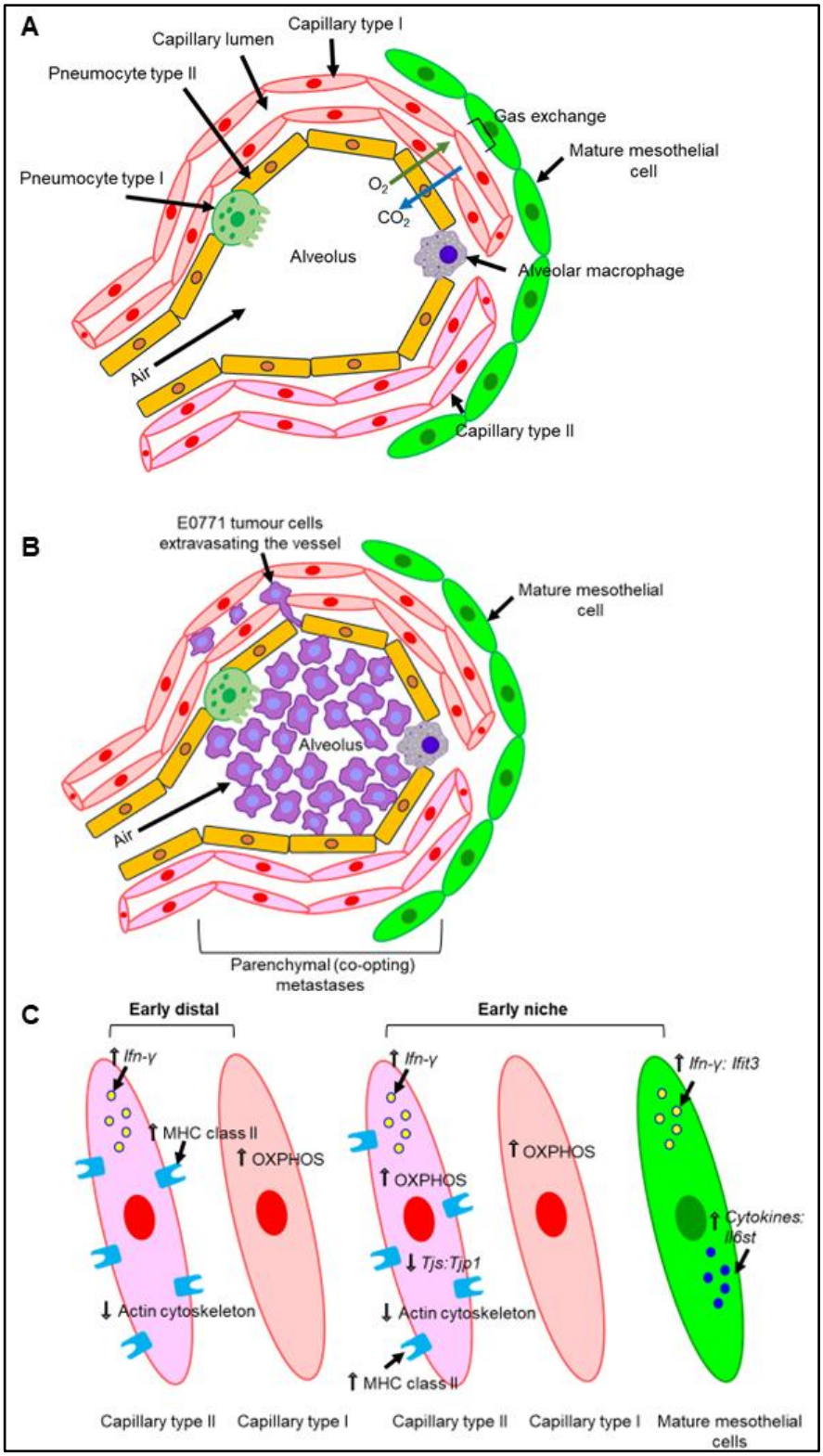

Figure 8-1. Schematic diagram summarising the transcriptional changes occurring in the early (parenchymal/vessel co-opting) E0771 metastases (B and C) in comparison to non-tumour-bearing lungs (A). *B: E0771 tumour cells grow in an alveolar growth pattern, filling the alveoli and co-opting lung vessels; C: in response to tumour colonisation, capillaries ECs in the metastatic niche and distal regions increased their OXPHOS metabolism. Co-opted capillary type II downregulated their tight junctions and actin cytoskeleton genes. Mature mesothelial cells were increased in the early niche, and upregulated inflammatory genes, including Il6st and Ifit3. A subset of capillary type II changed its expression profile upregulating MHC class II Ag-presenting and IFN response genes in early niche and distal regions.*

My scRNA-seq data identified a subtype of ECs which highly expressed tip cell, breach, and neophalanx genes and emerged in late E0771 metastases. This finding is in concordance with the angiogenesis observed in the histological assessment of the E0771 metastatic lung tissue section. This scRNA-seq data also indicate the cell types that drive VEGFR2-mediated angiogenesis. Cap I cells were found to highly express *Vegfr2,* while cancer-associated mesenchymal cells (CAMCs) were the primary cell cluster that highly expressed the pro-angiogenic factor *Vegfa* **(Figure 8-2)**. The *Vegfr2*-overexpressing cap I cells detected in our scRNA-seq data are probably the EC subtype targeted by pazopanib, leading to the inhibition of angiogenesis observed in advanced subpleural metastases. Inhibition of angiogenesis in the E0771 lung metastasis model by targeting VEGFR2 is broadly consistent with the sensitivity of angiogenic ECs (tip and breach ECs) in primary LLC lung tumour model to both anti-angiogenic VEGFR2 antibody (DC101) and VEGFR tyrosine kinase inhibitor (PTK787) treatments (Goveia et al., 2020), and with the sensitivity of tip ECs in the RENCA renal lung metastasis model to sunitinib (Teuwen et al., 2021).

These angiogenic ECs detected in the E0771 lung metastasis model are predicted to originate from lung capillaries in my analysis. This contrasts with previous morphological observations using a tumour-inserted rabbit corneal model, which suggested that angiogenic ECs originated from venules (Folkman, 1982). Another recent study supported this observation in Choroidal neovascularisation (CNV), in which they reported that post-capillary venules gave rise to angiogenic ECs (Rohlenova et al., 2020). These findings suggest that different organs might contribute to different cell of origin of angiogenic ECs, which could be considered when targeting angiogenesis in different diseases.

As discussed above, co-opted lung capillaries in early metastases increased OXPHOS metabolism. However, the capillaries in the late metastases switched to increasing glycolysis/gluconeogenesis. In addition to the capillaries, angiogenic ECs also increased their glycolytic flux, speeding up ATP production to meet their cellular building capacity **(Figure 8-2)**. Angiogenic ECs in other in *vivo* models such as primary LLC lung tumours

and corneal injury, also upregulated their glycolysis process, suggesting that angiogenesis relies on glycolysis in a disease-independent fashion (Rohlenova et al., 2020).

Interestingly, I detected an EC subtype annotated as “stressed ECs” that was enriched in the late distal region. This subtype expressed stress-response genes as well as genes reported to modulate EC survival, IFN signalling, and limit angiogenesis **(Figure 8-2)**, suggesting a role in controlling angiogenesis in the distal region at a late stage of metastasis. Angiogenesis in the late distal region was also found to be potentially influenced by cap I ECs via an upregulation of *Cd36*, which is known to have an anti-angiogenic effect (Hale et al., 2012). Capillaries in human breast cancer were also reported to upregulate CD36 in the peripheral region, suggesting a similar function in both primary and metastatic human tumours (Geldhof et al., 2022). Using a preclinical mouse tumour model and in breast cancer patients, CD36 has been reported to be upregulated following HER2 inhibition, suggesting its role in also mediating drug resistance (Feng et al., 2019). Future studies could examine the effect of targeting CD36 on metastatic growth and vascularisation in our E0771 metastasis model using anti-mouse CD36 antibodies such as the one developed recently by (Xu et al., 2021a).

Further analysis of my scRNA-seq data found that pleural mesothelial cell numbers increased in the early niche, whereas multiple CAMC populations had emerged in the late niche of E0771 lung metastases. An unsupervised (unbiased) clustering analysis also found that these CAMCs were composed of three subclusters, each with a distinct transcriptome. These were annotated as proliferating CAMCs (identified as mesenchymal cells with an upregulation of proliferation genes such as *Mki67* and *Top2a*), inflammatory fibroblast-like CAMCs (upregulating inflammatory genes such as *Cxcl5* and *Saa3)* and hypoxia-responsive perivascular CAMCs (upregulating perivascular genes such as *Tagln* and hypoxia genes such as *Car9* and *Ndrg1*) **(Figure 8-2)**.

In comparison to mesothelial cells present in the early niche, gene set enrichment analysis (GSEA) found an upregulation of gene sets related to the EMT process in CAMCs

in the late niche, suggesting high plasticity of these cells with transdifferentiating potential. Previous literature studies also reported the plasticity of mesothelial cells to undergo EMT giving rise to vascular smooth muscle cells (SMCs) and fibroblasts during development and lung diseases (Gordillo et al., 2020; Huang et al., 2022b; Rinkevich et al., 2012; Rynne-Vidal et al., 2017; Sontake et al., 2018; Tanaka et al., 2017; Wörthmüller et al., 2018; Zolak et al., 2013). Therefore, I also examined whether mesothelial cells in the early metastases could transdifferentiate into CAMCs at late timepoint. This analysis used a lineage tracing model, an inducible *Wt1-CreERT2*;tdTomato reporter mice, where mesothelial cells are labelled with tdTomato to enable tracking the fate of these cells when challenged with metastatic breast cancer. However, this analysis found that mesothelial cells minimally contributed to the late metastatic niche. Instead, these cells gave rise to only a limited number of CAMCs in the late (subpleural/angiogenic) metastases. This finding suggests that 1) mesothelial cells have limited capacity to undergo EMT and transdifferentiate to CAMCs confined to the metastatic region beneath the pleura with no contribution to the development of micrometastases and 2) CAMCs in the late niche originated from other cell types. These may be resident lung fibroblasts, which requires further investigation. Consequently, my analysis indicates that mesothelial cells partially contribute to CAMCs in the subpleural region, and that heterogenous CAMCs support the growth late E0771 lung metastases. This migratory phenotype of mesothelial cells is in line with what is observed in human primary invasive colorectal carcinomas, where visceral mesothelial cells support cancer invasion through a restricted EMT (differentiating) capacity. These cells were histologically demonstrated to give rise to CAFs only in the region near the visceral mesothelial layer (Gordillo et al., 2020). Based on these findings, we propose therapeutic strategies should be tailored based on the stage and the type of vascularisation in metastases targeting OXPHOS and vascular hyperpermeability in co-opting metastases, and glycolysis and CAMCs to prevent the development of angiogenic metastases.

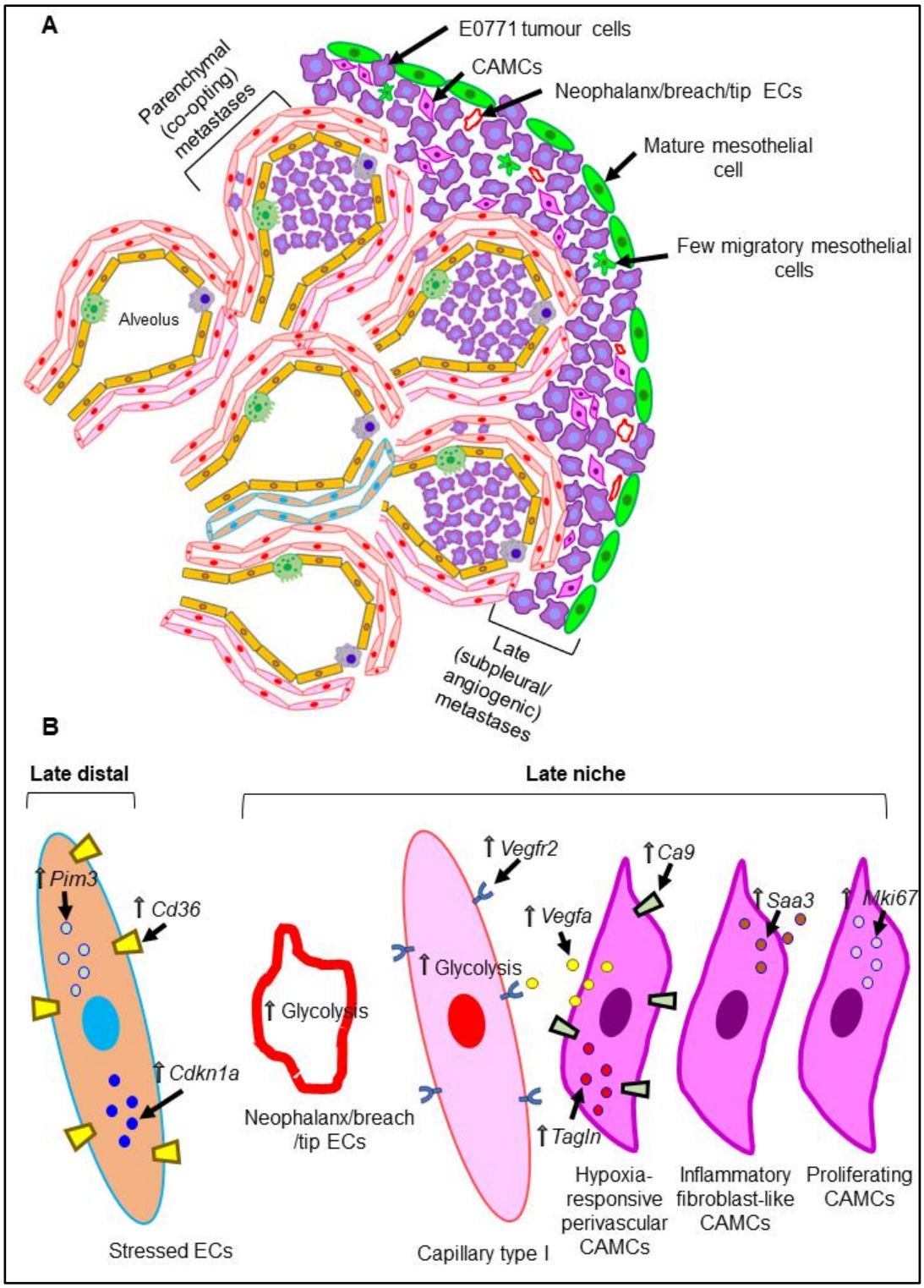

Figure 8-2. Schematic diagram summarising the transcriptional changes occurring in the late (angiogenic and vessel co-opting) E0771 metastases (A and B) in comparison to non-tumour-bearing lungs (Figure 8-1A). *A: in addition to their vessel co-opting growth inside the lung parenchyma, E0771 tumours expand and develop subpleural metastases inducing angiogenesis to sustain their progression; B: three CAMC populations, including proliferating, inflammatory-like, and hypoxia-responsive perivascular CAMCs were enriched in the late niche with an upregulation of Mki67, Saa3, and TagIn and Ca9, respectively. Hypoxia-responsive perivascular CAMCs were identified as the major source of Vegfa that mediated angiogenesis by predicted binding to the receptor Vegfr2, which was upregulated in capillary type I ECs. To meet this high proliferative demand, angiogenic (neophalanx/breach/tip and capillary type I ECs in the late niche upregulated their glycolysis metabolism. Few pleural mesothelial cells found to migrate into the intratumoural region and partially contribute to the development of subpleural metastases. Stressed ECs with high expression of Cd36, Pim3 and Cdkn1a emerged in the distal region of late-stage metastasis.*

One of the limitations of my study is that stromal cells from only one replicate (one well in 10xGenomic chip) per condition were sequenced. Sequencing three replicates per condition would have helped to validate the cellular composition per condition. However, this would have significantly increased the cost of the experiment and it is important to mention that several lungs were pooled per condition. Furthermore, the cell subtypes detected using the scRNA-seq data were consistent with the findings from histological and immunolabelling analyses of normal and tumour-bearing lungs. Thus, despite these limitations useful conclusions could be drawn from the study.

An additional potential limitation is that the *in vivo* model used was an experimental metastasis model, where tumour cells were inoculated into the circulation. This skips earlier metastatic stages present in a spontaneous (orthotopic) tumour model that might also contribute to the development of the metastatic niche. However, this E0771 breast cancer lung metastasis model demonstrated a unique mouse model with which to study tumours which combine non-angiogenic (co-option) and angiogenic methods of vessel access in a single model with spatial and temporal separation. Such a model enables the interrogation of the metastatic niche in both of these two heterogeneous vasculatures.

In conclusion, these findings provide in-depth molecular insights into vessel co-option, angiogenesis, and stromal remodelling in the early and late metastatic niches and distal regions. We also uncovered potential future therapeutic targets in TNBC lung metastases.

Future studies directly coming out of my research could potentially include:

- Immunostaining human tumours to determine whether CAMCs and candidate markers of vessel co-option are clinically relevant.
- Further study the molecular profiles of niche and distal stromal cells in relation to their localisation in lung tissue using spatial transcriptomics. This method would enable us to also validate the gene expression profiles and cell types identified using scRNA-seq and niche labelling technologies.

- An investigation of the intrinsic transcriptional changes in the E0771 tumour cells in vessel co-opting (parenchymal) and angiogenic (subpleural) metastases. We have established a method of manual microdissection of surface subpleural metastases and FACS validated the tumour burden in both compartments **(Figure 8-3).**

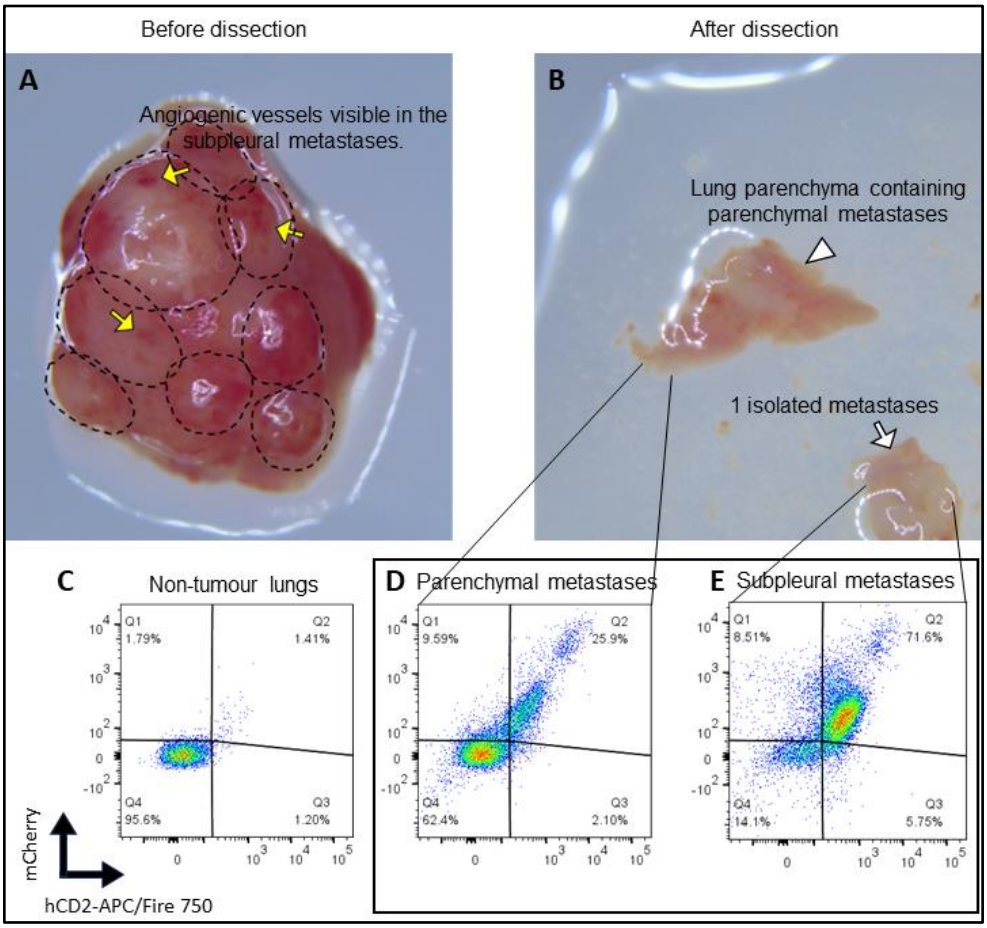

Figure 8-3. Gross view and FACS analysis of E0771 vessel co-opting (parenchymal) and angiogenic (subpleural) metastases. *Angiogenic metastases showed angiogenic vessels at macroscopic level (yellow arrows). C57BL/6 mouse were injected with mCherry-labelling hCD2 E0771 tumour cells and lungs were harvested 13 days post-tumour injection. A and B: gross view of tumour-bearing lung lobe before and after microdissection of subpleural metastases (white arrow) from parenchymal ones (white arrowhead); C-E: hCD2-APC/Fire750 density plot to identify E0771 tumour cells (hCD2+ mCherry+) from lung stromal cells (non-labelled (hCD2- mCherry-) and labelled cells (only mCherry+). C: FACS analysis of non-tumour-bearing lungs; D and E: FACS analysis of vessel co-opting metastases-containing lung parenchyma (D) and angiogenic metastases (E).*

- An assessment of the transcriptional profiles of EC subtypes upon inhibiting angiogenic ECs in the E0771 metastasis model using scRNA-seq, which might reveal vascular remodelling that underlie drug resistance.

These future studies will extend the explanations of metastatic niche formation, resistance mechanisms, and provide novel avenues for targeting metastatic disease.

References

Adighibe, et al. (2016). Why some tumours trigger neovascularisation and others don't: the story thus far. *Chinese journal of cancer, 35*, 18-18. doi:10.1186/s40880-016-0082-6

Adighibe, et al. (2006). Is nonangiogenesis a novel pathway for cancer progression? A study using 3-dimensional tumour reconstructions. *British journal of cancer, 94*(8), 1176-1179. doi:10.1038/sj.bjc.6603039

Ahn, & Brown. (2008). Matrix Metalloproteinase-9 Is Required for Tumor Vasculogenesis but Not for Angiogenesis: Role of Bone Marrow-Derived Myelomonocytic Cells. *Cancer Cell, 13*(3), 193-205. doi:10.1016/j.ccr.2007.11.032

Al-Hajj, et al. (2003). Prospective identification of tumorigenic breast cancer cells. *Proceedings of the National Academy of Sciences of the United States of America, 100*(7), 3983-3988. doi:10.1073/pnas.0530291100

Altorki, et al. (2019). The lung microenvironment: an important regulator of tumour growth and metastasis. *Nature reviews. Cancer, 19*(1), 9. doi:10.1038/s41568-018-0081-9

Ang. (2019). *The biology of ADGRL4/ELTD1 in angiogenesis and tumour development.* (A Doctor of Philosophy). Oxford University,

Angelidis, et al. (2019). An atlas of the aging lung mapped by single cell transcriptomics and deep tissue proteomics. *Nature Communications, 10*(1), 963. doi:10.1038/s41467-019-08831-9

Annabi, et al. (2004). Vascular progenitors derived from murine bone marrow stromal cells are regulated by fibroblast growth factor and are avidly recruited by vascularizing tumors. *Journal of Cellular Biochemistry, 91*(6), 1146-1158. doi:10.1002/jcb.10763

Annese, et al. (2022). Differential P-Glycoprotein/CD31 Expression as Markers of Vascular Co-Option in Primary Central Nervous System Tumors. *Diagnostics (Basel), 12*(12). doi:10.3390/diagnostics12123120

Aokage, et al. (2011). Dynamic molecular changes associated with epithelial-mesenchymal transition and subsequent mesenchymal-epithelial transition in the early phase of metastatic tumor formation. *Int J Cancer, 128*(7), 1585-1595. doi:10.1002/ijc.25500

Asahara, et al. (1999). Bone marrow origin of endothelial progenitor cells responsible for postnatal vasculogenesis in physiological and pathological neovascularization. *Circulation research, 85*(3), 221. doi:10.1161/01.RES.85.3.221

Augustin, et al. (2009). Control of vascular morphogenesis and homeostasis through the angiopoietin–Tie system. *Nature Reviews Molecular Cell Biology, 10*(3), 165-177. doi:10.1038/nrm2639

Bacci, et al. (2021). Fat and Furious: Lipid Metabolism in Antitumoral Therapy Response and Resistance. *Trends in cancer, 7*(3), 198-213. doi:https://doi.org/10.1016/j.trecan.2020.10.004

Bae, et al. (2005). Anti-Flt1 peptide, a vascular endothelial growth factor receptor 1-specific hexapeptide, inhibits tumor growth and metastasis. *Clin. Cancer Res., 11*(7), 2651-2661.

Baker, et al. (2014). Mechanisms of glioma formation: iterative perivascular glioma growth and invasion leads to tumor progression, VEGF-independent vascularization, and resistance to antiangiogenic therapy. *Neoplasia (New York, N.Y.), 16*(7), 543-561. doi:10.1016/j.neo.2014.06.003

Bao, et al. (2022). SNAIL Induces EMT and Lung Metastasis of Tumours Secreting CXCL2 to Promote the Invasion of M2-Type Immunosuppressed Macrophages in Colorectal Cancer. *International Journal of Biological Sciences, 18*(7), 2867-2881. doi:10.7150/ijbs.66854

Barnhill, et al. (2022). L1CAM and laminin vascular network: Association with the high-risk replacement histopathologic growth pattern in uveal melanoma liver metastases. *Lab Invest, 102*(11), 1214-1224. doi:10.1038/s41374-022-00803-w

Becker, et al. (2020). Epigenetic Reprogramming of Cancer-Associated Fibroblasts Deregulates Glucose Metabolism and Facilitates Progression of Breast Cancer. *Cell reports, 31*(9), 107701. doi:10.1016/j.celrep.2020.107701

Bednarek, et al. (2020). Functional inhibition of F11 receptor (F11R/junctional adhesion molecule-A/JAM-A) activity by a F11R-derived peptide in breast cancer and its microenvironment. *Breast Cancer Research and Treatment, 179*(2), 325-335. doi:10.1007/s10549-019-05471-x

Beigneux, et al. (2009). Highly conserved cysteines within the Ly6 domain of GPIHBP1 are crucial for the binding of lipoprotein lipase. *J Biol Chem, 284*(44), 30240-30247. doi:10.1074/jbc.M109.046391

Benedito, et al. (2009). The Notch Ligands Dll4 and Jagged1 Have Opposing Effects on Angiogenesis. *Cell, 137*(6), 1124-1135. doi:10.1016/j.cell.2009.03.025

Bergers, & Fendt. (2021). The metabolism of cancer cells during metastasis. *Nature Reviews Cancer, 21*(3), 162-180. doi:10.1038/s41568-020-00320-2

Bergers, et al. (2003). Benefits of targeting both pericytes and endothelial cells in the tumor vasculature with kinase inhibitors. *The Journal of clinical investigation, 111*(9), 1287-1295. doi:10.1172/JCI17929

Bernier-Latmani, et al. (2022). Apelin-driven endothelial cell migration sustains intestinal progenitor cells and tumor growth. *Nat Cardiovasc Res, 1*(5), 476-490. doi:10.1038/s44161-022-00061-5

Bernsen, et al. (2005). Gliomatosis cerebri: quantitative proof of vessel recruitment by cooptation instead of angiogenesis. *Journal of neurosurgery, 103*(4), 702. doi:10.3171/jns.2005.103.4.0702

Bhattacharya, et al. (2005). Inhibition of vascular permeability factor/vascular endothelial growth factor-mediated angiogenesis by the Kruppel-like factor KLF2. *J Biol Chem, 280*(32), 28848-28851. doi:10.1074/jbc.C500200200

Blanco, & Gerhardt. (2013). VEGF and Notch in tip and stalk cell selection. *Cold Spring Harbor perspectives in medicine, 3*(1), a006569-a006569. doi:10.1101/cshperspect.a006569

Blomberg, et al. (2018). Immune regulation of metastasis: mechanistic insights and therapeutic opportunities. *Disease models & mechanisms, 11*(10), dmm036236. doi:10.1242/dmm.036236

Bodogai, et al. (2015). Immunosuppressive and Prometastatic Functions of Myeloid-Derived Suppressive Cells Rely upon Education from Tumor-Associated B Cells. *Cancer Research, 75*(17), 3456-3465. doi:10.1158/0008-5472.CAN-14-3077

Bonnans, et al. (2014). Remodelling the extracellular matrix in development and disease. *Nature Reviews Molecular Cell Biology, 15*(12), 786-801. doi:10.1038/nrm3904

Bottos, et al. (2016). Decreased NK-cell tumour immunosurveillance consequent to JAK inhibition enhances metastasis in breast cancer models. *Nature Communications, 7*, 12258. doi:10.1038/ncomms12258

Brantley-Sieders, et al. (2006). Ephrin-A1 Facilitates Mammary Tumor Metastasis through an Angiogenesis-Dependent Mechanism Mediated by EphA Receptor and Vascular Endothelial Growth Factor in Mice. *Cancer Research, 66*(21), 10315. doi:10.1158/0008-5472.CAN-06-1560

Bray, et al. (2018). Global cancer statistics 2018: GLOBOCAN estimates of incidence and mortality worldwide for 36 cancers in 185 countries. *CA: a cancer journal for clinicians, 68*(6), 394. doi:10.3322/caac.21492

Bremnes, et al. (2011). The role of tumor stroma in cancer progression and prognosis: emphasis on carcinoma-associated fibroblasts and non-small cell lung cancer. *J Thorac Oncol, 6*(1), 209-217. doi:10.1097/JTO.0b013e3181f8a1bd

Brennan, et al. (2018). Generation of Luciferase-expressing Tumor Cell Lines. *Bio-protocol, 8*(8), e2817. doi:10.21769/BioProtoc.2817

Brenner, & Adams. (1999). First MAb approved for treatment of metastatic breast cancer. *J Am Pharm Assoc (Wash), 39*(2), 236-238.

Brichkina, et al. (2016). p38MAPK builds a hyaluronan cancer niche to drive lung tumorigenesis. *Genes Dev, 30*(23), 2623-2636. doi:10.1101/gad.290346.116

Bridgeman, et al. (2017). Vessel co-option is common in human lung metastases and mediates resistance to anti-angiogenic therapy in preclinical lung metastasis models. *Journal of Pathology, 241*(3), 362-374. doi:10.1002/path.4845

Brown. (2014). Vasculogenesis: a crucial player in the resistance of solid tumours to radiotherapy. *The British journal of radiology, 87*(1035), 20130686-20130686. doi:10.1259/bjr.20130686

Brunner, et al. (2014). Prognosis according to histochemical analysis of liver metastases removed at liver resection. *British Journal of Surgery, 101*(13), 1681-1691. doi:10.1002/bjs.9627

Burikhanov, et al. (2017). Chloroquine-Inducible Par-4 Secretion Is Essential for Tumor Cell Apoptosis and Inhibition of Metastasis. *Cell reports, 18*(2), 508-519. doi:10.1016/j.celrep.2016.12.051

Burri, et al. (2004). Intussusceptive angiogenesis: Its emergence, its characteristics, and its significance. In (Vol. 231, pp. 474-488). Hoboken.

Caduff, et al. (1986). Scanning electron microscope study of the developing microvasculature in the postnatal rat lung. *Anat Rec, 216*(2), 154-164. doi:10.1002/ar.1092160207

Cangul. (2004). Hypoxia upregulates the expression of the NDRG1 gene leading to its overexpression in various human cancers. *BMC Genet, 5*, 27. doi:10.1186/1471-2156-5-27

Cannell, et al. (2023). FOXC2 promotes vasculogenic mimicry and resistance to anti-angiogenic therapy. *Cell reports*, 112791. doi:10.1016/j.celrep.2023.112791

Cantelmo, et al. (2016). Inhibition of the Glycolytic Activator PFKFB3 in Endothelium Induces Tumor Vessel Normalization, Impairs Metastasis, and Improves Chemotherapy. *Cancer Cell, 30*(6), 968-985. doi:10.1016/j.ccell.2016.10.006

Capillo, et al. (2003). Continuous infusion of endostatin inhibits differentiation, mobilization, and clonogenic potential of endothelial cell progenitors. *Clinical cancer research : an official journal of the American Association for Cancer Research, 9*(1), 377.

Carmeliet, & Jain. (2011). Molecular mechanisms and clinical applications of angiogenesis. *Nature, 473*(7347), 298-307. doi:10.1038/nature10144

Casanovas, et al. (2005). Drug resistance by evasion of antiangiogenic targeting of VEGF signaling in late-stage pancreatic islet tumors. *Cancer Cell, 8*(4), 299-309. doi:https://doi.org/10.1016/j.ccr.2005.09.005

Caspani, et al. (2014). Glioblastoma: a pathogenic crosstalk between tumor cells and pericytes. *PLoS ONE, 9*(7), e101402-e101402. doi:10.1371/journal.pone.0101402

Cavallaro, et al. (2006). Endothelial cadherins and tumour angiogenesis. *Experimental Cell Research, 312*(5), 659-667. doi:https://doi.org/10.1016/j.yexcr.2005.09.019

Celia-Terrassa, & Kang. (2018). Metastatic niche functions and therapeutic opportunities. *Nat. Cell Biol., 20*(8), 868-877. doi:10.1038/s41556-018-0145-9

Celus, et al. (2022). Plexin-A4 Mediates Cytotoxic T-cell Trafficking and Exclusion in Cancer. *Cancer immunology research, 10*(1), 126-141. doi:10.1158/2326-6066.Cir-21-0061

Chafe, et al. (2015). Carbonic anhydrase IX promotes myeloid-derived suppressor cell mobilization and establishment of a metastatic niche by stimulating G-CSF production. *Cancer Res, 75*(6), 996-1008. doi:10.1158/0008-5472.Can-14-3000

Chait, et al. (2020). Presence of serum amyloid A3 in mouse plasma is dependent on the nature and extent of the inflammatory stimulus. *Scientific Reports, 10*(1), 10397. doi:10.1038/s41598-020-66898-7

Chakraborty, et al. (2019). Promoters to Study Vascular Smooth Muscle. *Arteriosclerosis, thrombosis, and vascular biology, 39*(4), 603-612. doi:10.1161/ATVBAHA.119.312449

Chavakis, et al. (2007). High-mobility group box 1 activates integrin-dependent homing of endothelial progenitor cells. *Circulation research, 100*(2), 204. doi:10.1161/01.RES.0000257774.55970.f4

Chellappan, et al. (2017). The role of pazopanib on tumour angiogenesis and in the management of cancers: A review. *Biomedicine & Pharmacotherapy, 96*, 768-781. doi:https://doi.org/10.1016/j.biopha.2017.10.058

Chen, et al. (2017). Notch1 promotes vasculogenic mimicry in hepatocellular carcinoma by inducing EMT signaling. *Oncotarget, 8*(2), 2501-2513. doi:10.18632/oncotarget.12388

Chen, et al. (2011). CCL18 from tumor-associated macrophages promotes breast cancer metastasis via PITPNM3. *Cancer Cell, 19*(4), 541-555. doi:10.1016/j.ccr.2011.02.006

Chidiac, et al. (2021). A Norrin/Wnt surrogate antibody stimulates endothelial cell barrier function and rescues retinopathy. *EMBO Mol Med, 13*(7), e13977. doi:10.15252/emmm.202113977

Chiossone, et al. (2018). Natural killer cells and other innate lymphoid cells in cancer. *Nature Reviews Immunology, 18*(11), 671-688. doi:10.1038/s41577-018-0061-z

Claxton, et al. (2008). Efficient, inducible Cre-recombinase activation in vascular endothelium. *genesis, 46*(2), 74-80. doi:10.1002/dvg.20367

Clever, et al. (2016). Oxygen Sensing by T Cells Establishes an Immunologically Tolerant Metastatic Niche. *Cell, 166*(5), 1117-1131.e1114. doi:10.1016/j.cell.2016.07.032

Coates, et al. (2015). Tailoring therapies--improving the management of early breast cancer: St Gallen International Expert Consensus on the Primary Therapy of Early Breast Cancer 2015. *Annals of oncology : official journal of the European Society for Medical Oncology, 26*(8), 1533-1546. doi:10.1093/annonc/mdv221

Coffelt, et al. (2015). IL-17-producing γδ T cells and neutrophils conspire to promote breast cancer metastasis. *Nature, 522*(7556), 345-348. doi:10.1038/nature14282

Collier. (2017). *Investigation of the role of eosinophils in pulmonary metastasis and primary tumours in mouse models of breast cancer.* (Master of Science - MSc). The University of British Columbia, Vancouver. Retrieved from

http://hdl.handle.net/2429/62442 Available from Vancouver : University of British Columbia Library

Coxon, et al. (2010). Context-dependent role of angiopoietin-1 inhibition in the suppression of angiogenesis and tumor growth: implications for AMG 386, an angiopoietin-1/2-neutralizing peptibody. *Molecular cancer therapeutics, 9*(10), 2641-2651. doi:10.1158/1535-7163.MCT-10-0213

Crivellato, et al. (2004). Recombinant human erythropoietin induces intussusceptive microvascular growth in vivo. *Leukemia, 18*(2), 331-336. doi:10.1038/sj.leu.2403246

Crivellato, et al. (2003). B-cell non-Hodgkin's lymphomas express heterogeneous patterns of neovascularization. *Haematologica, 88*(6), 671-678.

Cuiffo, et al. (2014). MSC-Regulated MicroRNAs Converge on the Transcription Factor FOXP2 and Promote Breast Cancer Metastasis. *Cell stem cell, 15*(6), 762-774. doi:https://doi.org/10.1016/j.stem.2014.10.001

Czubak-Prowizor, et al. (2022). The F11 Receptor (F11R)/Junctional Adhesion Molecule-A (JAM-A) (F11R/JAM-A) in cancer progression. *Mol Cell Biochem, 477*(1), 79-98. doi:10.1007/s11010-021-04259-2

David, et al. (2013). Visceral pleural invasion is not predictive of survival in patients with lung cancer and smaller tumor size. *Ann Thorac Surg, 95*(6), 1872-1877; discussion 1877. doi:10.1016/j.athoracsur.2013.03.085

Davies, et al. (2010). GPIHBP1 is responsible for the entry of lipoprotein lipase into capillaries. *Cell Metab, 12*(1), 42-52. doi:10.1016/j.cmet.2010.04.016

de Groot, et al. (2010). Tumor invasion after treatment of glioblastoma with bevacizumab: radiographic and pathologic correlation in humans and mice. *Neuro-oncology, 12*(3), 233-242. doi:10.1093/neuonc/nop027

de Looff, et al. (2019). Multiple Interactions Between Cancer Cells and the Tumor Microenvironment Modulate TRAIL Signaling: Implications for TRAIL Receptor Targeted Therapy. *Frontiers in immunology, 10*, 1530. doi:10.3389/fimmu.2019.01530

De Santo, et al. (2010). Invariant NKT cells modulate the suppressive activity of IL-10-secreting neutrophils differentiated with serum amyloid A. *Nature Immunology, 11*(11), 1039-1046. doi:10.1038/ni.1942

De Spiegelaere, et al. (2012). Intussusceptive Angiogenesis: A Biologically Relevant Form of Angiogenesis. *Journal of Vascular Research, 49*(5), 390-404. doi:10.1159/000338278

Denardo, et al. (2009). CD4 + T Cells Regulate Pulmonary Metastasis of Mammary Carcinomas by Enhancing Protumor Properties of Macrophages. *Cancer Cell, 16*(2), 91-102. doi:10.1016/j.ccr.2009.06.018

Depner, et al. (2016). EphrinB2 repression through ZEB2 mediates tumour invasion and anti-angiogenic resistance. *Nat Commun, 7*, 12329. doi:10.1038/ncomms12329

Descot, & Oskarsson. (2013). The molecular composition of the metastatic niche. *Experimental Cell Research, 319*(11), 1679-1686. doi:10.1016/j.yexcr.2013.04.017

Devilard, et al. (2013). Nectin-3 (CD113) interacts with Nectin-2 (CD112) to promote lymphocyte transendothelial migration. *PLoS ONE, 8*(10), e77424. doi:10.1371/journal.pone.0077424

Dhanabal, et al. (2005). Recombinant semaphorin 6A-1 ectodomain inhibits in vivo growth factor and tumor cell line-induced angiogenesis. *Cancer Biol Ther, 4*(6), 659-668. doi:10.4161/cbt.4.6.1733

di Tomaso, et al. (2011). Glioblastoma recurrence after cediranib therapy in patients: lack of "rebound" revascularization as mode of escape. *Cancer Research, 71*(1), 19-28. doi:10.1158/0008-5472.CAN-10-2602

Diehl, et al. (2008). Tolerogenic maturation of liver sinusoidal endothelial cells promotes B7-homolog 1-dependent CD8+ T cell tolerance. *Hepatology (Baltimore, Md.), 47*(1), 296.

Dilling, et al. (2017). Multiple protocadherins are expressed in brain microvascular endothelial cells and might play a role in tight junction protein regulation. *J Cereb Blood Flow Metab, 37*(10), 3391-3400. doi:10.1177/0271678x16688706

Ding, et al. (2019). Suppression of the SAP18/HDAC1 complex by targeting TRIM56 and Nanog is essential for oncogenic viral FLICE-inhibitory protein-induced acetylation of p65/RelA, NF-κB activation, and promotion of cell invasion and angiogenesis. *Cell Death Differ, 26*(10), 1970-1986. doi:10.1038/s41418-018-0268-3

Djonov, et al. (2001). Vascular remodelling during the normal and malignant life cycle of the mammary gland. *Microscopy Research and Technique, 52*(2), 182-189. doi:10.1002/1097-0029(20010115)52:2<182::AID-JEMT1004>3.0.CO;2-M

Djurec, et al. (2018). Saa3 is a key mediator of the protumorigenic properties of cancer-associated fibroblasts in pancreatic tumors. *Proceedings of the National Academy of Sciences of the United States of America, 115*(6), E1147-e1156. doi:10.1073/pnas.1717802115

Donnem, et al. (2013). Vessel co-option in primary human tumors and metastases: an obstacle to effective anti-angiogenic treatment? *Cancer medicine, 2*. doi:10.1002/cam4.105

Donnem, et al. (2018). Non-angiogenic tumours and their influence on cancer biology. *Nature reviews. Cancer, 18*(5), 323-336. doi:10.1038/nrc.2018.14

Du, & Shim. (2016). Targeting Epithelial-Mesenchymal Transition (EMT) to Overcome Drug Resistance in Cancer. *Molecules, 21*(7). doi:10.3390/molecules21070965

Duda, et al. (2010). Malignant cells facilitate lung metastasis by bringing their own soil. *Proceedings of the National Academy of Sciences, 107*(50), 21677. doi:10.1073/pnas.1016234107

Dykxhoorn, et al. (2009). miR-200 enhances mouse breast cancer cell colonization to form distant metastases. *PLoS ONE, 4*(9), e7181. doi:10.1371/journal.pone.0007181

Early Breast Cancer Trialists' Collaborative Group, et al. (2011). Relevance of breast cancer hormone receptors and other factors to the efficacy of adjuvant tamoxifen: patient-level meta-analysis of randomised trials. *Lancet (London, England), 378*(9793), 771-784. doi:10.1016/S0140-6736(11)60993-8

Early Breast Cancer Trialists' Collaborative Group, et al. (2012). Comparisons between different polychemotherapy regimens for early breast cancer: meta-analyses of long-term outcome among 100,000 women in 123 randomised trials. *Lancet (London, England), 379*(9814), 432-444. doi:10.1016/S0140-6736(11)61625-5

Efremova, et al. (2020). CellPhoneDB: inferring cell–cell communication from combined expression of multi-subunit ligand–receptor complexes. *Nature Protocols, 15*(4), 1484-1506. doi:10.1038/s41596-020-0292-x

Ehrentraut, et al. (2012). Adora2b adenosine receptor engagement enhances regulatory T cell abundance during endotoxin-induced pulmonary inflammation. *PLoS ONE, 7*(2), e32416. doi:10.1371/journal.pone.0032416

El-Botty, et al. (2023). Oxidative phosphorylation is a metabolic vulnerability of endocrine therapy and palbociclib resistant metastatic breast cancers. *Nature Communications, 14*(1), 4221. doi:10.1038/s41467-023-40022-5

Elia, et al. (2017). Proline metabolism supports metastasis formation and could be inhibited to selectively target metastasizing cancer cells. *Nature Communications, 8*(1), 15267. doi:10.1038/ncomms15267

Elia, et al. (2019). Breast cancer cells rely on environmental pyruvate to shape the metastatic niche. *Nature, 568*(7750), 117-121. doi:10.1038/s41586-019-0977-x

Elston, & Ellis. (1991). pathological prognostic factors in breast cancer. I. The value of histological grade in breast cancer: experience from a large study with long-term follow-up. *Histopathology, 19*(5), 403-410. doi:10.1111/j.1365-2559.1991.tb00229.x

Erler, et al. (2009). Hypoxia-induced lysyl oxidase is a critical mediator of bone marrow cell recruitment to form the premetastatic niche. *Cancer Cell, 15*(1), 35-44. doi:10.1016/j.ccr.2008.11.012

Ewens, et al. (2005). Distant metastasis from subcutaneously grown E0771 medullary breast adenocarcinoma. *Anticancer research, 25*(6B), 3905.

Eyles, et al. (2010). Tumor cells disseminate early, but immunosurveillance limits metastatic outgrowth, in a mouse model of melanoma. *The Journal of clinical investigation, 120*(6), 2030. doi:10.1172/JCI42002

Fack, et al. (2015). Bevacizumab treatment induces metabolic adaptation toward anaerobic metabolism in glioblastomas. *Acta Neuropathologica, 129*(1), 115-131. doi:10.1007/s00401-014-1352-5

Fairfax, et al. (2020). Peripheral CD8+ T cell characteristics associated with durable responses to immune checkpoint blockade in patients with metastatic melanoma. *Nature Medicine, 26*(2), 193-199. doi:10.1038/s41591-019-0734-6

Fang, et al. (2018). Tumor-derived exosomal miR-1247-3p induces cancer-associated fibroblast activation to foster lung metastasis of liver cancer. *Nature Communications, 9*(1), 191. doi:10.1038/s41467-017-02583-0

Fatehi-Hassanabad, & Chan. (2005). Transcriptional regulation of lipid metabolism by fatty acids: a key determinant of pancreatic β-cell function. *Nutrition & Metabolism, 2*(1), 1. doi:10.1186/1743-7075-2-1

Fear, et al. (2019). Neo-antigen specific T cell responses indicate the presence of metastases before imaging. *Scientific Reports, 9*(1), 14640. doi:10.1038/s41598-019-51317-3

Feng, et al. (2019). CD36-Mediated Metabolic Rewiring of Breast Cancer Cells Promotes Resistance to HER2-Targeted Therapies. *Cell reports, 29*(11), 3405-3420.e3405. doi:10.1016/j.celrep.2019.11.008

Fidler. (1970). Metastasis: Quantitative analysis of distribution and fate of tumor emboli labeled with 125I-5-Iodo-2'-deoxyuridine. *Journal of the National Cancer Institute, 45*(4), 773-782. doi:10.1093/jnci/45.4.773

Fischer, et al. (2015). Epithelial-to-mesenchymal transition is not required for lung metastasis but contributes to chemoresistance. *Nature, 527*(7579), 472-476. doi:10.1038/nature15748

Fleischer, et al. (2023). Molecular differences of angiogenic versus vessel co-opting colorectal cancer liver metastases at single-cell resolution. *Mol Cancer, 22*(1), 17. doi:10.1186/s12943-023-01713-1

Fleming, et al. (1993). Pulmonary carbonic anhydrase IV: developmental regulation and cell-specific expression in the capillary endothelium. *Am J Physiol, 265*(6 Pt 1), L627-635. doi:10.1152/ajplung.1993.265.6.L627

Folkman. (1971). Tumor Angiogenesis: Therapeutic Implications. *New England Journal of Medicine, 285*(21), 1182-1186. doi:10.1056/nejm197111182852108

Folkman. (1982). Angiogenesis: initiation and control. *Annals of the New York Academy of Sciences, 401*(1), 212-226. doi:https://doi.org/10.1111/j.1749-6632.1982.tb25720.x

Follain, et al. (2018). Hemodynamic Forces Tune the Arrest, Adhesion, and Extravasation of Circulating Tumor Cells. *Developmental Cell, 45*(1), 33-52.e12. doi:10.1016/j.devcel.2018.02.015

Fong, et al. (2015). Breast-cancer-secreted miR-122 reprograms glucose metabolism in premetastatic niche to promote metastasis. *Nature Cell Biology, 17*(2), 183-194. doi:10.1038/ncb3094

Francis, et al. (2018). Tailoring Adjuvant Endocrine Therapy for Premenopausal Breast Cancer. *The New England Journal of Medicine, 379*(2), 122-137. doi:10.1056/NEJMoa1803164

Frentzas, et al. (2016). Vessel co-option mediates resistance to anti-angiogenic therapy in liver metastases. *Nature Medicine, 22*(11), 1294-1302. doi:10.1038/nm.4197

Gadomski, et al. (2020). Id1 and Id3 Maintain Steady-State Hematopoiesis by Promoting Sinusoidal Endothelial Cell Survival and Regeneration. *Cell reports, 31*(4), 107572. doi:10.1016/j.celrep.2020.107572

Ganesh, & Massagué. (2021). Targeting metastatic cancer. *Nature Medicine, 27*(1), 34-44. doi:10.1038/s41591-020-01195-4

Gao, et al. (2016). Multi-organ Site Metastatic Reactivation Mediated by Non-canonical Discoidin Domain Receptor 1 Signaling. *Cell, 166*(1), 47-62. doi:https://doi.org/10.1016/j.cell.2016.06.009

Gao, et al. (2012). Myeloid Progenitor Cells in the Premetastatic Lung Promote Metastases by Inducing Mesenchymal to Epithelial Transition. *Cancer Research, 72*(6), 1384-1394. doi:10.1158/0008-5472.Can-11-2905

Gao, et al. (2008). Endothelial progenitor cells control the angiogenic switch in mouse lung metastasis. *Science (New York, N.Y.), 319*(5860), 195. doi:10.1126/science.1150224

Garbicz, et al. (2020). PIM Kinase Inhibition Decreases the Proangiogenic Properties of Multiple Myeloma Cells and Affects the Metabolic State of the Vascular Endothelium. *Blood, 136*, 16-17. doi:https://doi.org/10.1182/blood-2020-134979

Gay, & Felding-Habermann. (2011). Contribution of platelets to tumour metastasis. *Nature reviews. Cancer, 11*(2), 123-134. doi:10.1038/nrc3004

Geldhof, et al. (2022). Single cell atlas identifies lipid-processing and immunomodulatory endothelial cells in healthy and malignant breast. *Nature Communications, 13*(1), 5511. doi:10.1038/s41467-022-33052-y

Georgoudaki, et al. (2016). Reprogramming Tumor-Associated Macrophages by Antibody Targeting Inhibits Cancer Progression and Metastasis. *Cell reports, 15*(9), 2000-2011. doi:10.1016/j.celrep.2016.04.084

Géraud, et al. (2013). Endothelial transdifferentiation in hepatocellular carcinoma: loss of Stabilin-2 expression in peri-tumourous liver correlates with increased survival. *Liver International, 33*(9), 1428-1440. doi:10.1111/liv.12262

Ghaghada, et al. (2011). Evaluation of Tumor Microenvironment in an Animal Model using a Nanoparticle Contrast Agent in Computed Tomography Imaging. *Academic Radiology, 18*(1), 20-30. doi:https://doi.org/10.1016/j.acra.2010.09.003

Gianni, et al. (2016). 5-year analysis of neoadjuvant pertuzumab and trastuzumab in patients with locally advanced, inflammatory, or early-stage HER2-positive breast cancer (NeoSphere): a multicentre, open-label, phase 2 randomised trial. *The Lancet Oncology, 17*(6), 791-800. doi:10.1016/S1470-2045(16)00163-7

Gil-Bernabé, et al. (2012). Recruitment of monocytes/macrophages by tissue factor-mediated coagulation is essential for metastatic cell survival and premetastatic niche establishment in mice. *Blood, 119*(13), 3164-3175. doi:10.1182/blood-2011-08-376426

Gillich, et al. (2020). Capillary cell-type specialization in the alveolus. *Nature, 586*(7831), 785-789. doi:10.1038/s41586-020-2822-7

Ginestier, et al. (2007). ALDH1 is a marker of normal and malignant human mammary stem cells and a predictor of poor clinical outcome. *Cell stem cell, 1*(5), 555-567. doi:10.1016/j.stem.2007.08.014

Gomes, et al. (2019). Cardio-Respiratory synchronized bSSFP MRI for high throughput in vivo lung tumour quantification. *PLoS ONE, 14*(2), e0212172. doi:10.1371/journal.pone.0212172

Gorbunova, et al. (2016). The Andes Virus Nucleocapsid Protein Directs Basal Endothelial Cell Permeability by Activating RhoA. *mBio, 7*(5). doi:10.1128/mBio.01747-16

Gordillo, et al. (2020). Mesothelial-to-Mesenchymal Transition Contributes to the Generation of Carcinoma-Associated Fibroblasts in Locally Advanced Primary Colorectal Carcinomas. *Cancers, 12*(2). doi:10.3390/cancers12020499

Goveia, et al. (2020). An Integrated Gene Expression Landscape Profiling Approach to Identify Lung Tumor Endothelial Cell Heterogeneity and Angiogenic Candidates. *Cancer Cell, 37*(1), 21-36.e13. doi:10.1016/j.ccell.2019.12.001

Green, et al. (2017). A nonimmune function of T cells in promoting lung tumour progression. *Journal of Experimental Medicine, 214*(12), 3565-3575. doi:10.1084/jem.20170356

Griveau, et al. (2018). A Glial Signature and Wnt7 Signaling Regulate Glioma-Vascular Interactions and Tumor Microenvironment. *Cancer Cell, 33*(5), 874-889.e877. doi:10.1016/j.ccell.2018.03.020

Gromeier, et al. (2000). Intergeneric poliovirus recombinants for the treatment of malignant glioma. *Proceedings of the National Academy of Sciences of the United States of America, 97*(12), 6803-6808. doi:10.1073/pnas.97.12.6803

Gu, et al. (2009). Oral administration of pyrrolidine dithiocarbamate (PDTC) inhibits VEGF expression, tumor angiogenesis, and growth of breast cancer in female mice. *Cancer Biol Ther, 8*(6), 514-521. doi:10.4161/cbt.8.6.7689

Guillou, et al. (2010). The key roles of elongases and desaturases in mammalian fatty acid metabolism: Insights from transgenic mice. *Progress in Lipid Research, 49*(2), 186-199. doi:https://doi.org/10.1016/j.plipres.2009.12.002

Gujral, et al. (2014). A noncanonical Frizzled2 pathway regulates epithelial-mesenchymal transition and metastasis. *Cell, 159*(4), 844-856. doi:10.1016/j.cell.2014.10.032

Guo, et al. (2014). Targeting SREBP-1-driven lipid metabolism to treat cancer. *Curr Pharm Des, 20*(15), 2619-2626. doi:10.2174/13816128113199990486

Hafemeister, & Satija. (2019). Normalization and variance stabilization of single-cell RNA-seq data using regularized negative binomial regression. *Genome Biology, 20*(1), 296. doi:10.1186/s13059-019-1874-1

Hahnen, et al. (2017). Germline Mutation Status, Pathological Complete Response, and Disease-Free Survival in Triple-Negative Breast Cancer: Secondary Analysis of the GeparSixto Randomized Clinical Trial. *JAMA oncology, 3*(10), 1378-1385. doi:10.1001/jamaoncol.2017.1007

Hale, et al. (2012). Context dependent role of the CD36--thrombospondin--histidine-rich glycoprotein axis in tumor angiogenesis and growth. *PLoS ONE, 7*(7), e40033. doi:10.1371/journal.pone.0040033

Hamzah, et al. (2008). Vascular normalization in Rgs5-deficient tumours promotes immune destruction. *Nature, 453*(7193), 410-414. doi:10.1038/nature06868

Han, et al. (2001). Extracellular matrix protein 1 (ECM1) has angiogenic properties and is expressed by breast tumor cells. *Faseb j, 15*(6), 988-994. doi:10.1096/fj.99-0934com

Hanna, et al. (2015). Patrolling monocytes control tumor metastasis to the lung. *Science (New York, N.Y.), 350*(6263), 985-990. doi:10.1126/science.aac9407

Hansell, et al. (2018). The Atypical Chemokine Receptor Ackr2 Constrains NK Cell Migratory Activity and Promotes Metastasis. *J Immunol, 201*(8), 2510-2519. doi:10.4049/jimmunol.1800131

Harbeck, et al. (2019). Breast cancer. *Nature Reviews Disease Primers, 5*(1), 66. doi:10.1038/s41572-019-0111-2

He, et al. (2022). Lipid Droplet-Related PLIN2 in CD68(+) Tumor-Associated Macrophage of Oral Squamous Cell Carcinoma: Implications for Cancer Prognosis and Immunotherapy. *Front Oncol, 12*, 824235. doi:10.3389/fonc.2022.824235

He, et al. (2020). Remodeling of Metastatic Vasculature Reduces Lung Colonization and Sensitizes Overt Metastases to Immunotherapy. *Cell reports, 30*(3), 714-724.e715. doi:10.1016/j.celrep.2019.12.013

Heid, et al. (1998). Adipophilin is a specific marker of lipid accumulation in diverse cell types and diseases. *Cell Tissue Res, 294*(2), 309-321. doi:10.1007/s004410051181

Heindryckx, et al. (2010). Kinetics of angiogenic changes in a new mouse model for hepatocellular carcinoma. *MOLECULAR CANCER, 9*(1). doi:10.1186/1476-4598-9-219

Heissig, et al. (2002). Recruitment of Stem and Progenitor Cells from the Bone Marrow Niche Requires MMP-9 Mediated Release of Kit-Ligand. *Cell, 109*(5), 625-637. doi:10.1016/S0092-8674(02)00754-7

Helfrich, & Schadendorf. (2011). Blood vessel maturation, vascular phenotype and angiogenic potential in malignant melanoma: one step forward for overcoming anti-

angiogenic drug resistance? *Molecular oncology, 5*(2), 137-149. doi:10.1016/j.molonc.2011.01.003

Hendrix, et al. (2003). Vasculogenic mimicry and tumour-cell plasticity: lessons from melanoma. *Nature reviews. Cancer, 3*(6), 411-421. doi:10.1038/nrc1092

Hendrix, et al. (2001). Expression and functional significance of VE-cadherin in aggressive human melanoma cells: role in vasculogenic mimicry. *Proceedings of the National Academy of Sciences of the United States of America, 98*(14), 8018-8023. doi:10.1073/pnas.131209798

Hess, et al. (2001). Molecular regulation of tumor cell vasculogenic mimicry by tyrosine phosphorylation: role of epithelial cell kinase (Eck/EphA2). *Cancer Res, 61*(8), 3250-3255.

Hillen, & Griffioen. (2007). Tumour vascularization: sprouting angiogenesis and beyond. *Cancer metastasis reviews, 26*(3-4), 489-502. doi:10.1007/s10555-007-9094-7

Hirakawa, et al. (2007). VEGF-C-induced lymphangiogenesis in sentinel lymph nodes promotes tumor metastasis to distant sites. *Blood, 109*(3), 1010-1017. doi:10.1182/blood-2006-05-021758

Hirashima, et al. (2021). Wnt5a in cancer-associated fibroblasts promotes colorectal cancer progression. *Biochem Biophys Res Commun, 568*, 37-42. doi:10.1016/j.bbrc.2021.06.062

Hiratsuka, et al. (2002). MMP9 induction by vascular endothelial growth factor receptor-1 is involved in lung-specific metastasis. *Cancer Cell, 2*(4), 289-300. doi:10.1016/S1535-6108(02)00153-8

Hiratsuka, et al. (2006). Tumour-mediated upregulation of chemoattractants and recruitment of myeloid cells predetermines lung metastasis. *Nature Cell Biology, 8*(12), 1369-1375. doi:10.1038/ncb1507

Hodi, et al. (2014). Bevacizumab plus ipilimumab in patients with metastatic melanoma. *Cancer immunology research, 2*(7), 632-642. doi:10.1158/2326-6066.CIR-14-0053

Hoekstra, et al. (2020). Long-distance modulation of bystander tumor cells by CD8+ T-cell-secreted IFN-γ. *Nature Cancer, 1*(3), 291-301. doi:10.1038/s43018-020-0036-4

Holash, et al. (1999). Vessel Cooption, Regression, and Growth in Tumors Mediated by Angiopoietins and VEGF.(vascular endothelial growth factor). *Science, 284*(5422), 1994. doi:10.1126/science.284.5422.1994

Horton, et al. (2002). SREBPs: activators of the complete program of cholesterol and fatty acid synthesis in the liver. *J Clin Invest, 109*(9), 1125-1131. doi:10.1172/jci15593

Hu, et al. (2005). Gene expression signature for angiogenic and nonangiogenic non-small-cell lung cancer. *Oncogene, 24*(7), 1212-1219. doi:10.1038/sj.onc.1208242

Hu, et al. (2006). The molecular portraits of breast tumors are conserved across microarray platforms. *BMC Genomics, 7*, 96-96. doi:10.1186/1471-2164-7-96

Hu, et al. (2019). Sertad1 promotes prostate cancer progression through binding androgen receptor ligand binding domain. *Int J Cancer, 144*(3), 558-568. doi:10.1002/ijc.31877

Huang, et al. (2022a). ELTD1 deletion reduces vascular abnormality and improves T-cell recruitment after PD-1 blockade in glioma. *Neuro-oncology, 24*(3), 398-411. doi:10.1093/neuonc/noab181

Huang, et al. (2022b). Mesothelial cell-derived antigen-presenting cancer-associated fibroblasts induce expansion of regulatory T cells in pancreatic cancer. *Cancer Cell, 40*(6), 656-673.e657. doi:10.1016/j.ccell.2022.04.011

Hutchenreuther, et al. (2018). Activation of cancer-associated fibroblasts is required for tumor neovascularization in a murine model of melanoma. *Matrix Biology, 74*, 52-61. doi:10.1016/j.matbio.2018.06.003

Ibrahim, et al. (2019). Angiopoietin1 Deficiency in Hepatocytes Affects the Growth of Colorectal Cancer Liver Metastases (CRCLM). *Cancers, 12*(1). doi:10.3390/cancers12010035

Ikeda, et al. (2004). Nectin-like molecule-5/Tage4 enhances cell migration in an integrin-dependent, Nectin-3-independent manner. *J Biol Chem, 279*(17), 18015-18025. doi:10.1074/jbc.M312969200

Ingangi, et al. (2019). Role of Microenvironment on the Fate of Disseminating Cancer Stem Cells. *Front Oncol, 9*, 82. doi:10.3389/fonc.2019.00082

Jabouille, et al. (2015). Glioblastoma invasion and cooption depend on IRE1α endoribonuclease activity. *Oncotarget, 6*(28), 24922-24934. doi:10.18632/oncotarget.4679

Jain. (2003). Molecular regulation of vessel maturation. *Nature Medicine, 9*(6), 685-693. doi:10.1038/nm0603-685

Janssen, et al. (2017). The immune system in cancer metastasis: friend or foe? *Journal for ImmunoTherapy of Cancer, 5*(1), 79. doi:10.1186/s40425-017-0283-9

Ji, et al. (2018). Rutacecarpine Inhibits Angiogenesis by Targeting the VEGFR2 and VEGFR2-Mediated Akt/mTOR/p70s6k Signaling Pathway. *Molecules, 23*(8). doi:10.3390/molecules23082047

Jiang, et al. (2016). Primary breast cancer induces pulmonary vascular hyperpermeability and promotes metastasis via the VEGF–PKC pathway. *Molecular Carcinogenesis, 55*(6), 1087-1095. doi:https://doi.org/10.1002/mc.22352

Jiang, et al. (2022). Semaphorins as Potential Immune Therapeutic Targets for Cancer. *Front Oncol, 12*, 793805. doi:10.3389/fonc.2022.793805

Jin, et al. (2012). New Insight into the SDF-1/CXCR4 Axis in a Breast Carcinoma Model: Hypoxia-Induced Endothelial SDF-1 and Tumor Cell CXCR4 Are Required for Tumor Cell Intravasation. *Molecular Cancer Research, 10*(8), 1021. doi:10.1158/1541-7786.MCR-11-0498

Jin, et al. (2021). Inference and analysis of cell-cell communication using CellChat. *Nature Communications, 12*(1), 1088. doi:10.1038/s41467-021-21246-9

Jin, et al. (2018). Breast cancer lung metastasis: Molecular biology and therapeutic implications. In (Vol. 19, pp. 858-868).

Johansson-Percival, et al. (2017). De novo induction of intratumoral lymphoid structures and vessel normalization enhances immunotherapy in resistant tumors. *Nature Immunology, 18*(11), 1207-1217. doi:10.1038/ni.3836

Jolly, et al. (2017). EMT and MET: necessary or permissive for metastasis? *Molecular oncology, 11*(7), 755-769. doi:10.1002/1878-0261.12083

Jonas, & Carrington. (1969). Vascular patterns in primary and secondary pulmonary tumors in the dog. *The American journal of pathology, 56*(1), 79-95. Retrieved from https://pubmed.ncbi.nlm.nih.gov/4893319

https://www.ncbi.nlm.nih.gov/pmc/articles/PMC2013584/

Joseph, et al. (2021). CD8+ T cells inhibit metastasis and CXCL4 regulates its function. *British journal of cancer, 125*(2), 176-189. doi:10.1038/s41416-021-01338-5

Joyce, et al. (2011). VEGF-A and Tenascin-C produced by S100A4+ stromal cells are important for metastatic colonization. *Proceedings of the National Academy of Sciences, 108*(38), 16002. doi:10.1073/pnas.1109493108

Jung, et al. (2021). Tumor cell plasticity, heterogeneity, and resistance in crucial microenvironmental niches in glioma. *Nature Communications, 12*(1), 1014. doi:10.1038/s41467-021-21117-3

Kajiyama, et al. (2007). Chemoresistance to paclitaxel induces epithelial-mesenchymal transition and enhances metastatic potential for epithelial ovarian carcinoma cells. *Int J Oncol, 31*(2), 277-283.

Kanai, et al. (1987). Pathology of small hepatocellular carcinoma. A proposal for a new gross classification. *Cancer, 60*(4), 810-819. doi:10.1002/1097-0142(19870815)60:4<810::AID-CNCR2820600417>3.0.CO;2-1

Kanda, et al. (2020). Glucocorticoid-transactivated TSC22D3 attenuates hypoxia- and diabetes-induced Müller glial galectin-1 expression via HIF-1α destabilization. *Journal of cellular and molecular medicine, 24*(8), 4589-4599. doi:10.1111/jcmm.15116

Kaplan, et al. (2005). VEGFR1-positive haematopoietic bone marrow progenitors initiate the pre-metastatic niche. *Nature, 438*(7069), 820-827. doi:10.1038/nature04186

Kåre, et al. (2014). The morphological growth patterns of colorectal liver metastases are prognostic for overall survival. *Modern Pathology, 27*(12). doi:10.1038/modpathol.2014.4

Kawai, et al. (2019). Isolation and culture of pleural mesothelial cells. *Exp Lung Res, 45*(5-6), 151-156. doi:10.1080/01902148.2018.1511002

Keklikoglou, et al. (2018). Periostin Limits Tumor Response to VEGFA Inhibition. *Cell reports, 22*(10), 2530-2540. doi:10.1016/j.celrep.2018.02.035

Kenny, et al. (2014). Mesothelial cells promote early ovarian cancer metastasis through fibronectin secretion. *J Clin Invest, 124*(10), 4614-4628. doi:10.1172/jci74778

Keunen, et al. (2011). Anti-VEGF treatment reduces blood supply and increases tumor cell invasion in glioblastoma. *Proceedings of the National Academy of Sciences of the United States of America, 108*(9), 3749-3754. doi:10.1073/pnas.1014480108

Kida, & Yamaguchi. (2022). The vascular protective effect of matrix Gla protein during kidney injury. *Frontiers in Molecular Medicine, 2*. doi:10.3389/fmmed.2022.970744

Kigel, et al. (2011). Plexin-A4 promotes tumor progression and tumor angiogenesis by enhancement of VEGF and bFGF signaling. *Blood, 118*(15), 4285-4296. doi:10.1182/blood-2011-03-341388

Kimura, et al. (1996). Fluctuations in red cell flux in tumor microvessels can lead to transient hypoxia and reoxygenation in tumor parenchyma. *Cancer Res, 56*(23), 5522-5528.

Kitamura, et al. (2018). Monocytes Differentiate to Immune Suppressive Precursors of Metastasis-Associated Macrophages in Mouse Models of Metastatic Breast Cancer. *Frontiers in immunology, 8*, 2004-2004. doi:10.3389/fimmu.2017.02004

Kitamura, et al. (2015). Immune cell promotion of metastasis. *Nature reviews. Immunology, 15*(2), 73-86. doi:10.1038/nri3789

Klocke. (1980, 1980//). *Carbonic Anhydrase in Lung Tissue.* Paper presented at the Biophysics and Physiology of Carbon Dioxide, Berlin, Heidelberg.

Kofler, et al. (2011). Notch signaling in developmental and tumor angiogenesis. *Genes & cancer, 2*(12), 1106-1116. doi:10.1177/1947601911423030

Kong, et al. (2019). Extracellular vesicles of carcinoma-associated fibroblasts creates a pre-metastatic niche in the lung through activating fibroblasts. *MOLECULAR CANCER, 18*(1), 175. doi:10.1186/s12943-019-1101-4

Kowanetz, et al. (2010). Granulocyte-colony stimulating factor promotes lung metastasis through mobilization of Ly6G+Ly6C+ granulocytes. *Proceedings of the National Academy of Sciences of the United States of America, 107*(50), 21248-21255. doi:10.1073/pnas.1015855107

Krusche, et al. (2016). EphrinB2 drives perivascular invasion and proliferation of glioblastoma stem-like cells. *eLife, 5*, e14845. doi:10.7554/eLife.14845

Kučan Brlić, et al. (2019). Targeting PVR (CD155) and its receptors in anti-tumor therapy. *Cell Mol Immunol, 16*(1), 40-52. doi:10.1038/s41423-018-0168-y

Kuczynski, et al. (2019). Vessel co-option in cancer. *Nature reviews. Clinical oncology, 16*(8), 469. doi:10.1038/s41571-019-0181-9

Kuczynski, et al. (2016). Co-option of Liver Vessels and Not Sprouting Angiogenesis Drives Acquired Sorafenib Resistance in Hepatocellular Carcinoma. *Journal of the National Cancer Institute, 108*(8), djw030. doi:10.1093/jnci/djw030

Kuhnert, et al. (2011). Dll4-Notch signaling as a therapeutic target in tumor angiogenesis. *Vascular cell, 3*(1), 20-20. doi:10.1186/2045-824X-3-20

Kuo, et al. (2017). Lipid Droplet Biogenesis and Function in the Endothelium. *Circ Res, 120*(8), 1289-1297. doi:10.1161/circresaha.116.310498

Kurz, et al. (2003). Angiogenesis and vascular remodeling by intussusception: From form to function. *News Physiol. Sci., 18*, 65-70. doi:10.1152/nips.01417.2002

Lachapelle, & Foulkes. (2011). Triple-negative and basal-like breast cancer: implications for oncologists. *Current Oncology, 18*(4), 161-164. doi:10.3747/co.v18i4.824

Lars, et al. (1995). Dormancy of micrometastases: Balanced proliferation and apoptosis in the presence of angiogenesis suppression. *Nature Medicine, 1*(2), 149. doi:10.1038/nm0295-149

Lawson, et al. (2009). Cancer stem cells in breast cancer and metastasis. *Breast Cancer Research and Treatment, 118*(2), 241-254. doi:10.1007/s10549-009-0524-9

Lazaris, et al. (2018). Vascularization of colorectal carcinoma liver metastasis: insight into stratification of patients for anti-angiogenic therapies. *Journal of Pathology: Clinical Research, 4*(3), 184-192. doi:10.1002/cjp2.100

Le Naour, et al. (2020). EO771, is it a well-characterized cell line for mouse mammary cancer model? Limit and uncertainty. *Cancer medicine, 9*(21), 8074-8085. doi:10.1002/cam4.3295

Lee, & Djamgoz. (2018). Triple negative breast cancer: Emerging therapeutic modalities and novel combination therapies. *Cancer Treatment Reviews, 62*, 110-122. doi:10.1016/j.ctrv.2017.11.003

Lee, et al. (2016). LYVE1 Marks the Divergence of Yolk Sac Definitive Hemogenic Endothelium from the Primitive Erythroid Lineage. *Cell reports, 17*(9), 2286-2298. doi:10.1016/j.celrep.2016.10.080

Lee, & Haber. (2001). Wilms Tumor and the WT1 Gene. *Experimental Cell Research, 264*(1), 74-99. doi:https://doi.org/10.1006/excr.2000.5131

Leenders, et al. (2004). Antiangiogenic Therapy of Cerebral Melanoma Metastases Results in Sustained Tumor Progression via Vessel Co-Option. *Clinical Cancer Research, 10*(18), 6222. doi:10.1158/1078-0432.CCR-04-0823

Lehmann, et al. (2016). Refinement of Triple-Negative Breast Cancer Molecular Subtypes: Implications for Neoadjuvant Chemotherapy Selection. *PLoS ONE, 11*(6), e0157368. doi:10.1371/journal.pone.0157368

Lehuédé, et al. (2016). Metabolic Plasticity as a Determinant of Tumor Growth and Metastasis. *Cancer Res, 76*(18), 5201-5208. doi:10.1158/0008-5472.Can-16-0266

Levental, et al. (2009). Matrix crosslinking forces tumor progression by enhancing integrin signaling. *Cell, 139*(5), 891-906. doi:10.1016/j.cell.2009.10.027

Li, et al. (2023). An IGFBP7hi endothelial cell subset drives T cell extravasation in psoriasis via endothelial glycocalyx degradation. *J Clin Invest, 133*(9). doi:10.1172/jci160451

Liang, et al. (2007). CXCR4/CXCL12 axis promotes VEGF-mediated tumor angiogenesis through Akt signaling pathway. *Biochem Biophys Res Commun, 359*(3), 716-722. doi:10.1016/j.bbrc.2007.05.182

Liao, et al. (2002). Selective targeting of angiogenic tumour vasculature by vascular endothelial-cadherin antibody inhibits tumour growth without affecting vascular permeability. *Cancer Research, 62*(9), 2567-2575.

Liao, et al. (2022). CD36 and Its Role in Regulating the Tumor Microenvironment. *Current Oncology, 29*(11), 8133-8145. doi:10.3390/curroncol29110642

Lindberg, et al. (2016). GBM heterogeneity as a function of variable epidermal growth factor receptor variant III activity. *Oncotarget, 7*(48), 79101-79116. doi:10.18632/oncotarget.12600

Litton, et al. (2018). Talazoparib in Patients with Advanced Breast Cancer and a Germline BRCA Mutation. *N Engl J Med, 379*(8), 753-763. doi:10.1056/NEJMoa1802905

Liu, & Cao. (2016). Characteristics and Significance of the Pre-metastatic Niche. *Cancer Cell, 30*(5), 668-681. doi:10.1016/j.ccell.2016.09.011

Liu, et al. (2014). Dll4-Notch signaling in regulation of tumor angiogenesis. *Journal of Cancer Research and Clinical Oncology, 140*(4), 525-536. doi:10.1007/s00432-013-1534-x

Liu, et al. (2016). Tumor Exosomal RNAs Promote Lung Pre-metastatic Niche Formation by Activating Alveolar Epithelial TLR3 to Recruit Neutrophils. *Cancer Cell, 30*(2), 243-256. doi:10.1016/j.ccell.2016.06.021

Liu, et al. (2015). Genetic targeting of sprouting angiogenesis using Apln-CreER. *Nature Communications, 6*(1), 6020. doi:10.1038/ncomms7020

Liu, et al. (2021). Categorization of lung mesenchymal cells in development and fibrosis. *iScience, 24*(6), 102551. doi:10.1016/j.isci.2021.102551

Liu, et al. (2020a). High expression of PTPRM predicts poor prognosis and promotes tumor growth and lymph node metastasis in cervical cancer. *Cell death & disease, 11*(8), 687. doi:10.1038/s41419-020-02826-x

Liu, et al. (2011). Clinical significance of vasculogenic mimicry in human gliomas. *Journal of neuro-oncology, 105*(2), 173-179. doi:10.1007/s11060-011-0578-5

Liu, et al. (2020b). TRA2A-induced upregulation of LINC00662 regulates blood-brain barrier permeability by affecting ELK4 mRNA stability in Alzheimer's microenvironment. *RNA Biol, 17*(9), 1293-1308. doi:10.1080/15476286.2020.1756055

Lopes-Coelho, et al. (2018). Breast cancer metabolic cross-talk: Fibroblasts are hubs and breast cancer cells are gatherers of lipids. *Molecular and Cellular Endocrinology, 462*, 93-106. doi:https://doi.org/10.1016/j.mce.2017.01.031

Lu, et al. (2017). Developmental vascular remodeling defects and postnatal kidney failure in mice lacking Gpr116 (Adgrf5) and Eltd1 (Adgrl4). *PLoS ONE, 12*(8), e0183166. doi:10.1371/journal.pone.0183166

Luo, et al. (2022). Adding fuel to the fire: The lipid droplet and its associated proteins in cancer progression. *Int J Biol Sci, 18*(16), 6020-6034. doi:10.7150/ijbs.74902

Luo, et al. (2020). Vasculogenic mimicry in carcinogenesis and clinical applications. *Journal of Hematology & Oncology, 13*(1), 19. doi:10.1186/s13045-020-00858-6

Lyden, et al. (2001). Impaired recruitment of bone-marrow-derived endothelial and hematopoietic precursor cells blocks tumor angiogenesis and growth. *Nat Med, 7*(11), 1194-1201. doi:10.1038/nm1101-1194

Lyle, et al. (2016). Alterations in Pericyte Subpopulations Are Associated with Elevated Blood-Tumor Barrier Permeability in Experimental Brain Metastasis of Breast Cancer. *Clinical cancer research : an official journal of the American Association for Cancer Research, 22*(21), 5287-5299. doi:10.1158/1078-0432.CCR-15-1836

Ma, et al. (2020). SRGN, a new identified shear-stress-responsive gene in endothelial cells. *Molecular and Cellular Biochemistry, 474*(1), 15-26. doi:10.1007/s11010-020-03830-7

Madisen, et al. (2010). A robust and high-throughput Cre reporting and characterization system for the whole mouse brain. *Nature Neuroscience, 13*(1), 133-140. doi:10.1038/nn.2467

Makanya, et al. (2007). Microvascular endowment in the developing chicken embryo lung. *American journal of physiology. Lung cellular and molecular physiology, 292*(5), L1136. doi:10.1152/ajplung.00371.2006

Malhotra, et al. (2010). Histological, molecular and functional subtypes of breast cancers. In (Vol. 10, pp. 955-960).

Maniotis, et al. (2002). Control of Melanoma Morphogenesis, Endothelial Survival, and Perfusion by Extracellular Matrix. *Laboratory Investigation, 82*(8), 1031-1043. doi:10.1097/01.LAB.0000024362.12721.67

Maniotis, et al. (1999). Vascular channel formation by human melanoma cells in vivo and in vitro: vasculogenic mimicry. *The American journal of pathology, 155*(3), 739-752. doi:10.1016/S0002-9440(10)65173-5

Mao, et al. (2020). Nidogen 1-Enriched Extracellular Vesicles Facilitate Extrahepatic Metastasis of Liver Cancer by Activating Pulmonary Fibroblasts to Secrete Tumor Necrosis Factor Receptor 1. *Adv Sci (Weinh), 7*(21), 2002157. doi:10.1002/advs.202002157

Maru. (2015). The lung metastatic niche. *Journal of Molecular Medicine, 93*(11), 1185-1192. doi:10.1007/s00109-015-1355-2

Masiero, et al. (2013). A Core Human Primary Tumor Angiogenesis Signature Identifies the Endothelial Orphan Receptor ELTD1 as a Key Regulator of Angiogenesis. *Cancer Cell, 24*(2), 229-241. doi:10.1016/j.ccr.2013.06.004

Masson, et al. (2001). Overexpression of the CD155 gene in human colorectal carcinoma. *Gut, 49*(2), 236-240. doi:10.1136/gut.49.2.236

Masuda, et al. (2013). Differential response to neoadjuvant chemotherapy among 7 triple-negative breast cancer molecular subtypes. *Clinical cancer research : an official journal of the American Association for Cancer Research, 19*(19), 5533-5540. doi:10.1158/1078-0432.CCR-13-0799

Masuda, et al. (2017). Adjuvant Capecitabine for Breast Cancer after Preoperative Chemotherapy. *New England Journal of Medicine, 376*(22), 2147-2159. doi:10.1056/NEJMoa1612645

McInnes, et al. (2018). UMAP: Uniform Manifold Approximation and Projection. *Journal of open source software, 3*(29), 861. doi:10.21105/joss.00861

Mecham. (2018). Elastin in lung development and disease pathogenesis. *Matrix Biol, 73*, 6-20. doi:10.1016/j.matbio.2018.01.005

Medeiros, et al. (2020). Triple-Negative Primary Breast Tumors Induce Supportive Premetastatic Changes in the Extracellular Matrix and Soluble Components of the Lung Microenvironment. *Cancers, 12*(1). doi:10.3390/cancers12010172

Menssen, et al. (1995). Presence of Wilms' tumor gene (wt1) transcripts and the WT1 nuclear protein in the majority of human acute leukemias. *Leukemia, 9*(6), 1060-1067.

Michalik, et al. (2014). Long Noncoding RNA MALAT1 Regulates Endothelial Cell Function and Vessel Growth. *Circulation research, 114*(9), 1389-1397. doi:doi:10.1161/CIRCRESAHA.114.303265

Michiels, et al. (2016). Cycling hypoxia: A key feature of the tumor microenvironment. *Biochimica et Biophysica Acta (BBA) - Reviews on Cancer, 1866*(1), 76-86. doi:https://doi.org/10.1016/j.bbcan.2016.06.004

Milne, & Zerhouni. (1987). Blood supply of pulmonary metastases. *Journal of thoracic imaging, 2*(4), 15. doi:10.1097/00005382-198710000-00005

Mitzner, & Wagner. (2004). Vascular remodeling in the circulations of the lung. *J. Appl. Physiol., 97*(5), 1999-2004. doi:10.1152/japplphysiol.00473.2004

Montana, & Sontheimer. (2011). Bradykinin promotes the chemotactic invasion of primary brain tumors. *The Journal of neuroscience : the official journal of the Society for Neuroscience, 31*(13), 4858-4867. doi:10.1523/JNEUROSCI.3825-10.2011

Mosser, & Edwards. (2008). Exploring the full spectrum of macrophage activation. *Nature Reviews Immunology, 8*(12), 958-969. doi:10.1038/nri2448

Mutsaers. (2002). Mesothelial cells: Their structure, function and role in serosal repair. *Respirology, 7*(3), 171-191. doi:https://doi.org/10.1046/j.1440-1843.2002.00404.x

Nagarajan, et al. (2021). The diversity and breadth of cancer cell fatty acid metabolism. *Cancer & Metabolism, 9*(1), 2. doi:10.1186/s40170-020-00237-2

Nagy, et al. (2009). Why are tumour blood vessels abnormal and why is it important to know? *British journal of cancer, 100*(6), 865-869. doi:10.1038/sj.bjc.6604929

Nagy, & Dvorak. (2012). Heterogeneity of the tumor vasculature: the need for new tumor blood vessel type-specific targets. *Clinical & experimental metastasis, 29*(7), 657-662. doi:10.1007/s10585-012-9500-6

Nagy, et al. (2007). VEGF-A and the Induction of Pathological Angiogenesis. *2*(1), 251-275. doi:10.1146/annurev.pathol.2.010506.134925

Nagy, et al. (2008). THE ADENOVIRAL VECTOR ANGIOGENESIS/LYMPHANGIOGENESIS ASSAY. *Methods Enzymol., 444*, 43-64. doi:10.1016/S0076-6879(08)02803-6

Nakashima, et al. (1982). Histologic growth pattern of hepatocellular carcinoma: Relationship to orcein(hepatitis B surface antigen)-positive cells in cancer tissue. *Human Pathology, 13*(6), 563-568. doi:10.1016/S0046-8177(82)80272-4

Nakashima, et al. (1995). Pathomorphologic characteristics of small hepatocellular carcinoma: a special reference to small hepatocellular carcinoma with indistinct margins. *Hepatology (Baltimore, Md.), 22*(1), 101. doi:10.1016/0270-9139(95)90359-3

Neophytou, et al. (2018). Molecular Mechanisms and Emerging Therapeutic Targets of Triple-Negative Breast Cancer Metastasis. *Frontiers in oncology, 8*, 31-31. doi:10.3389/fonc.2018.00031

Nico, et al. (2011). Epo is involved in angiogenesis in human glioma. *Journal of neuro-oncology, 102*(1), 51-58. doi:10.1007/s11060-010-0294-6

Nico, et al. (2010). Intussusceptive microvascular growth in human glioma. *Clinical and Experimental Medicine, 10*(2), 93-98. doi:10.1007/s10238-009-0076-7

Niksic, et al. (2004). The Wilms' tumour protein (WT1) shuttles between nucleus and cytoplasm and is present in functional polysomes. *Hum Mol Genet, 13*(4), 463-471. doi:10.1093/hmg/ddh040

Nishimura, et al. (2010). Ki-67 as a prognostic marker according to breast cancer subtype and a predictor of recurrence time in primary breast cancer. *Experimental and therapeutic medicine, 1*(5), 747-754. doi:10.3892/etm.2010.133

Nomura, et al. (2010). Monoacylglycerol lipase regulates a fatty acid network that promotes cancer pathogenesis. *Cell, 140*(1), 49-61. doi:10.1016/j.cell.2009.11.027

Oatley, et al. (2020). Single-cell transcriptomics identifies CD44 as a marker and regulator of endothelial to haematopoietic transition. *Nature Communications, 11*(1), 586. doi:10.1038/s41467-019-14171-5

Obenauf, & Massagué. (2015). Surviving at a Distance: Organ-Specific Metastasis. *Trends in cancer, 1*(1), 76-91. doi:10.1016/j.trecan.2015.07.009

Offersen, et al. (2001). Patterns of angiogenesis in nonsmall-cell lung carcinoma. *Cancer, 91*(8), 1500-1509. doi:10.1002/1097-0142(20010415)91:8<1500::AID-CNCR1158>3.0.CO;2-M

Oji, et al. (2004). Overexpression of the Wilms' tumor gene WT1 in pancreatic ductal adenocarcinoma. *Cancer Sci, 95*(7), 583-587. doi:10.1111/j.1349-7006.2004.tb02490.x

Oji, et al. (2003). Overexpression of the Wilms' tumor gene WT1 in colorectal adenocarcinoma. *Cancer Sci, 94*(8), 712-717. doi:10.1111/j.1349-7006.2003.tb01507.x

Olkhanud, et al. (2011). Tumor-evoked regulatory B cells promote breast cancer metastasis by converting resting $CD4^+$ T cells to T-regulatory cells. *Cancer Research, 71*(10), 3505-3515. doi:10.1158/0008-5472.CAN-10-4316

Oltean, et al. (2006). Alternative inclusion of fibroblast growth factor receptor 2 exon IIIc in Dunning prostate tumors reveals unexpected epithelial mesenchymal plasticity. *Proceedings of the National Academy of Sciences, 103*(38), 14116-14121. doi:doi:10.1073/pnas.0603090103

Ombrato, et al. (2019). Metastatic-niche labelling reveals parenchymal cells with stem features. *Nature, 572*(7771), 603-608. doi:10.1038/s41586-019-1487-6

Ordóñez. (1998). Value of cytokeratin 5/6 immunostaining in distinguishing epithelial mesothelioma of the pleura from lung adenocarcinoma. *Am J Surg Pathol, 22*(10), 1215-1221. doi:10.1097/00000478-199810000-00006

Osaki, & Okada. (2019). Exosomes and Their Role in Cancer Progression. *Yonago acta medica, 62*(2), 182-190. doi:10.33160/yam.2019.06.002

Oskarsson, et al. (2011). Breast cancer cells produce tenascin C as a metastatic niche component to colonize the lungs. *Nature Medicine, 17*(7), 867-874. doi:10.1038/nm.2379

Otsuka, et al. (2016). The expression of embryonic globin mRNA in a severely anemic mouse model induced by treatment with nitrogen-containing bisphosphonate. *BMC Hematol, 16*, 4. doi:10.1186/s12878-016-0041-0

Ouyang, et al. (2021). ShinyCell: simple and sharable visualization of single-cell gene expression data. *Bioinformatics, 37*(19), 3374-3376. doi:10.1093/bioinformatics/btab209

Ouzounova, et al. (2017). Monocytic and granulocytic myeloid derived suppressor cells differentially regulate spatiotemporal tumour plasticity during metastatic cascade. *Nature Communications, 8*(1), 14979. doi:10.1038/ncomms14979

Pääkkö, et al. (1990). Immunohistochemical evidence that lung carcinomas grow on alveolar basement membranes. *The American journal of surgical pathology, 14*(5), 464. doi:10.1097/00000478-199005000-00006

Pace, et al. (2019). Exosomal L1CAM Stimulates Glioblastoma Cell Motility, Proliferation, and Invasiveness. *International journal of molecular sciences, 20*(16). doi:10.3390/ijms20163982

Paget. (1889). THE DISTRIBUTION OF SECONDARY GROWTHS IN CANCER OF THE BREAST. *The Lancet, 133*(3421), 571-573. doi:10.1016/S0140-6736(00)49915-0

Pan, et al. (2007a). Blocking Neuropilin-1 Function Has an Additive Effect with Anti-VEGF to Inhibit Tumor Growth. *Cancer Cell, 11*(1), 53-67. doi:10.1016/j.ccr.2006.10.018

Pan, et al. (2007b). Neuropilin-1 Binds to VEGF121 and Regulates Endothelial Cell Migration and Sprouting. *282*(33), 24049-24056. doi:10.1074/jbc.M703554200

Pasquale. (2010). Eph receptors and ephrins in cancer: bidirectional signalling and beyond. *Nature Reviews Cancer, 10*(3), 165-180. doi:10.1038/nrc2806

Passalidou, et al. (2002). Vascular phenotype in angiogenic and non-angiogenic lung non-small cell carcinomas. *British journal of cancer, 86*. doi:10.1038/sj.bjc.6600015

Patan. (1998). TIE1 and TIE2 Receptor Tyrosine Kinases Inversely Regulate Embryonic Angiogenesis by the Mechanism of Intussusceptive Microvascular Growth. *Microvascular Research, 56*(1), 1-21. doi:10.1006/mvre.1998.2081

Patan, et al. (1996). Intussusceptive Microvascular Growth in a Human Colon Adenocarcinoma Xenograft: A Novel Mechanism of Tumor Angiogenesis. *Microvascular Research, 51*(2), 260-272. doi:10.1006/mvre.1996.0025

Pende, et al. (2005). Analysis of the receptor-ligand interactions in the natural killer-mediated lysis of freshly isolated myeloid or lymphoblastic leukemias: evidence for the involvement of the Poliovirus receptor (CD155) and Nectin-2 (CD112). *Blood, 105*(5), 2066-2073. doi:10.1182/blood-2004-09-3548

Perou, et al. (2000). Molecular portraits of human breast tumours. *Nature, 406*(6797), 747-752. doi:10.1038/35021093

Peter, & Katarina. (2003). Tumour-cell invasion and migration: diversity and escape mechanisms. *Nature Reviews Cancer, 3*(5), 362. doi:10.1038/nrc1075

Pezzella, et al. (1996). Angiogenesis in primary lung cancer and lung secondaries. *Eur. J. Cancer, 32A*(14), 2494-2500.

Pezzella, et al. (1997). Non-small-cell lung carcinoma tumor growth without morphological evidence of neo-angiogenesis. *The American journal of pathology, 151*.

Pfister, et al. (2015). Mutant p53 cooperates with the SWI/SNF chromatin remodeling complex to regulate VEGFR2 in breast cancer cells. *Genes Dev, 29*(12), 1298-1315. doi:10.1101/gad.263202.115

Pietras, & Hanahan. (2005). A multitargeted, metronomic, and maximum-tolerated dose "chemo-switch" regimen is antiangiogenic, producing objective responses and survival benefit in a mouse model of cancer. *Journal of clinical oncology : official journal of the American Society of Clinical Oncology, 23*(5), 939-952. doi:10.1200/jco.2005.07.093

Psaila, & Lyden. (2009). The metastatic niche: adapting the foreign soil. *Nature reviews. Cancer, 9*(4), 285-293. doi:10.1038/nrc2621

Qi, et al. (2015). Wnt3a Promotes the Vasculogenic Mimicry Formation of Colon Cancer via Wnt/β-Catenin Signaling. *International journal of molecular sciences, 16*(8), 18564-18579. doi:10.3390/ijms160818564

Qi, et al. (2014). Wnt5a promotes vasculogenic mimicry and epithelial-mesenchymal transition via protein kinase Cα in epithelial ovarian cancer. *Oncol Rep, 32*(2), 771-779. doi:10.3892/or.2014.3229

Qian, et al. (2006). Preparing the “Soil”: The Primary Tumor Induces Vasculature Reorganization in the Sentinel Lymph Node before the Arrival of Metastatic Cancer Cells. *Cancer Research, 66*(21), 10365. doi:10.1158/0008-5472.CAN-06-2977

Qian, et al. (2011). CCL2 recruits inflammatory monocytes to facilitate breast-tumour metastasis. *Nature, 475*(7355), 222-225. doi:10.1038/nature10138

Que, et al. (2008). Mesothelium contributes to vascular smooth muscle and mesenchyme during lung development. *Proceedings of the National Academy of Sciences, 105*(43), 16626-16630. doi:doi:10.1073/pnas.0808649105

Rada, et al. (2021). Runt related transcription factor-1 plays a central role in vessel co-option of colorectal cancer liver metastases. *Commun Biol, 4*(1), 950. doi:10.1038/s42003-021-02481-8

Rakha, & Chan. (2011). Metastatic Triple-negative Breast Cancer. *Clinical Oncology, 23*(9), 587-600. doi:https://doi.org/10.1016/j.clon.2011.03.013

Rakha, et al. (2009). Triple-negative breast cancer: distinguishing between basal and nonbasal subtypes. *Clin Cancer Res, 15*(7), 2302-2310. doi:10.1158/1078-0432.Ccr-08-2132

Razani, et al. (2002). Caveolin-2-deficient mice show evidence of severe pulmonary dysfunction without disruption of caveolae. *Mol Cell Biol, 22*(7), 2329-2344. doi:10.1128/mcb.22.7.2329-2344.2002

Reis-Filho, & Tutt. (2008). Triple negative tumours: a critical review. In (Vol. 52, pp. 108-118). Oxford, UK.

Ribatti, et al. (2005). Microvascular density, vascular endothelial growth factor immunoreactivity in tumor cells, vessel diameter and intussusceptive microvascular growth in primary melanoma. *Oncol Rep, 14*(1), 81-84.

Rinkevich, et al. (2012). Identification and prospective isolation of a mesothelial precursor lineage giving rise to smooth muscle cells and fibroblasts for mammalian internal organs, and their vasculature. *Nat Cell Biol, 14*(12), 1251-1260. doi:10.1038/ncb2610

Roberts, et al. (2006). Inhibtion of VEGFR-3 activation with the antagonistic antibody more potently suppresses lymph node and distant metastases than inactivation of VEGFR-2. *Cancer Res., 66*(5), 2650-2657. doi:10.1158/0008-5472.CAN-05-1843

Robson, et al. (2017). Olaparib for Metastatic Breast Cancer in Patients with a Germline BRCA Mutation. *N Engl J Med, 377*(6), 523-533. doi:10.1056/NEJMoa1706450

Rocha, et al. (2014). Esm1 modulates endothelial tip cell behavior and vascular permeability by enhancing VEGF bioavailability. *Circ Res, 115*(6), 581-590. doi:10.1161/circresaha.115.304718

Roewe, et al. (2020). Bacterial polyphosphates interfere with the innate host defense to infection. *Nature Communications, 11*(1), 4035. doi:10.1038/s41467-020-17639-x

Rohlenova, et al. (2020). Single-Cell RNA Sequencing Maps Endothelial Metabolic Plasticity in Pathological Angiogenesis. *Cell Metab, 31*(4), 862-877.e814. doi:10.1016/j.cmet.2020.03.009

Rong, et al. (2016). Tumor-associated macrophages induce vasculogenic mimicry of glioblastoma multiforme through cyclooxygenase-2 activation. *Oncotarget, 7*(51), 83976-83986. doi:10.18632/oncotarget.6930

Rossen, et al. (2011). Arachidonic acid randomizes endothelial cell motion and regulates adhesion and migration. *PLoS ONE, 6*(9), e25196. doi:10.1371/journal.pone.0025196

Rugo, et al. (2016). Endocrine Therapy for Hormone Receptor–Positive Metastatic Breast Cancer: American Society of Clinical Oncology Guideline. *Journal of Clinical Oncology, 34*(25), 3069-3103. doi:10.1200/JCO.2016.67.1487

Russell, & Richardson. (2023). The good Samaritan glutathione-S-transferase P1: An evolving relationship in nitric oxide metabolism mediated by the direct interactions between multiple effector molecules. *Redox Biology, 59*, 102568. doi:https://doi.org/10.1016/j.redox.2022.102568

Rynne-Vidal, et al. (2017). Mesothelial-to-mesenchymal transition as a possible therapeutic target in peritoneal metastasis of ovarian cancer. *J Pathol, 242*(2), 140-151. doi:10.1002/path.4889

Saeg, & Anbalagan. (2018). Breast cancer stem cells and the challenges of eradication: a review of novel therapies. *Stem cell investigation, 5*, 39-39. doi:10.21037/sci.2018.10.05

Sakai, et al. (2022). Myo5b Transports Fibronectin-Containing Vesicles and Facilitates FN1 Secretion from Human Pleural Mesothelial Cells. *International journal of molecular sciences, 23*(9). doi:10.3390/ijms23094823

Sakariassen, et al. (2006). Angiogenesis-independent tumor growth mediated by stem-like cancer cells. *Proceedings of the National Academy of Sciences of the United States of America, 103*(44), 16466-16471. doi:10.1073/pnas.0607668103

Salzer. (2012). *Biomedical Imaging : Principles and Applications* (R. Salzer Ed. 1 ed.). Newark, United States: John Wiley & Sons, Incorporated.

Sangaletti, et al. (2008). Macrophage-Derived SPARC Bridges Tumor Cell-Extracellular Matrix Interactions toward Metastasis. *Cancer Research, 68*(21), 9050. doi:10.1158/0008-5472.CAN-08-1327

Sardari Nia, et al. (2008). Different Growth Patterns of Non-Small Cell Lung Cancer Represent Distinct Biologic Subtypes. *Ann Thorac Surg, 85*(2), 395-405. doi:https://doi.org/10.1016/j.athoracsur.2007.08.054

Satoh, et al. (2008). Angiopoietin-1 alters tumor growth by stabilizing blood vessels or by promoting angiogenesis. *Cancer Science, 99*(12), 2373-2379. doi:10.1111/j.1349-7006.2008.00961.x

Savai, et al. (2005). Analysis of Tumor Vessel Supply in Lewis Lung Carcinoma in Mice by Fluorescent Microsphere Distribution and Imaging with Micro- and Flat-Panel Computed Tomography. *The American journal of pathology, 167*(4), 937-946. doi:10.1016/S0002-9440(10)61184-4

Sawamiphak, et al. (2010). Ephrin-B2 regulates VEGFR2 function in developmental and tumour angiogenesis. *Nature, 465*(7297), 487-491. doi:10.1038/nature08995

Schindelin, et al. (2012). Fiji: an open-source platform for biological-image analysis. *Nature Methods, 9*(7), 676-682. doi:10.1038/nmeth.2019

Schmid, et al. (2018). Atezolizumab and Nab-Paclitaxel in Advanced Triple-Negative Breast Cancer. *New England Journal of Medicine, 379*(22), 2108-2121. doi:10.1056/NEJMoa1809615

Schoenfeld, & Hellmann. (2020). Acquired Resistance to Immune Checkpoint Inhibitors. *Cancer Cell, 37*(4), 443-455. doi:10.1016/j.ccell.2020.03.017

Seano, & Jain. (2020). Vessel co-option in glioblastoma: emerging insights and opportunities. *Angiogenesis, 23*(1), 9-16. doi:10.1007/s10456-019-09691-z

Seftor, et al. (2001). Cooperative interactions of laminin 5 gamma2 chain, matrix metalloproteinase-2, and membrane type-1-matrix/metalloproteinase are required for mimicry of embryonic vasculogenesis by aggressive melanoma. *Cancer Res, 61*(17), 6322-6327.

Segarra, et al. (2012). Semaphorin 6A regulates angiogenesis by modulating VEGF signaling. *Blood, 120*(19), 4104-4115. doi:10.1182/blood-2012-02-410076

Seifert, & Sontheimer. (2014). Bradykinin enhances invasion of malignant glioma into the brain parenchyma by inducing cells to undergo amoeboid migration. *The Journal of Physiology, 592*(22), 5109-5127. doi:https://doi.org/10.1113/jphysiol.2014.274498

Senkus, et al. (2015). Primary breast cancer: ESMO Clinical Practice Guidelines for diagnosis, treatment and follow-up †. *Annals of Oncology, 26*(suppl5), v8-v30. doi:10.1093/annonc/mdv298

Sharma, et al. (2015). Pulmonary Alveolar Macrophages Contribute to the Premetastatic Niche by Suppressing Antitumor T Cell Responses in the Lungs. *The Journal of Immunology, 194*(11), 5529. doi:10.4049/jimmunol.1403215

Sharma, et al. (2018). IL-8/CXCR1/2 signalling promotes tumor cell proliferation, invasion and vascular mimicry in glioblastoma. *Journal of Biomedical Science, 25*(1), 62. doi:10.1186/s12929-018-0464-y

Shield, & Koivurinne. (2008). The value of calretinin and cytokeratin 5/6 as markers for mesothelioma in cell block preparations of serous effusions. *Cytopathology, 19*(4), 218-223. doi:10.1111/j.1365-2303.2007.00482.x

Shiozawa, et al. (2013). Cancer stem cells and their role in metastasis. *Pharmacol Ther, 138*(2), 285-293. doi:10.1016/j.pharmthera.2013.01.014

Smith, & Dowsett. (2003). Aromatase Inhibitors in Breast Cancer. *The New England Journal of Medicine, 348*(24), 2431-2442. doi:10.1056/NEJMra023246

Smith, & Kang. (2013). The metastasis-promoting roles of tumor-associated immune cells. *Journal of molecular medicine (Berlin, Germany), 91*(4), 411-429. doi:10.1007/s00109-013-1021-5

Soh, et al. (2020). Surgical therapy for pulmonary metastasis of breast cancer. *Translational Cancer Research, 9*(8), 5044-5052. doi:10.21037/tcr.2020.03.63

Son, et al. (2018). Endothelial cell CD36 optimizes tissue fatty acid uptake. *J Clin Invest, 128*(10), 4329-4342. doi:10.1172/jci99315

Song, et al. (2018). Vasculogenic mimicry and expression of slug and vimentin correlate with metastasis and prognosis in non-small cell lung cancer. *International journal of clinical and experimental pathology, 11*(5), 2749-2758. Retrieved from https://pubmed.ncbi.nlm.nih.gov/31938392

https://www.ncbi.nlm.nih.gov/pmc/articles/PMC6958269/

Sontake, et al. (2018). Wilms' tumor 1 drives fibroproliferation and myofibroblast transformation in severe fibrotic lung disease. *JCI Insight, 3*(16). doi:10.1172/jci.insight.121252

Sophia, et al. (2016). Vessel co-option mediates resistance to anti-angiogenic therapy in liver metastases. *Nature Medicine, 22*(11). doi:10.1038/nm.4197

Sørlie, et al. (2001). Gene expression patterns of breast carcinomas distinguish tumor subclasses with clinical implications. *Proceedings of the National Academy of Sciences of the United States of America, 98*(19), 10869-10874. doi:10.1073/pnas.191367098

Spaderna, et al. (2008). The Transcriptional Repressor ZEB1 Promotes Metastasis and Loss of Cell Polarity in Cancer. *Cancer Research, 68*(2), 537-544. doi:10.1158/0008-5472.Can-07-5682

Stella, et al. (2019). Lung-Seeking Metastases. *Cancers, 11*(7), 1010. doi:10.3390/cancers11071010

Stessels, et al. (2004). Breast adenocarcinoma liver metastases, in contrast to colorectal cancer liver metastases, display a non-angiogenic growth pattern that preserves the stroma and lacks hypoxia. *British journal of cancer, 90*. doi:10.1038/sj.bjc.6601727

Stoletov, et al. (2013). Role of connexins in metastatic breast cancer and melanoma brain colonization. *J Cell Sci, 126*(Pt 4), 904-913. doi:10.1242/jcs.112748

Strand, et al. (2015). The percentage of lepidic growth is an independent prognostic factor in invasive adenocarcinoma of the lung. *Diagnostic pathology, 10*(1), 94. doi:10.1186/s13000-015-0335-8

Streef, et al. (2023). Single-cell analysis of human fetal epicardium reveals its cellular composition and identifies CRIP1 as a modulator of EMT. *Stem Cell Reports, 18*(7), 1421-1435. doi:10.1016/j.stemcr.2023.06.002

Stremitzer, et al. (2020). Immune phenotype and histopathological growth pattern in patients with colorectal liver metastases. *British journal of cancer, 122*(10), 1518-1524. doi:10.1038/s41416-020-0812-z

Su, et al. (2019). HIF1α, EGR1 and SP1 co-regulate the erythropoietin receptor expression under hypoxia: an essential role in the growth of non-small cell lung cancer cells. *Cell communication and signaling : CCS, 17*(1), 152-152. doi:10.1186/s12964-019-0458-8

Subramanian, et al. (2005). Gene set enrichment analysis: A knowledge-based approach for interpreting genome-wide expression profiles. *Proceedings of the National Academy of Sciences, 102*(43), 15545-15550. doi:doi:10.1073/pnas.0506580102

Suijkerbuijk, et al. (2016). Hormone Receptors in Breast Cancer. In S. Badve & Y. Gökmen-Polar (Eds.), *Molecular Pathology of Breast Cancer* (pp. 45-58). Cham: Springer International Publishing.

Sun, et al. (2019). DiVenn: An Interactive and Integrated Web-Based Visualization Tool for Comparing Gene Lists. *Front Genet, 10*, 421. doi:10.3389/fgene.2019.00421

Sun, et al. (2013). Slug promoted vasculogenic mimicry in hepatocellular carcinoma. *Journal of cellular and molecular medicine, 17*(8), 1038-1047. doi:10.1111/jcmm.12087

Sun, et al. (2006). Vasculogenic mimicry is associated with high tumor grade, invasion and metastasis, and short survival in patients with hepatocellular carcinoma. *Oncol Rep, 16*(4), 693-698.

Sun, et al. (2010). Expression and functional significance of Twist1 in hepatocellular carcinoma: Its role in vasculogenic mimicry. *Hepatology, 51*(2), 545-556. doi:10.1002/hep.23311

Sung, et al. (2011). Identification and Validation of SAA as a Potential Lung Cancer Biomarker and its Involvement in Metastatic Pathogenesis of Lung Cancer. *Journal of Proteome Research, 10*(3), 1383-1395. doi:10.1021/pr101154j

Sunitha, et al. (2019). Temporal VEGFA responsive genes in HUVECs: Gene signatures and potential ligands/receptors fine-tuning angiogenesis. *J Cell Commun Signal, 13*(4), 561-571. doi:10.1007/s12079-019-00541-7

Sussman, et al. (2003). Blood markers for vasculogenesis increase with tumor progression in patients with breast carcinoma. *Cancer Biol Ther, 2*(3), 255-256. doi:10.4161/cbt.2.3.363

Szabo, et al. (2015). Mechanism of tumour vascularization in experimental lung metastases. *J Pathol, 235*(3), 384-396. doi:10.1002/path.4464

Takeda, et al. (2011). IFN-γ production by lung NK cells is critical for the natural resistance to pulmonary metastasis of B16 melanoma in mice. *Journal of Leukocyte Biology, 90*(4), 777-785. doi:10.1189/jlb.0411208

Tanaka, et al. (2017). Mesothelial Cells Create a Novel Tissue Niche That Facilitates Gastric Cancer Invasion. *Cancer Res, 77*(3), 684-695. doi:10.1158/0008-5472.Can-16-0964

Tavora, et al. (2020). Tumoural activation of TLR3–SLIT2 axis in endothelium drives metastasis. *Nature, 586*(7828), 299-304. doi:10.1038/s41586-020-2774-y

Taylor, et al. (2010). Chronic whole-body hypoxia induces intussusceptive angiogenesis and microvascular remodeling in the mouse retina. *Microvascular Research, 79*(2), 93-101. doi:10.1016/j.mvr.2010.01.006

Telli. (2016). Triple-Negative Breast Cancer. In S. Badve & Y. Gökmen-Polar (Eds.), *Molecular Pathology of Breast Cancer* (pp. 71-80). Cham: Springer International Publishing.

Terayama, et al. (1996). Histologic growth patterns of metastatic carcinomas of the liver. *Japanese journal of clinical oncology, 26*(1), 24. doi:10.1093/oxfordjournals.jjco.a023174

Teuwen, et al. (2021). Tumor vessel co-option probed by single-cell analysis. *Cell reports, 35*(11), 109253. doi:10.1016/j.celrep.2021.109253

Thibaut, et al. (2020). Bystander IFN-γ activity promotes widespread and sustained cytokine signaling altering the tumor microenvironment. *Nature Cancer, 1*(3), 302-314. doi:10.1038/s43018-020-0038-2

Thordur, et al. (2011). Breast cancer cells produce tenascin C as a metastatic niche component to colonize the lungs. *Nature Medicine, 17*(7), 867. doi:10.1038/nm.2379

Tolaney, et al. (2017). Seven-year (yr) follow-up of adjuvant paclitaxel (T) and trastuzumab (H) (APT trial) for node-negative, HER2-positive breast cancer (BC). *J. Clin. Oncol., 35*(s15). doi:10.1200/JCO.2017.35.15_suppl.511

Trapnell, et al. (2014). The dynamics and regulators of cell fate decisions are revealed by pseudotemporal ordering of single cells. *Nature Biotechnology, 32*(4), 381-386. doi:10.1038/nbt.2859

Travaglini, et al. (2020). A molecular cell atlas of the human lung from single-cell RNA sequencing. *Nature, 587*(7835), 619-625. doi:10.1038/s41586-020-2922-4

Uhlar, & Whitehead. (1999). Serum amyloid A, the major vertebrate acute-phase reactant. *European Journal of Biochemistry, 265*(2), 501-523. doi:https://doi.org/10.1046/j.1432-1327.1999.00657.x

Vader, et al. (2014). Extracellular vesicles: emerging targets for cancer therapy. *Trends Mol Med, 20*(7), 385-393. doi:10.1016/j.molmed.2014.03.002

Vaillant, et al. (2008). The mammary progenitor marker CD61/beta3 integrin identifies cancer stem cells in mouse models of mammary tumorigenesis. *Cancer Research, 68*(19), 7711. doi:10.1158/0008-5472.CAN-08-1949

Vajkoczy, et al. (2003). Multistep nature of microvascular recruitment of ex vivo-expanded embryonic endothelial progenitor cells during tumor angiogenesis. *The Journal of experimental medicine, 197*(12), 1755-1765. doi:10.1084/jem.20021659

Valastyan, & Weinberg. (2011). Tumor metastasis: molecular insights and evolving paradigms. *Cell, 147*(2), 275-292. doi:10.1016/j.cell.2011.09.024

Valiente, et al. (2014). Serpins Promote Cancer Cell Survival and Vascular Co-Option in Brain Metastasis. *Cell (Cambridge), 156*(5), 1002-1016. doi:10.1016/j.cell.2014.01.040

Valpione, et al. (2020). Immune awakening revealed by peripheral T cell dynamics after one cycle of immunotherapy. *Nature Cancer, 1*(2), 210-221. doi:10.1038/s43018-019-0022-x

van Dam, et al. (2018). Histopathological growth patterns as a candidate biomarker for immunomodulatory therapy. *Seminars in Cancer Biology, 52*(Pt 2), 86-93. doi:10.1016/j.semcancer.2018.01.009

van Dam, et al. (2017). International consensus guidelines for scoring the histopathological growth patterns of liver metastasis. *British journal of cancer, 117*(10), 1427-1441. doi:10.1038/bjc.2017.334

van den Brink, et al. (2017). Single-cell sequencing reveals dissociation-induced gene expression in tissue subpopulations. *Nature Methods, 14*(10), 935-936. doi:10.1038/nmeth.4437

Van den Eynden, et al. (2012). The histological growth pattern of colorectal cancer liver metastases has prognostic value. *Official Journal of the Metastasis Research Society, 29*(6), 541-549. doi:10.1007/s10585-012-9469-1

Vandereyken, et al. (2017). Dusp3 deletion in mice promotes experimental lung tumour metastasis in a macrophage-dependent manner. *PLoS ONE, 12*(10), e0185786. doi:10.1371/journal.pone.0185786

Vartanian, et al. (2013). The involvement of Notch signaling in melanoma vasculogenic mimicry. *Clinical and Experimental Medicine, 13*(3), 201-209. doi:10.1007/s10238-012-0190-9

Vasudev, & Reynolds. (2014). Anti-angiogenic therapy for cancer: current progress, unresolved questions and future directions. *Angiogenesis, 17*(3), 471-494. doi:10.1007/s10456-014-9420-y

Vermeulen, et al. (2001). Liver metastases from colorectal adenocarcinomas grow in three patterns with different angiogenesis and desmoplasia. *Journal of Pathology, 195*(3), 336-342. doi:10.1002/path.966

Vila Ellis, et al. (2020). Epithelial Vegfa Specifies a Distinct Endothelial Population in the Mouse Lung. *Dev Cell, 52*(5), 617-630.e616. doi:10.1016/j.devcel.2020.01.009

Von Minckwitz, et al. (2019). Trastuzumab Emtansine for Residual Invasive HER2-Positive Breast Cancer. *The New England Journal of Medicine, 380*(7), 617-628. doi:10.1056/NEJMoa1814017

Von Minckwitz, et al. (2017). Adjuvant Pertuzumab and Trastuzumab in Early HER2-Positive Breast Cancer. *The New England Journal of Medicine, 377*(2), 122-131. doi:10.1056/NEJMoa1703643

Voutouri, et al. (2019). Experimental and computational analyses reveal dynamics of tumor vessel cooption and optimal treatment strategies. *Proceedings of the National Academy of Sciences of the United States of America, 116*(7), 2662-2671. doi:10.1073/pnas.1818322116

Wahba, & El-Hadaad. (2015). Current approaches in treatment of triple-negative breast cancer. *Cancer biology & medicine, 12*(2), 106-116. doi:10.7497/j.issn.2095-3941.2015.0030

Waks, & Winer. (2019). Breast cancer treatment: A review.(Report). *JAMA, The Journal of the American Medical Association, 321*(3), 288. doi:10.1001/jama.2018.19323

Wallin, et al. (2016). Atezolizumab in combination with bevacizumab enhances antigen-specific T-cell migration in metastatic renal cell carcinoma. *Nature Communications, 7*, 12624-12624. doi:10.1038/ncomms12624

Wang, et al. (2020). The Lipid Metabolic Landscape of Cancers and New Therapeutic Perspectives. *Front Oncol, 10*, 605154. doi:10.3389/fonc.2020.605154

Wang, et al. (2021). Targeting Pyrimidine Metabolism in the Era of Precision Cancer Medicine. *Frontiers in oncology, 11*. doi:10.3389/fonc.2021.684961

Wang, et al. (2003). Induction of tumor angiogenesis by Slit-Robo signaling and inhibition of cancer growth by blocking Robo activity. *Cancer Cell, 4*(1), 19-29. doi:10.1016/s1535-6108(03)00164-8

Wang, et al. (2018). Expression of periaxin (PRX) specifically in the human cerebrovascular system: PDZ domain-mediated strengthening of endothelial barrier function. *Scientific Reports, 8*(1), 10042. doi:10.1038/s41598-018-28190-7

Watkins, et al. (2014). Disruption of astrocyte–vascular coupling and the blood–brain barrier by invading glioma cells. *Nature Communications, 5*(1), 4196. doi:10.1038/ncomms5196

Weinländer, et al. (2008). Guanylate binding protein-1 inhibits spreading and migration of endothelial cells through induction of integrin alpha4 expression. *Faseb j, 22*(12), 4168-4178. doi:10.1096/fj.08-107524

Wen, et al. (2016). The Biodistribution and Immune Suppressive Effects of Breast Cancer–Derived Exosomes. *Cancer Research, 76*(23), 6816-6827. doi:10.1158/0008-5472.Can-16-0868

Wesseling, et al. (1994). Quantitative immunohistological analysis of the microvasculature in untreated human glioblastoma multiforme. Computer-assisted image analysis of whole-tumor sections. *Journal of neurosurgery, 81*(6), 902. doi:10.3171/jns.1994.81.6.0902

Wilkat, et al. (2020). Adenosine receptor 2B activity promotes autonomous growth, migration as well as vascularization of head and neck squamous cell carcinoma cells. *International Journal of Cancer, 147*(1), 202-217. doi:https://doi.org/10.1002/ijc.32835

Willett, et al. (2005). Surrogate Markers for Antiangiogenic Therapy and Dose-Limiting Toxicities for Bevacizumab With Radiation and Chemotherapy: Continued Experience of a Phase I Trial in Rectal Cancer Patients. *Journal of Clinical Oncology, 23*(31), 8136-8139. doi:10.1200/JCO.2005.02.5635

Williams, et al. (2013). An essential requirement for the SCAP/SREBP signaling axis to protect cancer cells from lipotoxicity. *Cancer Res, 73*(9), 2850-2862. doi:10.1158/0008-5472.Can-13-0382-t

Winkler, et al. (2009). Imaging glioma cell invasion in vivo reveals mechanisms of dissemination and peritumoral angiogenesis. *Glia, 57*(12), 1306-1315. doi:10.1002/glia.20850

Wolf, et al. (2018). Microglial MHC class II is dispensable for experimental autoimmune encephalomyelitis and cuprizone-induced demyelination. *Eur J Immunol, 48*(8), 1308-1318. doi:10.1002/eji.201847540

Won Jun, et al. (2016). Meta-Analysis of Tumor Stem-Like Breast Cancer Cells Using Gene Set and Network Analysis. *PLoS ONE, 11*(2), e0148818. doi:10.1371/journal.pone.0148818

Won, & Spruck. (2020). Triple-negative breast cancer therapy: Current and future perspectives (Review). *International Journal of Oncology, 57*(6), 1245-1261. doi:10.3892/ijo.2020.5135

Wong, et al. (2011). Hypoxia-inducible factor 1 is a master regulator of breast cancer metastatic niche formation. *Proceedings of the National Academy of Sciences of the United States of America, 108*(39), 16369-16374. doi:10.1073/pnas.1113483108

Woodcock, et al. (2017). The scavenging chemokine receptor ACKR2 has a significant impact on acute mortality rate and early lesion development after traumatic brain injury. *PLoS ONE, 12*(11), e0188305. doi:10.1371/journal.pone.0188305

World Health Organization. (2023). Breast cancer. Retrieved from https://www.who.int/news-room/fact-sheets/detail/breast-cancer

Wörthmüller, et al. (2018). Calretinin promotes invasiveness and EMT in malignant mesothelioma cells involving the activation of the FAK signaling pathway. *Oncotarget, 9*(91), 36256-36272. doi:10.18632/oncotarget.26332

Wu, et al. (2015). The lack of type I interferon induces neutrophil-mediated pre-metastatic niche formation in the mouse lung. *Int J Cancer, 137*(4), 837-847. doi:10.1002/ijc.29444

Wu, et al. (2019). Lipid droplet-dependent fatty acid metabolism controls the immune suppressive phenotype of tumor-associated macrophages. *EMBO Mol Med, 11*(11), e10698. doi:10.15252/emmm.201910698

Wu, et al. (2017). Autophagy-induced KDR/VEGFR-2 activation promotes the formation of vasculogenic mimicry by glioma stem cells. *Autophagy, 13*(9), 1528-1542. doi:10.1080/15548627.2017.1336277

Wu, et al. (2021). miR-181c-5p mediates apoptosis of vascular endothelial cells induced by hyperoxemia via ceRNA crosstalk. *Scientific Reports, 11*(1), 16582. doi:10.1038/s41598-021-95712-1

Xiao, et al. (2018). Risk factors and survival outcomes in patients with breast cancer and lung metastasis: a population-based study. *Cancer medicine, 7*(3), 922-930. doi:10.1002/cam4.1370

Xie, et al. (2018). Single-Cell Deconvolution of Fibroblast Heterogeneity in Mouse Pulmonary Fibrosis. *Cell reports, 22*(13), 3625-3640. doi:10.1016/j.celrep.2018.03.010

Xu, et al. (2021a). Successful prenatal therapy for anti-CD36-mediated severe FNAIT by deglycosylated antibodies in a novel murine model. *Blood, 138*(18), 1757-1767. doi:10.1182/blood.2021011131

Xu, et al. (2017). Breast tumor cell-specific knockout of Twist1 inhibits cancer cell plasticity, dissemination, and lung metastasis in mice. *Proceedings of the National Academy of Sciences, 114*(43), 11494-11499. doi:doi:10.1073/pnas.1618091114

Xu, et al. (2022). Sterol carrier protein 2: A promising target in the pathogenesis of atherosclerosis. *Genes & Diseases*. doi:https://doi.org/10.1016/j.gendis.2021.12.007

Xu, et al. (2021b). Unveiling Cancer Metabolism through Spontaneous and Coherent Raman Spectroscopy and Stable Isotope Probing. *Cancers, 13*(7), 1718. Retrieved from https://www.mdpi.com/2072-6694/13/7/1718

Xu, et al. (2021c). HDAC6 Negatively Regulates miR-155-5p Expression to Elicit Proliferation by Targeting RHEB in Microvascular Endothelial Cells under Mechanical

Unloading. *International journal of molecular sciences, 22*(19). doi:10.3390/ijms221910527

Yadav, et al. (2016). CXCR4 increases in-vivo glioma perivascular invasion, and reduces radiation induced apoptosis: A genetic knockdown study. *Oncotarget, 7*(50), 83701-83719. doi:10.18632/oncotarget.13295

Yae, et al. (2012). Alternative splicing of CD44 mRNA by ESRP1 enhances lung colonization of metastatic cancer cell. *Nature Communications, 3*(1), 883. doi:10.1038/ncomms1892

Yamamoto, et al. (2018). Lung-resident natural killer cells control pulmonary tumor growth in mice. *Cancer Science, 109*(9), 2670-2676. doi:10.1111/cas.13703

Yang, et al. (2015). Semaphorin-3C signals through Neuropilin-1 and PlexinD1 receptors to inhibit pathological angiogenesis. *EMBO Mol Med, 7*(10), 1267-1284. doi:10.15252/emmm.201404922

Yang, et al. (2013). Sox17 promotes tumor angiogenesis and destabilizes tumor vessels in mice. *J Clin Invest, 123*(1), 418-431. doi:10.1172/jci64547

Yang, et al. (2016). Vascular mimicry formation is promoted by paracrine TGF-β and SDF1 of cancer-associated fibroblasts and inhibited by miR-101 in hepatocellular carcinoma. *Cancer Letters, 383*(1), 18-27. doi:10.1016/j.canlet.2016.09.012

Yang, et al. (2004). Twist, a master regulator of morphogenesis, plays an essential role in tumor metastasis. *Cell, 117*(7), 927-939. doi:10.1016/j.cell.2004.06.006

Yang, et al. (2017). Immunocompetent mouse allograft models for development of therapies to target breast cancer metastasis. *Oncotarget, 8*(19), 30621-30643. doi:10.18632/oncotarget.15695

Yao, et al. (2011). Mechanism of the Mesenchymal–Epithelial Transition and Its Relationship with Metastatic Tumor Formation. *Molecular Cancer Research, 9*(12), 1608-1620. doi:10.1158/1541-7786.Mcr-10-0568

Ye, et al. (2015). TGFβ modulates inflammatory cytokines and growth factors to create premetastatic microenvironment and stimulate lung metastasis. *Journal of Molecular Histology, 46*(4-5), 365-375. doi:10.1007/s10735-015-9633-4

Ye, et al. (2013). Wnt5a uses CD146 as a receptor to regulate cell motility and convergent extension. *Nature Communications, 4*(1), 2803. doi:10.1038/ncomms3803

Yersal, & Barutca. (2014). Biological subtypes of breast cancer: Prognostic and therapeutic implications. *World journal of clinical oncology, 5*(3), 412-424. doi:10.5306/wjco.v5.i3.412

Yolla, et al. (2020). Resistance Mechanisms to Anti-angiogenic Therapies in Cancer. *Frontiers in oncology, 10*. doi:10.3389/fonc.2020.00221

Yousem. (2009). Peripheral squamous cell carcinoma of lung: patterns of growth with particular focus on airspace filling. *Human Pathology, 40*(6), 861-867. doi:10.1016/j.humpath.2008.11.008

Yu, et al. (2017). TNFα-activated mesenchymal stromal cells promote breast cancer metastasis by recruiting CXCR2(+) neutrophils. *Oncogene, 36*(4), 482-490. doi:10.1038/onc.2016.217

Zappia, & Oshlack. (2018). Clustering trees: a visualization for evaluating clusterings at multiple resolutions. *GigaScience, 7*(7). doi:10.1093/gigascience/giy083

Zarrin, et al. (2017). Acquired tumor resistance to antiangiogenic therapy: Mechanisms at a glance. *J. Res. Med. Sci., 22*(1). doi:10.4103/jrms.JRMS_182_17

Zeng, et al. (2018). Cancer-derived exosomal miR-25-3p promotes pre-metastatic niche formation by inducing vascular permeability and angiogenesis. *Nature Communications, 9*(1), 5395. doi:10.1038/s41467-018-07810-w

Zhan, et al. (2017). Wnt signaling in cancer. *Oncogene, 36*(11), 1461-1473. doi:10.1038/onc.2016.304

Zhang, et al. (2014). Twist1 expression induced by sunitinib accelerates tumor cell vasculogenic mimicry by increasing the population of CD133+ cells in triple-negative breast cancer. *MOLECULAR CANCER, 13*(1), 207. doi:10.1186/1476-4598-13-207

Zhao, et al. (2006). Erythropoietin stimulates phosphorylation and activation of GATA-1 via the PI3-kinase/AKT signaling pathway. *Blood, 107*(3), 907-915. doi:10.1182/blood-2005-06-2516

Zhao, et al. (2020). Pharmacologically reversible zonation-dependent endothelial cell transcriptomic changes with neurodegenerative disease associations in the aged brain. *Nature Communications, 11*(1), 4413. doi:10.1038/s41467-020-18249-3

Zhao, et al. (2018). Long noncoding RNA n339260 promotes vasculogenic mimicry and cancer stem cell development in hepatocellular carcinoma. *Cancer Science, 109*(10), 3197-3208. doi:10.1111/cas.13740

Zheng, et al. (2023). Multiregion single cell analysis reveals a novel subtype of cancer-associated fibroblasts located in the hypoxic tumor microenvironment in colorectal cancer. *Transl Oncol, 27*, 101570. doi:10.1016/j.tranon.2022.101570

Zhou, et al. (2014). Cancer-secreted miR-105 destroys vascular endothelial barriers to promote metastasis. *Cancer Cell, 25*(4), 501-515. doi:10.1016/j.ccr.2014.03.007

Zhou, et al. (2011). Regulation of angiogenesis and choroidal neovascularization by members of microRNA-23~27~24 clusters. *Proceedings of the National Academy of Sciences of the United States of America, 108*(20), 8287-8292. doi:10.1073/pnas.1105254108

Zhou, et al. (2008). Epicardial progenitors contribute to the cardiomyocyte lineage in the developing heart. *Nature, 454*(7200), 109-113. doi:10.1038/nature07060

Zhou, et al. (2020). G-MDSCs-Derived Exosomal miRNA-143-3p Promotes Proliferation via Targeting of ITM2B in Lung Cancer. *Onco Targets Ther, 13*, 9701-9719. doi:10.2147/ott.S256378

Zhu, & Sly. (1990). Carbonic anhydrase IV from human lung. Purification, characterization, and comparison with membrane carbonic anhydrase from human kidney. *J Biol Chem, 265*(15), 8795-8801.

Ziyad, & Iruela-Arispe. (2011). Molecular mechanisms of tumor angiogenesis. *Genes & cancer, 2*(12), 1085-1096. doi:10.1177/1947601911432334

Zolak, et al. (2013). Pleural mesothelial cell differentiation and invasion in fibrogenic lung injury. *Am J Pathol, 182*(4), 1239-1247. doi:10.1016/j.ajpath.2012.12.030

Zuazo-Gaztelu, & Casanovas. (2018). Unraveling the Role of Angiogenesis in Cancer Ecosystems. *Frontiers in oncology, 8*, 248-248. doi:10.3389/fonc.2018.00248

Appendices

Appendix A: The Quantification method used in the transwell invasion assays

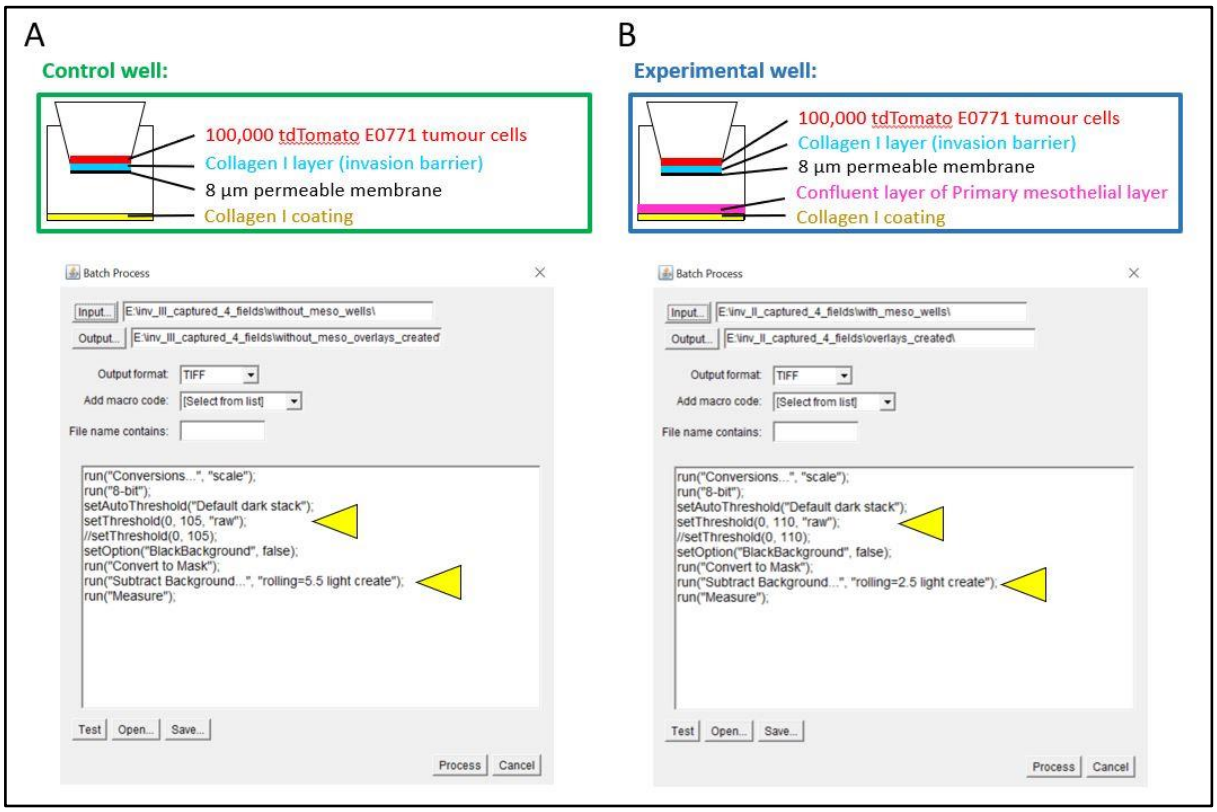

Figure A1. Macros (scripts) generated to automatically measure areas (as percentage) occupied by invaded E0771 tumour cells in presence or absence of pleural mesothelial cells. *A: depicts the script used for quantification of control wells with upper threshold of 105 and a radius of 5.5 to include only invaded cells and subtract background (yellow arrowheads), respectively; B: depicts the script used for quantification of experimental wells with upper threshold of 110 and a radius of 2.5 to include only invaded cells and subtract background (yellow arrowheads), respectively.*

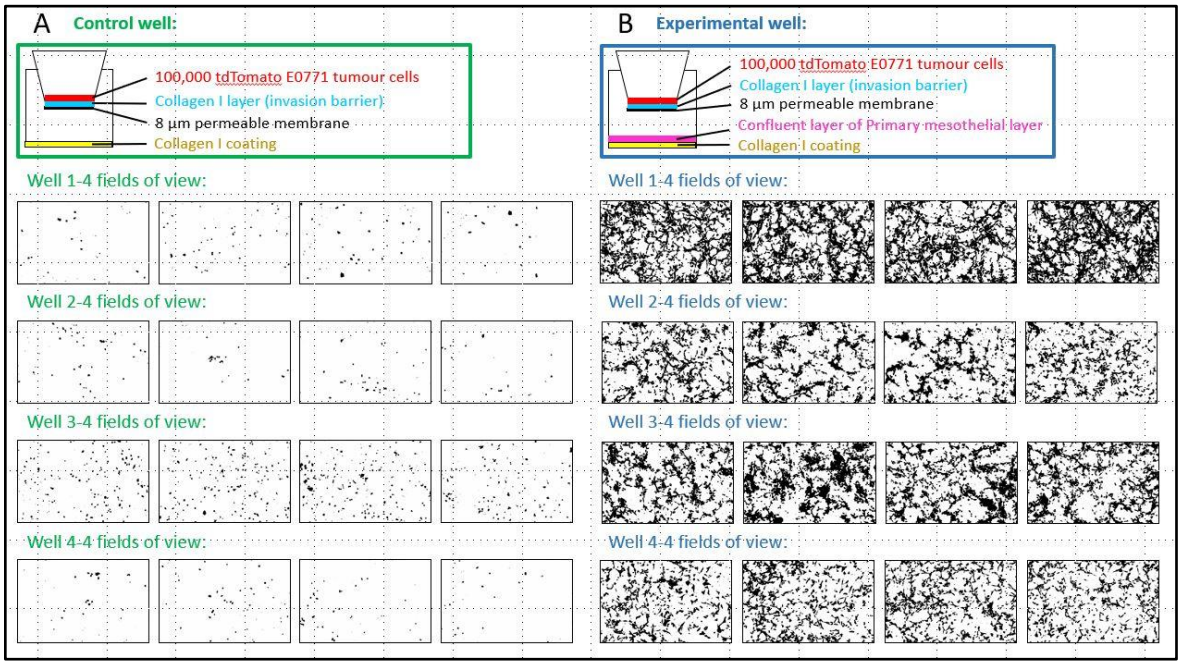

Figure A2. Overlays (masks) generated from control and experimental wells of transwell invasion assay replicate one using Fiji software. *A: depicts control wells which contain tdTomato E0771 tumour cells on the top of collagen I (invasion barrier) in inserts and no mesothelial cells in the lower compartment; B: Experimental wells which contain tdTomato E0771 tumour cells on the top of collagen I (invasion barrier) in inserts and pulmonary mesothelial monolayer in the lower compartment. Both A and B show four fields of view taken per well of a total number of four wells per control and experimental conditions*

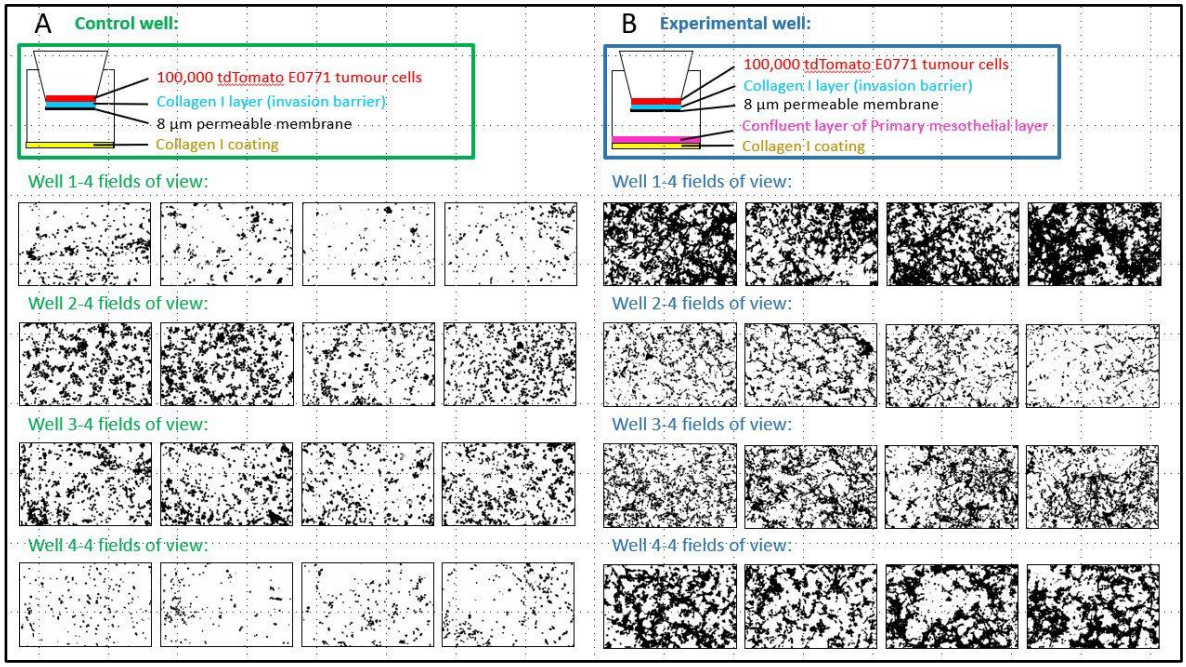

Figure A3. Overlays (masks) generated from control and experimental wells of transwell invasion assay replicate two using Fiji software*. A: depicts control wells which contain tdTomato E0771 tumour cells on the top of collagen I (invasion barrier) in inserts and no mesothelial cells in the lower compartment; B: Experimental wells which contain tdTomato E0771 tumour cells on the top of collagen I (invasion barrier) in inserts and pulmonary mesothelial monolayer in the lower compartment. Both A and B show four fields of view taken per well of a total number of four wells per control and experimental conditions.*

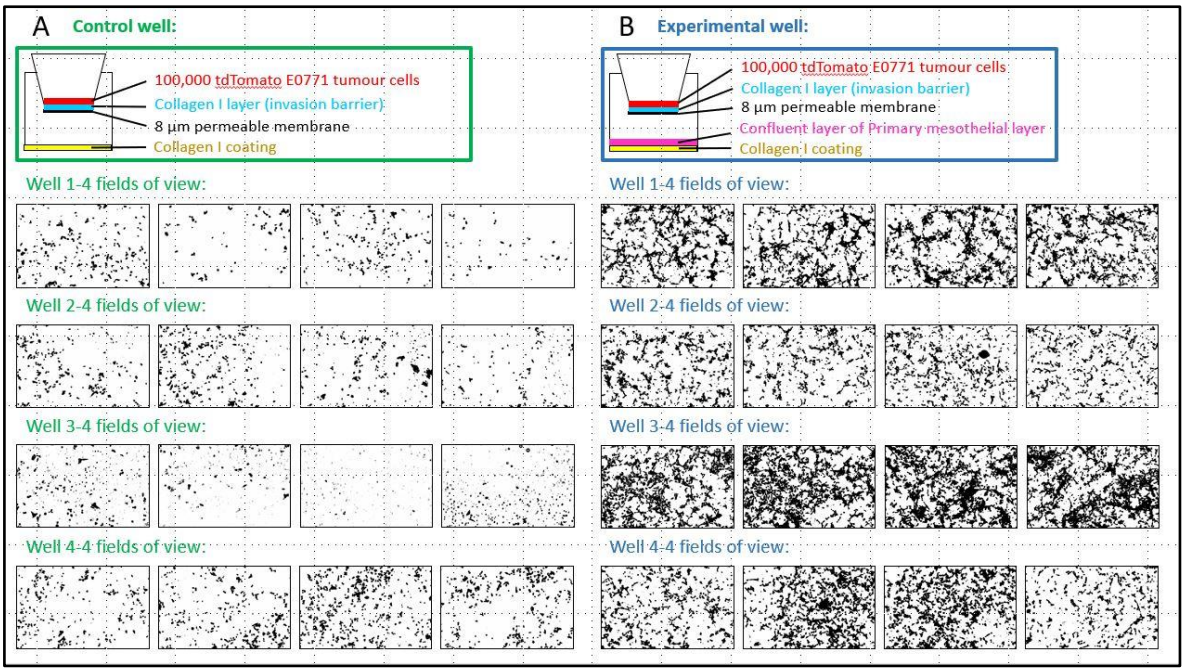

Figure A4. Overlays (masks) generated from control and experimental wells of transwell invasion assay replicate three using Fiji software. *A: depicts control wells which contain tdTomato E0771 tumour cells on the top of collagen I (invasion barrier) in inserts and no mesothelial cells in the lower compartment; B: Experimental wells which contain tdTomato E0771 tumour cells on the top of collagen I (invasion barrier) in inserts and pulmonary mesothelial monolayer in the lower compartment. Both A and B show four fields of view taken per well of a total number of four wells per control and experimental conditions.*

Appendix B: MRI orthogonal views of E0771 metastatic-bearing mouse lungs at early and late metastatic phases

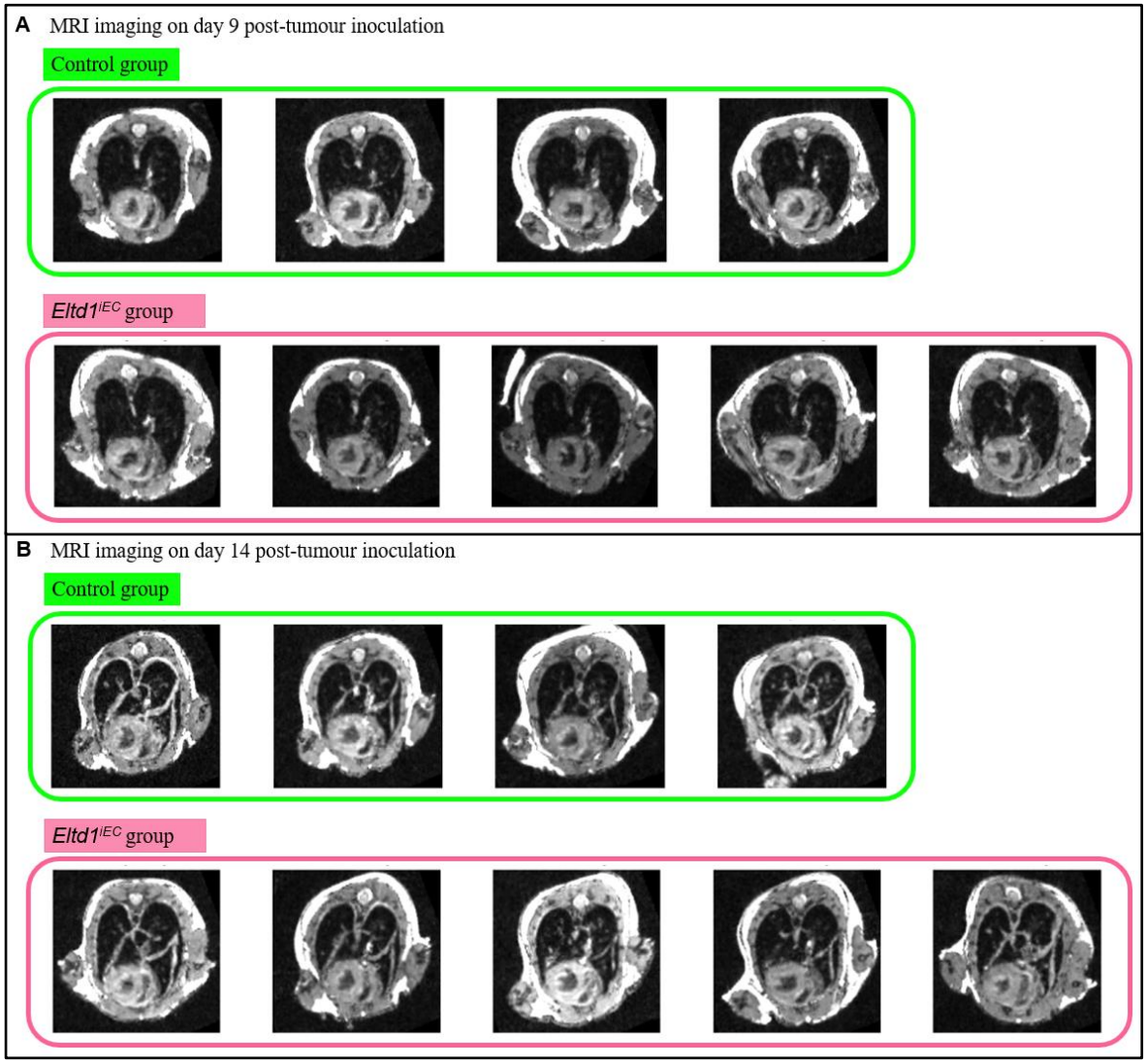

Figure B1. Segmented MRI images (Z plane cross-sectional view) of E0771 lung metastases showed no difference in tumour burden. *However, they showed interlobular strands (thickening) in both Eltd1^{iEC} and littermate control groups at day 14 compared to day 9. Green boxes indicate the control group (n=4 mice); pink boxes indicate Eltd1^{iEC} mice (n=5 mice).*

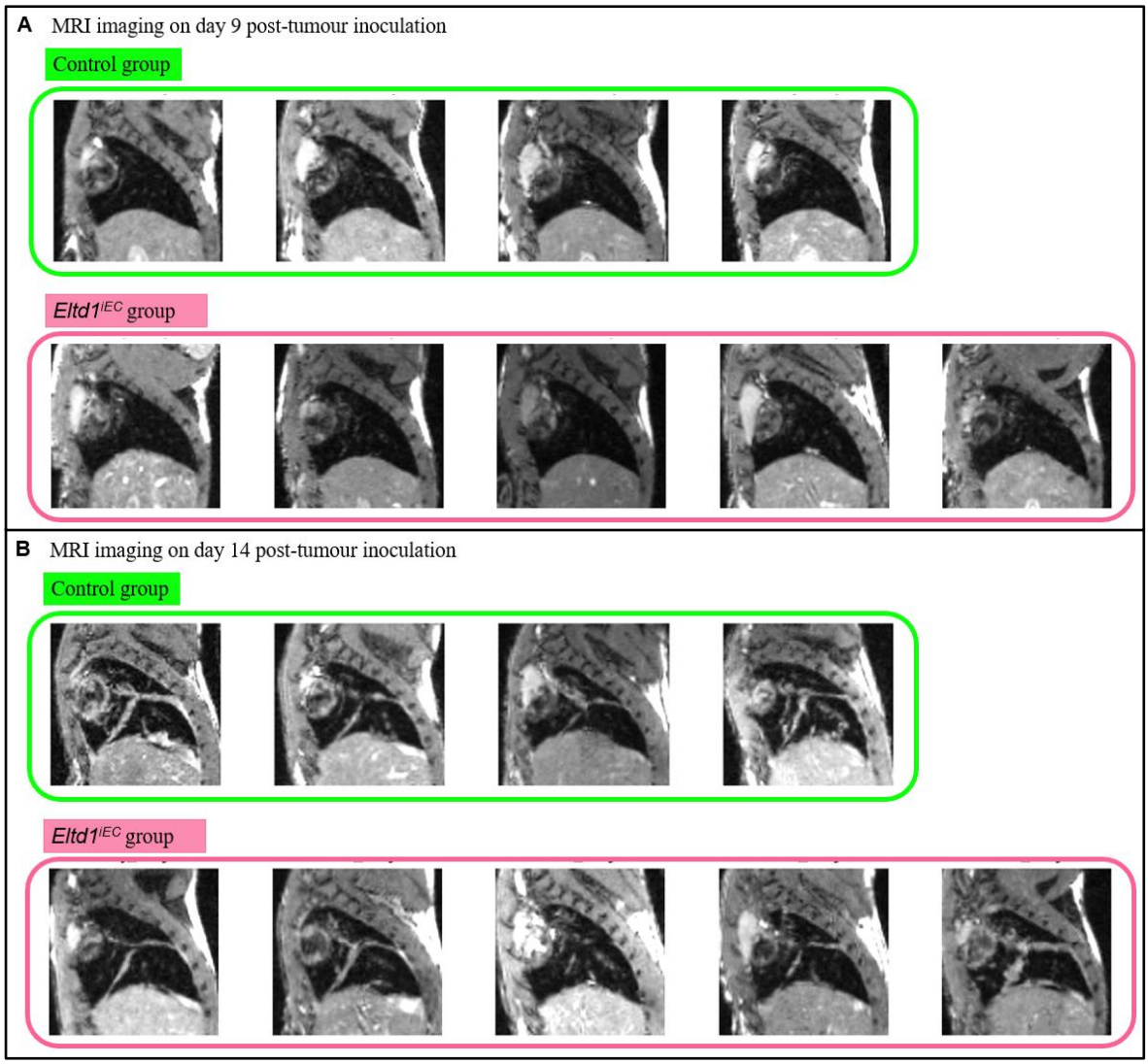

Figure B2. Segmented MRI images (Y plane cross-sectional view) of E0771 lung metastases showed no difference in tumour burden. *However, they showed interlobular strands (thickening) in both Eltd1^{iEC} and littermate control groups at day 14 compared to day 9. Green boxes indicate the control group (n=4 mice); pink boxes indicate Eltd1^{iEC} mice (n=5 mice).*

Appendix C: FACS strategy for gating and sorting lung stomal cells from non-tumour, early, and late metastatic lungs

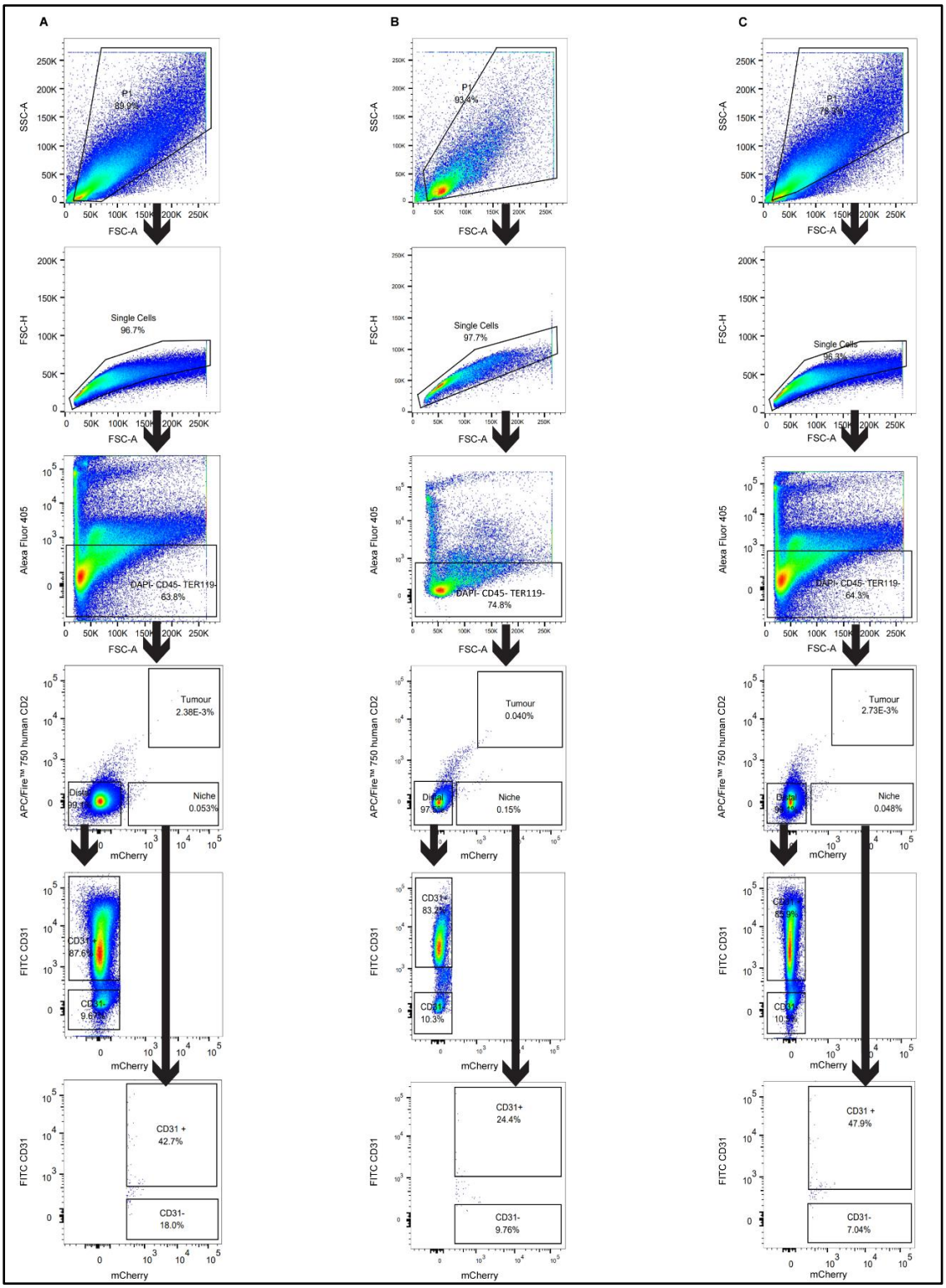

Figure C1. FACS sequential gating strategy of mouse non-tumour lungs gating the lung stroma including ECs*. A-C: FACS plots as follows: SSC-A vs. FSC-A density plot to gate population of interest (P1) excluding debris, FSC-H vs. FSC-A density plot to gate single cells, Alexa Fluor 405 vs. FSC-A density plot excluding immune cells (CD45+), RBC (TER119+) and dead cells (DAPI+) and grouping these populations into dump channel (gray box), APC/Fire750 hCD2 vs. mCherry density plot to identify E0771 tumour cells (hCD2+ mCherry+), distal normal stroma cells (non-labelled) and metastatic niche stroma cells (only mCherry+), and the latter two populations were further analysed for ECs marker (CD31).*

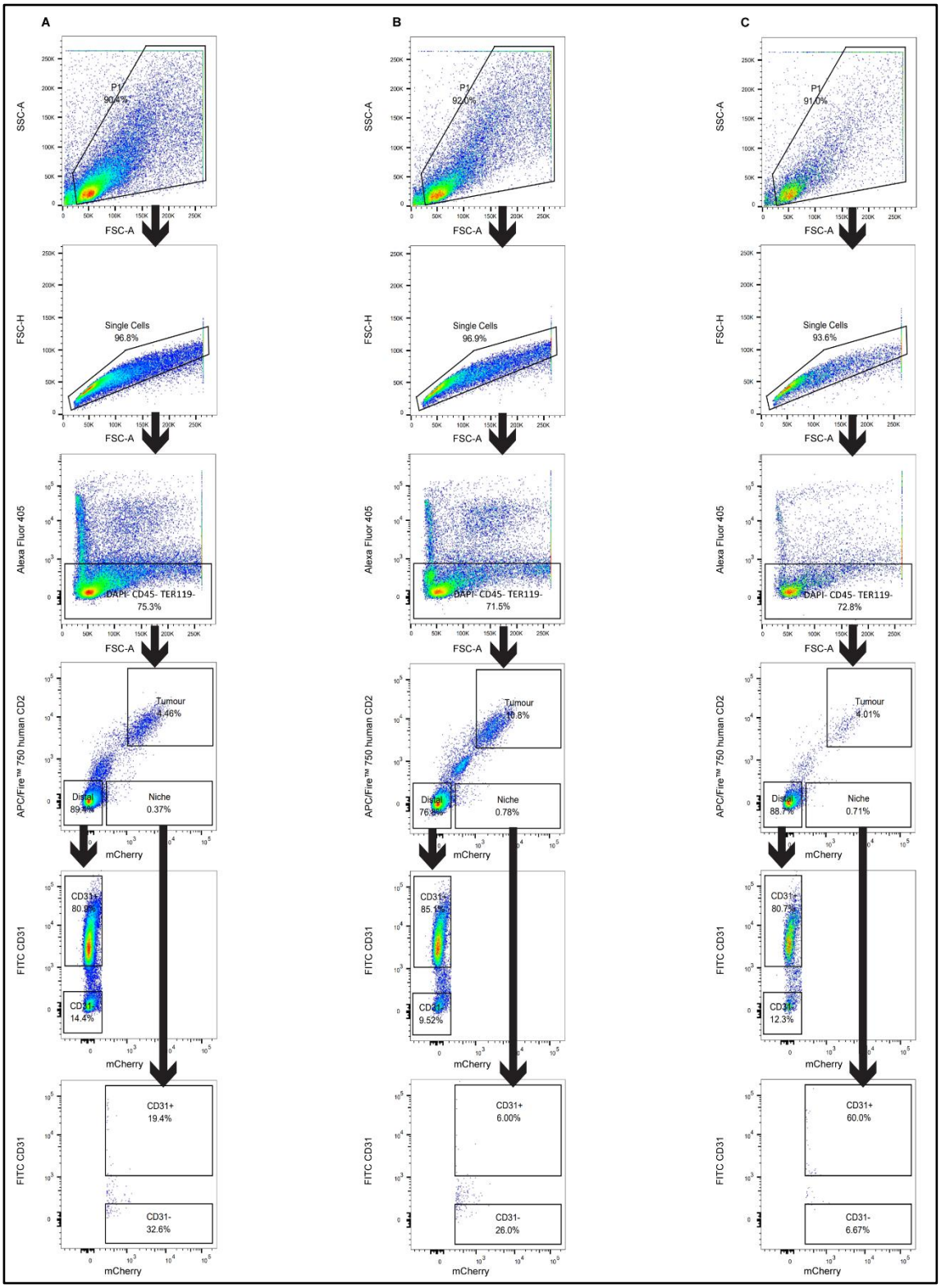

Figure C2. FACS sequential gating strategy of mouse early E0771 metastatic (day8) lungs identified E0771 tumour cells, metastatic niche, and distal (non-labelled) stroma including ECs*. A: non-tumour; B: early; C: late-tumour-bearing lungs; A-C: FACS plots as follows: SSC-A vs. FSC-A density plot to gate population of interest (P1) excluding debris, FSC-H vs. FSC-A density plot to gate single cells, Alexa Fluor 405 vs. FSC-A density plot excluding immune cells (CD45+), RBC (TER119+) and dead cells (DAPI+) and grouping these populations into dump channel (gray box), APC/Fire750 hCD2 vs. mCherry density plot to identify E0771 tumour cells (hCD2+ mCherry+), distal normal stroma cells (non-labelled) and metastatic niche stroma cells (only mCherry+), and the latter two populations were further analysed for ECs marker (CD31).*

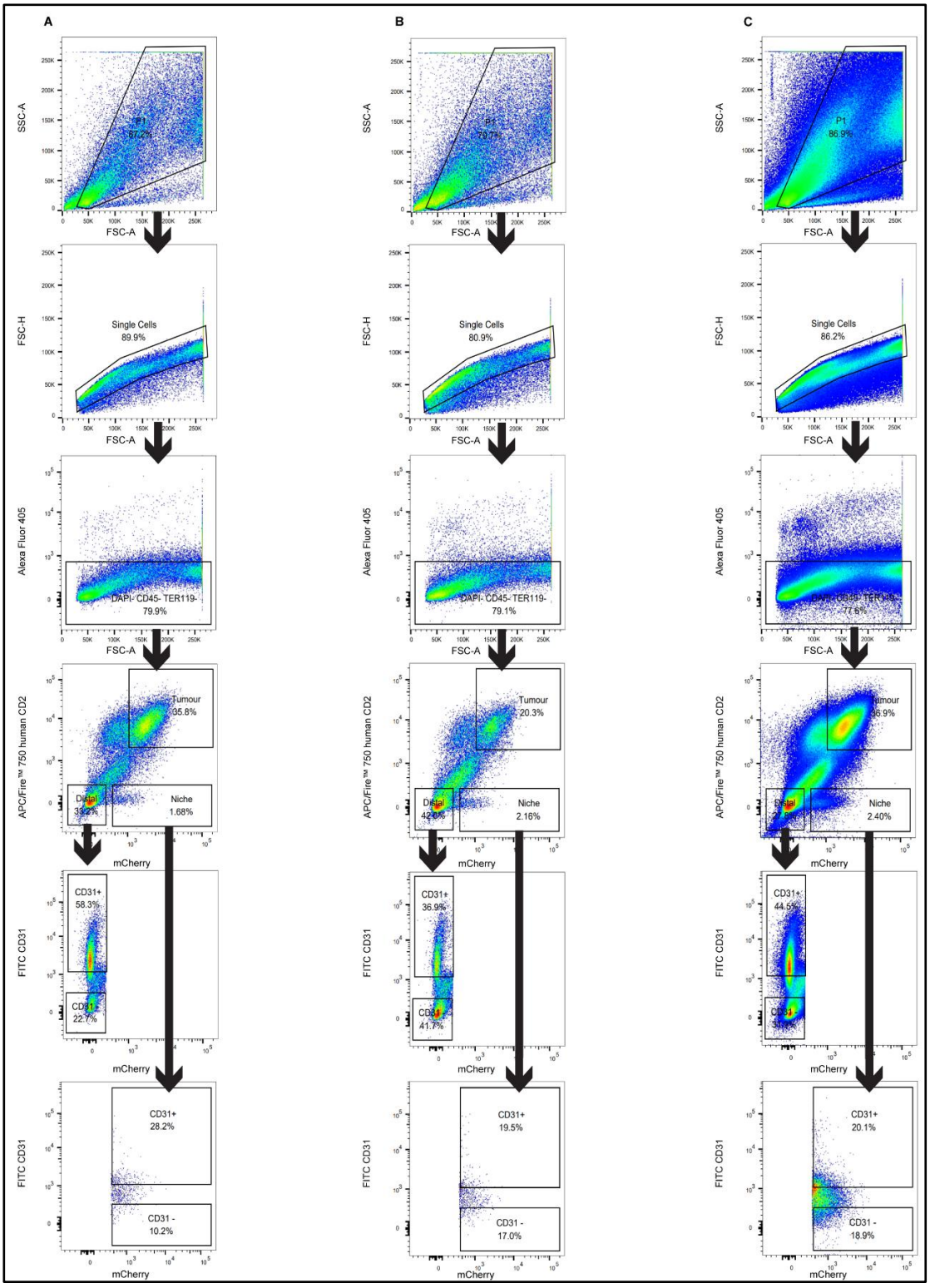

Figure C3. FACS sequential gating strategy of mouse late E0771 metastatic (day13) lungs identified E0771 tumour cells, metastatic niche, and distal (non-labelled) stroma including ECs. *A: non-tumour; B: early; C: late-tumour-bearing lungs; A-C: FACS plots as follows: SSC-A vs. FSC-A density plot to gate population of interest (P1) excluding debris, FSC-H vs. FSC-A density plot to gate single cells, Alexa Fluor 405 vs. FSC-A density plot excluding immune cells (CD45+), RBC (TER119+) and dead cells (DAPI+) and grouping these populations into dump channel (gray box), APC/Fire750 hCD2 vs. mCherry density plot to identify E0771 tumour cells (hCD2+ mCherry+), distal normal stroma cells (non-labelled) and metastatic niche stroma cells (only mCherry+), and the latter two populations were further analysed for ECs marker (CD31).*

Appendix D: Negative control for immunofluorescence staining of different proteins

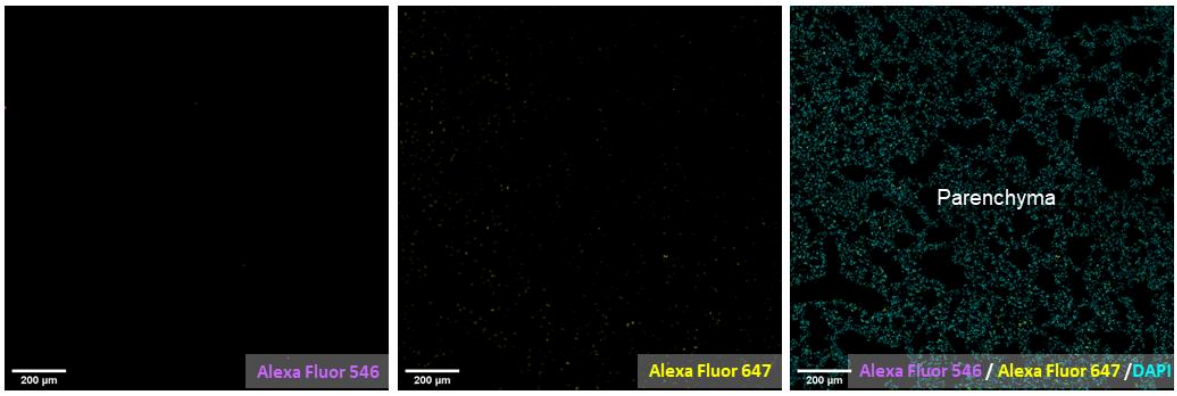

Figure D1. No primary antibody control tissue section, where only secondary antibodies (Abs) were used to immunofluorescently stain E0771 metastatic lung tissue sections to ensure the signal of primary Abs (mCherry and human CD2 Abs) are real. *The tissue section was stained with A: Alexa Fluor 546 Ab; B: Alexa Fluor 647 Ab; C: showed merged image with nuclear staining, DAPI.*

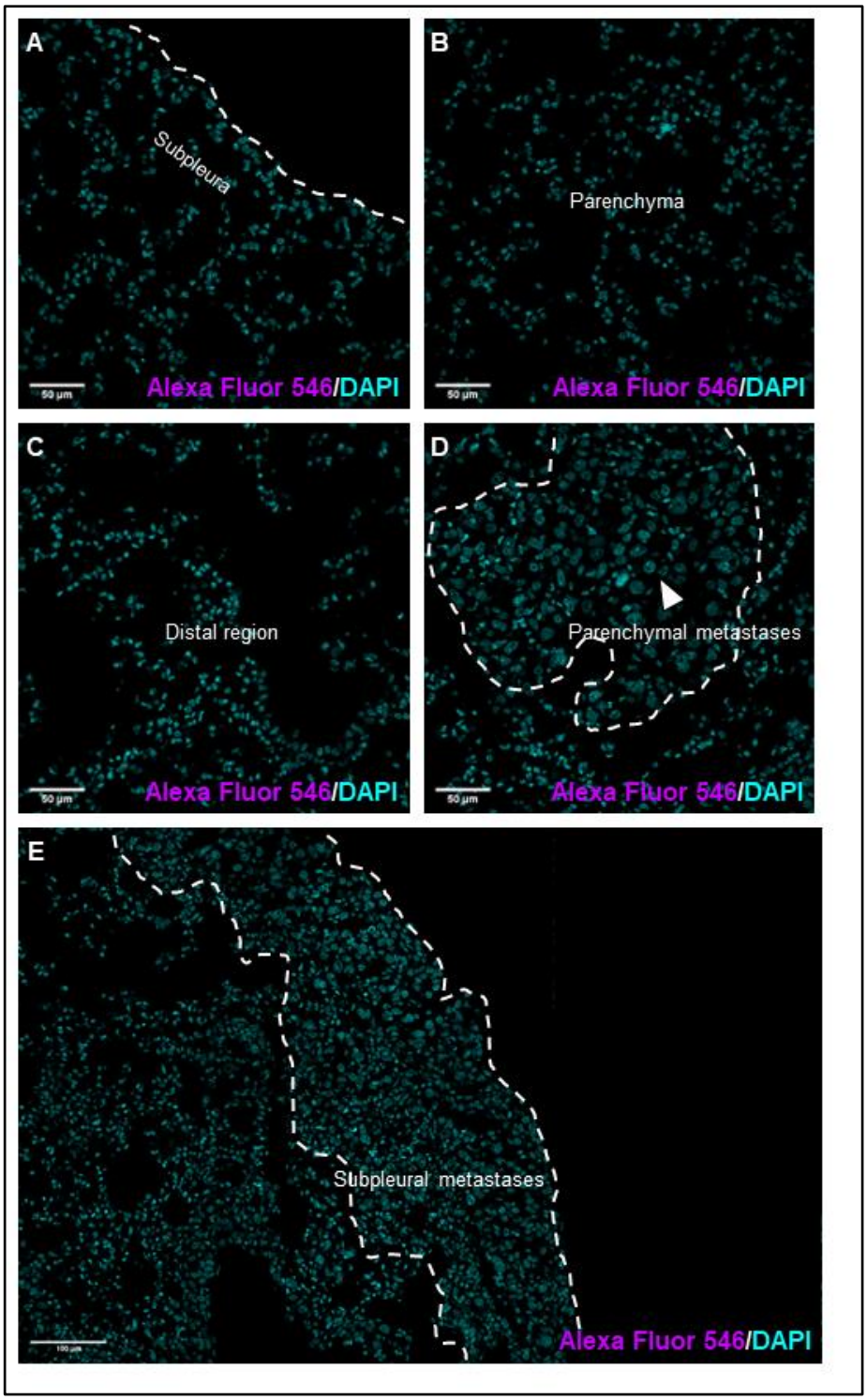

Figure D2. No primary antibody control tissue section, where only secondary Alexa Fluor 546 antibody (Ab) was used to immunofluorescently stain non-tumour-bearing and E0771 metastatic lung tissue sections to ensure the signal of the primary Ab (TJP1 Ab) is real. *A & B: non-tumour lung subpleura and parenchyma showing no non-specific signal of the secondary Ab; C-E: distal region, early (parenchymal) metastases, late (subpleural) metastases captured from E0771 metastatic lung sections with no non-specific signal. Dashed lines in (D) depicts parenchymal, while (E) depicts subpleural metastases. Nuclei were stained using the nuclear staining, DAPI.*

Appendix E: Upregulated and downregulated pathways determined by gene set enrichment analysis

Table E1. The top significantly upregulated and downregulated gene sets in capillary type I ECs with dual comparisons across the five conditions: normal (healthy) lungs, early distal, early niche, late distal, and late niche of E0771 metastatic lungs determined by gene set enrichment analysis (GSEA). *The top gene sets were selected based on the threshold of adjusted p values < 0.0005.*

EC subset	Comparison among conditions	Upregulated gene sets	Downregulated gene sets
Capillary type I	Early distal vs normal	Oxidative phosphorylation/Parkinsons disease/respiratory electron transport chain/Ag processing and presentation of peptide Ag and of exogenous peptide Ag via MHC class I/ATP synthesis coupled electron transport/mitochondrial respiratory chain complex assembly/NADH dehydrogenase complex assembly/mitochondrial electron transport NADH to ubiquinone	MARK signalling pathway/TNFA signalling via NFKB/response to endogenous stimulus/positive regulation of RNA metabolic process/positive regulation of transcription by RNA polymerase II/hypoxia/positive regulation of nucleobase containing compound metabolic process/SRF/cellular response to endogenous stimulus/positive regulation of cellular biosynthetic process
	Early niche vs normal	Oxidative phosphorylation/Parkinsons disease/Huntington disease/Alzheimer disease/proteasome/respiratory electron transport chain/ATP synthesis coupled electron transport/oxidation reduction process/cellular respiration/energy derivation by oxidation of organic compounds/generation of precursor metabolites and energy/ATP metabolic process/mitochondrial electron transport NADH to ubiquinone	Ribosome/response to CAMP/TNFA signalling via NFKB/positive regulation of RNA metabolic process/positive and negative regulation of nucleobase containing compound metabolic process/CTTTGT LEF1/positive regulation of transcription by RNA polymerase II/negative regulation of cellular biosynthetic process/SRF/response to CAMP
	Late distal vs normal	Cell adhesion_cams/Ag processing and presentation/IFN gamma response/IFN alpha response/allograft rejection/secretion/immune effector process/defense response/cytokine mediated signalling pathway/response to biotic stimulus/innate immune response	negative regulation of nucleobase containing compound metabolic process/negative regulation of RNA biosynthetic process/positive and negative regulation of transcription by RNA polymerase II/CTTTGT-LEF1/positive regulation of RNA metabolic process/positive regulation of nucleobase containing compound metabolic process/SMTTTTGT/AACTTT
	Late niche vs normal	Glycolysis_gluconeogenesis/ribosome/IFN gamma response/establishment of protein localization to ER/cotranslational protein targeting to membrane/IFN alpha response/nuclear transcribed mRNA catabolic process nonsense mediated decay/secretion/EMT/allograft rejection	positive and negative regulation of RNA metabolic process/positive and negative regulation of nucleobase containing compound metabolic process/positive regulation of transcription by RNA polymerase II/negative regulation of biosynthetic process/TNFA signalling via NFKB/CTTTGT_LEF1/AACTTT

	Late distal vs early distal	Cell adhesion_cams/Ag processing and presentation/TNFA signalling via NFKB/response to cytokine/IFN gamma response/immune effector process/response to biotic stimulus/regulation of response to stress/allograft rejection/cytokine mediated signalling pathway/defence response/secretion	Chromatin organization/covalent chromatin modification/histone methylation
	Late niche vs early niche	Ribosome/ ECM-receptor interaction/cotranslational protein targeting to membrane/establishment of protein localization to ER/nuclear transcribed mRNA catabolic process nonsense mediated decay/translational initiation/IFN gamma response/EMT/viral gene expression	Parkinsons disease/
	Early niche vs early distal	Oxidative phosphorylation/Parkinsons disease/electron transport chain/ATP synthesis coupled electron transport/	Ribosome/macrophage activation/chromosome organization/cytoskeleton organization
	Late niche vs late distal	Ribosome/nuclear transcribed mRNA catabolic process nonsense mediated decay/cotranslational protein targeting to membrane/translational initiation/establishment of protein localization to ER/viral gene expression/EMT/peptide biosynthetic process	allograft rejection/autoimmune thyroid disease/Ag processing and presentation/spliceosome/Type I diabetes mellitus/TNFA signalling via NFKB

Table E2. The top significantly upregulated and downregulated gene sets in capillary type II ECs with dual comparisons across the five conditions: normal (healthy) lungs, early distal, early niche, late distal, and late niche of E0771 metastatic lungs determined by gene set enrichment analysis (GSEA). *The top gene sets were selected based on the threshold of adjusted p values < 0.0005.*

EC subset	Comparison among conditions	Upregulated gene sets	Downregulated gene sets
Capillary type II (including IFN-Ag Capillary type II)	Early distal vs normal	Type I diabetes mellitus/Ag processing and presentation	Focal adhesion/ribosome/pathogenic Escherichia coli infection/neurotrophin signalling pathway/regulation of actin cytoskeleton/leukocyte transendothelial migration/Alzheimer disease/Huntington disease/MARK signalling pathway/protein localization to ER/translational initiation/TNFA signalling via NFKB/viral gene expression/cotranslational protein targeting to membrane/interspecies interaction between organisms

	Early niche vs normal	Oxidative phosphorylation/Cell adhesion_cams/Graft versus host disease/autoimmune thyroid disease/allograft rejection/Type I diabetes mellitus/Parkinsons disease/Ag processing and presentation/ATP synthesis coupled electron transport/respiratory electron transport chain/cellular respiration/IFN gamma response/mitochondrial electron transport NADH to ubiquinone/energy derivation by oxidation of organic compounds/ATP metabolic process	Focal adhesion/tight junction/ribosome/neurotrophin signalling pathway/regulation of actin cytoskeleton/leukocyte transendothelial migration/ protein localization to membrane/TNFA signalling via NFKB/viral gene expression/translational initiation/cellular macromolecule localization/protein localization to ER/nuclear transcribed mRNA catabolic process nonsense mediated decay/intracellular transport/establishment of protein localization to organelle
	Late distal vs normal	Oxidative phosphorylation/Cell adhesion_cams/Ag processing and presentation/Type I diabetes mellitus/Graft versus host disease/autoimmune thyroid disease/allograft rejection/viral myocarditis/intestinal immune network for IgA production/Parkinsons disease/IFN gamma response/IFN alpha response/innate immune response/defence response/defence response to other organisms/cytokine mediated signalling pathway/allograft rejection/response to biotic stimulus/response to type I interferon	negative regulation of biosynthetic process/negative regulation of nucleobase containing compound metabolic process/CEBP/negative regulation of transcription by RNA polymerase II/response to endogenous stimulus/TNFA signalling via NFKB/ATF3/CTTGT_LEF1
	Late niche vs normal	Ribosome/Ag processing and presentation/Type I diabetes mellitus/Graft versus host disease/autoimmune thyroid disease/allograft rejection/IFN gamma response/nuclear transcribed mRNA catabolic process nonsense mediated decay/cotranslational protein targeting to membrane/establishment of protein localization to ER/innate immune response/IFN alpha response/defence response to other organism	AACTTT/CTTTGT_LEF1/positive regulation of nucleobase containing compound metabolic process/positive regulation of RNA metabolic process/epithelial cell differentiation/tube morphogenesis/negative regulation of biosynthetic process/tube development/embryonic morphogenesis/locomotion
	Late distal vs early distal	Oxidative phosphorylation/Ribosome/Parkinsons disease/Ag processing and presentation/cardiac muscle contraction/Alzheimer disease/Huntington disease/viral myocarditis/autoimmune thyroid disease/allograft rejection/IFN gamma response/ion transport/response to cytokine/cation transport/cytokine mediated signalling pathway/transmembrane transport/defence response to other organism/ATP metabolic process/innate immune response	histone methylation/peptide lysine methylation/protein methylation/TGACAGNY_MEIS1/chromatin organization/HPI SITE factor/chromosome organization/sister chromatid cohesion/macromolecule methylation
	Late niche vs early niche	Ribosome/proteasome/nuclear transcribed mRNA catabolic process nonsense mediated decay/cotranslational protein targeting to membrane/establishment of protein localization to ER/translational initiation/viral gene expression/nuclear transcribed mRNA catabolic process	

	Early niche vs early distal	Oxidative phosphorylation/Parkinsons disease/ATP metabolic process/electron transport chain/generation of precursor metabolites and energy/respiratory electron transport chain/ATP synthesis coupled electron transport/cellular respiration/protein transmembrane transport/energy derivation by oxidation of organic compounds	chromatin organization/microtubule cytoskeleton organization/microtubule-based process/cytoskeleton organization/chromosome organization/
	Late niche vs late distal	Ribosome/nuclear transcribed mRNA catabolic process nonsense mediated decay/establishment of protein localization to ER/cotranslational protein targeting to membrane/translational initiation/nuclear transcribed mRNA catabolic process/viral gene expression	epithelial tube morphogenesis/endothelial development/embryonic organ development/locomotion/positive regulation of RNA metabolic process/epithelial cell differentiation/positive regulation of transcription by RNA polymerase II/tube morphogenesis/cell-cell adhesion

Table E3. The top significantly upregulated and downregulated gene sets in arteries with dual comparisons across the five conditions: normal (healthy) lungs, early distal, early niche, late distal, and late niche of E0771 metastatic lungs determined by gene set enrichment analysis (GSEA). *The top gene sets were selected based on the threshold of adjusted p values < 0.0005.*

EC subset	Comparison among conditions	Upregulated gene sets	Downregulated gene sets
Arteries	Early distal vs normal	Graft versus host disease/autoimmune thyroid disease/allograft reaction	Ribosome/establishment of protein localization to ER/TNFA signalling via NFKB/protein localization to membrane/cotranslational protein targeting to membrane/biological adhesion/translational initiation/cell activation/response to wounding/EMT/regulation of cell population proliferation/cell motility/hypoxia/blood vessel morphogenesis/supramolecular fibre organization/anatomical structure formation involved in morphogenesis/regulation of epithelial cell differentiation/apoptosis/actin filament bundle organization/response to ketone
	Early niche vs normal		Ribosome/establishment of protein localization to ER/cotranslational protein targeting to membrane/translational initiation/viral gene expression/nuclear transcribed mRNA catabolic process nonsense mediated decay/establishment of protein localization to organelle/biological adhesion/TNFA signalling via NFKB/circulatory system development/blood vessel morphogenesis/response to growth factor/regulation of cell population proliferation/cell-cell signalling by Wnt/regulation of anatomical structure morphogenesis/cell motility/cell activation/FC receptor signalling pathway/enzyme linked receptor protein signalling pathway

	Late distal vs normal	Oxidative phosphorylation/Cell adhesion_cams/Graft versus host disease/Ag processing and presentation/autoimmune thyroid disease/allograft rejection/Type I diabetes mellitus/viral myocarditis/Parkinsons disease/ribosome/IFN gamma response/IFN alpha response/defence response/response to biotic stimulus/innate immune response/allograft rejection/cytokine mediated signalling pathway/positive regulation of immune response/regulation of response to cytokine stimulus/regulation of multi organism process	LHX3 transcription factor/biological adhesion
	Late niche vs normal	Oxidative phosphorylation/Ribosome/cardiac muscle contraction/Parkinsons disease/nuclear transcribed mRNA catabolic process nonsense mediated decay/cotranslational protein targeting to membrane/establishment of protein localization to ER/viral gene expression/peptide biosynthetic process/RNA catabolic process/translational initiation/mRNA metabolic process/interspecies interaction between organisms/MYC targets/cytoplasmic translation/ribosome biogenesis/innate immune response/regulation of multi organism process/IFN gamma response/ATP metabolic process/protein containing complex assembly	LHX3 transcription factor/biological adhesion/locomotion/tube development/cardiovascular system development/circulatory system development/cell motility/blood vessel & tube morphogenesis/regulation of MARK cascade/vascular process in circulatory system/regulation of cell population proliferation/TAATTA_CHX10/regulation of epithelial differentiation
	Late distal vs early distal	Ribosome/protein targeting to membrane/protein localization to ER/translational initiation/nuclear transcribed mRNA catabolic process nonsense mediated decay/protein localization to membrane/viral gene expression/interspecies interaction between organisms/organonitrogen compound biosynthetic process/cytoplasmic translation/EMT/defence response/IFN gamma response/TNFA signalling via NFKB/response to cytokine/cell activation/immune effector process/secretion/hypoxia	CCAAT enhancer binding protein gamma (CEBP GAMMA)/positive regulation of GTPase activity
	Late niche vs early niche	Ribosome/cotranslational protein targeting to membrane/establishment of protein localization to ER/nuclear transcribed mRNA catabolic process nonsense mediated decay/viral gene expression/translational initiation/nuclear transcribed mRNA catabolic process/peptide biosynthetic process/RNA catabolic process/interspecies interaction between organisms/establishment of protein localization to organelle/mRNA metabolic process/MYC targets/cytoplasmic translation/ribonucleoprotein complex biogenesis/ribosome biogenesis & assembly/cellular protein containing complex assembly/post-transcriptional regulation of gene expression/defence response to other organism/response to cytokine/EMT	locomotion/cell motility/cardiovascular system development/circulatory system development/osteoblast differentiation/blood vessel & tube morphogenesis/positive regulation of EC differentiation

	Early niche vs early distal		
	Late niche vs late distal	Ribosome/nuclear transcribed mRNA catabolic process nonsense mediated decay/translational initiation/s/peptide biosynthetic process/cotranslational protein targeting to membrane/viral gene expression/protein localization to ER/nuclear transcribed mRNA catabolic process/protein localization to organelle/interspecies interaction between organisms/MYC targets/ribosome biogenesis/cytoplasmic translation/ribosomal large subunit biogenesis	Type I diabetes mellitus/allograft rejection/autoimmune thyroid disease/Graft versus host disease/cell motility/cardiovascular system development/regulation of osteoblast differentiation/positive regulation of locomotion/circulatory system process/outflow tract morphogenesis/regulation of cell population proliferation/biological adhesion/heart morphogenesis/regulation of MARK cascade/secretion

Table E4. The top significantly upregulated and downregulated gene sets in veins with dual comparisons across the five conditions: normal (healthy) lungs, early distal, early niche, late distal, and late niche of E0771 metastatic lungs determined by gene set enrichment analysis (GSEA). *The top gene sets were selected based on the threshold of adjusted p values < 0.0005.*

EC subset	Comparison among conditions	Upregulated gene sets	Downregulated gene sets
Veins	Early distal vs normal	Ribosome/ intestinal immune network for IgA production/establishment of protein localization to ER/cotranslational protein targeting to membrane/nuclear transcribed mRNA catabolic process nonsense mediated decay/translational initiation/mRNA metabolic process/protein localization to membrane/RNA processing and splicing/cytoplasmic translation	Insulin/ neurotrophins/ MARK signalling pathways/pathways in cancer/TNFA signalling via NFKB/anatomical structure formation involved in morphogenesis/regulation of cell population proliferation/response to endogenous stimulus/cardiovascular system development/circulatory system development/response to hormone/ response to oxygen containing compound/tube development/blood vessel morphogenesis/response to organic cyclic compound/response to nitrogen compound/hypoxia/biological adhesion/response to drug/regulation of cell adhesion/response to steroid hormone/cell motility/animal organ morphogenesis/positive regulation of developmental process

	Early niche vs normal		MARK signalling pathway/TNFA signalling via NFKB/hypoxia/cardiovascular system development/anatomical structure formation involved in morphogenesis/response to endogenous stimulus/positive regulation of development/circulatory system development/response to oxygen containing compound/CREB/regulation of cell population proliferation/cell-cell signalling/regulation of cell differentiation/response to mechanical stimulus/response to organic cyclic compound/enzyme linked receptor protein signalling pathway/epithelium development/regulation of cell death/response to drug/cell motility/ameboidal type cell migration/positive regulation of multicellular organismal process
	Late distal vs normal	Cell adhesion_cams/Oxidative phosphorylation/ ribosome/ Ag processing and presentation/autoimmune thyroid disease/allograft rejection/Graft versus host disease/Type I diabetes mellitus/Parkinsons disease/IFN gamma response/IFN gamma response/establishment of protein localization to ER/cotranslational protein targeting to membrane/nuclear transcribed mRNA catabolic process nonsense mediated decay/translational initiation/IFN alpha response/viral gene expression/protein targeting/defence to other organism/response to biotic stimulus/cytokine mediated signalling pathway/organic cyclic compound catabolic process/cellular nitrogen compound catabolic process/response to virus/interspecies interaction btw organisms/chaperone mediated protein folding/MYC targets	Neurogenesis/anatomical structure formation involved in morphogenesis/SRY/negative regulation of biosynthetic process/GCANCTGNY MYOD/tube morphogenesis and development/regulation of cell adhesion/PAX4/biological adhesion/cell junction organization/cell substrate adhesion/regulation of system process
	Late niche vs normal	Oxidative phosphorylation/ribosome/cardiac muscle contraction/Huntington disease/Parkinsons disease/nuclear transcribed mRNA catabolic process nonsense mediated decay/establishment of protein localization to ER/cotranslational protein targeting to membrane/translational initiation/protein targeting to membrane/viral gene expression/peptide biosynthetic process/RNA catabolic process/ribonucleoprotein complex biogenesis/interspecies interaction btw organisms/MYC targets/cytoplasmic translation/ribosome assembly/ribonucleoprotein complex subunit organization/ribosomal large & small subunit biogenesis/cellular containing complex assembly/nucleoside triphosphate biosynthetic process/ATP metabolic process	regulation of cell population proliferation/locomotion/biological adhesion/epithelial cell differentiation/TNFA signalling via NFKB/tube morphogenesis/regulation of cellular component movement/tube development/response to endogenous stimulus/circulatory system development/response to oxygen containing compound/regulation of cell adhesion/response to endogenous stimulus/epithelium development/anatomical structure formation involved in morphogenesis/response to organic cyclic compound/AACTTT/endothelium development/response to nitrogen compound/cell-cell signalling/neurogenesis/response to drug/heart morphogenesis

	Late distal vs early distal	MARK signalling pathway/Ag processing and presentation/TNFA signalling via NFKB/IFN gamma response/response to biotic stimulus/hypoxia/response to cytokine/cytokine mediated signalling pathway/cell activation/regulation of cell population proliferation/regulation of cell death/defence response/regulation of response to stress/positive regulation of immune system/SRF_Q5/chaperone mediated protein folding/response to oxygen containing compound/UV response up/P53 pathway/response to abiotic stimulus/response to topologically incorrect protein/SRF_Q4/positive regulation of developmental process	
	Late niche vs early niche	Oxidative phosphorylation/ribosome/Huntington disease/proteasome/establishment of protein localization to ER/cotranslational protein targeting to membrane/nuclear transcribed mRNA catabolic process nonsense mediated decay/translational initiation/viral gene expression/RNA catabolic process/cellular nitrogen compound catabolic process/peptide biosynthetic process/RNA catabolic process/MYC targets/interspecies interaction between organisms/ribonucleoprotein complex biogenesis/ribosome biogenesis & assembly/posttranscriptional regulation of gene expression/protein containing complex assembly/ribosomal large & small subunit biogenesis/response to topologically incorrect protein/ribonucleoside triphosphate biosynthetic process/	cytokine-cytokine receptor interaction/endothelial development/neurogenesis/OCT/biological adhesion/negative regulation of epithelial cell differentiation
	Early niche vs early distal		Ribosome/cotranslational protein targeting to membrane/establishment of protein localization to ER/viral gene expression/translational initiation
	Late niche vs late distal	Cell adhesion_cams/ribosome/establishment of protein localization to ER/nuclear transcribed mRNA catabolic process nonsense mediated decay/cotranslational protein targeting to membrane/viral gene expression/translational initiation/peptide biosynthetic process/RNA catabolic process/ribonucleoprotein complex biogenesis/RNA metabolic process/MYC targets/interspecies interaction between organisms/	TNFA signalling via NFKB/IFN gamma response/EC development/response to oxygen containing compound/regulation of cell population proliferation/locomotion/positive regulation of cell differentiation/cell motility/circulatory system development/response to mechanical stimulus/biological adhesion/response to bacterium/epithelial cell differentiation/response to cytokine/epithelial development/cell-cell adhesion/response to external stimulus/regulation of cell activation/cardiovascular system development/positive regulation of MARK cascade/positive regulation of transcription by RNA polymerase II

Table E5. The top significantly upregulated and downregulated gene sets in neophalanx/breach/tip ECs with dual comparisons across the five conditions: normal (healthy) lungs, early distal, early niche, late distal, and late niche of E0771 metastatic lungs determined by gene set enrichment analysis (GSEA). *The top gene sets were selected based on the threshold of adjusted p values < 0.0005.*

EC subset	Comparison among conditions	Upregulated gene sets	Downregulated gene sets
Neophalanx/breach/tip Ecs	Early distal vs normal	Cell adhesion_cams/Oxidative phosphorylation/Ag processing and presentation/Type I diabetes mellitus/Graft versus host disease/autoimmune thyroid disease/defence response/IFN gamma response/defence response to other organism/cytokine mediated signalling pathway/innate immune response/response to biotic stimulus/IFN alpha response/positive regulation of cytokine production/allograft rejection	ribosome
	Early niche vs normal	Cell adhesion_cams/Oxidative phosphorylation/autoimmune thyroid disease/allograft rejection/Graft versus host disease/Ag processing and presentation/Type I diabetes mellitus/IFN gamma response/defence response/defence response to other organism/cytokine mediated signalling pathway/innate immune response/response to biotic stimulus/IFN alpha response//allograft rejection/EMT	Ribosome/cotranslational protein targeting to membrane/establishment of protein localization to ER
	Late distal vs normal	Cell adhesion_cams/Ag processing and presentation/autoimmune thyroid disease/allograft rejection/Graft versus host disease/Type I diabetes mellitus/ intestinal immune network for IgA production/IFN gamma response/IFN alpha response/defence response to other organism/cytokine mediated signalling pathway/innate immune response/response to biotic stimulus/regulation of multi organism process/interspecies interaction between organisms	TTANTCA/GATA1
	Late niche vs normal	glycolysis_gluconeogenesis/Oxidative phosphorylation/ribosome/proteasome/Parkinsons disease/Ag processing and presentation/IFN gamma response/nuclear transcribed mRNA catabolic process nonsense mediated decay/interspecies interaction between organisms/IFN alpha response/defence response to other organism/innate immune response/cotranslational protein targeting to membrane/establishment of protein localization to ER/cytokine mediated signalling pathway/defence response	TATAAA_TATA/Sox5/cell fate specification
	Late distal vs early distal	cotranslational protein targeting to membrane/establishment of protein localization to ER/nuclear transcribed mRNA catabolic process nonsense mediated decay/viral gene expression/interspecies interaction between organisms/translational initiation	AACTTT/biological adhesion/TATAAA_TATA/TGGAAA_NFAT/locomotion/UV response/CTTTGA_LEF1/DEBPGAMMA/cellular component morphogenesis/TNFA signalling via NFKB

	Late niche vs early niche	Oxidative phosphorylation/ribosome/Alzheimer disease/Huntington disease/Parkinsons disease/translational initiation/nuclear transcribed mRNA catabolic process nonsense mediated decay/cotranslational protein targeting to membrane/establishment of protein localization to ER/peptide biosynthetic process	Cell adhesion_cams
	Early niche vs early distal	IFN gamma response/IFN /EMT/IFN alpha response	
	Late niche vs late distal	Ribosome/ECM receptor interaction/establishment of protein localization to ER/nuclear transcribed mRNA catabolic process nonsense mediated decay/cotranslational protein targeting to membrane/translational initiation/RNA catabolic process/peptide biosynthetic process/organic cyclic compound catabolic process	Cell adhesion_cams/Type I diabetes mellitus/allograft rejection/autoimmune thyroid disease/Graft versus host disease/Ag processing and presentation/viral myocarditis/axon guidance/cytokine cytokine receptor interaction/endothelium development

Table E6. The top significantly upregulated and downregulated gene sets in stressed ECs with dual comparisons across the five conditions: normal (healthy) lungs, early distal, early niche, late distal, and late niche of E0771 metastatic lungs determined by gene set enrichment analysis (GSEA). *The top gene sets were selected based on the threshold of adjusted p values < 0.0005.*

EC subset	Comparison among conditions	Upregulated gene sets	Downregulated gene sets
EC-stressed	Early distal vs normal		TNFA signalling via NFKB/response to endogenous stimulus/response to hormone/response to organic cyclic compound/hypoxia/response to lipid/negative regulation of nucleobase containing compound metabolic process/response to steroid hormone/cellular response to endogenous stimulus/cellular response to hormone stimulus
	Early niche vs normal	Cell adhesion_cams	Ribosome/translational initiation/macromolecule catabolic process/TNFA signalling via NFKB/regulation of cell differentiation/peptide biosynthetic process/response to endogenous process/hypoxia/cotranslational protein targeting to membrane/nuclear transcribed mRNA catabolic process nonsense mediated decay

	Late distal vs normal	Ag processing and presentation/ribosome/intestinal immune network for IgA production/Graft versus host disease/autoimmune thyroid disease/allograft rejection/Type I diabetes mellitus/IFN gamma response/IFN alpha response/response to biotic stimulus/cytokine mediated signalling pathway/establishment of protein localization to ER/defence response/cotranslational protein targeting to membrane/innate immune response	negative regulation of nucleobase containing compound metabolic process/negative regulation of RNA biosynthetic process/DBP/CTTTGT_LEF1/negative regulation of transcription by RNA polymerase II/POU6F1/CRX/response to endogenous stimulus/cell surface receptor signalling pathway involved in cell-cell signalling
	Late niche vs normal	Ribosome/nuclear transcribed mRNA catabolic process nonsense mediated decay/cotranslational protein targeting to membrane/establishment of protein localization to ER/translational initiation/RNA catabolic process/organic cyclic compound catabolic process/cellular nitrogen compound catabolic process	AACTT/CTTTGA_LEF1/epithelial cell differentiation/positive regulation of transcription by RNA polymerase II/sprouting angiogenesis/anatomical structure formation involved in morphogenesis/embryo development/negative regulation of RNA biosynthetic process/cellular response to endogenous stimulus
	Late distal vs early distal	Ribosome/TNFA signalling via NFKB/RNA catabolic process/nuclear transcribed mRNA catabolic process /nuclear transcribed mRNA catabolic process nonsense mediated decay/translational initiation/establishment of protein localization to ER/viral gene expression/cotranslational protein targeting to membrane/cellular nitrogen compound catabolic process	
	Late niche vs early niche	Ribosome/proteasome/translational initiation/nuclear transcribed mRNA catabolic process nonsense mediated decay/cotranslational protein targeting to membrane/establishment of protein localization to ER/peptide biosynthetic process/RNA catabolic process/amide biosynthetic process/peptide metabolic process	Cell adhesion_cams/allograft rejection/Graft versus host disease/autoimmune thyroid disease
	Early niche vs early distal		regulation of transcription from RNA polymerase II promoter in response to hypoxia
	Late niche vs late distal	Ribosome/establishment of protein localization to ER/nuclear transcribed mRNA catabolic process nonsense/cotranslational protein targeting to membrane/translational initiation/RNA catabolic process/peptide biosynthetic process/organic cyclic compound catabolic process	Cell adhesion_cams/Graft versus host disease/Type I diabetes mellitus/allograft rejection/autoimmune thyroid disease/Ag processing and presentation/endothelium development

Appendix F: Differentially expressed genes in co-opted lung capillaries in early niche compared to non-tumour, early distal, and late niche

Table F1. The gene signature of co-opted cap I present in the early niche compared to non-tumour cap I. *Differential expression analysis was performed using the Wilcoxon-Mann-Whitney test with log fold change threshold = 0.25.*

Gene name	Average log fold change	The adjusted p-value	Fraction of cap I expressing this gene in early niche	Fraction of non-tumour cap I expressing this gene
Cyp1a1	2.111	3.08601E-49	0.693	0.138
Scgb1a1	1.092	9.58311E-16	0.337	0.053
mt-Nd4l	0.865	6.4984E-31	0.693	0.248
Crip1	0.784	6.77024E-10	0.787	0.618
mt-Co2	0.684	1.35527E-18	0.989	0.922
mt-Cytb	0.681	2.65184E-21	0.984	0.962
Ly6c1	0.611	2.27465E-13	0.995	0.984
mt-Nd4	0.553	1.13394E-14	0.987	0.897
Sftpc	0.526	3.67425E-13	0.367	0.088
mt-Nd3	0.523	1.69809E-11	0.706	0.401
Gm10076	0.522	3.24182E-20	0.391	0.063
Car4	0.513	4.28815E-10	0.954	0.937
mt-Nd2	0.513	2.51658E-10	0.981	0.843
mt-Co1	0.508	9.02314E-12	0.978	0.906
mt-Atp6	0.486	3.37695E-09	0.995	0.95
Ly6a	0.472	8.43311E-12	0.995	1
Srgn	0.470	6.87428E-09	0.881	0.755
Hspa1b	0.449	1	0.057	0.135
Id3	0.440	1.05626E-08	0.935	0.843
mt-Nd5	0.440	3.30952E-08	0.601	0.342
Igfbp7	0.440	2.27651E-08	0.987	0.997
mt-Co3	0.436	3.59666E-06	0.992	0.94
Bcam	0.433	2.58911E-08	0.852	0.705
Itm2b	0.387	1.59096E-10	0.997	0.997
Tbx2	0.383	0.000289611	0.879	0.749
mt-Nd1	0.381	1.66267E-06	0.951	0.793
Psmb3	0.366	1.71016E-07	0.59	0.342
Ramp2	0.348	3.65974E-06	0.995	0.994
H2-D1	0.344	7.66329E-07	1	0.994
Prx	0.343	0.006620569	0.819	0.727
Hilpda	0.339	0.128035464	0.695	0.564
Gstp1	0.339	1.98418E-11	0.313	0.069
Ecm1	0.328	0.009408284	0.402	0.232
Pcdh1	0.326	0.028262938	0.889	0.812
Ftl1	0.325	0.001592343	0.949	0.875
Tmed10	0.309	0.003905492	0.779	0.633
Herpud1	0.294	0.018135621	0.48	0.31
Sap18	0.290	1.82283E-05	0.434	0.216
Rhoc	0.286	0.026496992	0.704	0.564
Clec2d	0.283	0.646530558	0.833	0.727
Mgll	0.283	0.04606816	0.774	0.618
Cavin3	0.283	0.004172686	0.456	0.27
Arhgap31	0.282	0.017298953	0.822	0.674
Anxa3	0.281	0.016426911	0.889	0.777
Aldoa	0.281	0.085579022	0.539	0.389

Grina	0.278	0.828267481	0.588	0.483
Adgre5	0.277	0.001894012	0.962	0.912
Gngt2	0.274	1	0.666	0.555
Gnas	0.273	0.015390046	0.898	0.793
Fibin	0.272	1	0.865	0.821
Ace	0.270	1	0.889	0.859
Rtl8a	0.268	0.120467857	0.709	0.558
Eif3j1	0.267	0.122104571	0.466	0.317
Mest	0.263	0.00599385	0.302	0.141
Hspa1a	0.263	0.000260041	0.032	0.157
Slc48a1	0.261	0.243300561	0.534	0.389
H2-K1	0.256	0.194580447	0.995	0.987
Dleu2	0.255	0.004197446	0.396	0.21

***Table F2. The gene signature of co-opted cap I present in the early niche compared to cap I in the early distal region**. Differential expression analysis was performed using the Wilcoxon-Mann-Whitney test with log fold change threshold = 0.25.*

Gene name	Average log fold change	Fraction of cap I expressing this gene in early niche	Fraction of cap I expressing this gene in early distal	The adjusted p value
Cyp1a1	1.309	0.693	0.395	4.0198E-24
Scgb1a1	1.154	0.337	0.017	7.1878E-33
mt-Cytb	0.588	0.984	0.99	1.6208E-20
Hopx	0.488	0.876	0.811	2.1315E-09
Sftpc	0.472	0.367	0.123	6.1329E-13
mt-Co2	0.445	0.989	0.985	1.0087E-10
Klf2	0.419	0.97	0.911	5.6522E-09
Crip1	0.419	0.787	0.699	0.01532946
mt-Nd4l	0.410	0.693	0.514	1.0691E-07
Sox18	0.401	0.612	0.439	1.3517E-07
mt-Atp6	0.393	0.995	0.988	5.4206E-05
Foxf1	0.378	0.895	0.802	2.201E-08
Srgn	0.363	0.881	0.792	6.5023E-06
mt-Co1	0.363	0.978	0.969	3.2268E-06
Cav2	0.361	0.903	0.815	2.8984E-07
Cd9	0.341	0.925	0.857	2.4722E-05
mt-Nd4	0.338	0.987	0.977	8.2945E-05
mt-Co3	0.337	0.992	0.99	0.04060258
Ecm1	0.336	0.402	0.26	0.00774334
Car4	0.327	0.954	0.967	0.00036792
Marcks	0.320	0.836	0.79	0.04201189
Itm2b	0.311	0.997	1	8.9176E-08
Gsn	0.306	0.202	0.04	1.0167E-09
Tsc22d3	0.280	0.38	0.233	0.01276942
Cdkn1a	0.276	0.774	0.684	1
Plaur	0.268	0.488	0.349	0.06001379
Myl12a	0.265	0.876	0.815	0.00854587
Ramp2	0.263	0.995	0.996	0.0018872
H2-D1	0.258	1	1	0.00083722
Rheb	0.253	0.544	0.364	0.00075918

***Table F3. The gene signature of co-opted cap I present in the early niche compared to cap I in the late niche**. Differential expression analysis was performed using the Wilcoxon-Mann-Whitney test with log fold change threshold = 0.25.*

Gene name	Average log fold change	Fraction of cap I expressing this gene in early niche	Fraction of cap I expressing this gene in late niche	The adjusted p value
Cyp1a1	2.405	0.693	0.035	2.6019E-26
Hopx	1.089	0.876	0.526	2.0819E-17
Scgb1a1	1.074	0.337	0.053	9.7595E-05
Sox18	0.975	0.612	0.061	1.7711E-19
Cyp4b1	0.934	0.981	0.895	1.2824E-18
Klf2	0.933	0.97	0.728	4.1207E-15
Fibin	0.896	0.865	0.623	2.1438E-07
mt-Nd3	0.836	0.706	0.289	5.3018E-12
mt-Nd4l	0.813	0.693	0.254	1.3501E-11
Klf4	0.785	0.852	0.518	9.6631E-11
Crip1	0.773	0.787	0.509	1.5499E-05
Tbx3	0.761	0.954	0.728	1.4329E-14
Tmem100	0.735	0.987	0.86	2.2338E-10
Id3	0.720	0.935	0.702	9.3664E-10
Map1lc3a	0.694	0.733	0.36	3.5397E-09
Fmo1	0.684	0.951	0.728	9.5822E-11
Hpgd	0.678	0.976	0.807	3.323E-08
Myl12b	0.665	0.844	0.518	6.9325E-10
Car4	0.656	0.954	0.965	4.9645E-07
Tbx2	0.642	0.879	0.623	9.6197E-07
Tspan18	0.624	0.838	0.561	4.8677E-07
Txnip	0.617	0.903	0.623	1.534E-07
Tmcc2	0.617	0.747	0.43	1.8226E-05
Hilpda	0.603	0.695	0.368	2.5789E-05
Id1	0.600	0.76	0.482	0.00031341
Pfn1	0.592	0.633	0.333	3.5482E-06
Malat1	0.590	0.995	1	3.855E-07
Gstm1	0.583	0.709	0.351	7.2735E-07
Gnb2	0.578	0.819	0.526	1.1627E-07
Foxf1	0.567	0.895	0.667	4.6922E-07
Smad6	0.565	0.582	0.237	3.0389E-06
Cdkn2b	0.563	0.472	0.175	4.3041E-05
Slc9a3r2	0.563	0.96	0.789	3.0847E-08
Gata2	0.522	0.642	0.351	0.00069014
Tspan7	0.507	0.96	0.807	1.1333E-06
Cnn3	0.505	0.644	0.377	0.00034662
Itm2b	0.505	0.997	1	4.6783E-07

Ednrb	0.484	0.927	0.825	0.00228766
Lars2	0.477	0.736	0.509	0.03773287
Rap1a	0.473	0.803	0.544	0.00108669
Srgn	0.465	0.881	0.605	0.00038074
Hmgn2	0.464	0.431	0.114	1.1154E-05
Rprml	0.455	0.45	0.184	0.00177857
Sema6a	0.454	0.806	0.474	0.00104687
Jun	0.453	1	0.939	1.6164E-06
Sftpc	0.451	0.367	0.132	0.05948826
Sept4	0.450	0.857	0.737	0.05945349
Marcks	0.448	0.836	0.632	0.13631646
Mgst3	0.447	0.569	0.272	0.00070668
Thbd	0.447	0.97	0.816	0.00429421

Table F4. The gene signature of co-opted cap II present in the early niche compared to non-tumour cap II ECs. *Differential expression analysis was performed using the Wilcoxon-Mann-Whitney test with log fold change threshold = 0.25.*

Gene name	Average log fold change	The adjusted p value	Fraction of cap II expressing this gene in early niche	Fraction of non-tumour cap II expressing this gene
Cd74	1.143	1.59569E-36	0.542	0.299
mt-Cytb	0.753	2.23313E-67	0.994	0.985
mt-Co2	0.733	1.45623E-65	0.991	0.971
mt-Nd4l	0.722	1.20623E-64	0.665	0.31
mt-Atp6	0.662	1.32357E-58	0.999	0.983
mt-Co1	0.646	2.36757E-54	0.987	0.937
mt-Nd2	0.646	1.19097E-48	0.962	0.854
mt-Nd3	0.606	4.05831E-45	0.716	0.437
mt-Co3	0.594	3.01501E-47	0.997	0.983
mt-Nd4	0.580	1.35774E-42	0.982	0.946
Malat1	0.525	2.07514E-55	1	0.999
Sftpc	0.523	1.01896E-54	0.391	0.096
Cyp1a1	0.467	2.1267E-21	0.179	0.041
Iigp1	0.445	0.000378186	0.435	0.339
Scgb1a1	0.443	1.91295E-57	0.299	0.035
mt-Nd5	0.439	4.05344E-25	0.568	0.337
Arhgap31	0.432	9.90618E-30	0.869	0.711
H2-Eb1	0.419	6.81127E-19	0.427	0.23
Gm10076	0.414	3.19093E-40	0.381	0.126
mt-Nd1	0.410	5.54598E-23	0.954	0.859
Clec2d	0.382	1.20569E-21	0.968	0.938
Gbp4	0.380	2.51944E-08	0.405	0.273
H2-Aa	0.353	2.42945E-14	0.5	0.309
Adgre5	0.346	2.50236E-17	0.944	0.871
Son	0.339	2.06188E-16	0.945	0.913
H2-K1	0.335	1.54797E-19	0.996	0.995
Sparcl1	0.312	7.13246E-06	0.395	0.281
Adgrl4	0.312	8.83272E-15	0.886	0.806
H2-Ab1	0.309	6.57607E-07	0.523	0.389
Vegfa	0.305	1.12547E-06	0.724	0.625
Tra2a	0.297	3.09318E-11	0.597	0.443
Dleu2	0.296	2.4081E-13	0.294	0.145
H2-D1	0.291	2.53748E-15	0.998	0.999
Git2	0.279	1.01765E-08	0.602	0.474
Rbpms	0.277	8.88715E-11	0.755	0.629
Trim35	0.276	5.43456E-11	0.472	0.311
Ttc14	0.273	1.9937E-11	0.537	0.371
Xdh	0.273	8.85751E-07	0.551	0.425
Trim12a	0.271	6.61861E-09	0.326	0.197
H2-T23	0.270	2.07358E-07	0.781	0.71
Clec14a	0.262	6.98422E-10	0.983	0.976
Oasl2	0.260	5.93735E-06	0.295	0.186
Gm26532	0.256	1.1428E-12	0.227	0.097
Rassf9	0.256	6.60991E-06	0.3	0.191
Gcc2	0.254	8.07158E-05	0.655	0.556
Srsf7	0.253	1.54911E-08	0.524	0.382
Ccnl2	0.250	3.77271E-14	0.38	0.209

***Table F5. The gene signature of co-opted cap II present in the early niche compared to cap II in the early distal region**. Differential expression analysis was performed using the Wilcoxon-Mann-Whitney test with log fold change threshold = 0.25.*

Gene name	Average log fold change	Fraction of cap II expressing this gene in early niche	Fraction of cap II expressing this gene in early distal	The adjusted p value
mt-Cytb	0.608	0.994	0.991	2.0465E-67
Scgb1a1	0.481	0.299	0.013	2.566E-220
mt-Atp6	0.451	0.999	0.999	4.3119E-36
Foxf1	0.406	0.775	0.62	9.1555E-39
mt-Co2	0.386	0.991	0.993	2.2934E-25
Sftpc	0.383	0.391	0.179	9.3343E-48
mt-Co1	0.371	0.987	0.983	6.9628E-22
mt-Nd4l	0.363	0.665	0.517	6.5686E-24
mt-Co3	0.340	0.997	0.993	1.4089E-18
Sox18	0.332	0.464	0.314	1.5306E-22
Cav2	0.319	0.827	0.743	5.7547E-23
Mgp	0.308	0.271	0.08	1.6703E-61
H2-D1	0.287	0.998	0.999	1.708E-22
Tmsb10	0.284	0.84	0.781	3.1146E-11
Myl12b	0.280	0.662	0.566	2.1124E-13
mt-Nd4	0.278	0.982	0.979	3.7617E-11
Klf2	0.278	0.874	0.833	1.1724E-08
Ramp2	0.265	0.993	0.997	1.2976E-12

***Table F6. The gene signature of co-opted cap II present in the early niche compared to cap II in the late niche**. Differential expression analysis was performed using the Wilcoxon-Mann-Whitney test with log fold change threshold = 0.25.*

Gene name	Average log fold change	Fraction of cap II expressing this gene in early niche	Fraction of cap II expressing this gene in late niche	The adjusted p value
mt-Nd3	1.049	0.716	0.212	1.1524E-22
mt-Nd4l	0.909	0.665	0.235	5.7773E-17
mt-Cytb	0.807	0.994	1	2.6295E-14
Sox18	0.769	0.464	0.053	1.2804E-14
Arhgap31	0.702	0.869	0.523	1.6429E-13
Malat1	0.701	1	1	5.4944E-23
mt-Co1	0.682	0.987	0.97	7.3763E-10
mt-Co2	0.664	0.991	0.985	2.6272E-09
Lars2	0.658	0.669	0.402	1.9193E-07
BC028528	0.621	0.948	0.811	1.9182E-10
Tspan7	0.587	0.979	0.902	7.337E-10
Sox11	0.584	0.453	0.189	0.00012167
Pcdh17	0.541	0.764	0.598	0.00319872
Cyp4b1	0.534	0.758	0.545	3.8198E-05
Glp1r	0.533	0.873	0.697	8.3649E-06
Adrb2	0.529	0.442	0.152	3.4868E-06
Sftpc	0.520	0.391	0.098	8.7356E-07
Kit	0.511	0.905	0.75	3.114E-05
Mcam	0.509	0.405	0.129	1.0772E-05
Luc7l2	0.508	0.726	0.447	1.1303E-05
Rbm39	0.506	0.919	0.788	2.2651E-08
Clec2d	0.494	0.968	0.902	5.4755E-06
Clec14a	0.493	0.983	0.932	9.2651E-07
Cyp1a1	0.488	0.179	0.038	0.4207273
Scgb1a1	0.472	0.299	0.023	2.6076E-07
Adgre5	0.460	0.944	0.848	0.00012114
Fmo1	0.458	0.87	0.75	4.2656E-05
Fendrr	0.455	0.679	0.455	0.0052729
Foxf1	0.450	0.775	0.583	0.00050539
Ghr	0.447	0.449	0.189	0.00053103
Ttc14	0.446	0.537	0.28	0.00208489
Hs3st1	0.437	0.377	0.129	0.00049167
H2-D1	0.428	0.998	1	5.5412E-05
Ptprk	0.421	0.522	0.242	0.00012269
Adrb1	0.418	0.604	0.402	0.03342339
Sema6a	0.415	0.579	0.356	0.03248174
Plvap	0.408	0.937	0.902	0.08978492
Nfat5	0.405	0.49	0.258	0.013431

Tap2	0.404	0.361	0.098	3.951E-05
Dll4	0.404	0.33	0.129	0.01757788
Tra2a	0.398	0.597	0.379	0.06332548
Hey1	0.397	0.397	0.182	0.02062218
Dleu2	0.385	0.294	0.098	0.0305035
Gm10076	0.385	0.381	0.129	0.00035655
Aplnr	0.384	0.414	0.159	0.00212529
Meis2	0.383	0.53	0.348	1
Cadm1	0.382	0.461	0.258	0.1333505
Irf2bp2	0.375	0.429	0.212	0.01456882
Thbd	0.371	0.923	0.871	0.72868997
Lyve1	0.367	0.741	0.667	1

Appendix G: *Gpihbp1* expression in lung capillaries and large vessels

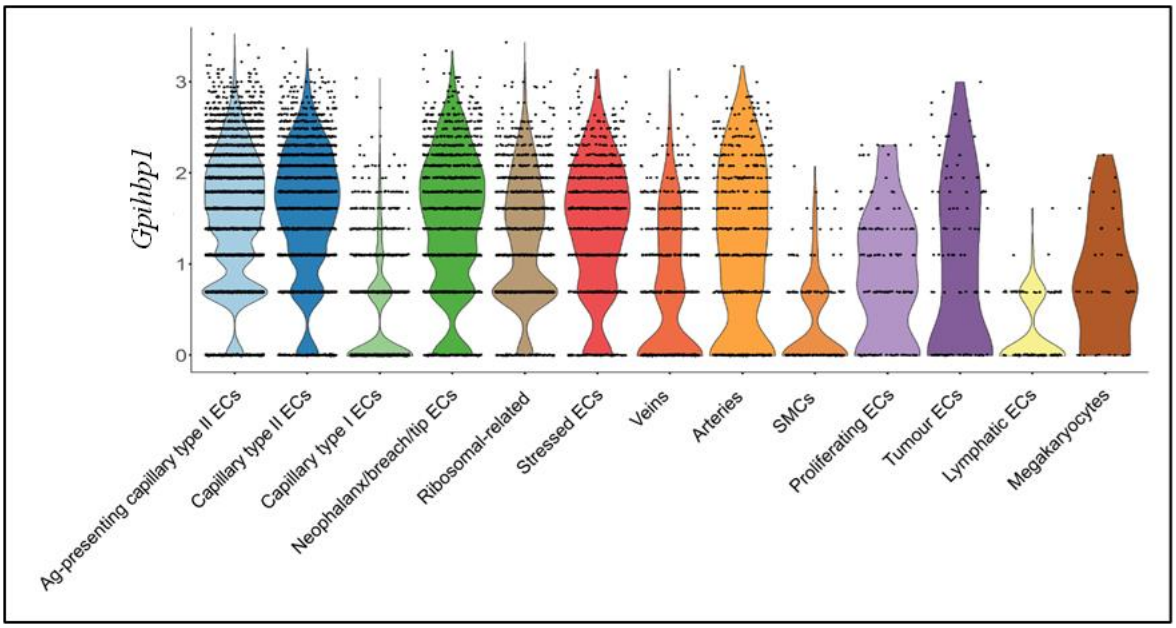

Figure G1. Violin plot depicting the expression distribution of Gpihbp1 across the subtypes of lung stromal cells, demonstrating that Gpihbp1 is expressed in large vessels (arteries and veins) but highly expressed in capillaries. *Gpihbp1: Glycosylphosphatidylinositol-anchored high-density lipoprotein–binding protein 1*

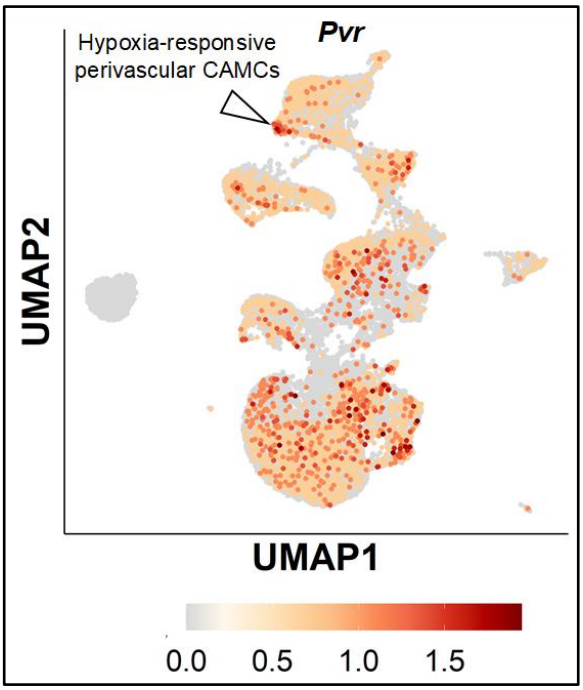

Figure G2. UMAP plot depicting the expression distribution of Pvr across the subtypes of lung stromal cells, with hypoxia-responsive perivascular CAMCs as one of the clusters that express high level of Pvr. *Pvr: poliovirus receptor.*

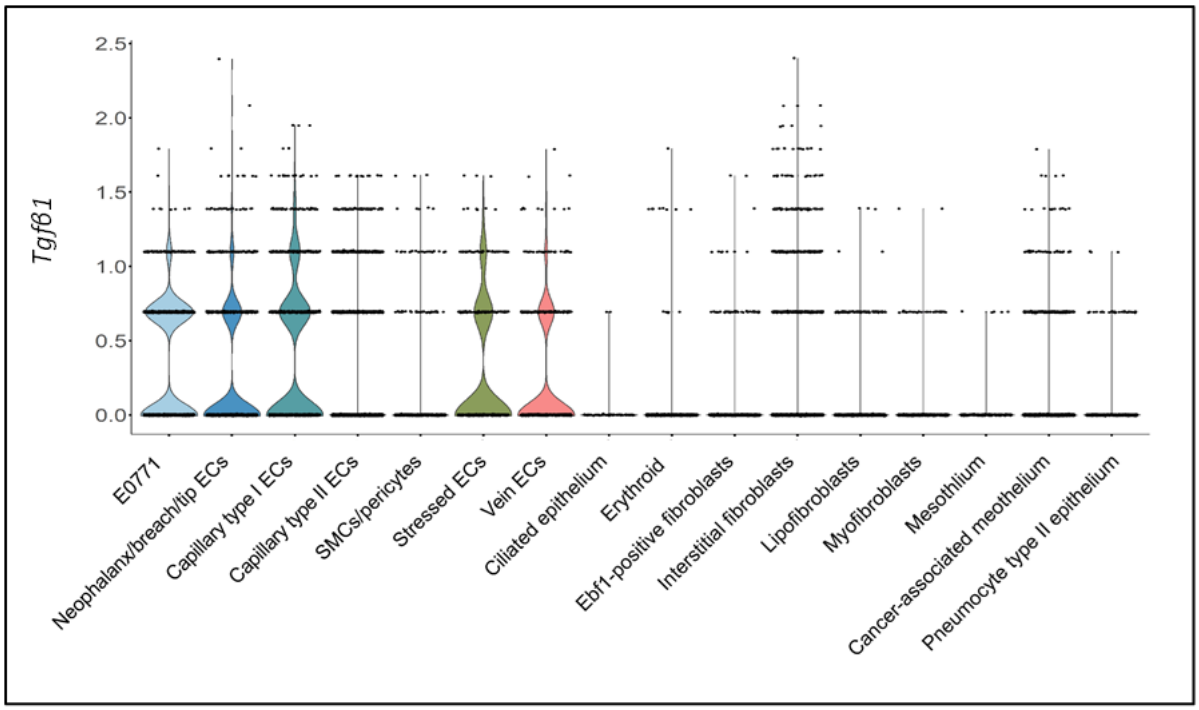

Figure G3. Violin plot depicting the expression distribution of Tgfβ1 across the subtypes of lung stromal cells in the late distal region, with E0771 tumour cells and capillary type I expressing the highest level.
Tgfβ1: transforming growth factor beta 1.